UNIVERSITÀ DI PARMA

UNIVERSITÀ DEGLI STUDI DI PARMA

DOTTORATO DI RICERCA IN
INGEGNERIA INDUSTRIALE

CICLO XXXV

FLEXURAL TENSEGRITY

Coordinatore:

Chiar.mo Prof. Gianni Royer-Carfagni

Tutore:

Chiar.mo Prof. Gianni Royer-Carfagni

Dottorando: **Claudio Boni**

Anni Accademici 2019/2020 – 2021/2022

UNIVERSITÀ DI PARMA

UNIVERSITÀ DEGLI STUDI DI PARMA

PH.D. COURSE IN
INDUSTRIAL ENGINEERING

XXXV CYCLE

FLEXURAL TENSEGRITY

Ph.D. Course Coordinator:

Cl. Prof. Gianni Royer-Carfagni

Thesis Advisor:

Cl. Prof. Gianni Royer-Carfagni

Candidate: **Claudio Boni**

ACADEMIC YEARS 2019/2020 – 2021/2022

Truth is ever to be found in simplicity, and not in the multiplicity and confusion of things.

Sir Isaac Newton

Abstract

The expression "flexural tensegrity" indicates an assembly of stiff segments held together by the tying action of prestressed tendons passing through them, in such a way that the *integrity* under *flexure* is provided by the *tensile* members (tendons). The key point is that the contact surfaces of any pair of consecutive segments are shaped according to properly-designed pitch profiles, such that a large relative rotation of the segments is allowed. As a result, the joints open up under bending, and this produces the straining of the tendons, which are free to move in properly-shaped cavities inside the segments and are anchored only to the ends of the beam (unbonded cables). The elongation of each cable, to an amount dictated by the shape of the contact surfaces, thus affects the elastic energy of the system and, hence, characterizes the constitutive bending properties of the segmental assembly, as a function of the design shape of contact profiles, as well as of the prestress and axial stiffness of the cable. A variational approach can be used to find the set of nonlinear equations that govern the response of the structural system, both in the static and dynamic equilibrium states.

The flexural-tensegrity concept can be explored in many forms. By changing the shape of the contact profiles, linear, sub-linear or super-linear constitutive responses can be obtained. As a function of the tendon stiffness, nonlinear Duffing-like vibrations are attained and can be controlled by varying the axial force in the tendon. Enhancing the mobility of the tendon in large cavities, the bending energy can be made non-convex in type, possibly achieving complex snap-through sequential motions. The limit, when the number of segments goes to infinity and their length to zero, corresponds to a particular type of Euler's elastica with nonlocal response, whose bent shape can be computed analytically (with elliptic integrals), or numerically. Field applications, yet to be fully explored, have been found in archery (a new type of deployable segmental bow) and soft robotics (limbs controlled by internal/external cables). Multi-stable flexural tensegrities can be used as basic constituents for metamaterials with tailored 3D mechanisms, in the form of plates and cubes, and for propulsion in fluids as flagellating tails. Larger scale applications in kinetic architecture, yet to be fully appreciated, can be found in the manufacturing of movable skeletons and envelopes. In the field of industrial design, the concept has been used in the manufacturing of a desk lamp, where the bent shape of the arm can be tuned by varying the tension force in the pair of prestressing cables, which also convoy electricity.

As a hint for future research, a different kinematics is finally introduced and preliminary investigated. This corresponds to the sliding of plates on initially-matching wavy contact surfaces (rather than rolling along pitch profiles), thus constituting the basis for the new concept of "shear tensegrity". The model can specifically find application in the interpretation of the mechanical behavior of nacre-like laminates.

Table of Contents

Chapter 1

Introduction

I present an innovative class of kinetic segmental structures, which has been named "flexural tensegrity" to refer to the fact that the integrity of the segmental assembly is granted by tensile members, which also give load bearing capacity to the structure and influence its constitutive response under bending.

1.1 Background: towards flexural tensegrity

The term "tensegrity" was first coined by R. B. Füller to refer to peculiar structures whose *integrity* is granted by *tensile* members [1]. In the original definition [2], here referred to as "pure tensegrities", these tensile members are represented by cables, pre-tensioned by matching a few floating compression struts. To illustrate such a design concept, Figure 1.1 reports two paradigmatic examples of pure tensegrities. In particular, Figure 1.1(a) shows the assembly of two wooden X-shaped modules connected by cables; peculiarly, the upper module is suspended and restrained by the thin cables, so that it seems to float in the air. Figure 1.1(b) displays a larger arched structure, made of aluminium and stainless steel, with straight floating bars connected by tendons. The aforementioned structures were manufactured by K. Snelson, who shares the authorship of the tensegrity concept with Füller.

Tensegrities are a paradigmatic example of "prestress stable" [4] pin-jointed structures. In fact, according to the mobility formula generally referred to as Maxwell rule [5], such structures do not have enough bars to be motionless, but potential mechanisms are stiffened by a state of self-stress induced by the prestressed cables. For example, a state of self-stress can be imparted by manufacturing some cables shorter than the prescribed distance between the connected bars, and by elastically forcing them into the design position.

The term "flexural tensegrity", appearing in the title, and often abbreviated

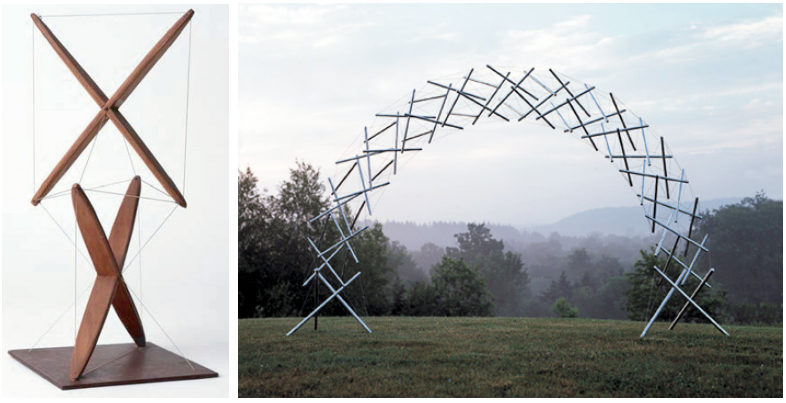

(a) (b)

Figure 1.1. Examples of pure tensegrity structures. (a) Wooden X-column by K. Snelson (1948), from [3]. (b) Rainbow arch by K. Snelson (2001), made of aluminium and stainless steel, from www.kennethsnelson.net.

as "flex-ten" in the following, is here used to represent a complementary concept, according to which the *integrity* under *flexure* of a mobile chain of coupled segments is ensured by *tensioned* tendons. More in detail, such an assembly is formed by stiff segments held together by the tying action of a prestressed tendon passing through them, so that the integrity and load bearing capacity is provided under flexure. The key point is that the contact surfaces of any pair of consecutive segments are shaped according to properly-designed pitch profiles, such that a finite-scale relative rotation of the segments is allowed and the joints macroscopically open up under service loads.

Because of their peculiar design, classical tensegrities are suitable to realize collapsible/deployable structures [6], also accounting for structural optimization [7] and form-finding [8]. Here, similar arguments hold: flexural tensegrities can be folded/deployed by slackening/pulling the cables, while the shape of the contact surfaces can be designed according to the specific need, to obtain a peculiar, possibly optimized, constitutive response.

The proposed system, especially when declined as one-dimensional chains of segments, recalls the segmental construction of beam-like structures with unbonded post-tensioned cables and prefabricated concrete ashlars, typically used to realize columns [9], arches [10] and bridges [11, 12]. The similarity is that the structure is assembled from segments, which are kept into contact by tendons encapsulated in ducts within the segments. These cables are tensioned (stressed) by pulling them through the anchorages while pressing against the end segments, so that the forces required to tension the tendons result in a significant permanent compression of the segments once the tendon is locked-off at the anchorage. On the other hand,

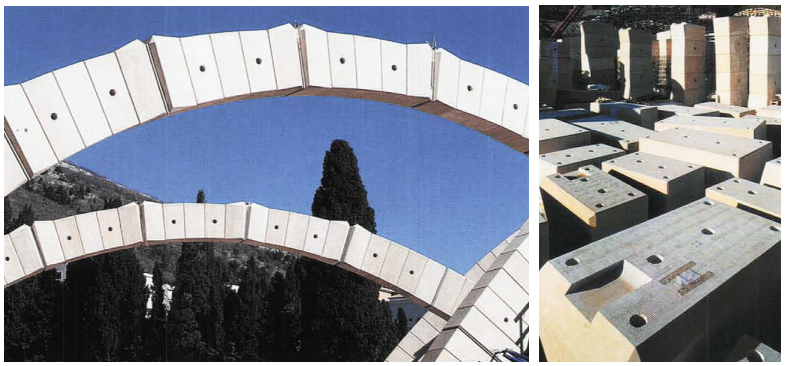

(a) (b)

Figure 1.2. Structural arches in Padre Pio Pilgrimage Church (San Giovanni Rotondo, FG, Italy), made with post-tensioned prefabricated-concrete ashlars: (a) segmental arches before the construction of the supported roof, and (b) disassembled segments before the erection of the arches, with evidence of the flat contact surface. Photographs from [10].

unbonded post-tensioning means that the tendons have freedom of longitudinal movement inside the prefabricated segments, thanks to the lubrication within the sheaths that house the cables.

Anyway, there is a substantial difference with prestressed reinforced concrete segmental beams. Indeed, the concrete segments are in reciprocal contact along approximately flat surfaces, and the joints are designed to remain tight (no opening) at least in the serviceability limit state. To explain, consider Figures 1.2 and 1.3, where representative examples are reported. More in detail, Figure 1.2(a) shows the segmental concrete arches erected for the Padre Pio Pilgrimage Church (San Giovanni Rotondo, FG, Italy), designed by R. Piano. The arches are portrayed before the construction of the supported roof and the planar contact surfaces are highlighted by the straight lines that visually tessellate the arch; these are also evidenced in Figure 1.2(b), which represents the disassembled ashlars lying on the ground before the erection. Figure 1.3(a) displays a segmental concrete bridge under construction: here the average mid plane for the contact is still planar, but the actual contact surfaces are undulated, by means of shear keys, and match each other to enhance interlocking. A detail view of the segment is reported in Figure 1.3(b). In both cases, the opening or the sliding of the joints is not expected under service loads, and the action of cables is basically that of generating a compression state in the segments so to avoid the onset of tensile stresses, under bending, in the no-tension-resistant concrete, and in order to increase the shear resistance by friction at the contact interfaces. Under loading the deformation is mainly due to the concrete matrix and the prestressed cables are not substantially further stretched. As a result the constitutive response is led by the concrete, and mini-

(a) (b)

Figure 1.3. Segmental bridge made with post-tensioned prefabricated-concrete segments: (a) bridge under construction, photograph from [13]; (b) detail of one segment with evidence of the flat contact surface with shear keys, photograph from [14].

mally influenced by the tendons. On the contrary, in the ultimate limit state (close to collapse), the joints can open and the cables are designed to yield, thus increasing the ductility of the structure before the total breakage. This means that, in traditional (concrete) segmental beams, the tendons do influence the structural behavior in the ultimate limit state, in terms of strength and ductility, while keeping the compressed segments together, but do not significantly affect the constitutive response in the serviceability limit state.

The case of flexural tensegrities is different and somehow complementary. Here, the opening of the joints is expected and tailor-designed to produce a specific straining of the tendons. The scope of post-tensioning is not that of inducing a permanent compression in a quasi-brittle material like concrete, but rather that of providing a relevant contribution to the elastic strain energy for a *prestress-stable* hinge-jointed structure, whose bending stiffness can be tuned according to the specific application. Then, the function of the cable is upgraded, and passes from that of a mere reinforcement element to that of a constitutive element.

The opening of the joints is obtained through a tailor-shaping of the contact surfaces according to curved profiles, so that any pair of consecutive segments, supposed rigid at least as a first-order approximation, can roll one another along design pitch lines. In particular, as a main deformation mode, a pure rolling motion along these pitch lines is assumed, and the desired kinematics is obtained with coupled conjugate profiles. A demonstrative example of such a structural system is provided in Figure 1.4. In particular, the straight and bent configurations of a 3D-printed cantilever are shown in Figure 1.4(a), where the segments are open to visualize the passing-through tendon (black cable). The magnification of Figure

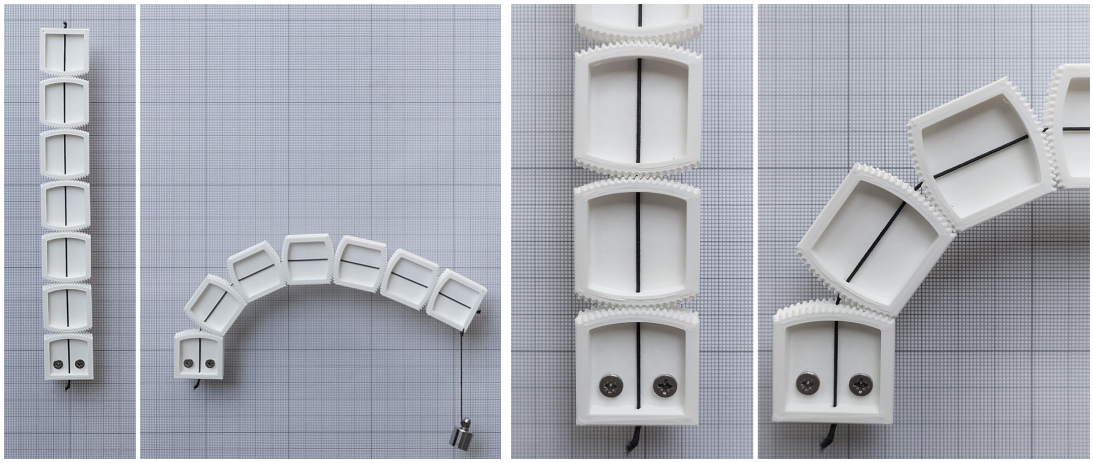

(a) (b)

Figure 1.4. Flexural-tensegrity cantilever: (a) reference straight configuration and bending deformation under a hanging weight; (b) detail of the contacts in the straight and rotated states, with evidence of the elongation of the tendon due to the opening of the joints. Millimeter grid paper on the background for dimensional reference.

1.4(b) evidences the part of the tendon that remains exposed when the joint opens up, and the segments roll one another along circular pitch lines. The elongation of the cable, to an amount dictated by the shape of the contact surfaces, thus affects the elastic energy of the system and, hence, characterizes the constitutive bending properties, as a function of the design shape of contact profiles.

Since a relative rotation of any two segments results in a localized elongation of the prestressing cable, the resulting internal constraint at the contact sections is similar to a *spring hinge* between the coupled segments. As the cable is unbonded in frictionless cavities and it passes through *all* the segments, these spring hinges result to be interconnected and the response of the assembly turns out to be *nonlocal* in type. By varying the design shape of the pitch lines, the initial tensile force in the tendon and its axial stiffness, and the type of allowed mobility of the cable inside the segments (from axial stretching only, to increased lateral degrees of freedom), it is possible to *functionally grade* the stiffness, and to obtain, at least in principle, any type of nonlinear, possibly non-monotone, moment vs. rotation constitutive relation at the joints, according to the requirement in service. In addition, an active tensioning device could automatically pull or release the cable, so to change the compliance of the system and reach diverse equilibrium configurations under the same applied loads, or control the vibrations.

As the system consists of segments that are strung by a cable, it is possible to fold and package them when the cable is slack (Figure 1.5), while their deployment

Figure 1.5. Packaging of a flex-ten assembly: beam in the deployed straight state, disassembled beam (segments, cable and clamps to anchor the cable) and components packed in a prismatic box for transportation.

is obtained by simply pulling the cable at one extremity, pressing against one end segment. All these properties make the system particularly suitable to manufacture (foldable) soft arms [15], especially for biomedical [16], robotics [17] and aerospace [18] applications.

1.2 Objectives

As a global objective, the kinematics and the static/dynamic response of innovative segmental assemblies, within the class of flexural tensegrity, will be investigated under multiple loading scenarios and for different design shapes of the contact profiles. More specifically, the principal scopes of such research can be listed as follows.

- Definition of the pure rolling kinematics for the contact joint and design of the corresponding constructive details, with specific reference to a possible manufacturing via 3D printing, CNC milling or casting in molds.
- Definition of the law that relates the opening of the joints to the elongation of the cable, once the shape of pitch profiles is given, or, alternatively, finding the shape of contact profiles for a target law of the cable elongation (as a function of the rotation at the joint).
- Enhancing the mobility of the cable inside the segments, to attain complex non-monotone constitutive relations for the joint, with the possibility to obtain structures able to harness elastic energy and suddenly release it, by

means of sequential snap-through instabilities, as a consequence of localized perturbations.

- Modeling the segmental assembly as a whole, for any given constitutive response of the contact joints, within a variational approach in order to find the set of nonlinear equations that govern the response of the structural system, both in the static and in the dynamic equilibrium states.
- Investigation of the continuum limit of the segmental assembly, with specific reference to beam-like segmental structures, and comparison with the model of Euler's elastica under large deflections.
- Extension of the structural concept from the one-dimensional beam to the cases of two-dimensional plates and three-dimensional assemblies, with a specific design for the contact joint that allows a full 3D mobility.
- Validation of theoretical models and analytical findings, as well as testing the manufacturing feasibility of the joint geometry, with experiments on 3D-printed or laser-cut prototypes, tested under static and dynamic conditions.
- Study on the possible field applications of the flexural-tensegrity concept, ranging from archery, to robotics, from marine propulsion with bio-inspired beating tails to the broad field of kinetic architecture and industrial design.
- Further hints for future research are found in the different kinematics of sliding plates on wavy surfaces (rather than rolling along pitch profiles), which can find application in the interpretation of the mechanical behavior of nacre-like laminates.

1.3 Outline

This work is divided into twelve chapters. In addition to the present introductory Chapter 1, the subject is exposed according to the following order.

Chapter 2 – The basic concept of flexural tensegrity

The concept of flexural tensegrity is presented, with specific reference to the case of cable-stiffened segmental beams. A way to manufacture a contact joint, such that consecutive segments move according to pure rolling along design pitch profiles, is proposed. The static equilibrium equations for the assembly under external loads are derived through a variational approach. Prototypes with different geometries for the pitch profiles are finally built via 3D printing, and tested to validate the theoretical model.

Chapter 3 – The continuum approximation

The continuum limit of flex-ten segmental beams is analyzed. This corresponds to the case in which the number of segments increases to infinity and their length decreases to zero. The model represents a peculiar elastica with nonlocal bending stiffness and hardening behavior under loading. Classical semi-analytical solutions, via elliptic integrals, that describe the bent shape of the thin lamina first analyzed by Euler, also apply to the nonlocal elastica here derived from flexural tensegrity. Such solutions are also compared with numerical results and with a simplified model that relies on a shape function. Examples are provided for axial buckling and bending under concentrated and distributed loads.

Chapter 4 – Dynamic aspects

The dynamic problem for flex-ten beams is analyzed, and the corresponding nonlinear governing equations are obtained thanks to Hamilton's principle. Experiments on simple cantilevers suggest how to model the possible sources of dissipation, by means of viscous damping and additional frictional moments. In the continuum limit, a simplified model is derived, based on the deflection of the beam described via shape function. This leads to a peculiar Duffing-like oscillator, whose vibrations can be excited/controlled by varying the cable stiffness and prestress.

Chapter 5 – Multi-stable flex-ten beams

An improved mobility of the cable in hourglass-shaped cavities inside the segments, rather than in tubular sheaths, allows for a multi-stable behavior of the contact joints. The response under bending of multi-stable flex-ten beams is theoretically analyzed, both in a hard and soft device (prescribed rotation angles or loads at the extremities of the beam, respectively), and analytical findings are corroborated by experiments on 3D-printed prototypes.

Chapter 6 – A snapping flex-ten cantilever

A further increased mobility of the cable within larger cavities inside the segments is the basis for the design of a snapping cantilever beam, that behaves like a flagellating tail. The sequential snapping of the joints causes the beam to reverse its shape, as a consequence of the rotation of just one driving segment. The dynamic equilibrium equations are obtained, and then used to describe the motion of prototypes whose snapping was recorded with a high-speed camera.

Chapter 7 – Two- and three-dimensional extensions

The extension from beam-like chains of segments to two- and three-dimensional assemblies is introduced. A specific joint that allows 3D relative motions between

the coupled segments is proposed. The requirement of a pure rolling contact can limit the allowed mobility of the segments when more than two segments are in reciprocal contact. Hence, a kinematic analysis is performed to find admissible mechanisms, and 3D-printed prototypes are tested to check the new design.

Chapter 8 – Application 1: a flex-ten bow

As a first field application, flex-ten beams are used to manufacture the limbs of a new type of bow. The bow is a case-study that involves the elastic return of the limbs coupled with the inertial effects due to their mass and to the accelerated arrow, thus representing a good benchmark problem to test the developed theoretical approach, by comparing results with experiments. Moreover, the possibility of tailor-shaping the pitch profiles, which represent the design variables for flex-tens, together with the cable stiffness and prestress, can be fully exploited to achieve such a bending response that meets the archer's needs and optimizes the firing performance. The design variables are theoretically investigated, and two bows, characterized by different shapes for the pitch profiles are finally built and tested.

Chapter 9 – Application 2: propulsion in fluids

The possibility of using the snapping cantilever beam, previously introduced, as a marine bio-inspired propeller is tested. The investigation is carried out only experimentally, since fluid-structure interaction is a challenging problem to tackle predictively because of the non-trivial coupling of elastic, inertial, and fluid forces, which specifically depend on time, geometry, and the physical properties of both fluid and structure. Thrust measurements on statically mounted tails are reported, as well as a proof-of-concept toy boat propelled by the snapping tail.

Chapter 10 – Other potential applications

Further applications of flex-ten structures are discussed. In particular, the envisaged fields of applications range from kinetic architecture, to soft robotics, to industrial design. More specifically, kinetic structures to support envelopes for shielding and water collection are proposed, cable-actuated robotic limbs are presented, and a desk lamp with a flex-ten tunable arm is designed and prototyped.

Chapter 11 – From rolling to sliding: introduction to shear tensegrity

A different type of kinematics is introduced. This corresponds to the sliding of initially-matching plates along wavy surfaces, rather than the case of pure rolling along pitch profiles, investigated so far. The segmental assembly is declined as a laminar brickwork, which is named "shear tensegrity" to refer to the sliding, in contrast to "flexural tensegrities", whose segments are rotated under bending.

Here, each lamella of the brickwork can relative slide with respect to the adjacent ones. As a result, the straining is due to the elasticity of the material and to the opening of gaps at the interfaces between consecutive lamellae. The response of the laminate is analyzed within structured deformation theory; it strongly depends on the shape of the contact profiles, as it happens for the complementary case of flextens under bending. The model, which deserves a specific research in the future, is suitable to interpret the complex structural behavior of nacre and nacre-inspired materials.

Chapter 12 – Final remarks

The results of the previous analyses are summarized and the main findings are highlighted. Possible future developments for the proposed structural concept are suggested, while open problems and hints for further research are discussed.

Chapter 2

The basic concept of flexural tensegrity

The flexural-tensegrity concept is here presented, theoretically analyzed and experimentally verified for the paradigmatic case of a simply supported segmental beam under different external loads.

A row of rigid voussoirs joined by a passing-through pre-tensioned cable was proposed at an embryonic level in [19], with the aim of obtaining a foldable *elastica* for architectural applications. However, that analysis was limited to the case of circular pitch lines, the theoretical modeling was for the linearized case only (small rotations) and relied upon strong simplifying hypotheses, no specific design of the joints to achieve the desired coupling along the pitch lines was considered, and the results were not corroborated by experiments. All these pending points are here analyzed in detail, and it is shown that the response of the beam is generally nonlocal in type, because the second-order elongation of the cable, under large deflections, depends upon the rotations of *all* the segments. On the other hand the response of each joint can be nonlinear in type, depending on the shape of the pitch lines.

In Section 2.1, the starting point is the definition of the spring contact hinges, appropriately designing the pitch lines and the corresponding internal constraint to realize a pure rolling motion along them, so to impart the desired nonlinear stiffness to the joint as a function of the tensile force and axial stiffness of the cable. The theoretical analysis of the discrete assembly correlates the bending stiffness with the geometry of the segments and the mechanical properties of the tendons. Section 2.2 is dedicated to the experimental verification. Prototypes of the system have been constructed with a 3D printer in order to obtain three different-in-type moment vs. rotation constitutive relations at the spring hinges: linear, super-linear and sub-linear. The physical models, tested under various static loads, show an excellent agreement with the theoretical predictions.

A selection of the main results here discussed can be found in [20].

2.1 The segmental beam

The simplest structural model for a flex-ten beam is that of a chain of rigid bodies (segments) connected by spring hinges. The model problem corresponds to a simply supported beam of the type indicated in Figure 2.1(a), composed of n longitudinal rigid segments of length ℓ_i, with $i = 1 \dots n$ and $\sum_{i=1}^{n} \ell_i = L$. Segments i and $i+1$, for $i = 1 \dots n-1$, are coupled together at the node i through a hinge fitted with a *nonlinear* rotational spring. On the other hand, node 0 of segment 1 and node n of segment n are constrained by a hinge and a roller, respectively. Introduce the reference system (x, y) as represented in Figure 2.1(b). The beam is loaded by a plane system of *vertical* forces, whose effect is assigned by the resultant P_i of all the forces acting on the segment i, considered positive in the direction of increasing y. This force is applied at a distance b_i from node i, as indicated in Figure 2.1(a). The deformation of the beam, represented in Figure 2.1(b), is completely described by the displacement components (u_i, v_i) of node i, for $i = 0, \dots, n$, considered positive in the same direction of the axes (x, y).

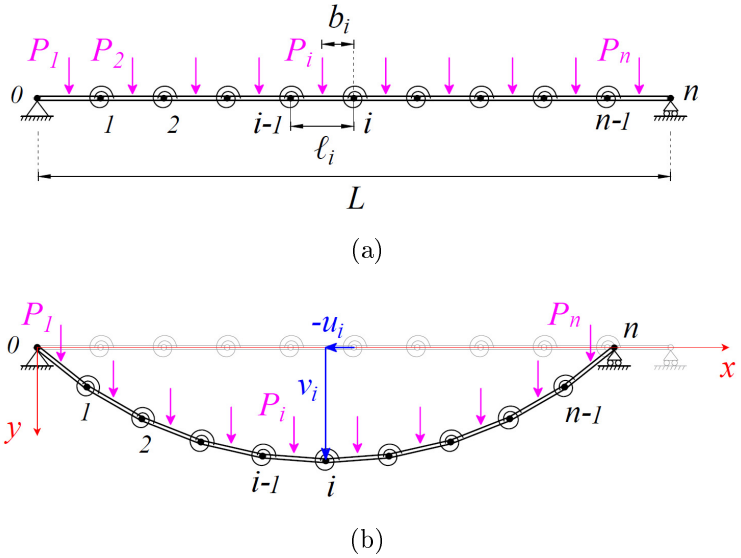

Figure 2.1. Scheme of a simply supported segmental beam with spring-hinged joints, in (a) the reference and (b) the deformed state.

The flexural-tensegrity concept will allow to tailor design the constitutive moment vs. rotation relationship of each spring hinge. The forthcoming analysis considers the case of a simply supported beam, but the results can be readily extended to constraints of more general type.

2.1.1 The contact joint

The construction of the spring hinges is the main aspect in the design of flex-tens. The constituent segments are pierced in the direction of the beam axis, housing a sheath through which an *elastic* cable can slide, approximately with *negligible friction*. When the cable is tensioned and later anchored at the end segments, the various parts are brought into contact, likewise in a prestressed precast-concrete segmental bridge. In our case, the contact surfaces of the segments are appropriately shaped so that, under bending, the adjacent segments can relatively move one another, as if they were in *pure rolling contact*, with *no sliding*, along the design *pitch lines*, as schematically represented in Figure 2.2(a).

At least as a first-order approximation, one can overlook the curvature of the fittings at the end points of the sheaths in each segment, which are certainly necessary to limit the contact stresses between the cable and the material, and consider that the diameter of the sheath is much smaller than the length of the segment. This means that in the deformed configuration the cable follows a polyline, defined by the actual placement of the end points of the sheath of each segment. The kinematics is completely described by the rolling contact along the design pitch lines. Therefore, at each joint i the cable elongates of the quantity Λ_i , represented in Figure 2.2(a), which depends only upon the relative rotation of the adjacent segments, once the shape of the pitch lines is given. The tensile force N in the cable correspondingly varies, but since sliding within the sheath is supposed to be frictionless, it remains homogenous along its length.

The bending response of the beam depends upon the shape of the pitch lines for segments i and $i+1$, since this affects the value of the cable elongation Λ_i and, consequently, its stored elastic energy. Following the general method for determining the forces and moments acting across any section of a slender member, imagine a hypothetical cut or section across the member. In this case, it is convenient to consider a section that passes through the surfaces in contact without trimming the segments, but cuts the cable in a point of the portion of length Λ_i , which remains exposed after the relative rotation of the segments. As represented in Figure 2.2(b), the mutual actions across such a section are the tensile force N in the cable, directed according to the line joining its exit points from the segments, and the resultant of the contact forces, which is a concentrated force R_i applied on a point of each segment that corresponds to the *pitch point*. Referring to the classical theory of beams, such internal forces can be resolved into the shear component V_i and the moment component M_i, which are represented in Figure 2.2(c). Indeed, V_i is the unbalanced resultant of N and R_i in the vertical direction, while $M_i = a_i\, N$, where the lever arm a_i is the distance between the pitch point and line of application of N, which depends only upon the relative rotation of the segments once the pitch lines have been assigned.

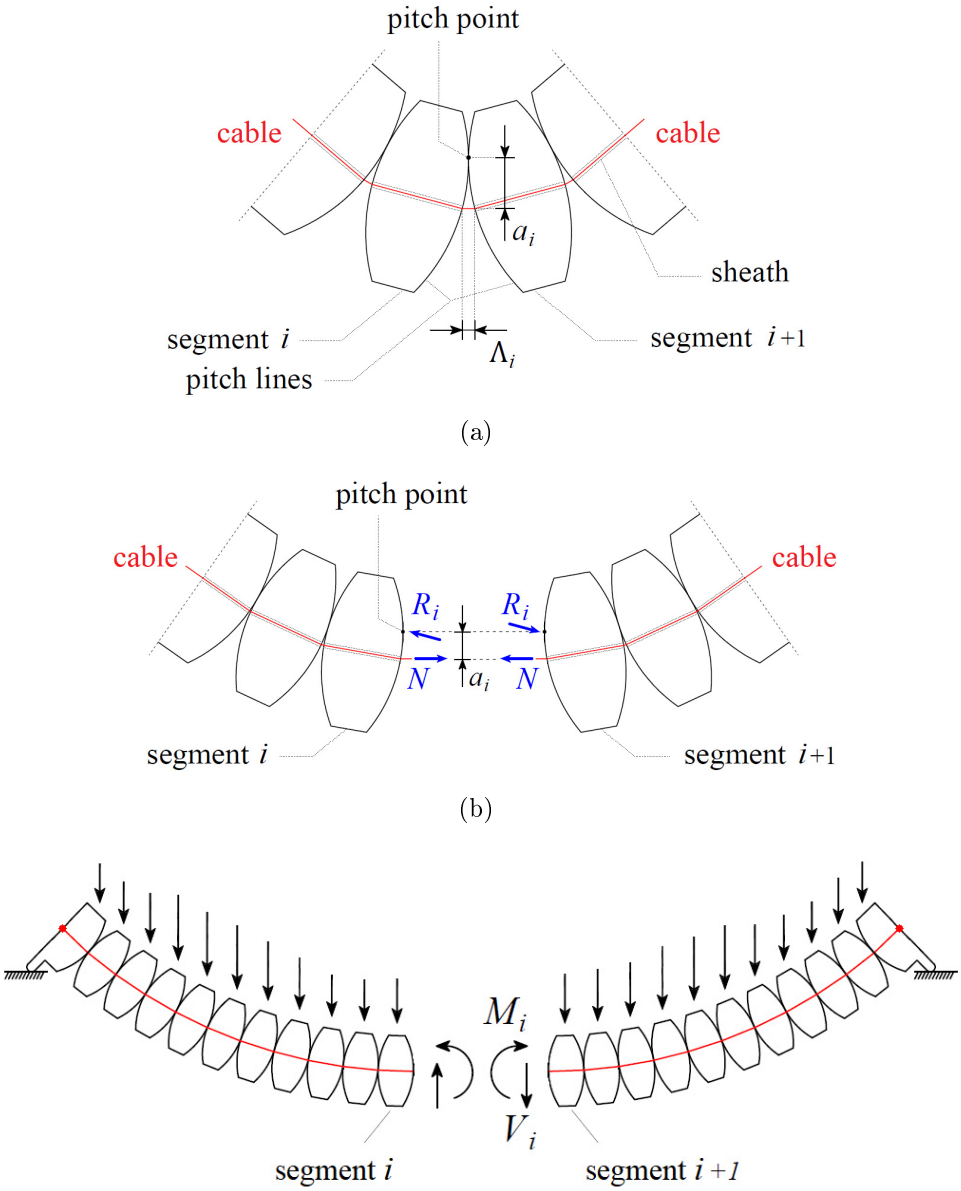

Figure 2.2. Configuration consequent to the relative rotation of the segments. (a) Cable elongation Λ_i at the $i-$th joint and lever arm a_i of the tensile force N with respect to the pitch point. (b) Schematics of the forces acting across a hypothetical section that cuts the cable and separates the segments i and $i+1$. These can be resolved (c) into the vertical shear V_i and the bending moment M_i for the bent segmental beam.

Observe that, in general, R_i is *not* parallel to N and it is *not* directed along the normal to the pitch lines, in order to fulfill the requisite of pure rolling contact with no sliding. To explain, consider the example given by a couple of toothed wheels, whose reciprocal motion is equivalent to the pure rolling along circular pitch lines. The resultant of the contact forces between the *lubricated* teeth, is equipollent to a concentrated force applied to the (ideal) contact point on the pitch lines, but it is never directed towards the center of the circles, otherwise no couple could be transferred through the mechanism.

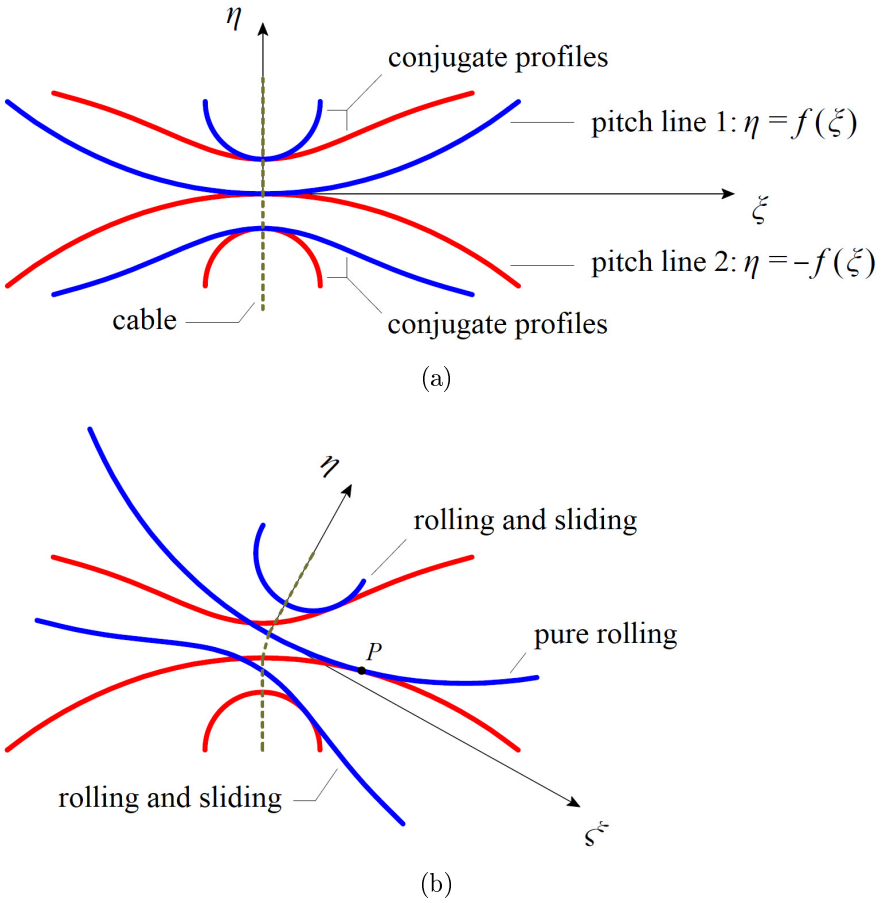

Figure 2.3. Schematics of the pitch lines with the double couple of conjugate profiles at the contact hinge. (a) Undistorted reference configuration; (b) actual configuration and actual pitch point P after the relative rotation of the segments.

If one simply designed the contact surfaces with the same shape of the pitch lines, frictional forces would be necessary to achieve the desired pure rolling motion, which may not be compatible with the friction coefficient of the material. Therefore, the desired kinematics is achieved by using the geometrical interlocking

provided by *conjugate profiles*, associated with the design pitch lines. Figure 2.3 represents a solution with just a double couple of smooth conjugate profiles. In particular, Figure 2.3(a) schematically represents, either in blue or in red color, the pitch line corresponding to one of the two segments in contact, and with the same color the profiles on the same beam segment that are conjugate with their counterparts on the other segment. In general, friction along the conjugated profiles is a parasitic action, to be limited by lubrication or non-stick interlayers like polytetrafluoroethylene; hence, the contact along the conjugate profiles is supposed to be frictionless, with the contact forces directed along the common normal to the profiles at the contact points. When the segments undergo a relative rotation, as represented in Figure 2.3(b), there is a unique configuration that fulfills the contact between both couples of conjugate profiles, and this corresponds to the configuration associated with the pure rolling motion along the pitch lines. The resultant of the contact forces on the conjugate profiles is equipollent to R_i, applied at the pitch point.

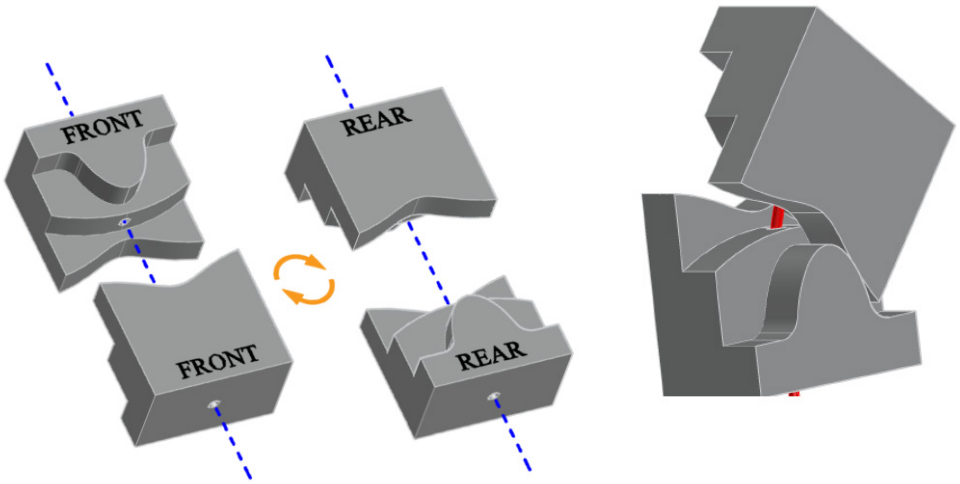

Figure 2.4. Three dimensional drawing of the smooth contact surfaces. (a) Exploded view of the joint evidencing the conjugate profiles and the pitch lines in two adjacent segments (blue dashed line indicates the cable axis); (b) the actual configuration of the joint, with the exposed portion of cable (in red), after a relative rotation of the segments.

Figure 2.4(a) shows a 3D drawing of one of the possible ways in which a joint achieving such a kinematics could be operatively constructed. Each segment is composed of three layers: the two external ones correspond to the two couples of conjugate profiles, whereas the central layer reproduces the pitch line. Strictly

speaking, the central layer is not necessary because the kinematics is achieved by using the conjugate profiles only. However, it is maintained in this design because, on the one hand, it hosts the cable and guides its deformed configuration; on the other hand, it helps to illustrate the concept from an experimental point of view. In any case, because of the presence of the conjugate profiles, the friction along the pitch lines is inessential for the desired kinematics. The contact configuration in the deformed state is represented in Figure 2.4(b). Here, one can see, evidenced with red color, the portion of cable that becomes exposed as a consequence of the rotation, which corresponds to the elongation Λ_i just indicated in Figure 2.2(a).

Note that the manufacturing can be conveniently carried out with a 3D printer (Figure 2.5(a)), through a deposition method [21], because each layer rests on the previous one. On the other hand, this design is also suitable for CNC milling (Figure 2.5(b)), with ordinary three-axis machinery, and for casting in simply-carved molds (Figure 2.5(c)).

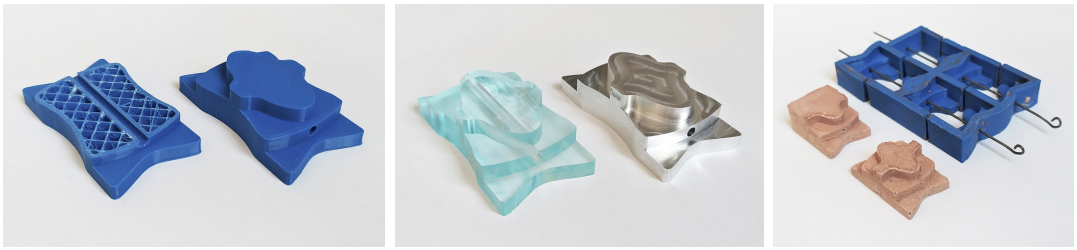

(a) (b) (c)

Figure 2.5. Different ways to manufacture the segments: (a) 3D printing with a plastic filament; (b) CNC milling from solid acrylic or aluminium; (c) casting in molds.

There are many ways to determine the conjugate profiles that achieve a rolling motion along the assigned pitch lines, and the solution is not unique. Here, a graphical method has been adopted, which is sometimes referred to as the *method of normals* [22]. This method is directly based upon the definition: since conjugate profiles are profiles in contact to each other during motion, the normal line to their contact point passes, at each time, through the corresponding pitch point of the primitive profiles [23]. Once one of the two profiles is given, the conjugate one can be drawn point to point, through the graphical construction represented in Figure 2.6. Here, r and ρ are the pitch lines, with initial pitch point P_0. Given the profile t, with initial contact point M_0, its conjugate τ is found by considering that any pair of points P' and P'', equidistant from P_0 along r and ρ, shall correspond to the contact points M' and M'' that are their normal projection on t and τ, respectively, so that the distances between P' and M' and between P'' and M'' are equal, and the angle between $P'M'$ and the normal to the pitch line r in P' is

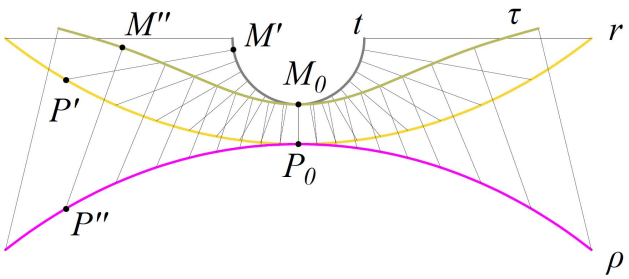

Figure 2.6. Graphical construction of the conjugate profiles: r and ρ are the pitch lines, t and τ the corresponding conjugate profiles.

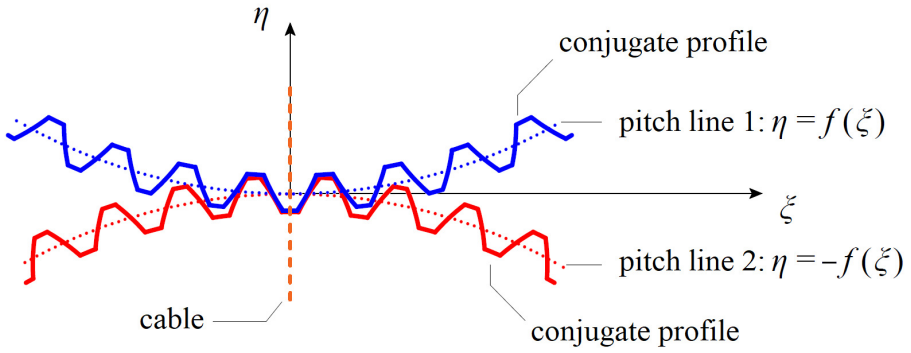

(a)

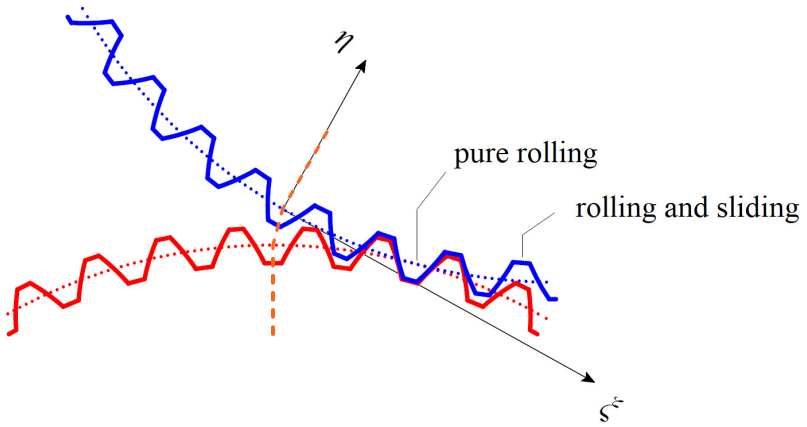

(b)

Figure 2.7. Schematics of the pitch lines with conjugate toothed profiles at the contact hinge. (a) Undistorted reference configuration; (b) actual configuration after the relative rotation of the segments.

equal to the angle between $P''M''$ and the normal to the pitch line ρ in P'' [22].

Once the pitch lines have been decided, the major difficulty consists in selecting the first one of the two conjugate profiles (the second one is uniquely determined from the first one), in such a way that kinematic interference is avoided and the contact stress remains within allowable limits. The construction shall be repeated in order to find the second couple of conjugate profiles. In the following we will limit to the case in which the pitch lines are symmetric with respect to both the tangent and the normal axes at their initial pitch point P_0. In this condition, the second couple of conjugate profiles can be obtained by mirroring the first couple with respect to the tangent axis of symmetry (Figure 2.3). In this case, all the segments composing the beam, except at most the end ones, are identical: the assembly is done by simply rotating half the segments of 180° about their longitudinal axis, so to bring the conjugate profiles in contact, as indicated in Figure 2.4(a).

Another possibility is to shape the contact profiles as toothed surfaces, designed according to standard methods for spur gears [24, 25]. Figure 2.7, which is the counterpart of Figure 2.3, schematically represents this second solution. The dotted line, either in blue or in red color, defines the pitch line corresponding to one of the two segments in contact, and the solid line with the same color describes the toothed profile on the same beam segment that is conjugate with its counterparts on the opposite segment. Figure 2.8(a) reports an exploded view of the joint, where the central layer reproducing the pitch lines is maintained, as before, to

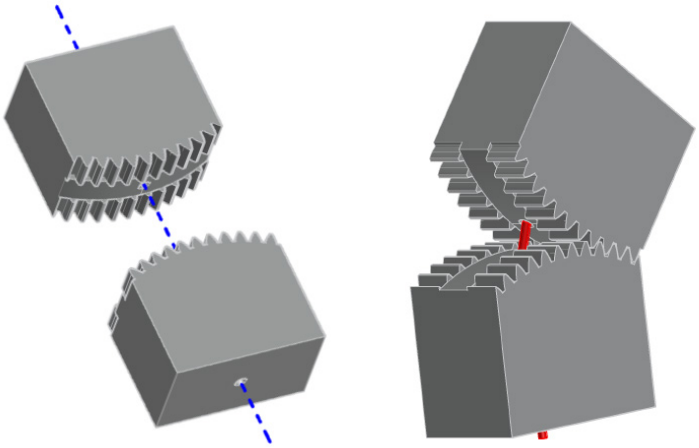

(a) (b)

Figure 2.8. Three dimensional drawing of the toothed contact surfaces. (a) Exploded view of the joint evidencing the toothed profiles and the pitch lines in two adjacent segments (blue dashed line indicates the cable axis); (b) the actual configuration of the joint, with the exposed portion of cable (in red), after a relative rotation of the segments.

guide the deformation of the cable; the assembled joint in a rotated configuration is represented in Figure 2.4(b).

The second design with toothed profiles (Figure 2.7) is well suited for classical circular pitch lines, the ones usually employed in gear transmissions; this also corresponds to a case in which the contact profiles can be easily machined. On the contrary, the first construction with a double couple of smooth conjugate profiles (Figure 2.3) is much more general and should be preferred for pitch lines whose shape differs from the simple geometry of the arc of circle/ellipse.

2.1.2 Constitutive equations

With reference to Figure 2.2(a), observe that, when a relative rotation occurs between the two consecutive segments i and $i+1$ at the $i-$th contact joint, the cable is constrained to vary its length of Λ_i. As the tendon is supposed to be unbonded, this quantity can be accommodated by the whole cable length. Denoting with K the equivalent axial stiffness of the tendon[1], the consequent increment of tensile force is $K\Lambda_i$. Globally, as a consequence of the bending of the whole beam composed of n segments, the variation of length of the tendon due to the rotation of the $n-1$ contact hinges reads $\Lambda = \sum_{i=1}^{n-1} \Lambda_i$ and its axial force passes from the initial prestressing value N_0 to $N = N_0 + K\Lambda$.

The static state at the $i-$th contact joint is also defined by the distance a_i from the pitch point to the line identified by the portion of the cable that becomes exposed after the relative rotation of the segments, also indicated in Figure 2.2(a). This represents the internal lever arm of the tensile force N, i.e., the contact joint is a spring hinge transmitting the bending moment $M_i = a_i N$.

Remarkably, the quantities Λ_i and a_i, for any given shape of the pitch lines, are correlated by pure kinematics. In particular, if $\Delta\varphi_i$ denotes the relative rotation between the consecutive segments i and $i+1$, one finds

$$a_i(\Delta\varphi_i) = \frac{\mathrm{d}}{\mathrm{d}\Delta\varphi_i}\Lambda_i(\Delta\varphi_i)\,. \tag{2.1.1}$$

To prove this relation, let $R = R(\Delta\varphi_i)$ denote the radius of curvature of the pitch line at the pitch point. Consider an infinitesimal incremental relative rotation $\mathrm{d}\Delta\varphi_i$ in a neighborhood of the rotated configuration $\Delta\varphi_i$ of Figure 2.2(a). Since the pure rolling motion is an infinitesimal rotation about the pitch point, but the pitch point moves as well, one can write

[1] If E, A and L_0 represent the Young's modulus, the cross sectional area and the undistorted length of the cable, respectively, one has that $K = EA/L_0$, with $L_0 < L$, being L the total length of the segmental beam. However, if an additional spring is added in series with the cable at the anchor point, the effective stiffness varies accordingly.

$$\mathrm{d}a_i = -\frac{\Lambda_i}{2}\frac{\mathrm{d}\Delta\varphi_i}{2} + R\frac{\mathrm{d}\Delta\varphi_i}{2}\,, \tag{2.1.2a}$$

$$\frac{\mathrm{d}\Lambda_i}{2} = a_i\frac{\mathrm{d}\Delta\varphi_i}{2}\,. \tag{2.1.2b}$$

Clearly, equation (2.1.1) comes from (2.1.2b). Moreover, using (2.1.2b) in (2.1.2a) one obtains

$$\frac{\mathrm{d}^2 a_i}{\mathrm{d}{\Delta\varphi_i}^2} = -\frac{1}{4}a_i + \frac{1}{2}\frac{\mathrm{d}R}{\mathrm{d}\Delta\varphi_i}\,. \tag{2.1.3}$$

This equation is the one that serves to design the shape of the pitch lines. For instance, from (2.1.3) the condition to achieve a linear dependence $a_i = B\Delta\varphi_i$, between the relative rotation and the internal lever arm, reads

$$\frac{\mathrm{d}R}{\mathrm{d}\Delta\varphi_i} = \frac{B}{2}\Delta\varphi_i \quad \Rightarrow \quad R = R_0 + \frac{B}{4}{\Delta\varphi_i}^2\,. \tag{2.1.4}$$

where R_0 is the radius of curvature of the pitch line at the contact point in the straight reference configuration $\Delta\varphi_i = 0$ of Figure 2.3(a). With respect to the reference frame $\xi - \eta$ of Figure 2.3, thanks to symmetry, one finds the analytic expression of the pitch line by considering that

$$\frac{1}{R} = \frac{\eta''}{[1+(\eta')^2]^{3/2}}\,, \quad \eta' = \tan\frac{\Delta\varphi_i}{2} \tag{2.1.5}$$

where we have used the notation $(\cdot)' = \partial(\cdot)/\partial\xi$.

A linear relationship is the simplest one that can be considered, and, left aside the variation of the tensile force in the cable associated with its straining, which is negligible in the case of highly prestressed cables for which $N_0 \gg K\Lambda$, this provides a linear relationship between the moment at the contact joint and the relative rotation. In the continuum limit, this corresponds to classical Euler's elastica, as explained in the following Chapter 3. From (2.1.4), it is evident that circular pitch lines $R = R_0$ can approximate a linear relationship up to infinitesimal that are of second order in $\Delta\varphi_i$. A better approximation is granted by elliptic pitch lines, as (2.1.4) indicates that the radius of curvature shall increase as a consequence of the relative rotation.

For the specific case of circular pitch lines (R equal to a constant value), the elongation Λ_i and the lever arm a_i can also be obtained from simple geometry. In particular, one has

$$\Lambda_i = 2R\Big(1 - \cos\frac{\Delta\varphi_i}{2}\Big)\,, \quad a_i = R\sin\frac{\Delta\varphi_i}{2}\,. \tag{2.1.6}$$

Note that the structure of (2.1.6), obtained from geometry, confirms the validity of (2.1.1). In addition, observe that the fact that circular pitch lines provide an approximated linear law of the lever arm a_i as a function of the rotation $\Delta\varphi_i$ of the joint can be also verified by expressing (2.1.6) through a truncated Taylor series for sine and cosine functions. In this case, one finds

$$\Lambda_i \simeq \frac{R}{4}\Delta{\varphi_i}^2\,, \quad a_i \simeq \frac{R}{2}\Delta\varphi_i\,. \tag{2.1.7}$$

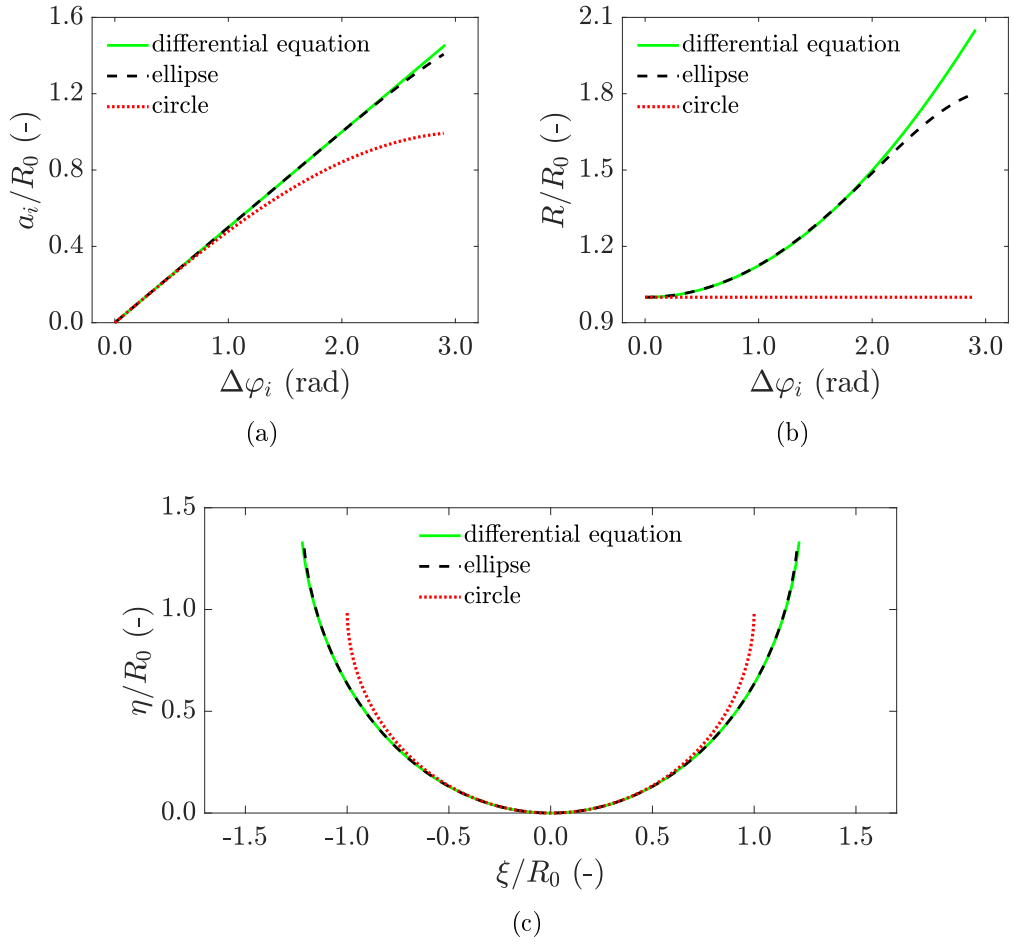

Figure 2.9. Linear case: solution of the differential equations (2.1.4) and (2.1.5) compared with the approximations with circular or elliptical pitch lines. Dimensionless plot of (a) the internal lever arm a_i and (b) of the radius of curvature R at the pitch point, as a function of the relative segmental rotation $\Delta\varphi_i$; (c) corresponding non-dimensional plot of pitch lines.

The pitch line profiles that achieve a linear relationship $a_i = B\Delta\varphi_i$ come from the solution of the differential equations (2.1.4) and (2.1.5), but, as previously said, they could be approximated with arcs of a circle or of an ellipse. Figure 2.9 indicates the level of approximation by considering the three aforementioned cases, labeled as "differential equation", "circle" and "ellipse". The graphs of $a_i(\Delta\varphi_i)$ represented in Figure 2.9(a), indicate that elliptical pitch lines provide an excellent approximation up to $\Delta\varphi_i \simeq 2\,\text{rad}$, while circular pitch lines can be used up to $\Delta\varphi_i \simeq 0.5\,\text{rad}$. Figure 2.9(b) reports the radius of curvature at the pitch point as a function of $\Delta\varphi_i$, and Figure 2.9(c) complements the analysis showing the corresponding pitch lines.

More in general, observe that the fact that the elongation of the cable Λ, and consequently its tensile force N, depends upon the rotation of *all* the joints is responsible of the *nonlocal* behavior of the beam. This is because the relative rotation of any two segments produces the elongation Λ_i, which modifies the overall cable elongation Λ from the hypothesis of perfectly unbonded prestressing tendon. Moreover, since N increases with Λ_i, or Λ, also in the case of a linear relationship between a_i and $\Delta\varphi_i$, the internal moment $M_i = a_i N$ becomes a super-linear function of $\Delta\varphi_i$. Only in the case of highly prestressed cables, or, equivalently, for a very compliant tendon ($K \to 0$), for which $N_0 \gg K\Lambda$, this provides an internal moment that reads $M_i \simeq a_i N_0$, and is characterized by a trend similar to that of the lever arm a_i as a function of the relative rotation $\Delta\varphi_i$. Note that, in this case, also the nonlocal interaction is (approximately) ineffective.

2.1.3 Static equilibrium equations

With reference to Figure 2.10(a), the absolute rotations φ_i of the segments i, $i = 1 \dots n$, positive if clockwise, are chosen as the Lagrangian variables to describe the deformation of the beam of Figure 2.2.

Since the segments are stiff, and can be assumed rigid as a first order approximation, the elastic strain energy U is due to the deformation of the cable only. Let K represent the elastic constant of the cable as a spring and denote with Λ_0 the cable elongation in the reference state of a straight beam, so that the initial pre-tension is $N_0 = K\,\Lambda_0$. If Λ is the successive variation of the cable length due to the inflexion of the beam, the increment ΔU of the elastic strain energy in the cable reads

$$\Delta U = \int_{\Lambda_0}^{\Lambda+\Lambda_0} K\bar{\Lambda}\,d\bar{\Lambda} = K\Lambda_0\Lambda + \frac{1}{2}K\Lambda^2 = N_0\sum_{i=1}^{n-1}\Lambda_i + \frac{1}{2}K\left(\sum_{i=1}^{n-1}\Lambda_i\right)^2. \qquad (2.1.8)$$

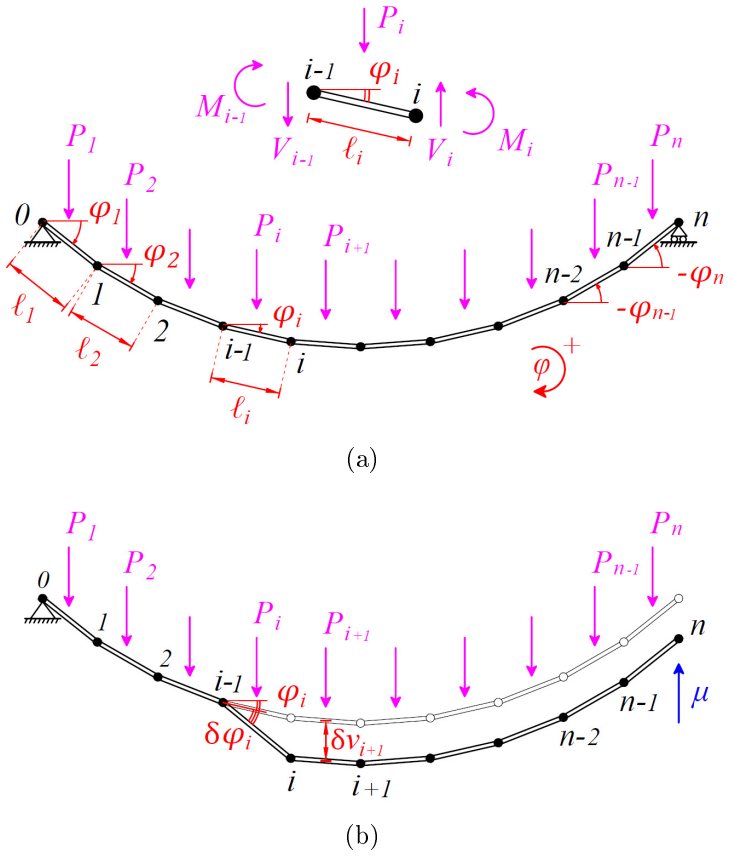

Figure 2.10. Lagrangian variables for the deformed beam. (a) The deformed state φ_i, $i = 1 \dots n$, and equilibrium on the $i-$th segment; (b) perturbation $\varphi_i + \delta\varphi_i$ from the deformed state.

Recall from Figure 2.1 that P_i is the resultant of all the vertical (conservative) forces acting on the $i-$th segment of length ℓ_i, and it is applied at a distance b_i from node i. Hence, the work ΔW of external loads from the undistorted straight state to the bent configuration reads

$$\Delta W = \sum_{i=1}^{n} P_i \, \bar{v}_i = \sum_{i=1}^{n} \left\{ P_i \left[\left(\sum_{j=1}^{i} \ell_j \sin \varphi_j \right) - b_i \sin \varphi_i \right] \right\}, \tag{2.1.9}$$

where $\bar{v}_i$ denotes the vertical displacement of the point where P_i is applied.

The problem to be solved is

$$\Delta U - \Delta W = \min, \quad G = \sum_{i=1}^{n} \ell_i \sin \varphi_i = 0, \tag{2.1.10}$$

where condition $G = 0$ is the kinematic constraint for a simply supported beam.

It is important to remark that $\Lambda = \sum_{i=1}^{n-1} \Lambda_i$, with Λ_i defined as *per* Figure 2.2(a), and that Λ_i is a function the relative rotation $\Delta\varphi_i = \varphi_i - \varphi_{i+1}$, i.e., $\Lambda_i = \Lambda_i(\varphi_i - \varphi_{i+1})$. Moreover, recalling from Figure 2.2(a) that a_i is the lever arm of the cable force N in the $i-$th joint, it is immediate to deduce that

$$\begin{cases} \partial\Lambda_j/\partial\varphi_i = 0\,, & \text{if } \; j \neq i-1 \wedge j \neq i\,, \\ \partial\Lambda_j/\partial\varphi_i = -a_{i-1}\,, & \text{if } \; j = i-1\,, \\ \partial\Lambda_j/\partial\varphi_i = a_i\,, & \text{if } \; j = i\,. \end{cases} \tag{2.1.11}$$

It should be observed that, due to assumed symmetry in the construction of the pitch lines of Figure 2.3, in general Λ_i is an even function of $\Delta\varphi_i$ and, consequently, a_i is an odd function of $\Delta\varphi_i$: the sign of a_i is consistent with the sign of the spring-hinge moment $M_i = a_i\, N$, which is positive if the beam curvature is as indicated in Figure 2.2, negative otherwise.

Therefore, one can write

$$\frac{\partial\Delta U}{\partial\varphi_i} = \frac{\partial\Delta U}{\partial\Lambda}\frac{\partial\Lambda}{\partial\varphi_i} = K(\Lambda_0 + \Lambda)\left(\sum_{j=1}^{n-1}\frac{\partial\Lambda_j}{\partial\varphi_i}\right) = N(a_i - a_{i-1})\,, \tag{2.1.12}$$

$$\frac{\partial\Delta W}{\partial\varphi_i} = \sum_{j=1}^{n} P_j\frac{\partial\bar{v}_j}{\partial\varphi_i} = \left(\sum_{j=i}^{n} P_j\right)\left(\ell_i\cos\varphi_i\right) - b_i P_i\cos\varphi_i\,, \tag{2.1.13}$$

$$\frac{\partial G}{\partial\varphi_i} = \ell_i\cos\varphi_i\,. \tag{2.1.14}$$

Setting $H = \Delta U - \Delta W + \mu\, G$, where μ is the Lagrange's multiplier, the system (2.1.10) is solved by the $n+1$ equations $\partial H/\partial\varphi_i = 0$ $(i = 1\ldots n)$ and $\partial H/\partial\mu = 0$, which read

$$N(a_i - a_{i-1}) - \left(\sum_{j=i}^{n} P_j\right)\left(\ell_i\cos\varphi_i\right) + b_i P_i\cos\varphi_i + \mu\ell_i\cos\varphi_i = 0\,, \tag{2.1.15a}$$

$$\sum_{j=1}^{n}\ell_j\sin\varphi_j = 0\,. \tag{2.1.15b}$$

Clearly, $N = K(\Lambda_0 + \Lambda)$ is the tensile force in the cable, uniform along its length from the hypothesis of negligible friction. Whereas Λ_0 is a datum from the initial prestress, $\Lambda = \sum_{i=1}^{n-1}\Lambda_i$ is a nonlinear function of all φ_i and depends upon the selected shape for the pitch lines at the contact sections. Also observe that the

Langrange's multiplier μ plays the role of the upward vertical constraint reaction at the right-hand-side roller of Figure 2.10(a), whereas the equation (2.1.15a) comes from the principle of virtual displacement for a variation $\varphi_i + \delta\varphi_i$ at $i-$th segment (Figure 2.10(b)). In fact, one has that the corresponding variation $\bar{v}_j + \delta\bar{v}_j$ reads

$$\delta\bar{v}_j = \begin{cases} 0\,, & \text{for} \quad j < i\,, \\ (\ell_i - b_i)\cos\varphi_i\,\delta\varphi_i\,, & \text{for} \quad j = i\,, \\ \ell_i \cos\varphi_i\,\delta\varphi_i\,, & \text{for} \quad j > i\,. \end{cases} \tag{2.1.16}$$

In particular, (2.1.15a) corresponds to the rotational equilibrium of the $i-$th segment about the $i-$th node, indicated at the top of Figure 2.10(a). In fact, the bending moments at the $(i-1)-$th and $i-$th nodes are equal to $M_{i-1} = a_{i-1}\,N$ and $M_i = a_i\,N$, respectively, whereas the vertical shear force at node $i-1$ is equal to $V_{i-1} = \mu - \sum_{j=i}^{n} P_j$. Consequently one has

$$M_i - M_{i-1} + V_{i-1}\,\ell_i \cos\varphi_i + P_i\,b_i \cos\varphi_i = 0\,, \tag{2.1.17}$$

which clearly coincides with (2.1.15a).

It is important to observe from (2.1.15) that the moment M_i at the $i-$th spring hinge is a function not only of its relative rotation $\Delta\varphi_i = \varphi_i - \varphi_{i+1}$, but also of *all* the relative rotations $\Delta\varphi_i$ for $i = 1 \ldots n-1$. This *nonlocal* dependence is a direct consequence of the quadratic term in Λ of (2.1.8). Consequently, in the schematic representation of Figure 2.1, the spring hinges should be intended in a *broader sense* than in the classical acceptation, since the stiffness of each one indeed depends upon the rotation of all the other hinges. Only in the case in which $\frac{1}{2}K\Lambda^2 \ll K\Lambda_0\Lambda$ in (2.1.8), which is equivalent to assume that the tensile force in the cable remains almost constant during bending, does the spring-hinge stiffness depend upon its relative rotation only, so that the nonlocal effect vanishes.

2.2 Examples

A few case-studies are now presented in order to illustrate the practical development of the flexural-tensegrity concept.

2.2.1 Construction of the pitch lines

Three prototypes have been designed and manufactured. As indicated in Figure 2.11(a), these represent three different-in-type relationships for the lever arm a_i of the tension force N, defined in Figure 2.2(a), as a function of the relative rotation $\Delta\varphi_i = \varphi_i - \varphi_{i+1}$: *linear*, *sub-linear* and *super-linear*. Figure 2.11(b) reports the

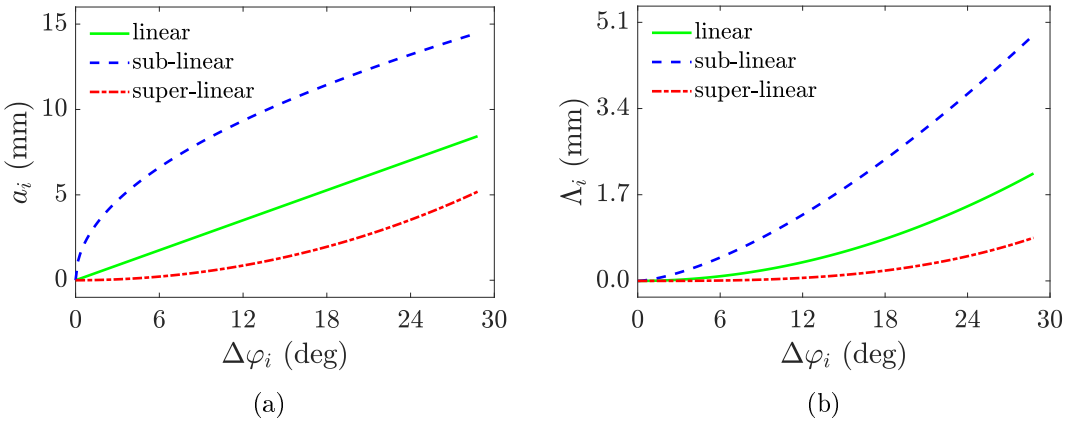

Figure 2.11. Constitutive relations for the prototyped beams. (a) Lever arm a_i of the tension force N in the cable and (b) local cable elongation Λ_i at the $i-$th spring hinge, as a function of the relative rotation $\Delta\varphi_i = \varphi_i - \varphi_{i+1}$.

corresponding local cable elongation Λ_i , as indicated in Figure 2.2(a). The graphs have been drawn only for $\Delta\varphi_i \geqslant 0$, but recall that a_i and Λ_i are, respectively, an odd and an even function of $\Delta\varphi_i$, as detailed in Section 2.1.3.

The analytical expression of such laws can be obtained by observing that the actual pitch point P of coordinates (ξ, η) with respect to the reference frame drawn in Figure 2.3, belongs to the pitch line of equation $\eta = f(\xi)$. Thanks to the symmetry in the construction, as discussed in Section 2.1.1, denoting with $f'(\cdot)$ the first derivative of the function $f(\cdot)$, one obtains from simple calculations that

$$a_i = \sqrt{\left(\xi - \frac{\xi f'(\xi) - f(\xi)}{f'(\xi) + 1/f'(\xi)}\right)^2 + \left(f(\xi) - \frac{f(\xi) - \xi f'(\xi)}{1 + f'(\xi)^2}\right)^2}, \tag{2.2.18}$$

$$\Lambda_i = 2\sqrt{\left(\frac{\xi f'(\xi) - f(\xi)}{f'(\xi) + 1/f'(\xi)}\right)^2 + \left(\frac{f(\xi) - \xi f'(\xi)}{1 + f'(\xi)^2}\right)^2}. \tag{2.2.19}$$

It is immediate to express these quantities as a function of $\Delta\varphi_i$ by observing that

$$f'(\xi) = \tan\frac{\Delta\varphi_i}{2} \quad \Rightarrow \quad \xi = f'^{-1}\left(\tan\frac{\Delta\varphi_i}{2}\right), \tag{2.2.20}$$

where $f'^{-1}(\cdot)$ denotes the inverse of the function $f'(\cdot)$.

For the *linear* case, the pitch lines can be well approximated by arches of ellipse, as detailed in Section 2.1.2, whereas power laws can be selected for the *sub-linear* and the *super-linear* cases. The graphs of Figure 2.11 correspond to the equations

$$\eta[\text{mm}] = f(\xi[\text{mm}]) = \begin{cases} \beta - \dfrac{\beta}{\alpha}\sqrt{\alpha^2 - \xi^2}\,, & \text{linear case}\,, \\ \alpha_1\,|\xi|^3\,, & \text{sub-linear case}\,, \\ \alpha_2\,|\xi|^{1.5}\,, & \text{super-linear case}\,, \end{cases} \tag{2.2.21}$$

with $\alpha = 40.9626$ mm, $\beta = 50$ mm, $\alpha_1 = 0.0004$ mm^{-2} and $\alpha_2 = 0.0756$ mm$^{-0.5}$. Observe that the local cable elongation Λ_i is convex function of $\Delta\varphi_i$ whenever the pitch lines are convex or, equivalently, a_i is a monotone increasing function of $\Delta\varphi_i$.

For a practical representation, the values of a_i from (2.2.18) were fitted with a polynomial of the 1^{st}, 8^{th} and 4^{th} order for the linear, sub-linear and super-linear cases, respectively. Recalling (2.1.1), the Λ_i from (2.2.19) were correspondingly fitted with polynomials of the 2^{nd}, 9^{th} and 5^{th} order. The average difference with respect to the theoretical value is always less than 0.6% within the range $|\Delta\varphi_i| \leqslant 30°$, in particular less than 0.01% for the linear case.

2.2.2 Manufacturing of prototypes

The prototypes were manufactured with a 3D printer in Polylactic Acid (PLA), a thermosoftening plastic obtained from renewable resources such as corn and sugar cane, using the deposition method (FDM) [21]. The typical segments for the three considered cases, with indication of their size, are represented in Figure 2.12. Each beam, made with 10 segments, has a free span of 613.5 mm, calculated from the midpoints of left- and right-hand-side supports in the reference undeformed configuration, with a total weight of 2.313 N, 2.948 N and 2.403 N for the linear, sub-linear and super-linear cases, respectively.

The prestressing cable is a polyamide 6.6 wire of diameter 1.1 mm, placed in series with one spring of stiffness $k_0 = 3.9$ N/mm at each end, as represented in Figure 2.13. In this way, the effective stiffness K of the system, introduced in (2.1.8), satisfies $1/K = 2/k_0 + L_0/EA$, where $EA/L_0 = 2.6$ N/mm is the stiffness of the nude cable, as mentioned in Footnote 1. The initial prestress has been calculated by measuring (through a Vernier caliper) the shortening δ_0 of one of the end springs after having tensioned the cable; in fact, since the springs and the cable are in series, one has that $N_0 = K\Lambda_0 = k_0\,\delta_0$.

The end segments are shaped with a vertical appendix, which, in the experimental setup, is in contact with a lubricated support to achieve a roller constraint. In Figure 2.13 it is also evident the horizontal cantilever at the extremity of which

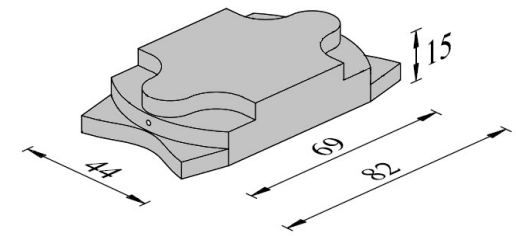

(a)

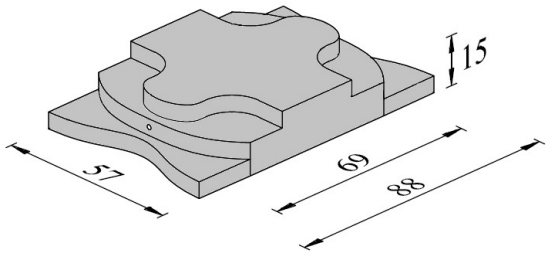

(b)

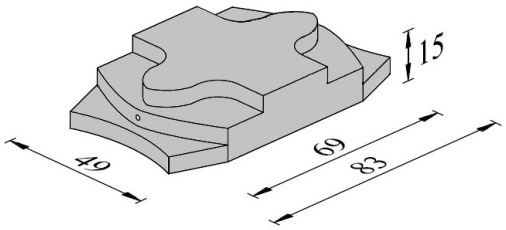

(c)

Figure 2.12. Geometry of the typical segment of the tensegrity beam: (a) linear case; (b) sub-linear case; (c) super-linear case.

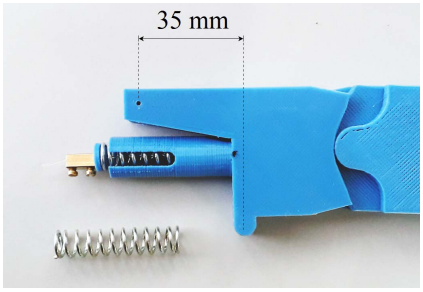

Figure 2.13. End segment of the beam, with indication of the additional compression spring, the vertical appendix in contact with the support and the cantilever at the extremity of which the force is applied for the four-point-bending test.

a *conservative* force, orthogonal to the beam axis in the undistorted (straight) configuration, is applied for the four-point-bending (4P-B) tests. The lever arm, initially 35 mm, varies because of geometric nonlinearity as the beam ends rotate.

All contact surfaces of the spring hinges, as well as the cable inserted in the ducts, were lubricated with silicone grease to minimize the effects of friction.

2.2.3 Experiments under bending

For three different values of the initial tensile force N_0 in the cable, the simply supported beams have been tested either under their self-weight or under the action of two end forces applied at the extremities of the cantilevers (4P-B), as indicated in Figures 2.14(a) and 2.14(b), respectively. In the 4P-B configuration, in order

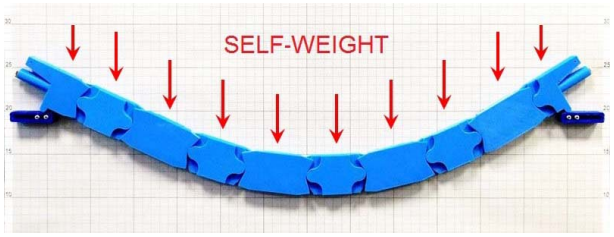

(a)

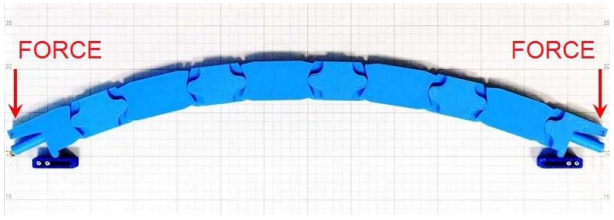

(b)

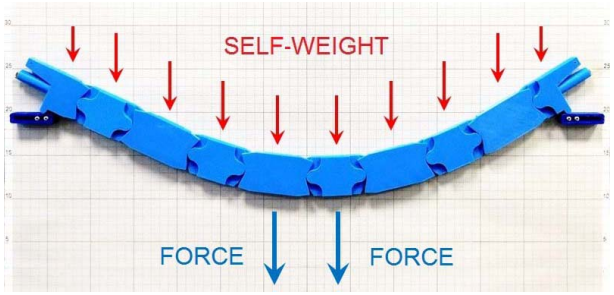

(c)

Figure 2.14. Experimental setup: (a) bending under self-weight; (b) four-point-bending; (c) bending under self-weight and tandem load at midspan.

to rule out the effects of the dead weight, the beam was lying on a horizontal plane, lubricated with oenological vaseline oil. The external forces were introduced through wires, directed to the vertical through lubricated pulleys, to which weights had been attached. Table 2.1 represents the test matrix. In total 9 configurations were considered, i.e., three configurations for each one of the linear, sub-linear and super-linear cases, indicated with the labels "lin", "sub" and "sup", respectively, which differ one another in the initial prestress N_0 . Each configuration was tested under 4P-B with external end forces indicated in the third column and under the self-weight, reported in the fourth column, for a total of 18 tests. Furthermore, 13 additional measurements were made, for the *linear* case only, in the configuration of Figure 2.14(c), in which, besides the self-weight, a variable tandem load is acting, with the two forces applied at the centroid of the two midspan segments. The tandem forces were applied through two clamps, to which two additional weights were hung. The background plane was graded for reference, and the beam deflection was measured with a Vernier caliper. The measurement error can be estimated to be ± 0.001 N for the applied forces, and ± 0.05 mm (caliper precision) for deflections. There are of course additional sources of error, but a precision of less than 1 mm for the sag of the beam can be confidently assured.

Under self-weight, the comparison between experimental and analytical results, obtained with the theory of Section 2.1.3, is shown in Table 2.2 in terms of maximum deflection. The beam response is highly nonlinear and the deflection is strongly affected by the initial prestress N_0. The error between measured values and the theoretical predictions is smaller than 3%, which is satisfactory taking into

Table 2.1. Test matrix: configuration reference for the linear (lin), sub-linear (sub) and super-linear (sup) cases, initial tensile force (prestress) N_0 in the cable, end forces under 4P-B, self-weight of the typical segment.

Configuration reference	Prestress N_0	External end force	Segment self-weight
lin 1	33.2 N		
lin 2	44.1 N	2.335 N	0.231 N
lin 3	51.1 N		
sub 1	23.0 N		
sub 2	32.4 N	5.337 N	0.295 N
sub 3	38.2 N		
sup 1	38.2 N		
sup 2	56.6 N	1.216 N	0.240 N
sup 3	64.0 N		

Table 2.2. Maximum deflections of the beam under self-weight. Comparison between theoretical predictions and experimental measurements.

Configuration	Theoretical	Experimental	Error
lin 1	126.5 mm	125.0 mm	1.2 %
lin 2	106.0 mm	107.0 mm	0.9 %
lin 3	95.5 mm	98.0 mm	2.7 %
sub 1	69.5 mm	71.0 mm	2.2 %
sub 2	43.6 mm	44.0 mm	0.9 %
sub 3	32.7 mm	33.0 mm	0.9 %
sup 1	189.1 mm	190.0 mm	0.5 %
sup 2	173.8 mm	174.0 mm	0.1 %
sup 3	168.6 mm	169.0 mm	0.3 %

Table 2.3. Maximum deflections of the beam under four-point-bending. Comparison between theoretical predictions and experimental measurements.

Configuration	Theoretical	Experimental	Error
lin 1	136.3 mm	135.0 mm	1.0 %
lin 2	109.6 mm	112.0 mm	2.2 %
lin 3	97.1 mm	99.0 mm	1.9 %
sub 1	140.1 mm	140.0 mm	0.1 %
sub 2	106.4 mm	106.0 mm	0.4 %
sub 3	81.1 mm	83.0 mm	2.3 %
sup 1	178.3 mm	176.0 mm	1.3 %
sup 2	158.1 mm	158.0 mm	0.1 %
sup 3	149.9 mm	151.0 mm	0.7 %

account the possible errors due to printing tolerances, measurement inaccuracies and the fact that our model neglects the straining of the segments (especially at the contact points) and their slight variation in length during the rolling motion, as well as the role of friction at the contact hinges, at the supports and between the cable and the duct.

Table 2.3 represents the counterpart of Table 2.2 for the four-point-bending tests. Again, the error remains smaller than 2.5%, despite of the fact that, now, there is an additional source of uncertainty due to the inevitable frictional contact between the supporting table and the beam resting on it. We have particularly verified that, in this case, the relative rotations $\Delta\varphi_i$ are the same at all the spring

hinges $i = 1 \dots n-1$, as it is qualitatively clear by observing Figure 2.14(b).

From a theoretical point of view, this finding is a direct consequence of the fact that the local cable elongation Λ_i is a convex function of $\Delta\varphi_i$, $i = 1 \dots n-1$, as shown in Figure 2.11(b). Pure bending can be equivalently obtained by imposing a relative rotation $(n-1)\overline{\Delta\varphi}$ to the ends of the beam, with $\overline{\Delta\varphi}$ the average hinge rotation. Therefore, recalling (2.1.8), since the external forces per unit length are null, the minimization problem (2.1.10) can be conveniently restated in the form

$$\begin{aligned} &U = K\Lambda_0\left(\sum_{i=1}^{n-1}\Lambda_i\right) + \frac{1}{2}K\left(\sum_{i=1}^{n-1}\Lambda_i\right)^2 =: H(\Delta\varphi_1,\dots,\Delta\varphi_{n-1}) = \min, \\ &\sum_{i=1}^{n-1}\Delta\varphi_i = (n-1)\overline{\Delta\varphi}, \end{aligned} \tag{2.2.22}$$

where $H(\Delta\varphi_1,\dots,\Delta\varphi_{n-1})$ is a convex function in the $(n-1)$ dimensional space. Denote with $H_{,i}$ the partial derivative of the function H with respect to the variable $\Delta\varphi_i$. It is straightforward to demonstrate that, since the pitch lines are the same for each hinge and the segments have the same length, $H_{,i}(\overline{\Delta\varphi},\dots,\overline{\Delta\varphi}) = H_{,j}(\overline{\Delta\varphi},\dots,\overline{\Delta\varphi})$, $\forall i,j = 1 \dots n-1$. Therefore, one can write

$$\begin{aligned} &H(\overline{\Delta\varphi},\dots,\overline{\Delta\varphi}) = H(\overline{\Delta\varphi},\dots,\overline{\Delta\varphi}) + \sum_{i=1}^{n-1}\left[H_{,i}(\overline{\Delta\varphi},\dots,\overline{\Delta\varphi})\left(\Delta\varphi_i - \overline{\Delta\varphi}\right)\right] \\ &\leqslant H(\Delta\varphi_1,\dots,\Delta\varphi_{n-1}) \quad \forall\Delta\varphi_i \quad \text{such that} \quad \sum_{i=1}^{n-1}\Delta\varphi_i = (n-1)\overline{\Delta\varphi}, \end{aligned} \tag{2.2.23}$$

where the inequality results from the fact that any tangent plane supports a convex function from below. This means that the condition $\Delta\varphi_i = \overline{\Delta\varphi}$, $i = 1 \dots n-1$, minimizes the energy.

In order to evidence the nonlinear response of the beam, an increasing tandem load composed by two twin forces F was superimposed to the dead weight, as *per* Figure 2.14(c). The experimental measurements, limited on the structure with a *linear* a_i vs. $\Delta\varphi_i$ relationship, were juxtaposed with the results from the model of Section 2.1.3. In particular, we are now considering, for the sake of comparison, also an approximation of the strain energy (2.1.8), here referred to as the "first-order approximation", in which the term $K\Lambda^2/2$ is neglected with respect to $N_0\Lambda$. This is equivalent to assume that the tensile force in the cable remains constant during the deformation of the beam ($N \simeq N_0$).

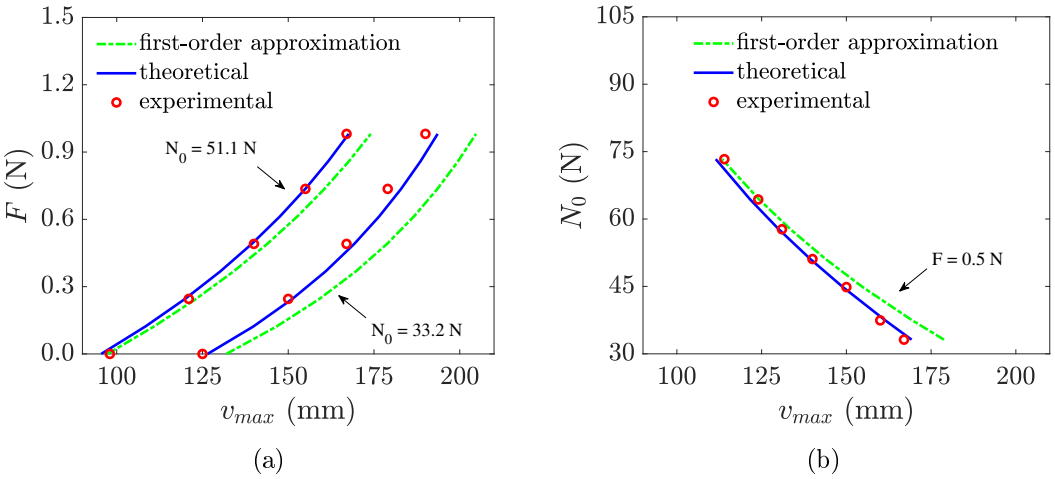

Figure 2.15. Maximum deflections v_{max} of the beam (linear case) under self-weight and tandem forces F. Comparison between experiments, theoretical model and its first-order approximation at: (a) constant N_0 and variable F; (b) constant F and variable N_0. Measurement errors of ± 0.1 N for N_0 and ± 1 mm for v_{max}.

This comparison is of importance, because it has been shown in Section 2.1.3 that, when the quadratic term in Λ is negligible, each spring hinge in the scheme of Figure 2.1 has a *local* response that depends upon its rotation only. Otherwise, a *nonlocal* effect arises due to the second-order straining of the cable.

For two values of the initial prestressing force ($N_0 = 33.2$ N or $N_0 = 51.1$ N) the maximum deflection v_{max} at the middle of the beam is reported in Figure 2.15(a) as a function of the tandem forces F. The model (continuous blue curve) provides an excellent agreement with the experimental results (red dots). As expected, the "first-order approximation" (dashed green line) slightly underestimates the stiffness of the beam, the error being higher the smaller the pre-stressing force N_0 is. Obviously, the difference increases as the load increases, because the second-order cable elongation becomes more important.

In order to evaluate the effect of the initial prestress, the tandem forces F were maintained constant to the value 0.5 N while N_0 was continuously varied. The corresponding deflection v_{max} is recorded in Figure 2.15(b). The model (continuous blue curve) again provides an excellent agreement with the experiments (red dots). The inaccuracy of the "first-order approximation" (dashed green line) diminishes as N_0 increases, because the more the beam is pre-stressed, the lower is the deflection and, correspondingly, the lower is the second-order elongation of the cable.

If the beam is used in practical structural applications, it cannot be too deformable. From an engineering point of view, it is reasonable to expect that the

initial prestress N_0 should be such that the maximum deflection under self-weight v_{max} should remain within the order of, say, $L/5$. For this prototype, approximately 62 cm long, this means a maximum sag of about 12 cm. From the graphs in Figure 2.15, one deduces that, in this case, the "first-order approximation" is quite accurate, and it can be used in a preliminary design phase.

2.2.4 Discussion on joints modeled as spring hinges

In the previous Section 2.1, the coupling between any pair of consecutive segments is that of a pure rolling contact along the pitch profiles, which affects the strain energy of the system through the cable elongation Λ. Such a coupling was used to deduce the constitutive relations for the joints; on the contrary, the joints were modeled as (nonlocal) spring hinges when macroscopically considering the segmental beam as a whole. This is obviously an approximation because the segments actually move one another in pure rolling along the pitch profiles, so that the pitch point moves as well during the rotation, while, in a (spring) hinge, the pivot point remains fixed.

As a consequence of the fact that the segments move on curved surfaces, their length slightly varies during the rotation of the joints, while in the model of Section 2.1.3, the segmental length ℓ_i was kept fixed under bending deformation. Hence, the validity of the simplified modeling of the joint as a spring hinge needs to be critically discussed. In particular, this assumption is validated whenever the variation in length of the segments, during the reciprocal rolling, represents a small percentage of ℓ_i, so that it can be overlooked. On the contrary, when this argument is not satisfied, or high accuracy in the description of the kinematics of the coupled segments is required, the model of Figure 2.1 should be updated.

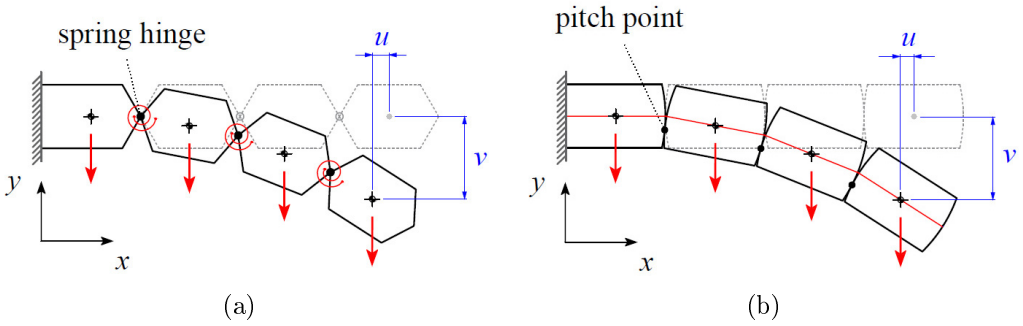

Figure 2.16. Comparison between the spring-hinge model and the actual flex-ten kinematics: (a) cantilever with 4 segments coupled by nonlocal spring hinges subjected to self-weight; (b) corresponding flex-ten beam with pure rolling along the pitch lines.

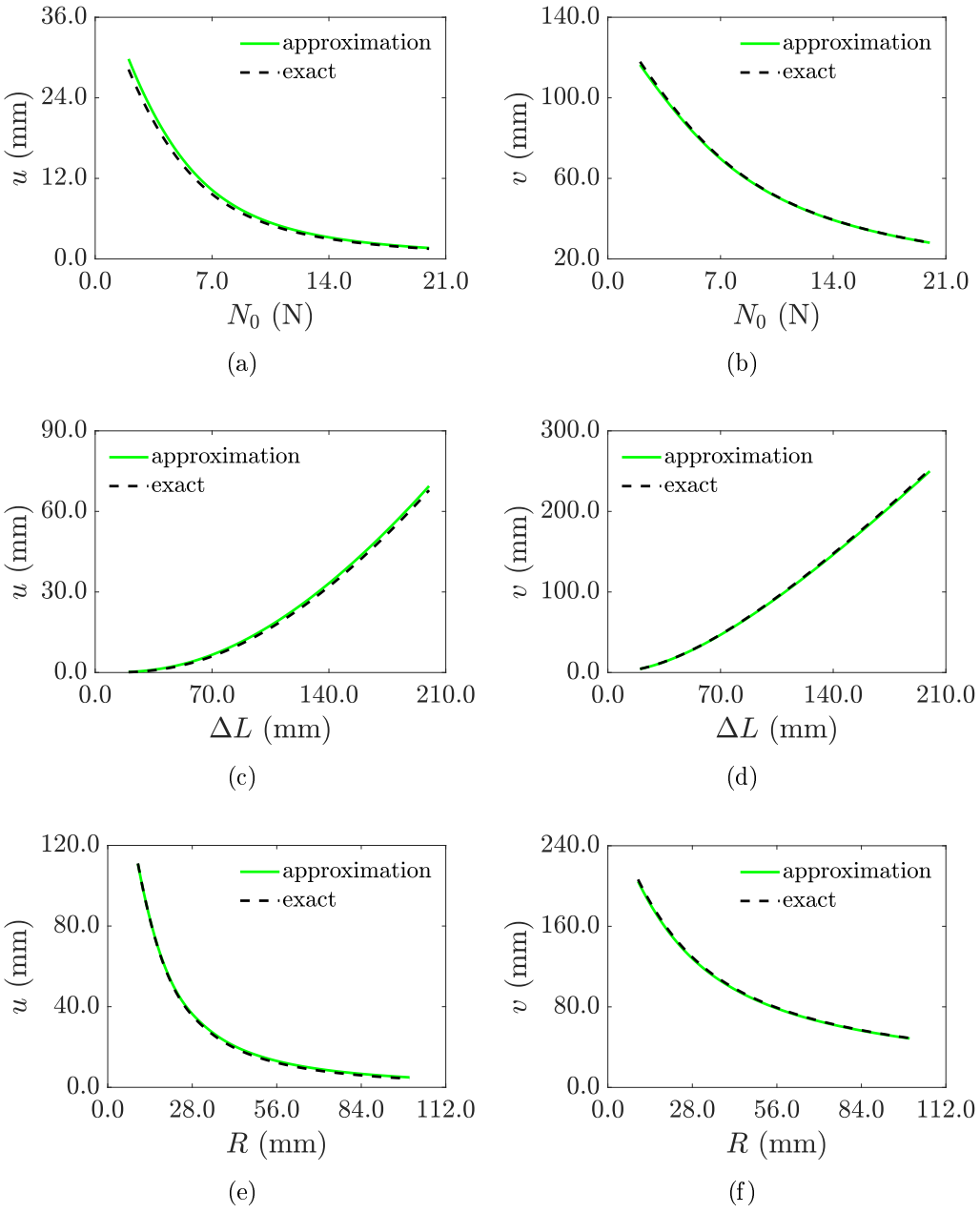

Figure 2.17. Comparison between the spring-hinge model and the actual flex-ten kinematics. Horizontal displacement u and vertical displacement v of the centroid of the tip segment for: (a)-(b) variable prestress N_0 in the cable and $R = 5\,\text{cm}$, $\Delta L = 10\,\text{cm}$, $m_i = 0.01\,\text{kg}$, $K = 1000\,\text{N/m}$; (c)-(d) variable segmental length ΔL and $R = 5\,\text{cm}$, $N_0 = 5\,\text{N}$, $m_i = 0.01\,\text{kg}$, $K = 1000\,\text{N/m}$; (e)-(f) variable pitch line radius R and $\Delta L = 10\,\text{cm}$, $N_0 = 5\,\text{N}$, $m_i = 0.01\,\text{kg}$, $K = 1000\,\text{N/m}$.

Consider the model problem of a cantilever beam subjected to self-weight and composed of $n = 4$ segments, coupled by means of circular pitch lines of radius R. Here, the segments have all the same length, so that $\ell_i = \Delta L$, and the same mass m_i. Hence, the applied load at each segment centroid is $m_i\, g$, being $g = 9.81\,\mathrm{m/s^2}$ the gravity acceleration. The simplified modeling with spring hinges, considered so far, is reported in Figure 2.16(a). This is now compared with a more refined modeling that accounts for the actual motion of the pitch point along the pitch lines while describing the deflection of the beam (Figure 2.16(b)). The deflection of the beam, obtained from the two models, is compared in terms of the displacements u and v of the centroid of the segment at the tip of the cantilever. These displacements are also indicated in Figure 2.16.

Figure 2.17 collects the results for such a comparison. In particular, a parametric investigation on how the deflection of the beam is affected by the initial prestress N_0 in the cable (Figure 2.17(a) and 2.17(b)), the segmental length ΔL (Figure 2.17(c) and 2.17(d)) and the radius R of pitch lines (Figure 2.17(e) and 2.17(f)) was carried out. In all cases, the difference between the spring-hinge model and the more refined rolling along pitch lines is small: always less than 1.3% for the vertical displacement v, and within the value of 1 mm for the horizontal displacement u. This demonstrates that the simple modeling with spring hinges is satisfactory, at least for the geometry at hand.

Note that the initial prestress N_0, the segmental length ΔL and the pitch line radius R are comparable with the values adopted in the experimental investigations presented in the previous Section 2.2.3, thus justifying the modeling of the joints as spring hinges also for that case.

2.2.5 Discussion on the deformation of contact profiles

In the previous Section 2.1, the segments were supposed to be very stiff (rigid in the limit case), so that their contribution to the variation ΔU of the strain energy can be overlooked. As a result, ΔU depends only upon the stretching of the tendon, as per (2.1.8). In addition to the specific contribution to strain energy, the deformability of the segments would also affect the shape of the contact profiles, thus influencing the cable elongation Λ_i and the internal lever arm a_i at each joint. Now, we want to evaluate this effect, and check if the assumption of macroscopically rigid segments is correct.

To exemplify, consider again the paradigmatic case of circular pitch lines of radius R, and assume that the contact profiles are shaped directly according to the pitch profiles. The simplest way to get a preliminary result about the deformation of the surfaces in contact is represented in Figure 2.18. Here, the initially-circular deformable contact profiles are modeled as a bed of springs à la Winkler, with

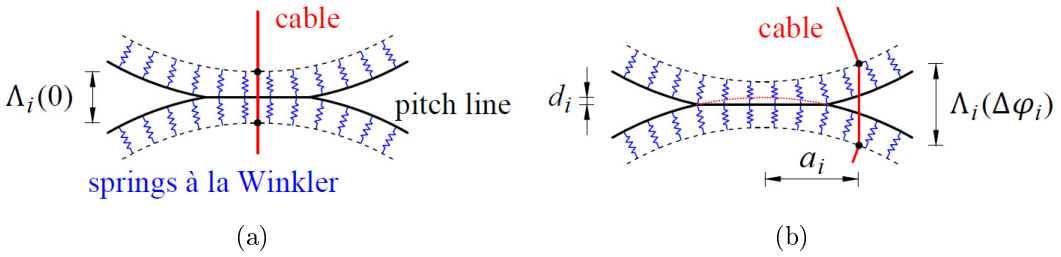

Figure 2.18. Deformable surfaces in contact modeled as a bed of springs à la Winkler: (a) joint in straight reference state and (b) rotated state under bending.

constant κ. Figure 2.18(a) reports the straight reference state of the joint, while the rotated state under bending is displayed in Figure 2.18(b), with indication of the lever arm a_i and the cable elongation Λ_i. Note that the cable exit point from the sheaths has been set back from the surface of pitch profiles, and placed at the interface between the bed of springs à la Winkler and the rigid underlying material matrix of the segments. From a physical point of view, this could account for "smoothened" fittings due to the deformability of the material of the segments.

Figure 2.19 reports the response of such a joint under bending, as a function of the relative rotation $\Delta\varphi_i$ and for different values of the spring constant κ. The trend of the internal lever arm a_i (Figure 2.19(a)) is practically unaffected by the deformation of pitch lines. On the contrary, the cable elongation Λ_i (Figure 2.19(b)) varies, especially for what concerns the initial distance between the exit points from the sheaths, referred to as $\Lambda_i(0)$, despite the quadratic trend of each curve is substantially maintained. The tension force N in the cable, given by $N = N_0 + K\ [\Lambda_i(\Delta\varphi_i) - \Lambda_i(0)]$ and reported in Figure 2.19(c), and the transmitted moment M_i at the joint, which reads $M_i = a_i\, N$ (Figure 2.19(d)), varies accordingly. The plots correspond to $R = 10\,\text{cm}$, $N_0 = 25\,\text{N}$. The shortening of Winkler's springs can be computed from equilibrium with the tension force in the cable.

To visually appreciate the deformation of the surfaces in contact, Figures 2.20(a) and 2.20(c) show the straight state of the joint, for $\kappa = 1 \cdot 10^8\,\text{N/m}^3$ and $\kappa = \infty$, respectively. Figures 2.20(b) and 2.20(d) depict the rotated state under bending for the corresponding values of κ. Here, the cable is represented with a red solid line, the deformable pitch lines with blue curves, and the bed of springs à la Winkler is highlighted by the shaded region.

To evaluate the flattening of contact profiles in the field, a compression test on a 3D-printed half segment was finally performed. The specimen, of length $\ell_i/2 = 4\,\text{cm}$, thickness equal to 1.5 cm, and with the radius of the pitch contact surface $R = 10\,\text{cm}$, as assumed in the plots of Figures 2.19 and 2.20, was compressed through a testing machine (MTS810 Universal Testing System) and

the force vs. shortening was measured. If all the deformation is concentrated at the pitch profiles, this shortening corresponds to the flattening of the contact surfaces, indicated as d_i in Figure 2.18(b). The value $d_i \simeq 0.1\,\text{mm}$ was found at a compression force of about 64 N for the test, while the case of $\kappa = 1 \cdot 10^9\,\text{N/m}^3$, theoretically analyzed in Figure 2.19, corresponds to $d_i \simeq 0.4\,\text{mm}$ at the same compression force.

Since the response of the joint for $\kappa = 1 \cdot 10^9\,\text{N/m}^3$ is close to the limit case $\kappa = \infty$ (Figure 2.19) and the value of d_i found in the compression test is smaller than the theoretical one for $\kappa = 1 \cdot 10^9\,\text{N/m}^3$, this validates the assumption of considering stiff segments, whose deformation minimally affects the shape of contact surfaces and whose straining can be neglected with respect to the variation of

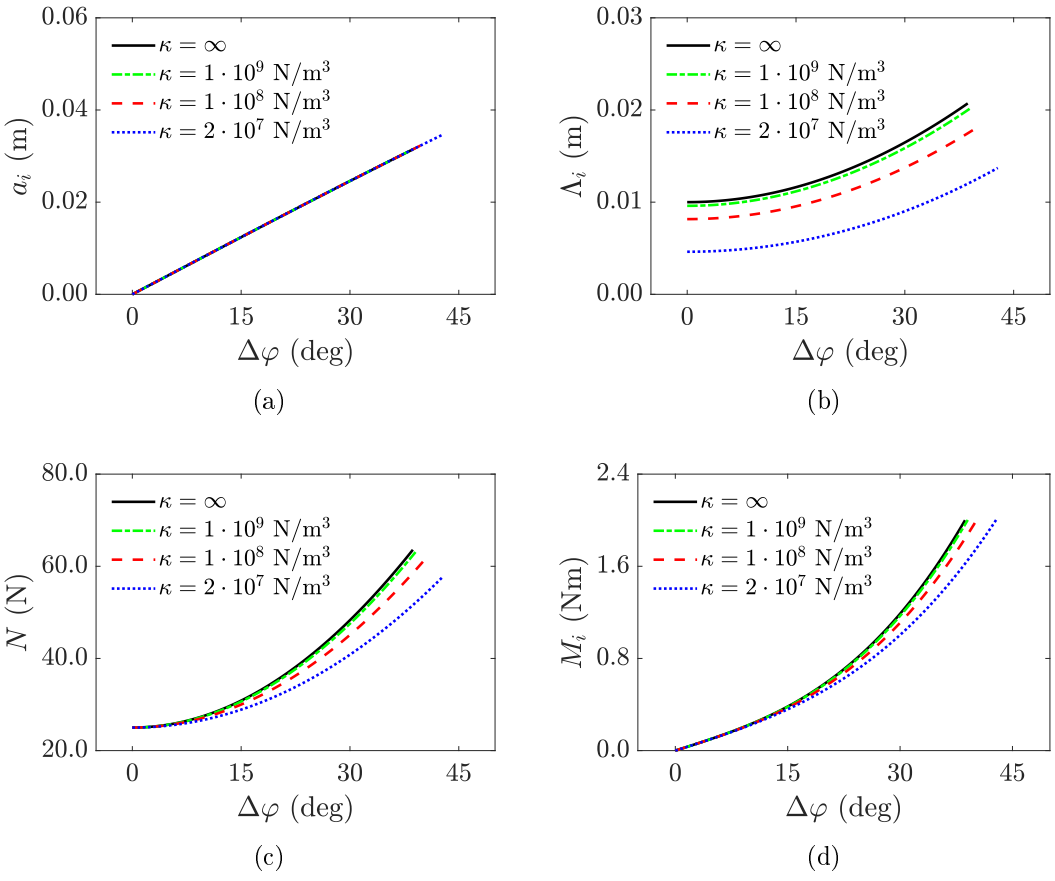

Figure 2.19. Response of the joint with deformable profiles under bending, as a function of the relative rotation $\Delta\varphi_i$, for variable spring constant κ: (a) internal lever arm a_i ; (b) cable elongation Λ_i ; (c) tension force N in the cable; (d) transmitted moment M_i at the joint. The plots correspond to $R = 10\,\text{cm}$, $N_0 = 25\,\text{N}$.

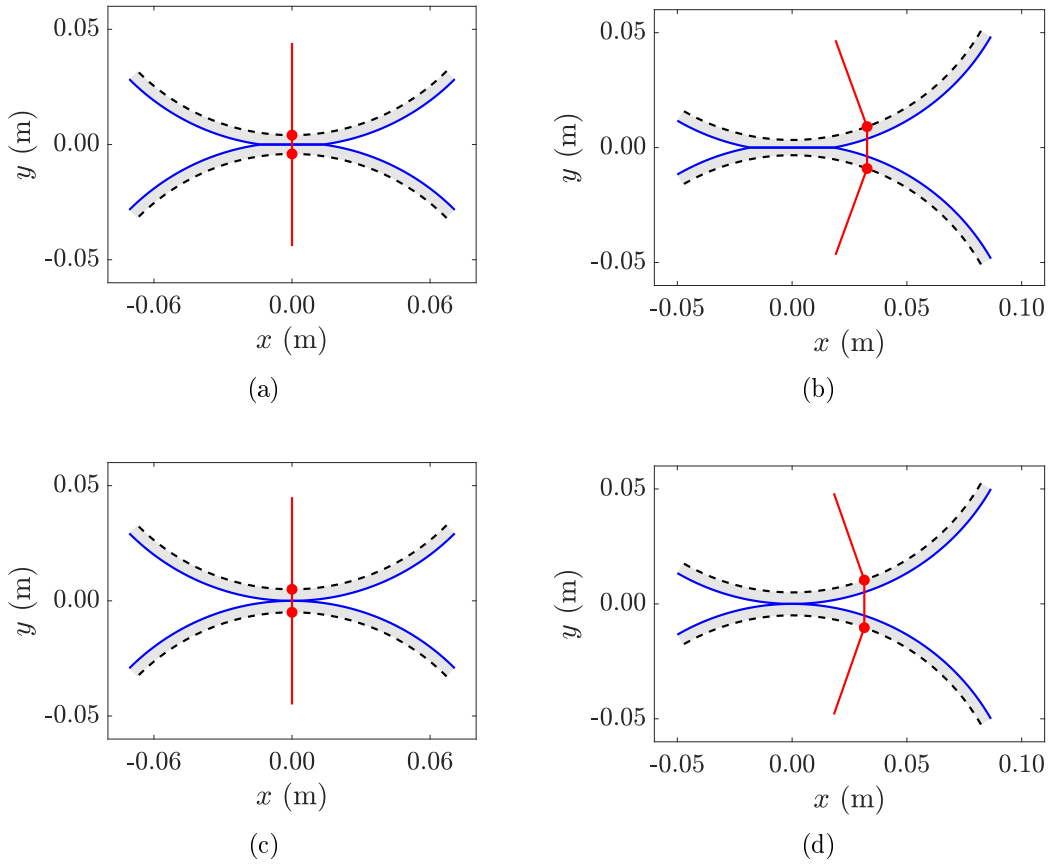

Figure 2.20. Response of the joint under bending: straight and rotated configurations for (a)-(b) $\kappa = 1 \cdot 10^8\,\mathrm{N/m^3}$ and (c)-(d) $\kappa = \infty$. The plots correspond to $R = 10\,\mathrm{cm}$, $N_0 = 25\,\mathrm{N}$; the cable is represented in red color, the deformable pitch lines in blue color, and the bed of springs à la Winkler is highlighted by the shaded region.

ΔU due to the compliant cable. In particular, as the tested specimen corresponds to the dimensions and the manufacturing process discussed in Section 2.2.2, the assumption of rigid segments adopted to theoretically interpret the experimental investigations of Section 2.2.3 is thus justified.

Chapter 3

The continuum approximation

The continuum limit of flex-ten segmental beams is here analyzed. This corresponds to the case in which the number of segments goes to infinity and their length decreases to zero. The model falls within the framework of Euler's *elastica*, but its peculiarity is represented by the nonlocal bending stiffness and hardening behavior under loading.

The classical model by Euler is first introduced in Section 3.1, while discussing the wide range of its possible fields of application, spanning from engineering to biology. With reference to the paradigmatic case-study of a simply supported rod under the most general loading conditions, the new nonlocal theory is then presented in Section 3.2. After detailing its derivation from flexural tensegrity, it is shown how the equilibrium states of the rod can be determined analytically modulo the calculation of elliptic integrals, as in the case of classical Euler's elastica. Indeed, the analysis of example cases (buckling and bending under concentrated and distributed loads), pursued in Section 3.3 either with the analytical approach or with a direct numerical calculation, demonstrates the strict correlation, but with fundamental differences, of the most well-known model by Euler with the nonlocal rod presented here.

The proposed *nonlocal elastica* represents an innovative flexible structure which, while respecting the orthodoxy of the classical elastica, can be tuned for a tailored design in a wide range of applications.

The main results here discussed are also collected in [20] and [26].

3.1 Introduction to the elastica

In *Additamentum I* "*De Curvis Elasticis*" to his famous treatise of 1744, Euler [27][1] celebrates Daniel Bernoulli for having suggested that the *universam vim* of a curved elastic lamina could be compacted in one single formula called *vim potentialem*, and such an expression shall be minimal for the *curva elastica*. Developing Bernoulli's idea, Euler showed that the differential equation determining the curve, or *elastica*, in which a thin rod, straight and prismatic in the unstressed state, is held by forces and couples when bent in a principal plane – so that the central line becomes a plane curve – could be found by making a minimum the integral of the square of the curvature taken along the rod [30, 31].

Euler's elastica is a simple model that is often advocated as the paradigm for compliant structures. It applies to biology, e.g., to conveniently describe the deformation of collagen fibers [32], or to study the locomotion provided by flexible flagella to bacteria [33]. The model is widely used in mechanical engineering and soft robotics [34, 35], as well as for biomedical tools [36]. "Unusual" applications can be found in a hot-cutting robot for the fabrication of formwork for concrete shell structures [37], in devices for timber transportation along rivers [38] and in cattle-catching tools like the *lasso* [39]. From a more fundamental point of view, flexible and inextensible elastic rods have been used by Bigoni and co-workers as the basic structural models to describe phenomena and applications yet to be fully appreciated. An elastic rod constrained within a frictionless sliding sleeve provides the simplest illustration of the role played by configurational, or Eshelby-like forces, on the statics [40] and dynamics [41] of one-dimensional structures. This finding has suggested novel ingenious devices, like a deformable arm scale [42], as an alternative to the traditional rigid arm balance. The elastica can be used to describe the effects of surface tension in fluids, such as self-encapsulation or dripping [43], with potential applications in electro-magnetic circuits. Drawing inspiration from antique weapons, the optimization of a flexible rod as a catapult [15] suggests the design for innovative robotic limbs.

All the aforementioned applications make use of the classical theory of the elastica. This has been geometrically linearized, treated with imperfections, analyzed for bifurcation points, relaxed to include extensibility but, fundamentally, the original stored-energy function has been maintained in its dependence on the square of the curvature. Non-quadratic energies have sometimes been used to describe non-linear constitutive responses between bending moment and local curvatures. Strain energy functionals derived from non-convex potentials in the curvature field [44] predict, as absolute minimizers, discontinuous curvatures of the central line even

[1] Reference [27] is the original Latin version of Euler's work, also available in [28]. An English translation with comments can be found in [29].

under pure bending (prescribed terminal slope-angles or couples), which recall the coexistent phases in stressed solid mixtures. Non-convex strain energy densities with linear growth at infinity (oblique asymptotes), providing moment-curvature relationships with strain-softening branches and horizontal asymptotes, can induce the localization of bending strains as in a plastic hinge [45]. Under the Euler-Bernoulli hypothesis that cross sections remain plane after the deformation, laws of this type were obtained in [46] for elastic-plastic materials exhibiting a transition from the upper to the lower yield point, commonly experienced in strain-driven tests on low-carbon-steel bars [47], which is equivalent to a strain-softening branch.

Nonlocal theories for inflexed rods have been inspired by the seminal work by Eringen [48]. Nonlocal *differential* (high-order gradient) elastic constitutive relations have been successfully used to describe the equilibrium states and vibration modes of carbon nanotubes [49]. The differential form is often considered as an approximation of the complete *integral* formulation, in which the bending depends upon the convolution between the elastic curvature and an averaging kernel, usually with compact support or with a fast decay at infinity. For models of this kind, an issue of paramount importance is the compatibility between the boundary conditions consequent to the nonlocal constitutive law and the equilibrium conditions that the bending field has to satisfy [50]. In order to overcome possible emerging paradoxes, stress-driven nonlocal theories have been also proposed in [51], where it is the elastic curvature field that depends upon convolution between the bending field and an averaging kernel.

In the following, a particular nonlocal constitutive law for the elastica, never considered before to the best of our knowledge, is proposed and analyzed in detail. The bending moment at each cross section depends linearly upon the curvature, but the bending stiffness, although remaining homogenously constant in the whole rod, is affected by the whole curvature field. This is fundamentally different from all the cases mentioned before, in which the bending moment at each point of the centroidal line is at most a nonlinear function of the local curvature and its gradients, or depends upon the values of the curvature field in a neighborhood of the point.

3.2 The model for a nonlocal elastica

After deriving the bending stiffness from the continuum limit of flex-ten beams, the analytical theory of the nonlocal elastica is presented. The nonlocal effect is discussed and methods of solution of the equilibrium equations are proposed.

3.2.1 From discrete to continuum

It has been evidenced in the previous Chapter 2 that the key point of flex-ten beams is the definition of the cable elongation Λ_i at the $i-$th joint, which is a function of the relative rotation $\Delta\varphi_i$ at the joint. In particular, referring to the quantities indicated in Figure 2.10, it is useful to introduce a re-normalization of such a function in the form

$$\begin{aligned}\Lambda_i = \Lambda_i(\Delta\varphi_i) = \Lambda_i(\varphi_i - \varphi_{i+1}) = \hat{\Lambda}_i\Big(\frac{\varphi_i - \varphi_{i+1}}{\ell_i}\Big) \\ = \frac{1}{\ell_i}\hat{\Lambda}_i\Big(\frac{\varphi_i - \varphi_{i+1}}{\ell_i}\Big)\ell_i = \hat{\lambda}_i\Big(\frac{\varphi_i - \varphi_{i+1}}{\ell_i}\Big)\ell_i\,,\end{aligned} \tag{3.2.1}$$

where $\hat{\lambda}_i(\cdot) = \hat{\Lambda}_i(\cdot)/\ell_i$ is the normalized cable elongation *per* unit length of the beam. Therefore, recalling (2.1.1), one can write

$$\begin{aligned}a_i = a_i(\Delta\varphi_i) = a_i(\varphi_i - \varphi_{i+1}) = \hat{a}_i\Big(\frac{\varphi_i - \varphi_{i+1}}{\ell_i}\Big) = \\ = \Lambda_i'(\varphi_i - \varphi_{i+1}) = \frac{1}{\ell_i}\hat{\Lambda}_i'\Big(\frac{\varphi_i - \varphi_{i+1}}{\ell_i}\Big) = \hat{\lambda}_i'\Big(\frac{\varphi_i - \varphi_{i+1}}{\ell_i}\Big)\,.\end{aligned} \tag{3.2.2}$$

where $f'(\cdot)$ denotes the first derivative of the function $f(\cdot)$. Consequently, the variation ΔU of the strain energy of (2.1.8) can be written in the form

$$\Delta U = K\Lambda_0\left[\sum_{i=1}^{n-1}\hat{\lambda}_i\Big(\frac{\varphi_i - \varphi_{i+1}}{\ell_i}\Big)\ell_i\right] + \frac{1}{2}K\left[\sum_{i=1}^{n-1}\hat{\lambda}_i\Big(\frac{\varphi_i - \varphi_{i+1}}{\ell_i}\Big)\ell_i\right]^2. \tag{3.2.3}$$

By letting $\ell_i \to 0$, one can define a smeared view of these quantities and refer to the continuum problem of a thin and prismatic, initially-straight, rod bent in a principal plane. Introduce the curvilinear coordinate s on the beam axis, and, if $\varphi(s)$ is the rotation of the beam at s, one can set

$$\lim_{\ell_i\to 0}\frac{\varphi_i - \varphi_{i+1}}{\ell_i} = -\varphi'(s)\,, \quad \lim_{\ell_i\to 0}\hat{\lambda}_i\Big(\frac{\varphi_i - \varphi_{i+1}}{\ell_i}\Big) = \tilde{\lambda}(-\varphi'(s))\,, \tag{3.2.4}$$

so that

$$\sum_{i=1}^{n-1} \hat{\lambda}_i \left(\frac{\varphi_i - \varphi_{i+1}}{\ell_i} \right) \ell_i \simeq \int_0^L \tilde{\lambda}(-\varphi'(s))\, ds\,. \tag{3.2.5}$$

This quantity represents the total elongation of the cable in the continuum limit, and, under this assumed equivalence, the elastic strain energy (3.2.3) should be written in the form

$$\Delta\mathcal{U} = K\Lambda_0 \left[\int_0^L \tilde{\lambda}(-\varphi'(s))\, ds \right] + \frac{1}{2} K \left[\int_0^L \tilde{\lambda}(-\varphi'(s))\, ds \right]^2 . \tag{3.2.6}$$

The first term in this equation is the contribution due to the initial prestress in the cable $N_0 = K\Lambda_0$, whereas the second term represents the second-order contribution, associated with the further increase in length of the cable.

3.2.2 The elastica with nonlocal bending stiffness

Consider the problem of determining the equilibrium states of a thin rod, straight in its undistorted reference configuration, which is bent in a principal plane so that the centerline becomes a plane curve. The rod, of length L, is simply supported at the ends as represented in Figure 3.1(a), and we take a system of fixed axes x, y, with x coinciding with the centerline in the unstressed state. The rod bends, as schematically indicated in Figure 3.1(b), under the action of a distributed load $p(s)$, being $s \in [0, L]$ the curvilinear abscissa identifying points on the centerline, two opposite horizontal end-forces F, positive if they induce compression, and two couples M_l and M_r, applied at the left- and right-hand-side ends, respectively. Let $u(s)$ and $v(s)$ denote the components on x, y of the displacement of the point at s, positive if opposite to the orientation of the axes, and let $\varphi(s)$ represent the angle here formed between the tangent to the deformed centerline and the x-axis, considered positive if it corresponds to a clockwise rotation. Hence, the curvature at s is given by $\chi = -\varphi'(s)$.

Assume that the increase $\Delta\mathcal{U}$ of the elastic strain energy, under applied external loads, is of the form

$$\Delta\mathcal{U} = \Delta\mathcal{U}[\varphi] = \frac{1}{2} K_L \int_0^L \left(-\varphi'(s)\right)^2 ds + \frac{l^2}{4L} K_{NL} \left[\int_0^L \left(-\varphi'(s)\right)^2 ds \right]^2 , \tag{3.2.7}$$

where K_L and K_{NL} are constants with dimension $[ML^3T^{-2}]$ and l denotes an intrinsic length scale. In the case in which $K_{NL} = 0$, the model falls in the category of classical Euler's elastica. With respect to this case, the term associated with K_{NL}

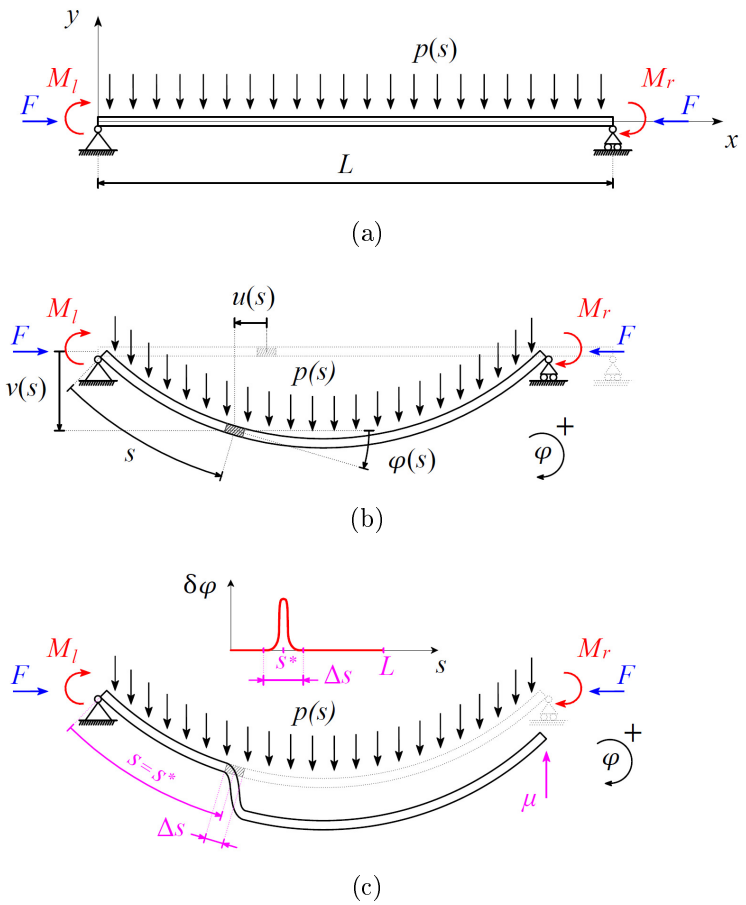

Figure 3.1. Schematic representation of the continuum problem: (a) beam in the straight reference state; (b) deformed configuration under external loads; (c) perturbation from the deformed state, and corresponding distortion of the beam.

provides a nonlocal effect and additional bending stiffness.

The physical role of these quantities is clear by comparison of (3.2.7) with (3.2.6), derived from flexural tensegrity. In particular, one has

$$\tilde{\lambda}(-\varphi'(s)) = \frac{l^2}{2}\,(-\varphi'(s))^2\,, \quad K_L = N_0\,l^2\,, \quad K_{NL} = \frac{1}{2}\,K\,L\,l^2\,. \tag{3.2.8}$$

Note that a quadratic law for $\tilde{\lambda}(-\varphi'(s))$ can be obtained with circular pitch lines of radius R in the corresponding flex-ten beam, as detailed in Section 2.1.2. Then, recalling (2.1.7) and (3.2.4), the counterpart in the discrete model of the intrinsic length-scale l of (3.2.7) is of the form $l^2 = R\,\Delta L/2$, where ΔL denotes the segmental length, now supposed to be uniform along the beam. To obtain a finite limit for

l^2 in the continuum model, one has to assume that $\lim_{\Delta L \to 0} R = +\infty$; this means that, for segments of infinitesimal length, the pitch lines at the contact joints are almost flat.

The work $\Delta\mathcal{W}$ of the external loads of Figure 3.1(a), under the hypothesis of conservative generalize forces, can be written as a function of $\varphi(s)$ in the form

$$\begin{aligned}\Delta\mathcal{W} = \Delta\mathcal{W}[\varphi] = \int_0^L p(s) \left[\int_0^s \sin\varphi(\bar{s})\, d\bar{s} \right] ds + \\ + F \int_0^L \Big[1 - \cos\varphi(s) \Big] ds + M_l\, \varphi(0) + M_r\, \varphi(L)\,.\end{aligned} \tag{3.2.9}$$

In addition, the kinematic compatibility with the roller constraint at $s = L$, for the simply supported beam of Figure 3.1(b), implies that

$$\mathcal{G} = \mathcal{G}[\varphi] = \int_0^L \sin\varphi(s)\, ds = 0\,. \tag{3.2.10}$$

The equilibrium states correspond to the solution of the minimization problem $\Delta\mathcal{U}[\varphi] - \Delta\mathcal{W}[\varphi] = \min$, under the constraint $\mathcal{G}[\varphi] = 0$. Consider the augmented functional $\mathcal{H}[\varphi] = \Delta\mathcal{U}[\varphi] - \Delta\mathcal{W}[\varphi] + \mu\,\mathcal{G}[\varphi]$, where μ is the Lagrange's multiplier. For a variation $\varphi + \delta\varphi$, the corresponding first variation of $\mathcal{H}[\varphi]$ reads

$$\begin{aligned}\mathcal{H}[\varphi|\delta\varphi] = \left[K_L + K_{NL} \frac{l^2}{L} \int_0^L (\varphi'(s))^2\, ds \right] \left[\int_0^L \varphi'(s)\, \delta\varphi'(s)\, ds \right] + \\ - \int_0^L p(s) \left[\int_0^s \cos\varphi(\bar{s})\, \delta\varphi(\bar{s})\, d\bar{s} \right] ds - M_l\, \delta\varphi(0) - M_r\, \delta\varphi(L) + \\ - F \int_0^L \sin\varphi(s)\, \delta\varphi(s)\, ds + \mu \int_0^L \cos\varphi(s)\, \delta\varphi(s)\, ds\,.\end{aligned} \tag{3.2.11}$$

Consider a variation $\delta\varphi$ with unit mass and centered at s^* with compact support in the interval $(s^* - \frac{\Delta s}{2},\ s^* + \frac{\Delta s}{2})$, as schematically indicated in Figure 3.1(c). One clearly has

$$\int_0^s \cos\varphi(\bar{s})\, \delta\varphi(\bar{s})\, d\bar{s} = \begin{cases} 0\,, & \text{for} \quad s < s^* - \frac{\Delta s}{2}\,, \\ \displaystyle\int_{s^* - \frac{\Delta s}{2}}^{s} \cos\varphi(\bar{s})\, \delta\varphi(\bar{s})\, d\bar{s}\,, & \text{for} \quad s \geqslant s^* - \frac{\Delta s}{2}\,. \end{cases} \tag{3.2.12}$$

By letting $\Delta s \to 0$, the distortion becomes a Dirac Delta distribution centered at $s = s^*$. After integration by parts, one obtains the field equations

$$\left[K_L + K_{NL}\frac{l^2}{L}\int_0^L (\varphi'(s))^2\,ds\right]\varphi''(s^*) + F\sin\varphi(s^*) + \\ + \left[\int_{s^*}^L p(s)\,ds - \mu\right]\cos\varphi(s^*) = 0\,, \tag{3.2.13a}$$

$$\int_0^L \sin\varphi(s)\,ds = 0\,, \tag{3.2.13b}$$

with integral conditions at the boundary

$$\left[K_L + K_{NL}\frac{l^2}{L}\int_0^L (\varphi'(s))^2\,ds\right]\varphi'(0) = -M_l\,, \tag{3.2.14a}$$

$$\left[K_L + K_{NL}\frac{l^2}{L}\int_0^L (\varphi'(s))^2\,ds\right]\varphi'(L) = M_r\,. \tag{3.2.14b}$$

Observe that boundary conditions of this kind do not present the inconvenience discussed in [50] because the nonlocal effect is not obtained as a convolution between the elastic curvature and an averaging kernel, which may provide spurious results when the convolution is evaluated in a neighborhood of the ends of the rod. Here, the flexural stiffness is *homogeneously* increased in the whole rod, according the quadratic mean of the curvature. The classical equations of Euler's (local) elastica are obtained when $K_{NL} = 0$ and, in this limit, the flexural stiffness is K_L.

It is worth mentioning that an interesting result in the classical problem of the elastica, in the case in which no forces or couples are applied to the rod except at the ends, is that there is a conserved quantity, equivalent to the energy-integral of the equations of motion in Kirchhoff's kinetic analogue, expressed by eq. (3) of art. 260 in the treatise by Love [31]. To be more explicit, consider, for example, the simplest case of a cantilever $s \in [0, L]$, initially straight, clamped at $s = 0$ and loaded by the axial force F at $s = L$. In this case, the governing equation can be derived from (3.2.13a) with $K_{NL} = 0$, $p(s) = 0$, $\mu = 0$, and reads $K_L\varphi'' + F\sin\varphi = 0$. In the kinetic analogue [31], substituting differentiation with respect to the variable s with the time derivative, this equation applies to the varying angle $\varphi(t)$ that a rigid pendulum turning around a fixed horizontal axis, with a hanging mass proportional to F, forms with the vertical in the time interval $t \in [0, L]$.

However, in the presented nonlocal theory, the bending stiffness is not constant,

but depends on the squared Lebesgue norm of the curvature, so that the classic argument does not hold. The *periodicity in space* of the curves representing a family of elastica solutions is lost in the nonlocal case, because the bending stiffness depends upon the length of the rod that is considered. Consequently, also the *periodicity in time* in the envisaged kinetic analogue would fail.

Remark. The discretized version of the equilibrium equations (3.2.13) for the nonlocal elastica provides the basis for their numerical solution with the finite difference method, but it also corresponds to the equations for the tensegrity beam of Figure 3.2. Denoting with n the number of subdivisions and with ΔL the discretization step, coinciding with the length of the segment in the flexural-tensegrity counterpart ($\ell_i = \Delta L$, for $i = 1 \dots n$), derivatives are substituted by difference quotients and integrals by summations. Of course, the distributed load $p(s)$ needs to be approximated by a set of forces P_i applied at the segment centroid, such that $p(s_i - \Delta L/2) = P_i/\Delta L$, being $s_i = i\,\Delta L$ the curvilinear abscissa at the $i-$th node. In particular, one can set

$$-\varphi'(s) \simeq \frac{\varphi_i - \varphi_{i+1}}{\Delta L}\,, \quad \varphi''(s) \simeq \frac{\varphi_{i+1} - 2\varphi_i + \varphi_{i-1}}{\Delta L^2}\,, \tag{3.2.15}$$

where φ_i is the absolute rotation of the discretization segment i for $i = 1 \dots n$. Recalling (3.2.8), the discretized form of equations (3.2.13) read

$$\begin{aligned} N\,\frac{a_i - a_{i-1}}{\Delta L} + \left(\mu + \frac{P_i}{2} - \sum_{j=i}^{n} P_j\right)\,\cos\varphi_i - F\,\sin\varphi_i + \\ - \mathbb{I}_1(i)\frac{M_l}{\Delta L} - \mathbb{I}_n(i)\frac{M_r}{\Delta L} = 0\,, \end{aligned} \tag{3.2.16a}$$

$$\sum_{j=1}^{n} \Delta L\,\sin\varphi_j = 0\,, \quad i = 1 \dots n\,, \tag{3.2.16b}$$

where $N = N_0 + K\,\Lambda$, $a_i = l^2\,(\varphi_i - \varphi_{i+1})/\Delta L$, $\Lambda_i = \frac{1}{2}\,l^2\,(\varphi_i - \varphi_{i+1})^2/\Delta L$, and $\Lambda = \sum_{i=1}^{n-1} \Lambda_i$. On the other hand, $\mathbb{I}_i(j)$ is the indicator function, which equals 1 when $i = j$, zero otherwise. Moreover, we have formally set $\varphi_k = 0$ when $k < 1$ or $k > n$, and $a_k = 0$ when $k < 1$ or $k \geqslant n$.

Note that equations (3.2.16) are the same found in Section 2.1.3 and represent an extension of (2.1.15) to a more general loading condition. Specifically, the quantity b_i, indicated in Figure 2.1, is here set to $b_i = \Delta L/2$ and the presence of end moments has been made explicit; in addition, the axial force F has been now introduced.

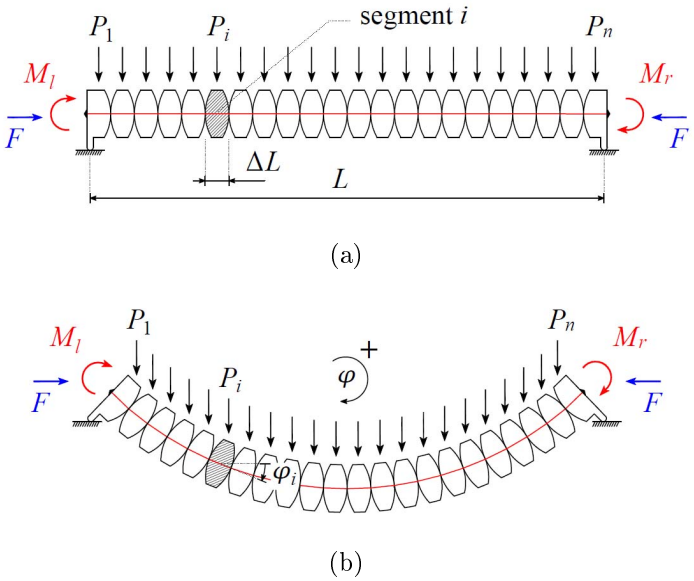

Figure 3.2. Schematic representation of the simply-supported flexural-tensegrity beam. (a) Reference undeformed configuration; (b) deformed state.

3.2.3 Nonlocal effect and the semi-analytical solution

The difference with classical Euler's elastica is represented by the nonlocal term in (3.2.13). In the physical flex-ten segmental model of Figure 3.2, this is consequent to the fact that the tendon (cable) is not bonded to the material matrix, so that its elongation Λ is affected by the whole curvature field. There is a remarkable difference between the present model and a nonlocal elastica for which the bending is governed by the convolution between the curvature field and an average kernel with compact support. In the second case, the nonlocal effect is localized in a neighborhood of the cross section, whereas in our case the bending stiffness is *homogeneously* and *uniformly* modified along the entire length of the rod.

Indeed, it is clear from (3.2.13) and (3.2.14) that the inflexion of the nonlocal elastica is identical to that of a classical Euler's elastica with *effective bending stiffness* K^*, of the form

$$K^* = K_L + K_{NL}\frac{l^2}{L}\int_0^L (\varphi'(s))^2 ds\,. \tag{3.2.17}$$

This observation suggests that, if the solution of the Euler's elastica is known as a function of its bending stiffness, then the solution can be found also for the nonlocal case.

To illustrate, consider the curve attained under applied loads by a classical

Euler's elastica of bending stiffness K^*, and let $\varphi^*(s)$ represent the angle of rotation of its tangent at s with respect to the undeformed straight configuration. Then, calculate the function

$$f(K^*) = \int_0^L \left[(\varphi^*(s))'\right]^2 ds\,. \tag{3.2.18}$$

In order to solve the nonlocal case, it is sufficient to observe from (3.2.17) that

$$K^* = K_L + K_{NL}\frac{l^2}{L}f(K^*) \quad \Rightarrow \quad \frac{(K^* - K_L)L}{l^2 K_{NL}} = f(K^*)\,. \tag{3.2.19}$$

Consequently, the *actual* curve taken by the *nonlocal elastica* is the one corresponding to the deformation of that *Euler's elastica*, whose bending stiffness is found from the intercept of the graph of the function $\eta = f(K^*)$ with the line $\eta = (K^* - K_L)L/(l^2 K_{NL})$.

In general, the solution of Euler's elastica prescribes the calculation of elliptic integrals. In the past, it was necessary to estimate them with tables [52], but, nowadays, they can be evaluated numerically using a commercial software. Since the method described above is based on a analytical formulation, but eventually a numerical approach will be used to solve the elliptic integrals, the solution found in this way will be referred to as the *semi-analytical solution.*

The method is firstly clarified in an elementary example for which the field $\varphi^*(s)$ can be found in closed form, i.e., the case in which the rod of Figure 3.1 is bent by the two couples $M_l = M$ and $M_r = -M$. The deformed shape is an arc of a circle and the rotation field takes the form

$$\varphi^*(s) = \frac{M}{2K^*}(L - 2s)\,. \tag{3.2.20}$$

From (3.2.18) and (3.2.19), the actual stiffness K^* coincides with the real root of the cubic equation

$$\frac{(K^* - K_L)L}{l^2 K_{NL}} = f(K^*) = \frac{M^2 L}{(K^*)^2}\,. \tag{3.2.21}$$

For the case $M = 50\,\mathrm{Nm}$, $K_L = 10\,\mathrm{Nm}^2$, $K_{NL} = 150\,\mathrm{Nm}^2$, $l^2 = 0.1\,\mathrm{m}^2$ and $L = 3\,\mathrm{m}$, its graphical solution, providing the value $K^* = 37.16\,\mathrm{Nm}^2$, is shown in Figure 3.3(a).

The cases in which a concentrated load P is applied at midspan or, alternatively, the rod is axially compressed by two end-forces F, can be similarly treated. The starting point is again the solution of Euler's elastica with arbitrary bending stiffness K^*. Using symmetry, one can equivalently consider a cantilever of length $L/2$ loaded at the free end by a force $P/2$ orthogonal to the undeformed centerline

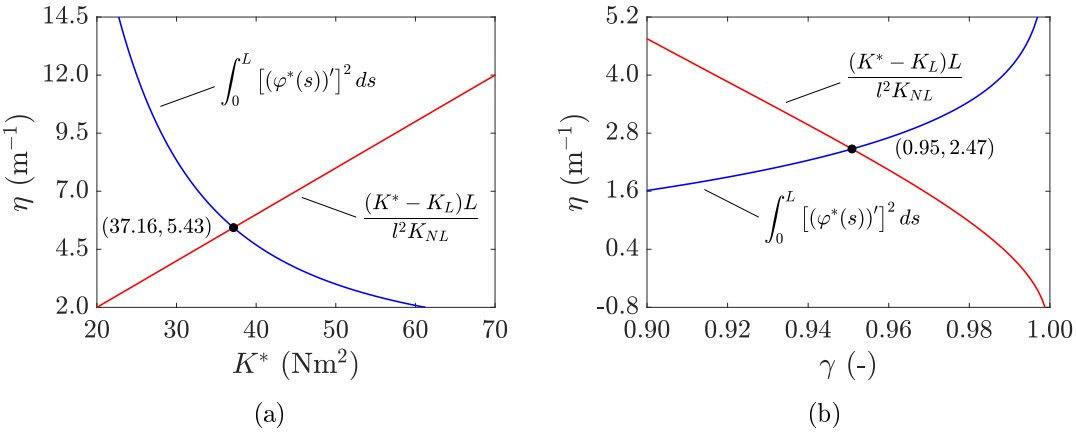

Figure 3.3. Graphs of the functions $\eta = \int_0^L \left[(\varphi^*(s))'\right]^2 ds$ and $\eta = (K^* - K_L)L/(l^2 K_{NL})$ for a simply supported rod subjected to (a) pure bending under end-couples $M_l = -M_r = M$ (plotted as a function of the effective stiffness K^*) and (b) a concentrated force P at midspan (plotted as a function of the elliptic parameter γ). Case $M = 50\,\mathrm{Nm}$, $P = 80\,\mathrm{N}$, $K_L = 10\,\mathrm{Nm}^2$, $K_{NL} = 150\,\mathrm{Nm}^2$, $l^2 = 0.1\,\mathrm{m}^2$ and $L = 3\,\mathrm{m}$.

or by an axial force F. The first case was solved by Bisshopp and Drucker [53], while the second one has been reported in classical books [30, 31] and, more recently, by Bigoni [54]. Let φ_0 represent the rotation at the tip of the cantilever, to be determined. Define the quantities $\mathcal{P}_0$, γ and ϑ_1 as

$$\left.\begin{aligned} &\mathcal{P}_0 = P/2 \\ &\gamma = (1+\sin\varphi_0)/2 \\ &\vartheta_1 = \arcsin(1/\sqrt{2\gamma}) \end{aligned}\right\} \text{ for midspan concentrated load } P\,,$$

$$\left.\begin{aligned} &\mathcal{P}_0 = F \\ &\gamma = (1-\cos\varphi_0)/2 \\ &\vartheta_1 = 0 \end{aligned}\right\} \text{ for compression axial load } F\,.$$

Then, for any value of the bending stiffness K^*, the value $\gamma = \gamma^*$ that solves the problem is found from the equation

$$K^* = \frac{\mathcal{P}_0 L^2}{4\left[\mathcal{F}(\frac{\pi}{2},\gamma) - \mathcal{F}(\vartheta_1,\gamma)\right]^2}\,, \tag{3.2.22}$$

where

$$\mathcal{F}(\phi,\gamma)=\int_0^{\phi}\frac{d\theta}{\sqrt{1-\gamma\sin^2\theta}}\,, \tag{3.2.23}$$

represents the incomplete elliptic integral of the first kind. The actual value ${\varphi_0}^*$ can be determined once γ^* is known. The corresponding curvature field $\chi^*=-(\varphi^*(s))'$ admits the representation

$$(\varphi^*(s))'=\begin{cases}\sqrt{\dfrac{P}{K^*}}\left[\sin{\varphi_0}^*-\sin\varphi^*(s)\right]^{\frac{1}{2}} & \text{for midspan load } P\,,\\[2ex] \sqrt{\dfrac{2F}{K^*}}\left[\cos\varphi^*(s)-\cos{\varphi_0}^*\right]^{\frac{1}{2}} & \text{for axial load } F\,.\end{cases} \tag{3.2.24}$$

Hence, one finds the intercept of $\eta=f(K^*)$ with the line $\eta=(K^*-K_L)L/(l^2K_{NL})$. It should be observed that (3.2.24) can be conveniently expressed through elliptic integrals as a function of the only variable γ, so that the elliptic parameter γ can be used to restate the condition (3.2.19). After some calculations, one finds that the solution $\gamma=\gamma^*$ for the *nonlocal elastica* is the solution of the equation

$$\begin{aligned}\eta&=f\left(K^*(\gamma)\right)=\int_0^L\left(\varphi'(s,\gamma)\right)^2ds=\\ &=\frac{16\,\gamma}{L}\left[\mathcal{F}(\tfrac{\pi}{2},\gamma)-\mathcal{F}(\vartheta_1,\gamma)\right]\left[\mathcal{F}(\tfrac{\pi}{2},\gamma)-\mathcal{F}(\vartheta_1,\gamma)-\mathcal{D}(\tfrac{\pi}{2},\gamma)+\mathcal{D}(\vartheta_1,\gamma)\right]=\\ &=\frac{\mathcal{P}_0L^3}{4\,l^2K_{NL}[\mathcal{F}(\frac{\pi}{2},\gamma)-\mathcal{F}(\vartheta_1,\gamma)]^2}-\frac{K_LL}{l^2K_{NL}}=\frac{[K^*(\gamma)-K_L]\,L}{l^2K_{NL}}\,,\end{aligned} \tag{3.2.25}$$

where $\mathcal{D}(\phi,\gamma)$ is a combination of the incomplete elliptic integral of the first kind $\mathcal{F}(\phi,\gamma)$ and the incomplete elliptic integral of the second kind $\mathcal{E}(\phi,\gamma)$, which take the form

$$\mathcal{E}(\phi,\gamma)=\int_0^{\phi}\sqrt{1-\gamma\sin^2\theta}\,d\theta\,, \tag{3.2.26}$$

$$\mathcal{D}(\phi,\gamma)=\frac{\mathcal{F}(\phi,\gamma)-\mathcal{E}(\phi,\gamma)}{\gamma}=\int_0^{\phi}\frac{\sin^2\theta\,d\theta}{\sqrt{1-\gamma\sin^2\theta}}\,. \tag{3.2.27}$$

For the same material parameters considered for the case of Figure 3.3(a), Figure 3.3(b) shows the graphical solution of (3.2.19) in terms of the elliptic parameter γ for the case of a midspan load $P = 80\,\mathrm{N}$. In this way, one obtains the value $\gamma^* = 0.95$ and, from this, $K^* = 22.35\,\mathrm{Nm}^2$ and ${\varphi_0}^* = 1.12\,\mathrm{rad}$.

The semi-analytical approach could also be used when the rod of Figure 3.1 is bent by a load $p(s)$ distributed along its length. When $p(s)$ follows a constant, triangular or sinusoidal law, the deformation of the Euler's elastica can be found [55] in terms of Lauricella ${F_D}^{(3)}$ hypergeometric functions [56]. However the calculations become very complicated, so that a simple numerical method based on finite differences, through equations (3.2.16), turns out to be much more convenient.

To conclude this section, it may be useful to estimate the "strength" of the nonlocal effect with reference to the physical interpretation of parameters via the flexural-tensegrity model. Assume that, in the flex-ten equivalent beam, the cable is characterized by Young's modulus E, cross sectional area A and undistorted length L_0, so that its axial stiffness is given by $K = EA/L_0$. Using (3.2.8), the effective stiffness (3.2.17) becomes

$$K^* = l^2 N_0 + \frac{l^4}{2}\frac{EA}{L_0}\int_0^L \left(-\varphi'(s)\right)^2 ds\,. \tag{3.2.28}$$

To be noticed is that the intrinsic length scale l affects both the local and the nonlocal stiffness, but with different powers. The term $l^2 N_0$ determines the tangent stiffness at the origin. When the tendon is highly pre-stressed with respect to its axial stiffness ($N_0 \gg EA\,L/L_0$) and/or the curvature is small ($\varphi'(s) \ll 1/L$), the model falls within the framework of Euler's (local) elastica. In the simplest case of pure bending according to an arc of a circle, the rotation field is given by (3.2.20). Setting ${\varphi_0}^* = \varphi^*(0) = -\varphi^*(L)$, one finds that $(\varphi^*(s))' = -2{\varphi_0}^*/L$, so that the radius of curvature is $\rho = 0.5L/{\varphi_0}^*$. Consequently, assuming for simplicity that $L_0 \simeq L$, equation (3.2.28) can be written in the form

$$K^* = l^2\left(N_0 + \frac{l^2}{2\rho^2}\,EA\right)\,. \tag{3.2.29}$$

As an order of magnitude $N_0 \simeq 10^{-4}AE$. Hence, the nonlocal term becomes greater than the local one when approximately $\rho < 70\,l$. This simple example highlights that there is a close correlation between macroscopic curvature and intrinsic length-scale l in the nonlocal term.

3.2.4 Numerical solutions

The semi-analytical method described in Section 3.2.3 makes it possible to establish a correspondence between the classical Euler's elastica and its nonlocal

counterpart. However, it is much faster nowadays to directly solve numerically the integro-differential equations (3.2.13) and (3.2.14). The comparison of the solutions obtainable with the semi-analytical and the numerical methods mutually proves their reliability, since the approaches are completely different in type.

The discretized version of the governing equations can be obtained through the approximation (3.2.15). The interval $[0, L]$ is divided into n equal segments of length $\Delta L = L/n$, and the nonlinear system of algebraic equations (3.2.16) is solved. Recall that such system corresponds to the solution for the flexural-tensegrity physical model represented in Figure 3.2, when the length of the segments coincides with the discretization step. Segmental beams composed of a limited number of segments (of the order of 10) have been analyzed in detail in Chapter 2, but our interest here is to tackle to continuum problem by means of its discrete approximation. Therefore, it is necessary to check the convergence of the numerical solution as the number of subdivisions increases.

For the discretized problem, we have used the numerical solver `fsolve` implemented in Matlab® [57], which is based on the Levenberg-Marquardt [58] and trust-region [59] methods developed from nonlinear least-squares algorithms.

For the rod of Figure 3.1, subjected only to a concentrated force $P = 30\,\mathrm{N}$ at midspan, with reference to the case $L = 3\,\mathrm{m}$, $K_L = 10\,\mathrm{Nm}^2$, $K_{NL} = 150\,\mathrm{Nm}^2$ and $l^2 = 0.1\,\mathrm{m}^2$, Figure 3.4(a) shows the plots of the deformation as the number n of subdivisions is augmented. On the other hand, Figure 3.4(b) reports the maximum deflection v_m again as a function n. A good approximation is obtained with $n = 49$ since the difference is less than 0.032% when passing to $n = 99$.

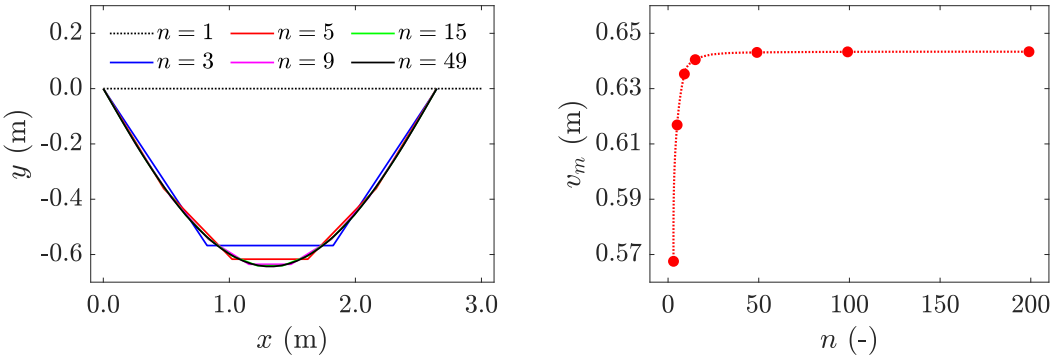

Figure 3.4. Numerical results obtained with an increasing number n of subdivisions for a simply supported rod under a concentrated load $P = 30\,\mathrm{N}$ at midspan: (a) Deformed curve for various n and (b) maximum midspan deflection v_m as a function of n. Case $L = 3\,\mathrm{m}$, $K_L = 10\,\mathrm{Nm}^2$, $K_{NL} = 150\,\mathrm{Nm}^2$ and $l^2 = 0.1\,\mathrm{m}^2$.

It should also be mentioned that fairly accurate estimates of the solution can be obtained by using appropriate shape functions for the rotation field $\varphi(s)$. In particular, consider

$$\varphi(s) = \varphi_0 \cos\frac{\pi s}{L}, \tag{3.2.30}$$

where φ_0 is the shape parameter, representing the rotation at the ends of the simply supported rod (Figure 3.1). The constraint equation (3.2.13b) is automatically satisfied. Then, the shape function is inserted in the energy functional represented by (3.2.7) and (3.2.9), which thus becomes an algebraic function of φ_0. The optimal value of φ_0 is found through minimization. A further useful simplification consists in expanding in Taylor's series the sine (up to the fifth order) and cosine functions (up to the fourth order), so that the energy reduces to a polynomial of the 5^{th} degree in φ_0. We have verified that when the midspan deflection is less than $L/5$, this method provides excellent results under uniformly distributed loads, but it is also sufficiently accurate under a concentrated load at midspan and for the first mode of axial buckling, as it will be shown in the forthcoming examples.

3.3 Examples

The rod of Figure 3.1 is here analyzed when subjected to axial load, concentrated load at midspan and uniformly distributed load. Results obtained with the semi-analytical method illustrated in Section 3.2.3 are compared with those obtainable with a direct numerical approach, as per Section 3.2.4. For the case of moderately inflexed rods, with no loops, we discuss the approximation via shape function. Unless stated otherwise, reference is made to the case $L = 3\,\mathrm{m}$, $K_L = 10\,\mathrm{Nm}^2$, $K_{NL} = 150\,\mathrm{Nm}^2$ and $l^2 = 0.1\,\mathrm{m}^2$.

In order to compare the theoretical curves obtained from the nonlocal continuum theory with the physical model of flex-ten beams, the prototype displayed in Figure 3.5 has been manufactured in the same way indicated in Section 2.1.1. The prototype, 3D printed in polyethylene terephthalate, is composed of 32 segments of length 17.3 mm (total length of 553.6 mm), for which $l^2 = 100.6\,\mathrm{mm}^2$. The prestressing cable is a polyamide 6.6 wire of diameter 0.8 mm, with two springs of constant $k = 2.8\,\mathrm{N/mm}$ added in series, as shown in Figure 3.5(a), so that $K_{NL} \simeq 21375\,\mathrm{Nmm}^2$. The deformation under self-weight is represented in Figure 3.5(b). The relative displacement of any two consecutive segments is a rolling motion along the design circular pitch lines, which has been obtained in the practice by shaping the contact surfaces with a double couple of conjugate profiles, according to the layered construction detailed in Section 2.1.1.

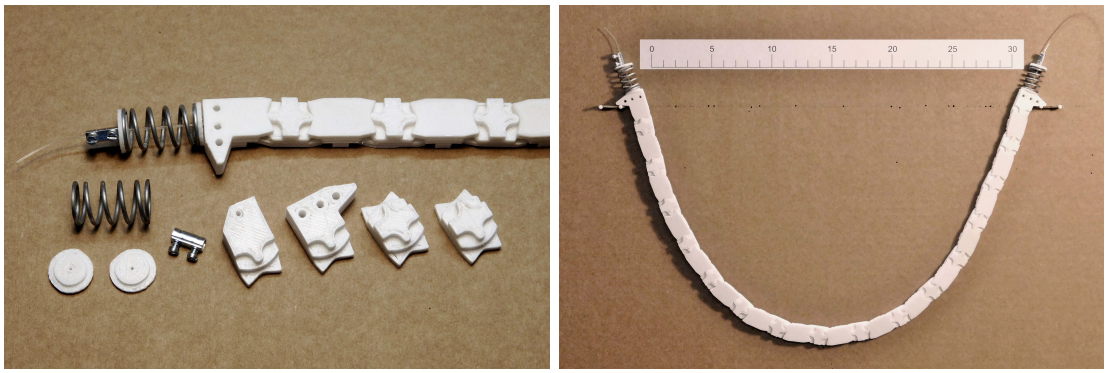

(a) (b)

Figure 3.5. Flexural-tensegrity segmental beam used for comparisons with the nonlocal elastica: (a) constituting segments for which the theoretical pitch lines at the contact surfaces are obtained with a double couple of conjugate profiles; (b) deflection of the prototype under self-weight.

3.3.1 Axial load and buckling

Suppose that only a compression force F is applied ($M_l = M_r = 0$ and $p(s) = 0$). The Lagrange's multiplier μ is null and the differential equation (3.2.13a) becomes

$$\left[K_L + K_{NL}\frac{l^2}{L}\int_0^L (\varphi'(s))^2 ds\right]\varphi''(s) + F\sin\varphi(s) = 0\,. \tag{3.3.31}$$

To determine the bifurcation limit for buckling, only small perturbations in a neighborhood of the reference straight configuration need to be considered. Assuming $\varphi \ll 1$, the nonlocal term becomes negligible; setting $\sin(\varphi(s)) \simeq \varphi(s)$, the critical load $F_{cr} = K_L\pi^2/L^2$ is found. For the case at hand $F_{cr} \simeq 10.97\,\mathrm{N}$.

The post-critical deformation (first mode) has been evaluated in three different ways: with the semi-analytical approach, numerically and by using the shape function (3.2.30). In the latter case, the equilibrium condition furnishes the shape parameter φ_0 as the solution of the equation

$$\left(\frac{K_{NL}l^2\pi^4}{2L^4} + \frac{F}{8}\right)\varphi_0^2 + \left(\frac{K_L\pi^2}{L^2} - F\right) = 0\,. \tag{3.3.32}$$

Figure 3.6(a) shows the deformation corresponding to four different values of $F > F_{cr}$. The curves associated with the two lower loads ($F = 20,\ 40\,\mathrm{N}$), calculated with all the three aforementioned methods (semi-analytical, numerical, shape-function), show an excellent correspondence. The other curves ($F = 60,\ 80\,\mathrm{N}$) cannot be accurately determined with the shape function. A quantitative compar-

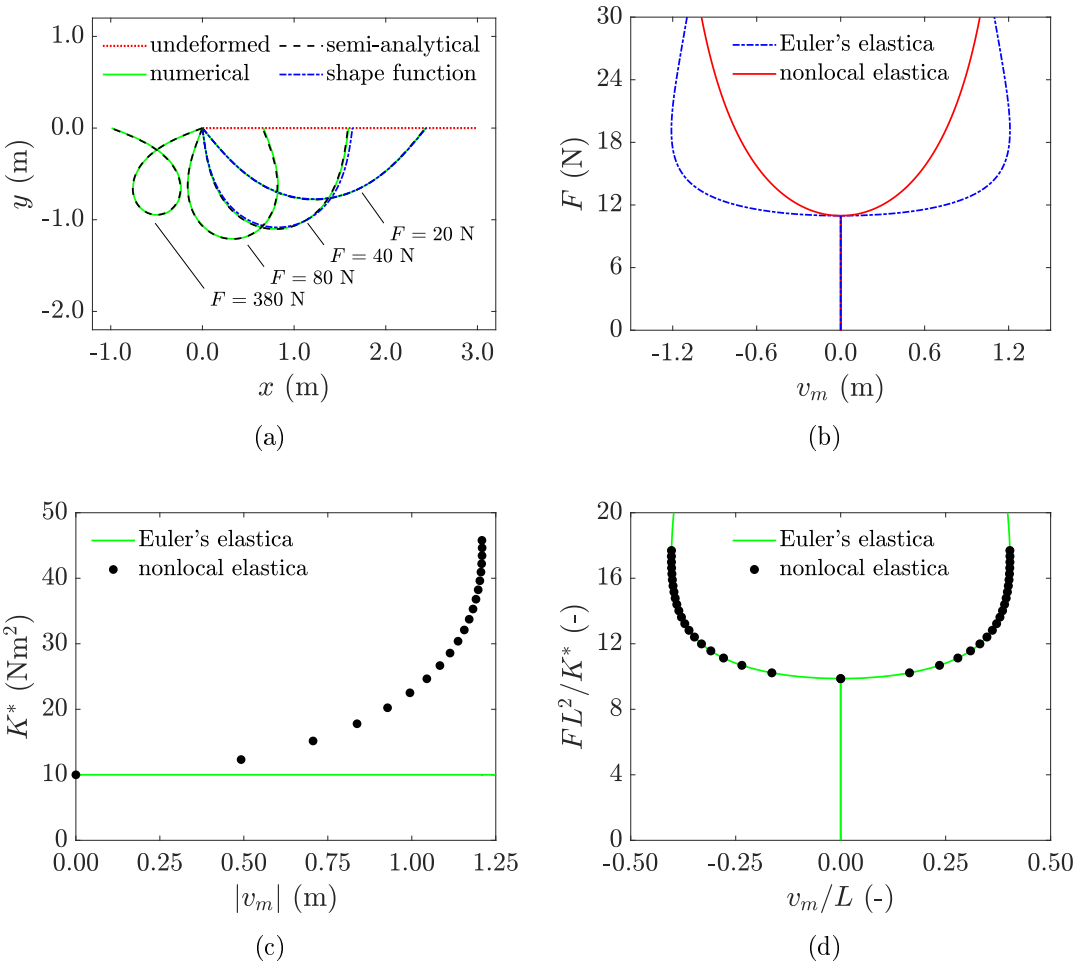

Figure 3.6. Nonlocal elastica under the axial load $F \geqslant F_{cr}$. (a) Post-buckling deformation for different values of F; (b) graph of F as a function of the inflexion v_m at midspan and comparison with Euler's elastica; (c) effective stiffness K^* as a function of $|v_m|$; (d) non-dimensional plot of the load-displacement curves.

ison is made in Table 3.1 in terms of maximum inflexion $|v_m|$ at midspan.

The plot of F against v_m is shown in Figure 3.6(b), together with the graph corresponding to the case $K_{NL} = 0$, from now on referred to as *Euler's elastica* or *local elastica*. It is clear that the nonlocal term provides additional stiffness since a slight increase of $|v_m|$ with respect to the bifurcation point is associated with an almost quadratic increment of F; on the other hand, in the Euler's elastica, F remains almost constant within the range $|v_m| \leqslant 0.5\,\mathrm{m}$.

Figure 3.6(c) reports the bending stiffness K^* as per (3.2.17) as a function of $|v_m|$. Observe that for large deflections the contribution from the nonlocal term

Table 3.1. Maximum inflexion $|v_m|$ at midspan under the axial load $F > F_{cr}$. Results obtained with the semi-analytical approach, the numerical method and the shape function, and corresponding difference (in percentage) with respect to the semi-analytical solution.

Axial Load F	Semi-analytical	Numerical ($n = 199$)	Percentage difference	Shape function	Percentage difference
20 N	0.7800 m	0.7781 m	0.24 %	0.7742 m	0.74 %
40 N	1.1017 m	1.0997 m	0.18 %	1.0831 m	1.69 %
80 N	1.2097 m	1.2087 m	0.08 %	-	-
380 N	0.9453 m	0.9474 m	0.22 %	-	-

may overcome several times the tangent stiffness, which coincides with the stiffness of Euler's elastica.

Figure 3.6(d) is the most interesting one since it shows the non-dimensional quantity FL^2/K^*, plotted as a function of v_m/L. While presenting the semi-analytical method in Section 3.2.3, it has been demonstrated that a nonlocal elastica responds as an Euler's elastica with bending stiffness K^* given by (3.2.17). This means that the deformed shape of Euler's elastica, with bending stiffness K_L, under the force F, perfectly overlaps with the curve attained by the nonlocal elastica when bent by the generic force $F\,K^*/K_L$. Hence, it is not surprising that the black dots, associated with the *nonlocal* model, perfectly overlap with the curve corresponding to the *local* case. In other words, the ratio F/K^* represents the invariant describing the self-similarity associated with the same deformed shape for the local and the nonlocal cases.

For the sake of comparison with a physical model, consider now the flex-ten beam that was illustrated in Figure 3.5, for which $L = 553.6\,\text{mm}$, $l^2 = 100.6\,\text{mm}^2$, $K_L = 3475\,\text{Nmm}^2$ and $K_{NL} = 21375\,\text{Nmm}^2$. The deformed shapes consequent to the application of the two forces F can be equivalently obtained by imposing the relative displacement of the ends, so that F represents the constraint reaction. Figure 3.7 reports four different configurations which correspond to the cases illustrated in Figure 3.6(a) with respect to the aforementioned self-similarity. The blue dots that are overdrawn on the photographs indicate the deformation predicted by the theoretical continuum model with the same material parameters, calculated by using the semi-analytical method. The comparison shows a very good agreement.

3.3.2 Rod bent by a concentrated force at midspan

When only a concentrated force P acts at midspan ($F = 0$ and $M_l = M_r = 0$), the Lagrange's multiplier is $\mu = P/2$ and the differential equation (3.2.13a) becomes

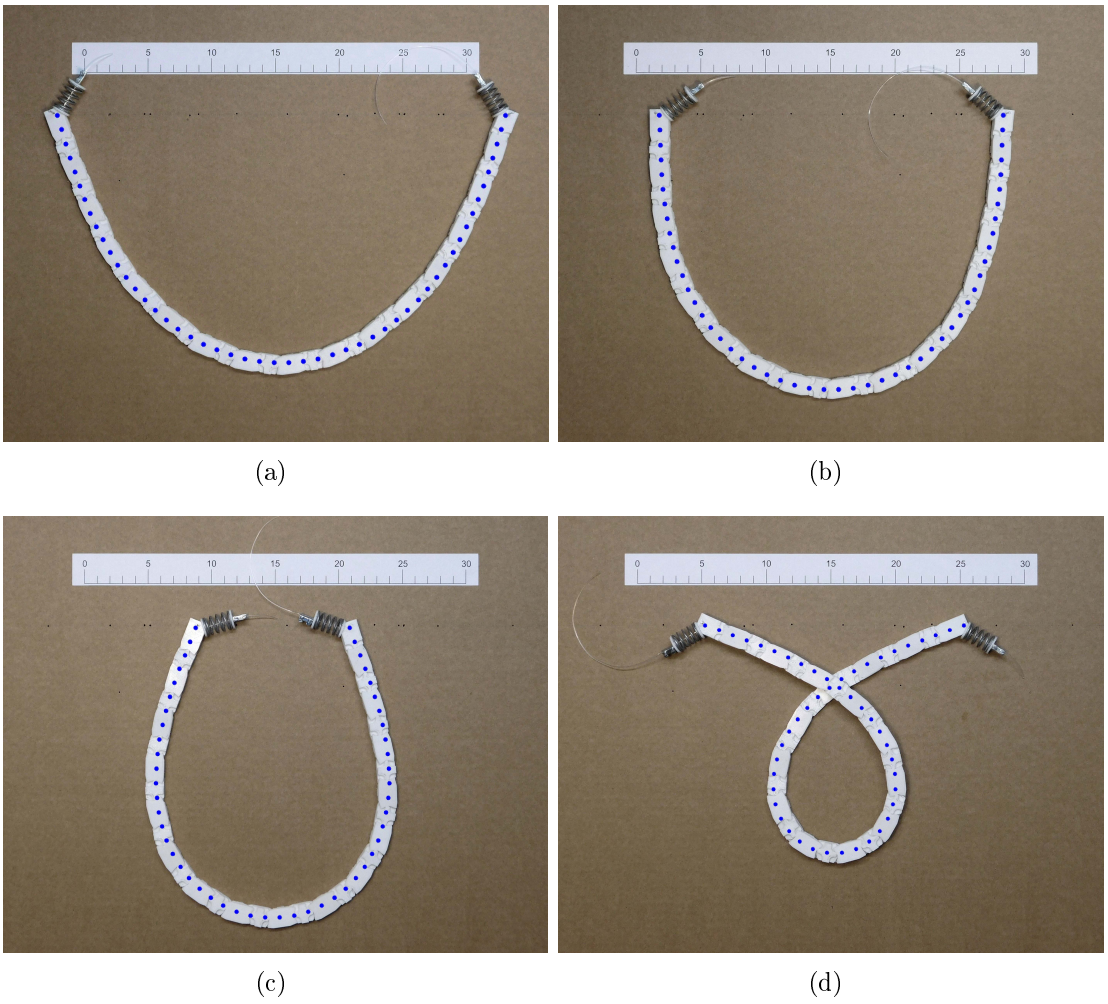

Figure 3.7. Post-buckling deformations of the flex-ten beam for different values of the relative displacement assigned at the ends. Imposed end displacements correspond to axial force: (a) $u(L) = 198\,\mathrm{mm}$, (b) $u(L) = 286\,\mathrm{mm}$, (c) $u(L) = 432\,\mathrm{mm}$ and (d) $u(L) = 755\,\mathrm{mm}$ (closed loop). The overdrawn blue dots correspond to the semi-analytical solution of the nonlocal-elastica continuum model.

$$\left[K_L + K_{NL}\frac{l^2}{L}\int_0^L (\varphi'(s))^2 ds\right]\varphi''(s) \pm \frac{P}{2}\cos\varphi(s) = 0\,, \tag{3.3.33}$$

where the "plus" ("minus") sign holds for $L/2 \leqslant s \leqslant L$ $(0 \leqslant s < L/2)$.

Using the shape function (3.2.30) and expanding in Taylor's series the trigonometric functions, as indicated in Section 3.2.4, one obtains the polynomial equation

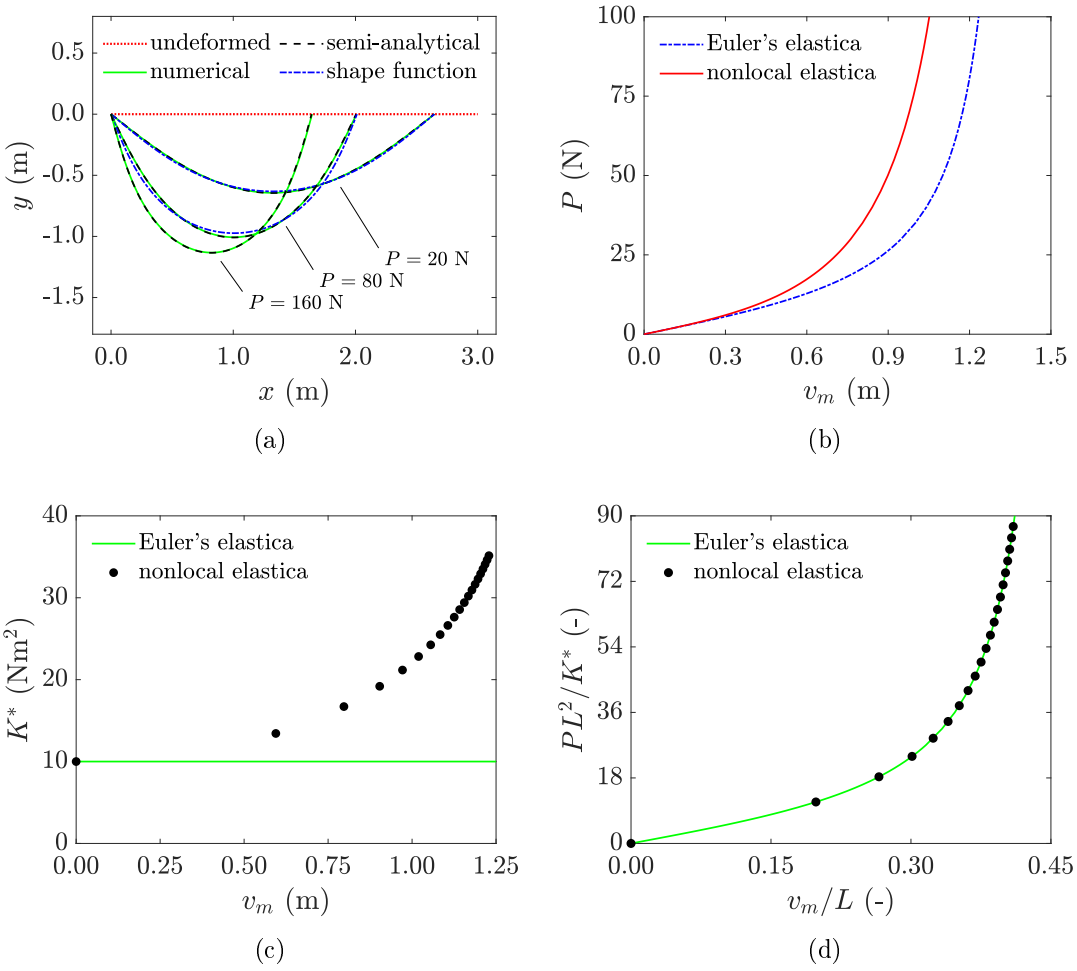

Figure 3.8. Nonlocal elastica under the concentrated load P at midspan. (a) Deformation for different values of P; (b) graph of P as a function of maximum inflexion v_m at midspan and comparison with Euler's elastica; (c) effective stiffness K^* as a function of v_m; (d) non-dimensional plot of the load-displacement curves.

$$P\,\frac{1}{45}\,\frac{L}{\pi}\,\varphi_0^4 - \frac{K_{NL}l^2\pi^4}{4L^3}\,\varphi_0^3 - P\,\frac{1}{3}\,\frac{L}{\pi}\,\varphi_0^2 - \frac{K_L\pi^2}{2L}\,\varphi_0 + P\,\frac{L}{\pi} = 0\,. \tag{3.3.34}$$

The plots of the deformed shape obtained with the semi-analytical method, the numerical approach and the shape function are juxtaposed in Figure 3.8(a). The agreement between the semi-analytical and numerical methods is again excellent. The accuracy of the shape function is still rather good, with maximum differences

Table 3.2. Maximum inflexion v_m under concentrated load P at midspan. Results obtained with the semi-analytical approach, the numerical method and the shape function, and corresponding difference (in percentage) with respect to the semi-analytical solution.

midspan Load P	Semi-analytical	Numerical ($n = 199$)	Percentage difference	Shape function	Percentage difference
20 N	0.6448 m	0.6434 m	0.22 %	0.6314 m	2.08 %
80 N	1.0085 m	1.0068 m	0.17 %	0.9734 m	3.48 %
160 N	1.1340 m	1.1325 m	0.13 %	-	-

in terms of v_m of about 3.5%, at least for the loads $P = 20, 80\,N$ (the case $P = 160\,\mathrm{N}$ is not considered because accuracy is lost). The quantitative comparison in terms of maximum deflection v_m is recorded in Table 3.2, which is the counterpart of Table 3.1.

The relationships between P and v_m are plotted in Figure 3.8(b) and compared with the local model of Euler's elastica: the additional stiffness provided by the nonlocal term is evident. Figure 3.8(c) reports the effective stiffness K^* for increasing inflexion, measured through the variable v_m. Figure 3.8(d), which is the counterpart of Figure 3.6(d), shows the non-dimensional plot of the load-displacement curves for Euler's elastica and the nonlocal elastica. Again the black dots, corresponding to the nonlocal case, perfectly overlap with the graph corre-

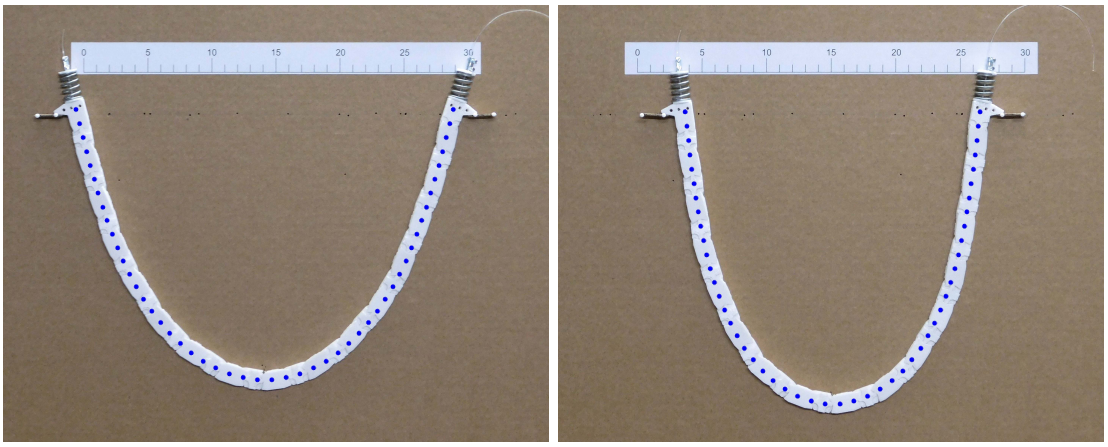

(a) (b)

Figure 3.9. Flexural-tensegrity segmental beam under imposed displacements at midspan (equivalent to concentrated load at midspan): (a) $v(L/2) = 211\,\mathrm{mm}$ and (b) $v(L/2) = 226\,\mathrm{mm}$. The overdrawn blue dots correspond to the semi-analytical solution of the nonlocal-elastica continuum model.

Table 3.3. Maximum inflexion v_m under uniformly distributed load p_0. Results obtained numerically and with the shape function, and corresponding difference (in percentage).

Distributed Load p_0	Numerical ($n = 199$)	Shape function	Percentage error
10 N/m	0.6082 m	0.6097 m	0.25 %
30 N/m	0.8897 m	0.8861 m	0.40 %
100 N/m	1.0962 m	1.0719 m	2.22 %

sponding to local case. This confirms what already indicated for case of the axial force: the nonlocal elastica is equivalent to a local Euler's elastica with a bending stiffness that depends upon the deformation.

Figure 3.9 reports the comparison between the response of the flexural tensegrity segmental beam of Figure 3.5, with the same constitutive parameters, and that of the nonlocal model (blue dots). The effect of a concentrated load at midspan has been equivalently evaluated by imposing a vertical displacement at the same point. The agreement is again very good.

3.3.3 Rod bent by uniformly distributed load per unit length

Having set $M_l = M_r = 0$ and $F = 0$, the effect of a uniformly distributed load $p(s) = p_0$ is now investigated. The solution has been obtained either by means of the shape function (3.2.30) or numerically. For this case, the semi-analytical method is not feasible. An analytical solution for Euler's elastica has been presented by [55] in terms of Lauricella's hypergeometric functions, but it is limited to the range $0.0594 < p_0 L^3/K^* < 6$ and its expression is really complicated.

For this case, the Lagrange's multiplies is $\mu = p_0 L/2$ and the differential equation (3.2.13a) becomes

$$\left[K_L + K_{NL}\frac{l^2}{L}\int_0^L (\varphi'(s))^2 ds\right]\varphi''(s) + p_0\,\frac{L-2s}{2}\,\cos\varphi(s) = 0\,. \tag{3.3.35}$$

By using the shape function (3.2.30) and expanding in Taylor's series the trigonometric functions, one obtains the polynomial equation

$$p_0\,\frac{149}{2700}\,\frac{L^2}{\pi^2}\,\varphi_0^4 - \frac{K_{NL}l^2\pi^4}{4L^3}\,\varphi_0^3 - p_0\,\frac{7}{9}\,\frac{L^2}{\pi^2}\,\varphi_0^2 - \frac{N_0 l^2\pi^2}{2L}\,\varphi_0 + 2\,p_0\,\frac{L^2}{\pi^2} = 0\,. \tag{3.3.36}$$

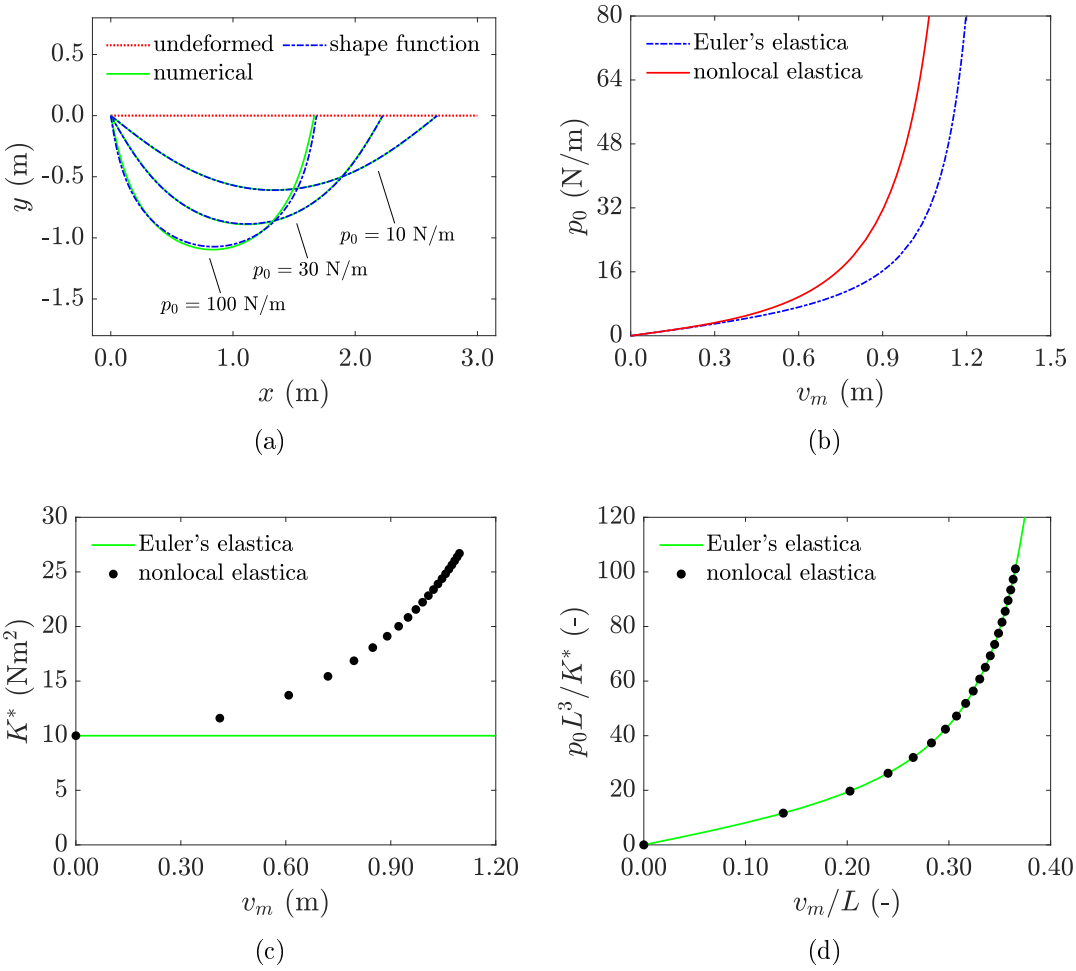

Figure 3.10. Nonlocal elastica under uniformly distributed load p_0. (a) Deformation for different values of p_0; (b) graph of p_0 as a function of maximum inflexion v_m at midspan and comparison with Euler's elastica; (c) effective stiffness K^* as a function of v_m; (d) non-dimensional plot of the load-displacement curves.

The deformations resulting from the two approaches (numerical and shape function) are juxtaposed in Figure 3.10(a) for $p_0 = 10,\ 30,\ 100\,\mathrm{N/m}$. Table 3.3 records the maximum deflection v_m as a function of p_0. Observe that the shape function provides a difference less than 0.5% with respect to the numerical calculation when $v_m < L/3$.

The dependence of v_m on p_0 is shown in Figure 3.10(b). Figure 3.10(c) compares the values of K^* against v_m for the nonlocal case (black dots) and the local Euler's elastica (continuous line). The same conclusions drawn in the previous Sections

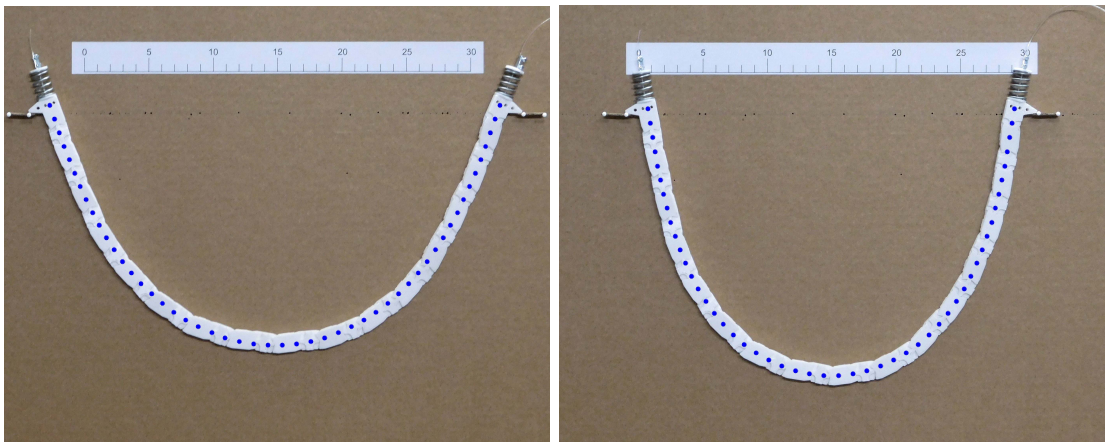

(a) (b)

Figure 3.11. Flexural-tensegrity segmental beam under uniformly distributed load. The distributed load was self-weight ($P_i = 0.02\,\mathrm{N}$ for each segment i, $i = 1 \dots 32$) and the different value of deflection is obtained by varying the tension force in the cable: (a) $N_0 = 44.1\,\mathrm{N}$ and (b) $N_0 = 23.7\,\mathrm{N}$. The overdrawn blue dots correspond to the numerical solution of the nonlocal-elastica continuum model.

3.3.1 and 3.3.2 also apply in this case. The non-dimensional plot of the function $p_0 L^3/K^*$ vs. v_m/L, shown in Figure 3.10(d), confirms again that the nonlocal elastica perfectly corresponds to an equivalent Euler's elastica with appropriate stiffness.

Figure 3.11 shows the comparison between the deformation of nonlocal elastica (blue dots), numerically calculated, and the flex-ten beam of Figure 3.5 under the uniformly distributed load corresponding to self-weight. The two different deflections have been obtained by varying the initial tensile force in the cable (either $N_0 = 23.7\,\mathrm{N}$ or $N_0 = 44.1\,\mathrm{N}$), which is equivalent to a variation in the initial stiffness, so that, for the tested model, one has $L = 553.6\,\mathrm{mm}$, $l^2 = 100.6\,\mathrm{mm}^2$, either $K_L = 2383\,\mathrm{Nmm}^2$ or $4435\,\mathrm{Nmm}^2$, and $K_{NL} = 21375\,\mathrm{Nmm}^2$. Again the theoretical and the physical models provide overlapping results.

Chapter 4

Dynamic aspects

The problem of vibrations of flexural-tensegrity segmental assemblies is here considered. Specifically, the case of flex-ten beams is analyzed and it is shown that this can represent a sufficiently rich model to illustrate, with paradigmatic examples, complex nonlinear effects in the mechanics of vibrations. Most of the properties are consequent to the way in which the unbonded cable, after prestressing, is fixed to the end segments. In particular, elastic springs in parallel with viscoelastic dampers, as in a Kelvin-Voigt model, can be interposed between the end segments and the anchorage points of the cable, in order to achieve a passive control of the vibrations; moreover, the cable tensile force could also be modified by an actuator, for an active control on the basis of a sensor input.

The variation of tensile force in the cable consequent to its inflexion-induced elongation provokes the bending stiffening of the beam. This represents a higher order term that renders the oscillations nonlinear [60,61] from a constitutive point of view (*nonlinear stiffness*). The classical example is represented by a Duffing oscillator [62], where a cubic term is present.

Another source of nonlinearity results from the viscoelastic damper at the cable ends, even when this is a simple dashpot whose force is a *linear* function of the velocity only, because the beam inflexion nonlinearly affects the relative displacement of the points connected by the dashpot. *Nonlinear damping* has been measured in aerospace structures, such as real-scale aircraft wings [63], in graphene and carbon nanotubes at the nano-scale [64], but also in common shock absorbers for automotive applications [65]. However, it is perhaps much less known that even in beams, plates and shells made of a homogenous material like steel, and even more so in laminated sandwich panels, the most significant effect during nonlinear vibrations is the increase of damping with the vibration amplitude [66,67]. Based on this evidence, in [68] a consistent derivation of nonlinear damping was obtained for rectangular plates made of a viscoelastic material within a geometric nonlin-

ear theory. In flex-ten beams, the nonlinear character of the damping is naturally obtained, in the gross structural response, from simple kinematics.

The possibility of modifying the tensile force in the cable through an actuator permits to artfully manipulate the bending stiffness of the beam. A periodically variable stiffness represents a parametric excitation that can lead to phenomena of *parametric resonance*, similar to those occurring in cables with harmonically excited supports [69], when the external excitation frequency equals twice the natural frequency of the system. Such phenomenon may lead to instabilities that are interpreted by Mathieu's equation [70] for a linear oscillator but, in the case at hand, the nonlinear character of the bending stiffness allows to reach a limit amplitude at any frequency. On the other hand, the parametric excitation can be imposed in opposition of phase to the natural oscillations, measured by a sensor, in order to produce an *active control* of the vibrations [71]. Remarkably, since the structure is characterized by a strongly nonlinear damping, the active control may be directed at modifying the amplitude of the oscillations in order to obtain the maximum dissipation in the shortest time. This represents, to our knowledge, a possibility that has never been explored before, whose potentialities are yet to be fully appreciated.

This chapter intends to be illustrative about the topic of vibrations in flex-ten beams and, for this reason, simplified approaches are used. In particular, after a detailed derivation, in Section 4.1, of the dynamic equations for the segmental beam, the equivalent continuum model is adopted in Section 4.2 under the hypothesis that the length of the segments is much smaller than the length of the beam. Then, by using an appropriate shape function for the rotation field of the continuous beam, which proved to be accurate also for large deflections under transversal loads (see Section 3.3), the problem can be reduced to that of a single-degree-of-freedom (SDOF) oscillator. The nonlinear response of a simply supported beam under harmonic uniformly-distributed transversal actions is analyzed, evidencing the role played by nonlinear damping and by the presence of an initial camber due, e.g., to self-weight. Furthermore, the possibility of artfully controlling the tensile axial force in the cable is investigated. This may lead to nonlinear phenomena of parametric resonance, or may serve to suppress pre-existing oscillatory motions.

Some of the results presented here are also available in [72].

4.1 The dynamic problem for a segmental beam

The dynamic problem for flex-ten segmental beams is here introduced, and the corresponding nonlinear governing equations are obtained thanks to Hamilton's principle. Experiments on simple SDOF cantilevers, composed of two segments

coupled by one joint, suggest how to model the possible sources of dissipation, by means of viscous damping and additional frictional moments.

4.1.1 Dynamic equilibrium equations

Postponing to the next sections the detailed discussion about the possible sources of damping, the response of the flex-ten beam is governed by the variation ΔU of elastic potential energy from the reference state under null external loads, the work ΔW of external (conservative) forces from such reference state and the kinetic energy T of the moving segments. With reference to the notation introduced in Figures 2.1 and 2.10, and recalling Section 2.1.3, these quantities take the form

$$\Delta U = N_0\Lambda + \frac{1}{2}K\Lambda^2 = N_0\sum_{i=1}^{n-1}\Lambda_i + \frac{1}{2}K\left(\sum_{i=1}^{n-1}\Lambda_i\right)^2, \tag{4.1.1a}$$

$$\begin{aligned}\Delta W = &\sum_{i=1}^{n}\left\{P_i\left[\left(\sum_{j=1}^{i}\ell_j\sin\varphi_j\right) - \frac{\ell_i}{2}\sin\varphi_i\right]\right\} + \\ &+ \sum_{i=1}^{n}\left\{F_i\left[\left(\sum_{j=1}^{i}\ell_j\Big(1-\cos\varphi_j\Big)\right) - \frac{\ell_i}{2}\Big(1-\cos\varphi_i\Big)\right]\right\},\end{aligned} \tag{4.1.1b}$$

$$\begin{aligned}T = &\frac{1}{2}\sum_{i=1}^{n}m\ell_i\left\{\frac{\partial}{\partial t}\left[\left(\sum_{j=1}^{i}\ell_j\sin\varphi_j\right) - \frac{\ell_i}{2}\sin\varphi_i\right]\right\}^2 + \\ &+ \frac{1}{2}\sum_{i=1}^{n}m\ell_i\left\{\frac{\partial}{\partial t}\left[\left(\sum_{j=1}^{i}\ell_j\Big(1-\cos\varphi_j\Big)\right) - \frac{\ell_i}{2}\Big(1-\cos\varphi_i\Big)\right]\right\}^2,\end{aligned} \tag{4.1.1c}$$

where N_0 is the initial prestress of the cable, K its equivalent elastic axial stiffness, P_i and F_i are the external (conservative) loads applied at the $i-$th segment in the transverse and longitudinal direction, respectively, with respect to the beam axis in the initial straight state (positive if directed as the displacements v and u displayed in Figure 3.1(b)); $m\ell_i$ is the mass of the $i-$th segment of length ℓ_i. Here, it has been assumed that the mass m per unit length is constant and that the loads P_i and F_i are applied at the midpoint of the $i-$th segment, so that the quantity b_i, indicated in Figure 2.1(a), reads $b_i = \ell_i/2$. The total elongation of the cable is $\Lambda = \sum_{i=1}^{n-1}\Lambda_i$, where n is the number of segments, as usual.

Observe that, in the definition of T, the rotational inertia of each segment has been neglected with respect to translational contribution: this is reasonable if the segments are much shorter than the beam length. More in detail, the kinetic energy

of the $i-$th segment can be rigorously written as $T_i = (I_i\dot{\varphi}_i{}^2 + m\ell_i\,\dot{v}_i{}^2 + m\ell_i\,\dot{u}_i{}^2)/2$, where I_i is the moment of inertia of the segment, $m\ell_i$ is the segmental mass, φ_i the segmental rotation, and u_i and v_i are the longitudinal and transverse displacement, respectively, of the centroid of the segment from the straight reference state; the latter two quantities correspond to the terms between square brackets in (4.1.1c), first and second line respectively. For the case at hand, we are assuming that the rotational contribution of each segment is negligible, i.e., $I_i\dot{\varphi}_i{}^2 \ll m\ell_i\,\dot{v}_i{}^2 + m\ell_i\,\dot{u}_i{}^2$.

The equations of equilibrium can be found with a variational approach, according to Hamilton's principle [73], under the constraint related to the compatibility with boundary conditions. For the paradigmatic case of cantilevers (clamped at segment $i = 1$) and simply supported beams (pin at node $i = 0$ and roller at node $i = n$), this reads

$$G = \begin{cases} \varphi_1 = 0\,, & \text{for cantilever beams,} \\ \displaystyle\sum_{j=1}^{n} \ell_j\,\sin\varphi_j = 0\,, & \text{for simply supported beams.} \end{cases} \tag{4.1.2}$$

The Euler-Lagrange's equations of motion, in terms of variables $\varphi_i = \varphi_i(t)$, resulting from Hamilton's principle [73], takes the well-known form

$$\frac{\partial}{\partial t}\left(\frac{\partial T}{\partial\dot{\varphi}_i}\right) - \frac{\partial T}{\partial\varphi_i} + \frac{\partial\Delta U}{\partial\varphi_i} = Q_W - \mu\,Q_G\,, \tag{4.1.3a}$$

$$G = 0\,, \quad i = 1\ldots n\,, \tag{4.1.3b}$$

where μ is the Lagrange's multiplier and we have set

$$\delta\Delta W = \frac{\partial\Delta W}{\partial\varphi_i}\,\delta\varphi_i = Q_W\,\delta\varphi_i\,, \tag{4.1.4}$$

$$\delta G = \frac{\partial G}{\partial\varphi_i}\,\delta\varphi_i = Q_G\,\delta\varphi_i = \begin{cases} 0\,, & \text{for cantilever beams } (i \neq 1), \\ 1\,, & \text{for cantilever beams } (i = 1), \\ \ell_i\,\cos\varphi_i\,, & \text{for simply supported beams.} \end{cases} \tag{4.1.5}$$

Note that for cantilever beams, the equation (4.1.3a), for $i = 1$, can be disregarded during the computation of variables φ_i. In fact, the constraint $\varphi_1 = 0$ and the $n-1$ equations (4.1.3a), for $i = 2\ldots n$, suffice to find the n unknowns φ_i $(i = 1\ldots n)$.

On the other hand, the equation (4.1.3a), for $i = 1$, can be later used to calculate the constraint moment reaction, which is expressed by the additional unknown represented by the Lagrange's multiplier μ.

To exemplify, consider a flex-ten cantilever with n segments and assume, for simplicity, that $\ell_i = \Delta L$, for $i = 1 \dots n$. The governing equations (4.1.3), describing the undamped vibrations of such a beam, can be detailed as follows

$$\begin{aligned} & N\big(a_i - a_{i-1}\big) - \Big(\sum_{j=i}^{n} P_j\Big)\Big(\Delta L \cos\varphi_i\Big) + \frac{\Delta L}{2} P_i \cos\varphi_i \; + \\ & - \Big(\sum_{j=i}^{n} F_j\Big)\Big(\Delta L \sin\varphi_i\Big) + \frac{\Delta L}{2} F_i \sin\varphi_i + \mathbb{I}_1(i)\,\mu + \\ & + \frac{m\,\Delta L^3}{4} \cos\varphi_i \Big(\sum_{j=1}^{n} \bar{\mu}_{ij} \ddot{\varphi}_j \cos\varphi_j - \sum_{j=1}^{n} \bar{\mu}_{ij} \dot{\varphi}_j{}^2 \sin\varphi_j \Big) + \\ & + \frac{m\,\Delta L^3}{4} \sin\varphi_i \Big(\sum_{j=1}^{n} \bar{\mu}_{ij} \ddot{\varphi}_j \sin\varphi_j + \sum_{j=1}^{n} \bar{\mu}_{ij} \dot{\varphi}_j{}^2 \cos\varphi_j \Big) = 0 \;, \end{aligned} \tag{4.1.6a}$$

$$\varphi_1 = 0\,, \quad i = 1 \dots n, \tag{4.1.6b}$$

where we have formally set $\varphi_k = 0$ when $k < 1$ or $k > n$, and $a_k = 0$ when $k < 1$ or $k \geqslant n$. Recall that $\mathbb{I}_i(j)$ is the indicator function, which equals 1 when $i = j$, zero otherwise, and that $N = N_0 + K\Lambda$ with $\Lambda = \sum_{i=1}^{n-1} \Lambda_i$. To further detail, one can assume, for example, that $a_i = l^2\,(\varphi_i - \varphi_{i+1})/\Delta L$ and $\Lambda_i = \frac{1}{2}\, l^2\,(\varphi_i - \varphi_{i+1})^2/\Delta L$, as discussed in the previous Section 3.2.2. The mass coefficients $\bar{\mu}_{ij}$ can be expressed through a recursive formulation that reads

$$\bar{\mu}_{ij} = \begin{cases} \bar{\mu}_{i-1\,j-1} + 4\,, & \text{for} \quad 1 < i = j \leqslant n\,, \quad \text{with} \quad \bar{\mu}_{nn} = 1\,, \\ \bar{\mu}_{i\,j-1} + 4\,, & \text{for} \quad 1 < i < j \leqslant n\,, \quad \text{with} \quad \bar{\mu}_{in} = 2\,, \\ \bar{\mu}_{i-1\,j} + 4\,, & \text{for} \quad 1 < j < i \leqslant n\,, \quad \text{with} \quad \bar{\mu}_{nj} = 2\,. \end{cases} \tag{4.1.7}$$

These mass coefficients $\bar{\mu}_{ij}$ can be collected in a symmetric matrix of the form

$$\big[\bar{\mu}_{ij}\big] = \begin{bmatrix} 21 & 18 & 14 & 10 & 6 & 2 \\ 18 & 17 & 14 & 10 & 6 & 2 \\ 14 & 14 & 13 & 10 & 6 & 2 \\ 10 & 10 & 10 & 9 & 6 & 2 \\ 6 & 6 & 6 & 6 & 5 & 2 \\ 2 & 2 & 2 & 2 & 2 & 1 \end{bmatrix}, \tag{4.1.8}$$

which corresponds to $n = 6$ segments of equal mass, but its recursive structure allows for a direct extension/reduction to $n \neq 6$.

4.1.2 Focus on the SDOF oscillator

The simplest case of a SDOF oscillator is now considered. This corresponds to a flex-ten cantilever composed two segments ($n = 2$) coupled by one joint. Such "reduced" assembly is introduced, and dynamic governing equations are detailed, in view of the following Section 4.1.3, where the observed free vibration of a 3D-printed prototype are compared with theoretical findings, which will include different modelings for the damping contribution at the joint.

Recall that schematizing flex-ten beams as a sequence of segments connected by spring hinges, as per Figure 2.1, is adequate for long chains of ashlars and limited angles of rotation (see Section 2.2.4). Since the structure here analyzed is composed by one single joint under large deflections, a higher level of detail is needed to describe the kinematics, rather than the modeling of the coupling between the segments as a macroscopic spring hinge. Hence, equations (4.1.1), for $n = 2$, have to be upgraded and adapted to the case at hand. On the contrary, equations (4.1.1) are adequate for the larger assembly with $n = 5$, introduced later on in Section 4.1.3 for comparison.

Refer to Figure 4.1, which reports a schematic representation of the SDOF

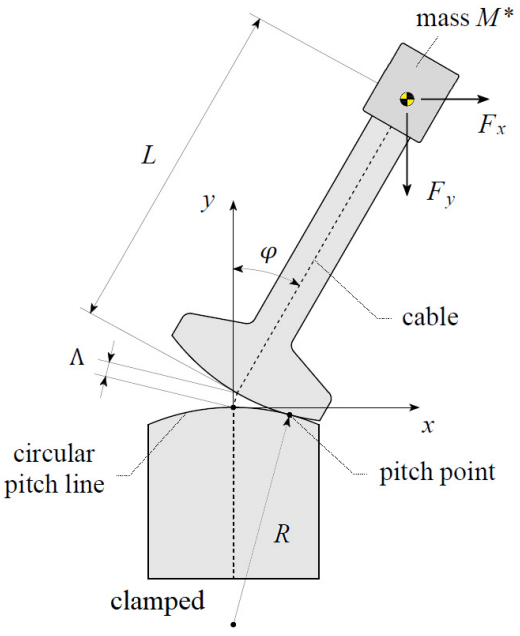

Figure 4.1. Schematic of the SDOF cantilever composed of two segments coupled by a joint with circular pitch lines of radius R.

cantilever. The coupling between the segments relies on circular pitch lines of radius R; the bottom segment is clamped, while the upper one is free to rotate. The inertial forces are modeled through a lumped mass M^*, which is concentrated on the tip of the cantilever, at a distance $\hat{L}$ from the initial pitch point in the straight state at rest. External forces F_x and F_y are applied at the centroid of mass M^*, and they are positive if directed as indicated in Figure 4.1. Since only one joint is considered, one has that the absolute rotation of the free segment coincides with its relative rotation with respect to the clamped segment; this is indicated as φ in Figure 4.1.

For the case at hand, equations (4.1.1) can be rewritten as

$$\Delta U = N_0\Lambda + \frac{1}{2}K\Lambda^2 \tag{4.1.9a}$$

$$\Delta W = F_x\Big(\hat{L}\sin\varphi + \Lambda\sin\frac{\varphi}{2}\Big) + F_y\Big(\hat{L} - \hat{L}\cos\varphi - \Lambda\cos\frac{\varphi}{2}\Big)\,, \tag{4.1.9b}$$

$$T = \frac{1}{2}M^*\bigg[\frac{\partial}{\partial t}\Big(\hat{L}\sin\varphi + \Lambda\sin\frac{\varphi}{2}\Big)\bigg]^2 + \frac{1}{2}M^*\bigg[\frac{\partial}{\partial t}\Big(\hat{L} - \hat{L}\cos\varphi - \Lambda\cos\frac{\varphi}{2}\Big)\bigg]^2, \tag{4.1.9c}$$

and the Euler-Lagrange's equation of motion, resulting from Hamilton's principle, takes the form

$$\frac{\partial}{\partial t}\left(\frac{\partial T}{\partial\dot{\varphi}}\right) - \frac{\partial T}{\partial\varphi} + \frac{\partial\Delta U}{\partial\varphi} - \frac{\partial\Delta W}{\partial\varphi} = 0\,. \tag{4.1.10}$$

In particular, recalling the differential condition (2.1.1) and that, for circular pitch lines, formula (2.1.6) holds, one finds

$$\frac{\partial\Delta U}{\partial\varphi} = \bigg[N_0 + 2KR\Big(1 - \cos\frac{\varphi}{2}\Big)\bigg]\Big(R\sin\frac{\varphi}{2}\Big)\,, \tag{4.1.11a}$$

$$\begin{aligned}\frac{\partial\Delta W}{\partial\varphi} = {}& F_x\bigg[\hat{L}\cos\varphi + R\Big(1 - \cos\frac{\varphi}{2}\Big)\cos\frac{\varphi}{2} + R\sin^2\frac{\varphi}{2}\bigg] + \\ & + F_y\bigg[\hat{L}\sin\varphi + R\Big(1 - \cos\frac{\varphi}{2}\Big)\sin\frac{\varphi}{2} - R\sin\frac{\varphi}{2}\cos\frac{\varphi}{2}\bigg]\,,\end{aligned} \tag{4.1.11b}$$

$$\begin{aligned}\frac{\partial}{\partial t}\left(\frac{\partial T}{\partial\dot{\varphi}}\right) - \frac{\partial T}{\partial\varphi} = {}& M^*\bigg[\Big(\frac{R}{2} - \frac{\hat{L}}{2}\Big)R\sin\frac{\varphi}{2}\bigg]\dot{\varphi}^2 + \\ & + M^*\bigg[2R^2 - 2\hat{L}R + \hat{L}^2 + 2R\Big(\hat{L} - R\Big)\cos\frac{\varphi}{2}\bigg]\ddot{\varphi}\,,\end{aligned} \tag{4.1.11c}$$

where the only unknown is represented by the function $\varphi = \varphi(t)$; its derivatives can be approximated, through finite differences, as follows

$$\dot{\varphi}(t) \simeq \frac{\varphi(t + \Delta t) - \varphi(t - \Delta t)}{2\,\Delta t}\,, \tag{4.1.12a}$$

$$\ddot{\varphi}(t) \simeq \frac{\varphi(t + \Delta t) - 2\varphi(t) + \varphi(t - \Delta t)}{\Delta t^2}\,. \tag{4.1.12b}$$

Here, Δt is the time step adopted for the numerical integration of equation (4.1.10), once initial conditions for the motion are set.

4.1.3 Experiments on free vibrations of cantilevers

The cantilever schematically represented in Figure 4.1 has been prototyped via 3D printing in order to test its response under free vibrations. The geometry of the prototype, depicted in the photograph of Figure 4.2, is characterized by the length $\hat{L} = 65.3\,\text{mm}$ and by the radius $R = 48.0\,\text{mm}$ of the pitch lines, indicated in Figure 4.1. The total mass at the tip of the cantilever is $M^* = 0.035\,\text{kg}$, which accounts for the lumped self-weight of the 3D-printed segment (made of white polylactide) and for an additional weight (made of lead).

The tendon is a dark-brown braided wire made of cotton, waxed to diminish friction, with effective diameter of 0.5 mm. In addition, a steel compression spring is placed in series to the cable, to achieve the effective axial stiffness $K = 0.84\,\text{N/mm}$. As described in Section 2.2.3, the initial prestress N_0 in the cable is measured from the shortening of the spring with a Vernier caliper.

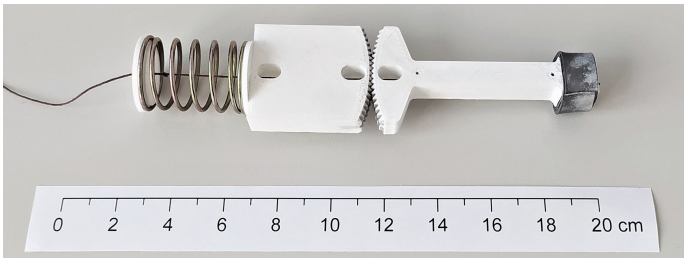

Figure 4.2. Photograph of the SDOF cantilever prototyped via 3D printing according to the schematic drawing of Figure 4.1.

In the experimental procedure, the cantilever was placed vertically in the gravity field, so that force F_y, indicated in Figure 4.1, is equal to M^*g, being $g = 9.81\,\text{m/s}^2$ the gravity acceleration. The force F_x, also indicated in Figure 4.1, was first applied quasi-statically to deform the cantilever, then it was suddenly made to vanish in order to excite the free vibration of the cantilever. The motion

was filmed with a camera (Samsung S5KGM1) and the position of the centroid of lumped mass M^* has been recorded with respect to the reference frame indicated in Figure 4.1. It was observed, as expected, that oscillations progressively reduced their amplitude. Since viscous drag in the air is negligible, a source of damping at the level of the joint should be introduced to catch this phenomenon.

The simplest way to consider such damping contribution is to append to the governing equation (4.1.10) a damping moment of the form

$$M_d = c\,\dot{\varphi}\,, \tag{4.1.13}$$

which is proportional through the constant c to the speed of relative rotation $\dot{\varphi}$ between the two coupled segments.

Figure 4.3 compares the experimental and theoretical findings, when damping is modeled as a linear function of the rotation speed. In particular, the x- and y-position of the centroid of lumped mass M^* is reported for two different values of the prestress, $N_0 = 9.36\,\mathrm{N}$ and $N_0 = 1.83\,\mathrm{N}$, respectively. The best agreement between theory and experiments is obtained for the corresponding values $c = 0.0005\,\mathrm{N\,m\,s}$ and $c = 0.0003\,\mathrm{N\,m\,s}$. Numerical integration of (4.1.10), with the additional contribution (4.1.13), is computed though the approximation (4.1.12) with a time step $\Delta t = 0.0001\,\mathrm{s}$.

Note that distinct values of c correspond to different values of prestress N_0, suggesting that a (nonlinear) dependence between these quantities could be established, but this would require a wide campaign of experimental tests to have coherent statistical data, which goes beyond the scope of the present section.

The theoretical results almost perfectly overlap to the experimental ones when the amplitude of oscillations is large (Figure 4.3). Conversely, accuracy is lost when small amplitudes are reached, which demonstrates that a different damping mechanism comes into play at this stage. In particular, observe that, in the recorded experiments, the oscillations stop abruptly and the initial straight state $x = 0$ is not perfectly recovered (Figure 4.3(a)). This evidence can indicate the presence of frictional dissipative moments.

To this aim, instead of the linear damping moment M_d, a parasitic-friction moment is now appended to the governing equation (4.1.10). This frictional contribution can be due, for example, to the rough contact (despite lubrication with graphite powder) of the toothed contact profiles that define the pitch profiles. Such dynamic-friction moment is considered in the form

$$M_f = \mathrm{sgn}(\dot{\varphi})\,\bar{M}\,, \tag{4.1.14}$$

where $\bar{M} > 0$, and the sign depends on the rotation speed $\dot{\varphi}$.

Figure 4.4, which is the counterpart of Figure 4.3, shows the experimental and

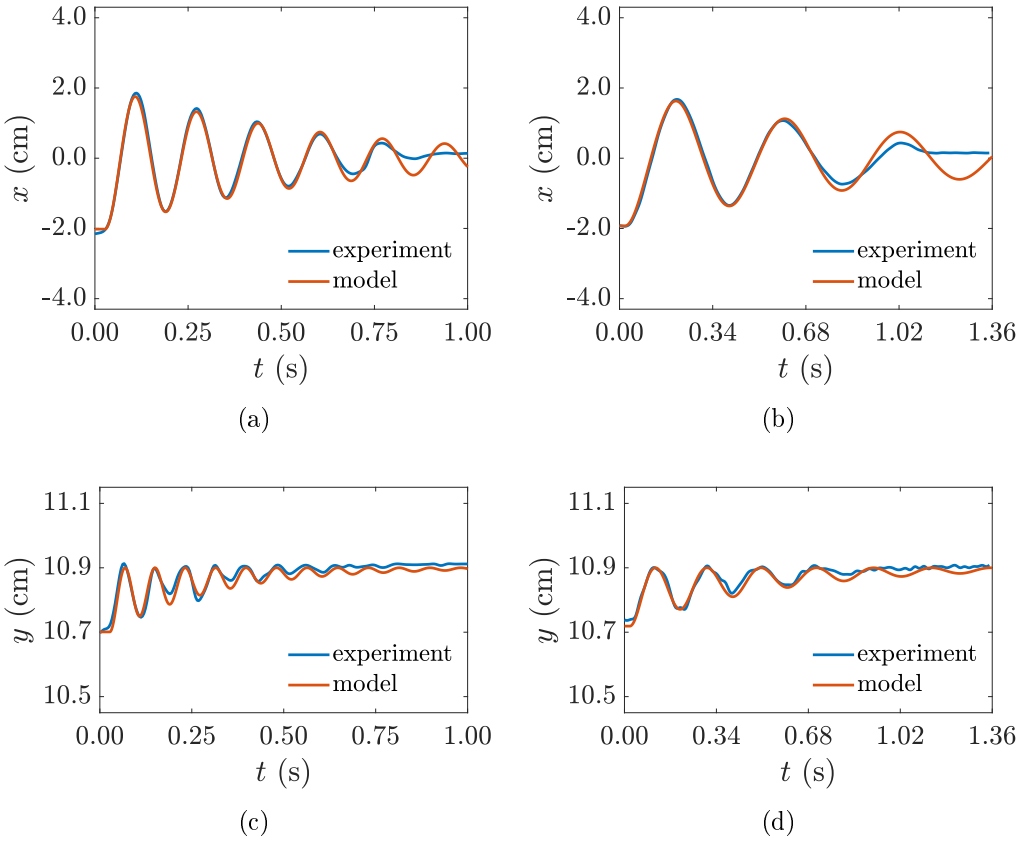

Figure 4.3. Comparison between experimental and theoretical findings, when damping is modeled as a linear function of the rotation speed: x-position of the centroid of lumped mass M^* for (a) $N_0 = 9.36\,\mathrm{N}$ and $c = 0.0005\,\mathrm{Nm\,s}$, and (b) $N_0 = 1.83\,\mathrm{N}$ and $c = 0.0003\,\mathrm{Nm\,s}$; (c)-(d) y-position of the centroid of lumped mass M^* for the corresponding cases.

theoretical findings, when damping is modeled with an additional friction moment. The x- and y-position of the centroid of lumped mass M^* is plotted for the aforementioned values of the prestress ($N_0 = 9.36\,\mathrm{N}$ and $N_0 = 1.83\,\mathrm{N}$, respectively), and the best fit is obtained for the corresponding values $\bar{M} = 0.0031\,\mathrm{Nm}$ and $\bar{M} = 0.0003\,\mathrm{Nm}$. Again the selected time step is $\Delta t = 0.0001\,\mathrm{s}$.

Also in this case, distinct values of $\bar{M}$ are found for different values of prestress N_0. This is consistent with the fact that a higher value of the prestress, i.e., higher compression stresses along the profiles in contact, does induce larger frictional forces at the surfaces in contact.

Observe that now the sudden stop of the oscillations is caught by the model (Figure 4.4), though at the price of having singularities in the mathematical com-

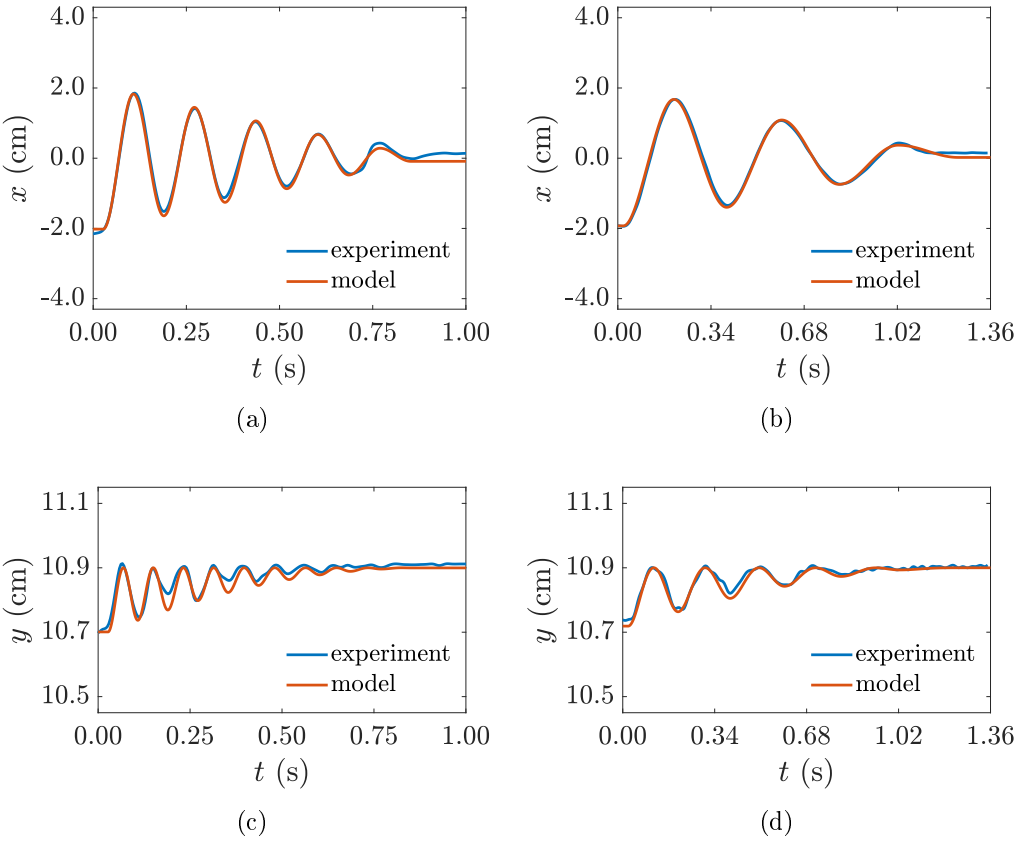

Figure 4.4. Comparison between experimental and theoretical findings, when dissipation is modeled as a parasitic friction moment: x-position of the centroid of lumped mass M^* for (a) $N_0 = 9.36\,\mathrm{N}$ and $\bar{M} = 0.0031\,\mathrm{Nm}$, and (b) $N_0 = 1.83\,\mathrm{N}$ and $\bar{M} = 0.0003\,\mathrm{Nm}$; (c)-(d) y-position of the centroid of lumped mass M^* for the corresponding cases.

putations due to the change in sign of the friction moment M_f during the time history. For this reason, in the following, the linear damping, as per (4.1.13), will be preferred, when only large oscillations are involved. Indeed, for large oscillations (4.1.13) proves to be adequate, as evidenced by Figure 4.3. To further demonstrate this point, another example is considered, which corresponds to the cantilever beam depicted in Figure 4.5.

The new prototype is composed of $n = 5$ segments coupled according to circular pitch profiles, and it has been prototyped via 3D printing. The beam is clamped at segment $i = 1$, as indicated in Figure 4.5(a), and the position of a reference point on segment $i = 5$, also highlighted in Figure 4.5(a), has been recorded as before. Each segment is made of black polylactide and an additional lead lamina is glued at its centroid to increase the segmental inertia (Figure 4.5(a)); the segmental mass

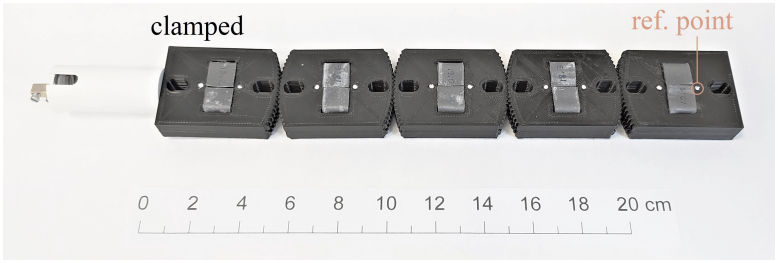

(a)

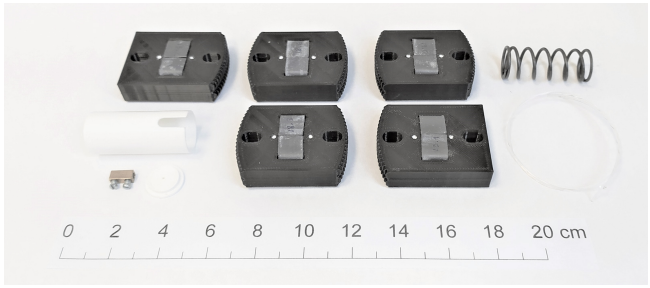

(b)

Figure 4.5. Photograph of the cantilever with $n = 5$ segments prototyped via 3D printing to test the modeling of dissipation through linear damping: (a) assembled and (b) disassembled beam, with evidence of the various components (segments, cable, spring, clamp to anchor the cable).

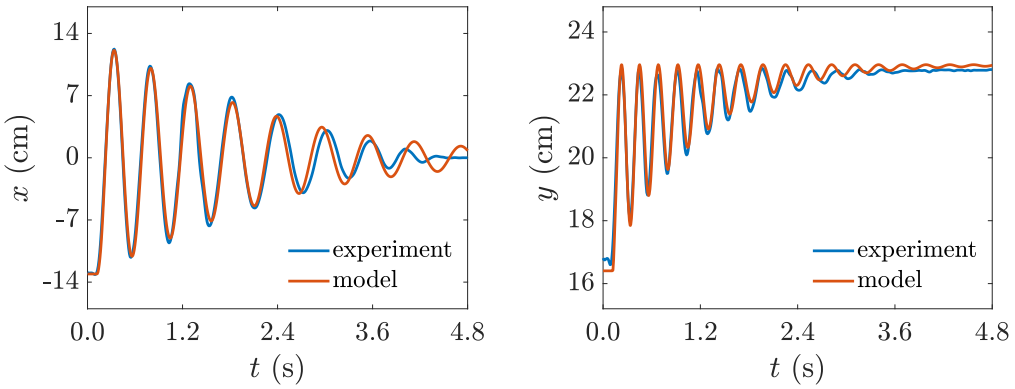

(a) (b)

Figure 4.6. Comparison between experimental and theoretical findings, for the longer cantilever with $n = 5$ segments: (a) x-position and (b) y-position of the reference point indicated in Figure 4.5(a), for $c = 0.0016\,\mathrm{Nm\,s}$.

results $m\Delta L = 0.0188\,\mathrm{kg}$, being $\Delta L = 49.2\,\mathrm{mm}$ the segmental length and m the equivalent mass per unit length. The radius of the pitch lines is $R = 48.0\,\mathrm{mm}$. The prestressing cable is a polyamide 6.6 wire of diameter 0.8 mm, placed in series with a steel spring, which are shown in Figure 4.5(b) together with the disassembled segments; the equivalent axial stiffness of the tendon is $K = 1.72\,\mathrm{N/mm}$, while the initial prestress was set to $N_0 = 11.32\,\mathrm{N}$. During the experimental test, the cantilever was placed vertically in the gravity field, and oscillations are caused by the release from a bent configuration due to an external load at the free tip.

In this case, the modeling of the joints as spring hinges is acceptable, since the beam is longer and the global response of the assembly is analyzed, rather than that of a single joint. Hence, equations (4.1.6) can be used, with the additional moment $M_{d,i} = c\,\Delta\dot{\varphi}_i = c\,(\dot{\varphi}_i - \dot{\varphi}_{i+1})$ transmitted at each joint. For clarity, the generic governing equation (4.1.6a) is here rewritten including such a damping contribution, and it reads

$$
\begin{aligned}
&N\big(a_i - a_{i-1}\big) - \left(\sum_{j=i}^{n} P_j\right)\left(\Delta L\cos\varphi_i\right) + \frac{\Delta L}{2} P_i \cos\varphi_i \; + \\
&- \left(\sum_{j=i}^{n} F_j\right)\left(\Delta L\sin\varphi_i\right) + \frac{\Delta L}{2} F_i \sin\varphi_i + \mathbb{I}_1(i)\,\mu + \\
&+ \frac{m\,\Delta L^3}{4}\cos\varphi_i\left(\sum_{j=1}^{n}\bar{\mu}_{ij}\ddot{\varphi}_j\cos\varphi_j - \sum_{j=1}^{n}\bar{\mu}_{ij}\dot{\varphi}_j{}^2\sin\varphi_j\right) + \\
&+ \frac{m\,\Delta L^3}{4}\sin\varphi_i\left(\sum_{j=1}^{n}\bar{\mu}_{ij}\ddot{\varphi}_j\sin\varphi_j + \sum_{j=1}^{n}\bar{\mu}_{ij}\dot{\varphi}_j{}^2\cos\varphi_j\right) + \\
&+ M_{d,i} - M_{d,i-1} = 0\;, \quad i = 1\ldots n\,,
\end{aligned}
\tag{4.1.15}
$$

where, for the case at hand, $P_i = 0$ during the oscillations and $F_i = mg\Delta L$.

Figure 4.6 compares the experimental and theoretical results, concerning the position of the reference point during oscillations. The adopted damping coefficient is $c = 0.0016\,\mathrm{Nm\,s}$, and the time step is $\Delta t = 0.0001\,\mathrm{s}$. The accuracy of the model with linear damping is good up to $t \simeq 3.6\,\mathrm{s}$, then experimental oscillations quickly decay to zero, whereas the model still computes small vibrations with slower decay.

Since the present prototype (Figure 4.5) is totally different from the previous SDOF oscillator (Figure 4.2), but in both cases a good accuracy is reached in reproducing experimentally measured vibrations, we believe that the linear damping contribution, expressed through the additional dissipative moments $M_{d,i} = c\,\Delta\dot{\varphi}_i$, can represent a satisfactory way to model dissipative forces, at least when large oscillations are observed. On the other hand, the additional frictional moment

$M_{f,i} = \mathrm{sgn}(\Delta\dot{\varphi}_i)\,\bar{M}$ should be considered to catch the fast decay of oscillations at small amplitudes.

4.2 The dynamic problem in the continuum limit

The description of the dynamic problem in the continuum limit is now considered. By using the appropriate shape function (3.2.30) for the rotation field of a simply supported beam (selected as paradigmatic case-study), the problem can be reduced to that of a SDOF oscillator. The nonlinear response of the simply supported beam under harmonic uniformly-distributed transversal actions is analyzed: the role played by the introduction of dampers at the anchoring points of the cable is considered and the effect of an initial camber due, e.g., to self-weight, is investigated. The possibility of artfully tuning the tensile force in the cable to actively control vibration is finally tested.

4.2.1 Governing equations and damping

Consider equations (4.1.1). By letting $\ell_i \to 0$, one can replace summations with integrals and incremental quotients with derivatives, in order to define, as represented in Figure 3.1, the continuum counterpart of the discrete problem. Referring to Section 3.2 for the detailed derivation, the final result is here recalled.

Having introduced the curvilinear coordinate s on the beam axis, if $\varphi(s,t)$ is the rotation of the beam at s at the time t, with the notation $(\cdot)' = \partial(\cdot)/\partial s$, the expressions (4.1.1) become

$$\Delta\mathcal{U}(t) = \frac{l^2 N_0}{2}\int_0^L \Big[-\varphi'(s,t)\Big]^2 ds + \frac{K}{2}\frac{l^4}{4}\left\{\int_0^L \Big[-\varphi'(s,t)\Big]^2 ds\right\}^2, \tag{4.2.16a}$$

$$\begin{aligned}\Delta\mathcal{W}(t) = &\int_0^L p(s,t)\left\{\int_0^s \sin\varphi(\bar{s},t)\,d\bar{s}\right\} ds + \\ &+ \int_0^L f(s,t)\left\{\int_0^s \Big[1-\cos\varphi(\bar{s},t)\Big]\,d\bar{s}\right\} ds\,,\end{aligned} \tag{4.2.16b}$$

$$\begin{aligned}\mathcal{T}(t) = &\frac{1}{2}\int_0^L m(s)\left\{\frac{\partial}{\partial t}\int_0^s \sin\varphi(\bar{s},t)\,d\bar{s}\right\}^2 ds \\ &+ \frac{1}{2}\int_0^L m(s)\left\{\frac{\partial}{\partial t}\int_0^s \Big[1-\cos\varphi(\bar{s},t)\Big]\,d\bar{s}\right\}^2 ds\,,\end{aligned} \tag{4.2.16c}$$

where $p(s,t)$ and $f(s,t)$ are the smeared counterpart of loads P_i and F_i, while $m(s)$ is the mass per unit length. The cable elongation depends upon the local curvature $\chi(s,t)$ of the beam, and it is such that $d\Lambda(s,t) = \frac{1}{2}l^2\chi^2(s,t)ds = \frac{1}{2}l^2[-\varphi'(s,t)]^2ds$, i.e., the local cable elongation $d\Lambda(s,t)$, corresponding to Λ_i in the discrete model, is a quadratic function of the curvature at s, as assumed in Section 3.2. Recall that the quantity l is an intrinsic length scale for the structure.

Again, the equilibrium equations can be found through Hamilton's principle [73], under the continuum limit of the constraint (4.1.2), which, for a simply supported beam, reads

$$\mathcal{G}(t) = \int_0^L \sin\varphi(s,t)\, ds = 0\,. \tag{4.2.17}$$

This is the same formulation as per (3.2.10), but now the dependence on time t is considered and highlighted. The associated Lagrange's multiplier represents the vertical reaction force at the right-hand roller restraint (Figure 3.1(c)).

The solution of the problem requires a step-by-step numerical integration. However, it has been demonstrated in Section 3.3 that for different static load conditions, including uniformly distributed loads, the rotation field is very well approximated by a cosinusoidal function. Hence, now in the dynamic case, we consider a shape function (3.2.30) in the time-depending version of the form

$$\varphi(s,t) = \varphi_0(t)\, \cos\frac{\pi s}{L}\,, \tag{4.2.18}$$

where $\varphi_0(t)$ is the shape parameter at time t, representing the rotation at the left-hand end of the rod. The constraint equation (4.2.17) is automatically satisfied by this choice. Then, the variational problem via Hamilton's principle allows to obtain the optimal value of $\varphi_0(t)$. A further useful simplification consists in expanding in Taylor's series the sine and cosine functions appearing in (4.2.16), so that the integrals can be readily calculated in closed form. In the following, the presence of axial force $f(s,t)$ will also be dropped.

It is clear that (4.2.18) can only account for the first vibration mode, which is indeed a very strong limitation. However, this is certainly the leading mode when considering the forced vibrations under uniformly distributed harmonic loads, or other conditions similar to this, as it will be done in the sequel. In addition, observe that the first mode is also driven by the nonlinear character of the bending stiffness, associated with the variation of the cable length and/or, equivalently, of the springs in series to it. Kept fixed the maximum amplitude of vibrations, the deformation associated with the first mode provokes a cable elongation much smaller than that for the higher modes, i.e., less elastic energy is involved. Of course, by numerically solving the equilibrium equations for the discrete case, obtained from

(4.1.1), it would be possible to clarify the role played by the higher natural modes of vibrations. However, the simplifications introduced here will provide a concise, though accurate, view of the response of the flexural-tensegrity beam.

There may be many possible sources of damping and one is certainly associated with relative rotation at each contact joint, as introduced in the previous Section 4.1.3 for the discrete case. In this simplest case, for a continuous beam, assume that the first variation of dissipated energy is of the form

$$\begin{aligned}\delta\mathcal{W}_D{}^{(1)}(t) &= -c_1 L^3 \int_0^L \dot{\chi}(s,t)\,\delta\chi(s,t)\,ds \\ &= -c_1 L^3 \int_0^L \Big[-\dot{\varphi}'(s,t)\Big]\Big[-\delta\varphi'(s,t)\Big]ds\,,\end{aligned} \tag{4.2.19}$$

where c_1 is the damping coefficient, which dimensions are $[M][T]^{-1}$, and we have used the notation $\dot{(\cdot)} = \partial(\cdot)/\partial t$ and, again, $(\cdot)' = \partial(\cdot)/\partial s$. Substituting the shape function (4.2.18) in (4.2.19), after integration by parts, one obtains

$$\delta\mathcal{W}_D{}^{(1)}(t) = -c_1\frac{\pi^2 L^2}{2}\dot{\varphi}_0(t)\delta\varphi_0(t) = Q_{D1}(t)\delta\varphi_0(t)\,. \tag{4.2.20}$$

However, an additional contribution to damping may be considered, now associated with the unbonded tendon. This may be naturally due to the sliding of the tendon inside the sheath or, equivalently, it can be artfully obtained by adding a linear viscous dashpot at each end of the prestressing cable. The resulting scheme is that represented in Figure 4.7, where k_C is the effective stiffness constant for the elasticity of the cable, whereas k_A and k_B are the additional elastic springs at the beam ends. In parallel with the springs k_A and k_B, one can insert the dashpots with damping coefficients c_A and c_B, respectively, with dimensions $[M][T]^{-1}$.

With reference to Figure 4.7(b), let Λ_A and Λ_B denote the variation of length of the end springs, of length L_A and L_B in the reference state as per Figure 4.7(a), considered positive if they induce compression in the springs. As before, let Λ represent the increase of length of the centroid line of the beam, where the cable is placed, consequent to the inflection. For simplicity, assume that $c_A = c_B = c_2$, $k_A = k_B = k$ and $k/k_C \to 0$. Hence, recalling that $d\Lambda(s,t) = \frac{1}{2}l^2[-\varphi'(s,t)]^2 ds$, one obtains by symmetry

$$\Lambda_A = \Lambda_B = \frac{\Lambda}{2} = \frac{l^2}{4}\int_0^L \Big[-\varphi'(s,t)\Big]^2 ds\,, \tag{4.2.21}$$

so that the variation of dissipated energy, after substituting the shape function (4.2.18), takes the form

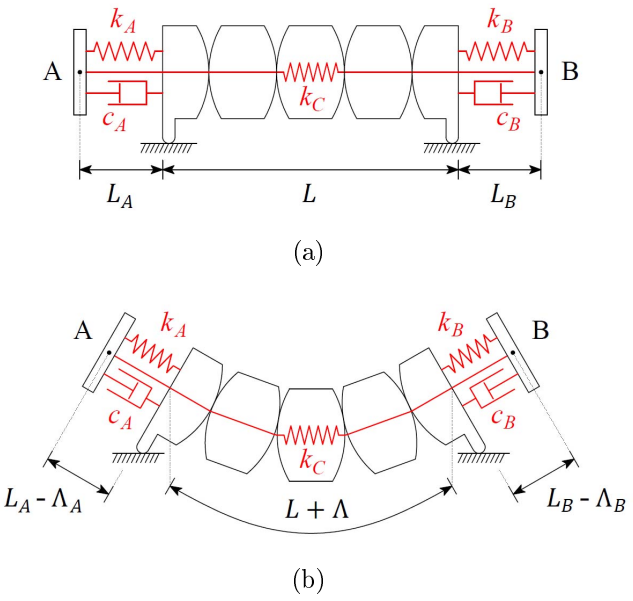

Figure 4.7. Schematic representation of the system formed by the prestressing cable and the two additional dashpots in parallel with the end springs of the flex-ten beam. (a) Reference straight configuration and (b) configuration after bending.

$$\begin{aligned}\delta\mathcal{W}_D{}^{(2)}(t) &= -c_A\dot{\Lambda}_A(t)\delta\Lambda_A(t) - c_B\dot{\Lambda}_B(t)\delta\Lambda_B(t) \\ &= -c_2\frac{l^4\pi^4}{8L^2}\varphi_0{}^2(t)\dot{\varphi}_0(t)\delta\varphi_0(t) = Q_{D2}(t)\delta\varphi_0(t)\,.\end{aligned} \tag{4.2.22}$$

Observe that $\delta\mathcal{W}_D{}^{(1)}$ provides a linear contribution to damping directly proportional to the deformation speed $\dot{\varphi}_0(t)$. More interesting, the term $\delta\mathcal{W}_D{}^{(2)}$ is nonlinear, since the resulting damping depends upon both $\dot{\varphi}_0(t)$ and $\varphi_0{}^2(t)$. The possibility of a nonlinear source of damping of this type has been either postulated, or theoretically derived under specific assumptions, in order to correctly interpret the dynamic response of homogenous plates [68]. Here it is naturally obtained for a simple mechanical system.

4.2.2 Simplified governing equation

The Euler-Lagrange's equation of motion in terms of $\varphi_0(t)$, resulting from Hamilton's principle [73], can be written as

$$\frac{\partial}{\partial t}\left(\frac{\partial \mathcal{T}}{\partial \dot{\varphi}_0}\right) - \frac{\partial \mathcal{T}}{\partial \varphi_0} + \frac{\partial \Delta \mathcal{U}}{\partial \varphi_0} = Q_W + Q_{D1} + Q_{D2}\,, \tag{4.2.23}$$

where we have set $\delta \Delta \mathcal{W} = Q_W \delta \varphi_0$. After some calculations, assuming that both the mass m and the load per unit length p are uniformly distributed along the beam, that axial force $f = 0$, and using Taylor's expansion for the sine and cosine functions and neglecting terms of order higher than 5, one obtains

$$\begin{aligned}
&m\frac{L^3}{\pi^2}\left[\frac{1}{2} - \frac{3}{8}{\varphi_0}^2(t) + \frac{7}{72}{\varphi_0}^4(t)\right]\ddot{\varphi}_0(t) - m\frac{L^3}{\pi^2}\left[\frac{3}{8}\varphi_0(t) - \frac{7}{36}{\varphi_0}^3(t)\right]{\dot{\varphi}_0}^2(t) + \\
&+ m\frac{L^3}{\pi^2}\left[\frac{8\pi^2 - 9}{96}{\varphi_0}^2(t) - \frac{16\pi^2 - 21}{768}{\varphi_0}^4(t)\right]\ddot{\varphi}_0(t) + \\
&+ m\frac{L^3}{\pi^2}\left[\frac{8\pi^2 - 9}{96}\varphi_0(t) - \frac{16\pi^2 - 21}{384}{\varphi_0}^3(t)\right]{\dot{\varphi}_0}^2(t) + \\
&+ c_1\frac{\pi^2 L^2}{2}\dot{\varphi}_0(t) + c_2\frac{l^4\pi^4}{8L^2}{\varphi_0}^2(t)\dot{\varphi}_0(t) + \frac{l^2 N_0 \pi^2}{2L}\varphi_0(t) + \\
&+ \frac{l^4 k \pi^4}{16L^2}{\varphi_0}^3(t) - p(t)\frac{L^2}{\pi^2}\left[2 - \frac{7}{9}{\varphi_0}^2(t) + \frac{149}{2700}{\varphi_0}^4(t)\right] = 0\,.
\end{aligned} \tag{4.2.24}$$

which is the equation of a nonlinear SDOF oscillator. If the oscillations are very small, one may neglect all the terms of order higher than 1 in equation (4.2.24) and obtain a harmonic oscillator, but the nonlinear character is provided by cubic and higher order terms. It will be verified in Section 4.2.3 that terms of order higher than 3 do not provide a significant contribution even when resonant conditions are approached. Of course, some of the cubic terms are negligible with respect to others depending on the model parameters.

In order to estimate which are the leading terms in the expansion, it is convenient to define suitable quantities that provide the mechanical similitude for the oscillating system. To this end, consider the following nondimensional quantities:

$$\gamma = \frac{mL\bar{\omega}^2}{N_0/L} = \frac{\text{inertia force per unit length}}{\text{local stiffness}}\,, \tag{4.2.25}$$

$$\beta = \frac{k}{N_0/L} = \frac{\text{nonlocal stiffness}}{\text{local stiffness}}\,, \tag{4.2.26}$$

$$\alpha = \frac{l}{L} = \frac{\text{intrinsic length scale}}{\text{macroscopic length}}\,, \tag{4.2.27}$$

where $\bar{\omega}$ can be either the natural frequency of the equivalent harmonic system or the frequency of the forcing term, if any.

Assume that the general solution of equation (4.2.24) is of the type

$$\varphi_0(t) \simeq \psi \cos(\bar{\omega} t + \phi)\,, \tag{4.2.28}$$

where ψ is the amplitude of oscillations and ϕ is the phase. In particular, one has $|\varphi_0(t)| \leqslant \psi$, $|\dot{\varphi}_0(t)| \leqslant \bar{\omega}\psi$ and $|\ddot{\varphi}_0(t)| \leqslant \bar{\omega}^2\psi$. We can define ψ as the order parameter, which is also associated with the ratio v_m/L between the maximum sag v_m at midspan and the beam length L.

Considering mass, stiffness and load terms up to third order in (4.2.24), dividing each term by $N_0\,L$ and substituting the order parameter, one finds

$$\begin{aligned}
&m\frac{L^3}{\pi^2}\frac{1}{2}\ddot{\varphi}_0\frac{1}{N_0 L} \simeq \frac{\gamma\psi}{19.7}\,, && m\frac{L^3}{\pi^2}\frac{3}{8}{\varphi_0}^2\ddot{\varphi}_0\frac{1}{N_0 L} \simeq \frac{\gamma\psi^3}{26.3}\,,\\
&m\frac{L^3}{\pi^2}\frac{3}{8}\varphi_0{\dot{\varphi}_0}^2\frac{1}{N_0 L} \simeq \frac{\gamma\psi^3}{26.3}\,, && m\frac{L^3}{\pi^2}\frac{8\pi^2-9}{96}{\varphi_0}^2\ddot{\varphi}_0\frac{1}{N_0 L} \simeq \frac{\gamma\psi^3}{13.5}\,,\\
&m\frac{L^3}{\pi^2}\frac{8\pi^2-9}{96}\varphi_0{\dot{\varphi}_0}^2\frac{1}{N_0 L} \simeq \frac{\gamma\psi^3}{13.5}\,, && \frac{pL^2}{\pi^2}\left(2-\frac{7}{9}{\varphi_0}^2\right)\frac{1}{N_0 L} \simeq \frac{pL\,(2-0.8\psi^2)}{10N_0}\,,\\
&\frac{l^2 N_0\pi^2}{2L}\varphi_0\frac{1}{N_0 L} \simeq 4.9\,\alpha^2\psi\,, && \frac{l^4 k\pi^4}{16L^2}{\varphi_0}^3\frac{1}{N_0 L} \simeq 6.1\,\alpha^4\beta\psi^3\,.
\end{aligned}$$

Hence, if oscillations are sufficiently small (say when $\psi < 15^\circ$ or $v_m < L/12$), one can neglect terms proportional to $\gamma\psi^3$ with respect to those proportional to $\gamma\psi$, as well as the quadratic contribution in the forcing term. On the other hand, the cubic stiffness, proportional to $\alpha^4\beta\psi^3$, will affect the solution in the case that β is big enough, of the order of $\beta > 0.08\,\alpha^{-2}\psi^{-2}$: this represents a condition of practical interest.

Passing to the damping, the linear contribution is proportional to $4.9\,c_1\psi$, while the nonlinear contribution is proportional to $12.2\,c_2\alpha^4\psi^3$. Hence the nonlinear effect is comparable with the linear one if $c_2 \simeq c_1/(2.5\,\alpha^4\psi^2)$.

In conclusion, neglecting all the terms of order higher than 1 in ψ, but keeping the significative terms in the cubic stiffness and nonlinear damping, one obtains

$$\begin{aligned}
&m\frac{L^3}{2\pi^2}\ddot{\varphi}_0(t) + c_1\frac{\pi^2 L^2}{2}\dot{\varphi}_0(t) + c_2\frac{l^4\pi^4}{8L^2}{\varphi_0}^2(t)\dot{\varphi}_0(t) +\\
&+\frac{l^2 N_0\pi^2}{2L}\varphi_0(t) + \frac{l^4 k\pi^4}{16L^2}{\varphi_0}^3(t) - p(t)\frac{2L^2}{\pi^2} = 0\,.
\end{aligned} \tag{4.2.29}$$

This represents a hard-spring Duffing oscillator [61] with linear and nonlinear damping under forced oscillations. In the following, we will assume that $p(t)$ is proportional to $mg\,\hat{f}(t)$, where $\hat{f}(t)$ is a periodic function of time and mg is the self-weight per unit length of the beam, being g the acceleration of gravity.

4.2.3 Examples

The dynamical response of the beam of Figure 3.1 is here analyzed by numerically integrating equation (4.2.29) and by using the harmonic balance method [74] to capture unstable branches. Unless stated otherwise, in the following reference is made to the case $L = 0.4\,\mathrm{m}$, $l^2 = 0.00109\,\mathrm{m}^2$, $N_0 = 20\,\mathrm{N}$ and $m = 0.3\,\mathrm{kg/m}$, while $k = 1400\,\mathrm{N/m}$. Such parameters are consistent with a flex-ten beam of the type represented in Figure 3.5, composed of $n = 32$ segments of equal length $\Delta L = 12.5\,\mathrm{mm}$ and coupled according to circular pitch lines of radius $R = 174.4\,\mathrm{mm}$, where the prestressing cable is a steel tendon, much stiffer than the end springs.

Harmonic and duffing oscillator

Equation (4.2.29), which corresponds to a nonlinear Duffing oscillator, can be rewritten in the more compact form

$$M\ddot{\varphi}_0(t) + C_1\dot{\varphi}_0(t) + C_2{\varphi_0}^2(t)\dot{\varphi}_0(t) + K_1\varphi_0(t) + K_2{\varphi_0}^3(t) - F(t) = 0\,, \quad (4.2.30)$$

where

$$\begin{aligned} M &= m\frac{L}{2\pi^2}\,, & C_1 &= c_1\frac{\pi^2}{2}\,, & C_2 &= c_2\frac{l^4\pi^4}{8L^4}\,, \\ K_1 &= \frac{l^2N_0\pi^2}{2L^3}\,, & K_2 &= \frac{l^4k\pi^4}{16L^4}\,, & F(t) &= \frac{2}{\pi^2}\,p(t)\,. \end{aligned} \quad (4.2.31)$$

For the corresponding harmonic oscillator the natural frequency is $\omega_1 = \sqrt{K_1/M}$ and the critical linear damping reads $C_{cr} = 1/\sqrt{4K_1M}$. The nonlinearity in stiffness is due to the cubic term with coefficient K_2 (Duffing term) with positive sign (hard spring).

For the case in which C_1 is 10% of the critical value and $C_2 = 0$, the response under a harmonic excitation of the type $p(t) = p_0\cos(\Omega t)$ is evidenced in Figure 4.8, which reports the maximum displacement at midspan v_m, normalized by the beam length L, as a function of the frequency Ω, normalized by the natural frequency ω_1. The two pictures refer to different values of the Duffing term K_2 and show graphs

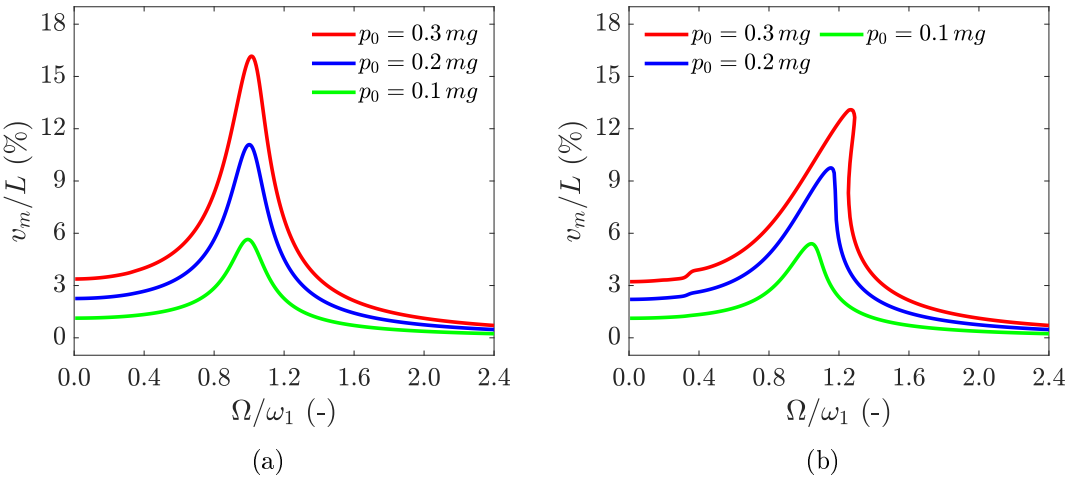

Figure 4.8. Frequency-displacement response chart for the beam under the harmonic load $p(t) = p_0 \cos(\Omega t)$, when C_1 is 10% of the critical value and $C_2 = 0$. (a) Small Duffing term ($K_2 = 0.396\,\mathrm{N/m}$) and (b) large Duffing term ($K_2 = 8.307\,\mathrm{N/m}$).

corresponding to various values of p_0, expressed in terms of the weight per unit length mg. For a small K_2, as indicated in Figure 4.8(a), the response is similar to a harmonic oscillator. Increasing K_2, as per Figure 4.8(b), an unstable branch becomes visible for sufficiently high values of p_0. The fundamental resonance is at $\Omega/\omega_1 \simeq 1$, but for sufficiently high K_2 a subharmonic resonance begins to emerge, for frequencies about 1/3 of the fundamental resonance.

Having set $p_0 = 0.3\,mg$ and having defined $\bar{K}_2 = 0.396\,\mathrm{N/m}$, Figure 4.9(a) shows how the response chart is affected by the Duffing term K_2, indicated as a multiple of $\bar{K}_2$. When K_2 is small, the structure tends to a harmonic oscillator. On the contrary, when K_2 increases, the nonlinear response typical of the Duffing oscillator emerges. This fact is also evident by the comparison of Figure 4.8(a) and 4.8(b). Observe, in passing, that, from (4.2.31), K_1 depends upon the initial prestress N_0 in the cable, whereas K_2 is affected by the effective stiffness of the cable, in particular by the end springs with elastic constant k.

Figure 4.9(b) reports the influence of linear damping C_1, indicated as a percentage of C_{cr}, when $C_2 = 0$. The considered values should take into account the rolling friction of the contact surfaces and the friction between the sheath and cable in proximity of the joint. Friction is certainly enhanced here by the change of direction of the cable consequent to the rotation of the segments, which locally increases the contact pressure between cable and sheath.

Figure 4.10(a) shows the response in terms of maximum deflection for different values of p_0 when the vibrations are around the deformed shape due to self-weight

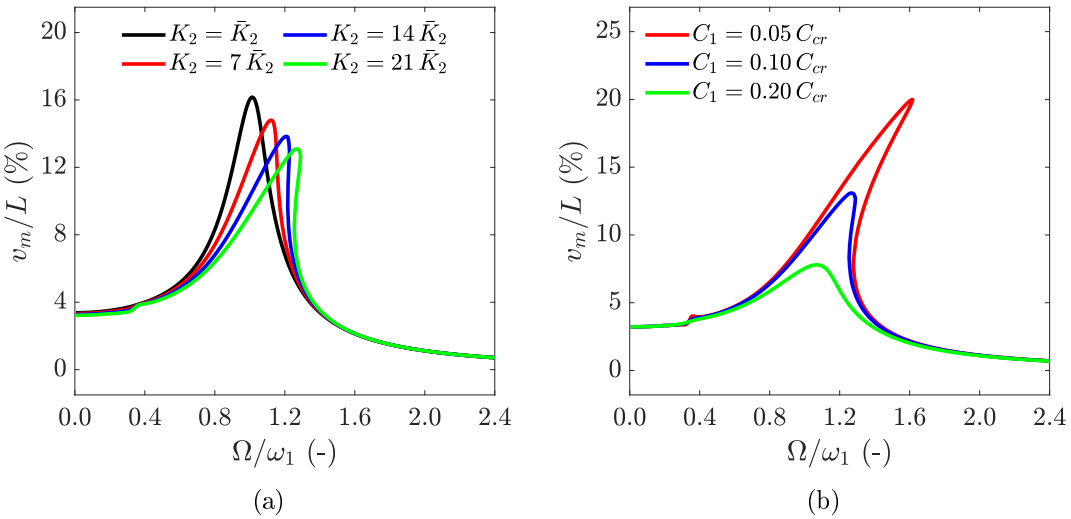

Figure 4.9. Frequency-displacement response chart for the beam subjected $p(t) = 0.3\,mg\cos(\Omega t)$ when $C_2 = 0$. (a) Influence of the Duffing term K_2, expressed as a multiple of the reference value $\bar{K}_2 = 0.396\,\mathrm{N/m}$, when $C_1 = 0.1\,C_{cr}$; (b) influence of damping C_1, indicated as a percentage of C_{cr}, when $K_2 = 8.307\,\mathrm{N/m}$.

in the gravity field. Note that the fundamental resonance moves from $\Omega/\omega_1 \simeq 1.0$ to $\Omega/\omega_1 \simeq 1.5$. Moreover, a subharmonic resonance emerges for frequencies about one half of those corresponding to fundamental resonance. These differences may be attributed to the "arch-effect" of the configuration around which the oscillations take place. When p_0 is sufficiently high, the amplitude becomes so large that the initial camber is recovered and the curvature changes sign in the oscillations. This is evident in Figure 4.10(b) that reports, for $p_0 = 0.5\,mg$, the minimum and the maximum sag as well as their arithmetic mean. Figure 4.10(c) shows the phase diagram at a frequency corresponding to the subharmonic resonance ($\Omega = 12.1\,\mathrm{rad/s} \simeq 0.75\,\omega_1$ when $p_0 = 0.5\,mg$), whereas Figure 4.10(d) displays the corresponding time history for the oscillator.

Figure 4.11(a) is dedicated to the illustration of the influence of the additional nonlinear damping. As the dissipation depends on $\varphi_0{}^2\dot{\varphi}_0$, its contribution increases for large oscillations. Hence, only in a neighborhood of the fundamental resonance the effect of the nonlinear damping is relevant, while the remaining part of the frequency-displacement response chart is left almost completely unaffected.

It may be argued that, in proximity of the fundamental resonance, the hypothesis of small oscillations ($|\varphi_0| < 15°$), at the basis of the simplifications presented in Section 4.2.2, may be violated. However, it is possible to verify that, at least for the case at hand, the error is limited. This is confirmed by the graphs of Figure

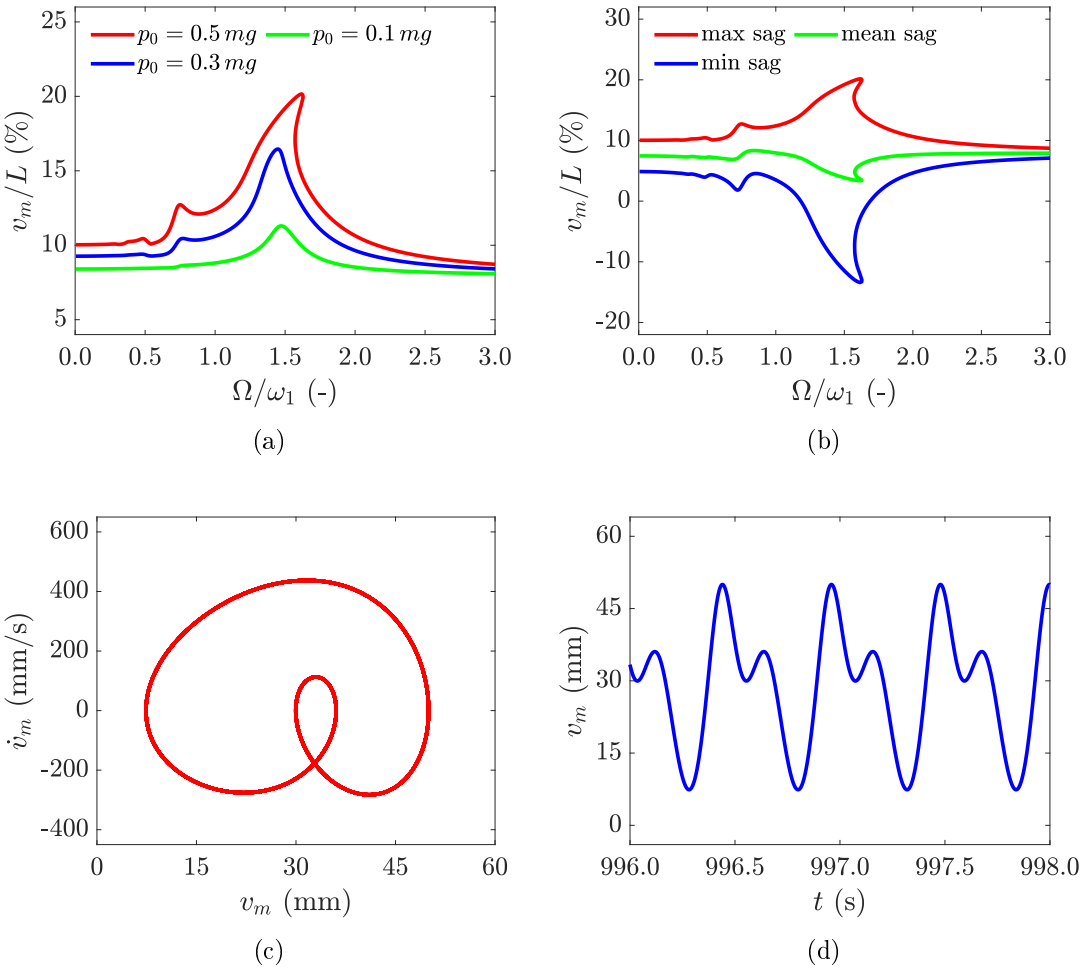

Figure 4.10. Frequency-displacement response chart for the simply supported beam under $p(t) = mg + p_0 \cos(\Omega t)$, for the case $C_1 = 0.1 C_{cr}$, $C_2 = 0$ and $K_2 = 11.076\,\mathrm{N/m}$. (a) Maximum sag under variable p_0; (b) maximum, minimum and mean sag when $p_0 = 0.5\,mg$; (c) phase diagram in proximity of subharmonic resonance at $\Omega = 12.1\,\mathrm{rad/s} \simeq 0.75\,\omega_1$ at $p_0 = 0.5\,mg$ and (d) corresponding time history.

4.11(b), which provide the comparison between the results obtainable with the simplified equation (4.2.30) and the equation (4.2.24), where terms up to the fifth order are preserved. Only a slight deviation is observed for the largest oscillations: the error is less than 2% at resonance, less than 3% at the frequency corresponding to maximum amplitude, and remains in any case within 4% on stable branches.

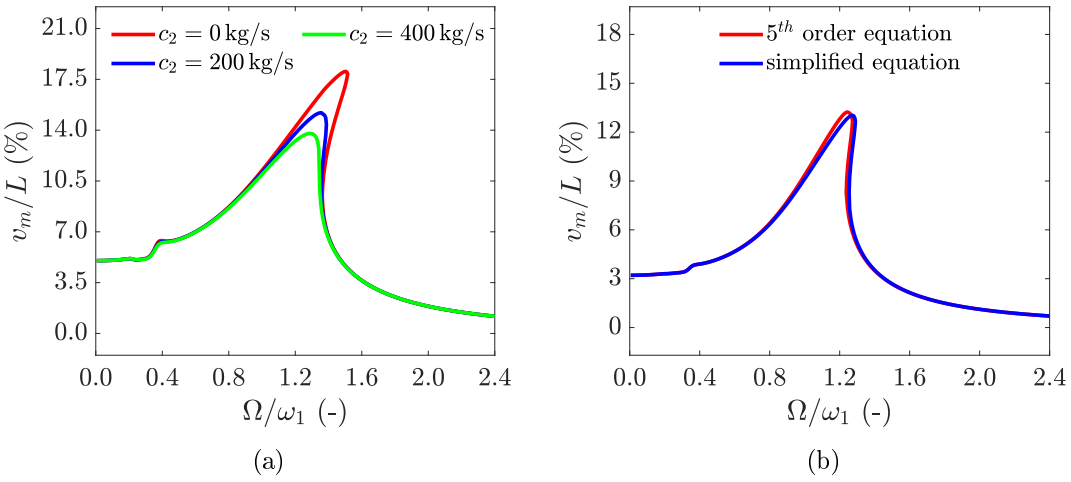

Figure 4.11. Frequency-displacement response chart for the simply supported beam under $p(t) = p_0\, mg\, \cos(\Omega t)$, for $C_1 = 0.1\, C_{cr}$ and $K_2 = 8.307\,\mathrm{N/m}$. (a) Case $p_0 = 0.5\, mg$ and variable c_2. (b) Comparison between the responses predicted by the simplified equation (4.2.30) and the equation (4.2.24), where terms up to the fifth order are considered (case $c_2 = 0$ and $p_0 = 0.3\, mg$).

Parametric resonance

The coefficient K_1, which represents the linear stiffness of the oscillator, depends on the cable initial prestress N_0. By varying in time the prestress value, a condition of parametric resonance may be achieved. If one neglects all sources of damping, as well as the nonlinear Duffing term, the oscillations consequent to a prestressing force $N_0 + \Delta N_0 \cos(\omega t)$ correspond to the solutions of Mathieu's equation

$$M\ddot{\varphi}_0(t) + [K_1 + \Delta K_1 \cos(\omega t)]\, \varphi_0(t) = 0\,, \tag{4.2.32}$$

where $\Delta K_1 = (l^2 \Delta N_0 \pi^2)/(2L^3)$ represents the effect of ΔN_0, which is equivalent to a variation in the bending stiffness. With the change of variable $\omega t = 2\tau$, (4.2.32) can be written in the canonical form

$$\ddot{x}(\tau) + [\delta + 2\epsilon \cos(2\tau)]\, x(\tau) = 0\,, \tag{4.2.33}$$

where $\delta = (4K_1)/(M\omega^2)$ and $\epsilon = (2\Delta K_1)/(M\omega^2)$. The corresponding stability chart is reported in Figure 4.12(a). The addition of the Duffing term to equation (4.2.32) does not modify the shape of the curves that, in the stability chart of Figure 4.12(a), mark a transition between different-in-type responses, but its presence makes the solution bounded also in instability regions [60]. To illustrate Figure

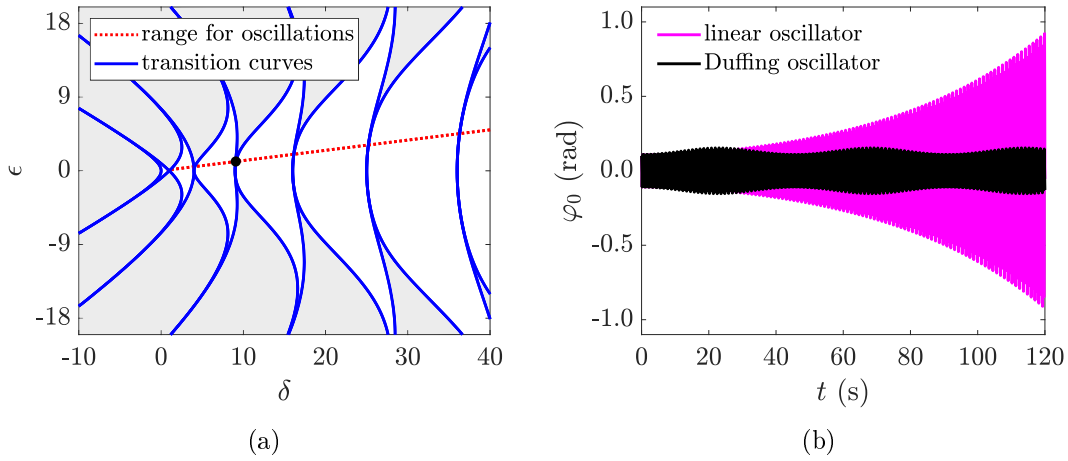

(a) (b)

Figure 4.12. Parametric resonance: (a) stability chart for Mathieu's equation (instability regions are shaded in light grey); (b) unbounded response (in magenta) for the point corresponding to the black dot in the first plot, which becomes bounded (in black) when the Duffing term is added ($K_2 = 1.187\,\mathrm{N/m}$).

4.12(b) represents the time history in terms of $\varphi_0(t)$ for values of the parameters $(\delta, \epsilon) = (9.080, 1.135)$ corresponding to the point indicated with a black dot in Figure 4.12(a). The addition of the Duffing term makes the solution to pass from that plotted in magenta, which diverges, to the one indicated in black, which remains bounded. The plot corresponds to $k = 4200\,\mathrm{N/m}$, so that $K_2 = 1.187\,\mathrm{N/m}$.

The complete equation for parametric resonance, also accounting for damping, Duffing and forcing terms, reads

$$\begin{aligned} &M\ddot{\varphi}_0(t) + C_1\dot{\varphi}_0(t) + C_2{\varphi_0}^2(t)\dot{\varphi}_0(t) + \frac{c_2}{k}\Delta K_1 \dot{f}_k(t)\varphi_0(t) + \\ &+ \left[K_1 + \Delta K_1 f_k(t)\right]\varphi_0(t) + K_2{\varphi_0}^3(t) - F(t) = 0\,, \end{aligned} \tag{4.2.34}$$

where we assume that $f_k(t) = \cos(\omega t)$.

An initial camber, like that corresponding to the inflexion under self-weight, triggers the onset of the oscillations due to the variation of the cable prestress: this is a classical example of self excitation due to parametric resonance. On the contrary, if the reference configuration is straight, an initial perturbation is necessary to induce the onset of oscillations.

Consider a cambered beam under self-weight. Setting $C_1 = 0.1\,C_{cr}$ and $C_2 = 0$, and assuming $\bar{K}_2 = 0.396\,\mathrm{N/m}$ as a reference value, Figure 4.13 reports the maximum displacement at mid-span as a function of the ratio ω/ω_1. In Figure

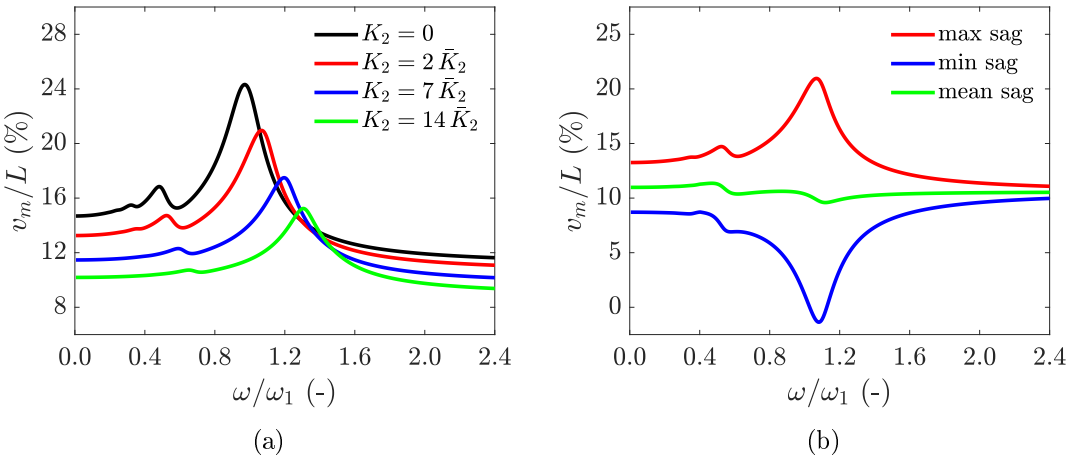

Figure 4.13. Parametric resonance: self-excitation of the beam, cambered under self-weight. Case $C_1 = 0.1\,C_{cr}$, $C_2 = 0$, $K_1 = 1.680\,\mathrm{N/m}$, $\Delta K_1 = 0.420\,\mathrm{N/m}$ ($\Delta N_0 = N_0/4$) and $\bar{K}_2 = 0.396\,\mathrm{N/m}$. (a) Influence of the Duffing K_2 expressed as a multiple of $\bar{K}_2$; (b) maximum, minimum and mean sag when $K_2 = 2\,\bar{K}_2$.

4.13(a), $K_1 = 1.680\,\mathrm{N/m}$ and $\Delta K_1 = 0.420\,\mathrm{N/m}$ ($\Delta N_0 = N_0/4$) are kept constant, while the Duffing term K_2 is varied and indicated as a multiple of $\bar{K}_2$. Observe that the Duffing term stiffens the beam, so that the maximum sag diminishes when K_2 increases, and also affects the peak position of curves at resonance, which moves rightwards as K_2 is increased.

Also in this case, in proximity of the fundamental parametric-resonance values, the oscillation amplitude may overcome the initial camber. This is represented in Figure 4.13(b) that reports, for $K_2 = 2\,\bar{K}_2$, the minimum and the maximum sag as well as their arithmetic mean. In particular, the mean value remains almost constant and equal to the initial camber, with slight deviations in correspondence of the fundamental and subharmonic resonances.

Active control

The variation of cable prestress can also be used to reduce or suppress the oscillations by means of an active control system.

In order to investigate this potentiality, consider first the case of free vibrations without damping ($c_1 = c_2 = 0$). A possible way to reduce the oscillations amplitude may consists in introducing impulsive variations in the cable prestress: Figure 4.14(a) compares the free vibrations with the controlled vibrations. A sensor detects the oscillator natural period and then an actuator applies the variation of stress in the cable with a doubled frequency and in phase opposition. Observe

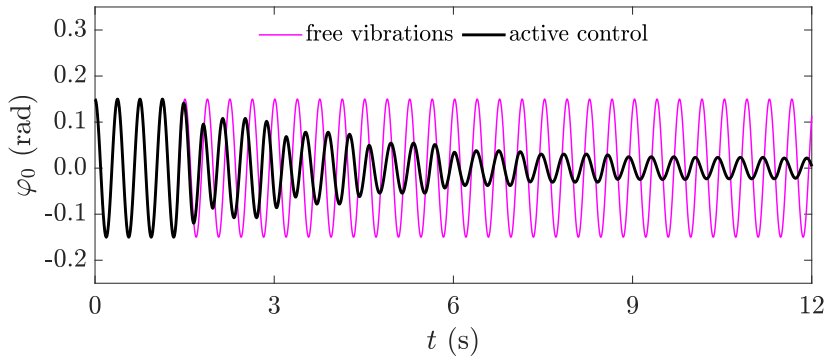

(a)

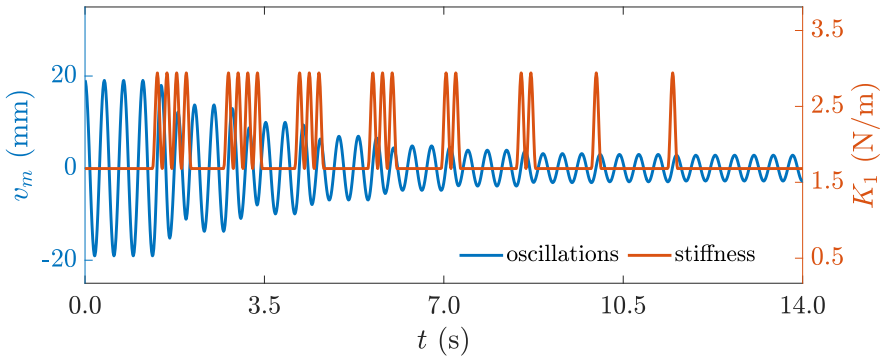

(b)

Figure 4.14. Active control of free vibrations with no damping (case $K_2 = 0.791\,\mathrm{N/m}$, $c_1 = c_2 = 0$), obtained with impulsive variations of the cable tensile force. (a) Comparison between free and controlled vibrations; (b) time history for the maximum displacement at midspan and for the stiffness K_1 , with impulsive variations induced by the actuator.

that the period of oscillation changes with the amplitude of the vibrations because of the nonlinear term; hence, it would be necessary to change accordingly the frequency of the impulses from the actuator. For this case, a stepwise variation has been considered, in the sense that the frequency of the impulses is maintained constant for the time in which they are effective, and it is updated successively following the new natural period detected by the sensor. Figure 4.14(b) reports the maximum displacement as a function of time, with indication of the variation of the stiffness K_1 , which is correlated with the variation of the cable prestress N_0 , as induced by the actuator. Observe that the number of the impulses at constant frequency is decreased because, as the oscillation amplitude diminishes, just a few impulses result effective; then, the control detects the new natural period and runs

again the actuator, decreasing the number of impulses if necessary (from 4 to 1 in the figure).

The introduction of damping can itself provide a strong decay in the oscillatory motion and render superfluous the active control. Nevertheless, the nonlinear character of the damping may suggest a new form of active control that is worth mentioning, at least for its theoretical value. To illustrate, consider the case in which only the nonlinear damping is present ($c_1 = 0$ and $c_2 = 880\,\mathrm{kg/s}$). The damping depends on $\varphi_0{}^2\dot{\varphi}_0$, so that its contribution is the higher, the larger the amplitude of oscillations is. If one artfully reduces the tensile force in the cable, the oscillations correspondingly increase their amplitude and, consequently, render the nonlinear dissipation more effective; when the initial prestress is restored, the vibrations are much smaller than in the case in which the cable tensile force had been kept constant. Figure 4.15 provides an example for this method. Figure 4.15(a) compares the free and controlled vibrations when the stiffness K_1 varies according to the graph of Figure 4.15(b), as a consequence of the release of the tensile force in the prestressing cable.

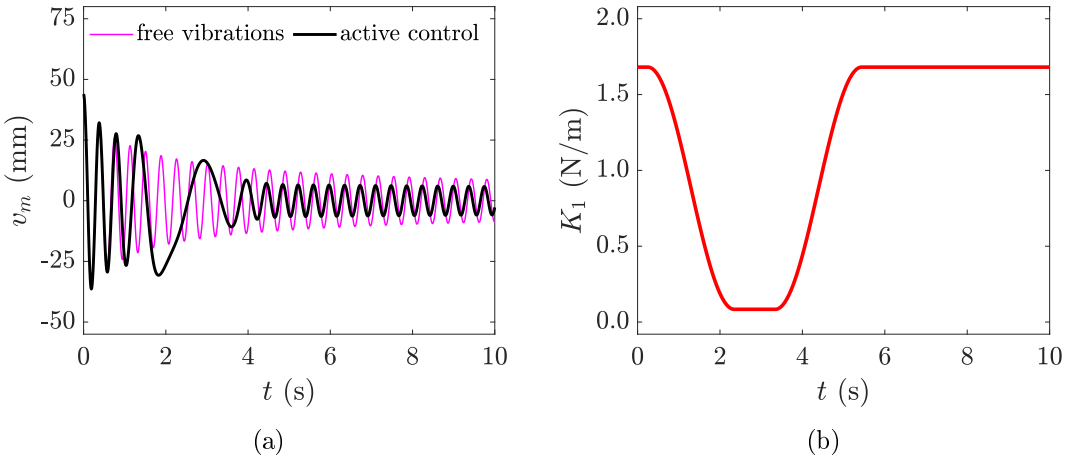

Figure 4.15. Alternative active control of free vibrations with nonlinear damping ($c_1 = 0$, $c_2 = 880\,\mathrm{kg/s}$, $K_2 = 0.791\,\mathrm{N/m}$). (a) Comparison between free and controlled vibrations; (b) Variation of stiffness K_1 in time, induced by releasing the tensile force in the cable.

In the case of forced vibrations induced by a periodic external perturbation, an active control may be much more effective than a strong damping, because the system can be stiffened by tensioning the cable when the external action is applied. Figure 4.16 reports the time histories of the forced vibrations, either uncontrolled or controlled, of a beam excited by a series of sinusoidal impulses, indicated in

Figure 4.16(a); the control detects, by means of a sensor, when a limit value for the sag at midspan is exceeded; at this point an actuator starts to pull the cable so to modify the stiffness K_1, as indicated in Figure 4.16(b), in order to reduce oscillations amplitude. When the limit value for the sag is no more exceeded, the cable is released and the initial prestress is restored. For the case represented in the figure, the reduction of amplitude is about 30% as a consequence of an increase of stiffness K_1 of the order of 50%.

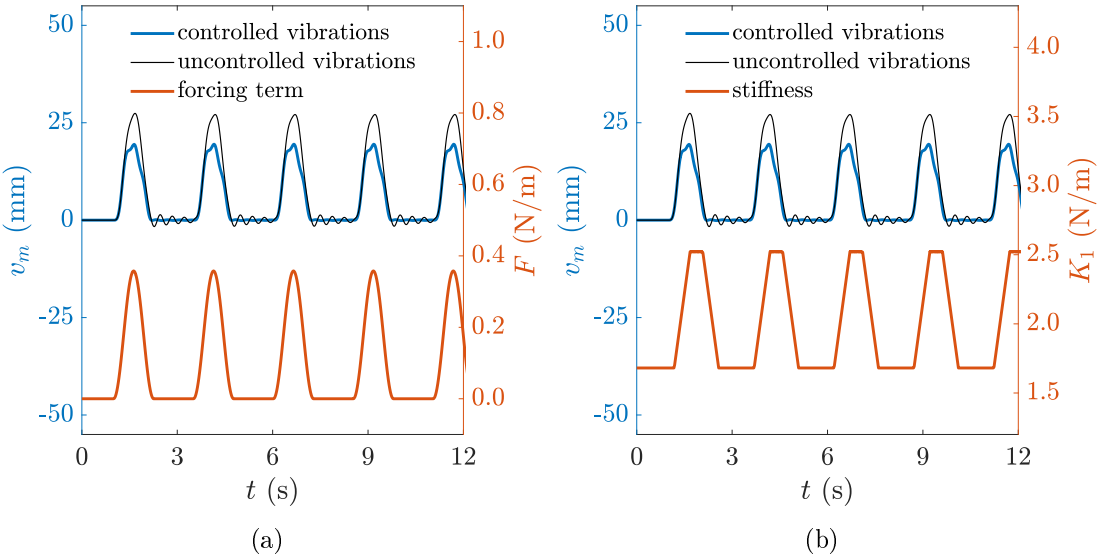

Figure 4.16. Comparison of uncontrolled and controlled forced vibrations (case $C_1 = 0.1\,C_{cr}$, $C_2 = 0$, $K_2 = 0.791\,\mathrm{N/m}$) with evidence of (a) the forcing term and (b) the variation in time of the stiffness K_1, as a consequence of the control on the axial force in the cable.

Certainly, other types of active controls can be obtained by acting directly on the cable tensile force, and/or by using more than one cable eccentrically located with respect to the beam axis. For example, inserting a certain number of actively controlled tendons, a cable-actuated robotic limb could be manufactured, with properties similar to the prototype presented in [75]. The cases reported above are only examples of the potentiality of the proposed structural system.

Chapter 5

Multi-stable flex-ten beams

The possibility to design a multi-stable flex-ten joint is here concerned. In the previous chapters, the simplest class of flexural tensegrities, i.e., the case of segmental beams for which the bending moment is a monotonic increasing function of the relative rotation of the segments (convex bending energy), was theoretically analyzed, prototyped and tested under static and dynamic loads. The aim now is to present a new class of flex-ten beams, characterized by a *nonlocal* and *non-convex* strain energy function, described in terms of the rotations at the segmental contact sections. This represents the extension to the case of bending of the chains formed by snap-springs under tension [76], with additional nonlocal interaction. The bi-stable behavior now depends not only upon the shape of the pitch lines, but also on a tailored increased mobility of the prestressing tendon inside the sheaths, which produces an effect similar to the snap-through buckling.

For illustrative purposes, the case analyzed here is that of pure bending. One of the most remarkable properties of the model is that the Maxwell path is described by a stepped *strain-hardening* curve. Real scale prototypes have been 3D printed and tested to compare the experimental results with the theoretical predictions. As derived for flexional loading, this concept could be immediately adopted to develop foldable devices, to store binary data, or to interpret different configurations of biological structures.

Simple models for bi-stable bars are recalled in Section 5.1, and the motivation from natural/engineered materials is highlighted. The concept of bi-stable flex-ten beams is indicated in Section 5.2.1, and the governing equations are presented in Section 5.2.2. Section 5.2.3 is dedicated to the testing of two representative 3D-printed physical models, for which the experimental findings are compared with the theoretical results. These results here presented are also summarized in [77].

The extension to a more complicated multi-stable behavior, with a more elaborated geometry for the contact joints, is finally analyzed in Section 5.3.

5.1 Multi-stable materials and their modeling

New materials characterized by a morphing capacity are often derived from the possibility of supporting multi-stable equilibrium states under prescribed boundary conditions. Such materials arouse the interest of engineers and material scientists, for their specific applications in the electronic, mechanical and biomedical fields.

Multi-stable configurations may be obtained at the molecular level thanks to microstructural transformations, which can be driven by variations in terms of stress, temperature and electro-magnetic field. A paradigmatic example is represented by shape memory alloys, for which the austenite-martensite phase transformation permits multiple simultaneous equilibrium states for a fixed value of external actions, which results in large deformations at the macroscopic level. To illustrate, Figure 5.1(a) represents the experimentally-measured uniaxial *macroscopic* response under cyclic loading [78] of a specimen made of a shape memory alloy in a constant magnetic and temperature environment. There is an evident hysteresis loop, where the largest part of the deformation is associated with a plateau, apparently horizontal but actually *strain-harding* in type. A similar behavior has been observed in foldable molecules, such as DNA and other biological structures and proteins, as a consequence of the breakage and rearrangement of molecular bonds (hydrogen and van der Waals bonds) under external actions. For example, Figure 5.1(b) reports [79] the *strain-hardening sawtooth* force vs. displacement path for titin, the giant sarcomeric protein of striated muscle, measured in *microscopic* tests under uniaxial tension.

In a continuum approach, the equilibrium states for structures made of materials of this type are usually associated with the local and global minimizers of energy functionals, possibly incorporating the effects of temperature and electro-magnetic fields, peculiarly characterized by a non- (quasi) convex dependence on the stretch tensor. Since the seminal work by Ericksen [80] on uniaxially stretched elastic bars, it has been clear that the plateau in the macroscopic stress-strain response is due the coexistence of solid phases. There are multiple equilibrium states, since the location of the phases in the bar can be rearranged without affecting the statics. The coexistence of material phases was discussed in more general thermodynamic framework by Dunn and Fosdick [81].

The continuum models have their justification in the material underlying crystalline microstructure, or in a rearrangement of the protein constituents, a fact that has led many authors to consider discrete lattices whose points are coupled by centripetal interactions. A key aspect is that the interaction forces between the points, which depend upon their relative distance, are described by non-convex potentials permitting bi-stable equilibrium configurations. Müller and Villaggio [82] proposed an interesting interpretation with reference to a mechanical model made by chains

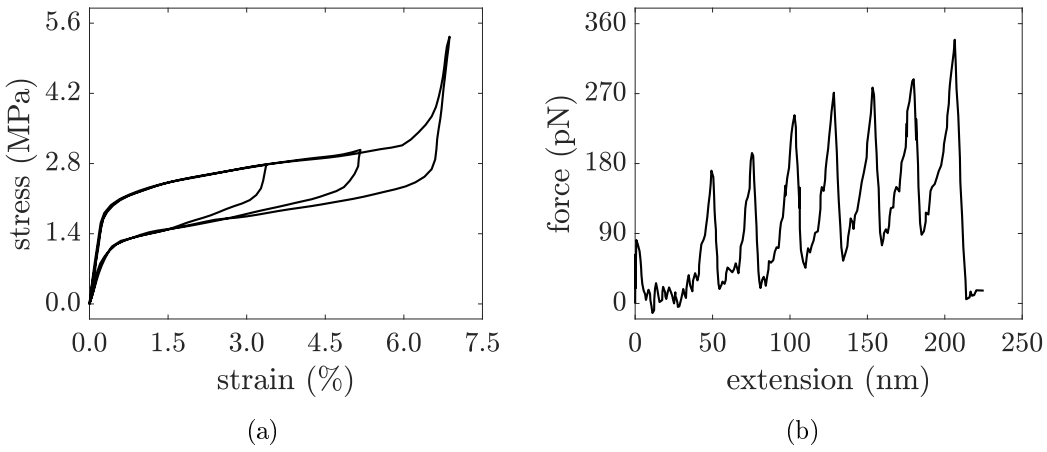

Figure 5.1. Typical response of real materials: (a) magnetic shape memory alloy under a uniaxial cyclic loading in a controlled temperature and magnetic environment at 6 kOe (picture adapted from [78]); (b) uniaxial tension test on titin, the protein constituting striated muscles (picture adapted from [79]).

of bi-stable two-bar-linkage elements, amenable of snap-through buckling. The sequential occurrence of snaps in the units provides a macroscopic response in which large deformations occur under a stress oscillating around a constant value, reminiscent of the onset of plastic flow. The bi-stable character of the interaction forces can also be considered in a physical model where the units consists of springs and dashpots [47]; connecting the points with multiple units, it is possible to reproduce the slow wave of plastic flow and the Portevin-Le Chatelier effect in tensile bars, as measured by experiments [83].

Truskinovsky and coauthors were among the first to develop and exploit the concept model of uniaxial chains composed by atoms interacting through bi-stable springs, usually referred to as snap-springs to recall the properties of snap-through buckling. Such a simple arrangement, considering either interconnections of type NN (nearest neighbor) or NNN (next nearest neighbor), is sufficiently rich to represent complex stability paths [76], which can reproduce the response of shape memory alloys [84] or plastic flow [85]. More recently, Benichou and Givli have revisited the discrete chain model [86] to study the behavior of proteins or shape memory alloys, providing an experimental verification with a finite-scale physical model consisting of units susceptible to snap-through buckling, connected to linear springs. The system proposed by Caruel et al. [87] to model the response of contractile units in skeletal muscles is composed of bi-stable units connecting two rigid backbones, where each crosslinker is represented by a bi-stable potential, representing two folding configurations, connected in series to a linear spring.

When uniaxially stretched, chains of snap-springs evolve according to equilibrium paths where large displacements derive from the sequential occurrence of snap-through instabilities of the constituent units. Such paths may be associated with points representative of configurations where each unit is in a locally stable equilibrium state; however, since the fluctuation consequent to the snaps can cause the exit from the domain of local equilibrium, the structure is prone to follow the Maxwell path, corresponding to absolute minima of the energy. Anyway, the discrete nature of the model implies a stepped response around a constant value of stress, with an amplitude that decreases as the number of units is increased, as evidenced from the graphs recorded in [76]. In the limit of infinite units, there is a convergence to a horizonal plateau, as in the continuum model [80]. On the other hand, the graphs of Figure 5.1, which typically refer to tensile experiments on shape memory alloys and on proteins amenable of folding/unfolding, indicate that in the branches of large deformation the response is indeed strain-hardening in type. The model presented in [88] consists of a simple chain of snap-springs with NN interactions with diverse constitutive properties but characterized by the same Maxwell force (computable with the equal-area rule): correspondingly, the Maxwell stress vs. average strain path corresponds to a stress that fluctuates around a constant value as the deformation is increased, whereas the maximum hysteresis path, associated with local minima, exhibits a strain-harding trend because of the orderly snaps of the springs, from the weakest to the strongest ones. A strain-hardening Maxwell path can be obtained by introducing the dependence upon temperature [89–91], which affects the mechanical properties of the links due to entropic effects [91].

All the discrete models mentioned above consider the uniaxial response of chains composed, in practice, of extensional snap-springs. Continuum theories for the bending of beams that are based on the minimization of a non-convex strain energy functional of the curvature field have been proposed as an extension of the classical Euler's theory of the inextensible elastica, in order to overcome the classical quadratic energetic dependence on the curvature. Fosdick and James [44] considered the simplest problem of the pure bending, showing that under prescribed end-couples a set of many inhomogeneous strain configurations is possible. These kinds of equilibrium configurations are related to those that are observed in a casual experiment on the pure bending of a steel pocket measuring tape. Non-convex strain energy densities with linear growth at infinity (oblique asymptotes) can induce the localization of bending strains similar to what occurs in a plastic hinge [45]. Energies of this type can be theoretically derived [46] for elastic-plastic materials exhibiting a transition from the upper to the lower yield point [83].

The discretized version of models of this type for bending has seldom been attempted. On the one hand, the experimental verification is difficult because, whereas the snap-spring under tension can be conceptualized in the snap-through

buckling of lowered arches, or two-bar-linkages, and manufactured accordingly, the practical way to fabricate snap-spring hinges that link rigid segments is not straightforward. On the other hand, it is difficult to conceive, for the case of bending, the counterpart of the interconnections of the type "next nearest neighbor", which induce in uniaxial models that great variety of behaviors such as to make them particularly effective for the description of complex interaction phenomena at the molecular level. Despite this, the characterization of the bending behavior is of great importance to describe the peculiar capacities of elongated structures, with applications especially in the biological field, e.g., for the interpretation of the mechanical properties of folding molecules such as DNA and of protein chains, capable of adapting and replicating also by virtue of their flexural properties [92].

The issues above are readily solved thanks to the versatility of flexural tensegrities. In the following, the problem of bending is investigated for a flex-ten chain of segments, and the practical manufacturing of the bi-stable joint is obtained thanks to the geometry of the contact surfaces and the additional mobility of the cable. The nonlocal interconnection of all the segments through the unbonded tendon preserves some features of the next nearest neighbor, or higher order, interactions. In fact, the rotation of any contact joint stiffens all the other joints, so that the orderly snaps of the spring-hinges occur at an increasing bending moment. Remarkably, this leads to a strain-hardening character of the Maxwell path, which renders the model suitable to reproduce experimentally the measured responses for elements of the type represented in Figure 5.1.

5.2 Bi-stable segmental beams

A particular construction of the joints is proposed in order to achieve a non-convex strain energy. The governing equilibrium equations are analyzed for the paradigmatic case of pure bending of an initially straight beam. Experiments on 3D-printed prototypes are finally considered to evidence the inhomogeneous strain configurations for given loads at the extremities of the beam.

5.2.1 The contact joint

In principle, any type of nonlinear moment-curvature relationship could be obtained with a tailored design of the pitch lines; the limit, however, is represented by possible slip and material interpenetration between the segments, which is dictated by the geometry and roughness of the contact surfaces. By using toothed conjugate profiles, in theory, relative rotations between the segments up to $\pm 180^\circ$ can be achieved. In practice, only convex pitch lines can avoid the interpenetration

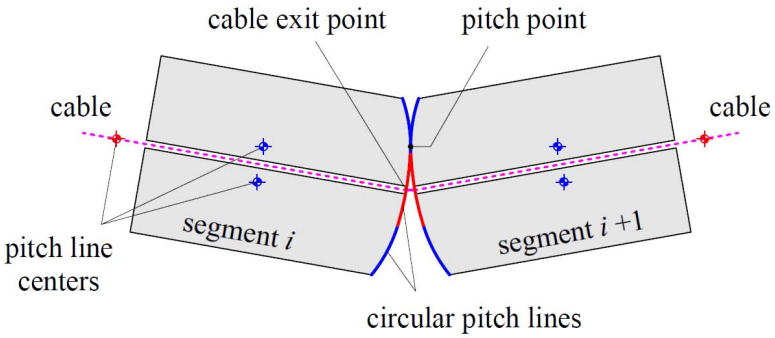

(a)

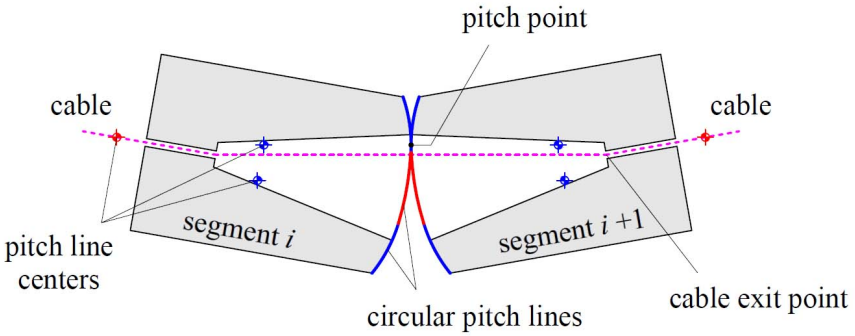

(b)

Figure 5.2. Schematic representation of a contact joint in which the pitch lines are smoothly connected arcs of circle: (a) configuration with the cable exit point on the pitch line; (b) configuration with the cable exit point set back with respect to the pitch line.

of the segments in contact during the pure rolling motion. More precisely, one of the pitch lines can be convex and the other one concave, but in any case, the profiles that avoid material interpenetration corresponds to conditions (see Section 2.2.1) in which the lever arm a_i , indicated in Figure 2.2(a), is a monotone increasing function of the relative rotation $\Delta\varphi_i = \varphi_{i+1} - \varphi_i$. Since the axial force N in the cable is also a monotone increasing function of the relative rotation, the bending moment $M_i = a_i N$ is monotonically increasing as well. No bi-stable equilibrium states are thus possible.

A way to obtain a non-monotone moment-rotation relationship, without running into problems of material interpenetration, consists in setting back the cable exit point with respect to the pitch profile. Figure 5.2 shows a schematic example to represent this concept. The design pitch lines consist of three smoothly connected arcs of circle: the central one (red color line) has twice the radius of the external

ones (blue color line), which are symmetric with respect to the longitudinal axis of the segment. Globally, the pitch lines are convex and represented by regular curves, so to provide a smooth rolling motion without interpenetration. Figure 5.2(a) reports the standard case, analyzed so far, in which the cable exit point is right on the pitch line: the area hatched in grey, representing the material matrix cut by a longitudinal section, indicates the location of the sheath and the region where the cable is constrained. This configuration shall provide a monotonically increasing dependence of the lever arm on the relative rotation of the contact segments. On the contrary, Figure 5.2(b) represents the case in which the cable exit point is set back with respect to the pitch profile: the hatched portions indicate the corresponding mobility of the cable when the segments are rotated apart. In particular, the cable exit point is located between the centers of curvature of the pitch lines and the segments are hollowed in such a way that there is no contact of the cable with the matrix, at least until the relative rotation does not exceed a certain limit. During the pure rolling motion of the contact surface, the cable moves and its distance from the pitch point varies. By varying the distance of the exit point, one can obtain a non-monotone relationship between the lever arm a_i and the relative rotation $\Delta\varphi_i$ of the type represented in Figures 5.3(a) and 5.3(b), both characterized by bi-stable equilibrium configurations.

The trilinear graphs result from an assumed piecewise circular shape of the pitch lines and to the allowed movement of the cable inside the hollow segments[1]. Of course, by varying the shape of the pitch lines one can obtain any kind of smooth curves. The cable elongation Λ_i at each contact joint is indicated in Figures 5.3(c) and 5.3(d), respectively. The non-convex graphs are composed of arches of parabolas since, as it will be explained in the sequel, formula (2.1.1) holds also in this case, i.e., $a_i = a_i(\Delta\varphi_i)$ is the first derivative of $\Lambda_i = \Lambda_i(\Delta\varphi_i)$.

The graphs of a_i and Λ_i in Figure 5.3 are drawn only for positive values of the relative rotation $\Delta\varphi_i$, but they can be directly extended to negative values since they are odd and even functions, respectively. In fact, due to geometric symmetry, the bending response is specular for opposite values of the applied actions. In Figure 5.3, points A and B delimit the spinodal region (for positive relative rotations), which is the region of instability: if the load is quasi-statically increased (decreased), once reached point A (point B), the equilibrium configuration jumps to a distant branch of the graphs.

The graphs of Figure 5.3 correspond to pitch lines for which the internal (red) arc has radius 48 mm and length 11.73 mm, whereas the external (blue) arcs have radius 24 mm and length of 14.44 mm. The difference between the case of Figures

[1]More precisely, this construction provides a trilinear graph only approximately, as it will be clear later on while discussing equations (5.2.4). However, the accuracy is excellent: the maximum deviation from linearity is of about 0.5% for the case of Figure 5.3(a), and of about 1.0% for Figure 5.3(b) when $\Delta\varphi_i \simeq 1$ rad, the difference being the smaller, the smaller the rotation.

5.3(a) and 5.3(c), on the one hand, and of Figures 5.3(b) and 5.3(d), on the other hand, consists in the location of the exit point of the cable, which is set back with respect to the pitch line of 31.6 mm, in the first case, and of 39.2 mm, in the second case. In both cases, the cable can freely span an arc length of 17.59 mm measured along the pitch line profile, corresponding to the cavity of the segments indicated in Figure 5.2(b). These two different designs will be prototyped in 3D-printed physical models, hereafter referred to as *Prototype A* and *Prototype B*.

Remarkably, such a small difference in the location of the exit point can greatly affect the joint response. The peculiarity of prototype B is that null values of the

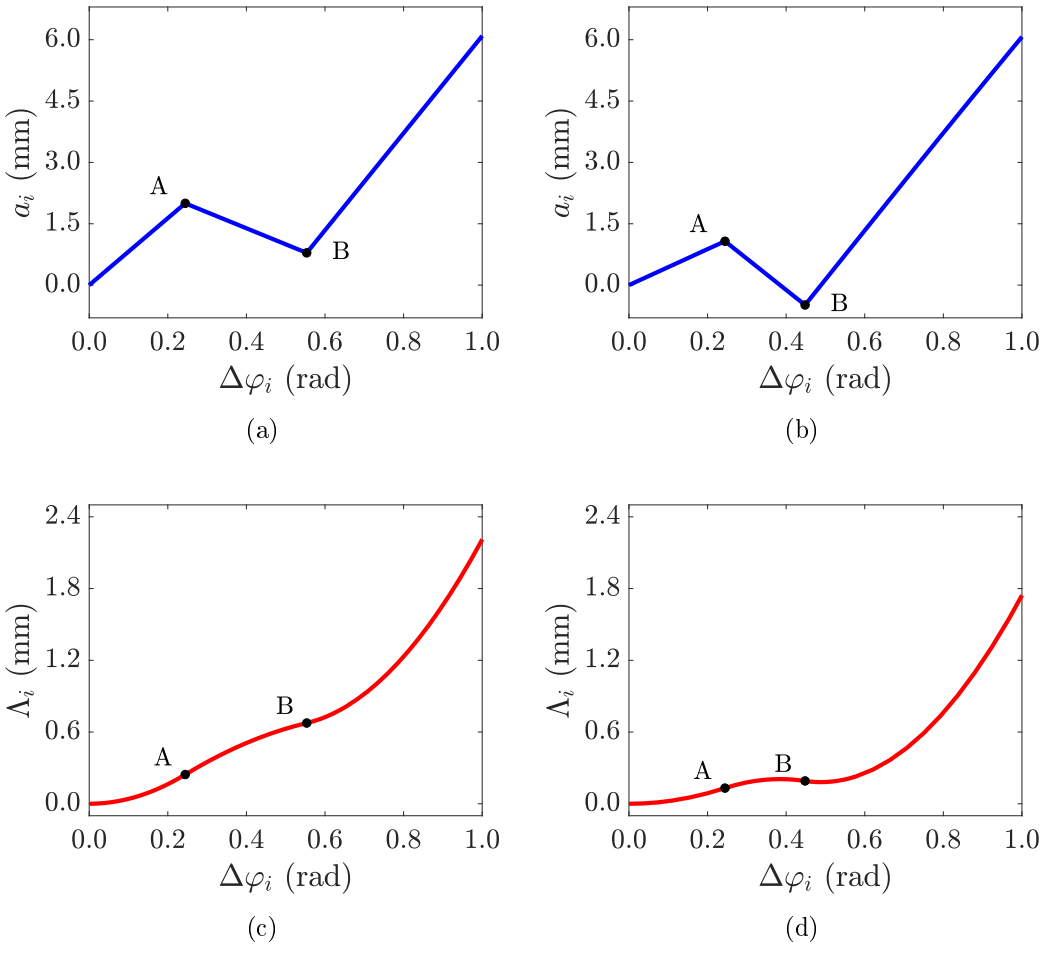

Figure 5.3. Constitutive relationships for two designs that will be prototyped and tested: (a) lever arm a_i as a function of $\Delta\varphi_i$ for *Prototype A*; (b) lever arm a_i for *Prototype B*; (c) and (d) corresponding cable elongation Λ_i . Points A and B delimit the spinodal region and correspond to each other in their respective figures.

lever arm a_i can be attained for a non-null relative rotation $\Delta\varphi_i$, as indicated in Figure 5.3(b): this means that there are bent configurations in equilibrium with null bending moment. This is not the case for prototype A, as it is clear from Figure 5.3(a): the only configuration in equilibrium with null external forces is the straight state. A response of this type could be referred to as "pseudoelastic in bending", in accordance with a similar term used to characterize the tensile response of SMA wires. The two prototypes thus represent paradigmatic examples, but of course they cannot cover all possible cases.

It may be worth remarking that the bi-stable behavior of the joint depends only upon the shape of the pitch lines and on the placement of the prestressing cable, i.e., the location of its exit points with respect to the pitch lines and the region where it can freely move inside the segments. Indeed, the constitutive properties depend only upon the geometry of the structure.

5.2.2 Governing equations and analytical results

Consider the equilibrium under pure bending of a flexural-tensegrity beam composed of n segments coupled one another with the bi-stable joints represented in Figure 5.2(b).

If the beam is constrained in a hard device (strain-driven test), then the relative rotation $\Delta\bar{\varphi}$ on the ends of the beam is prescribed. If the segments are supposed rigid, the equilibrium problem reduces to the study of critical points of the increase ΔU of the elastic strain energy, which is expressed by (2.1.8). This is here rewritten, for clarity, and reads

$$\Delta U = N_0\Lambda + \frac{1}{2}K\Lambda^2\,, \quad \Lambda = \sum_{i=1}^{n-1}\Lambda_i\,. \tag{5.2.1}$$

The constraint equation is given by

$$\sum_{i=1}^{n-1}\Delta\varphi_i = \Delta\bar{\varphi}\,. \tag{5.2.2}$$

Again, N_0 is the cable initial prestress, K is the elastic constant of the cable, possibly taking into account the presence of springs in series, while

$$\Lambda_i = \Lambda_i(\Delta\varphi_i)\,, \tag{5.2.3}$$

is the elongation of the cable in the $i-$th contact joint, $i = 1\ldots n-1$, due to the relative rotation $\Delta\varphi_i = \varphi_{i+1} - \varphi_i$ of the coupled segments. This produces the straining of the cable. With reference to (5.2.1), this function is associated

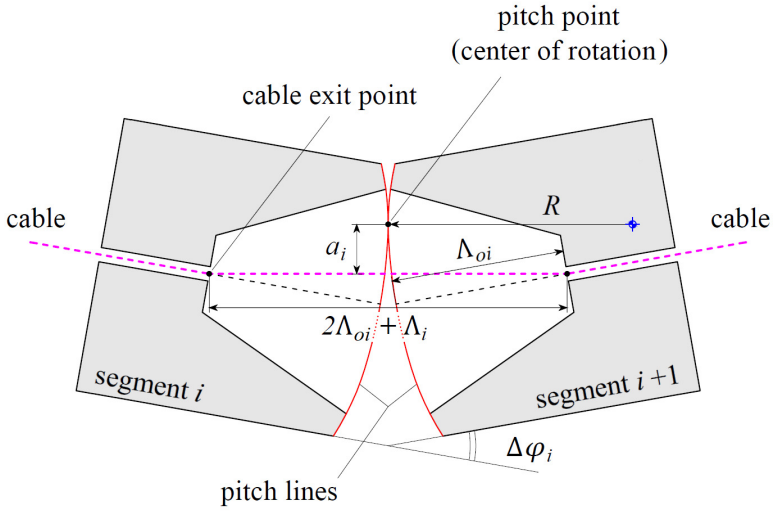

Figure 5.4. Schematic representation of the $i-$th contact joint, with indication of the lever arm a_i , the exposed portion of the cable $2\Lambda_{oi} + \Lambda_i$ and the radius of curvature R of the pitch line at the pitch point.

with the strain energy stored in the flexural-tensegrity beam, dictated only by the shape of the contact pitch lines and the location of the exit point of the cable, as schematically represented in Figure 5.2(b). We will assume for such a function a non-convex dependence, of the type indicated in Figures 5.3(c) or 5.3(d).

Geometric considerations indicate that, as confirmed by the shape of the graphs of Figures 5.3, the lever arm of the cable force $a_i = a_i(\Delta\varphi_i)$ is the first derivative of the local cable elongation $\Lambda_i = \Lambda_i(\Delta\varphi_i)$. In fact, with reference to Figure 5.4, which displays two adjacent segments subjected to the relative rotation $\Delta\varphi_i$, consider the effects of an incremental infinitesimal relative rotation $\mathrm{d}\Delta\varphi_i$. Let $2\Lambda_{oi}$ denote the distance between the two exit points of the cable in the reference straight configuration. In the configuration $\Delta\varphi_i$ this becomes $2\Lambda_{oi} + \Lambda_i$, while $R = R(\Delta\varphi_i)$ will denote the radius of curvature of the pitch line at the pitch point. The incremental relative motion of the segments is an infinitesimal rotation about the pitch point, but the pitch point moves as well with the rotation. Therefore, one can write

$$\mathrm{d}a_i = -\frac{2\Lambda_{oi} + \Lambda_i}{2}\frac{\mathrm{d}\Delta\varphi_i}{2} + R\frac{\mathrm{d}\Delta\varphi_i}{2}\,, \tag{5.2.4a}$$

$$\frac{\mathrm{d}(2\Lambda_{oi} + \Lambda_i)}{2} = a_i\frac{\mathrm{d}\Delta\varphi_i}{2}\,. \tag{5.2.4b}$$

These represent an extension of equations (2.1.2) discussed in Section 2.1.2. For the case at hand, since Λ_{oi} is a constant quantity, it is immediate to deduce

from (5.2.4b) that $\mathrm{d}\Lambda_i/\mathrm{d}\Delta\varphi_i = a_i$, which is the equation (2.1.1). Moreover, using (5.2.4b) in (2.1.2a) one recovers (2.1.3), i.e., the equation that serves to design the shape of pitch lines.

In the special case in which the pitch line is an arc of a circle so that the radius of curvature R is constant, from the condition that $a_i = 0$ when $\Delta\varphi_i = 0$, one finds from (2.1.3) that $a_i = A\sin(\Delta\varphi_i/2)$, where A is a constant that depends on the radius of the pitch line. In particular, $A = R - \Lambda_{oi}$ for the configuration reported in Figure 5.4, where the cable moves still in the hollow portion[2]. When $\Delta\varphi_i$ is small, with very good approximation[3] one can write $a_i = A\,\Delta\varphi_i/2$. This provides a direct verification that circular pitch lines provide almost a linear dependence of a_i on $\Delta\varphi_i$, as anticipated in Section 5.2.1 while discussing the piecewise linear trend of the graphs in Figures 5.3(a) and 5.3(b).

Taking into account that $a_i = a_i(\Delta\varphi_i)$ is the first derivative of $\Lambda_i = \Lambda_i(\Delta\varphi_i)$, as per (2.1.1), the stationary points of the energy correspond to the solution of the system of equations

$$\left[N_0 + K\left(\sum_{i=1}^{n-1}\Lambda_i(\Delta\varphi_i)\right)\right] a_i(\Delta\varphi_i) = M\,, \quad i = 1\ldots n-1\,, \tag{5.2.5}$$

in the $n-1$ unknowns $\Delta\varphi_i$, where $M = \text{const.}$ is the Lagrange's multiplier originating from the constraint (5.2.2), which corresponds to the constant bending moment along the beam.

When the beam is loaded in a soft device (stress-driven test), then the uniform bending moment M is prescribed. Denoting with ΔU the increase in strain energy function, as per (5.2.1), and with ΔW the work of the external end couples M, the equilibrium configurations coincide with the stationary points of the total energy

$$\Delta U - \Delta W = N_0\Lambda + \frac{1}{2}K\Lambda^2 - M\Delta\bar{\varphi}\,, \tag{5.2.6}$$

where $\Delta\bar{\varphi}$ takes the same expression of (5.2.2). The corresponding equilibrium equations take a form analogous to (5.2.5), where now M is given.

In the following, two different types of bi-stable flexural-tensegrity segmental beams will be analyzed in detail. These are the ones referred to in Section (5.2.1) as *Prototype A* and *Prototype B*, for which the geometric parameters have been indicated in the same section. The laws for $a_i = a_i(\Delta\varphi_i)$ and $\Lambda_i = \Lambda_i(\Delta\varphi_i)$ are those represented in the graphs of Figures 5.3(a) and 5.3(c) and Figures 5.3(b) and 5.3(d) for *Prototypes A* and *B*, respectively. The peculiarity of *Prototype B*

[2]When the pitch line is an arc of a circle of radius R and the cable moves in the hollow portion of the segment, the derivation of this result is straightforward. In fact, with elementary trigonometry, one finds $\Lambda_i = 2R - 2(R - \Lambda_{oi})\cos(\Delta\varphi_i/2) - 2\Lambda_{oi}$ and $a_i = (R - \Lambda_{oi})\sin(\Delta\varphi_i/2)$.

[3]When $\Delta\varphi_i = 1\,\mathrm{rad}$, $\sin(1/2) = 0.48$.

is that null values of the lever arm a_i correspond to non-null relative rotations: this implies that non-straight configurations at null external moment are expected for the beam. More in general, a variety of nontrivial equilibrium configurations, characterized by an inhomogeneous distribution of relative rotations, are possible even under uniform bending.

Response in the hard device

For $N_0 = 1.96\,\mathrm{N}$ and $K = 1.03\,\mathrm{N/mm}$, Figure 5.5 shows the graphs of all possible states, in terms of energy ΔU and of end-couple M, as a function of the relative rotation $\Delta\bar{\varphi}$ for *Prototype A* with three bi-stable joints ($n = 4$ segments). Figure 5.6 reports the same plots for five bi-stable joints ($n = 6$ segments). In this latter case N_0 is still $1.96\,\mathrm{N}$, but $K = 0.89\,\mathrm{N/mm}$, because the length of the beam changes (it is longer) and, accordingly, the stiffness of the tendon varies (it decreases). Absolute minima (stable states) are shown with bold (black) lines, metastable states with solid (red) lines and unstable states with dotted (magenta) lines. Note that, if the number of segments is increased while keeping fixed the geometry of the joints, for example from 3 to 5 as shown in Figures 5.5 and 5.6, we move from the configuration that in the snap-spring chain analyzed in [76] was called *supercritical*, to the one referred to as *subcritical*.

Similar to what discussed in [76], in the *supercritical* configuration the absolute minima of the energy function, represented with black bold lines in Figures 5.5(a) and 5.6(a), form a smooth curve, whereas in the *subcritical* configuration angular points appear where the curve changes slope. This effect depends upon the extension of the spinodal region of the single joint, i.e., the distance between point A and point B in Figure 5.3, with respect to the number of segments. If the beam is formed by a limited number of segments, the unstable branch of one snap-spring can be stabilized by the angle-control of the hard device. This is evident in Figure 5.5(b), where unstable branches characterized by steep and negative slope connect, without gaps, the two adjacent stable branches with positive slope. The analytical demonstration of this finding, reported at the end of this section, follows the same arguments presented in [76].

Figure 5.7 shows the expected macroscopic response of *Prototype A* with $n = 6$ segments in a monotone strain-drive test (increasing $\Delta\bar{\varphi}$). The beam could follow two different main paths, evidenced in the graphs with a black bold line. The first one corresponds to the *Maxwell path* associated with absolute minima of ΔU, represented in the ΔU-$\Delta\bar{\varphi}$ and M-$\Delta\bar{\varphi}$ graphs of Figures 5.7(a) and 5.7(c), respectively. The second one, referred to as *maximum hysteresis path*, includes also metastable states, i.e., local minima of the strain energy ΔU, and is indicated in the corresponding Figures 5.7(b) and 5.7(d). This latter path prescribes energy dissipation by hysteresis under loading and unloading path, with the appearance

of rhomboidal loops in Figure 5.7(d).

What should be observed is the main peculiarity of these graphs: both the Maxwell and the maximum hysteresis paths are characterized by a *strain-hardening* trend. This is essentially due to the nonlocal character provided by the unbonded

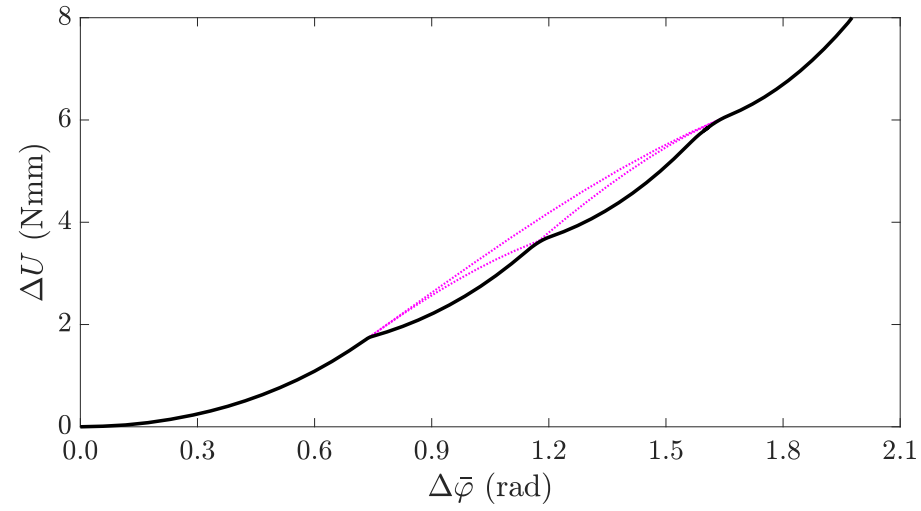

(a)

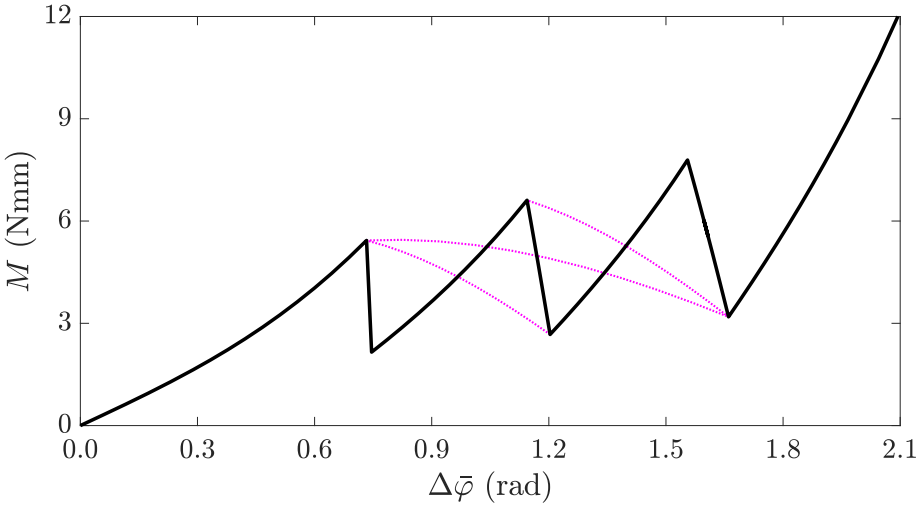

(b)

Figure 5.5. Response in a hard device of the bi-stable flex-ten *Prototype A* with n=4 (supercritical configuration): (a) energy as a function of relative end rotation $\Delta\bar{\varphi}$ and (b) moment M vs. $\Delta\bar{\varphi}$. Stable states are shown with bold (black) lines and unstable states with dotted (magenta) lines. Parameters: $N_0 = 1.96\,\mathrm{N}$ and $K = 1.03\,\mathrm{N/mm}$.

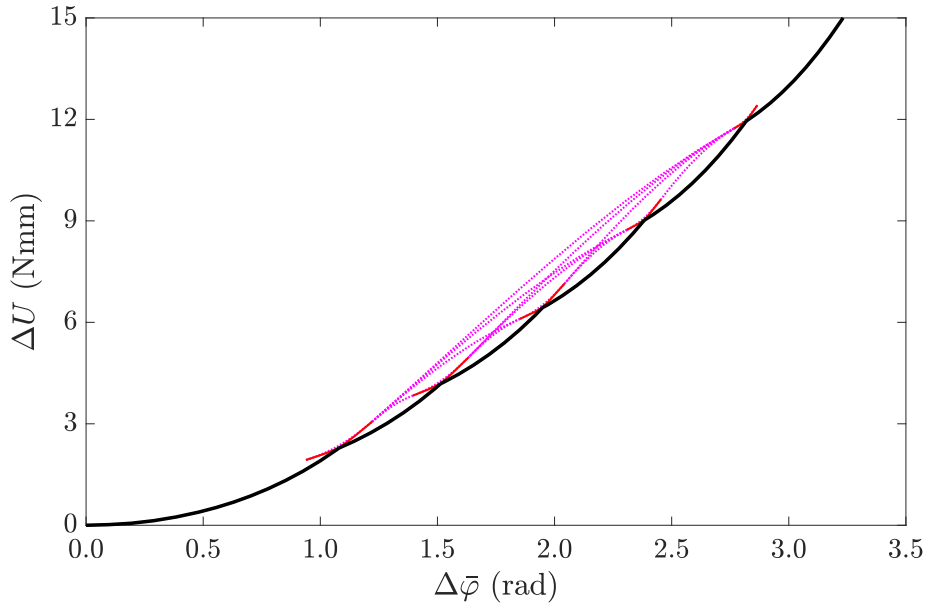

(a)

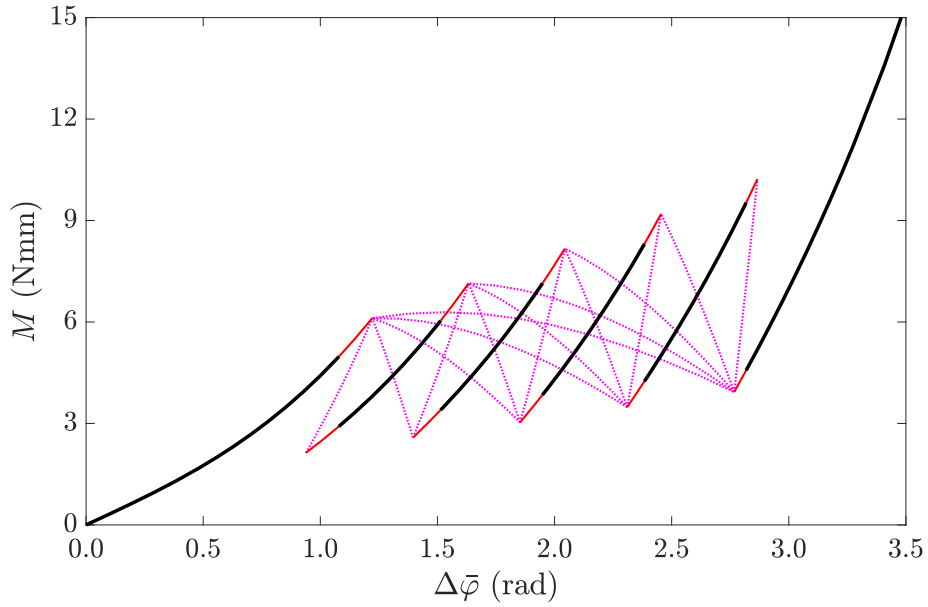

(b)

Figure 5.6. Response in a hard device of the bi-stable flex-ten *Prototype A* with $n = 6$ segments (subcritical configuration): (a) energy as a function of relative end rotation $\Delta\bar{\varphi}$ and (b) moment M vs. $\Delta\bar{\varphi}$. Stable states are shown with bold (black) lines, metastable states with solid (red) lines and unstable states with dotted (magenta) lines. Parameters: $N_0 = 1.96\,\mathrm{N}$ and $K = 0.89\,\mathrm{N/mm}$.

prestressing cable, which produces the stiffening of the beam with increasing rotation. The branches for stable and metastable states progressively become steeper as the deformation $\Delta\bar{\varphi}$ increases; moreover, both the Maxwell path and the hysteresis path follow a stepped curve that increases with the overall rotation. This is qualitatively different from what occurs in chains of snap-springs [76,82].

In order to recover the same qualitative response predicted by models of this kind, in the flex-ten beam one should disregard the increment in the cable axial

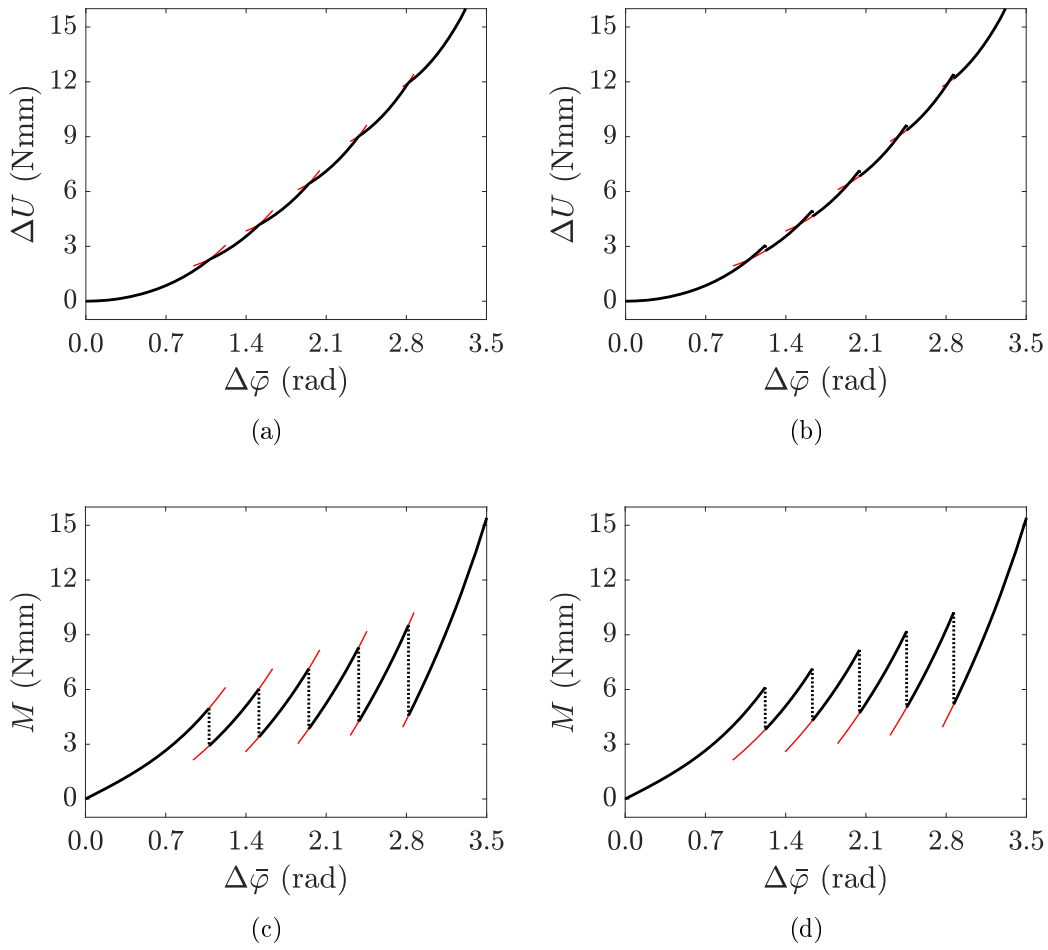

Figure 5.7. Response of the bi-stable flex-ten *Prototype A* with $n = 6$ segments in a strain-driven test (increasing $\Delta\bar{\varphi}$): (a) Maxwell path and (b) maximum hysteresis path in the ΔU-$\Delta\bar{\varphi}$ (energy-strain) chart; (c) Maxwell path and (d) maximum hysteresis path in the M-$\Delta\bar{\varphi}$ (load-strain) chart. Followed paths are drawn with bold (black) lines, stable and metastable states are shown with solid (red) lines and unstable states are omitted. Parameters: $N_0 = 1.96\,\mathrm{N}$ and $K = 0.89\,\mathrm{N/mm}$.

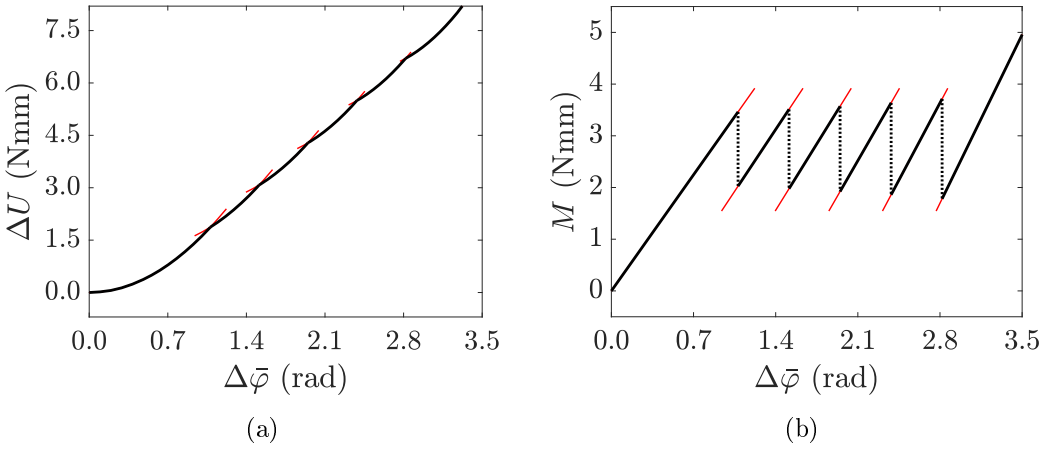

Figure 5.8. Response of the bi-stable flex-ten *Prototype A* with $n = 6$ segments in a strain driven test (increasing $\Delta\bar{\varphi}$), when the nonlocal effect is neglected (the increment in the cable axial force is overlooked): (a) ΔU-$\Delta\bar{\varphi}$ (energy-strain) chart and (b) M-$\Delta\bar{\varphi}$ (load-strain) chart. Maxwell path is shown with bold (black) lines and metastable states with solid (red) lines; unstable states are omitted. Parameters: $N_0 = 1.96\,\mathrm{N}$ and $K = 0$.

force $\Delta N = K\Lambda$ due to the elongation of the cable. In fact, by assuming $K = 0$ in the relevant equation, the counterpart of Figures 5.7(a) and 5.7(c) for the Maxwell path becomes the graphs of Figure 5.8. The stable and metastable branches are now linear, and the steps occur around a horizontal plateau. This trend is qualitatively equal to that found in [76, 84] for NN chains formed by trilinear springs. In fact, in flex-ten beams, circular pitch lines for the contact surfaces provide a pseudo-linear dependence of the lever arm a_i on the relative rotation $\Delta\varphi_i$. In other words, the case $K = 0$ corresponds to the case of *snap-spring hinges*. In fact, when the nonlocal dependence from the unbonded tendon is disregarded or becomes negligible, also the strain-hardening behavior is lost.

We believe that, because of the aforementioned properties, in particular the possibility of describing strain-hardening equilibrium paths, models based on bi-stable flexural tensegrities could interpret, better than classical models with snap-springs chains, the macroscopic response of crystalline and biological structures of the type presented in Figure 5.1. Remarkably, the path of Figure 5.7(c) is qualitatively analogous to the one experimentally observed and reported in Figure 5.1(b).

Response in the soft device

The equilibrium configuration under a soft device of *Prototypes A* is reported in Figures 5.9 and 5.10, referring to the cases with three and five joints ($n = 4$ and

$n = 6$ segments, respectively). As previously, stable states (absolute minima) are shown with bold (black) lines, metastable states (local minima) with solid (red) lines and unstable states with dotted (magenta) lines.

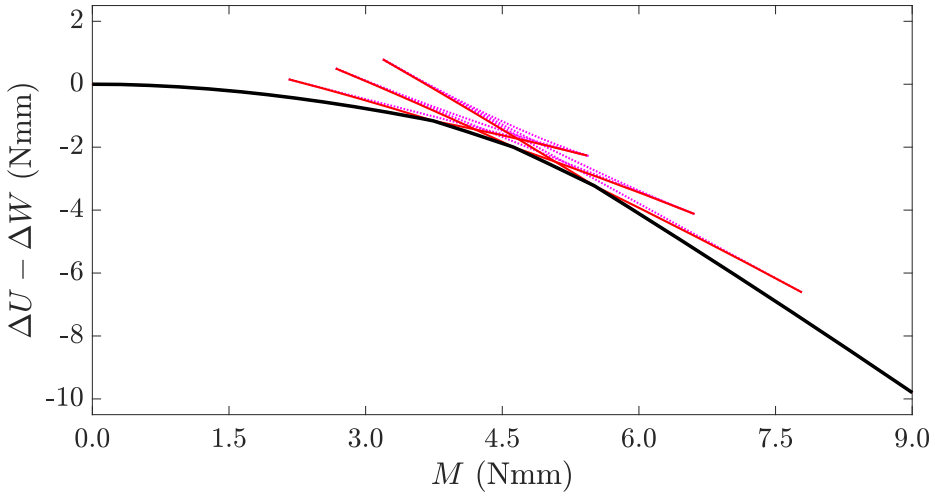

(a)

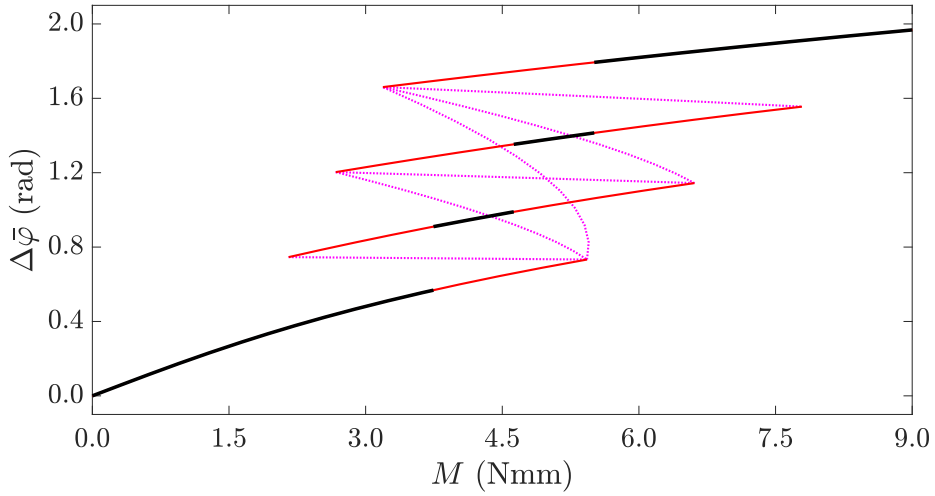

(b)

Figure 5.9. Response in a soft device of the bi-stable flex-ten *Prototype A* with n=4 segments: (a) energy as a function of the applied end couple M and (b) moment M vs. relative end rotation $\Delta\bar{\varphi}$. Stable states are shown with bold (black) lines, metastable states with solid (red) lines and unstable states with dotted (magenta) lines. Parameters: $N_0 = 1.96\,\mathrm{N}$ and $K = 1.03\,\mathrm{N/mm}$.

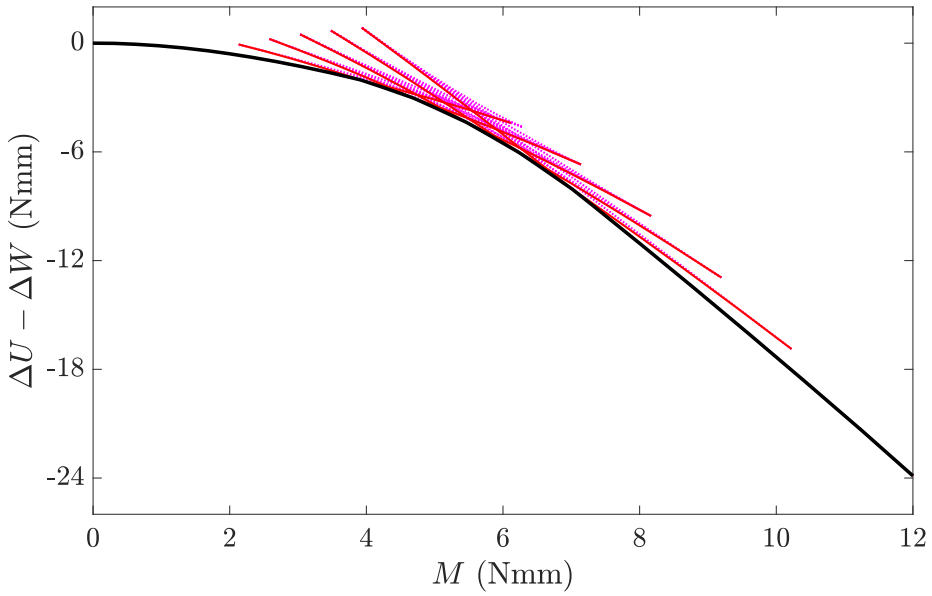

(a)

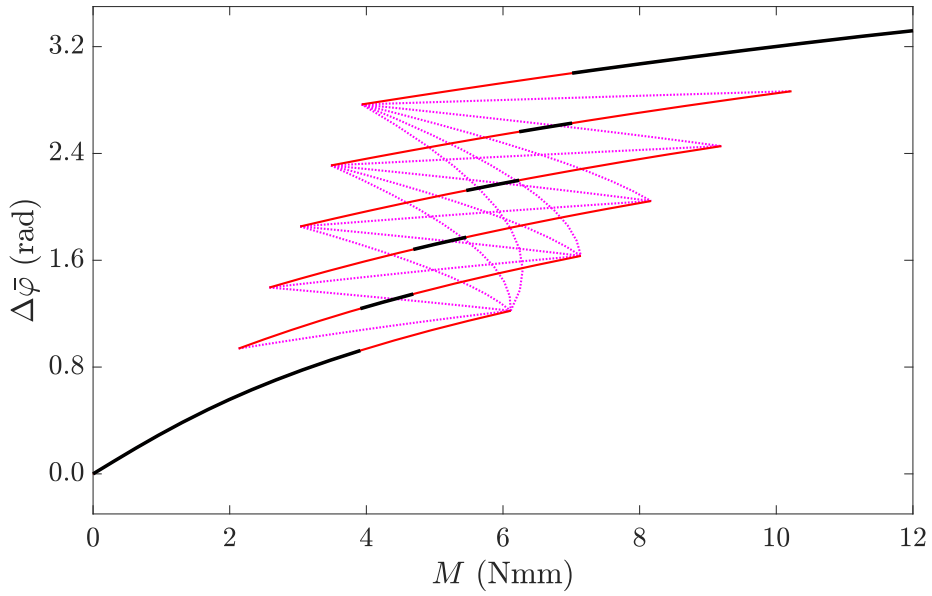

(b)

Figure 5.10. Response in a soft device of the bi-stable flex-ten *Prototype A* with $n = 6$ segments: (a) energy as a function of the applied end couple M and (b) moment M vs. relative end rotation $\Delta\bar{\varphi}$. Stable states are shown with bold (black) lines, metastable states with solid (red) lines and unstable states with dotted (magenta) lines. Parameters: $N_0 = 1.96\,\mathrm{N}$ and $K = 0.89\,\mathrm{N/mm}$.

Figure 5.11, which is the counterpart for the soft device of Figure 5.7, shows the response of the bi-stable beam *Prototype A* with $n = 6$ segments for an increasing load M. Again, the structure can follow two different main paths, evidenced with black bold lines in the figure: again, the first one is the *Maxwell path*, associated with absolute minima of the total energy $\Delta U - \Delta W$, and the second one is the *maximum hysteresis path*, associated with local minima. Loading and unloading stress histories following local minima in the soft device lead to a strong energy

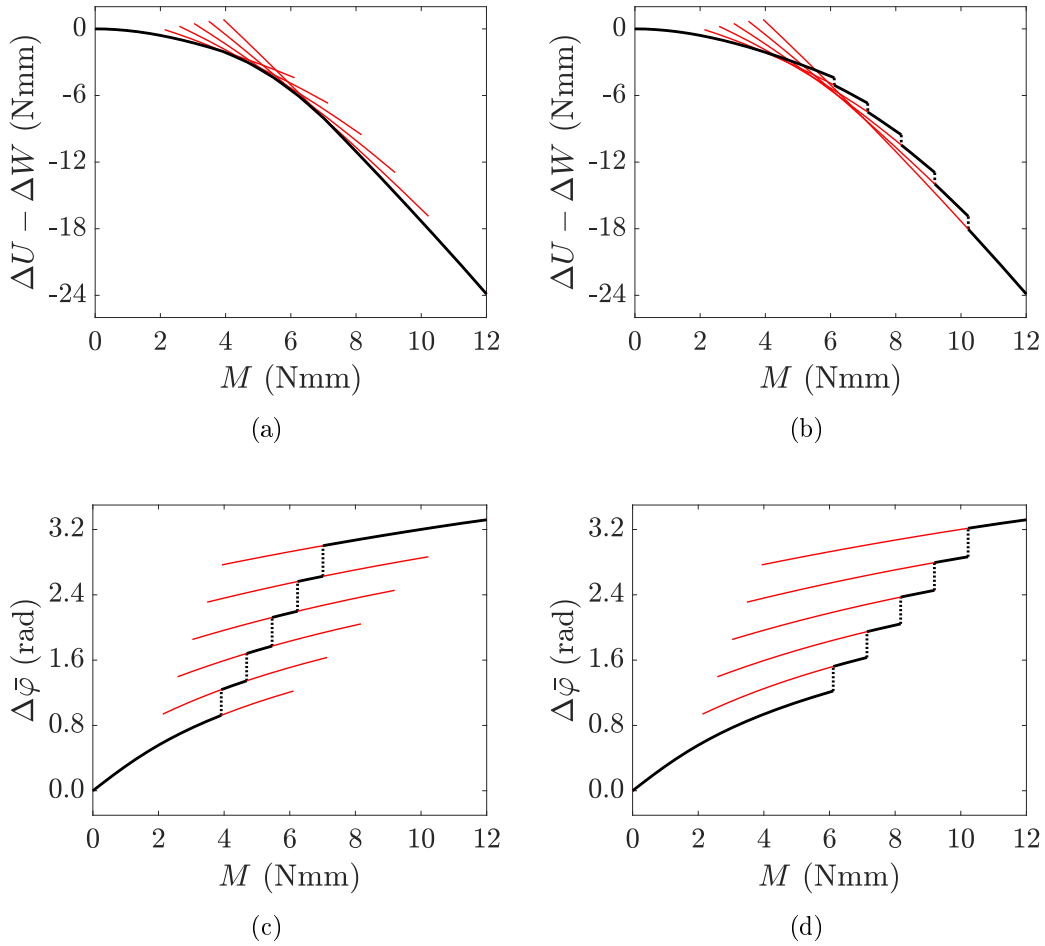

Figure 5.11. Response of the bi-stable flex-ten *Prototype A* with $n = 6$ segments in a stress-driven test (increasing M): (a) Maxwell path and (b) maximum hysteresis path in the $\Delta U - \Delta W$ vs. M (energy-load) chart; (c) Maxwell path and (d) maximum hysteresis path in the $\Delta\bar{\varphi}$ vs. M (strain-load) chart. The followed path is evidenced with black color, stable and metastable states are shown with red lines and unstable states are omitted. Parameters: $N_0 = 1.96\,\mathrm{N}$ and $K = 0.89\,\mathrm{N/mm}$.

dissipation by hysteresis: a large closed loop would appear in Figure 5.11(d).

The complete hysteresis path for *Prototype A* under a cyclic quasi-static load is shown in Figure 5.12, which also compares the same load history for *Prototype B*. The hysteresis loop is much larger for this latter case.

Again the nonlocal character of flexural tensegrity provides a strain-hardening behavior and both the Maxwell path and the hysteresis path of Figure 5.12 are increasing stepped curves. Focusing on $\Delta\bar{\varphi} > 0$, Figure 5.12(b) has a noteworthy

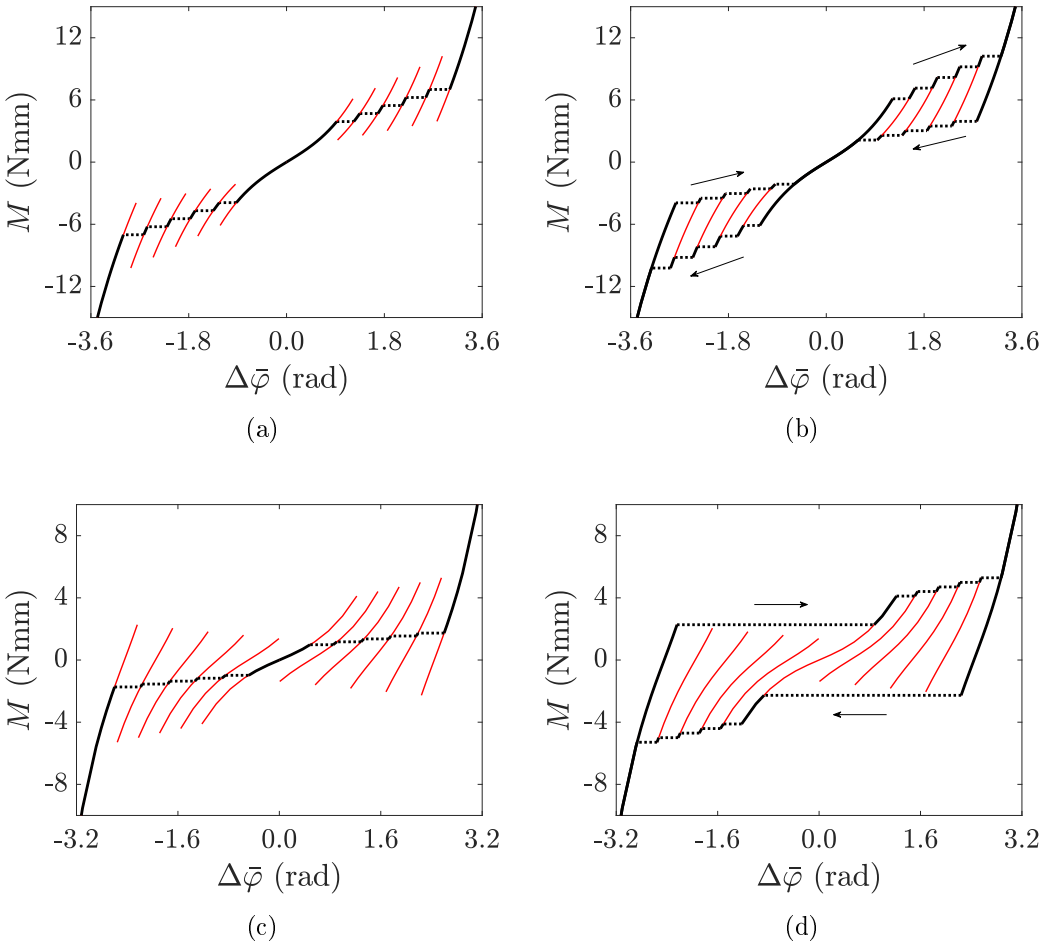

Figure 5.12. Load-strain charts (M vs. $\Delta\bar{\varphi}$) for a bi-stable flex-ten with $n = 6$ segments in a stress-driven test under cycling load M. (a) Maxwell path and (b) maximum hysteresis path for *Prototype A*; (c) Maxwell path and (d) maximum hysteresis path for *Prototype B*. The followed path is evidenced with black color, stable and metastable states are shown with red lines and unstable states are omitted. Parameters: $N_0 = 1.96\,\mathrm{N}$ and $K = 0.89\,\mathrm{N/mm}$ for *Prototype A*; $N_0 = 2.00\,\mathrm{N}$ and $K = 2.80\,\mathrm{N/mm}$ for *Prototype B*.

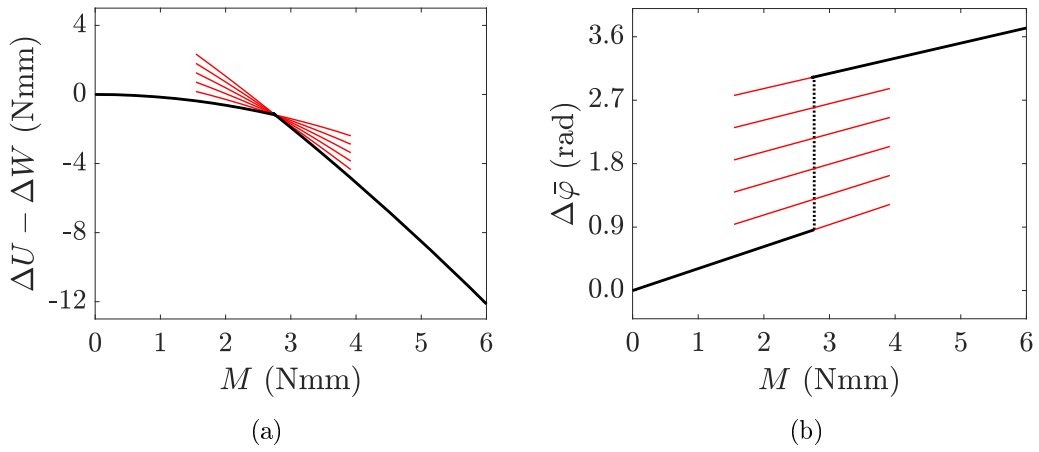

Figure 5.13. Response of the bi-stable flex-ten *Prototype A* with $n = 6$ segments in a stress-driven test (increasing M), when the nonlocal effect is neglected (the increment in the cable axial force is overlooked): (a) $\Delta U - \Delta W$ vs. M (energy-load) chart and (b) $\Delta\bar{\varphi}$ vs. M (strain-load) chart. Maxwell path is shown with bold (black) lines and metastable states with solid (red) lines; unstable states are omitted. Parameters: $N_0 = 1.96\,\mathrm{N}$ and $K = 0$.

similarity with the hysteresis loops observed in Figure 5.1(a). Note that, now, also the Maxwell line shows a strain-hardening behavior, while in the model of [88] only the hysteresis path is of this type.

Of course, if one disregards the nonlocal character of flexural tensegrity by setting $K = 0$, the usual horizontal Maxwell line is found, as indicated in Figure 5.13. Such a condition can be used to reproduce a perfectly plastic response.

Stability analysis

The possibility of attaining supercritical states is strictly correlated to the local stability of the corresponding equilibrium configurations, dictated by the second variation of the energy. For this system, defined by a finite number of variables $\Delta\varphi_i$, $i = 1 \dots n-1$, the stability analysis consists in discussing the positive definiteness of the Hessian matrix of the energy function.

Let $\Delta\bar{\varphi}$ represent the relative rotation of the end segments in a hard-device testing. This datum can be conveniently used to restate the total elongation of the cable, $\Lambda = \sum_{i=1}^{n-1} \Lambda_i$, as a function of $n-2$ variables only, by setting

$$\Delta\varphi_{n-1} = \Delta\bar{\varphi} - \sum_{j=1}^{n-2} \Delta\varphi_j \,, \tag{5.2.7a}$$

$$\Lambda_i = \Lambda_i(\Delta\varphi_i)\,, \qquad i = 1\ldots n-2\,, \tag{5.2.7b}$$

$$\Lambda_{n-1} = \Lambda_{n-1}(\Delta\varphi_{n-1}) = \Lambda_{n-1}\Big(\Delta\bar{\varphi} - \sum_{j=1}^{n-2}\Delta\varphi_j\Big)\,. \tag{5.2.7c}$$

The elastic strain energy function ΔU, expressed by (5.2.1), now depends on $\Delta\varphi_i$ for $i = 1\ldots n-2$. Let $\mathbf{H}$ denote the Hessian matrix. For $j,k = 1\ldots n-2$ one has

$$[\mathbf{H}]_{jk} = \frac{\partial^2}{\partial\Delta\varphi_k\,\partial\Delta\varphi_j}\Delta U = \frac{\partial^2}{\partial\Delta\varphi_k\,\partial\Delta\varphi_j}\Big[N_0\sum_{i=1}^{n-1}\Lambda_i + \frac{1}{2}K\Big(\sum_{i=1}^{n-1}\Lambda_i\Big)^2\Big]\,. \tag{5.2.8}$$

Recalling equation (2.1.1), i.e., the fact that $a_i = a_i(\Delta\varphi_i)$ is the first derivative of $\Lambda_i = \Lambda_i(\Delta\varphi_i)$, and expressing $\Delta\varphi_{n-1}$ as per equation (5.2.7a), for $j,k = 1\ldots n-2$, one obtains

$$\frac{\partial}{\partial\Delta\varphi_k}\Big(\sum_{i=1}^{n-1}\Lambda_i\Big) = a_k + \frac{\partial\Lambda_{n-1}}{\partial\Delta\varphi_{n-1}}\frac{\partial\Delta\varphi_{n-1}}{\partial\Delta\varphi_k} = a_k - a_{n-1}\,, \tag{5.2.9a}$$

$$\begin{aligned}\frac{\partial}{\partial\Delta\varphi_j}(a_k - a_{n-1}) &= \frac{\partial a_k}{\partial\Delta\varphi_j} - \frac{\partial a_{n-1}}{\partial\Delta\varphi_{n-1}}\frac{\partial\Delta\varphi_{n-1}}{\partial\Delta\varphi_j} = \\ &= \frac{\partial a_k}{\partial\Delta\varphi_j} + \frac{\partial a_{n-1}}{\partial\Delta\varphi_{n-1}}\,.\end{aligned} \tag{5.2.9b}$$

Consequently, the Hessian matrix can be rewritten as

$$[\mathbf{H}]_{jk} = N\Big(\frac{\partial a_k}{\partial\Delta\varphi_j} + \frac{\partial a_{n-1}}{\partial\Delta\varphi_{n-1}}\Big) + K(a_k - a_{n-1})(a_j - a_{n-1})\,, \tag{5.2.10}$$

for $j,k = 1\ldots n-2$, where $N = N_0 + K\Lambda$ is the tension force in the cable, supposed homogenous along its length (perfectly-unbonded prestressing tendon).

Equilibrium under pure bending implies that $M_i = a_i N$ is a constant quantity, for $i = 1\ldots n-1$, so that also $a_i = \text{const}$. This means that the second term on the r.h.s. of (5.2.10) is null. Moreover, recall that Λ_i is a function of the only variable $\Delta\varphi_i$, so that $\partial a_k/\partial\Delta\varphi_j = 0$ when $j \neq k$. Therefore, (5.2.10) can be simplified as

$$[\mathbf{H}]_{jk} = \begin{cases} N\Big(\dfrac{\partial a_j}{\partial\Delta\varphi_j} + \dfrac{\partial a_{n-1}}{\partial\Delta\varphi_{n-1}}\Big)\,, & \text{for} \quad k = j\,, \\[2ex] N\dfrac{\partial a_{n-1}}{\partial\Delta\varphi_{n-1}}\,, & \text{for} \quad k \neq j\,. \end{cases} \tag{5.2.11}$$

Recall that $\partial a_i/\partial\Delta\varphi_i$ represents the gradient of the internal lever arm with respect to the relative rotation (Figure 5.3), which is negative in the spinodal region and positive otherwise.

Since the tendon is unbonded, rearrangements of the order of the relative rotations of the joints are energetically equivalent. If there are two joints in the spinodal state configuration, without loosing generality, these can be assumed to be the first one ($i = 1$) and the last one ($i = n - 1$). This readily implies that the first principal minor of the Hessian matrix has negative determinant, i.e.,

$$\det\left(N\frac{\partial a_1}{\partial\Delta\varphi_1} + N\frac{\partial a_{n-1}}{\partial\Delta\varphi_{n-1}}\right) = N\frac{\partial a_1}{\partial\Delta\varphi_1} + N\frac{\partial a_{n-1}}{\partial\Delta\varphi_{n-1}} < 0\,. \tag{5.2.12}$$

because $N > 0$, $\partial a_1/\partial\Delta\varphi_1 < 0$ and $\partial a_{n-1}/\partial\Delta\varphi_{n-1} < 0$. Since the Hessian matrix, from Sylvester's criterion, cannot be positive-definite, the configuration cannot be stable. The same argument can be repeated if there are more than two joints in the spinodal region, to conclude that configurations of this type are also unstable.

If there is only one joint in the spinodal region, thanks to the energetic equivalence of the rearrangements, this can be considered in the position $i = n - 2$. In general, all the principal minors of the Hessian matrix up to the $(n-3)-$th order have positive determinant since $N > 0$, $\partial a_{n-1}/\partial\Delta\varphi_{n-1} > 0$ and $\partial a_k/\partial\Delta\varphi_k > 0$, for $k = 1\ldots n-3$. Therefore, the positive-definitiveness of the Hessian matrix depends only upon the sign of the determinant of the $(n-2)-$th principal minor.

Consider, as an illustrative example, the structure represented in Figure 5.5, for which $n = 4$. For a piecewise-linear law a_i vs. $\Delta\varphi_i$, of the type represented in Figure 5.3(a), the derivatives $\partial a_i/\partial\Delta\varphi_i$ attain constant values, which are positive (negative) on the increasing (decreasing) branches.

For $n = 4$, the determinant of the $(n-2)-$th principal minor is proportional, modulo the tendon force N, to the quantity

$$\frac{\partial a_1}{\partial\Delta\varphi_1}\frac{\partial a_2}{\partial\Delta\varphi_2} + \frac{\partial a_1}{\partial\Delta\varphi_1}\frac{\partial a_3}{\partial\Delta\varphi_3} + \frac{\partial a_2}{\partial\Delta\varphi_2}\frac{\partial a_3}{\partial\Delta\varphi_3}\,. \tag{5.2.13}$$

This is equal, for instance, to $18.57\,\mathrm{mm/rad} > 0$ when one joint is on the central decreasing branch of Figure 5.3(a) (between points A and B), and the remaining two joints are on the l.h.s. increasing branch (below point A) and on the r.h.s. increasing branch (above point B), respectively. One can thus conclude that supercritical configurations, where only one of the joints is in the spinodal region, are admissible for this structure.

When there are no joints in the spinodal region, it is possible to verify that, since now $\partial a_k/\partial\Delta\varphi_k > 0$, for $k = 1\ldots n-1$, all the principal minors of the Hessian matrix have positive determinant. Therefore, equilibrium configurations of this type are locally stable.

5.2.3 Experiments on prototypes

Experiments on 3D-printed bi-stable flex-ten beams are now performed for a comparison with the theoretical predictions. In order to visually evaluate the position assumed by the cable in the various configurations as per Figure 5.2(b), the segments are "open" in the central portion, so that the cable, made of white polyamide, can be distinguished against the dark material of which the segments are made.

The shape of the pitch lines for the contact surface and the location of the exit point for the cable are as described in Section 5.2.1, so to obtain the constitutive relations for the lever arm a_i and the gap Λ_i as a function of the relative segmental rotation $\Delta\varphi_i$ respectively represented in Figures 5.3(a) and 5.3(c) for *Prototype A*, and in Figures 5.3(b) and 5.3(d) for *Prototype B*.

In the case of pure bending, the moment $M_i = a_i N$ transmitted by each one of the contact joints shall be the same; but since the tensile force N in the *unbonded* tendon is constant at all joints, this equilibrium condition requires that the lever arm a_i , indicated in Figure 5.4, does not vary from joint to joint for any given value of N. Figure 5.14 recalls, from Figure 5.3, the constitutive equation a_i vs. $\Delta\varphi_i$ where, for completeness, also the negative branches have been drawn. Observe that, for *prototype A*, there may be one (case of lines a and c) or three (line b) values of $\Delta\varphi_i$ that provide the same value of a_i , whereas for *prototype B* the values of $\Delta\varphi_i$ can be one (line a), three (line b) or five (line c).

Any equilibrium configuration for *prototype A* with n segments and $n-1$ joints, either stable, metastable, or unstable, will be characterized by k joints whose lever

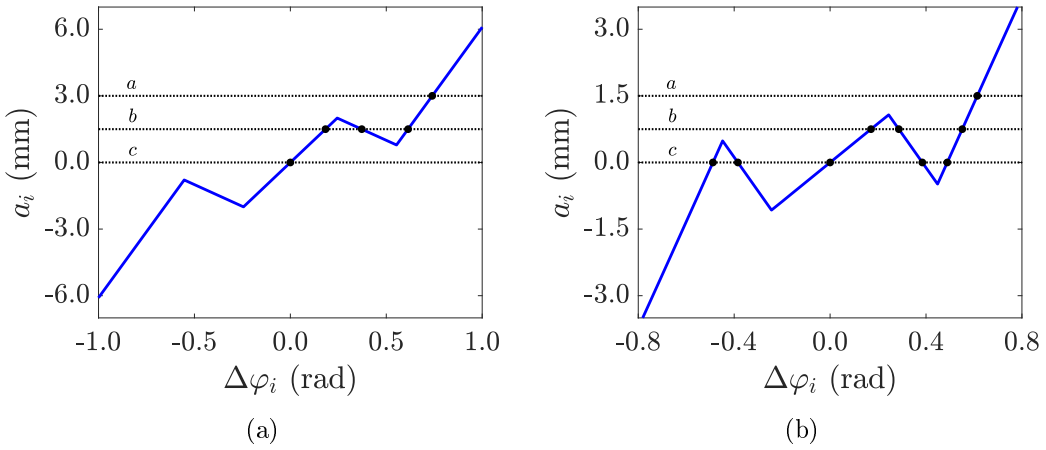

Figure 5.14. Constitutive relations for the lever arm a_i as a function of relative segmental rotation $\Delta\varphi_i$, with indication of the possible coexistent states for a given value of a_i: (a) *Prototype A* and (b) *Prototype B*.

arm is on the stable branch passing through the origin, h joints laying on one of the other stable branches and j joints in the spinodal branch, with $j, h, k \geqslant 0$ and $j + h + k = n - 1$; of course, one is free to change the location of the joints without affecting the static equilibrium. Therefore, the number of *equivalent* configurations equals the number of permutations with repetition

$$P_{n-1}^{(j,h,k)} = \frac{(n-1)!}{j!\,h!\,k!}\,. \tag{5.2.14}$$

For *Prototype B*, there are up to five values of the relative rotation $\Delta\varphi_i$ corresponding to the same a_i at each joint and, consequently, the number of equivalent configurations can be much higher. In the noteworthy case, analyzed in the following, of an unconstrained beam in its natural state ($M = 0$), besides the null value there are other two values of $\Delta\varphi_i$ ($\pm 0.4887\,\mathrm{rad}$) corresponding to (locally) stable states in equilibrium with null bending moment: this case is attained by 3^{n-1} configurations.

When the end segments are relatively rotated of $\Delta\bar{\varphi}$ (hard device), one of the joints may be trapped in the spinodal region and stabilized by the hard-device control of the global angle $\Delta\bar{\varphi}$: this condition was referred to as *supercritical* in [76]. In a soft device (prescribed end couples M), all the lever arms a_i at the various joints shall be on the stable branches.

Prototype A - Hard device

Physical models of *Prototype A* with either three ($n = 4$ segments) or five ($n = 6$ segments) bi-stable joints were 3D printed. The end segments were relatively rotated of $\Delta\bar{\varphi}$ and the resulting deformed shapes were compared with those analyzed in Section 5.2.2. In particular, the end rotations have been imposed by pinning the end segments to a rigid support, in such a way that only the rotation is prevented. The forcing was done gradually by hand, paying great care at not touching the intermediate segments in any way, acting only on the end segments. At this point, we have verified whether the intermediate segments actually described the theoretical deformation, using as reference for the measurements a graph paper background.

Three bi-stable joints (4 segments). The prototype has a total length $L = 198.8\,\mathrm{mm}$, with end segments of length about one half ($33.8\,\mathrm{mm}$) of the central ones ($65.6\,\mathrm{mm}$). The initial prestress of the cable and its effective axial stiffness, taking into account the presence of the springs in series, are the same of the case reported in Figure 5.5, i.e., $N_0 = 1.96\,\mathrm{N}$ and $K = 1.03\,\mathrm{N/mm}$.

At $\Delta\bar{\varphi} = 36.56^\circ = 0.6381\,\mathrm{rad}$, as well as at $\Delta\bar{\varphi} = 99.23^\circ = 1.7319\,\mathrm{rad}$, the equilibrium branches indicate the possibility of just one homogeneous configuration

(relative rotations of the segments are all equal), corresponding to a theoretical constraint reaction $M = 4.41\,\text{Nmm}$. These are represented in Figure 5.15(a) and 5.15(b), respectively.

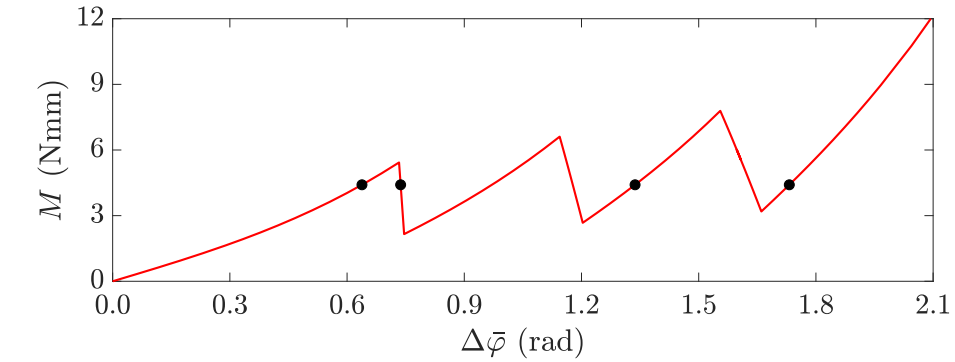

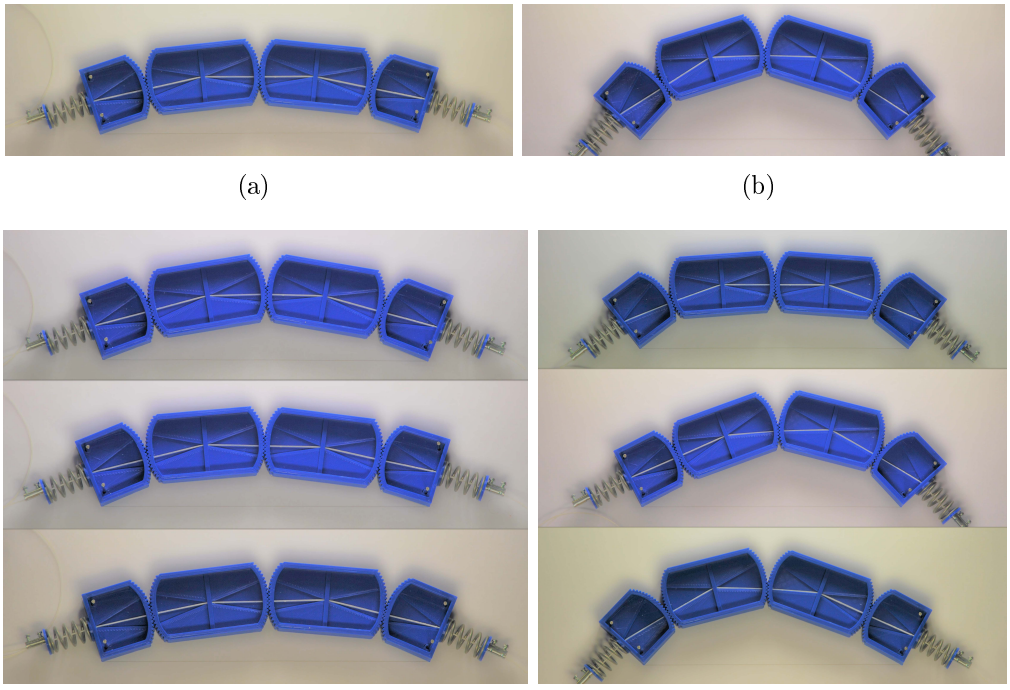

(a) (b)

(c) (d)

Figure 5.15. Experiments on the prototype of the bi-stable flex-ten beam considered in Figure 5.5 ($n = 4$, *Prototype A*). Homogeneous equilibrium configuration in the hard device for: (a) $\Delta\bar{\varphi} = 36.56^\circ = 0.6381\,\text{rad}$ and (b) $\Delta\bar{\varphi} = 99.23^\circ = 1.7319\,\text{rad}$. Three inhomogeneous equilibrium configuration in the hard device for: (c) $\Delta\bar{\varphi} = 42.23^\circ = 0.7371\,\text{rad}$ and (d) $\Delta\bar{\varphi} = 76.61^\circ = 1.3371\,\text{rad}$.

Figure 5.15(c) corresponds to $\Delta\bar{\varphi} = 42.23^\circ = 0.7371\,\text{rad}$, for which there are three possible stable configurations corresponding to $M = 4.41\,\text{Nmm}$. Two joints are in a state corresponding to the l.h.s. stable branch of Figure 5.3(a) (below point A) and one joint is on the spinodal branch (between points A and B). This is due to the fact that the beam is in a *supercritical* state [76], so that one joint is in the spinodal (unstable) region, but it is stabilized thanks to the hard device. There are three possible stable configurations also at $\Delta\bar{\varphi} = 76.61^\circ = 1.3371\,\text{rad}$, as indicated in Figure 5.15(d), but in this case two joints are in a state corresponding to the r.h.s. stable branch (above point B) and one joint is on the l.h.s. stable branch (below point A).

Figure 5.16 displays the six possible stable configurations of the beam for $\Delta\bar{\varphi} = 67.48^\circ = 1.1777\,\text{rad}$, to which corresponds $M = 4.41\,\text{Nmm}$. This is again

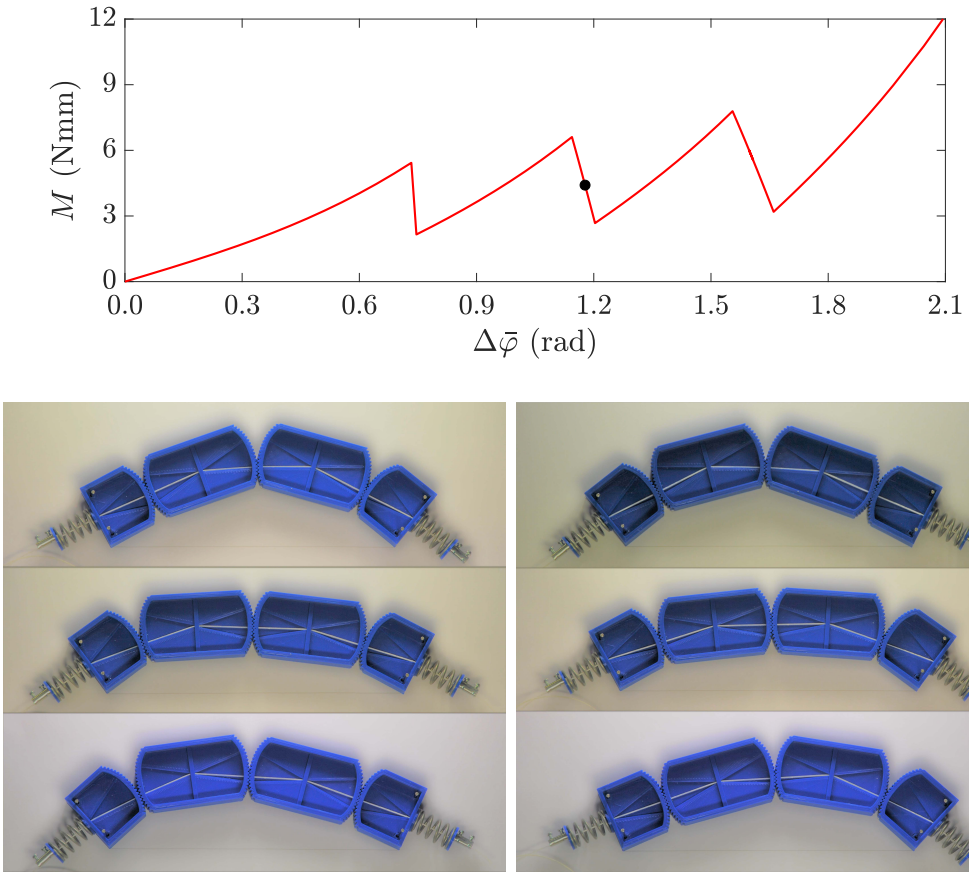

Figure 5.16. Experiments on the prototype of the bi-stable flex-ten beam considered in Figure 5.5 ($n = 4$, *Prototype A*). Six inhomogeneous equilibrium configuration in the hard device for $\Delta\bar{\varphi} = 67.48^\circ = 1.1777\,\text{rad}$.

a supercritical configuration for the beam in which one joint is on the spinodal branch of Figure 5.3(a) (between points A and B), but it is stabilized by the hard device; the remaining two joints are on the l.h.s. stable branch (below point A) and on the r.h.s. stable branch (above point B), respectively. Since $j = h = k = 1$, from (5.2.14) one has $P_3^{(1,1,1)} = 6$, corresponding to the number of equivalent configurations.

Five bi-stable joints (6 segments). A physical model of *Prototype A* with five bi-stable joints ($n = 6$ segments) was manufactured by adding two more central segments of length 65.6 mm to the prototype with three bi-stable joints ($n = 4$ segments), so to reach a total length $L = 330$ mm. The initial prestress of the cable and its effective axial stiffness, taking into account the presence of the springs in series, are the same of the case reported in Figure 5.6, i.e., $N_0 = 1.96$ N and $K = 0.89$ N/mm. The major difference with the case of the previous subsection is that now all equilibrium configurations of the beam are *subcritical*, according to the definition of [76]: with respect to the length of the spinodal branch, the number of joints is such that no joint in the instability region can be stabilized even in the hard device. In fact, from Figure 5.6(b), one has that there is at least one value of M corresponding to a stable or metastable state for any rotation $\Delta\bar{\varphi}$.

At $\Delta\bar{\varphi} = 65.00^\circ = 1.1345$ rad, there is one homogeneous configuration (all relative rotations of the segments are equal) corresponding to a theoretical constraint reaction $M = 5.40$ Nmm, and five inhomogeneous configurations (different rotations) at $M = 3.24$ Nmm. These respectively correspond to the first photograph in Figure 5.17 and to the successive five pictures in the same figure. For the inhomogeneous configurations, four joints are on the l.h.s. stable branch of Figure 5.3(a), one joint is on the r.h.s. stable branch and none on the spinodal branch.

Figure 5.18 displays the possible stable configurations of the beam at $\Delta\bar{\varphi} = 120.00^\circ = 2.0944$ rad, corresponding to $M = 5.18$ Nmm. There are ten possible stable configurations: two joints are in a state corresponding to the l.h.s. stable branch of Figure 5.3(a) (below point A) and three joints on the r.h.s. stable branch (above point B). Since $j = 0$, $h = 3$, $k = 2$, from (5.2.14) one has $P_5^{(0,2,3)} = 10$, corresponding to the number of equivalent configurations.

It is worth remarking that, in the theoretical model, all contact joints are identical and the tendon is supposed to be free to frictionless slide. At least in theory, it is totally equivalent if one or the other spring hinge snaps: only the number of snapping springs is prescribed, neither their order, nor the sequence of snapping. On the other hand, in the real prototype there are many sources of inaccuracy (one for all, parasitic friction), which may drive the sequence to follow a preferential order. Non-locality also influences the hardening response, in the sense that the beam becomes stiffer as deformation increases. However,

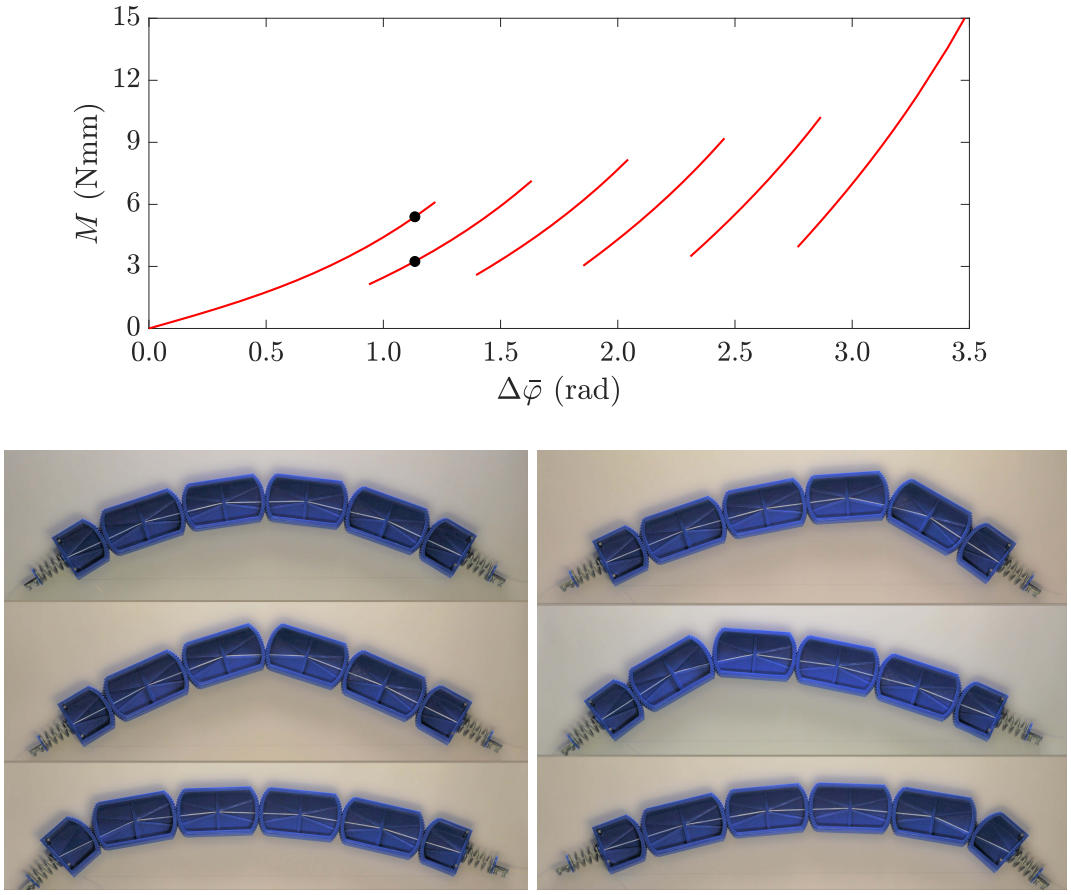

Figure 5.17. Experiments on the prototype of the bi-stable flex-ten beam considered in Figure 5.6 ($n = 6$, *Prototype A*). Homogeneous and inhomogeneous equilibrium configuration in the hard device for $\Delta\bar{\varphi} = 65.00^\circ = 1.1345\,\text{rad}$.

since the tendon is supposed to be perfectly unbonded, the nonlocal effect is the same in all the contact hinges composing the chain; consequently, for fixed relative rotation between the end segments, the order of the snapped contact joints can be interchanged without affecting the resulting strain energy. In any case, nonlocality does influence the energetic barrier that separates one inhomogeneous configuration from any other energetically equivalent to it because, in order to pass from one configuration to the other, the cable has to be further strained. The detailed dynamic characterization of the sequence of snaps is not considered here, and it will be the subject of a successive work.

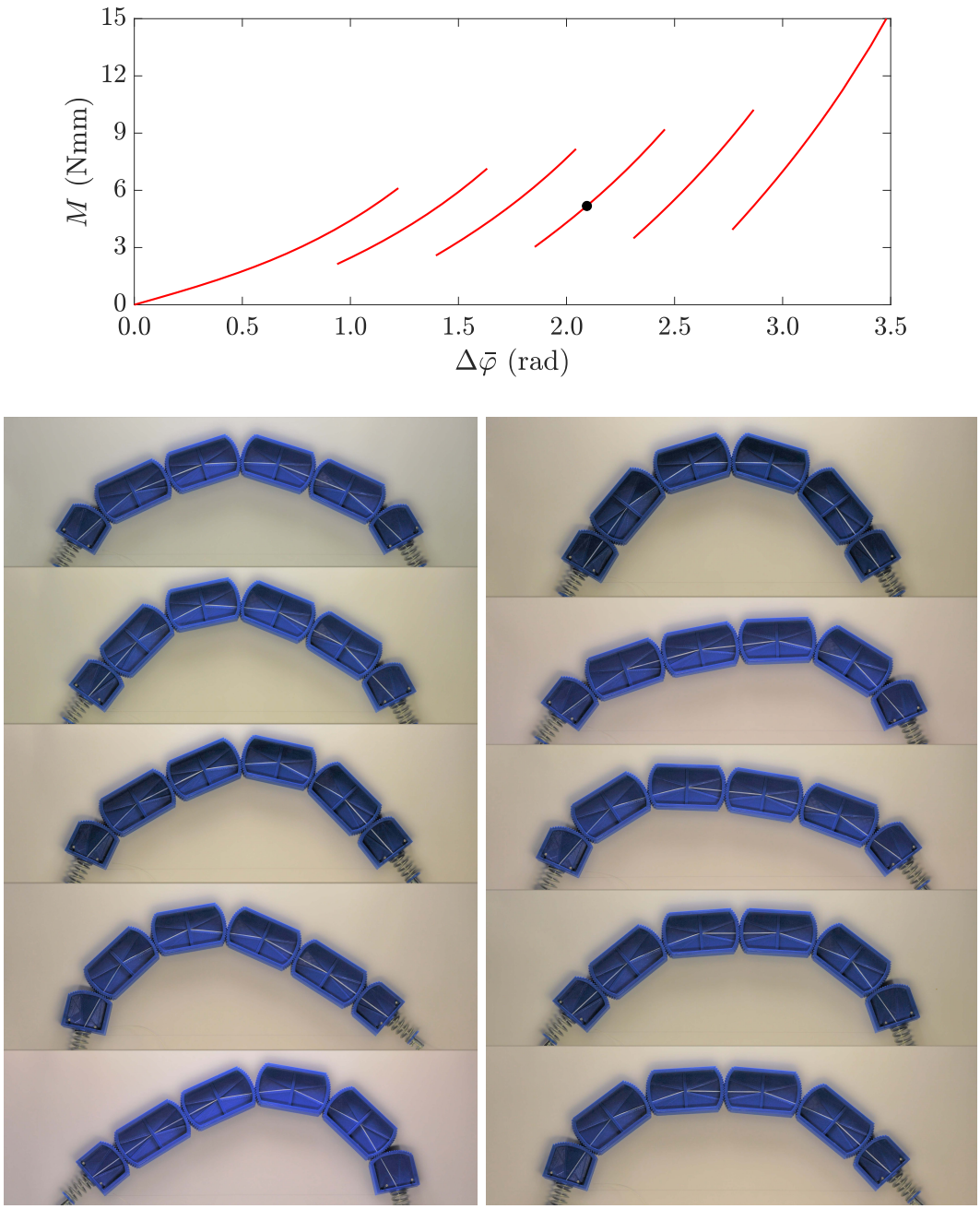

Figure 5.18. Experiments on the prototype of the bi-stable flex-ten beam considered in Figure 5.6 ($n = 6$, *Prototype A*). The ten inhomogeneous equilibrium configuration in the hard device for $\Delta\bar{\varphi} = 120.00^\circ = 2.0944\,\text{rad}$.

Prototype A - Soft device

Prototype A is now tested in a soft device. Only the results under stress-driven testing on one single joint and the shorter prototype are recorded, since the longer chain does not add any conceptual difference.

One single joint (2 segments). The two coupled segments, of length 33.8 mm, lay in the vertical plane, as indicated in Figure 5.19(a). The initial prestress is 4.70 N, the cable equivalent stiffness is 1.80 N/mm and the contact profiles are the same of *Prototype A*. The upper segment is hinged to a horizontal pin passing through its centroidal point, while a constant weight of 1.00 N is hanged to the lower segment. Then, the upper segment is gradually rotated, so that the self-weight of the lower segment, equal to 0.08 N, together with the hanging weight, produces a moment with respect to the pitch point of the contact joint, which can be estimated by geometrically measuring the lever arm.

Despite the many sources of inaccuracy (friction between profiles, friction in the sheaths, imperfections and manufacturing tolerances, creep of the tendon, parasitic bending stiffness of the tendon, measurement errors), the graph reported in

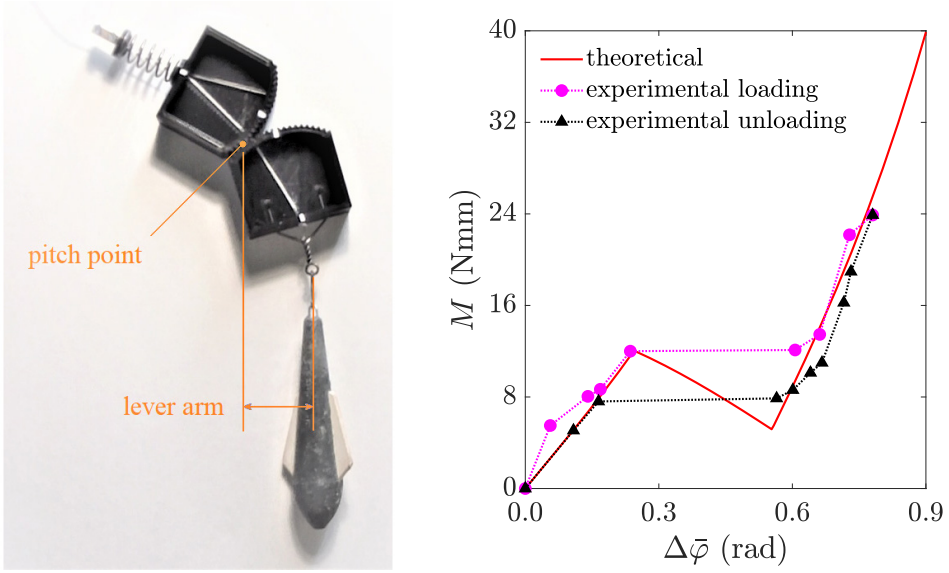

(a) (b)

Figure 5.19. Stress-driven test of one bi-stable joint of *Prototype A* ($n = 2$, $N_0 = 4.7$ N and $K = 1.80$ N/mm): (a) layout, with indication of the lever arm for the hanging weight with respect to the pitch point; (b) measured M vs. $\Delta\bar{\varphi}$ graph in loading-unloading paths, compared with the theoretical predictions.

Figure 5.19(b) confirms the good agreement between the experimentally-measured points and the theoretical prediction, in particular for what concerns the loading-unloading paths and the consequent "pseudoelastic" response.

Three bi-stable joints (4 segments). The physical model of *Prototype A* with three bi-stable joints ($n = 4$ segments) is tested in the soft device under four-point-bending. Structural parameters for this case are $N_0 = 5.6\,\mathrm{N}$, in order to span larger values of the bending moment, and $K = 1.00\,\mathrm{N/mm}$, because the cable is a bit longer than in the hard-device-tested beam due to the new design of the end segments.

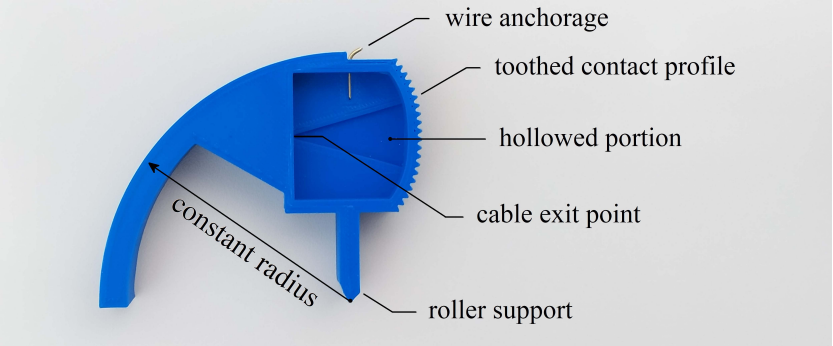

Figure 5.20. New design of the end segment for the soft-device testing of the bi-stable flexural-tensegrity beam.

The prototype lies on a well-lubricated horizontal plane, in order to rule out the effects of the dead weight. The external forces are introduced through wires, redirected towards the vertical by means of pulleys, to which weights have been attached. It is important to assure that the moment applied at the end segments remains constant regardless of their rotation: hence, the end segments have been designed as indicated in Figure 5.20. Observe that they are characterized by two appendices: the vertical one is placed in contact with a straight fixed support, well lubricated so to minimize the effects of friction, in order to become a roller constraint; the cable to which the weights are attached is convoluted on the circular appendix with radius 60 mm, centered on the tip of the vertical appendix. When the end segment rotates, the cable unwinds from the circular guide and its tensile force maintains a constant lever arm with respect to the center of rotation. Hence, the bending moment at the beam ends depends only on the weights that are attached to the loading wires.

Figure 5.21 represents the results of the test. The moment-rotation (M vs. $\Delta\bar{\varphi}$) chart reports the theoretical analysis, with indication of the Maxwell path (black

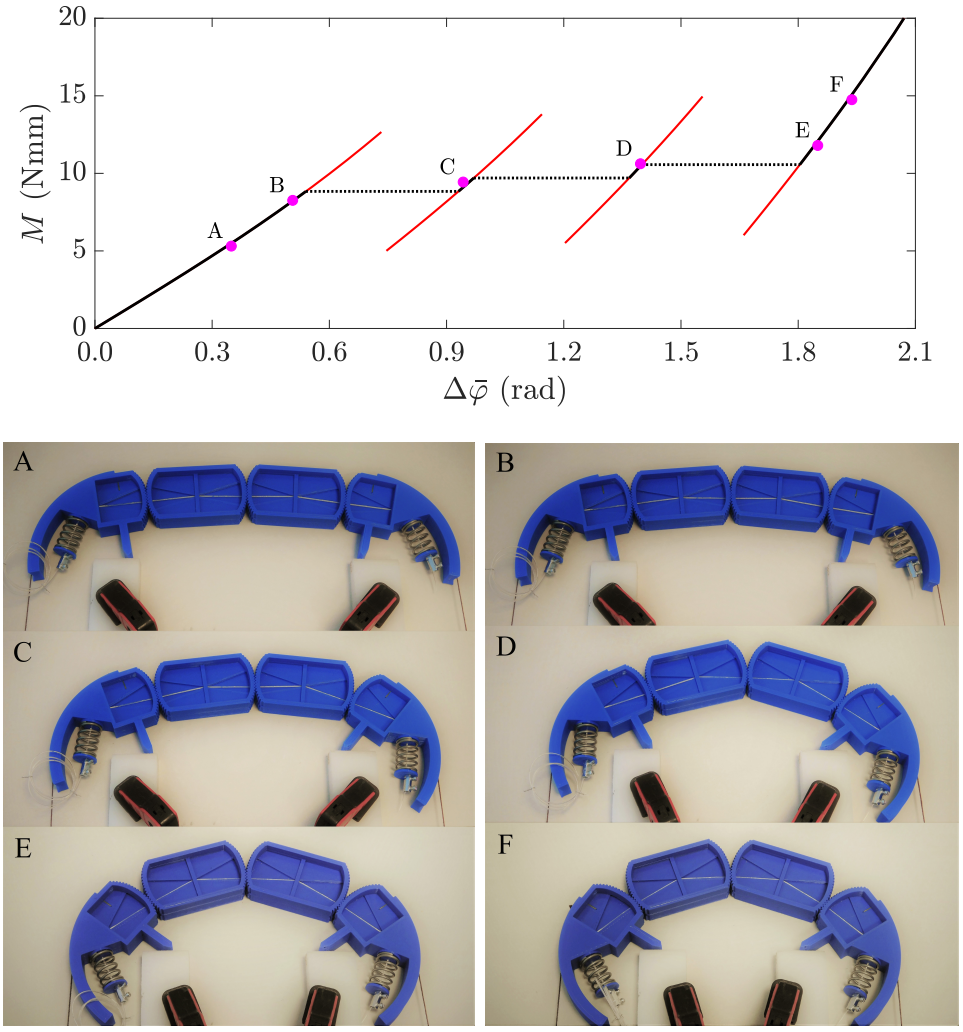

Figure 5.21. Testing in a soft device of the bi-stable flex-ten *Prototype A* with four segments ($n = 4$). Chart M vs. $\Delta\bar{\varphi}$, with indication of metastable states (red lines), Maxwell path (black line) and experimentally measured data (magenta dots). Photographs of the prototype in the configurations represented by the points indicated with A-F in the chart. Parameters: $N_0 = 5.6\,\mathrm{N}$ and $K = 1.00\,\mathrm{N/mm}$.

line) and the branches corresponding to metastable states (red line). The measured points are those represented with magenta dots in the chart and indicated with the letters A-F: the photographs of the structure in these states are shown below. End-couples have been applied to the prototype and, at each value of the load, the structure has been gently shaken in order to reduce the parasite effects of friction, so to reach the equilibrium configuration. As a result of the applied perturbations, the prototype essentially follows the Maxwell line, with slight deviations on the

metastable branches in proximity of the point where each contact joints snaps.

There are of course the same sources of inaccuracy as in the test on the single joint, but also additional uncertainties: friction between the structure and the horizontal plane; friction in the pulleys and inside the sheath that host the prestressing cable (despite lubrication); friction at the roller supports; measurement errors with the caliper, the scale and the protractor; 3D printing tolerances; creep and parasitic bending stiffness of the cable. In any case, the experimental results well agree with the theoretical predictions.

Prototype B - Multiple natural states

Consider now the *Prototype B* with five bi-stable joints ($n = 6$ segments), for which the constitutive relations for a_i and Λ_i as a function of the relative segmental rotation $\Delta\varphi_i$ are reported in Figures 5.3(b) and 5.3(d), respectively. The beam has a total length $L = 406\,\text{mm}$ and again the end segments have a length about one half (41.4 mm) of the central ones (80.8 mm). The initial prestress of the cable and its effective axial stiffness, taking into account the presence of the series springs, are now $N_0 = 2.73\,\text{N}$ and $K = 0.84\,\text{N/mm}$. With respect to *Prototype A*, the main peculiarity is that equilibrium states either than the straight configuration are possible for null applied external couples $M = 0$.

Figure 5.22 shows just a few of the possible natural configurations in equilibrium with null external couples. These range from the straight reference state to the uniformly bent state with constant relative rotations, and comprehend zig-zag and V-shaped configurations or a combination of them. This possibility is due to the fact that, as it is clear from Figures 5.3(b) and 5.14(b), also negative values of the lever arm a_i are possible for certain rotations: there are values of $\Delta\varphi_i > 0$ for which the bending moment is null even if the deformation is not, one corresponding to spinodal region and another one on the stable branch (of course the same result holds on the specular branch, for $\Delta\varphi_i < 0$).

There are many locally stable configurations, besides the straight reference one. For the case of five bi-stable joints ($n = 6$ segments), considering that each joint has three natural states for $M = 0$ corresponding to the stable branches (rotation positive, null or negative), there are $3^{n-1} = 3^5 = 243$ possible configurations corresponding to null end-couples, for the unconstrained beam. The particular shape of the contact surface and the location of the exit points of the cable are such that the globally-stable natural state (absolute minimum for the energy) is the straight one. It should be observed, however, that in the configuration shown in the second picture from the top in the first column of Figure 5.22, the cable is just slightly longer than in the straight configuration represented above. By slightly changing the shape of contact surface, it would be possible to render this configuration, and the symmetric one, energetically equivalent to the straight state,

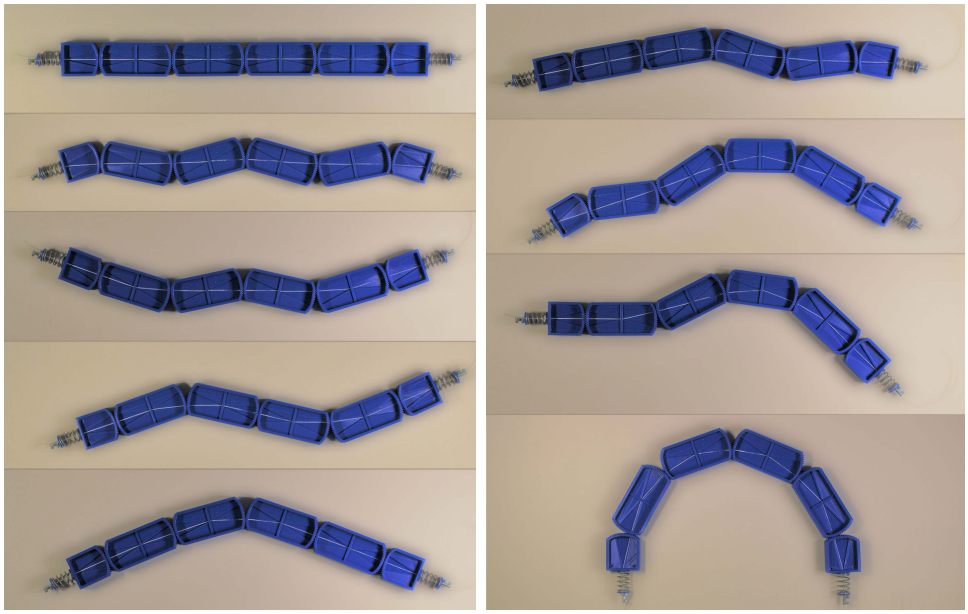

Figure 5.22. Multiple natural states (in equilibrium with $M = 0$) for a bi-stable flex-ten beam with $n = 6$ segments, manufactured as *Prototype B*: examples of straight, zig-zag, V-shaped, homogenously bent configurations and a combination of them.

in order to achieve a structure where there are multiple globally-stable natural states. This is just an example that confirms the great versatility of structures of this type which, with a tailored design, can adapt to any path.

Indeed, bi-stable flexural-tensegrity beams of this type, arranged as long structures or as a single joint, have properties that recall the multiple natural states of shape memory alloys in the martensitic phase. Multiple natural states are also possible in elastic isotropic material with polyconvex stored energy [93]. With the geometric parameters used for the construction of *Prototype B*, presented in Section 5.2.1, the relative rotations of the joints when $M = 0$, corresponding to $a_i = 0$, can be initialized to zero and then set equal to either a positive or a negative value ($\Delta\varphi_i = \pm 28^\circ = \pm 0.4887\,\text{rad}$ for the constitutive relation of Figure 5.3(b)). The resulting structure could be used to store binary data, similarly to old hard disks based on magnetic hysteresis, to construct switches in electric circuits, or to manufacture adaptive catheters for biomedical applications.

5.3 Multi-stable segmental beams

The possibility of increasing the number of energy wells at the level of the single contact joint is now investigated. Using the design concept illustrated in Figure

5.2(b), which consists in setting back the exit point of the cable with respect to the pitch line, just two energy wells can be obtained (bi-stable response) for monotonically increasing rotations ($\Delta\varphi_i > 0$). In order to increase their number, one can conceive a layout that repeats this construction multiple times, thus obtaining a contact joint where the pitch lines consist of many smoothly connected arcs of circle, and the internal cavities are delimited by convex segmented profiles (instead of one straight line). In the following, reference is made to the case in which this construction is repeated twice, so that a "tri-stable" response is obtained for rotations $\Delta\varphi_i \geqslant 0$ that are monotonically increasing.

5.3.1 The contact joint

To this aim, consider Figure 5.23. Each segment is carved to increase the mobility of the cable inside it, but as the relative rotation increases, the cable comes into contact with the ridges of the segmented edge profile of the cavity. The result is that the pivotal point for the cable attains different positions as a function of the relative rotation. If the pitch lines are properly designed, a new energy well can be associated with each one of the new pivotal points. In Figure 5.23, these pitch lines are smoothly connected arcs of circle with decreasing radius, and each arc is highlighted with a different color.

The graphs of Figures 5.24(a) and 5.24(c), representing the internal lever arm a_i and the local cable elongation Λ_i as a function of the relative rotation $\Delta\varphi_i$ of the joint, correspond to pitch lines for which the internal (red) arc has radius 96 mm and length 23.46 mm, the adjacent (blue) arc has radius 48 mm and length 5.86 mm, the consecutive (green) arc has radius 36 mm and length 3.32 mm, whereas the external (magenta) arc has radius 18 mm and length of 9.52 mm; the cable exit point is set back with respect to the pitch line of 63.21 mm in the straight state reported in Figure 5.23(a).

On the other hand, the graphs of Figures 5.24(b) and 5.24(d) correspond to pitch lines where each arc has the same radius as before, but different arc length. In particular, the internal (red) arc is 10.05 mm long, the adjacent (blue) arc is 8.38 mm long, the consecutive (green) arc is 5.65 mm long, and the external (magenta) arc is 9.52 mm long, while the cable exit point is now set back with respect to the pitch line of 63.20 mm.

In the first case (Figures 5.24(a) and 5.24(c)), the cable can freely span an angle of $\pm 20.14^\circ$ along the pitch line and centered at the cable exit point, whereas the ridges of the internal cavities are at $\pm 14.00^\circ$ with polar distance from the cable exit point equal to 36.11 mm. In the second case (Figures 5.24(b) and 5.24(d)), the cable can freely span the angle of $\pm 14.17^\circ$ along the pitch line, centered again at the cable exit point, whereas the ridges of the internal cavities are at $\pm 6.41^\circ$ with

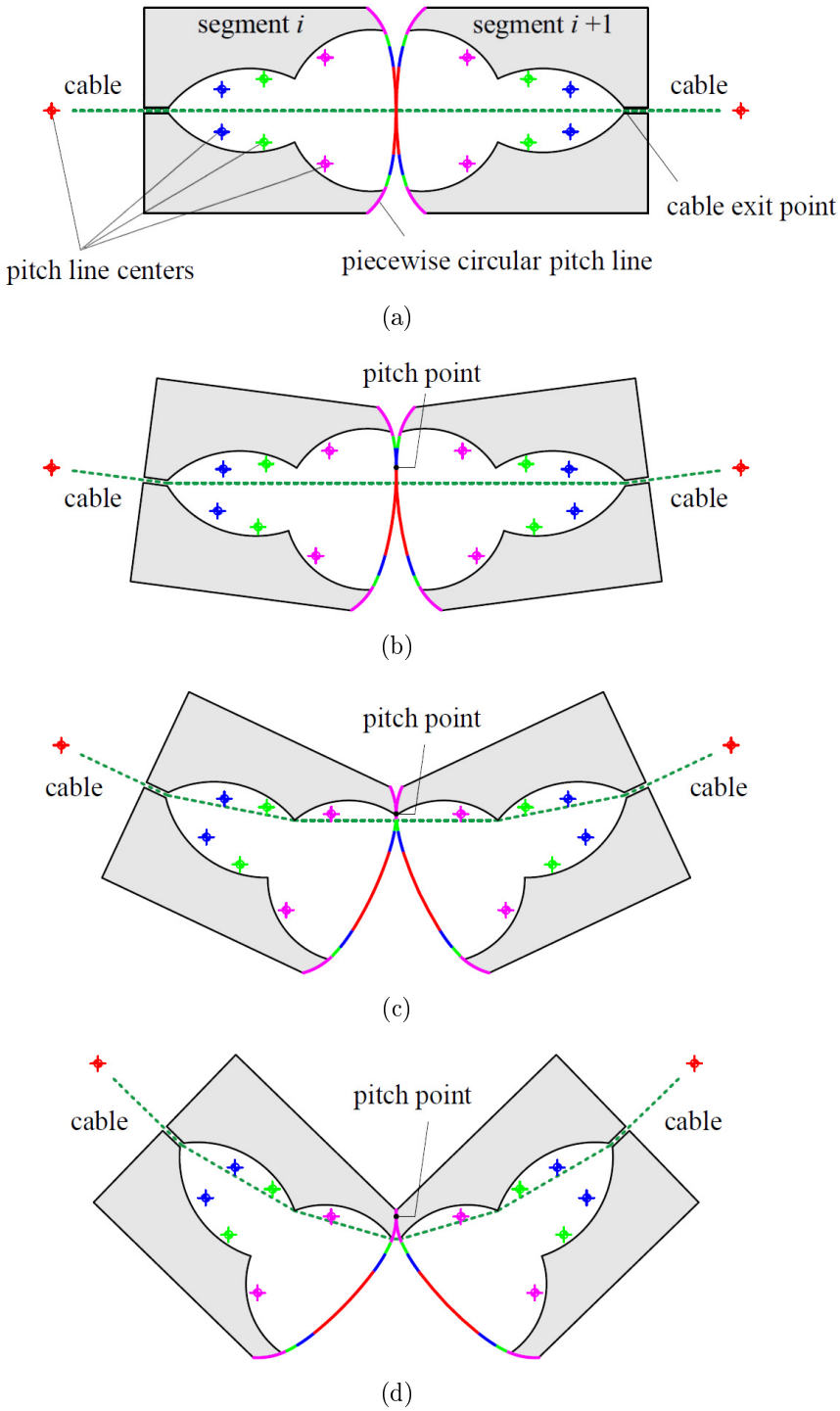

Figure 5.23. Schematics of a contact joint where the pitch lines are smoothly connected arcs of circle, and the cavities are delimited by curved segmented profiles. Various positions of the pivotal point for the cable as the relative rotation increases: (a) $\Delta\varphi_i = 0.0°$, (b) $\Delta\varphi_i = 14.9°$, (c) $\Delta\varphi_i = 50.4°$ and (d) $\Delta\varphi_i = 88.2°$.

polar distance from the pitch point equal to 35.69 mm.

Note that the peculiar design of pitch lines and internal cavities allows to obtain the additional branch, indicated as BC in Figure 5.24, interposed between the two spinodal (unstable) regions AB and CD. Observe, in particular, that, with the design corresponding to Figure 5.24(b), it is possible to have two rotated stable states under null applied loads ($M = 0$) for positive rotations ($\Delta\varphi_i > 0$). Recalling that a_i is an odd function of the relative rotation $\Delta\varphi_i$ of the joint, one has up to 5 natural states at $M = 0$ for the joint, corresponding to $\Delta\varphi_i = 0$, $\Delta\varphi_i = \pm 0.6370$ rad and $\Delta\varphi_i = \pm 1.1884$ rad in Figure 5.24(b).

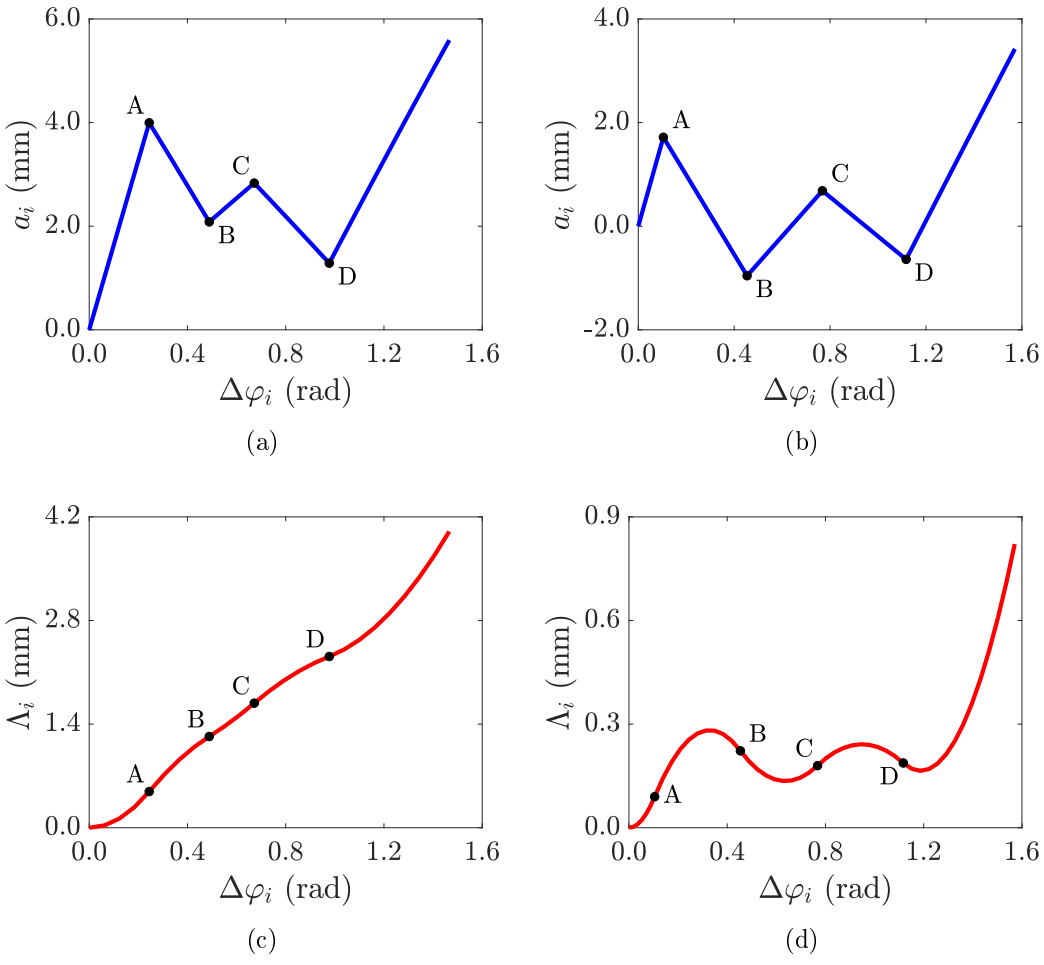

Figure 5.24. Two possible constitutive relationships for the multi-stable joint of Figure 5.23 by varying the geometrical parameters: (a)-(b) lever arm a_i as a function of $\Delta\varphi_i$; (c)-(d) corresponding cable elongation Λ_i. Points A, B, C and D delimit the spinodal regions and correspond to each other in the respective pictures.

5.3.2 Analytical results in the hard device

The response of a beam, composed of $n = 3$ segments coupled by means of joints with such a geometry to achieve the constitutive laws of Figures 5.24(b) and 5.24(d), is shown in Figure 5.25. This analysis is limited to one example for the hard device testing, as the soft device case does not provide additional relevant information, and the energy landscape is already incredibly rich, with many bifurcations and possible paths for a given external constraint/load.

For $N_0 = 5.00\,\mathrm{N}$ and $K = 5.60\,\mathrm{N/mm}$, Figure 5.25(a) shows the graphs of all possible states in terms of energy ΔU as a function of the relative rotation $\Delta\bar{\varphi}$ of the extremities of the beam. Figure 5.25(b) reports the corresponding plot in terms of end-couple M. As before, absolute minima (stable states) are shown with bold (black) lines, metastable states with solid (red) lines and unstable states with dotted (magenta) lines. The stability of the various paths has been assessed by studying the positive definitiveness of the Hessian matrix, as detailed in the last paragraphs of Section 5.2.2.

As evidenced by Figure 5.25, which refers just to the case of two multi-stable joints, the energy landscape can rapidly become richer by adding segments to the beam. Multiple equilibrium paths are possible, both stable and metastable, which can find specific applications in material science, to realize tailor-designed structured materials or as phenomenological model for the interpretation of the nature of solids with poly-convex energy. More in general, flexural tensegrities of this kind can also serve as a didactic laboratory, to explain the complex behavior of materials with multiple energy wells.

5.3.3 Multiple natural states

The structural response of a beam with the multi-stable joints of Figure 5.24(b) can apparently recall the multi-stable behavior of the segmental beam presented in [94], but, here, the scenario is much broader. Indeed, each joint is characterized by 5 stable configurations (instead of two) under null external loads, and one cable connects all the joints, thus giving to the assembly a nonlocal response. Moreover, the contact surfaces are shaped according to smooth and regular curves without angular points, so that the transition from one configuration to any other occurs smoothly and without large stress concentrations.

Similarly to what discussed in the previous Section 5.2.3 for the bi-stable joint, a flex-ten beam, whose multi-stable joints are manufactured according to constitutive relations of Figures 5.24(b) and 5.24(d), is characterized by many locally stable configurations, besides the straight one. For the case with four multi-stable joints ($n = 5$ segments), each joint has five natural states for $M = 0$, so that there

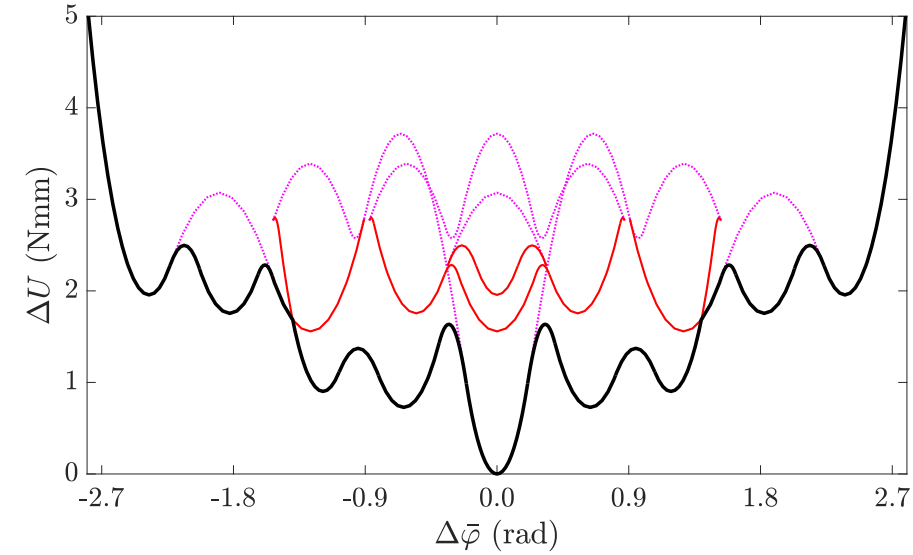

(a)

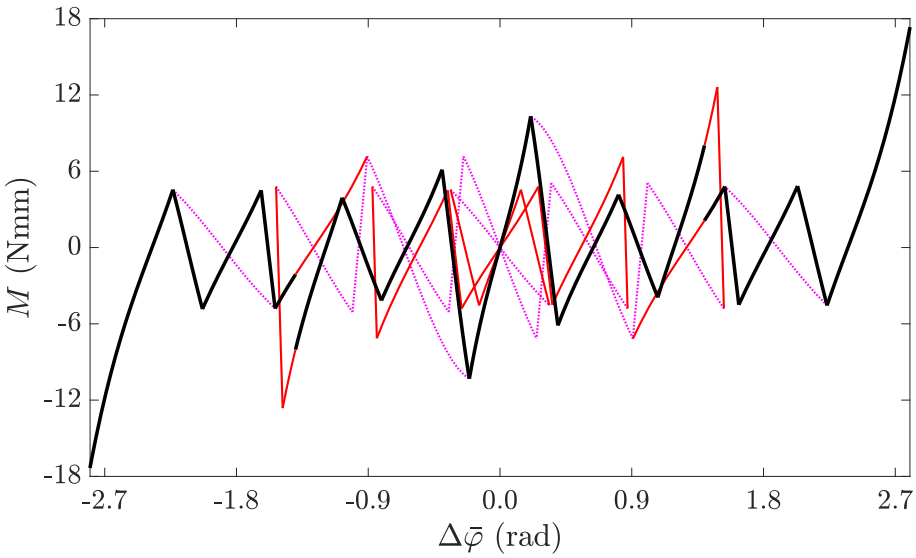

(b)

Figure 5.25. Response in a hard device of the multi-stable flex-ten beam with $n = 3$ segments corresponding to constitutive relations of Figures 5.24(b) and 5.24(d): (a) energy as a function of relative end rotation $\Delta\bar{\varphi}$ and (b) moment M vs. $\Delta\bar{\varphi}$. Stable states are shown with bold (black) lines, metastable states with solid (red) lines and unstable states with dotted (magenta) lines. Parameters: $N_0 = 5.00\,\mathrm{N}$ and $K = 5.60\,\mathrm{N/mm}$.

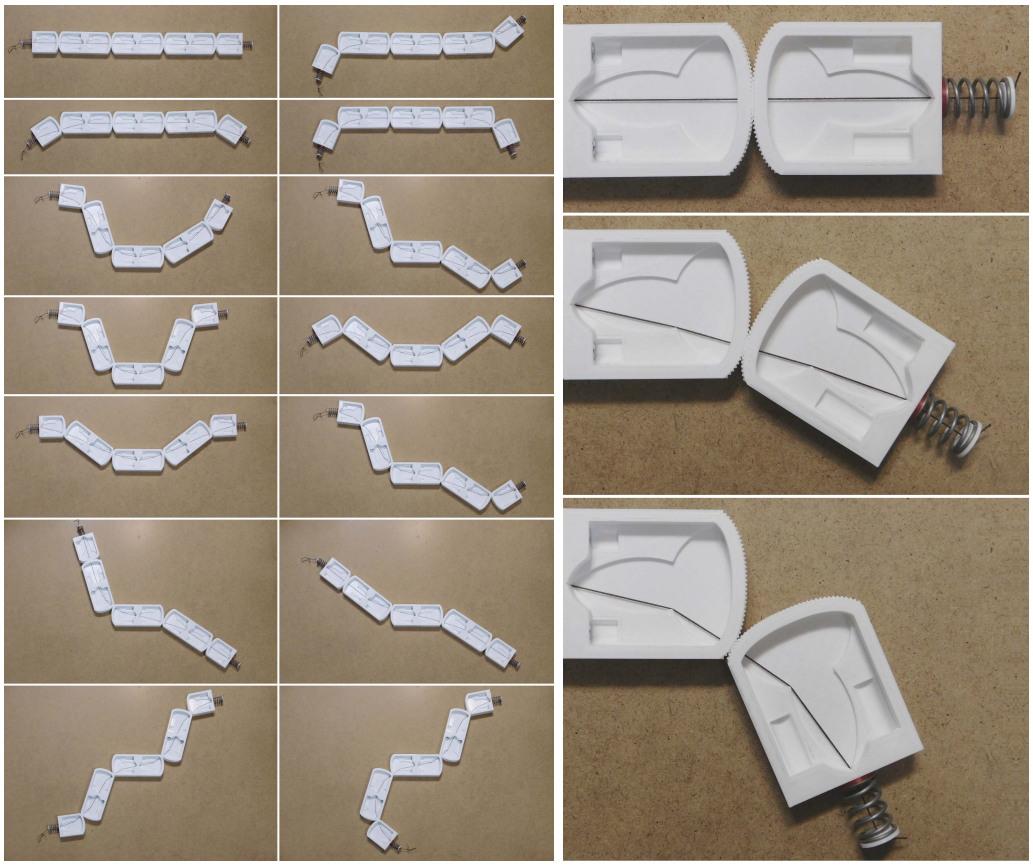

(a) (b)

Figure 5.26. Prototyped multi-stable flex-ten beam with $n = 5$ segments, manufactured according to constitutive relations of Figures 5.24(b) and 5.24(d). (a) Selection of the many possible multiple natural states (in equilibrium with $M = 0$) (b) Detail of the joint with evidence of the three stable states under null external loads for relative rotations $\Delta\varphi_i \geqslant 0$.

are $5^{n-1} = 5^4 = 625$ possible configurations corresponding to null end-couples, for the unconstrained beam. Figure 5.26(a) reports just a selection of such natural states, while Figure 5.26(b) displays a detail of the 3D-printed joint, depicted in the three stable states under null external loads for relative rotation $\Delta\varphi_i \geqslant 0$.

Obviously, this was just one example to evidence the great versatility of flex-ten structures and to show how a custom design of the joints can enlarge the energy landscape, including multiple energy wells.

Chapter 6

A snapping flex-ten cantilever

Structures that present two, or more, stable-equilibrium configurations, are referred to as bi-stable, or multi-stable, respectively. A bi- and multi-stable response, at the level of the single joint, was analyzed in the previous Chapter 5 by modifying the segments with hourglass-like internal cavities, where the cable can move. Anyway, the load was considered quasi-static and the focus was only on the different equilibrium configurations attainable for the same given external load.

Here, a new type of flex-ten structure is presented, and the full dynamic problems during snapping is considered in detail. The beam, arranged as a cantilever, is characterized by an enhanced mobility of the cable, which allows for a *reversible* multi-articulated global motion, driven by a localized perturbation, between two distant stable-equilibrium configurations. The new design provides a bi-stable response at the level of the *whole* structure. This is much more than simply modifying the energy wells of the multi-stable contact joints considered in Chapter 5, by reshaping the contact profiles or the hourglass-like internal cavities. If this was done, only the blending between inertial and elastic forces could possibly trigger the snapping of the links [95], through the propagation of transition waves [96].

The major novelty here consists in the new design of the internal cavities, such that the enhanced mobility of the tendon defines only two stable-equilibrium configurations for the chain as a whole. Remarkably, the structure will snap in its entirety in response to the imposed relative rotation of any two adjacent segments, without the need for inertial triggering via transition waves. When the first joint snaps, the others are forced to snap in cascade by the movement of the cable inside the cavities, which is driven by elastic energy minimization regardless of the inertia forces, without any control device. Of course, the dynamics of the problem must be considered because the performance of the system is dictated by the sudden release of energy at snapping, balanced by the inertial contribution.

The energetic barrier separating these states provides that the structure can

snap from one equilibrium configuration to another in response to external actions. In particular, the energy resulting from localized perturbations of an equilibrium configuration may be harnessed in the structural system, and make it snap towards another state when the perturbation reaches a critical threshold. The interest for systems of this kind has considerably grown in recent years in view of morphing and adaptive applications.

In Section 6.1, the detailed design of the new flexural-tensegrity structure is presented; the dynamic equations for the assembled system are derived and solved. In Section 6.2, three cantilevers, characterized by a different number of segments, are designed, prototyped and tested, in order to validate the theoretical predictions. The results here discussed are also collected in [97].

6.1 The design for a snapping cantilever

We consider the paradigmatic arrangement of a segmental flex-ten cantilever, entailing large deflections between two stable configurations. The motion is produced by the *sequential snaps* of the constituent contact joints in response to one single perturbation, represented by the slow cyclic rotation of one contact joint in proximity of the clamped segment. The system is *simple and robust*, and its movement is autonomous once snapping is triggered.

A similar example was presented in [96]. This is represented by a chain of hinged rigid segments, coupled in a next-nearest-neighbor (NNN) interaction scheme by extensional elastic springs, with an eccentricity with respect to the axis of the elements. If an initial low-energy perturbation is introduced at the free tip, the chain, clamped at the opposite end, folds from the straight configuration and needs to be manually restored back. On the contrary, one of the most interesting features of the flex-ten cantilever is that the *motion can be reversed* by changing the sign of the perturbation, although only *one tendon* is used. Thus, the system can represent the basic unit of complex articulated systems, in particular for deployable-collapsible structures. The two stable configurations are separated by a high energetic barrier: *no locking device* is thus needed to secure one of them after snapping, as is the case in other proposed devices [98].

The full dynamical problem is stated and the resulting equations are solved numerically. Since the harvested energy is suddenly released, the deformation rate is strongly influenced by dissipative phenomena, such as: friction/cohesion between the segmental contact surfaces (affected by the deformation of the conjugate profiles) and between the cable and the sheaths; viscosity of the medium where the device operates (air) and the aerodynamic characteristics of the segments. These are taken into account through equivalent terms in the theoretical formulation,

according to the findings of Section 4.1.3, and the corresponding parameters will be later calibrated by comparison with experiments on 3D-printed prototypes.

The aforementioned properties suggest applications as (micro) propulsion units, such as a flagellating tail for a robot fish [99], or jumping legs for a locust-inspired robot [100], for which the desired curvatures can be obtained by shaping the pitch profiles of the contact joints. The actuation mechanism would be simpler than that proposed, e.g., in [101], for a dolphin-like tail (adjustable Scotch yoke mechanism vs. a basic crank and crankshaft connected to a motor). The whipping of multiple flagella has application in a snake robot like that in [102], which locomotes in pipes using trapezium-like traveling wave. A classical flexural-tensegrity can be used to manufacture a bow (see next Chapter 8), but the new concept suggests applications for a new type of snapping catapult, outperforming the classical elastica-based design [15]. A miniaturized version may represent the basic cell of metamaterials with a modular 2D pattern, with a multi-stable response similar to the proposal of [103], where the basic snap-through instability of thin elastic arches is coupled with the Eulerian buckling of initially-straight thin elastic rods. If these were substituted by a flexural-tensegrity assembly, the metamaterial would acquires also memory properties, because the snap rewinds only if one changes the load sign, but not if the load is brought to zero.

6.1.1 Flexural tensegrity with enhanced tendon mobility

Increasing the mobility of the cable within the segments, that compose the flex-ten assembly, opens up a broader scenario because it can confer a multi-stable character to the contact joints. The evolution of the structural concept is summarized in Figure 6.1, which represents a schematic view of longitudinal sections of the segments, with indication of the passing-through cable. The sectioned portions are hatched, to distinguish them from the cavities where the cable is free to move. Adjacent to each section, on the right-hand side, the corresponding standing-alone segment is shown in a X-ray view.

The primitive configuration, first introduced in Chapter 2, is represented in Figures 6.1(a) and 6.1(b). The cable is constrained within a thin tubular sheath inside the segment, and its exit point is located exactly at the mid-point of pitch profile, here coinciding with the arc of circle drawn in red. The mobility of the cable is limited to axial stretching only. In general, the lever arm a_i, represented in Figure 2.2(a), is a monotone function of the relative rotation $\Delta\varphi_i$, so that the corresponding energy is a convex function of $\Delta\varphi_i$ and no snapping occurs.

The scheme of Figures 6.1(c) and 6.1(d) was analyzed in Chapter 5, and differs from the previous one because the exit point is located behind the pitch line: thanks to the presence of triangular-shaped cavities, the cable can move while keeping the

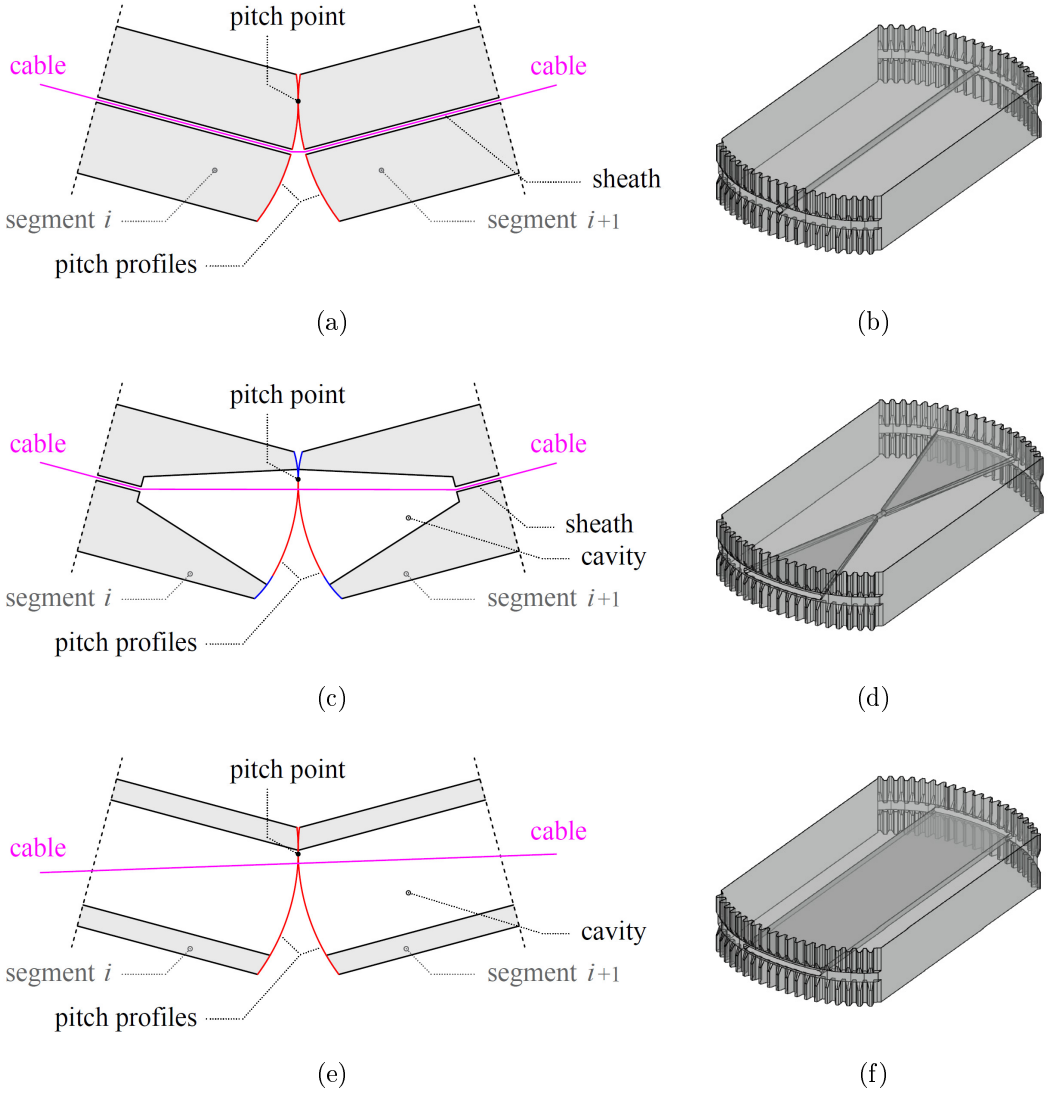

Figure 6.1. Schematic sections of adjacent segments with increased mobility of the cable, and corresponding X-ray view of the standing-alone segment: (a)-(b) tubular sheath and circular pitch lines, first introduced in Chapter 2; (c)-(d) triangular-shaped cavity and short sheaths, with piecewise circular pitch lines, analyzed in Chapter 5; (e)-(f) broader cavities, with circular pitch lines.

exit point as the pivot point. Designing the pitch lines as three smoothly-connected arcs of circle (blue and red curves in the picture), as pursued in Chapter 5, it is possible to obtain a multi-stable joint, with three stable configurations under null external actions, of which one is represented by the undistorted straight state.

The new geometry, that will be investigated in the present chapter, is that

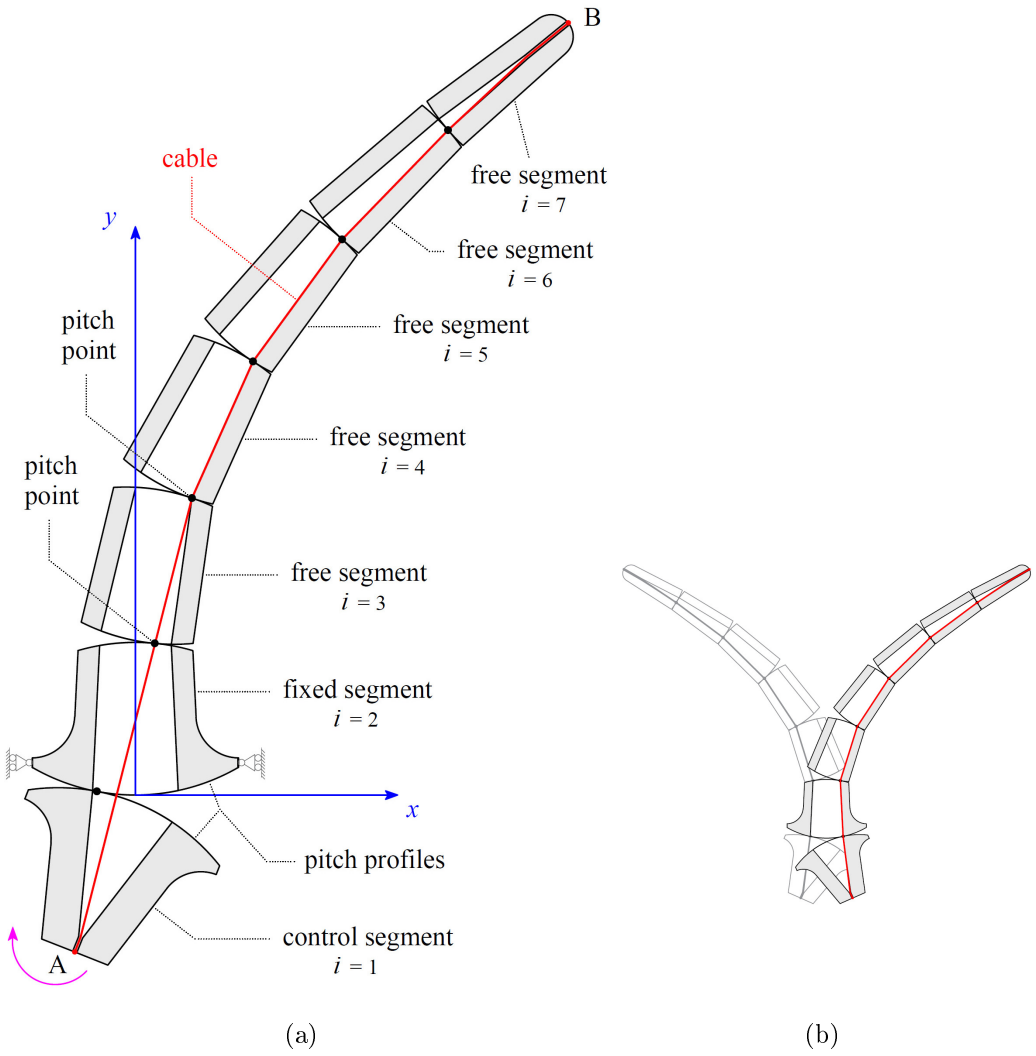

Figure 6.2. Schematic section of a snapping cantilever with $n = 7$ segments: (a) detailed view of the shape of the cavities and the passing-through cable; (b) the two symmetric configurations corresponding to minima for the strain energy.

depicted in Figures 6.1(e) and 6.1(f), where the cavity is broader and the sheath has been eliminated, so that there is no more the constraint for the exit point of the cable, as in the previous cases. The result is that the cable can more freely move inside the cavity, since there is no more the geometric restraint to pass through a fixed point within the single segment. The residual constraint is unilateral in type, being activated only when the cable touches the walls of the internal cavity.

The new concept is specialized to the model-problem of a cantilever, represented in Figure 6.2 as the assembly of $n = 7$ segments. The most important feature,

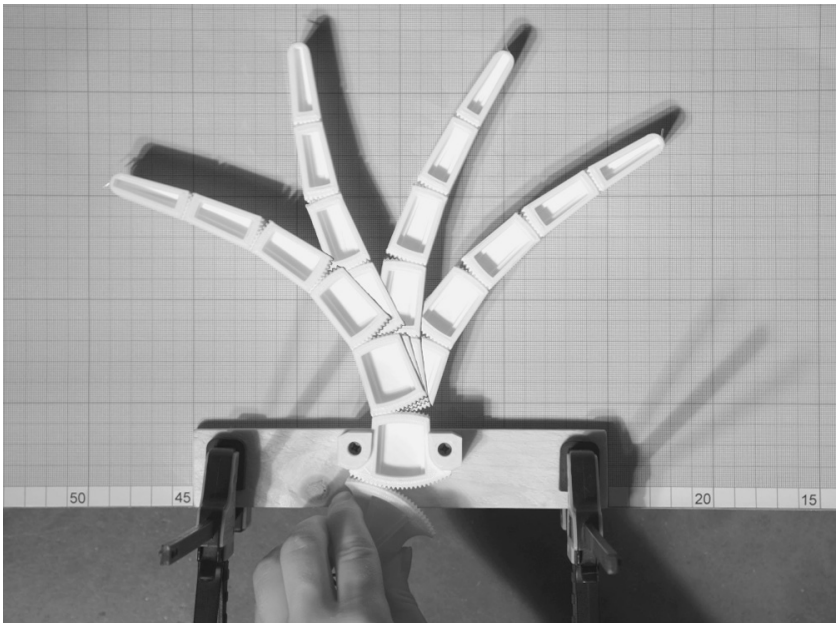

Figure 6.3. Frame sequence during the snapping of a cantilever prototyped via 3D-printing according to the schematic of Figure 6.2: the tip of the cantilever is initially pointing to the right-hand side, then the beam reverses its shape with a sequential snap of the joints.

evidenced in the longitudinal schematic section of Figure 6.2(a), is that the cavities, symmetric with respect to the axis of the segments, are tapered and gradually narrow while passing from the bottom to the top of the structure. More precisely, the cavities for $i = 2 \dots 6$ are trapezoidal in shape, while those at $i = 1$ and $i = 7$ are triangular because the anchoring point of the cable is located at the vertices (points A and B). The pitch profiles for the contact joints are arcs of circle and their radius is kept constant along the beam, while the length of the segments is less than the radius of the pitch lines (segmental length equal to 74% of the pitch line radius in the figure).

The peculiar geometry of the segments and their cavities, as well as of the contact profiles, is such that there are, by symmetry, only two configurations that correspond to the minimal length of the cable, when this is in contact with the walls of the cavities. These two configurations, which are represented in Figure 6.2(b), correspond to states of minimal strain energy and, therefore, define the only two symmetric stable configurations of equilibrium under null external actions.

We are interested in studying the dynamics of this structure when the segment $i = 2$ is kept fixed and the segment $i = 1$ is gradually rotated, as indicated in Figure 6.2(a). The cable thus moves inside the cavities: static equilibrium is obtained when the cable passes through the pitch point of each contact joint $i \neq 1$

(null lever arm). However, gradually increasing the rotation of the first segment, the equilibrium becomes unstable, because the length of the cable may be lowered by an infinitesimal perturbation of the configuration. At this instant, the structure is prone to snap towards the symmetric stable equilibrium state, as indicated in Figure 6.2(b). For a real cantilever, prototyped via 3D printing according to the schematic of Figure 6.2, the frame sequence during the snapping is reported in Figure 6.3: the tip of the cantilever is initially pointing to the right-hand side and the segment $i = 1$ is rotated by hand; when a certain limit angle is reached, then the beam is forced to reverse its shape.

One observes the orderly snap of the contact joints, because the relative rotation of two segments produces the movement of the cable that, in turn, triggers the snapping of the adjacent couple of segments. This is the major difference between structures of this type, and those corresponding to the construction of Figure 6.1(c). There, the energetic barrier between the equilibrium states of the contact joints is in general such that snapping occurs independently from one joint to the other. Here, for the case at hand, the snap-through instability of one joint produces instead a chain reaction that affects all the other joints. As a consequence, the structure snaps as a whole.

Of course, the dynamics is complicated by the blending between inertial and elastic forces. In particular, the acceleration is such that the stable equilibrium states are overtaken and the system starts to oscillate. The length of the arc of the pitch profiles that the cable can span without touching the walls of the cavities gradually diminishes from the bottom to the top, corresponding to an angle that passes from $2\pi/15$ for the first joint (between segments 1 and 2) to $\pi/45$ for the last joint (between segments 6 and 7). When the extremal points are reached, the cable is bound by the walls of the cavities and this produces the springing-back of the link. By changing the sign of the rotation of the control segment, the motion is reversed. Since a considerable elastic energy is released when the entire structure snaps, the structure behaves like a tail that flagellates. The cyclic rotation of the end segments produces alternating whipping, which can find specific applications.

6.1.2 Dynamic equilibrium

The solution procedure consists in solving the nonlinear system of equations that define dynamic equilibrium, coupled with a minimization algorithm that determined the position of the cable. We neglect the mass of the cable and the rotatory inertia of the segments[1], so that their mass is concentrated in the corresponding

[1]We have checked, a posteriori, that this contribution is inessential. The verification is provided in the remark at the end of Section 6.2.3, while discussing the experiments on the prototyped cantilever with $n = 5$ segments.

centroid (lumped mass model).

With reference to Figure 6.2(a), for a cantilever composed of n segments, let $\Delta\varphi_i(t)$, $i = 1 \dots n-1$, denote the relative rotation, positive if clockwise, between the segment $i+1$ and i, at time t. Recall that the segment 1 is gradually rotated, whereas segment 2 is kept fixed. Hence, the first rotation $\Delta\varphi_1(t)$ is the control parameter, whereas $\Delta\varphi_i(t)$, $i = 2 \dots n-1$, are the Lagrangian variables that define the actual configuration at time t. Introduce the global reference system (x, y) as represented in the same figure. If the values of the rotations are known, then the coordinates $\left(x_{\bar{P}_i}(t), y_{\bar{P}_i}(t)\right)$ of the pitch point $\bar{P}_i$ at the $i-$th contact joint, $i = 1 \dots n-1$, the coordinates $(x_A(t), y_A(t))$ and $(x_B(t), y_B(t))$ of the end points A and B where the cable is anchored, and the position $\left(x_{\bar{G}_i}(t), y_{\bar{G}_i}(t)\right)$ of the centroid $\bar{G}_i$ of the $i-$th segment, $i = 1 \dots n$ are completely determined by elementary geometry as a function of $\Delta\varphi_i(t)$, $i = 1 \dots n-1$.

The cable is free to move in the space determined by the cavities of the segments at time t, which is again completely defined by $\Delta\varphi_i(t)$, $i = 1 \dots n-1$. Since we neglect the mass of the cable, its position is such that its length is minimal at each instant t. This is found by solving a minimization problem, subjected to the unilateral constraints that the walls of the cavities cannot be overcome. Since the walls of the cavities are straight and the cable has negligible bending stiffness, such tendon is represented by a polyline. Thus, the minimization problem can be stated by considering as variables the coordinates $\left(x^-_{C_i}, y^-_{C_i}\right)$ and $\left(x^+_{C_i}, y^+_{C_i}\right)$, $i = 1 \dots n-1$, that represent the vertices of the polyline, being respectively associated with the position of the cable in correspondence of the pitch profiles of the lower $(^-)$ and

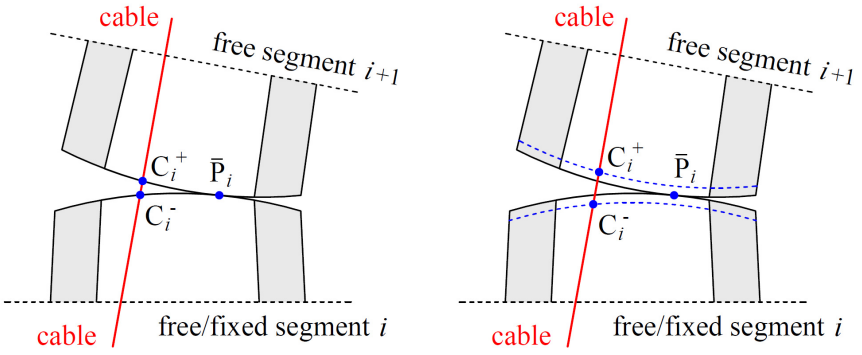

Figure 6.4. Location of the cable in the deformed configuration: (a) variables $C_i^- \equiv (x^-_{C_i}, y^-_{C_i})$ and $C_i^+ \equiv (x^+_{C_i}, y^+_{C_i})$ that define the vertices of the polyline as the points of intersection with the pitch profiles at joint i; (b) offset of the pitch profiles to avoid numerical instabilities in the minimization problem.

upper ($^+$) segments at the $i-$th joint, as indicated in Figure 6.4(a). With the same notation used in the previous chapters, once the length of the cable is determined, its elongation Λ is found and, correspondingly, the tensile force reads $N = N_0 + K\Lambda$.

The objective function is represented by the length of the cable expressed in terms of the aforementioned variables, subjected to the constraints, expressed in terms of inequalities, that the walls of the cavities cannot be surpassed. This is solved by using a procedure implemented in Wolfram Mathematica® [104], that adopts a Karush-Kuhn-Tucker approach. However, numerical instabilities may occur when the cable is close to the pitch points, because in this case $\left(x^-_{C_i}, y^-_{C_i}\right) \cong \left(x^+_{C_i}, y^+_{C_i}\right)$. Even a small approximation of such values can produce noteworthy errors for the evaluation of the internal moment at the contact joint. In fact, this is given by $M_i = a_i N$, but the lever arm a_i is determined by the coordinates $\left(x^\pm_{C_i}, y^\pm_{C_i}\right)$, which define the orientation of the exposed portion of the cable. In order to by-pass this problem, the pitch profiles are artificially offset of a small quantity (offset-length = 0.5 mm for the case at hand), as indicated in Figure 6.4(b). This implies that, even in proximity of the pitch point, the intersection points are well spaced apart, and the minimization algorithm is stabilized.

Dissipation can also play a decisive role. According to the findings of Section 4.1.3, this is modeled by assuming that at each joint i there is a parasite moment $M_{d,i} = c\,\Delta\dot{\varphi}_i$, proportional through the constant c to the speed of relative rotation $\Delta\dot{\varphi}_i$. An additional contribution is due to the frictional contact of the conjugate profiles that define the pitch profiles, manufactured as toothed wheels in the prototypes. A dynamic-friction moment is considered in the form $M_{f,i} = \mathrm{sgn}(\Delta\dot{\varphi}_i)\,\bar{M}$, where $\bar{M} > 0$.

The equilibrium of each joint shall be satisfied. To define the corresponding equation, the structure is ideally separated at the $i-$th contact joint, for $i = 2 \dots n-1$, by cutting the exposed portion of the cable: the internal forces at the node are the contact reactions, concentrated at the pitch point, and the axial force N in the cable. Consider the free body diagram of the portion, formed by the assembled segments j, for $j = i+1 \dots n$. For the configuration at time t, defined by the variables $\Delta\varphi_i(t)$ for $i = 2 \dots n$ (recall that $\Delta\varphi_1(t)$ is the control parameter representing the load history), one calculates the position of the cable from the minimization problem and, hence, the axial force $N(t)$. Elementary geometry also provides the lever arm $a_i(t)$ of the cable force with respect to the pitch point $\bar{P}_i \equiv \left(x_{\bar{P}_i}(t), y_{\bar{P}_i}(t)\right)$ at the $i-$th joint, the coordinates of the centroid $\bar{G}_j \equiv \left(x_{\bar{G}_j}(t), y_{\bar{G}_j}(t)\right)$ and the corresponding components of the inertial forces $F_{x,j}(t) = -m_j\,\ddot{x}_{\bar{G}_j}(t)$ and $F_{y,j} = -m_j\,\ddot{y}_{\bar{G}_j}(t)$, where m_j is the mass of the segment. Then, there are $n-2$ independent nonlinear equations at joints $i = 2 \dots n-1$, which correspond to the rotational equilibrium with respect to the pitch point and can be written as

$$N(t)\,a_i(t) + \sum_{j=i+1}^{n} \Big[m_j \ddot{x}_{\bar{G}_j}(t) \left(y_{\bar{G}_j}(t) - y_{\bar{P}_i}(t) \right) - m_j \ddot{y}_{\bar{G}_j}(t) \left(x_{\bar{G}_j}(t) - x_{\bar{P}_i}(t) \right) \Big] + \\ + \operatorname{sgn}\left(\Delta\dot{\varphi}_i(t) \right) \bar{M} + c\,\Delta\dot{\varphi}_i(t) = 0\,, \quad i = 2 \ldots n-1\,. \tag{6.1.1}$$

For the sake of illustration, the various quantities represented in this equations are detailed in Figure 6.5(a) for the case $n = 4$. Observe that in general $a_i(t)$ may achieve either positive or negative values, depending on the fact that the cable line is located on the right-hand side or the left-hand side with respect to the pitch point, as indicated in Figure 6.5(b).

Experiments have provided further evidence that there is an initial resistance to the rotation of the segments, which should be attributed to the static friction

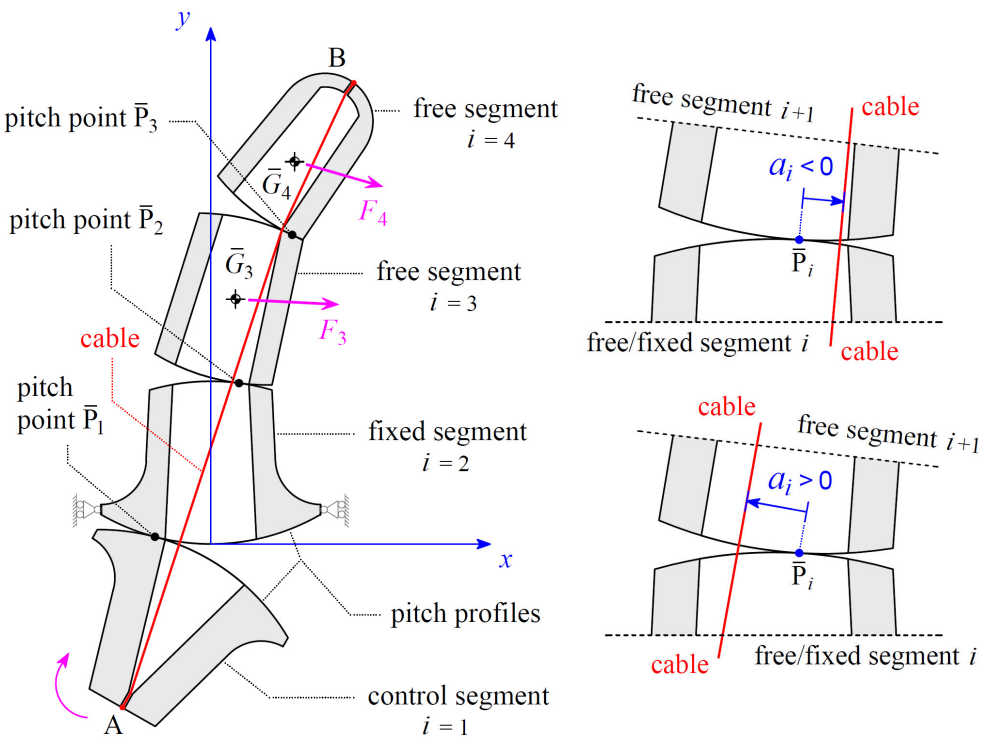

Figure 6.5. Cantilever with $n = 4$ segments: (a) indications of inertial forces, centroids and pitch points; (b) different signs of the level arm a_i according to the position of the cable line with respect to the pitch points.

between the conjugate profiles, i.e., a threshold that should be overcome before dynamic friction comes into play when the motion starts. We consider this effect by introducing a value for the moment of static friction $\bar{M}_s > \bar{M}$. Therefore, the problem is subjected to the further condition that the relative rotation at the $i-$th joint does not occur as long as

$$\begin{aligned}\Bigg| N(t)\, a_i(t) + \sum_{j=i+1}^{n} m_j \ddot{x}_{\bar{G}_j}(t) \left(y_{\bar{G}_j}(t) - y_{\bar{P}_i}(t)\right) + \\ - \sum_{j=i+1}^{n} m_j \ddot{y}_{\bar{G}_j}(t) \left(x_{\bar{G}_j}(t) - x_{\bar{P}_i}(t)\right) \Bigg| < \bar{M}_s \,.\end{aligned} \tag{6.1.2}$$

The problem is solved through a step-by-step integration coupled with the minimization algorithm that finds the position of the cable associated with each configuration. Let Δt denote the time step. As detailed in equation (4.1.12) for the specific case of the relative rotation, the time-derivatives (velocity and acceleration) of any function $\theta(t)$ of the time t can be approximated as

$$\dot{\theta}(t) \simeq \frac{\theta(t+\Delta t) - \theta(t-\Delta t)}{2\,\Delta t}\,, \tag{6.1.3a}$$

$$\ddot{\theta}(t) \simeq \frac{\theta(t+\Delta t) - 2\theta(t) + \theta(t-\Delta t)}{\Delta t^2}\,. \tag{6.1.3b}$$

The x and y components of the acceleration $\ddot{x}_{\bar{G}_j}(t)$ and $\ddot{y}_{\bar{G}_j}(t)$, as well as the angular velocity $\Delta\dot{\varphi}_i(t)$, featuring in equations (6.1.1) and (6.1.2), are approximated as per (6.1.3). In conclusion the solution is found according to the following procedure.

- The variables $\Delta\varphi_i(t)$, $i = 1 \dots n-1$, are supposed to have been determined up to the time t. The polyline defining the position of the cable is then found by solving the minimization problem. Hence, the tensile force $N(t)$, the lever arm $a_i(t)$, the pitch points $\bar{P}_i \equiv \left(x_{\bar{P}_i}(t), y_{\bar{P}_i}(t)\right)$, $i = 1 \dots n-1$, and the centroids $G_j \equiv \left(x_{\bar{G}_j}(t), y_{\bar{G}_j}(t)\right)$, $j = 3 \dots n$, are determined.
- At the time $t + \Delta t$, $\Delta\varphi_1(t+\Delta t)$ is assigned. The values of $\Delta\dot{\varphi}_i(t)$, for $i = 2 \dots n-1$, and of $\ddot{x}_{\bar{G}_j}(t)$ and $\ddot{y}_{\bar{G}_j}(t)$, for $j = 3 \dots n$, are approximated with a formula of the type (6.1.3). Since $x_{\bar{G}_j}(t+\Delta t)$ and $y_{\bar{G}_j}(t+\Delta t)$ depend on $\Delta\varphi_i(t+\Delta t)$, $i = 2 \dots n-1$, all quantities depend upon this value.
- Solving the nonlinear equations (6.1.1), under the condition (6.1.2), the values of $\Delta\varphi_i(t+\Delta t)$, $i = 2 \dots n-1$ are found.
- The calculation is repeated for the time $t + \Delta t$.

In the following, we will consider the motion of cantilevers composed of $n = 3, 4, 5$ segments. The theoretical results will be compared with experiments on 3D-printed physical models.

6.2 Examples

This section presents theory and experiments. A high-speed camera has been used to record the snap-through instability of physical models of the structure, to make comparisons with the predictions of the theoretical model.

6.2.1 Construction of prototypes

Three cantilevers, made of $n = 3, 4, 5$ segments, were 3D printed in white polylactide (PLA) through the deposition method (FDM). These are shown in Figure 6.6(a). The tendon is a dark-brown braided wire made of cotton, waxed to diminish friction, with effective diameter of 0.5 mm. Each segment is open in proximity of the cavity, so that the movement of the cable can be visualized. To increase its compliance, a steel elastic spring was added in series with the cable at the anchor point, as displayed in Figure 6.6(a). The initial prestress N_0 was evaluated by measuring the deformation of the spring. The elastic constant of the spring (measured in a compression test) is 5.45 N/mm, so that the effective axial stiffness of the cable, with the spring in series, results to be $K = 2.47\,\mathrm{N/mm}$ for $n = 3$, $K = 2.17\,\mathrm{N/mm}$ for $n = 4$ and $K = 1.91\,\mathrm{N/mm}$ for $n = 5$. The difference is because the length, and hence the compliance, of the cable itself increases with the number of segments.

Figure 6.6(b) shows the design drawings, with indication of the main dimensions of the segments and the corresponding cavities. The pitch lines are arcs of circle with radius equal to 48 mm and the pure rolling motion, with no sliding, is obtained with toothed conjugate profiles, as evidenced in Figure 6.6. In the same picture, the $x - y$ reference frame used for the representation, as well as the points used as reference to measure the motion, are evidenced in red.

6.2.2 Static analysis

The first analysis concerns the static equilibrium configurations of the structure, irrespective of their stability. When inertia, dissipative and frictional forces are not considered, the only way in which the equilibrium can be achieved is that the polyline representing the position of the cable passes through the pitch points of all the contact joints, except for the first one $i = 1$, because the first segment is

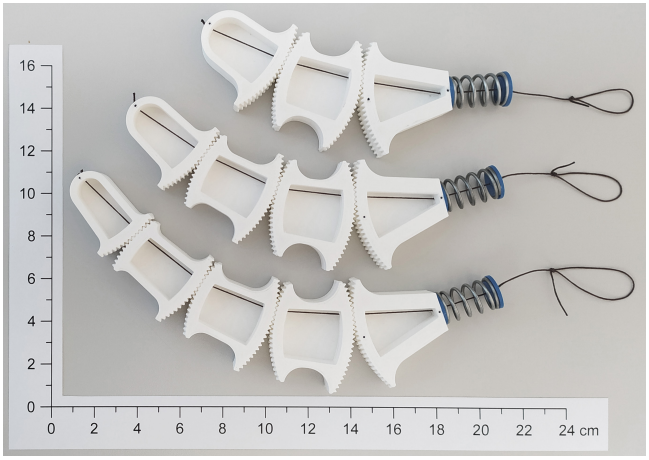

(a)

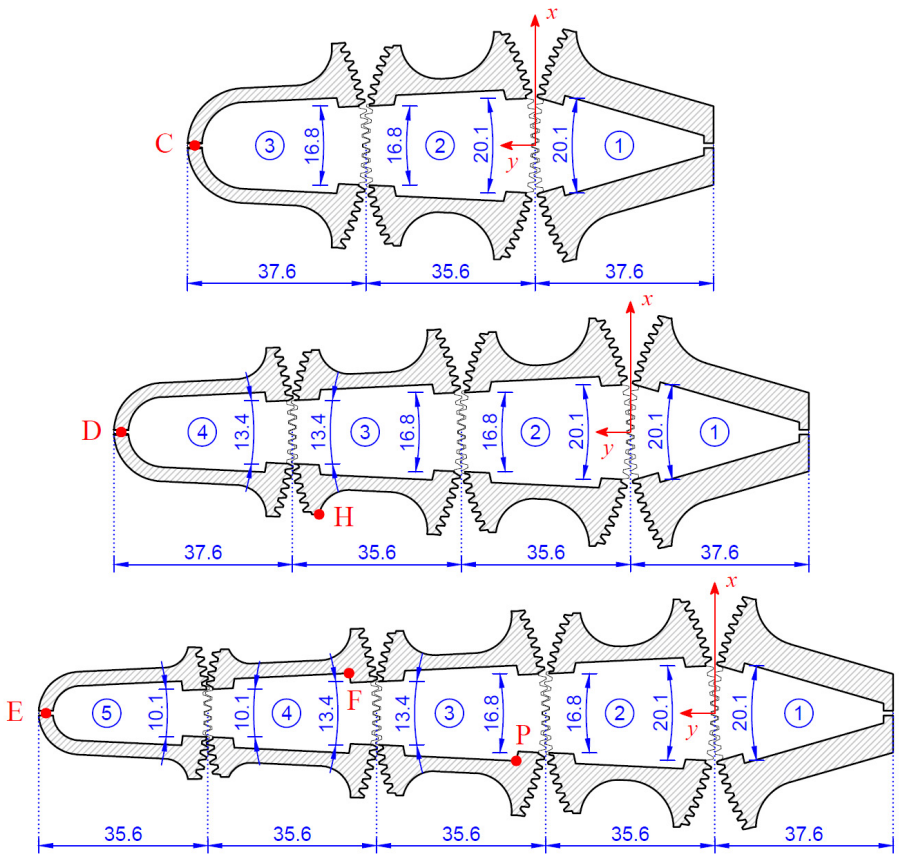

(b)

Figure 6.6. Physical models of the cantilever: (a) 3D-printed prototypes composed by $n = 3, 4, 5$ segments; (b) corresponding design drawings of the prototypes, with indication of the dimensions [mm].

constrained to rotate. In fact, only in this case the internal moment $M_i = a_i N$ is zero, because the lever arm a_i is null. Hence, the equilibrium configurations are obtained from pure geometric considerations. As the control parameter $\Delta\varphi_1$ is gradually varied, one finds the rotation angles $\Delta\varphi_i$, $i = 2 \dots n-1$, such that compatibility with the cable position is satisfied.

The construction is particularly simple for $n = 3$, because only the angle $\Delta\varphi_2$ needs to be determined as a function of just $\Delta\varphi_1$. For the geometry indicated in Figure 6.6(b) and an initial prestress $N_0 = 2.73\,\mathrm{N}$, as in the experiments of the following Section 6.2.3, the results are summarized in Figure 6.7. The variation of elastic strain energy $\Delta U = N_0\Lambda + \frac{1}{2}K\Lambda^2$, as first detailed in Section 2.1.3, is plotted as a function of $\Delta\varphi_1$ in Figure 6.7(a). This exhibits two convex branches

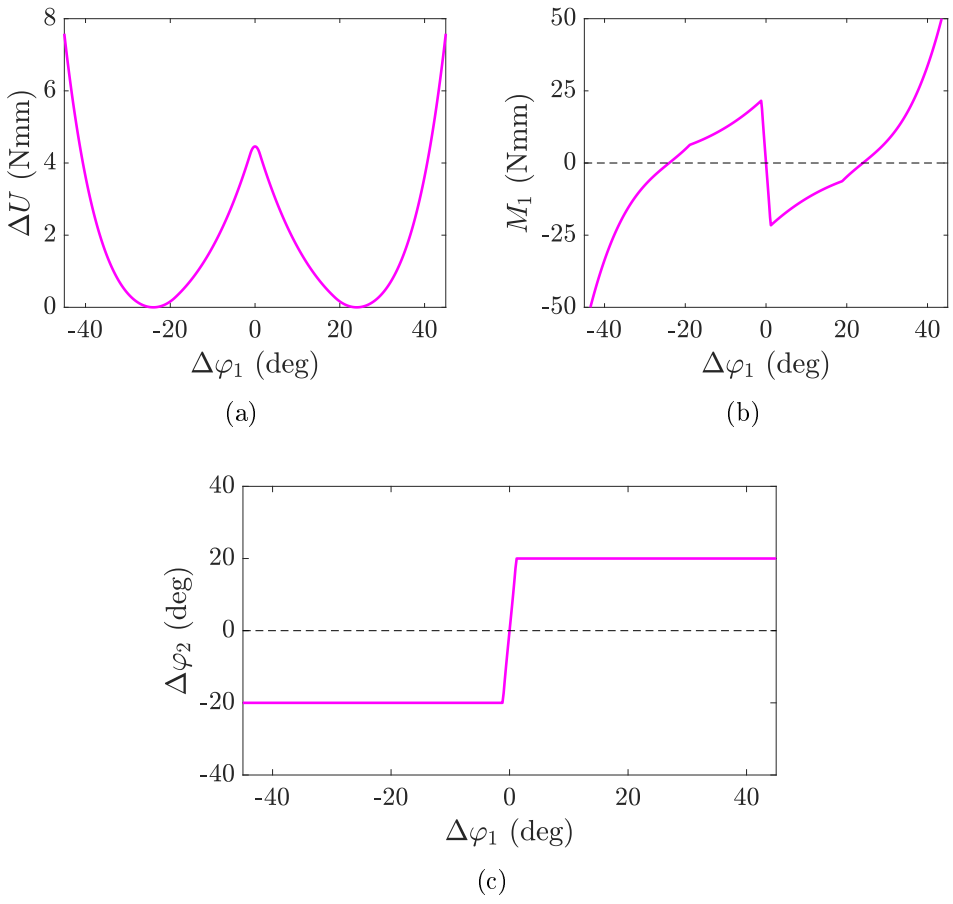

Figure 6.7. Static equilibrium configurations of a cantilever composed of $n = 3$ segments, for varying $\Delta\varphi_1$: (a) variation of the elastic strain energy ΔU; (b) internal moment M_1 at the first joint; (c) relative rotation $\Delta\varphi_2$.

with absolute minima at $\Delta\varphi_1 = \pm 24^\circ$ (corresponding to $\Delta\varphi_2 = \pm 20^\circ$), connected by a narrow spinodal region where the curvature changes sign. Figure 6.7(b) reports the internal moment M_1 at the first joint, corresponding to the reaction offered by the system as the angle $\Delta\varphi_1$ is varied. There is a steep descending branch, in correspondence of the spinodal region. Finally, Figure 6.7(c) shows $\Delta\varphi_2$ as a function of $\Delta\varphi_1$.

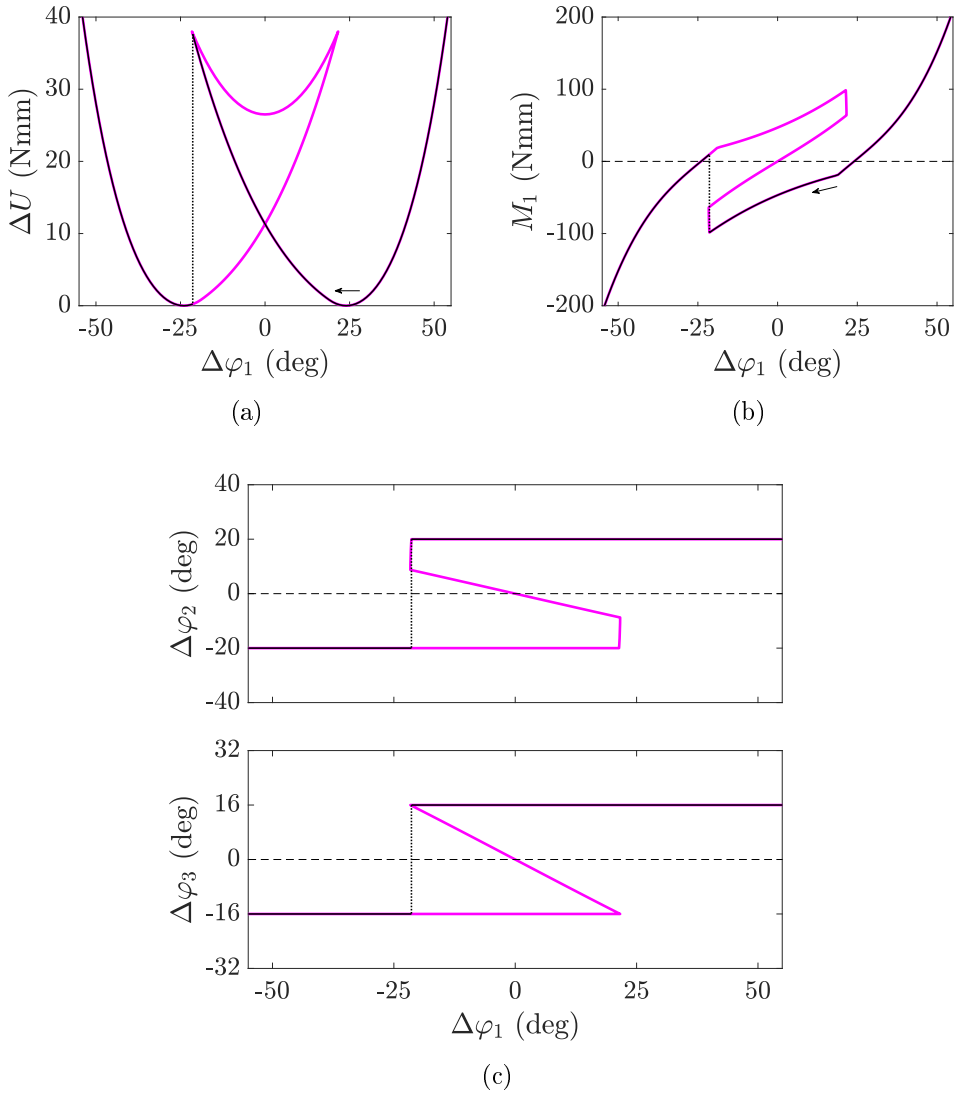

Figure 6.8. Static equilibrium configurations of a cantilever composed of $n = 4$ segments, for varying $\Delta\varphi_1$: (a) variation of elastic strain energy ΔU; (b) internal moment M_1 at the first joint; (c) relative rotations $\Delta\varphi_2$ and $\Delta\varphi_3$.

Figure 6.8 corresponds to the case of $n = 4$ segments for the geometry of Figure 6.6(b) and initial prestress $N_0 = 8.72\,\mathrm{N}$. Now the free variables are $\Delta\varphi_2$ and $\Delta\varphi_3$, so that there can be three equilibrium configurations corresponding to the same value of control variable $\Delta\varphi_1$. The graph of the energy ΔU becomes that represented in Figure 6.8(a). Again, there are two absolute minima at $\Delta\varphi_1 = \pm 24^\circ$, corresponding to $\Delta\varphi_2 = \pm 20^\circ$ and $\Delta\varphi_3 = \pm 16^\circ$, and equivalent to the natural equilibrium states at rest. As $\Delta\varphi_1$ is gradually diminished from the initial value $+50^\circ$, the system jumps from one branch to the other corresponding to a lower energy: the system snaps, following the path drawn with a black line. Figure 6.8(b) reports the internal moment M_1 at the first joint, where the correspondence with the various branches in the energy graph is evidenced by an equal color. Figure 6.8(c) shows $\Delta\varphi_2$ and $\Delta\varphi_3$ as a function of $\Delta\varphi_1$, and, according to the same chromatic characterization of the other graphs, the snap path is drawn in black.

The analysis for a structure made by a higher number of segments is similar. More equilibrium paths and more complicated snap-through instabilities would be possible. However, at the conceptual level, there is not a substantial difference with respect to the case $n = 4$.

6.2.3 Dynamic analysis and comparisons with experiments

Three prototypes following the design of Figure 6.6(b), respectively composed of $n = 3, 4, 5$ segments, were tested. Their motion was filmed with a high-speed camera and compared with the theoretical predictions. The segment $i = 2$ was clamped and angle $\Delta\varphi_1$ was gradually varied by moving the segment $i = 1$ by hand. During the test, the specimens were placed horizontally, in order to rule out the effects of gravity in the plane where the motion took place. Of course, the cantilever bends also in the vertical direction and twists, but we have verified that the corresponding deformation is negligible. The high-speed camera was a Phantom v1840 and the recordings were performed at 2000 fps for the prototype with $n = 3$ segments, and at 1000 fps for the other two prototypes. The values of prestress N_0, the effective stiffness of the cable K, and the segmental mass m_i are reported in Table 6.1.

Table 6.1. Values of the prestress N_0, the effective stiffness of the cable K, and the segmental mass m_i for the three prototypes composed by $n = 3, 4, 5$ segments.

n	N_0	K	m_3	m_4	m_5
3	2.73 N	2.47 N/mm	0.0063 kg	–	–
4	8.72 N	2.17 N/mm	0.0068 kg	0.0059 kg	–
5	11.00 N	1.91 N/mm	0.0068 kg	0.0060 kg	0.0049 kg

Cantilever with $n = 3$ segments

The frames from the high-speed video, collected in Figure 6.9, represent the motion of the cantilever with $n = 3$ segments while snapping. The chart above the pictures reports, as a function of time, the x-coordinate x_C of the tip point C, defined with respect to the reference frame represented in Figure 6.6(b). Here the dots numbered from 1 to 8 correspond to the labels of the photographs.

Figure 6.10 reports the results from the theoretical model, calculated with a time step $\Delta t = 0.0005\,\mathrm{s}$. The rotation history $\Delta\varphi_1(t)$ of the end segment has been determined from the high-speed video and used as input for the calculations. Figure 6.10(a) shows the elastic strain energy contribution ΔU as a function of time, whereas Figures 6.10(b) and 6.10(c) respectively report the internal moments M_i and the segmental relative rotations $\Delta\varphi_i$, for $i = 1, 2$. Here, the instant where the structure snaps and the successive oscillations are well defined. The comparison between experiments and theory is represented in Figures 6.10(d) and 6.10(e), respectively in terms of the coordinates $x_C(t)$ and $y_C(t)$ of the tip point C indicated in Figure 6.6(b). The agreement is very good if one assumes, as dissipative and friction parameters, the values $c = 0.03\,\mathrm{Nmm\,s}$, $\bar{M} = 0.33\,\mathrm{Nmm}$ and $\bar{M}_s = 3.30\,\mathrm{Nmm}$.

Note that the condition (6.1.2) provides the initial delay of the motion, in agreement with the experimental findings. This can be attributed by the initial static character of the friction and/or the interlocking of the teeth of the conjugate

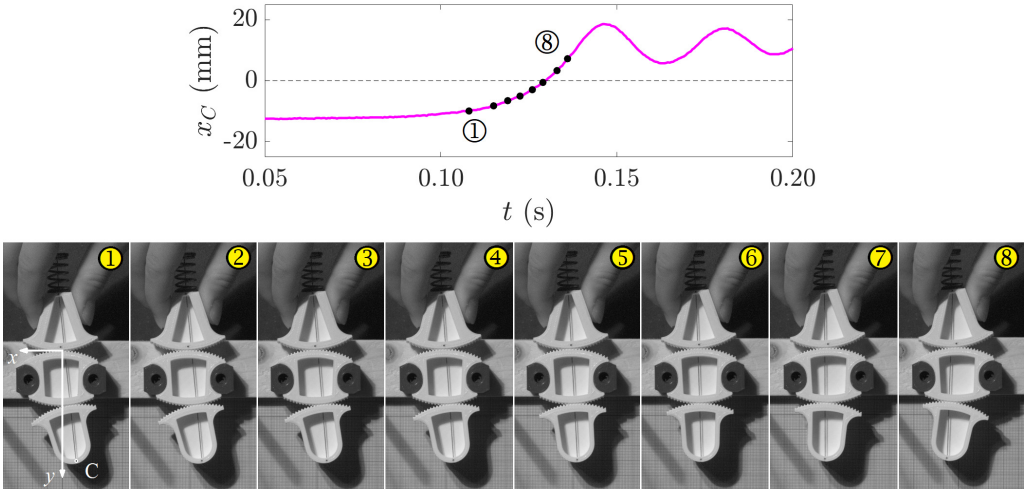

Figure 6.9. Images of the snapping cantilever with $n = 3$ segments from high-speed recording. The graph above shows, as a function of time, the x-coordinate x_C of the tip point C with respect to the reference frame represented in Figure 6.6(b), with indication of the configurations $1 - 8$ corresponding to the pictures.

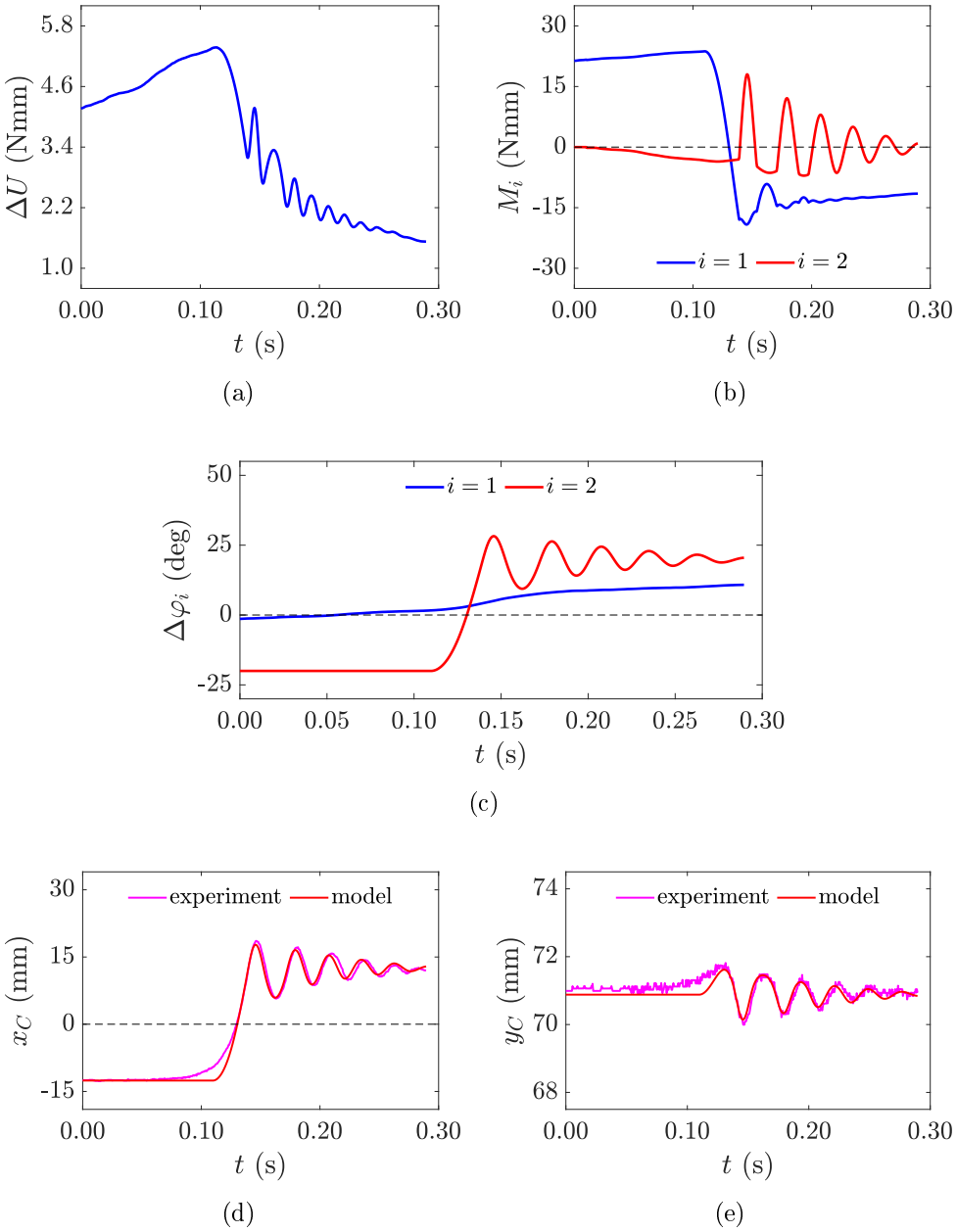

Figure 6.10. Cantilever with $n = 3$ segments subjected to a gradual rotation $\Delta\varphi_1(t)$ of the first segment: (a) variation of the elastic strain energy ΔU as a function of time t; (b) internal moments $M_i(t)$ at the contact joints $i = 1, 2$; (c) segmental relative rotations $\Delta\varphi_i(t)$, $i = 1, 2$. Comparison between experimental data and theoretical results: coordinates (d) $x_C(t)$ and (e) $y_C(t)$ of the tip point C.

profiles that have been used in the design. Of course, the phenomenon is complex, and the assumption of a relatively-high value for the static-friction moment $\bar{M}_s$ of first movement, is just an approximation. This is why the experimental (magenta) curve of Figure 6.10(d) does not perfectly overlap with the theoretical branch in the neighborhood of $t = 0.10\,\mathrm{s}$, but the agreement may be reputed satisfactory.

Cantilever with $n = 4$ segments

The counterpart of Figure 6.9 for the case of $n = 4$ segments is represented by Figure 6.11; now the tip point is denoted by D as per Figure 6.6(b). On the other hand, Figure 6.12 is the counterpart of Figure 6.10. The time step in the finite difference approach is again $\Delta t = 0.0005\,\mathrm{s}$, and, again the rotation $\Delta\varphi_1(t)$ has been calculated from the video and used as input for the model. For this case there are three values, for $i = 1\ldots3$, of the bending moments $M_i(t)$ and the relative rotation $\Delta\varphi_i(t)$. With respect to the case $n = 3$, the response is more complicated and the oscillations of larger amplitude, as expected.

The comparison between experimental data and theoretical prediction can be found in Figure 6.13. This is done in terms of the coordinates $(x_D(t), y_D(t))$ and $(x_H(t), y_H(t))$ respectively of the tip point D and the point H of segment $i = 3$, indicated in Figure 6.6(b) with respect to the relevant reference frame. The agree-

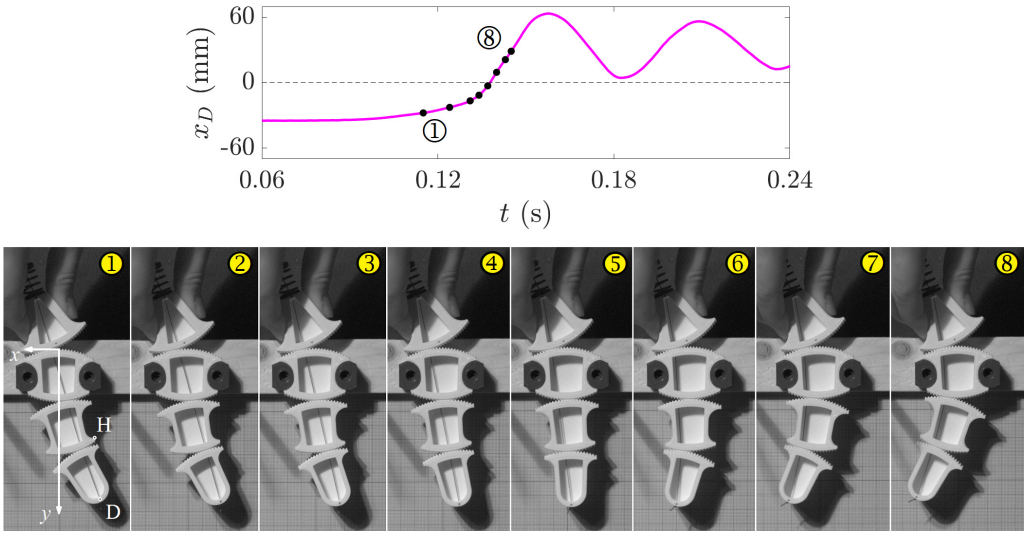

Figure 6.11. Images of the snapping cantilever with $n = 4$ segments from high-speed recording. The graph above shows, as a function of time, the x-coordinate x_D of the tip point D with respect to the reference frame represented in Figure 6.6(b), with indication of the configurations $1 - 8$ corresponding to the pictures.

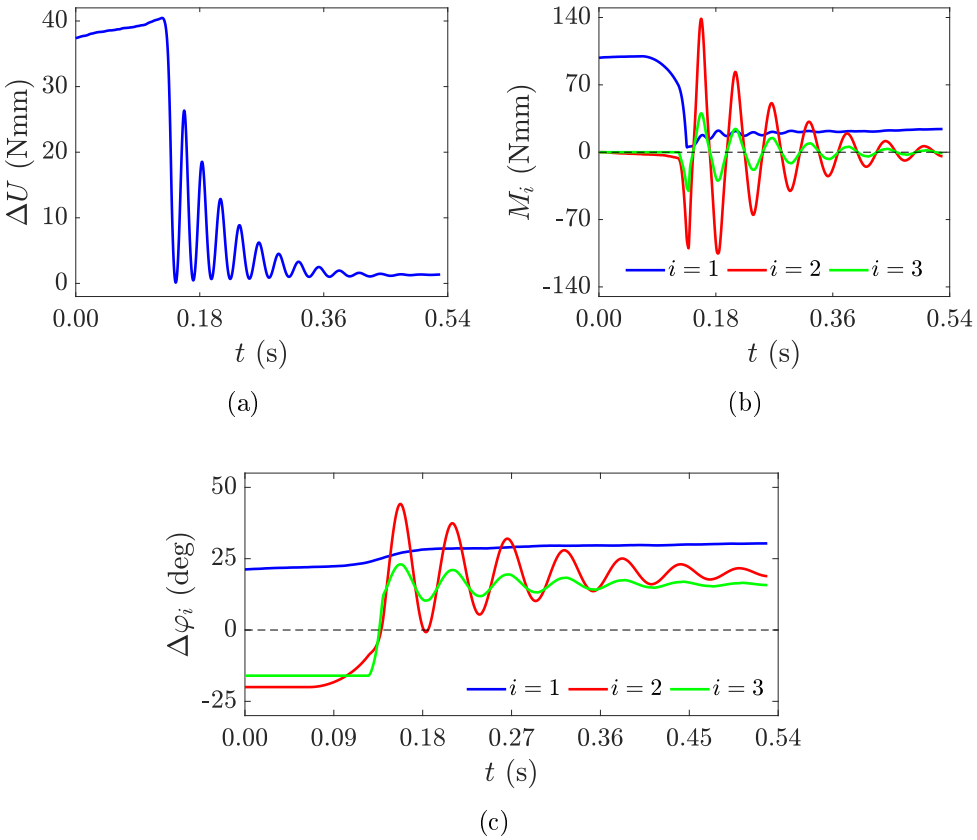

Figure 6.12. Cantilever with $n = 4$ segments subjected to a gradual rotation $\Delta\varphi_1(t)$ of the first segment: (a) variation of the elastic strain energy ΔU as a function of time t; (b) internal moments $M_i(t)$ at the contact joints $i = 1 \dots 3$; (c) segmental relative rotations $\Delta\varphi_i(t)$, $i = 1 \dots 3$.

ment between the theory and the experiment is excellent if one sets $c = 0.25\,\mathrm{Nmm\,s}$, $\bar{M} = 0.40\,\mathrm{Nmm}$ and $\bar{M}_s = 2.00\,\mathrm{Nmm}$. Again, the static-friction moment $\bar{M}_s$ is necessary to reproduce the delay in the motion observed in the test.

The parameters defining the dissipation terms in the equations have been calibrated for the best fit with the experimental data. Since multiple parameters need to be found, corresponding to phenomena that all restrain the motion, the precise calibration of each single parameter would require a greater number of tests and a statistical analysis, especially for the pair $(\bar{M}, c)$. Moreover, notice that the values change with respect to the previous case of $n = 3$ segments. Indeed, one expects nonlinear effects which depend upon the level of the inertial forces and their ratio with the elastic constraining forces for the tendon. In particular, for the short prototypes, the mass and the prestress are low, so that frictional forces may

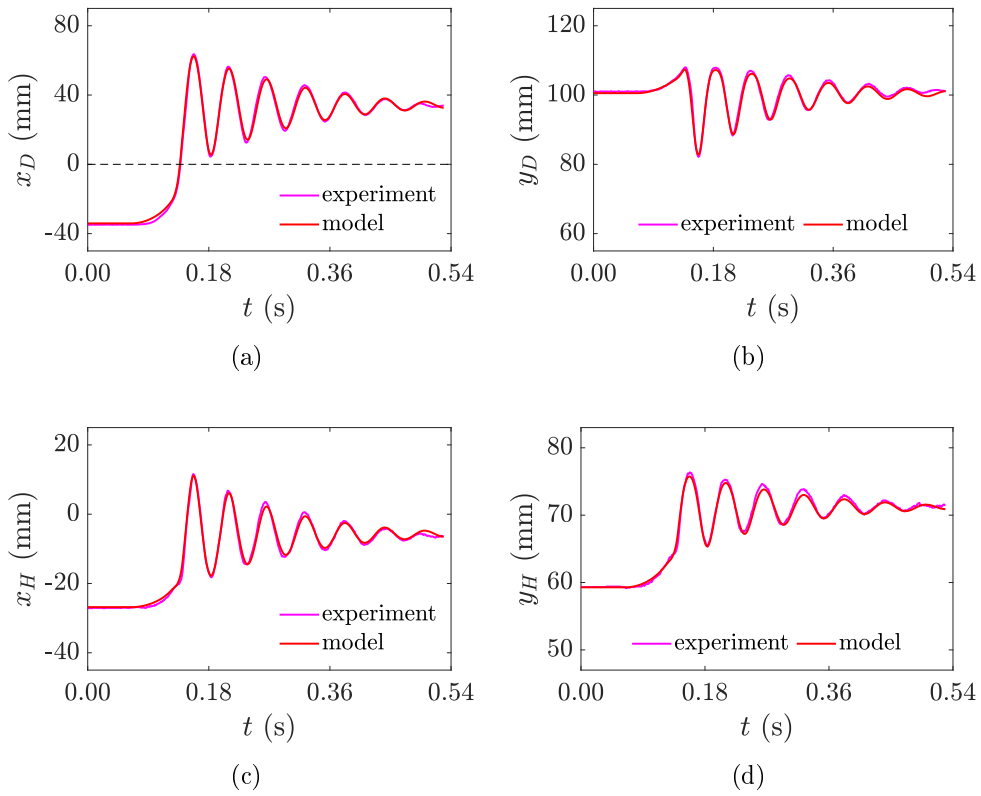

Figure 6.13. Comparison between experimental data and theoretical results for a cantilever with $n = 4$ segments: coordinates (a) $x_D(t)$, (b) $y_D(t)$, (c) $x_H(t)$ and (d) $y_H(t)$, of points C and H indicated in Figure 6.6(b).

be decisive. On the contrary, in long prototypes, inertia, prestress and aeroelastic damping are much higher, so that the friction at the joints becomes less important with respect to damping. In addition, one should mention the physiological tolerances associated with FDM 3D printing: these could certainly provide a further source of uncertainty.

Cantilever with $n = 5$ segments

The situation becomes more complicated for a cantilever made of $n = 5$ segments. Relevant images during the snapping are reported in Figure 6.14(a). The instant at which they have been taken is evidenced in the graph which reports the coordinate $x_E(t)$ of the tip point E with respect to the reference frame represented in Figure 6.6(b). A subtle movement now occurs because in a neighborhood of $t = 0.25\,\mathrm{s}$ the segment $i = 3$ counter-rotates, because this renders minimal the length of the cable

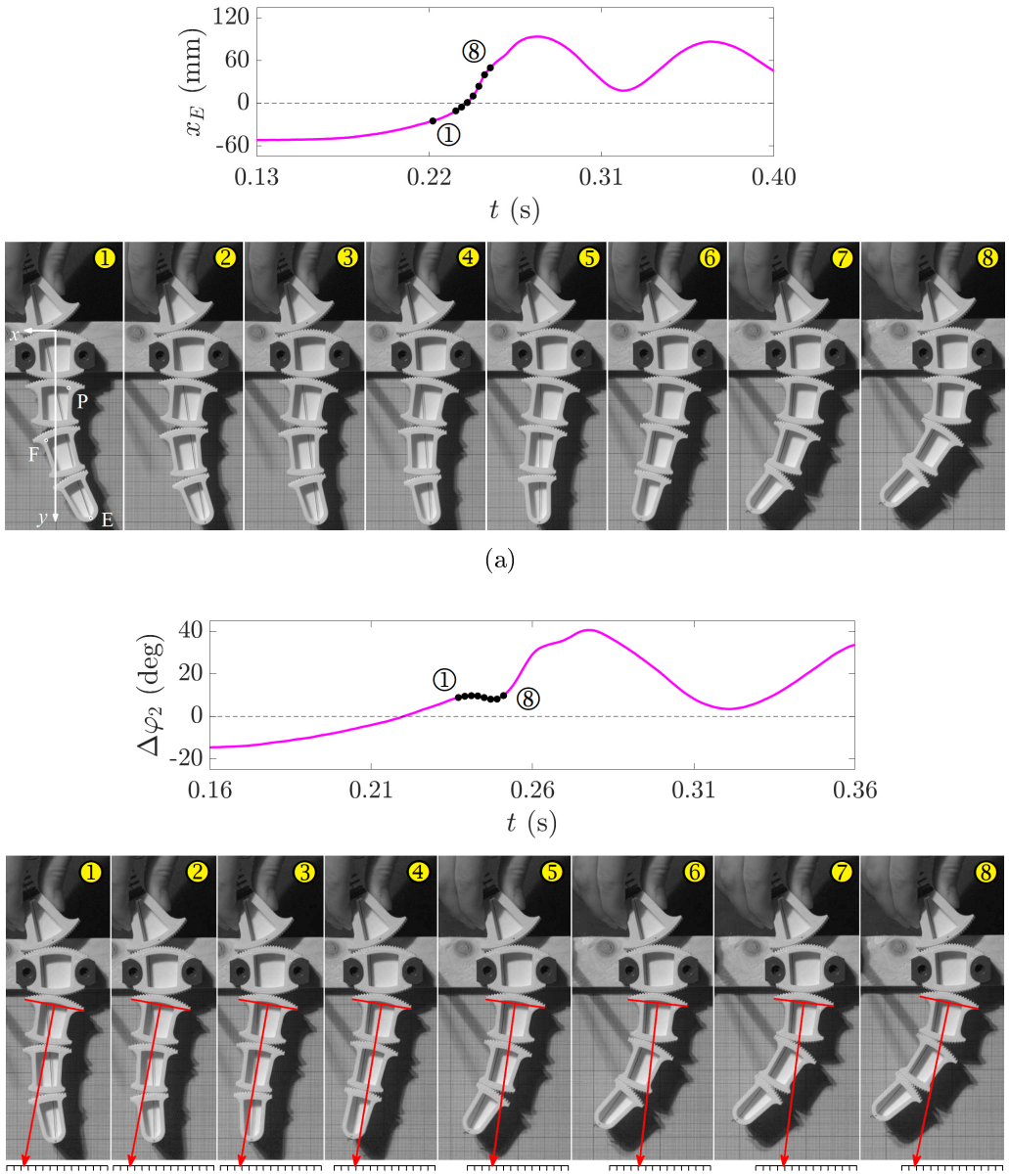

Figure 6.14. Snapping cantilever with $n = 5$ segments. (a) Images from high speed recording (the graph shows, as a function of time, the x-coordinate x_E of the tip point E with respect to the reference frame represented in Figure 6.6(b), with indication of the configurations $1 - 8$ corresponding to the pictures). (b) Detail representation in a restricted time interval when the segment $i = 3$ counter-rotates (the graph indicates the rotation $\Delta\varphi_2(t)$ and the points refers to the images $1 - 8$).

at this stage. This is evidenced in the detail representation of Figure 6.14(b), where the rotation of such segment is emphasized by drawing its axis while indicating its intercept with a horizontal graduated scale. The associated graph reports the trend of $\Delta\varphi_2(t)$, with the dots denoting again the labels of the photographs: the counter-rotation is associated with the descending branch.

Figure 6.15 reports the theoretical findings for a time step $\Delta t = 0.0005\,\mathrm{s}$. Also in this case $\Delta\varphi_1(t)$ has been traced from the high-speed video and used as input. Figure 6.15(a) shows the elastic strain energy contribution ΔU as a function of time t, while Figures 6.15(b) and 6.15(c) show the internal moments $M_i(t)$ and the segmental rotations $\Delta\varphi_i(t)$ for $i = 1 \dots 4$. The comparison between experimental

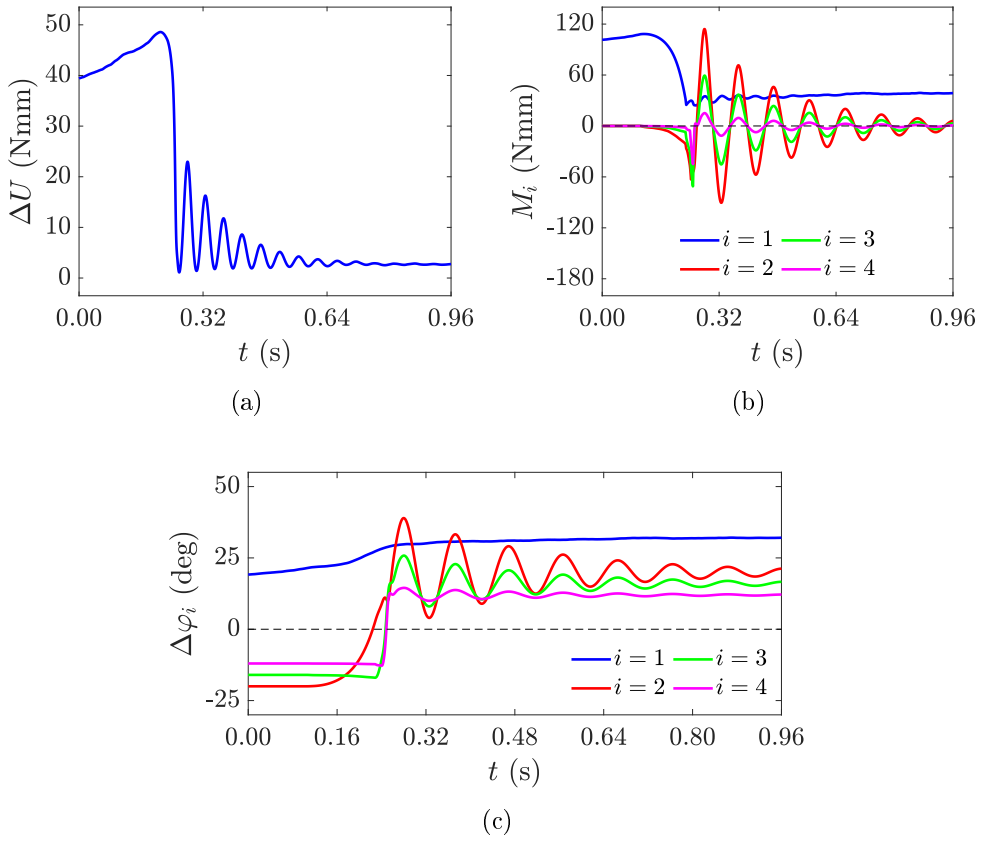

Figure 6.15. Cantilever with $n = 5$ segments subjected to a gradual rotation $\Delta\varphi_1(t)$ of the first segment: (a) variation of elastic strain energy ΔU as a function of time t; (b) internal moments $M_i(t)$ at the contact joints $i = 1 \dots 4$ and corresponding (c) segmental relative rotations $\Delta\varphi_i(t)$.

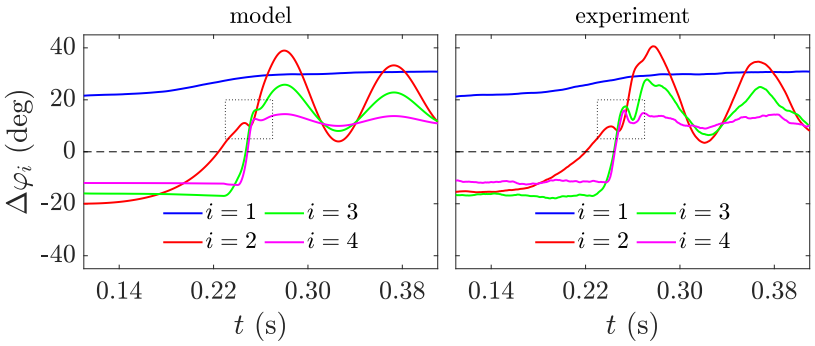

Figure 6.16. Comparison between experimental data (r.h.s. graphs) and theoretical results (l.h.s. graphs) in terms of the rotation $\Delta\varphi_i(t)$, $i = 1 \dots 4$, for the cantilever with $n = 5$ segments subjected to a gradual rotation $\Delta\varphi_1(t)$ of the first segment.

and theoretical rotations $\Delta\varphi_i(t)$, $i = 1 \dots 4$, results from the observation of the graphs of Figure 6.16 in the restricted interval $t \in [0.11, 0.41]$ s. Despite a certain background noise is observed in the experimentally-obtained curves, the trend can be reproduced by the theoretical model. The time at which the segment $i = 3$ counter-rotates, is indicated by the black rectangle reported in the same picture. This phenomenon is precisely caught by the theory.

A more comprehensive comparison between experiments and theory is shown in Figure 6.17. This is done in terms of the coordinates $(x_E(t), y_E(t))$ of the tip point E (Figures 6.17(a) and 6.17(b) respectively), $(x_F(t), y_F(t))$ of the point F on segment $i = 4$ (Figures 6.17(c) and 6.17(d), respectively) and $(x_P(t), y_P(t))$ of the point P on segment $i = 3$ (Figures 6.17(e) and 6.17(f), respectively), where the position of the points on the prototype is shown in Figure 6.6(b). The agreement is again good when the dissipative and friction parameters are $c = 0.55\,\mathrm{Nmm\,s}$, $\bar{M} = 0\,\mathrm{Nmm}$ and $\bar{M}_s = 0\,\mathrm{Nmm}$.

Observe that now the best fit is obtained by considering viscous dissipation only. On the one hand, the dynamic-friction moment may loose importance as the number of segments is increased and the amplitude of oscillations enlarged (see also Section 4.1.3), because of the major role played by the inertial and viscous/drag forces, but this is yet to be verified through more tests and comparisons, in order to obtain statistically reliable data. On the other hand, in this case, we have experimentally observed that there is not a noteworthy delay in the response, of the same type of the one that, in the other cases $n = 3$ or $n = 4$, has suggested to consider the static friction moment $\bar{M}_s$. More in particular, the starting of the experimentally-observed motion is characterized by a single relatively-high jump (Figure 6.17), which however occurs a few time steps before that the theoretically-predicted onset of the snap-through motion, corresponding to $\Delta\varphi_1 \simeq 21.38°$, is reached. This may also be due to 3D printing inaccuracies.

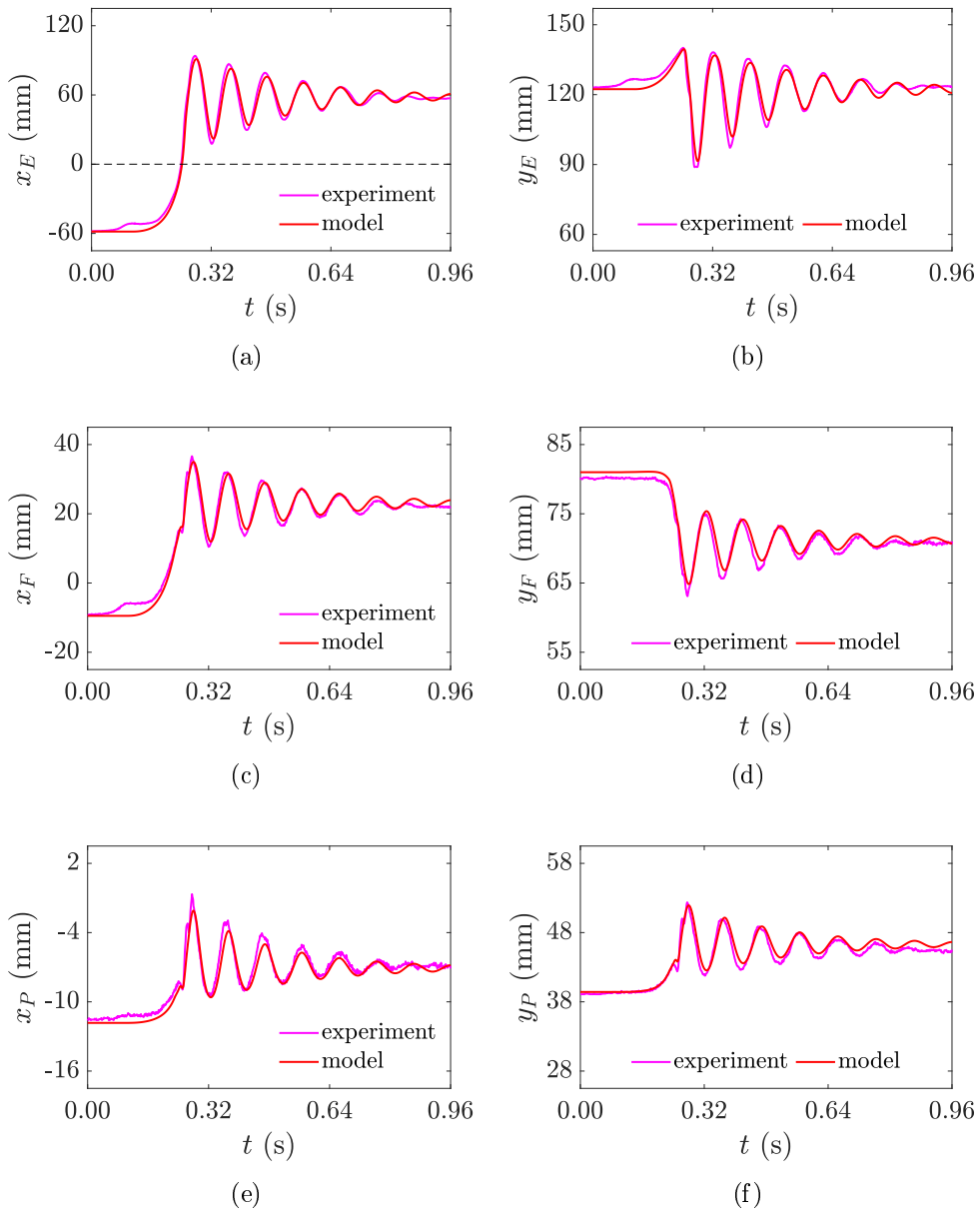

Figure 6.17. Comparison between experimental data and theoretical results for a cantilever with $n = 5$ segments. Coordinates (a) $x_E(t)$, (b) $y_E(t)$, (c) $x_F(t)$, (d) $y_F(t)$, (e) $x_P(t)$ and (f) $y_P(t)$, of points E, F and P represented in Figure 6.6(b), with respect to the indicated reference frame.

Another remark is that the damping coefficient c, calibrated from the experimental results, increases with the number of segments. However, one should com-

pare this value with a quantity somehow related with the critical damping for a vibrating linear system. To do so, although the system is highly nonlinear, one can consider the mean value $\bar{N}$ for the tensile force N in the cable, which varies during the motion, and approximate the effective rotational stiffness of the contact joint, as detailed in Section 3.2.2, as $\tilde{k}_\varphi = R\bar{N}/2$, where R is the radius of pitch lines. Although the pitch lines have the same radius R, the resulting $\tilde{k}_\varphi$ varies from case to case, because oscillations of larger amplitude increase the tension in the cable.

Now, by measuring the frequency ω of oscillations from experimental data, the value of the critical damping can be set equal to $c_{cr} = 2\tilde{k}_\varphi/\omega$. Left aside the case $n = 3$, for which the frictional dissipation is found to be quite high with respect to the viscous contribution (frictional moment about 30% of maximum damping moment), one finds that the ratio c/c_{cr} is almost the same for the cases $n = 4$ and $n = 5$, of the order of 6%. This indicates that the calibrated value of c is somehow related with dynamical properties of the joints, thus confirming the consistency of the theoretical approach.

Remark. The model was developed by neglecting the rotary inertia of the segments and the mass of the cable, as well as the energy dissipation due to the impact of the cable on the internal surfaces of the cavities. These could be considered in an updated version, but even the present model can reproduce fairly well the experimental findings. Indeed, the manufactured segments are short and the cable is a thin lightweight cotton string.

We can verify a posteriori that the rotary inertia of the segments plays a minor role, with specific reference, for example, to the case of the cantilever with $n = 5$ segments. The kinetic energy $T_i(t)$ of the $i-$th segment at time t, reads

$$T_i(t) = T_{i,\mathrm{TR}}(t) + T_{i,\mathrm{ROT}}(t) = \frac{1}{2}\, m_i \left[\dot{x}_{\bar{G}_i}{}^2(t) + \dot{y}_{\bar{G}_i}{}^2(t)\right] + \frac{1}{2}\, I_i\, \dot{\varphi}_i{}^2(t)\,, \qquad (6.2.4)$$

where, we recall, m_i is the mass of the segment and I_i its rotational inertia with respect to the centroid $\bar{G}_i$; $x_{\bar{G}_i}$ and $y_{\bar{G}_i}$ denote the position of the centroid and φ_i is the absolute segmental rotation. Here, $T_{i,\mathrm{TR}}$ and $T_{i,\mathrm{ROT}}$ represent the translational and rotational contributions, respectively. The total kinetic energy is $T(t) = \sum_{i=1}^{n} T_i(t)$, where n is the number of segments, but the kinetic energy of the control segment $i = 1$ is negligible because this is slowly rotated, while the second segment $i = 2$ provides a null contribution since it is clamped.

For the prototype with $n = 5$ segments, Figure 6.18(a) reports the experimentally measured relative segmental rotation $\Delta\varphi_i(t)$, for $i = 1 \dots n-1$ in the restricted interval $t \in (0.2, 0.4)\,\mathrm{s}$, while Figure 6.18(b) displays the corresponding total kinetic energy, sorted out into translational and rotational contributions. The

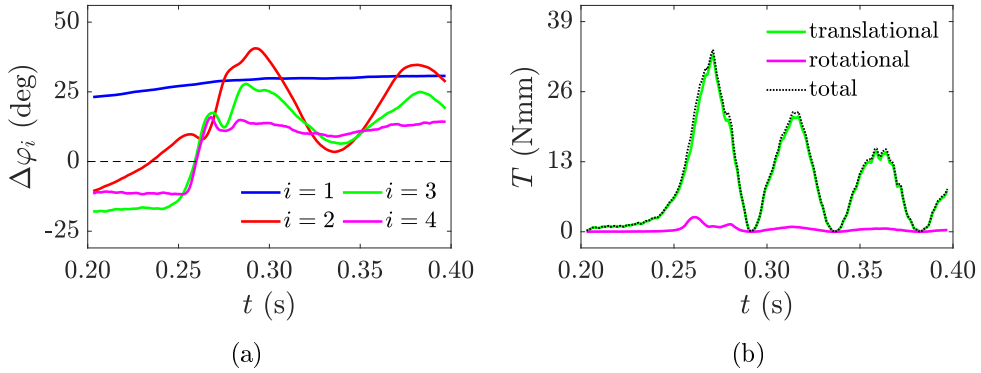

Figure 6.18. Cantilever with $n = 5$ segments subjected to a gradual rotation $\Delta\varphi_1(t)$ of the first segment: (a) experimentally measured relative rotations $\Delta\varphi_i(t)$, $i = 1 \ldots 4$, between the segments and (b) corresponding kinetic energy for the beam, divided into translational and rotational contributions.

rotational contribution is always less than 5%. There is just one exception, when the segment $i = 3$ counter-rotates, as previously discussed in this section: at this instant ($t \simeq 0.26\,\mathrm{s}$), it momentarily reaches a peak of 15%, but this happens in a very limited time interval. Hence, we think that, at least for the considered cases, it is legitimate to overlook the rotational contribution.

Chapter 7

Two- and three-dimensional extensions

Flexural tensegrities have been analyzed, so far, for the one-dimensional case, corresponding to beam-like chains of segments. The concept has been declined in many ways: different shapes for the contact profiles are responsible for diverse constitutive responses, either linear, or sub-linear, or super-linear (Chapter 2), while further improvements for the cable mobility inside the segments, passing from tubular sheaths to a broader cavities, modify the bending energy landscape, including non-convex relationships (Chapter 5), with possibly the activation of sequential snap-through instabilities in response to localized perturbations (Chapter 6); on the other hand, the limit case of the segmental beam, when the number of segments goes to infinity and their length to zero, turned out to be a particular type of Euler's elastica (Chapter 3) with nonlocal bending stiffness.

Here, we focus on flexural-tensegrity two- and three-dimensional assemblies, where the segments are in mutual contact according to spherical pitch surfaces of radius R, whose center is placed at the corners of a square/cube of side equal to $2R$. This configuration immediately recalls a crystalline lattice, which represents a motivation to deepen the study. Indeed, flex-ten 3D assemblies could represent a suitable way to interpret, with a simple physical model, the complex phenomena that occur at the molecular level in solids.

In Section 7.1, the parallelism between 3D flex-tens and crystalline microstructure is highlighted, and, in Section 7.2, the design of the joints for 1D beams is extended to a 3D motion. In Section 7.3, we present manufactured prototypes for flex-ten plates and cubes, analyzed under the hypothesis of either large or small deflections, while possible hints for further research and open problems are finally explored in Section 7.4. The main results here discussed are also collected in [105].

7.1 Motivation from crystalline lattices

Modeling the response of materials is a key point for a correct understanding of the macroscopic behavior of solids and structures. Halfway between the microscopic level of detail, where sub-atomic particles are directly taken into account through quantum physics, and the macroscopic level generally dealing with the classical mechanics of continua, there is the mesoscopic approach [106]. In this case, the material is assumed to be composed of small-sized structural elements, such as masses, springs, or beams (structural approach), to form a microstructure for the medium. The assembly should be such that it degenerates into a continuum mechanics medium when the investigated phenomenon involves larger length scales, and, on the other hand, each constituent should behave in a way that approaches quantum mechanics or classical physics depending on its size.

In the remarkable *Robert Boyle Lecture*, delivered before the Oxford University Junior Scientific Club on May 16th 1893 (reprinted in Appendix H of the Baltimore Lectures [107]), Sir William Thomson, 1st Baron Kelvin, while discussing the "The Molecular Tactics of a Crystal", presents his insightful view of the constitution of matter. Every crystal is a homogenous assemblage of small bodies (molecules), *all equal, similar and in precisely similar attitudes*. Each member of the assemblage may be regarded as a single point but this is a drastic approximation. One should consider that each member is a group of points, or a globe, or a cube, or another geometrical (possibly chiral) figure, in reciprocal contact on a set of points, or lines, or surfaces. The solids may be perfectly smooth and frictionless, or in frictional contact, or connected by forces operating at a distance. The coherent assemblage constitutes a kinematic frame or skeleton for an elastic solid of very peculiar properties: change of shape of the whole can only take place in virtue of rotation of the constituent members, relative to each other. An interesting problem is represented by supposing any mutual forces, such as may be produced by springs, to act between the solid molecules, and investigating configurations of equilibrium on the supposition of frictionless contacts. The solution of it is that the potential energy of the springs must be stationary for equilibrium, and a minimum for stable equilibrium, but the constitutive properties are dictated, besides the nature of intermolecular forces, by pure geometric consideration of kinematic compatibility. This interpretation of the macroscopic properties of a crystal, defined by the geometry of the constituent members, the nature of their contact, and the type of intermolecular forces, is actually within the *mesoscopic* approach [106], being halfway between the microscopic level of detail, where particles are taken into account through the laws of quantum physics, and the macroscopic level of continuum mechanics.

Mesoscopic models are usually discrete lattices of points, where lumped masses

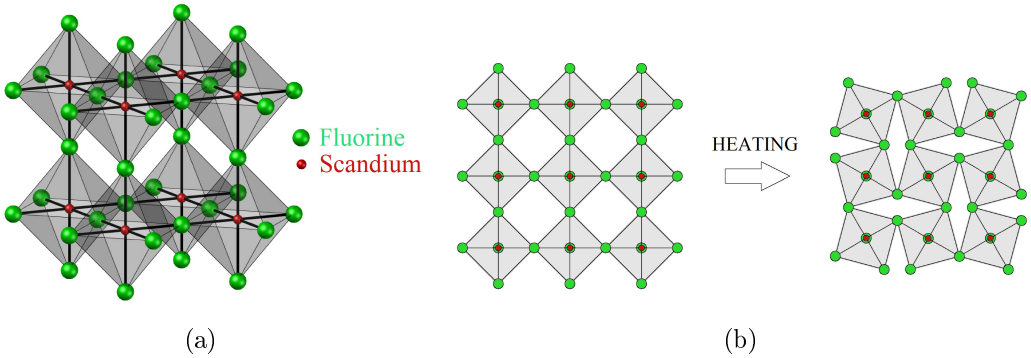

Figure 7.1. Scandium fluoride lattice: (a) schematics of the crystalline lattice with indication of octahedral meso-structures; (b) octahedral rotation at increasing temperature, causing bulk contraction.

interact through elastic forces that depend on mutual distance, schematized as extensional spring linkages [108], possibly amenable of multi-stable equilibrium states [76, 84]. The field of application of such *mass-spring* models is very wide, ranging from the analysis of propagating acoustic waves in elastic media [109] to the modeling of vibrations of tensioned membranes [110], from fluid-structure interaction [111] to the reproduction of facial movements [112]. On the other hand, micropolar bodies can be represented by grid frameworks, where meso-particles are linked by beam-like connectors [113, 114], and the plastic flow in metals can be interpreted via chains of two-bar-linkage elements amenable of snap-through instability [82]. A major limitation in models of this kind is that the points are seen as irrotational entities; instead, there are materials composed by the aggregation of subelements (meso-particles) whose relative rotations cannot be disregarded. An illustrative example is that of scandium fluoride (ScF_3) whose microstructure, shown in Figure 7.1(a), is represented by octahedral-shaped meso-particles. These can relatively rotate when heating is provided [115], causing a reduction of volume according to the mechanism of Figure 7.1(b), responsible of a negative thermal-expansion coefficient at the macroscopic level. For such a material the basic mesoscopic element cannot be point, but a member with geometric shape, whose configuration is defined by its rotation.

In order to account for "rotational" effects and, specifically, torsional vibrations of the lattice members, it is common to conceive mass-spring models where additional eccentric springs connect the body of two adjacent meso-constituents, with anchoring points different from their centroids [106]. This approach is followed for the representation of chiral metamaterials, when the connectors are not symmetrically placed [116, 117]. Another class is represented by lattice solid models [118], consisting of non-pointwise particles linked by bond of various nature. This "dis-

crete element modeling" of matter can interpret macroscopic mechanical properties of structured materials [119].

Here, a new conceptual structure for two- and three-dimensional lattices, with non-chiral structure, is presented. Since these are based on the structural concept of flexural tensegrity and represent its extension to the spatial case, they will be specifically referred to as *flextegrity lattices*. When passing to spatial grid assemblies, the major difficulty certainly consists in the design of the contact joints. Here, the simplest case is analyzed, in which the kinematics of the segments mimics that of balls of radius R in pure rolling contact (no sliding), with their centers at the points of simple cubic lattice of size $2R$. The segments are hold together by straight tendons, following the direction of the primitive vectors of the lattice. The skeletal structure constrains the kinematics; the energy of the system results from the straining of the tendons consequent to the relative rotation of the segments.

Flextegrity lattices can define mesoscopic models for crystals. Remarkable are the similarities with the nanostructure of fullerite, composed of fullerene balls as indicated in Figure 7.2(a). The spherical structure of fullerene, with a diameter of 0.714 nm [106], is shown in Figure 7.2(b) with reference to Buckminsterfullerene C_{60} [120] with 60 carbon atoms. It recalls the same tessellation (hexagons and pentagons) of soccerballs, as well as the geometric structure of the geodesic domes theorized by Buckminster Füller (hence, the name Fullerene). The fullerite crystal at room temperature [121] is a face-centered cubic (FCC) lattice with parameter

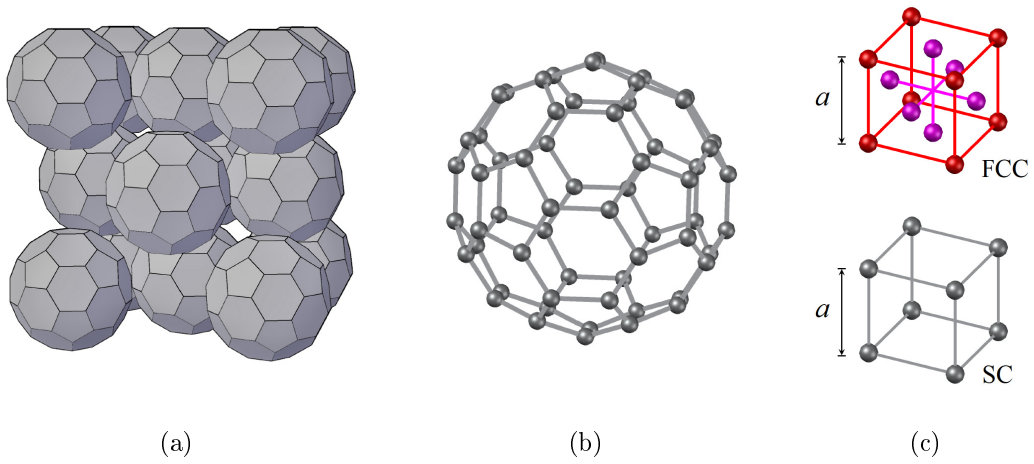

Figure 7.2. Fullerite and fullerene crystalline structure. (a) Basic unit of fullerite lattice at room temperature, composed of members of (b) Buckminsterfullerene (type of fullerene with formula C_{60}). (c) Face-centered cubic (FCC) lattice for fullerite at room temperature, and simple cubic (SC) lattice for fullerite at lower temperature.

$a = 1.417\,\text{nm}$ (Figure 7.2(c)), whose points are the centers of fullerene balls. At 260 K a phase transition begins, in which the mesoscopic arrangement is transformed from FCC to simple cubic (SC) lattice (Figure 7.2(c)). At room temperature fullerenes are free to rotate [121] independently one another at high frequency, but at lower temperature (SC lattice, below 200 K) the mobility is restrained: the orientation of the rotation axis is always the same and the molecules perform torsional vibrations, relatively rotating with jump-like movement [106] only when a certain energy barrier is occasionally overcome.

The analogy with crystalline lattices is kinematical, because flextegrity grid assemblies are characterized by the relative rotation of the segments as main deformation mechanism. Although the model accounts for relative rotations of subconstituents with finite amplitude, not for their spin, it appears suitable for those materials in which torsional vibrations play a major role. The flextegrity lattice can also inspire metamaterial with tailor properties, depending on the shape of the contact surface and the mutual spatial placement of segments. Anyway, this study is a field of research *per se*, as it represents the nontrivial spatial extension of the structural principle introduced in Chapter 2.

7.2 The spatial assembly

Recall the geometry of a flex-ten joint, of the type introduced in Chapter 2. Such a joint is schematically redrawn in Figure 7.3(a), where the contact surfaces between any two consecutive segments are shaped according to toothed profiles, as in gears, to prevent sliding. The corresponding pitch lines are arcs of circle, which are drawn in red, while the passing-through tendon is represented by the green line. Consider a deformation scenario as general as possible. Under tensile forces, when the prestress induced by the tendon is overcome, the segments detach as indicated in Figure 7.3(b), so that the axial stiffness is due to the elasticity of the tendon. When subjected to shear loading, as in Figure 7.3(c), the deformation depends on the elastic compliance of the teeth. Under compression, the contact surfaces flatten due to Hertzian contact, as per Figure 7.3(d). The response to pure bending is led by the relative rotation of the segments along the design pitch lines, as shown in Figure 7.3(e): the tendon is strained due to the opening of the joint, while the segments are subjected to localized compression at the contact point.

If the tendon is compliant, as in most practical applications and as usually supposed in the previous chapters, the bulk deformation of the segments can be neglected. In this case, the joint is almost rigid under shear and compression (Figures 7.3(c) and 7.3(d)). The deformation due to tensile actions (Figure 7.3(b)) depends on the cable prestress and its axial stiffness: in the following we will as-

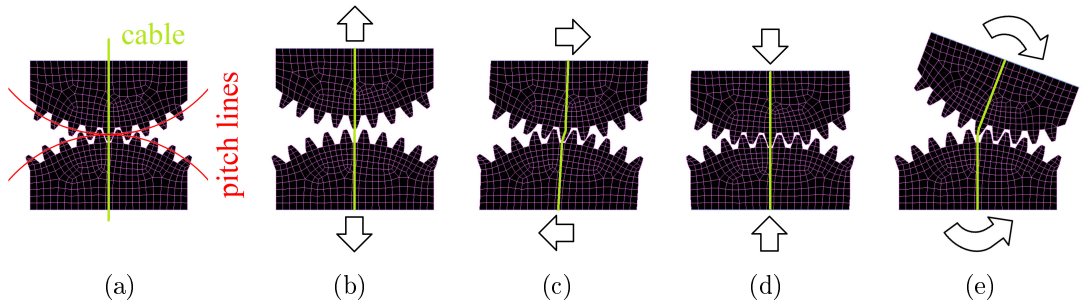

Figure 7.3. Schematics of a flex-ten joint for beam-like structures, with toothed contact profiles corresponding to circular pitch lines. (a) Reference state, with indication of the cable (green line) and the pitch lines (in red); (b) detachment of segments under tensile forces; (c) deformation of teeth and segments under shear forces; (d) deformation of segments under compression loading; (e) relative rotation of segments under bending.

sume that the prestress induced by the tendon is never exceeded by tensile loads. Under bending (Figure 7.3(e)), the response is governed by the straining of the cable, which is forced to elongate by the relative rotation of the segments, while the segments remain practically undeformed.

Focus od the response under bending, and consider the schematic of Figure 7.4(a), which illustrates the paradigmatic case of circular pitch lines of radius R. Let N_0 denote the initial prestress of the cable, as usual, and K its effective axial stiffness. When the consecutive segments i and $i+1$ are relatively rotated by the quantity $\Delta\varphi_i$, the segments follow pure rolling along the pitch lines. The pitch point moves from the cable exit point to the position P_i, while the cable elongates of the quantity Λ_i. The distance between the portion of the cable that becomes exposed (of length Λ_i, between the two exit points from the segments) and the pitch point P_i, indicated as a_i in Figure 7.4(a), is the internal lever arm. Hence, the internal bending moment M_i at the joint, computed with respect to the pitch point, can be written as $M_i = N\,a_i$, where N is the tension force in the cable. If the cable can frictionless slide inside the holes and it is anchored at the end-segments only, its elongation is the sum of all the joint elongations Λ_i. For a segmental beam composed of n segments and $n-1$ contact joints, the total elongation of the cable is $\Lambda = \sum_{i=1}^{n-1} \Lambda_i$, while the axial force in the cable passes from the initial pre-tension N_0 at rest, to the value $N = N_0 + K\,\Lambda$ after bending.

For the case of circular pitch lines of Figure 7.4(a), Λ_i and a_i are given by (2.1.1) and (2.1.6); these equations are here retyped for clarity and read

$$\Lambda_i = 2R\Big(1 - \cos\frac{\Delta\varphi_i}{2}\Big)\,, \quad \text{and} \quad a_i = \frac{\mathrm{d}\Lambda_i}{\mathrm{d}\Delta\varphi_i} = R\sin\frac{\Delta\varphi_i}{2}\,. \tag{7.2.1}$$

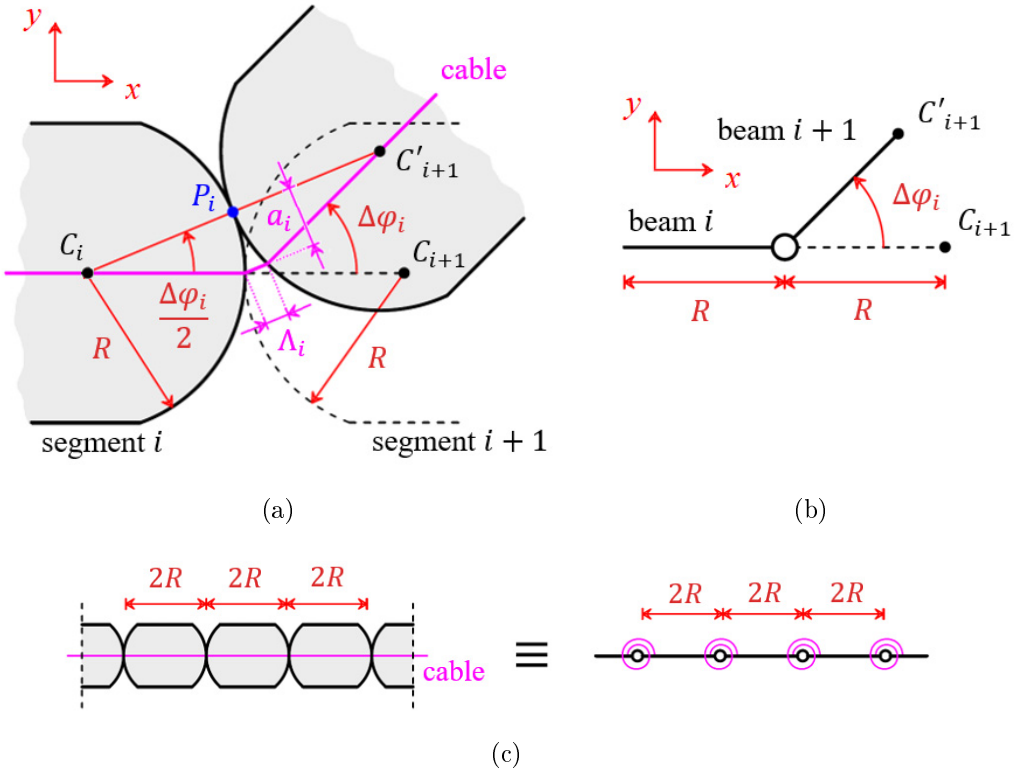

Figure 7.4. Schematics of a flex-ten joint and comparison with a pin joint. (a) Flex-ten joint between segments i and $i+1$, with indication of the cable elongation Λ_i and the lever arm a_i : the reference point C_{i+1} moves to C'_{i+1} after a relative rotation of $\Delta\varphi_i$. (b) Pin joint, connecting beam segments i and $i+1$. (c) Equivalence between the flexural-tensegrity and the spring-hinged joint under the hypothesis of small deflections.

In order to analyze the mobility of the joint under bending, assume, for simplicity, that $2R$ is the segmental length along the longitudinal centroidal axis, so that the reference point C_{i+1} corresponds to the segment centroid. If the segments i and $i+1$ relatively rotate of $\Delta\varphi_i$, C_{i+1} moves to the new position C'_{i+1} . With respect to the reference frame shown in Figure 7.4(a), define the displacements

$$\Delta x_i = -2R\Big(1-\cos\frac{\Delta\varphi_i}{2}\Big)\,, \quad \text{and} \quad \Delta y_i = 2R\sin\frac{\Delta\varphi_i}{2}\,, \tag{7.2.2}$$

while the lever arm and the cable elongation are defined by (7.2.1). If $\Delta\varphi_i$ is an infinitesimal quantity (small deflections and rotations), one can write

$$\Delta x_i \simeq 0\,, \quad \Delta y_i \simeq R\,\Delta\varphi_i\,, \quad \Lambda_i \simeq 0\,, \quad \text{and} \quad a_i \simeq R\,\Delta\varphi_i/2\,, \tag{7.2.3}$$

while the internal bending moment reads $M_i = N\,a_i \simeq N_0 R\,\Delta\varphi_i/2$.

It should be observed that the kinematics is equivalent to that of a pin hinge, indicated in Figure 7.4(b), only in the case of infinitesimal rotations. In fact, for finite deformations, one would find $\Delta x_i = -R(1-\cos\Delta\varphi_i)$ and $\Delta y_i = R\sin\Delta\varphi_i$. There is therefore a substantial difference, associated with rolling motion of the segments along the pitch profiles. Anyway, such a difference is negligible for many practical applications, where the rotations are small enough to approximate the sine and cosine functions with a Taylor's series truncated at the first or second order (see also Section 2.2.4). Under the hypothesis of small rotations, the flexural-tensegrity joint is equivalent to a spring hinge with constant $k_\varphi = N_0\,R/2$. In this case, the flexural-tensegrity assembly can be modeled as a chain of segments connected by 3D spring hinges, representing the spatial extension of the 2D case of Figure 7.4(c). In the limit in which the prestressing force in the cable vanishes ($N_0 \to 0^+$), the flexural-tensegrity joint is equivalent to a spherical hinge. However, in this condition, the detachment of the segments under tensile forces (Figure 7.3(b)), is not prevented, unless $K \to \infty$.

Consider now the kinematic skeleton of spheres of radius R in pure rolling contact (no sliding) along their surfaces. This represents a possible extension to spatial assemblies of the flexural-tensegrity kinematics, thus defining the concept of flextegrity lattices. Figure 7.5(a) refers to a SC lattice, where the sphere centers are placed at the vertices of the cubic unit cell of size $2R$. The spheres are kept in contact by three orthogonal families of straight prestressing cables (tendons) passing through holes drilled in them, as indicated in Figure 7.5(b). If the cables are compliant, one can neglect the deformation of the spheres and regard them as rigid bodies. Clearly, the resulting assembly is incompressible under uniformly distributed positive (inwards) pressures applied to the boundary; under negative (outward) pressures, it will not be deformed as long as the prestress from the tendons is not exceeded.

The spheres are supposed to be in pure rolling contact: this is a strong kinematic constraint that limits their mobility. Consider, for example, one layer of the assembly, indicated in Figure 7.5(c). If one sphere rotates in the clockwise direction, the condition of no-sliding requires that the neighboring ones rotate counter-clockwise. Remarkably, the rotation of one sphere affects the rotations of *all* the other spheres of the layer, which are forced to rotate of the same angle (in absolute value), alternatively clockwise or counter-clockwise. This is a *nonlocal* interaction that affects instantaneously the whole layer where the sphere, which is first rotated, is placed. Another noteworthy property is that shear-like distortion of the lattice, of the type represented in Figure 7.5(d), is not allowed, because this would involve the reciprocal slipping of some of the surfaces in contact. Moderate shear distortion would be permitted only by the deformation of the material of which the spheres are made.

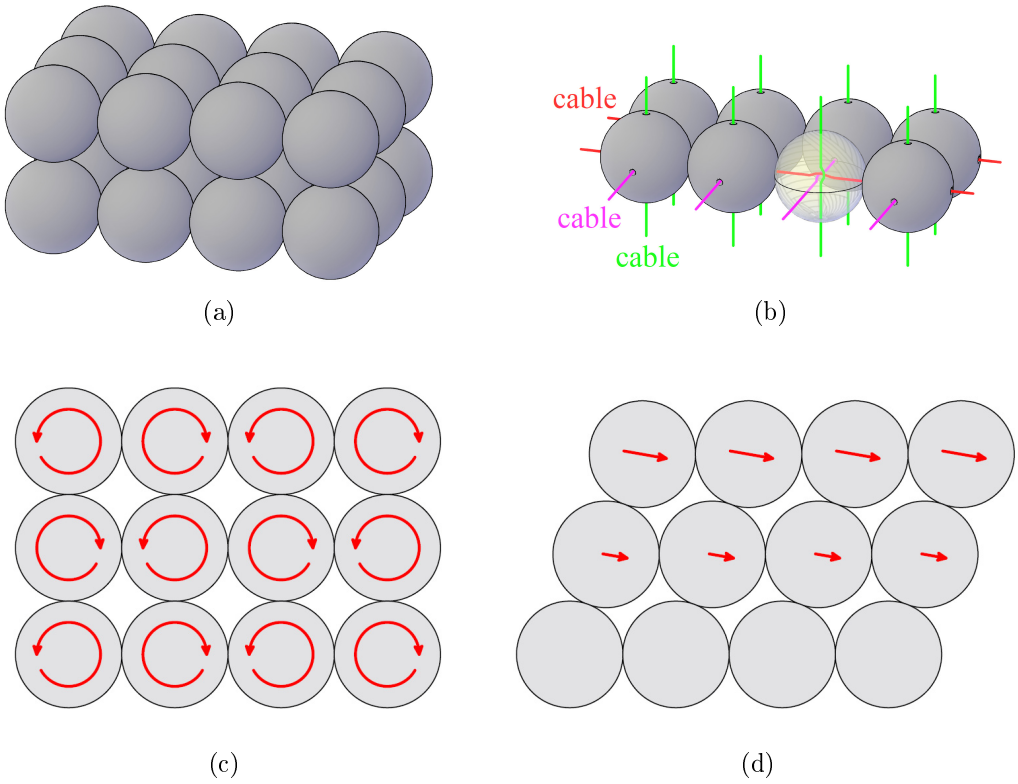

Figure 7.5. Spheres in contact: (a) assembly of spheres in the SC lattice and (b) detail of one layer with indication of the three family of prestressing tendons. The spheres are in pure rolling contact: (c) allowed relative rotation, and (d) forbidden shear-like deformation.

Here, we consider a particular kinematic constraint, represented in Figure 7.6(a), where the relative motion between any two "rigid" spheres i and j is fully described by the torsion angle $\Delta\psi_{ij}$, the longitude angle $\Delta\vartheta_{ij}$, and the angle $\Delta\varphi_{ij}$ corresponding to pure rolling along the meridian. In the reference (undistorted) state, in which the tendons are straight, the center of the spheres, C_i and C_j, and the cable exit points, E'_{ij} and E''_{ij}, which coincides in the same point E_{ij}, are aligned on a straight line. Starting from this configuration, the sphere j can *freely* rotate (without straining the tendon) with respect to the adjacent sphere i of the angle $\Delta\psi_{ij}$ around the axis passing through C_i, C_j and E_{ij} (the cable cannot provide any stiffness against twist). Then, the spheres can pure roll one another along that meridian (with the "North" pole in E_{ij}) identified by the longitude angle $\Delta\vartheta_{ij}$. The motion takes place for an arc length equal to $R\,\Delta\varphi_{ij}\,/\,2$, so that points P'_{ij} and P''_{ij} are going to coincide in P_{ij}. This path is represented by the arcs drawn in red and distinguished by solid dots in Figure 7.6(a).

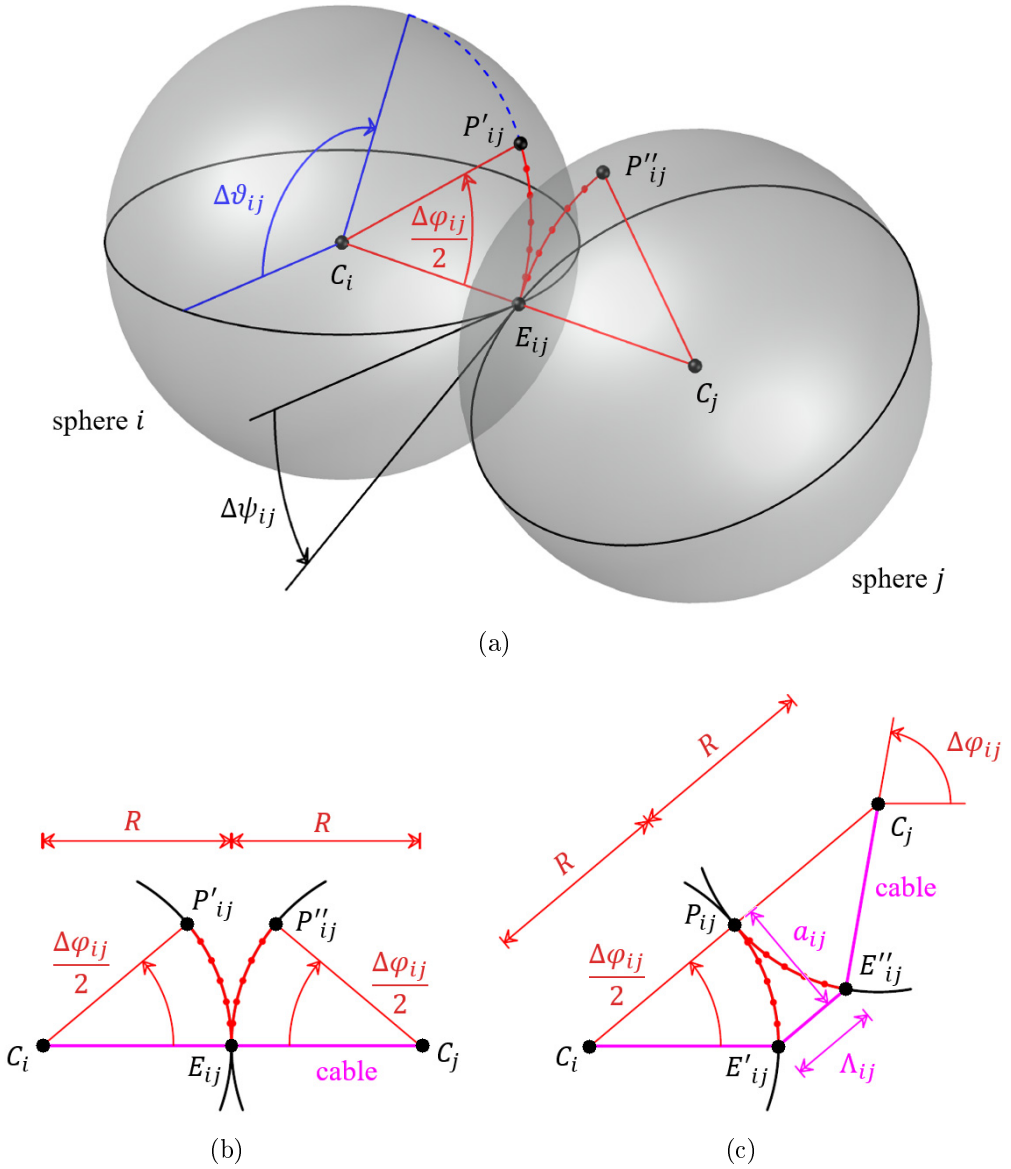

Figure 7.6. Kinematics of the 3D joint. (a) Degrees of freedom of the spherical contact surfaces: torsion $\Delta\psi_{ij}$, longitude $\Delta\vartheta_{ij}$, and pure rolling along the meridian achieving the relative rotation $\Delta\varphi_{ij}$. (b) Reference (undistorted) state on the slicing plane passing through points C_i, C_j, P'_{ij} and P''_{ij}, and (c) rotated (distorted) state on the same plane, with indication of the cable elongation Λ_{ij} and lever arm a_{ij}.

Figures 7.6(b) and 7.6(c) respectively report a section of the reference undistorted state and the distorted state, obtained with a slicing plane passing through points C_i , C_j , P'_{ij} and P''_{ij} . The motion on this plane is analogous to that of a one-dimensional joint, discussed in Figure 7.4(a). In particular, the cable elongates of the quantity Λ_{ij} between the spheres i and j, while the distance a_{ij} corresponds to the lever arm of the cable axial force with respect to the pitch point P_{ij} . If R is the radius of the spheres, the expressions for Λ_{ij} and a_{ij} are again defined by equations (7.2.1).

Observe that the assumed kinematics does not cover all possible configurations of two spheres in pure rolling contact. This is in general a strong non-holonomic

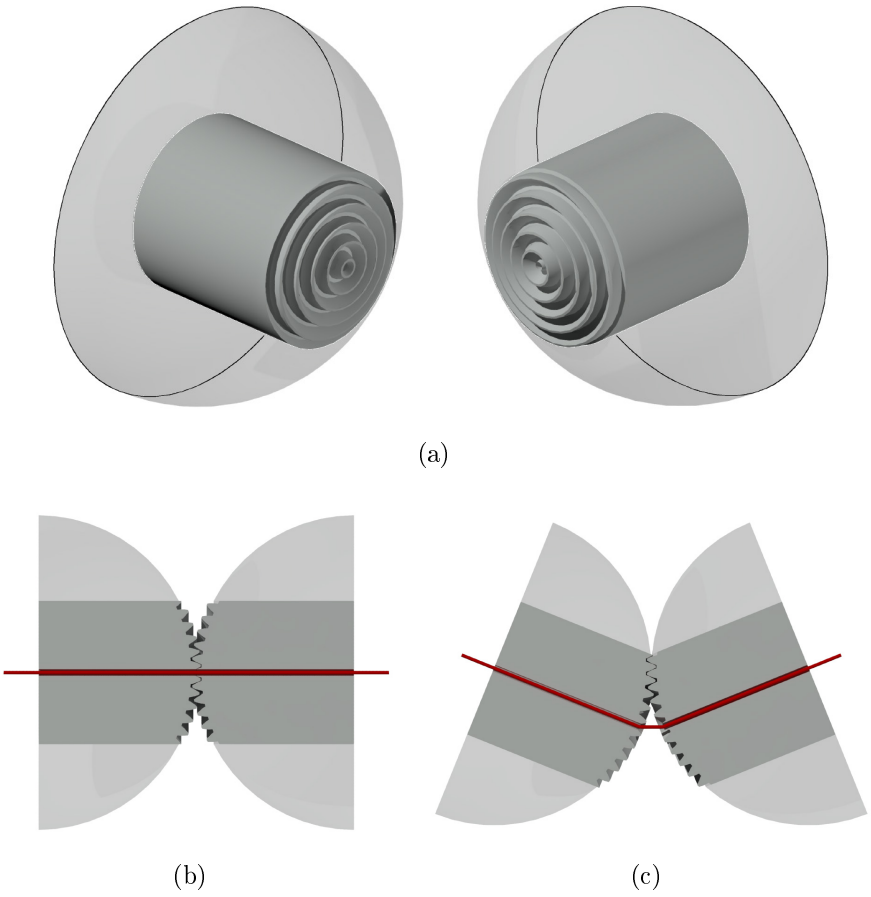

Figure 7.7. Physical model of the contact joint, with axial-symmetric toothed contact profiles, achieving the kinematic constraint schematized in Figure 7.6. (a) View of the disassembled joint with the axial-symmetric toothed contact surfaces; longitudinal section of the joint (cable represented by the red solid line) in (b) the reference state and (c) the rotated configuration.

constraint: in principle, any two arbitrary points laying on the two spherical surfaces can be brought into contact by following a proper contact path. On the contrary, the motion indicated in Figure 7.6(a) requires that the arcs of circle $\widehat{E_{ij}P'_{ij}}$ and $\widehat{E_{ij}P''_{ij}}$ have the same length, a property that is not satisfied by all rolling motions. This simplification is such that the relative position of the spheres is completely determined by the angles $\Delta\psi_{ij}$, $\Delta\vartheta_{ij}$ and $\Delta\varphi_{ij}$, which can thus be considered as generalized coordinates to describe the configuration of system.

The constraint just described can be directly achieved within the category of flexural-tensegrity structures, since it represent the natural three-dimensional extension of the toothed beam joint represented in Figure 7.3. The concept is illustrated in Figure 7.7. An exploded view of the disassembled joint is shown in Figure 7.7(a): the portions of the spheres that remain in contact during movements associated with a limit admissible value for the angle $\Delta\varphi_{ij}$, are grooved according to toothed contact profiles, axially symmetrical with respect to the axis of the prestressing tendon. The conjugate profiles are shaped in such a way that relative rotation between the bodies achieves a pure rolling motion along two meridians. A side view of the sections of the two bodies, obtaining by cutting them with a plane passing through the contact meridians, is represented in Figures 7.7(b) and 7.7(c) for the undistorted reference state and the rotated state, respectively.

This joint corresponds to a pin coupling for the spinning around cable axis (rotation $\Delta\psi_{ij}$ is unconstrained). The contact meridians are defined by the angle $\Delta\vartheta_{ij}$. The elasticity of the cable and its pre-stress define the stiffness of the joint against the relative rotation $\Delta\varphi_{ij}$.

7.3 Physical models

Flextegrity grids forming two-dimensional plates and three-dimensional cubes are now analyzed. Physical prototypes are manufactured via 3D printing to demonstrate how the assembly works and deforms under loading.

7.3.1 Kinematic analysis of flextegrity plates

Figure 7.8 shows two physical models of segmental plates, representative of two-dimensional flextegrity lattices. The assembled basic unit, composed of 4 segments manufactured via 3D printing, is indicated in Figure 7.8(a), whereas Figure 7.8(b) shows the corresponding exploded view. The contact surfaces, which correspond to spherical pitch surfaces of radius $R = 30\,\text{mm}$, are shaped according to toothed gears, axial symmetric with respect to axis of the tendons, made with two couples of black-colored parallel elastic rods visible in Figure 7.8(a). The size of the segments

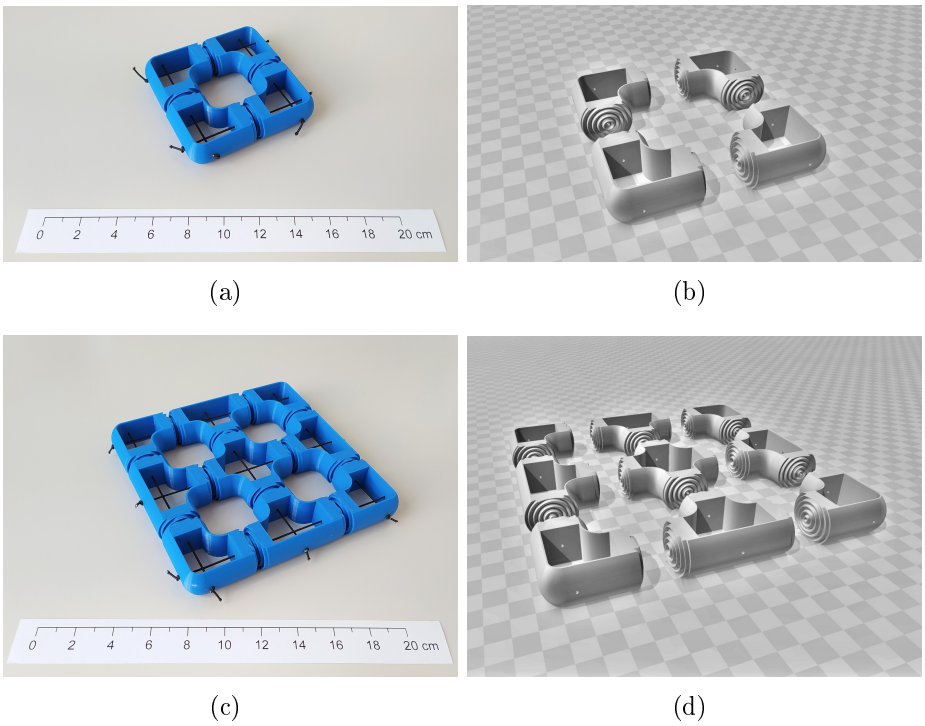

(a) (b)

(c) (d)

Figure 7.8. Segmental plates with flexural-tensegrity skeleton. (a) Photograph of the manufactured basic unit composed of 4 segments, and (b) corresponding exploded view. (c) Photograph of a larger plate with 9 segments (4 basic units) and (d) corresponding exploded view. Tendons are black-colored elastic strings.

is such that the distance between the pitch surfaces and the center of the segments, defined as the point of intersection of two orthogonal tendons passing through them, is equal to R, so that the system reproduces the assembly of a plane of spheres in contact. Figures 7.8(c) and 7.8(d) are the counterpart of the previous ones for a larger assembly, made of 4 basic units coupled together, with 9 segments in total. The tendons are elastic strings of diameter 1.2 mm, with axial stiffness equal to $K = 0.058\,\mathrm{N/mm}$ for the prototype of Figure 7.8(a) and $K = 0.029\,\mathrm{N/mm}$ for the case of Figure 7.8(c). The difference is due to the fact that the length of the cables of the first prototype is one-half of the second one. The cables are equally prestressed (modulo tolerances) by $N_0 \simeq 1.2\,\mathrm{N}$.

Supposing that the angles of rotation are infinitesimal of the first order (linearized kinematics), the contact joints can be approximated by spherical (spring) hinges, as discussed in Section 7.2. The physical model of Figure 7.8(a) is thus schematized as in Figure 7.9(a), which represents the assembly of 4 L-shaped bars connected by hinges, numbered counterclockwise. One can assume, as degrees of

freedom, the absolute rotations of each segment α_h, β_h and γ_h, for $h = 1 \dots 4$, defined by the triad of Figure 7.9(a). The corner of element 4 is clamped to rule out rigid-body displacements.

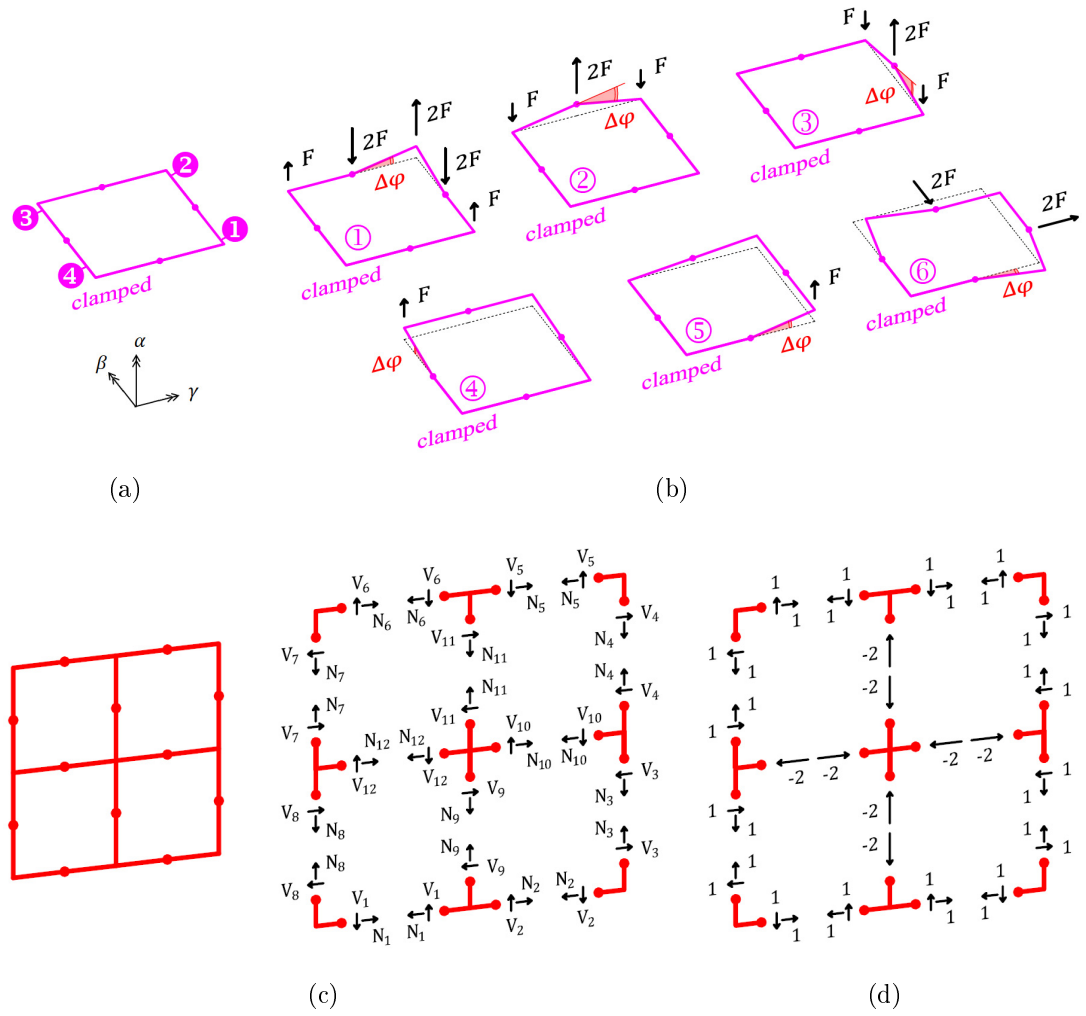

Figure 7.9. Infinitesimal mobility of the plate and states of self-stress. (a) Equivalent chain of pinned L-shaped bars (element 4 is clamped), representative of the basic unit of Figure 7.8(a), and (b) corresponding six independent mechanisms, with indication of possible systems of external loads to achieve them. (c) Equivalent scheme with pin joints for the larger structure of Figure 7.8(c), with indication of in-plane internal actions at joints and (d) corresponding state of self-stress.

The kinematic matrix $\boldsymbol{C}$ for such a structural system can be written as

$$\boldsymbol{C} = \begin{bmatrix} -1 & 0 & 0 & -1 & 0 & 0 & 1 & 0 & 0 & 0 & 0 & 0 \\ 1 & 0 & 0 & -1 & 0 & 0 & -1 & 0 & 0 & 0 & 0 & 0 \\ 0 & -1 & 1 & 0 & 1 & 1 & 0 & 1 & -1 & 0 & 0 & 0 \\ 0 & 0 & 0 & 0 & 0 & 0 & 0 & 0 & 0 & 1 & 0 & 0 \\ 0 & 0 & 0 & 0 & 0 & 0 & 0 & 0 & 0 & 0 & 1 & 0 \\ 0 & 0 & 0 & 0 & 0 & 0 & 0 & 0 & 0 & 0 & 0 & 1 \end{bmatrix}, \tag{7.3.4}$$

being the degrees of freedom ordered in the array $\mathbf{d}$ defined as

$$\mathbf{d} = \begin{Bmatrix} \alpha_1 & \beta_1 & \gamma_1 & \alpha_2 & \beta_2 & \gamma_2 & \alpha_3 & \beta_3 & \gamma_3 & \alpha_4 & \beta_4 & \gamma_4 \end{Bmatrix}^T . \tag{7.3.5}$$

The kinematic matrix (7.3.4) is rank deficient with respect to the number of degrees of freedom. There are 6 independent mechanisms, associated with the non-trivial solutions of $\boldsymbol{C}\,\mathbf{d} = \mathbf{0}$, which are shown in Figure 7.9(b). Since the pre-tension of the cable renders the contact joints equivalent to spring hinges, the aforementioned mechanisms can be obtained with the external loads, reported in the same figure. Here, $F = k_\varphi \, \Delta\varphi \, / \, R$, where the angle $\Delta\varphi$ defines the deformation. Observe that the mechanisms of Figure 7.9(b) corresponds to infinitesimal mobility, but they can be achieved also with finite rotations, with the only exception of mechanism (1). This is not allowed by the actual geometry of the joint, as it is incompatible with the rolling motion of the contact surfaces along meridians, as detailed in Section 7.2.

The plate of Figure 7.8(a) cannot accommodate any other state of self-stress but the pre-compression introduced by the cables. This is not the case of the larger structure of Figure 7.8(c). Consider the corresponding pinned-joint assembly, composed of 4 L-shaped, 4 T-shaped and 1 X-shaped bars connected by hinges. This is shown in Figure 7.9(c) together with the relevant in-plane internal actions. The static unknowns are 36, while the rank of the static matrix $\boldsymbol{S}$, collecting the static equilibrium equations, is equal to 35. This means that it is possible one state of self-stress, schematically shown in Figure 7.8(d). This could be obtained, e.g., by providing to the central X-shaped segment a positive thermal variation, causing its expansion.

In practical terms, this state of self-stress could be used to reduce the number of prestressing cables, as the two tendons passing through the inner segment are no longer needed to keep the segments in contact. On the other hand, the state of self-stress is not stable, and it can be lost by means of out-of-plane deflections of the plate.

7.3.2 Kinematic analysis of flextegrity cubes

Figure 7.10 shows two 3D-printed prototypes of flextegrity cubes. The basic unit, now composed of 8 segments, is displayed in Figure 7.10(a) and is kept together by 12 tendons. The exploded view is shown in Figure 7.10(b). Figures 7.10(c) and 7.10(d) refer to a larger system of 27 segments, formed by the assembly of 8 basic units, coupled by 27 tendons. The contact conjugate profiles are shaped similarly to the two-dimensional case of Section 7.3.1, forming spherical pitch surfaces of radius $R = 30\,\text{mm}$. In this way, one aims at reproducing a set of spheres in pure rolling contact whose centers follow a SC lattice. Each tendon is again an elastic

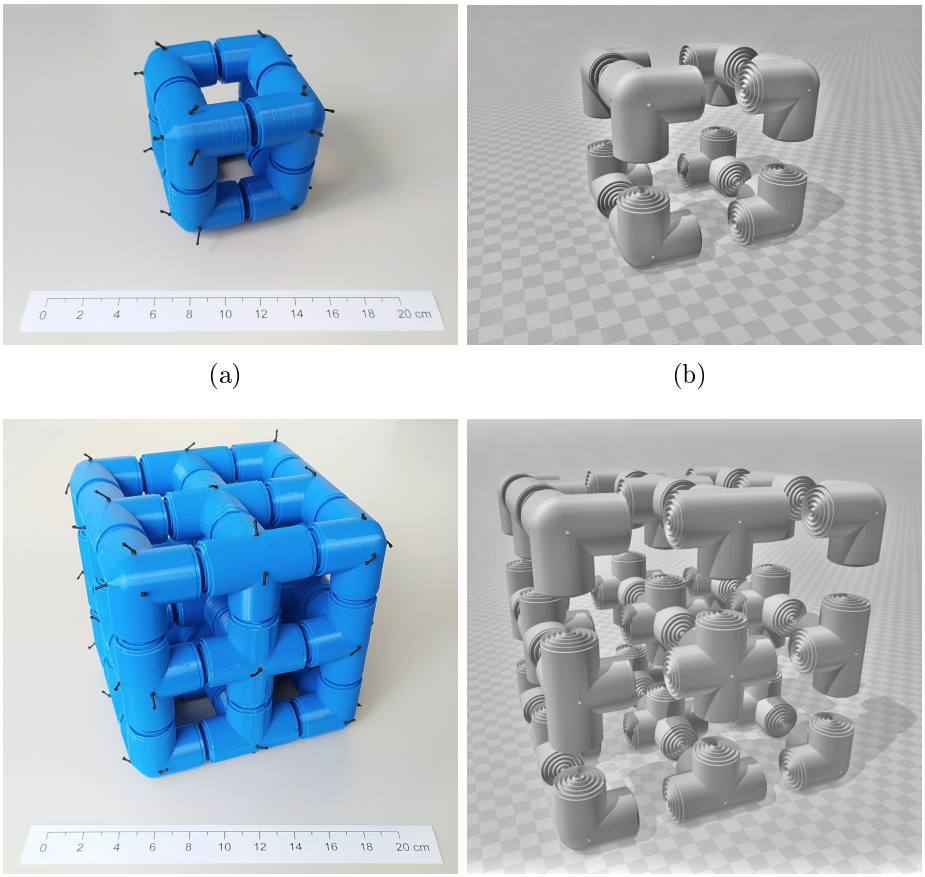

(a) (b)

(c) (d)

Figure 7.10. Flextegrity cubes. (a) Photograph of the manufactured basic unit composed of 8 segments and 12 tendons (black-colored elastic strings); (b) corresponding exploded view. (c) Photograph of a larger cube with 27 segments (8 basic units) and 27 tendons; (d) corresponding exploded view.

thread of diameter 1.2 mm, with axial stiffness equal to $K = 0.058\,\mathrm{N/mm}$ for the prototype of Figure 7.10(a) and $K = 0.029\,\mathrm{N/mm}$ for the prototype of Figure 7.10(c), due to the different cable lengths. Again, the cables are equally prestressed at $N_0 \simeq 1.2\,\mathrm{N}$.

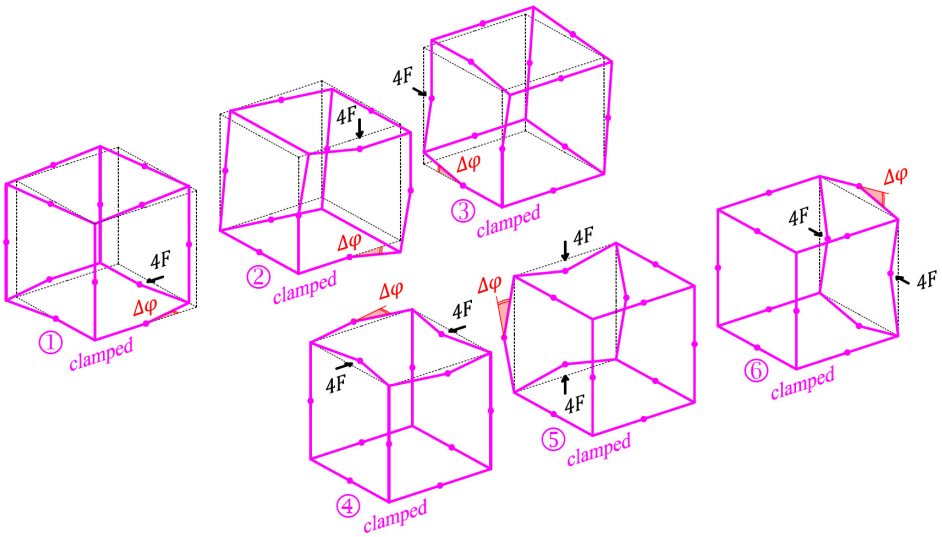

(a)

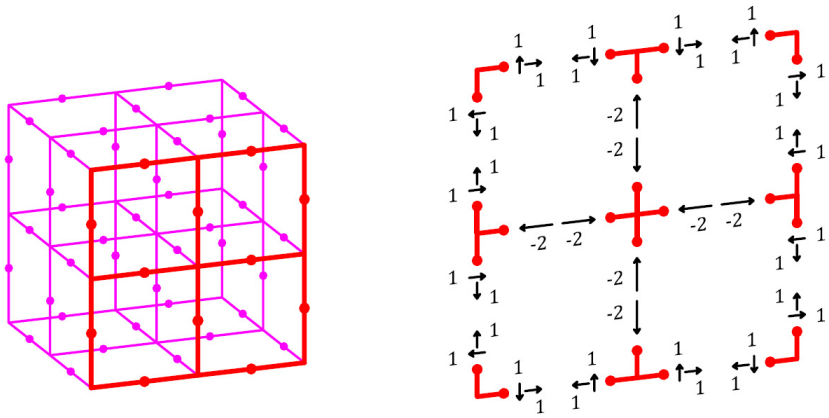

(b)

Figure 7.11. Infinitesimal mobility of the segmental cube and states of self-stress. (a) The six independent mechanisms for the cubic basic unit of Figure 7.10(a), with indication of possible systems of external loads to achieve the mechanisms. (b) Equivalent scheme with pin joints for the larger cube of Figure 7.10(c), with indication of one of the 9 possible states of self-stress.

As done in the previous Section 7.3.1, independent mechanisms can be caught from the equivalence between the flexural-tensegrity assembly and an assembly of hinged beams under the hypothesis of infinitesimal mobility. Figure 7.11(a) collects the six independent mechanisms, obtained for the basic cubic unit of Figure 7.10(a). For each mechanism, a possible set of external loads is also indicated, with $F = k_\varphi \, \Delta\varphi \, / \, R$, where k_φ is the stiffness of the spring hinges, defined in Section 7.2. All these mechanisms are also allowed in large deflections for the geometry at hand, corresponding to spherical contacts.

For the larger cube of Figure 7.10(c), nine states of self-stress are possible. These correspond to the state of self-stress already found for the two-dimensional case of Figure 7.8(c), which can be now achieved in each planar face and intermediate symmetry plane of the cubic assembly, as shown in Figure 7.11(b). The major difference, with respect to the case of plates, is that now each state of self-stress is stable, thanks to the confinement of the cubic lattice, which avoid out-of-plane deformations.

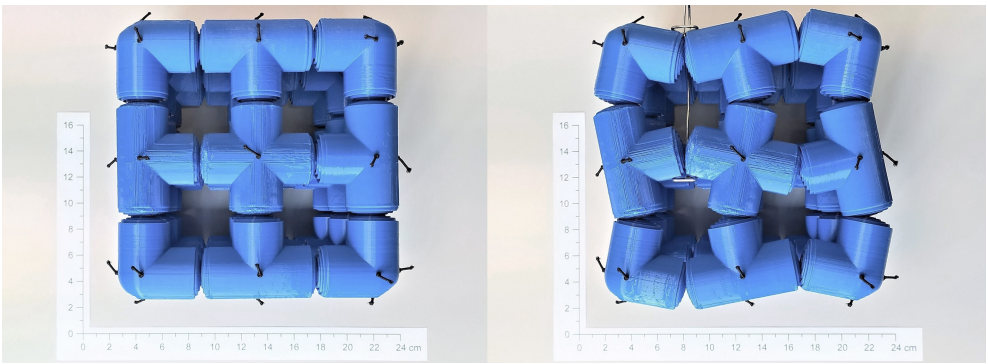

Figure 7.12. Mobility of each face of the larger cube with 27 segments.

The structure of Figure 7.10(c) may represent a mesoscopic model for a crystalline lattice with strong asymmetry between the responses under tension and compression. Remarkably, the particular form of the eigenstress states could provide an insight about the strategy of crystalline growth in thin films, or the way through which the molecular skeleton could be strengthened via thermal processes or oversized solutes. A certain freedom is maintained for the rotations of subelements, which is a peculiar property of flextegrity lattices. For example, the comparison of Figure 7.12 with Figure 7.1(b) recalls the molecular re-organization of the scandium fluoride lattice consequent to heating. If the segments were circumscribed by a surface different from a sphere (e.g., an ellipsoid), a deformation of this type could also be associated with a thermal differential expansion of the

central segments with respect to the neighboring ones, where the rotation render the elongation compatible.

7.3.3 Examples of finite deformation

The kinematic analysis under large rotations presents no conceptual difficulty, but requires a robust numerical approach. An example, instructive for its simplicity, is represented by the out-of-plane bending of flextegrity plates under conservative external forces, such as self-weight. Since in the manufactured prototypes the deformation of the segments is negligible, the strain energy is associated only with the tendons.

Let Q indicate the total number of tendons, e.g., $Q = 6$ for the case of Figure 7.8(c). Let $\Delta\boldsymbol{\psi}$, $\Delta\boldsymbol{\vartheta}$ and $\Delta\boldsymbol{\varphi}$ denote the arrays respectively containing all the rotations $\Delta\psi_{ij}$, $\Delta\vartheta_{ij}$, and $\Delta\varphi_{ij}$, as indicated in Section 7.2. With the notation of Figure 7.6, the increase of strain energy ΔU when the segments (spheres) roll on each another, starting from the reference state with straight tendons, can be written as

$$\begin{aligned} \Delta U &= \sum_{q=1}^{Q} N_{0,q}\,\Lambda_q + \frac{1}{2}\sum_{q=1}^{Q} K_q\,{\Lambda_q}^2 \\ &= \sum_{q=1}^{Q} N_{0,q}\left(\textstyle\sum_{i,j}\,\Lambda_{ij}\right)_q + \frac{1}{2}\sum_{q=1}^{Q} K_q\left(\textstyle\sum_{i,j}\,\Lambda_{ij}\right)_q^2 . \end{aligned} \tag{7.3.6}$$

Here, $N_{0,q}$ $(q = 1, \ldots, Q)$ represents the initial prestress of the $q-$th tendon, K_q its axial stiffness, whereas Λ_q denotes its total elongation, which is the sum of the contributions Λ_{ij} (detailed in Figure 7.6(c)) due to the relative rotation of the two spheres i and j in contact, through which the $q-$th cable passes. Since Λ_{ij} is a function of $\Delta\varphi_{ij}$, the strain energy ΔU results to be a function of $\Delta\boldsymbol{\varphi}$.

The work ΔW of the external conservative loads F_s , for $s = 1, \ldots, S$, applied orthogonally to the initially-planar (mid) surface of the plate at S points, depends upon the out-of-plane displacements w_s of these points, i.e.,

$$\Delta W = \sum_{s=1}^{S} F_s\, w_s\,. \tag{7.3.7}$$

Observe that the displacements w_s depend on the position of the segments (spheres) in the distorted state, which is defined by the rotations $\Delta\psi_{ij}$, $\Delta\vartheta_{ij}$, and $\Delta\varphi_{ij}$. Hence, ΔW is a function of the vectors $\Delta\boldsymbol{\psi}$, $\Delta\boldsymbol{\vartheta}$ and $\Delta\boldsymbol{\varphi}$.

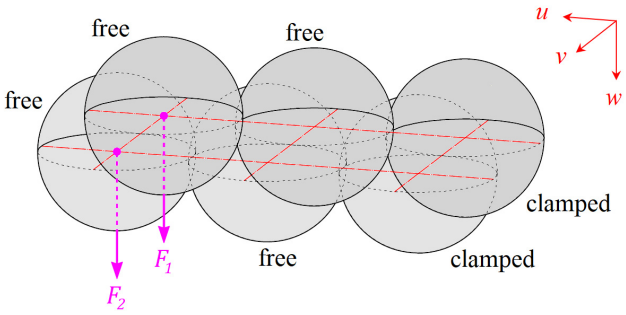

(a)

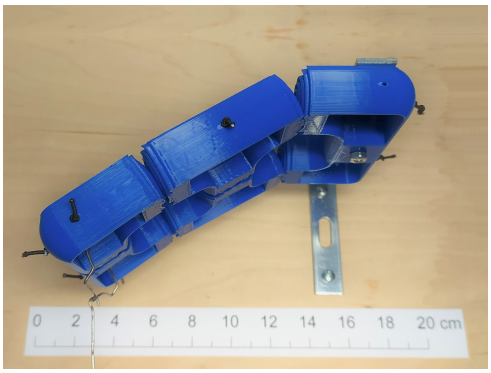

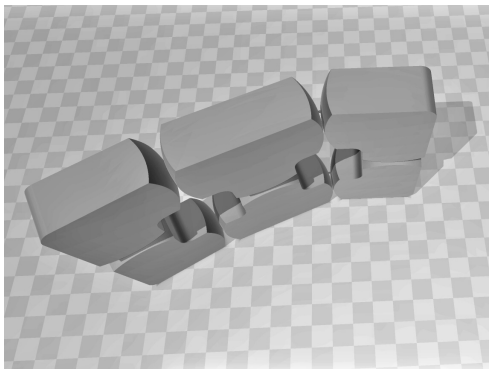

(b) (c)

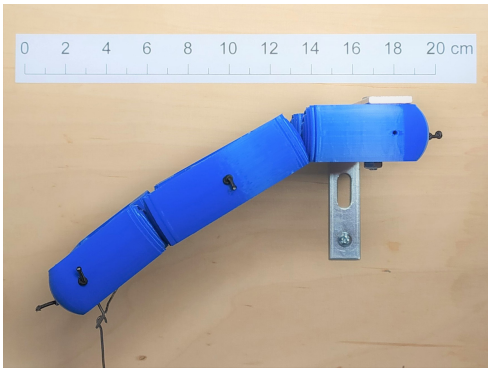

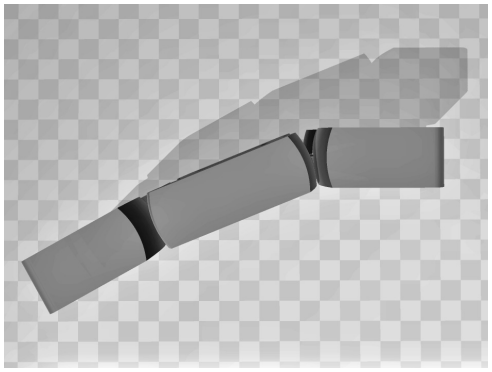

(d) (e)

Figure 7.13. Flextegrity plate composed of 6 segments (two basic units of Figure 7.8(a)) under symmetric external loads. (a) Schematic of the spherical contact profiles with indication of the constraints and the points of application of the loads. (b)-(d) Different views of the deformed shape for the manufactured prototype, and (c)-(e) corresponding views for the shape obtained via computations.

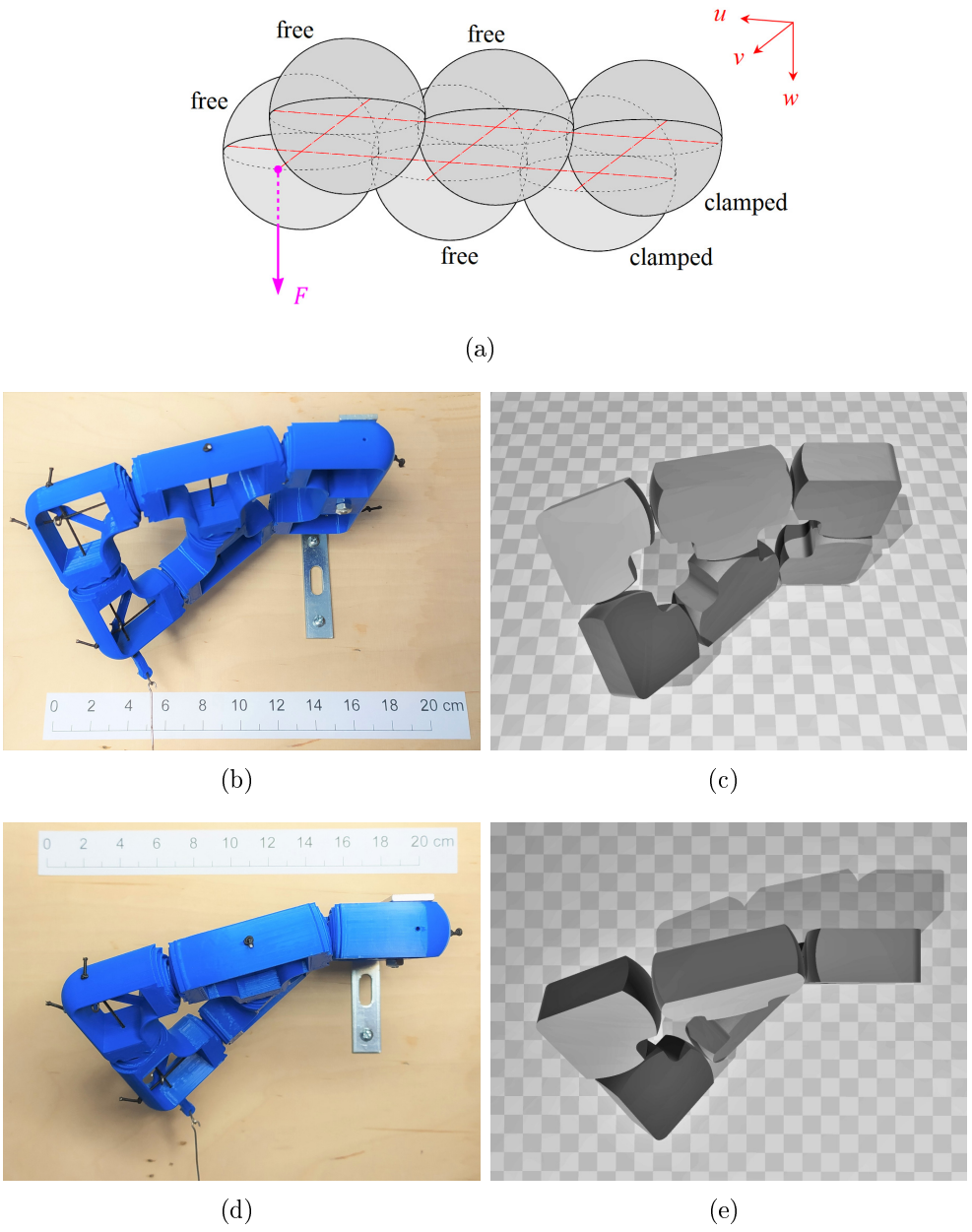

Figure 7.14. Flextegrity plate composed of 6 segments (two basic units of Figure 7.8(a)) under eccentric external loads. (a) Schematic of the spherical contact profiles with indication of the constraints and the points of application of the load. (b)-(d) Different views of the deformed shape for the manufactured prototype, and (c)-(e) corresponding views for the shape obtained via computations.

The equilibrium condition is defined by

$$\Delta U - \Delta W = \Delta U(\Delta\boldsymbol{\varphi}) - \Delta W(\Delta\boldsymbol{\psi}, \Delta\boldsymbol{\vartheta}, \Delta\boldsymbol{\varphi}) = \min\,, \tag{7.3.8}$$

under the constraints introduced, besides the boundary conditions, by the kinematic skeleton. The latter correspond to the kinematic conditions that each ring of the grid, following the path of segments in contact, must be a closed loop: starting from one segment, one shall recover the same position after the composition of displacements dictated by rotations $\Delta\psi_{ij}$, $\Delta\vartheta_{ij}$, and $\Delta\varphi_{ij}$ at each pair of consecutive segments.

The 3D-printed plate first considered consists in the assembly of 2 basic units (6 segments), of the type indicated in Figure 7.8(a), now coupled in series. The kinematic skeleton is that of 6 spheres of radius $R = 30\,\mathrm{mm}$ in mutual contact, arranged as in Figure 7.13(a). The tendons parallel to the short sides are characterized by axial stiffness equal to $K_q = 0.058\,\mathrm{N/mm}$ and they have been pre-tensioned at $N_{0,q} \simeq 1.7\,\mathrm{N}$ $(q = 1, 2, 3)$, while for those following the long sides one has $K_q = 0.029\,\mathrm{N/mm}$ and $N_{0,q} \simeq 1.4\,\mathrm{N}$ $(q = 4, 5)$.

The test of Figure 7.13 was preliminary carried out. As indicated in Figure 7.13(a), the structure is clamped at one of the short sides and it is subjected to the forces $F_1 = F_2 = 0.1\,\mathrm{N}$, applied at the opposite sides. The tested plate is placed vertically, in such a way that the planar face of the undeformed plate is parallel to the gravity field, acting along the direction of the short sides: this allows to disregard the action of the self-weight. The symmetry of the problem is such that the structure deform as a one-dimensional beam, for which an analytic solution can be found. This served to validate the numerical computations, which used the Nelder-Mead algorithm [122], implemented in Mathematica®, used for energy minimization [123]. Figures 7.13(b) and 7.13(d) show different views of the deformation of the prototype, which are juxtaposed to the deformed shapes obtained via calculation, reproduced with a CAD tool and reported in Figures 7.13(c) and 7.13(e), respectively. Analytical and numerical solutions coincide in practice. The agreement between theory and experiment is very good.

The same physical model was tested under the eccentric force $F = 0.4\,\mathrm{N}$ indicated Figure 7.14(a). Figures 7.14(b)-7.14(d) and Figures 7.14(c)-7.14(e) again compare the observed deflection with that obtained via numerical calculations. The flexural-torsional deformation is correctly reproduced by the model.

The last test regards the square 3D-printed plate of Figure 7.8(c), placed horizontally in the (vertical) gravity field. This is composed of 9 segments (4 basic units), and it is supported at the mid central segment and subjected to self-weight. The pitch surface radius is again $R = 30\,\mathrm{mm}$, and the tendons, whose axial stiffness is $K_q = 0.029\,\mathrm{N/mm}$ for $q = 1, \ldots, 6$, are pre-tensioned by $N_{0,q} = 1.2\,\mathrm{N}$. The loads $F_s \simeq 0.1\,\mathrm{N}$ represent the self-weight of each segment. Figure 7.15 collects

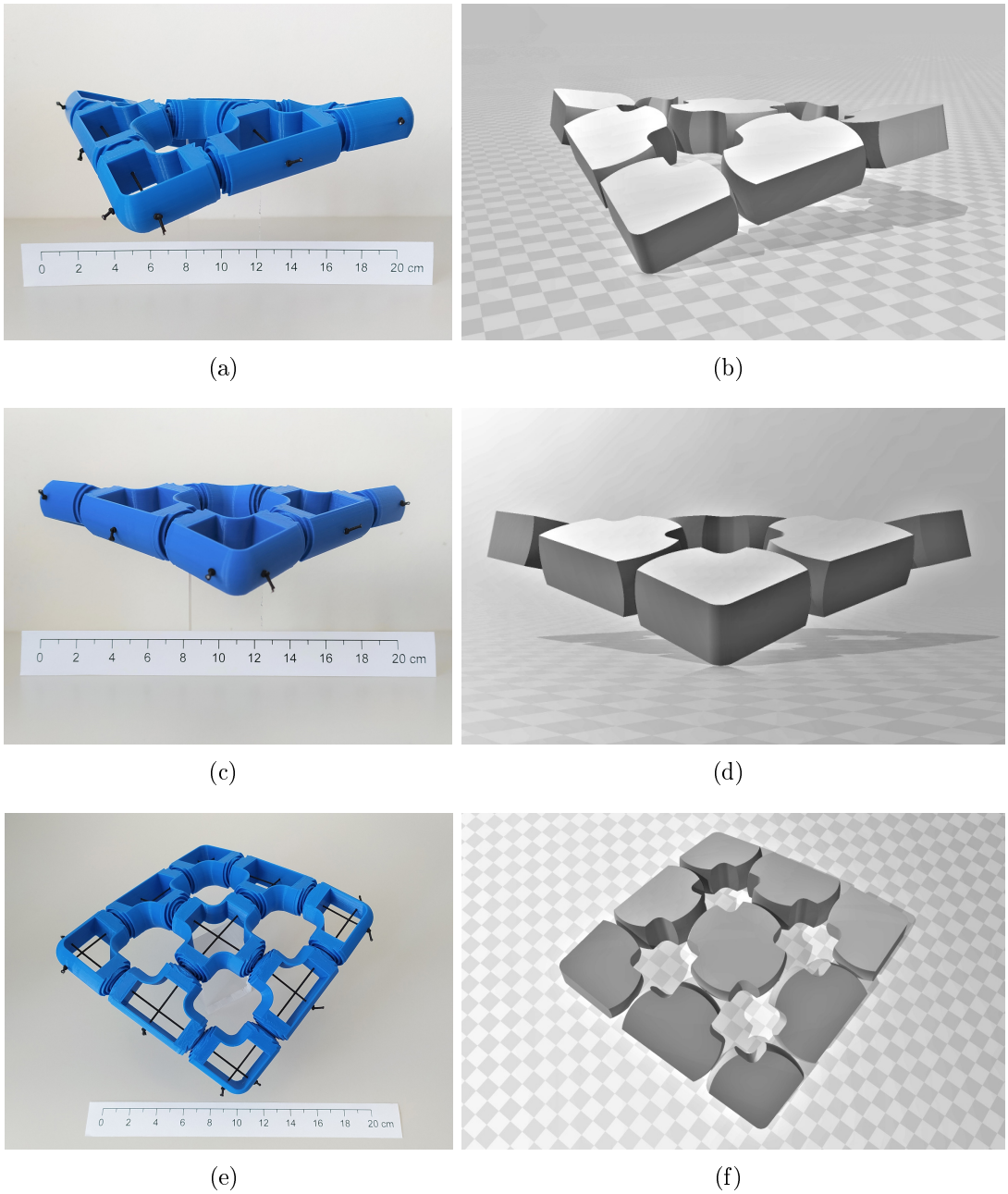

Figure 7.15. Deformation of a flextegrity plate composed of 9 segments (4 basic units), under self-weight and supported at the middle. (a)-(c)-(e) Different views of the deformed shape for the manufactured prototype, and (b)-(d)-(f) corresponding views for the shape obtained via computation.

three different views for the plate in the deformed state, and compares them with the corresponding shapes, obtained via calculations. The deformation recalls the shape of a hyperbolic paraboloid, which is perfectly caught by the model.

On the whole, the agreement between theory and experiments is very good, at least at the qualitative level, taking into account the uncertainties in the physical model, in terms of measured tensile force and stiffness of the tendons, effects of parasitic friction at the contact joints and with the cables, and 3D printing tolerances.

7.4 Discussion

Flextegrity lattices, mimicking an assembly of rolling spheres, can represent the basis for mesoscopic models of crystalline microstructure, where the molecular rotations are non-negligible degrees of freedom. Similarly, the mesoscopic model can represent the actual microstructure of metamaterials, with mechanical properties dictated by the kinematic skeleton. However, the conceptual model can be declined in many other forms. In fact, by varying the tendon stiffness/prestress, as well as the shape of the pitch surfaces of the contact joints, with geometries departing from the spherical paradigm (paraboloid, ellipsoid or more complex surfaces), a surprising wide range of different in-type responses can be attained. As discussed in Chapters 2 and 3 for beam-like structures, the stiffness and prestress of the tendons would affect the equivalent elasticity of the lattice; the shape of pitch surfaces dictates the cable elongation Λ_{ij} and the lever arm a_{ij} at each joint, thus modifying the form of constitutive relations.

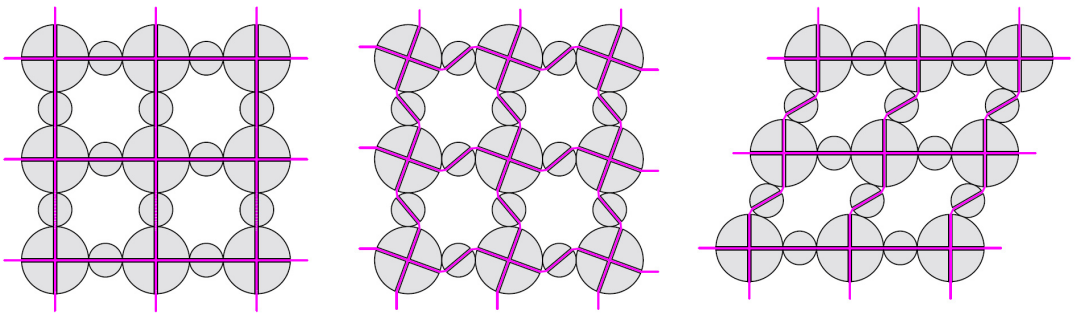

Figure 7.16. Lattices made with spherical segments with diverse radius. (a) Schematics of the arrangement (tendons represented by magenta lines), which allows for both (b) relative rotations and (c) shear-like deformation between the sub-particles.

The assemblies so far considered are, in practice, SC lattices of spheres with the same radius R in pure rolling contact, but this is just one particular category. Figure 7.16(a) reports a plan view of a lattice made with spheres of two different sizes, connected by tendons represented in magenta color. Figure 7.16(b) indicates that the system permits the relative rotation of the spheres, with a motion similar to that already observed in Figure 7.5(c). Note, however, that also a shear-like deformation, following the scheme of Figure 7.16(c), can be achieved. A motion of this type is prevented in the assembly of equal spheres by the constraint of pure rolling contact, as discussed in Figure 7.5(d).

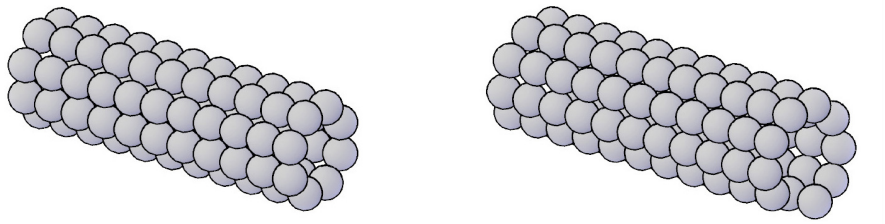

(a) (b)

Figure 7.17. Two possible arrangements for (nano-)tube lattices. Arrangement with (a) parallel rings and (b) helically wound chains.

Spherical segments of equal size could also be conveniently arranged in the form of (nano-)tube lattices. Figure 7.17(a) schematically represents a tube formed by parallel rings of spheres. In this case the integrity is granted by straight longitudinal tendons, as well as by circular tendons that hoop the rings. Another possible configuration follows the helical arrangement of Figure 7.17(b). Apart from straight tendons parallel to the axis of the tube, here the segments are kept in contact by tendons that follow the helix defined by the sphere centers.

In Chapter 5, it has been shown that the contact joints of a segmental beam can achieve multiple equilibrium states (non-convex energy) when the mobility of the tendon is increased by enlarging the segmental cavities. The possible extension of this concept to flextegrity lattices is shown in Figure 7.18. The multi-stable behavior is obtained by shaping the internal cavity hollowed inside the segments as indicated in Figure 7.18(a), so that the pivot point of the cable (exit point from the tubular sheath) is set back with respect to the pitch profile. This is formed, as discussed in Section 5.2.1 for the one-dimensional case, by three smoothly-connected arcs of circle with radii R and $2R$. The joint is multi-stable, because there are more than one configurations associated with the minimal length of the tendon. Two-dimensional structures can be obtained by assembling cross-shaped segments

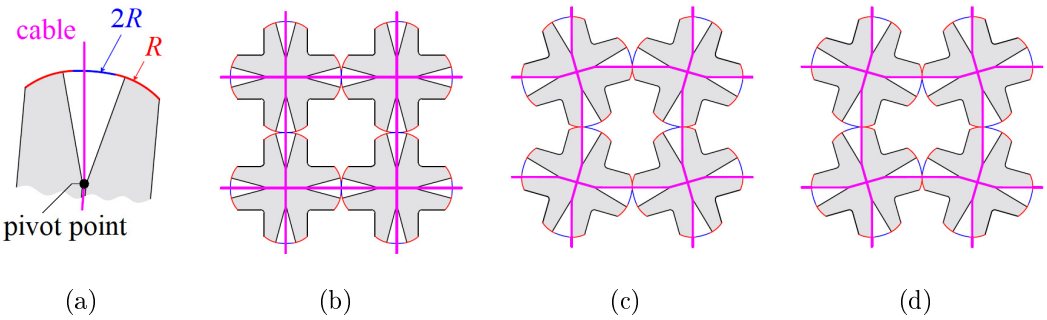

Figure 7.18. Other types of flexural-tensegrity lattices, with multi-stable contact joints. (a) Schematics of the segmental cavity (blank region), which increases the mobility of the cable inside the segment, and pitch lines consisting of 3 smoothly-connected arcs of circle, as suggested in Chapter 5, with radii R and $2R$. Equilibrium configurations under null external actions: (b) "straight" (non-chiral) state and (c)-(d) "rotated" (chiral) states.

according to the scheme of Figure 7.18(b): this "straight" configuration depicts a non-chiral lattice. There are, however, other two "rotated" equilibrium states, as per Figures 7.18(c) and 7.18(d), that provide a chiral micro-arrangement, stable under null external actions. This is an example of how a homogeneous assemblage of non-chiral objects can have chirality. The concept could also be extended to three-dimensional multi-stable flextegrity lattices, although the design of joints with complete 3D mobility certainly requires additional investigation. The possibility, leveraging the variant proposed in Chapter 6 for a globally-snapping flexural-tensegrity beam, of making such a 3D bi-stable coupling between the segments that the solid lattice snaps as a whole is yet to be fully investigated.

In all the aforementioned cases, rolling motions rely on the hypothesis that all the segments remain in contact along the pitch surfaces but, in general, some components may detach under tension. Moreover, the hypothesis of rigid segments should be relaxed when the segmental contact is achieved by very stiff, highly pre-tensioned, tendons. In this case, the change of shape of the pitch profiles under contact forces will produce a modification of the constitutive equations, according to the straining mechanisms of Figure 7.3.

Chapter 8

Application 1: a flex-ten bow

The invention of the bow, one of the first man-made tools used for hunting and for warfare, dates back to the dawn of time; but the bow also represents an instructive and clever application of the theory of the elastica and elastica-related models. Here, reference is made to the application of flexural-tensegrity beams to manufacture the limbs of a new type of foldable bow. The focus is on the technical and theoretical problems related to the development and optimization of elastic bows, in order to present the potentialities of flex-ten structures. Indeed, the bow is a model problem that involves the elastic return of the limbs coupled with the inertial effects due to their mass and to the accelerated arrow, thus representing a good benchmark to test the developed theoretical approach, comparing results with experiments. Moreover, the possibility of tailor-shaping the pitch profiles, which represents the design variable for flex-tens, together with the cable stiffness and prestress, can be fully exploited to achieve such a bending response that meets the archer's needs and optimizes the firing performance.

For centuries the bow has been the best performing long-range hunting device and weapon [124]. Nowadays, these uses have been outdated by the development of firearms, at least in the industrialized countries, so that the bow is mainly used in a sport known as archery, but transportability, low-technology, robustness, effectiveness and silence are still appreciated. The scheme of a classical bow is indicated in Figure 8.1(a). It consists of [125] a central stiff portion (the *grip* or *handle*), with two elastic staves on both sides (the *limbs*); the side of the limb facing the archer is the *belly*, while the opposite side is called the *back*; the two free tips of the limbs, called *nocks*, are coupled together with the *string*, which should be as inextensible as possible. When the limbs are free, the bow is said to be *unbraced* or *unstrung*; when they are tied together by the string, the bow is *braced* or *strung*. In this configuration, the distance between the grip and the string is the *brace height*. In order to shoot, the arrow is set in contact with the string

and the archer holds the bow at the handle with one hand and pulls the string at the middle, hooking it with the fingers of the other hand or clip devices: this is the *drawing* phase. The force applied by the archer at full draw is referred to as the *weight* of the bow and represents a parameter of paramount importance, because aiming is facilitated by a low weight, but a low weight is usually associated with a limited power of the device.

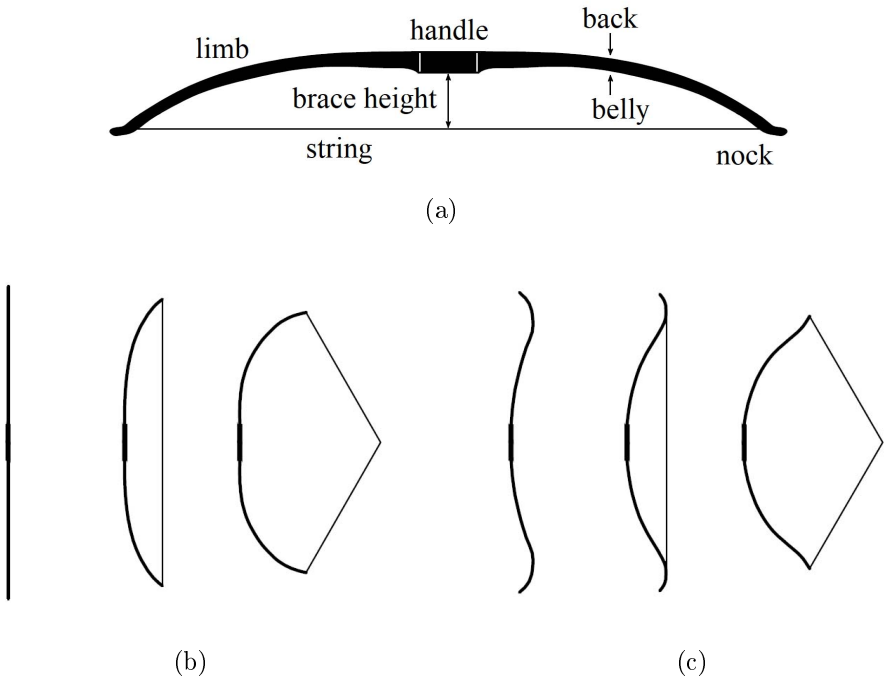

Figure 8.1. Schematic representation of a classical bow. (a) Parts of the bow; (b) non-recurve bow in the unbraced, braced and fully-drawn configuration; (c) recurve bow in the unbraced, braced and fully-drawn configuration (pictures adapted from [125]).

Over the centuries there have been many technical innovations, which allowed some populations to obtain war supremacy. Most of the theory and technology has been addressed to limiting the weight, without going to the detriment of power. From a geometrical point of view, one can distinguish two types of traditional bows: the *non-recurve* bow of Figure 8.1(b) and the *recurve* bow of Figure 8.1(c). In the former case, the limbs are straight in the unbraced configuration and the string touches only at their tips both in the braced and in any drawn state. In the second case, the limbs are curved away from the archer in the unbraced configuration, so that in the braced configuration the string is in contact with the limbs on a certain length in proximity of the tips; such length diminishes as the bow is drawn [125]. By properly shaping the limbs, the recurve bow can perform much better than

non-recurve bows. Nowadays, modern compound bows use advanced technology, having passed from single stave bows to complex mechanisms operated by means of cams and pulleys.

Passing to materials, traditional bows were mostly made of wood (*self bow*), or a composition of wood and other natural materials, such as sinew, horn and bone (*composite bow*), providing suitable materials where it is required to resist tension (sinew on the back) and compression (horn on the belly). The classical example of traditional self bow is the English longbow [126], while a paradigmatic historical composite bow is the Turkish bow [127–129]. Modern bows can be made of steel and/or glass/carbon fibers in a resin matrix, while nylon, dacron and kevlar are used for the string in substitution of sinew, silk, hemp or cotton [125]. Moreover, since the 1960s, eccentric cams, to which the string is wound, have been added at the tips of the limbs in order to provide a better performance (modern compound bow [130, 131]).

Many are the parameters that determine the performance of the bow: its length and shape, the ultimate drawing force, the compliance of the string. In any case, the bending stiffness and mass of the limbs [124, 132] play a dominant role. These were traditionally functionally graded by recurving and tapering the bows and/or using composite materials and, more recently, by introducing additional devices, such as the cams in the compound bow. However, the constitutive law for the flexible parts remains essentially linear elastic. Here, we consider a new design approach. Left aside the important aspect of the optimization of geometry for the recurve bow, which is a classical and well studied subject, we start with the simplest case of a non-recurve bow, being interested in increasing its performance via a tailored functionally-graded nonlinear nonlocal constitutive bending law for the limbs. To manufacture elements with such properties, the flexural-tensegrity concept appears to be particularly suitable.

The plan of the chapter is as follows. After some historical insights on classical bows (Section 8.1), the dynamic equations for a non-recurve segmental flex-ten bow are detailed in Section 8.2. Two different types of flex-ten bows are then designed, prototyped and tested in Section 8.3, comparing their efficiency with that of a classical non-recurve bow. The main results here concerned are also collected in [133].

8.1 Insights on historical bows

The bow is a fascinating machine that has undergone a continuous evolution during the centuries, in order to improve its performance in throwing projectiles faster and farther.

Traces of stone-tipped arrows, namely of a bow, were reported in South Africa 64000 years ago [134]. The invention of the bow as a machine to throw shaped projectiles at a long distance required great cognitive ability by primitive humans [135]. Our ancestors had first to recognize that elastic rods can store energy in the form of deformation, which can be transformed, thanks to the elastic return, into kinetic energy of the arrow. Manufacturing required the right materials, whose combination and shaping was made with manual skill and coordination, using state-of-the-art tools for smoothing, carving, cutting and glueing. Certainly, its use in hunting requires the right muscular effort to provide the initial deformation energy, and skills to direct this released energy (aiming and shooting).

There have been many famous bows, such as Ulysses's, classically known to be very difficult to draw, and the longbow used by Robin Hood, the English outlaw who steals from the rich to give to the poor. One should also recall the primitive short bows of African Bushmen, the fearsome recurve bows used by Mongolians under the guide of Genghis Khan and the weapons of American Indians. From a theoretical and historical point of view, the most noteworthy examples are the English longbow, the Turkish recurve bow and the modern compound bow.

The longbow [126], represented in Figure 8.2(a), is a huge non-recurve self bow traditionally made of yew or wych elm in England. Although probably already used as a hunting tool in the Neolithic period (10000 BC), the first written reference of the longbow dates back to 1449 AD in a letter by Margaret Paston to her husband John who, at that time, were involved in a private war against Robert Moleyns.

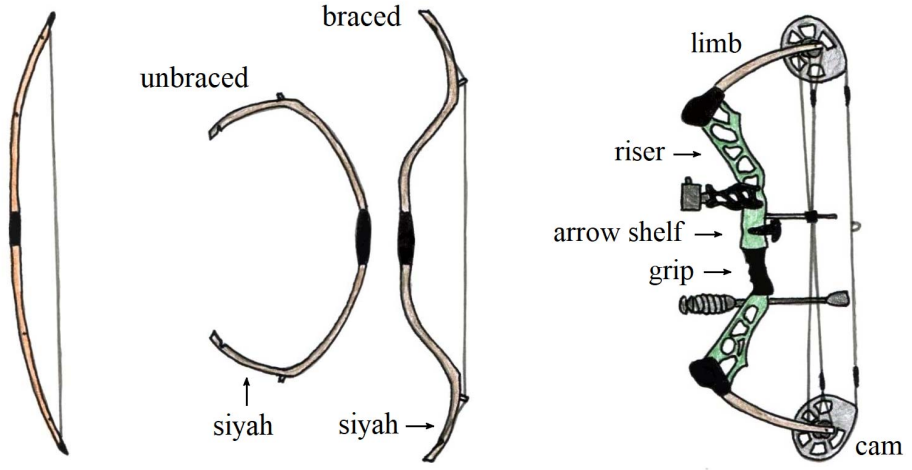

Figure 8.2. Different types of bow: (a) English longbow, (b) Turkish-Mongolian bow, and (c) modern compound bow.

Mrs. Paston suggested to employ the crossbow instead of the "long bowe" because the inter-floor height of their house was too small for a longbow archer [126]. The longbow is also famous for its massive employment in the battlefields of the Scottish Wars (1296-1357), the Hundred Years' War (1337-1453) and the War of the Roses (1455-1485); indeed, it was very popular in Eastern Europe, particularly in England, during the Middle Age. Its main characteristic is the length of its limbs, which is dictated by the fact that it is a self bow made of wood: compatibly with material strength, the longer the arms, the higher the elastic energy that can be stored. However, since the length could exceed the height of the archer[1], it was difficult to handle [126]; hence, it was mainly used as a "defensive" weapon by a *static* crowd of archers against the approaching hord of enemies [129].

The Turkish bow, sketched in Figure 8.2(b), is a strongly-recurved composite bow representative of the technology developed by Asian bowyers. The oldest traces of this type of bow are reported in Mesopotamia, in Anatolia and in the steppes of Northern Asia since the third millennium BC [137]. This consists of a central core made of wood to which a layer made of horn is glued on the belly and a strip of sinew is placed on the back. The horn was generally from buffalos or antelopes, the sinew from the leg tendons of oxen and the wood from maple trees, while the adhesive was a animal collagen-based glue [128, 129]. The composite layered rod was protected from the weather by a thin covering of tree bark, leather or lacquer [127, 128]. In this way, the appropriate materials are placed where it is required to resist tension (sinew on the back) and compression (horn on the belly), while the wooden core, being close to the neutral axis in bending, provides axial stiffness and the support for the other layers. The structure is actually prestressed, since the shrinkage of the sinew contributes to provide a reflexed shape for the unbraced bow. The cross-section has a variable shape along the limb in order to better distribute the stiffness [128], but it is the recurve that provides a peculiar elastic law for the drawing force, which increases quickly at first, but it softens as drawing progresses [127]. A peculiar "trick" introduced by the Turks was represented by a rigid tip in proximity of the limb-ends called *siyah*, shown in Figure 8.2(b), which plays a benefic lever action [127, 129]. The curved shape provides a convenient energy-draw function and, on the other hand, the composite material can withstand extreme bending, so that a short bow can be made without loss of weight and efficiency. In this way, the archer could shoot both light-weight missiles at a long-distance and heavy arrows to perforate soldiers armor, but, the greatest advantage was that the archer could handle the bow while on horseback,

[1] The Japanese Yumi was even longer ($210 \div 230$ cm), with draw lengths of about $80 \div 90$ cm, so that the string had to be pulled beyond the shooter's ear. This is a bow worth mentioning because of its unique *asymmetric* shape with the handle at about one-third of the its length from the bottom [136]. As the longbow, it was traditionally made of wood, specifically of bamboo strips glued together, with no rigid parts.

following the "attack and retreat" Saracen strategy [129].

It should be mentioned that in traditional bows, such as the aforementioned examples, the arrow does not follow the straight line (*aim line*), connecting the target with the nock of the arrow and parallel to the arrow when the bow is fully drawn. The arrow cannot travel straight along this line, because it is resting on the archer's hand and there is the thickness of the handle, which would deflect its trajectory (Figure 8.3(a)). Nevertheless, the arrow actually directs towards the target: the effect is usually referred to as the *archer's paradox* [138, 139]. This is a consequence of the *missile oscillations* (Figure 8.3(b)), due to the deflection of the arrow against the handle when it is fired and the interaction with the string perturbed by the archer's fingers at release. In addition to the archer skill in properly releasing the string, the arrow will fly accurately to the target only if its elastic bending stiffness is properly functionally graded along the centroidal line.

The compound bow, represented in Figure 8.2(c), is a modern composite bow, first reported to be built in 1938 by the physicist Claude Lapp [125], but patented and commercialized by H.W. Allen in the 1960s [130]. Apart from the string, whose constitutive properties are more or less the same in all bows, its main constituents are, as indicated in Figure 8.2(c), the *riser*, the *grip*, the *arrow shelf*, the *limbs* and the *cams*. The riser is a central stiff portion of the bow, usually made of aluminium or magnesium alloys, which supports, in the middle, both the grip and the arrow shelf. The arrow shelf allows to hold the arrow in place according to the aim line (in the plane of the bow), so that the missile can follow a rectilinear trajectory, with no need of the effects of the archer's paradox. The limbs, generally

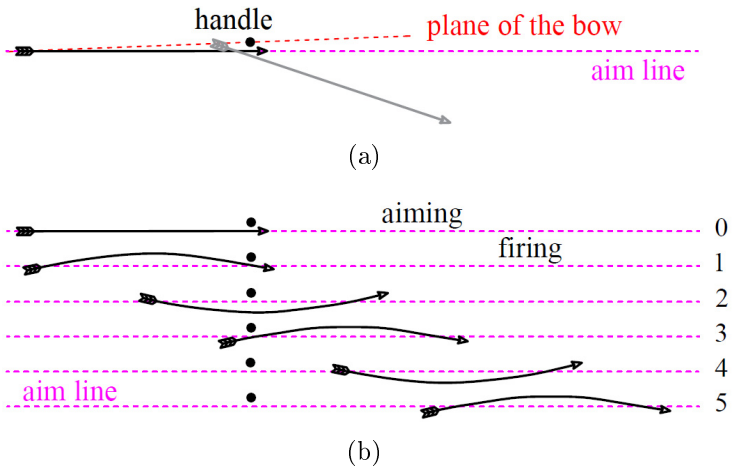

Figure 8.3. Illustration of archer's paradox: (a) deflection of the arrow trajectory against the handle if the arrow were rigid and the string remained in the plane of the bow; (b) schematic representation of the shapes actually assumed by the arrow, which is deformable in bending and interacts with the string during its passage of the bow.

made of laminated layers of fiberglass glued with resin, represent the flexible part of the bow, bolted to the tips of the riser. Other accessories are available, such as viewfinder, stabilizers and special hooks for aid during drawing and releasing. Remarkably, the cams to which the string is wound are eccentric pulleys, placed at the limbs tips. The main properties of the compound bow are consequent to this eccentricity: by gradually changing the lever arm, the peak force is reached much before the full draw and, from this point on, the required force to complete the drawing decreases. This facilitates aiming [130], because the holding weight at full draw is not too high while, by properly shaping the cams and limbs, the stored elastic energy remains sufficiently high to provide power. A way to design cams for an arbitrary function generation is presented in [131]; although the wrapping device is indicated to obtain torsional nonlinear spring-hinges, an application to the cams of a compound bow is envisaged.

More in general, the elastic limbs are the key elements of more complicated and enlarged launching systems. A first example is represented by the portable crossbow, reported in China since the third century BC [140], in which the limbs are quite short but rigid and attached to a wooden tiller [128]; the string is then hooked to the tiller itself and released with a trigger, so that the shooter can aim without any muscular effort. A further development in size, and hence and in stored elastic energy, probably dates back to the inventions by Archimedes [141, 142]: here the limbs are large and the wooden staves are connected at the basis to torsion motors, as in Figure 8.4(a); because of the huge weight, drawing is done via toothed wheels, racks and chains. Also Leonardo da Vinci explored the theme of the catapult and the siege-crossbow, as indicated in the tabulae of the Codex Atlanticus [143], one of which is reported in Figure 8.4(b); this example is characterized by the functionally-graded laminar conformation of the bow.

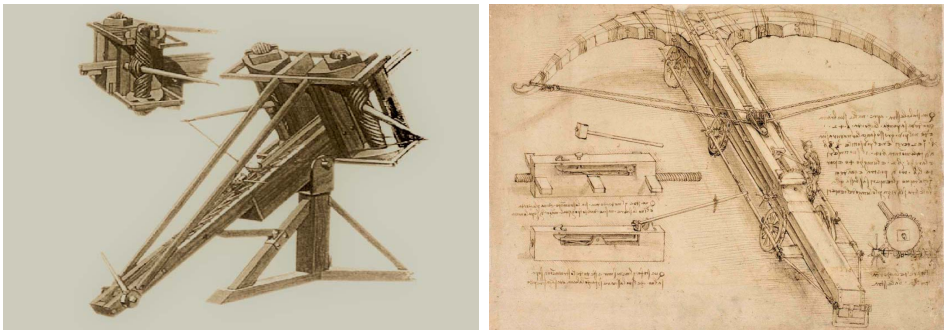

(a) (b)

Figure 8.4. Evolution of the bow: (a) Greek-Roman catapult (picture adapted from [141]); (b) drawing of a siege-crossbow by Leonardo da Vinci (picture adapted from [143]).

8.2 Dynamic equilibrium of the bow

The aim is to investigate the possible application of the flexural-tensegrity concept to the manufacturing of an innovative type of bow. This represents a challenging problem in dynamics, characterized by the interaction of a nonlinear nonlocal elastic structure with a moving mass. Now, the dynamic equilibrium equations for a flex-ten segmental bow are derived.

Figure 8.5 shows the scheme of a non-recurve bow in which the flexural-tensegrity concept is applied. Each limb, made of five rigid segments, is connected to a rigid handle, twice as long as the segments, and its pieces are kept together by one prestressing tendon. The limb tips are connected by an inextensible string of length L_s , with negligible mass, the brace height is f_0 , while the draw is indicated as f_d in Figure 8.5(a). The drawing force P, which is a function of f_d according to the elastic return of the limbs, accelerates the arrow after that the string is released. Thanks to symmetry, the problem can be simplified, as per Figure 8.5(b), in that of a flexural-tensegrity cantilever with $n = 6$ segments of equal length ΔL, under the force applied by the string.

The dynamic response of bows and arrows after the release of the string from the full draw has been analyzed by a few authors. A simplified approach was first presented in [144], under the assumptions that the limbs deform according to arcs of a circle and an effective percentage of their mass is concentrated at tips (lumped mass model). An improved model was proposed in [145] by considering the limbs as thin elastic Euler-Bernoulli beams, but a discretization was used to solve the equations numerically, i.e., the limbs were treated as chains of rigid segments

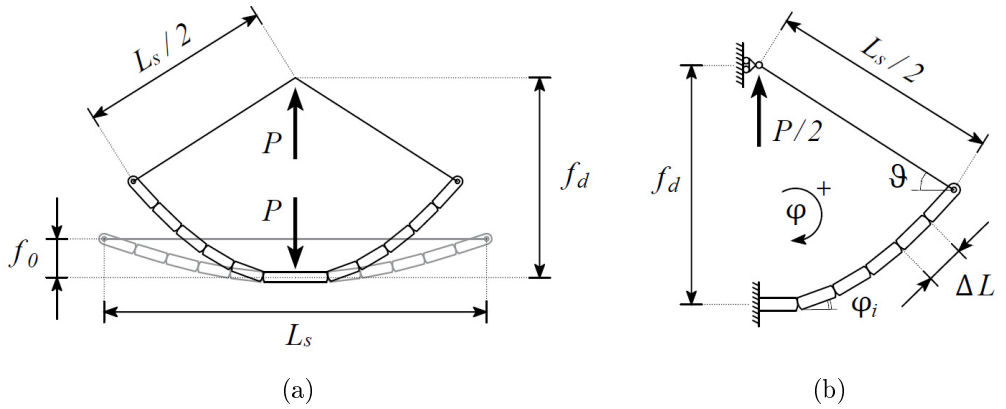

Figure 8.5. Schematic representation of the flex-ten bow: (a) scheme of the whole bow in the braced (light grey) and drawn (black) configurations; (b) equivalent problem thanks to symmetry, with indication of the Lagrangian variables.

coupled by linear elastic spring hinges. Also the proposed flex-ten bow is actually a segmental structure, but the spring hinges are governed by a nonlinear nonlocal constitutive relation.

The Lagrangian variables for the problem, represented in Figure 8.5(b), are the absolute rotations φ_i , $i = 1 \dots n$, of the $n = 6$ segments, positive if clockwise, and the inclination ϑ of the string, which are related because the segments and the string are inextensible. The increase of elastic strain energy ΔU from the unbraced straight state, under the assumption of rigid segments and compliant tendon, takes the form expressed by (2.1.8) or (4.1.1a). Its variation reads

$$\Delta U = N_0 \Lambda + \frac{1}{2} K \Lambda^2 \quad \Rightarrow \quad \delta \Delta U = N_0 \, \delta\Lambda + K \Lambda \, \delta\Lambda = N \, \delta\Lambda \,, \tag{8.2.1}$$

where N_0 is the initial prestressing force of the tendon and K its effective stiffness, while $N = N_0 + K\Lambda$ is the actual tension force in the cable, being $\Lambda = \sum_{i=1}^{n-1} \Lambda_i$, with Λ_i indicating the elongation of the cable at each joint (Figure 2.2(a)).

Recall that the quadratic term in the left-hand formula of equation (8.2.1) is responsible of the nonlocal behavior of the structure. If this term is negligible, as in the case of a highly prestressed beam ($N_0 \gg K\Lambda$), all the contact joints behave as spring hinges, one independent from the other. Otherwise, the term $\frac{1}{2} K \Lambda^2$ provides the "interconnection" of the spring hinges.

With reference to Figure 8.5(b), the force $P/2$ is in general a function of time, and can indicate either the (static) drawing force, or the force that accelerates the arrow at firing. Let ΔW denote the work done by such force. Then, the incremental work $\delta \Delta W$ of $P/2$, for a variation δf_d of the draw f_d , is given by

$$\delta \Delta W = \frac{P(f_d)}{2} \, \delta f_d \,, \quad \text{with} \quad f_d = \sum_{i=1}^{n} \Delta L \sin \varphi_i + \frac{L_s}{2} \sin \vartheta \,, \tag{8.2.2}$$

where ΔL the length of each segment and L_s the length of the string.

Let us denote with $\bar{f}_d$ the full draw and with M_a the mass of the arrow. When the bow is released from the full draw configuration $f_d = \bar{f}_d$ and the arrow is fired, the following conditions apply:

$$\varphi_1(t) = 0 \,, \tag{8.2.3a}$$

$$\sum_{i=1}^{n} \Delta L \cos \varphi_i(t) - \frac{L_s}{2} \cos \vartheta(t) = 0 \,, \tag{8.2.3b}$$

$$M_a \, \ddot{f}_d(t) = -P(t) \,, \quad \text{with} \quad f_d(0) = \bar{f}_d \,, \; \dot{f}_d(0) = 0 \,. \tag{8.2.3c}$$

Here, the notation $\dot{(\cdot)} = \partial(\cdot)/\partial t$ has been used. The clamped handle constraint

provides (8.2.3a). Equation (8.2.3b) is the kinematic compatibility of inextensible segments and string, which relates the inclination ϑ of the string with the absolute rotations φ_i, $i = 1 \dots n$, of the $n = 6$ segments. Equation (8.2.3c) is Newton's second law of motion with initial conditions for the arrow. Left aside the inertial contributions, the equations can also be used to describe the quasi-static process of drawing.

The drawing phase can be assumed to be a quasi-static process, where accelerations are negligible and, hence, condition (8.2.3c) does not apply. One thus finds the relationship between drawing load $P/2$ and the draw f_d from the minimization of the elastic energy of the limbs and the potential energy of the load. On the contrary, in the process of firing, one has also to consider the inertia of the bow. The kinetic energy T of the limb of Figure 8.5(b) can be expressed according to (4.1.1c). For the case at hand, where $\ell_i = \Delta L, \forall\, i = 1 \dots 6$, this reads

$$\begin{aligned} T = &\frac{1}{2}\sum_{i=1}^{n} m\Delta L \left\{ \frac{\partial}{\partial t}\left[\left(\sum_{j=1}^{i} \Delta L \sin\varphi_j \right) - \frac{\Delta L}{2}\sin\varphi_i \right] \right\}^2 \\ &+ \frac{1}{2}\sum_{i=1}^{n} m\Delta L \left\{ \frac{\partial}{\partial t}\left[\left(\sum_{j=1}^{i} \Delta L(1-\cos\varphi_j) \right) - \frac{\Delta L}{2}(1-\cos\varphi_i) \right] \right\}^2 , \end{aligned} \tag{8.2.4}$$

where $m\Delta L$ is the mass of each segment of length ΔL. Observe that the mass m per unit length of the segments has been assumed constant and uniform, neglecting the rotational inertia with respect to translational contribution[2].

It is worth mentioning that one could have considered the system bow + arrow. In this case, the drawing force P is an internal force between the string and the arrow that makes no work, but the mass M_a of the arrow should be included in the kinetic energy contribution. By adding to T the quantity $M_a \dot{f}_d^2/4$ corresponding to one half of the mass of the arrow associated with the half-bow of Figure 8.5(b), the variational derivation of the equation of motion would imply (8.2.3c). However, the proposed formulation has the advantages that it can be applied both to the dynamic (firing) and the static (drawing) case.

In order to consider possible sources of dissipation, a conventional linear-

[2]As already pointed out in Chapter 4, the kinetic energy of the $i-$th segment can be written as $T_i = (I\dot{\varphi}_i{}^2 + m\Delta L\, \dot{u}_i{}^2 + m\Delta L\, \dot{v}_i{}^2)/2$, where I is the moment of inertia of the segment (here assumed to be all same), $m\Delta L$ is the segmental mass, φ_i the segmental rotation, u_i the longitudinal displacement of the centroid of the segment, from the straight reference state, and v_i the corresponding transverse displacement; the latter two quantities correspond to the terms between square brackets in (8.2.4), first and second line respectively. For the case at hand, the rotational contribution is negligible. In fact, it has been verified *a posteriori* that the term $\sum_{i=1}^{n} I\dot{\varphi}_i{}^2/2$ accounts only for 1% of the total kinetic energy T when this reaches its maximum; in general, the contribution is always much less than 5%.

damping term, associated with the parameter c, is added at each joint, so that the resulting incremental dissipated work reads

$$\delta W_D = -c \sum_{i=1}^{n-1} \frac{\partial \Delta\varphi_i}{\partial t}\, \delta\Delta\varphi_i = -c \sum_{i=1}^{n-1} \left[\frac{\partial}{\partial t} \left(\varphi_i - \varphi_{i+1}\right) \right] \left[\delta\varphi_i - \delta\varphi_{i+1} \right]. \qquad (8.2.5)$$

This represents a conventional idealization and a simplification of the real mechanisms of dissipation, which occur at the level of the contact hinges, as well as between the cable and the sheaths. The sliding of the conjugate profiles certainly dissipates energy through friction; frictional contact also comes into play, despite lubrication, between the cable and the sheaths, and this may also affect the distribution of axial stress along the cable itself. Many authors have suggested models to take into account friction while analyzing cables sliding on pulleys, such as in [146] and [147], via a complementary approach, or in [148], via a dynamic relaxation formulation. Postponing to further studies a more detailed characterization of the dissipation mechanisms[3], here we limit to consider the conventional expression (8.2.5). Of course, dissipations do not come into play in the quasi-static case of the bow drawing; in particular, the parasite effects of friction can be ruled out if the bow, at full draw, is shaken by hand, so that the external perturbations allows to reach the configuration of minimum potential energy.

The governing equations can be found via Hamilton's principle [73] from (8.2.1), (8.2.2), (8.2.4) and (8.2.5), under conditions (8.2.3) and recalling the differential relation (2.1.1) between the cable elongation Λ_i and the internal lever arm a_i, which are reported in Figure 2.2(a). These governing equations can be written in the general form

$$\begin{aligned} & N\big(a_i - a_{i-1}\big) - \frac{P\,\Delta L}{2\tan\vartheta}\sin\varphi_i + \frac{P\,\Delta L}{2}\cos\varphi_i + c\big(2\dot\varphi_i - \dot\varphi_{i-1} - \dot\varphi_{i+1}\big) + \\ & + \frac{m\,\Delta L^3}{4}\cos\varphi_i \left(\sum_{j=1}^{n} \mu_{ij}\ddot\varphi_j \cos\varphi_j - \sum_{j=1}^{n} \mu_{ij}\dot\varphi_j{}^2 \sin\varphi_j \right) + \\ & + \frac{m\,\Delta L^3}{4}\sin\varphi_i \left(\sum_{j=1}^{n} \mu_{ij}\ddot\varphi_j \sin\varphi_j + \sum_{j=1}^{n} \mu_{ij}\dot\varphi_j{}^2 \cos\varphi_j \right) = 0\,, \quad i = 1\ldots n, \end{aligned} \qquad (8.2.6)$$

[3]Preliminary experiments on the free vibrations of cantilevers, reported in Section 4.1.3, for which the theoretical modeling of different sources of dissipation has been considered, indicate that a conventional viscous dissipation, of the same type considered in (8.2.5), can very well reproduce the oscillatory response, at least when the oscillations are wide enough. When the arrow is fired, the deformation of the bow is large: we conjecture that such a condition is similar to that corresponding to oscillations of wide amplitude in the dynamical test.

where we have formally set $\varphi_k = 0$ when $k < 1$ or $k > n$, and $a_k = 0$ when $k < 1$ or $k \geqslant n$. Recall that $N = N_0 + K\Lambda$ is the tensile force in the tendon, a_i is the internal lever arm and $\Lambda = \sum_{i=1}^{n-1} \Lambda_i$, where both a_i and Λ_i are functions of the relative rotation $\Delta\varphi_i = \varphi_i - \varphi_{i+1}$. The mass coefficients μ_{ij} result from the symmetric matrix (4.1.8), introduced in Section 4.1.1.

In the dynamic problem, when the archer releases the string, the unknowns are the segmental rotations φ_i , the drawing force P and the angle ϑ, as per Figure 8.5(b). In the quasi-static process of drawing, one shall set $m = 0$ and $c = 0$ in equations (8.2.6), while condition (8.2.3c) becomes ineffective. Hence, the unknowns are the segmental rotations φ_i and the drawing force P, while the angle ϑ is the datum that describes the amount of drawing.

8.3 Design of the bow

The flex-ten bow is a composite bow, since it is made of two distinct categories of elements: the segments, which resist compression, and the compliant prestressing cable, which provides tension and is the main source of elastic energy. By simply changing the shape of the contact surfaces of the segments, it is possible to design the elastic properties of the limbs according to the specific needs of the archer. Moreover, the length of the bow can be changed by simply adding or removing segments, while the stiffness can be tuned by varying the cable prestress. In addition, the weapon can be folded/unfolded for easy packaging and transportation. The modular construction permits industrialized manufacture: the hard components, which are massive and hardly subjected to breakage, could be obtained by using milling cutters. It should also be mentioned that the desired relative motion of the segments, conceived as pure rolling along the design pitch lines, could alternatively be obtained by manufacturing the joints not as surfaces in contact, but as optimized compliant mechanisms [149] or cross-axis flexural pivots [150]. Although the final assembly would be more complicated, this represents a promising conceptual development of the flexural-tensegrity concept, to be considered in further work.

After recalling the parameters that measure the bow performance, two prototypes of flex-ten bow are presented for the sake of comparison, corresponding to either a linear or a sub-linear constitutive relation for the internal lever arm. Finally, theoretical predictions for the prototypes are experimentally corroborated.

8.3.1 The good design

Two main aspects need to be considered while evaluating the performance of a bow. The first one [138] is the speed that the bow can impart to an arrow of given

mass for fixed draw and drawing force. In particular, the interest of designers is to investigate how different masses for the arrow affect the exit speed. In fact, in general the elastic strain energy is not entirely converted into kinetic energy of the arrow because of the contribution of the mass of the limbs, which induces their vibrations; moreover, when the string suddenly achieves the straight configuration there is an impact that can induce further energy loss. Hence, one has to consider the full dynamic problem for arrows of different mass. The second aspect to be taken into account [138] is the efficiency of the bow, defined as the ratio between the kinetic energy of the arrow when it leaves the bow and the work done by the archer in the drawing operation.

A further important parameter [132] is the ratio between the energy stored in drawing and the product between the weight of the bow and the full draw height (distance of the middle of the string from the grip at full draw). When this quantity is small, the drawing force increases quite sharply. Since slight variations of the draw correspond to appreciable variations in the energy stored in the limbs, the archer has a harder time taking a good aim. Hence, in a user-friendly bow, this ratio should be as large as possible.

8.3.2 The shape of pitch profiles

The lever arm $a_i = a_i(\Delta\varphi_i)$ of the tension force N in the cable, or equivalently the elongation $\Lambda_i = \Lambda_i(\Delta\varphi_i)$ required at each joint for the cable, defines the constitutive response at the $i-$th contact joint of the flex-ten bow. Here, we consider either a *linear* or a *sub-linear* law for a_i, which are represented in Figures 8.6(a) and 8.6(c), respectively. The corresponding primitives Λ_i are plotted in Figures 8.6(b) and 8.6(d), respectively.

The linear case, represented in Figures 8.6(a) and 8.6(b), can be very well approximated with elliptic pitch lines whose equation, with respect the reference frame $\xi - \eta$ of Figure 2.3(a), reads

$$\eta = \pm\,\beta\left[1 - \sqrt{1 - \left(\frac{\xi}{\alpha}\right)^2}\right], \tag{8.3.7}$$

with $\alpha = 118.14\,\mathrm{mm}$ and $\beta = 144.21\,\mathrm{mm}$, where the plus (minus) holds for pitch line 1 (pitch line 2) labeled in Figure 2.3(a). From this, one finds that $a_i \simeq B\Delta\varphi_i$, with $B = 48.39\,\mathrm{mm}$. On the other hand, the sub-linear case of Figures 8.6(c) and 8.6(d) results from power-law pitch lines of the form

$$\eta = \pm\,\gamma\,\xi^4, \tag{8.3.8}$$

where $\gamma = 32.63 \cdot 10^{-6}\,\mathrm{mm}^{-3}$. From this geometry, one finds that $a_i \simeq C{\Delta\varphi_i}^{1/3}$,

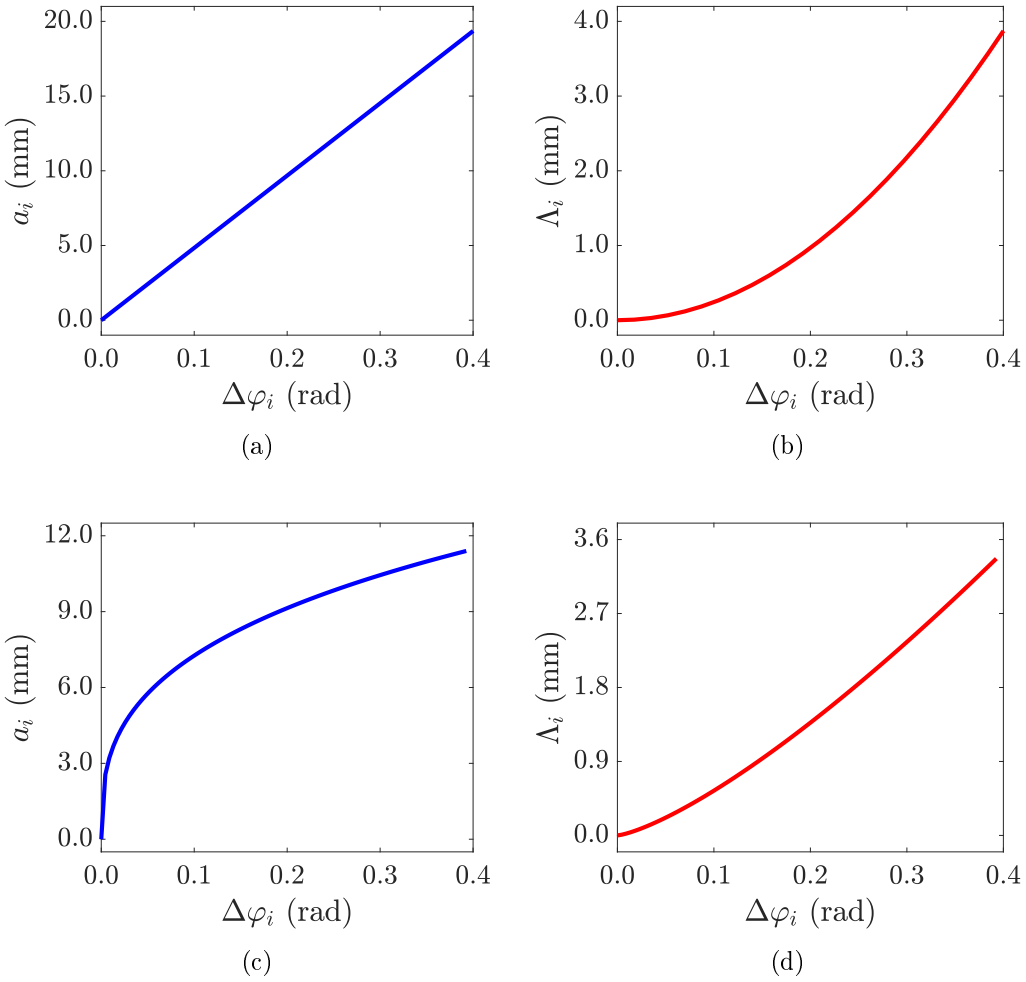

Figure 8.6. Constitutive relations for two types of joints used in the design of the flex-ten bow: (a) internal lever arm a_i and (b) local elongation Λ_i for the linear case; the curves plotted in (c) and (d) respectively correspond to the sub-linear case.

with $C = 15.60\,\text{mm}$. The graphs of Figure 8.6, obtained from pure kinematic considerations, confirm that the lever arm a_i is the first derivative with respect to $\Delta\varphi_i$ of the local elongation Λ_i, as per (2.1.1).

8.3.3 Theoretical results

We now theoretically compare two different designs for the flex-ten bow, corresponding either to the linear or sub-linear constitutive relations represented in Figure 8.6 for the contact joints, from now on referred to as "linear" and "sub-

linear" cases. Assumed parameters are $\Delta L = 60\,\text{mm}$, $L = 12\Delta L$, $f_0 = 105\,\text{mm}$ ($L_s \simeq 0.94\,L$), $m = 0.1515\,\text{kg/m}$ and $K = 2.19\,\text{N/mm}$, which are compatible with the prototypes considered in the following Section 8.4. The initial prestressing force of the tendon is $N_0 = 13.00\,\text{N}$ for the linear case and $N_0 = 15.35\,\text{N}$ for its sub-linear counterpart, in order to have the same value of full draw height and weight. For this example, the arrow mass is $M_a = 0.0096\,\text{kg}$.

The time-dependent system of algebraic equations (8.2.6) and conditions (8.2.3), has been numerically solved using the function `fsolve` implemented in Matlab®, which is based on the Levenberg-Marquardt [58] and trust-region [59] methods de-

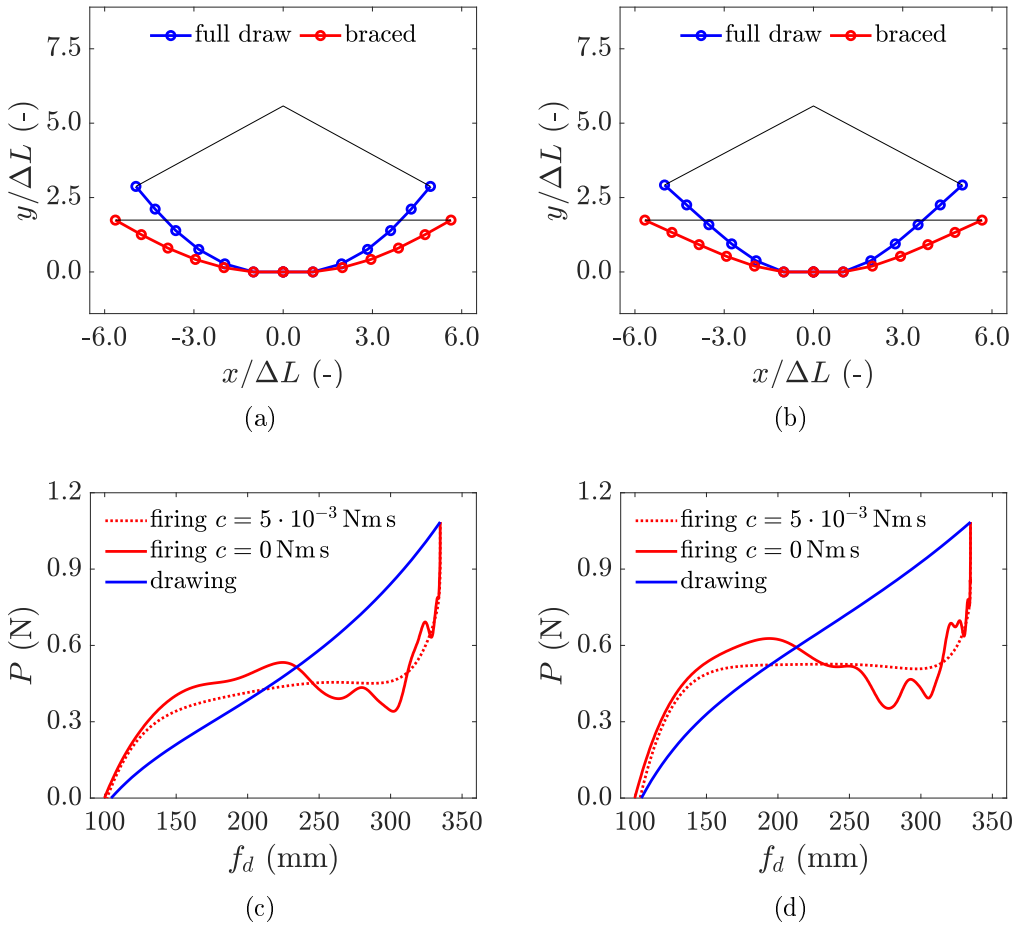

Figure 8.7. Dimensionless shapes of flex-ten bow in the braced state and in the fully-drawn configuration for the (a) linear and (b) sub-linear design. Response curves for the drawing and firing stages for the (c) linear and (d) sub-linear cases. The two different firing scenarios correspond to damping coefficients $c = 0$ or $c = 5 \cdot 10^{-3}\,\text{Ns}$.

veloped from nonlinear least-squares algorithms. The time-depending aspect has been computed according to a finite difference explicit Euler method, with a time step equal to $\Delta t = 0.0002\,\mathrm{s}$. Since we are interested in the firing of the arrow, we assume that the *impact* that occurs when the string achieves the straight configuration has consequences only on the vibration and dissipation in the limbs; in other words, we suppose that, at the same instant, the arrow detaches from the string and is no more affected by the dynamics of the bow.

Figures 8.7(a) and 8.7(b) show the braced and fully-drawn shape for the linear and sub-linear cases, respectively, obtained for the quasi-static case. The corresponding response curves are indicated in Figures 8.7(c) and 8.7(d). The quasi-static drawing curve, reported in blue solid line, is juxtaposed to those corresponding to two different firing scenarios, associated with the conditions in which the damping coefficient c is either null (red solid line) or equal to $5 \cdot 10^{-3}\,\mathrm{N\,m\,s}$ (red dotted line), respectively.

Observe that the drawing curve is much more "concave" in the sub-linear than in the linear case, corresponding to a higher stored energy for the same force at full draw. Although more effort is needed to draw the bow in the sub-linear case, the ratio between the energy spent for drawing and the product between the weight of the bow and the full draw height is bigger, so that small fluctuations of the draw while aiming affect less the exit speed of the arrow. Indeed, the difference in the slope of the curves measures the variation in stored energy for fluctuation of the drawing force: the smaller it is, the easier is the aiming process for the archer (more user-friendly bow).

Let E_d denote the stored elastic energy in the bow and E_f the kinetic energy of the fired arrow with exit speed v_e, and let $\bar{f}_d$ and $\bar{P}$ represent the full draw and weight, respectively, then the efficiency of the bow is measured by the ratios E_f/E_d and $E_d/(\bar{f}\bar{P})$, and by the value of the exit speed v_e. Referring to Figure 8.7(c) or 8.7(d), one has

$$E_d = \int_{f_0}^{\bar{f}_d} P(f_d)\, df_d\,, \quad \text{along the blue curve of drawing}\,, \tag{8.3.9}$$

$$E_f = -\int_{\bar{f}_d}^{f_d(P=0)} P(f_d)\, df_d = \frac{1}{2} M {v_e}^2\,, \quad \text{along the red curve of firing}\,, \tag{8.3.10}$$

where f_0 is the brace height. Note that the value of the draw f_d, for which the arrow detaches from the string when fired, i.e., the value $f_d(P=0)$ indicated in the integral of (8.3.10), may be slightly different from f_0 because the limb deflection is influenced by the inertial effects due to its own mass. For the case at hand, numerical data about the efficiency of flex-ten bows are collected in Table 8.1.

Table 8.1. Performance of the flex-ten bow, measured by the energetic ratios E_f/E_d and $E_d/(\bar{f}_d\bar{P})$ and by the exit speed v_e of the arrow.

prototype	linear		sub-linear	
damping c	$0\,\mathrm{N\,m\,s}$	$5\cdot10^{-3}\,\mathrm{N\,m\,s}$	$0\,\mathrm{N\,m\,s}$	$5\cdot10^{-3}\,\mathrm{N\,m\,s}$
E_f/E_d (–)	0.88	0.83	0.84	0.81
$E_d/(\bar{f}_d\bar{P})$ (–)	0.31	0.31	0.38	0.38
v_e (m/s)	4.55	4.42	4.92	4.85

Observe that the sub-linear case always provides a higher exit speed v_e , about 7.6% higher than the linear case with no dissipation and 8.8% higher when damping is considered. Results confirm that the linear prototype requires less work by the archer (18.7% lower than the sub-linear case), but there is a negative effect on both v_e and the ratio $E_d/(\bar{f}_d\bar{P})$. The linear bow is more efficient in terms of the ratio E_f/E_d when no dissipation is present, but the difference strongly decreases when damping comes into play, as it passes from 5.1% to 2.4% (less than one half) with respect to the sub-linear prototype. This is due to the fact that, in the sub-linear design, as shown in Figure 8.7(b), the deformation mainly concentrates at the first joint (the one that connects the limb with the handle). Hence, dissipation is minimized, at least with respect to the model of damping assumed here. On the contrary, in the linear prototype the curvature is more uniform along the limbs, as indicated in Figure 8.7(a).

Figure 8.8 reports the curves for the arrow exit speed v_e and for the ratio E_f/E_d as a function of the arrow mass M_a for various values of the mass per unit length m of the limbs. As expected, Figure 8.8 shows that the lighter the limbs, the faster the arrow and the higher the efficiency, regardless of the arrow mass. On the other hand, both bows show a similar trend for the response in terms of arrow speed as a function of the arrow mass. In the linear bow the exit speed is lower than in the other case (Figure 8.8(a)), but the efficiency (Figure 8.8(b)) is comparable to that of a sub-linear prototype (Figure 8.8(d)). On the contrary, the sub-linear bow excels in exit speed (Figure 8.8(c)), but the efficiency is poor if the mass of the limbs is high.

In conclusion, the sub-linear bow results to be the most performing, although it requires more drawing work with respect to the other case.

8.3.4 Comparison with a traditional bow

For the sake of comparison, we consider now the case of a bow made of a single stave of linear elastic material, whose width is functionally graded in such a way

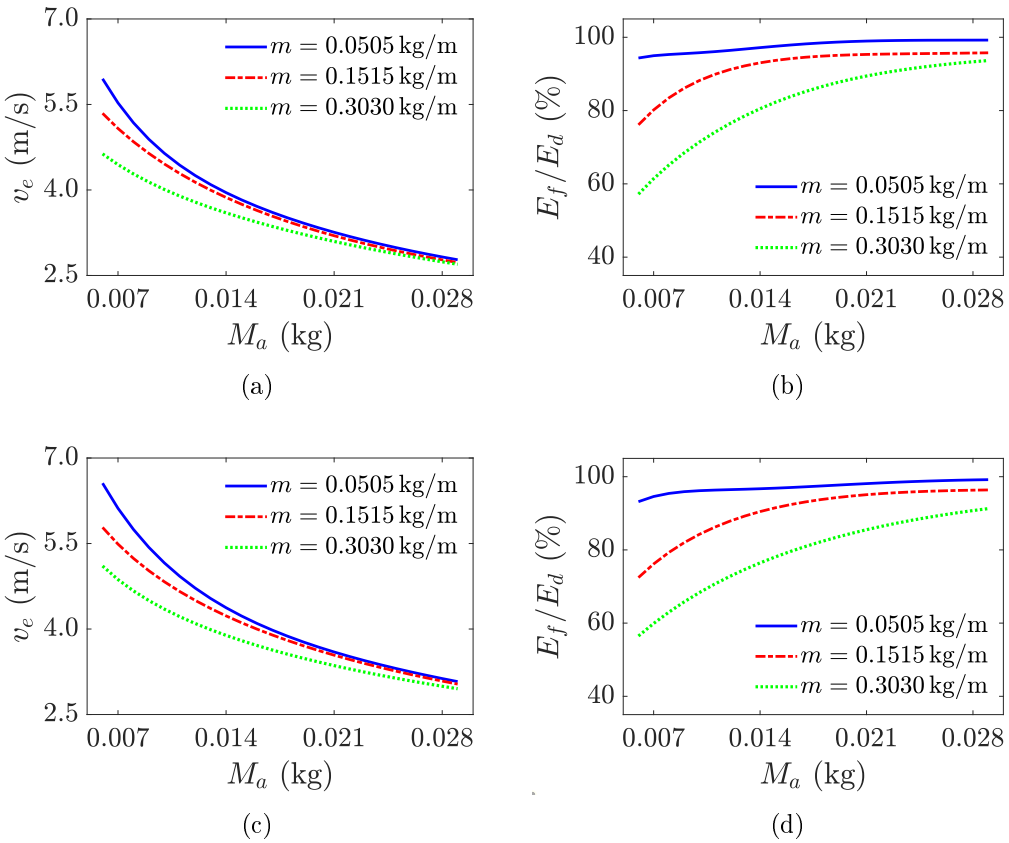

Figure 8.8. Efficiency of the flex-ten bow with variable arrow mass M_a and for different values of the limb mass per unit length m: (a) arrow exit speed v_e and (b) efficiency ratio E_f/E_d for the linear case; graphs plotted in (c) and (d) correspond to the sub-linear case. Condition with no dissipation.

that the limb deforms according to an arc of circle. This case, referred to as the "circular" bow, is suggested in [144], where it is stated that practically all bowyers construct their (self) bows so that they bend in such a shape, corresponding to a homogenous stress along the limb consequent to the constant curvature.

Although the cross sectional area of the limbs is in theory variable, in order to grade the stiffness and obtain the circular bend, their mass per unit length has been considered constant in order to facilitate the comparisons with the flex-ten bow; moreover, the limbs have been discretized into six segments, as for the flex-ten bow, but now they are coupled by "local" spring-hinges whose stiffness is constant at each joint but varies along the limb, from joint to joint, in order to approximate the circular deformed shape with a polygonal line.

The response of the circular bow is detailed in Figure 8.9, which is the coun-

terpart of Figure 8.7. In particular, Figure 8.9(a) displays the bow in the braced and fully-drawn configuration. Figure 8.9(b) shows the static drawing curve in blue color and the firing scenario corresponding to no dissipation in red color, for $M_a = 0.0096\,\mathrm{kg}$ and $m = 0.1515\,\mathrm{kg/m}$, while the full draw height and weight, as well as the brace height, are the same as for the flex-ten bow.

Figures 8.9(c) and 8.9(d) qualitatively compare the response of the circular bow with that of the flex-ten bow, for the linear and sub-linear cases, respectively. Corresponding quantitative data are collected in Table 8.2. On the one hand, the circular (traditional) bow is much less efficient than the flex-ten linear bow, as

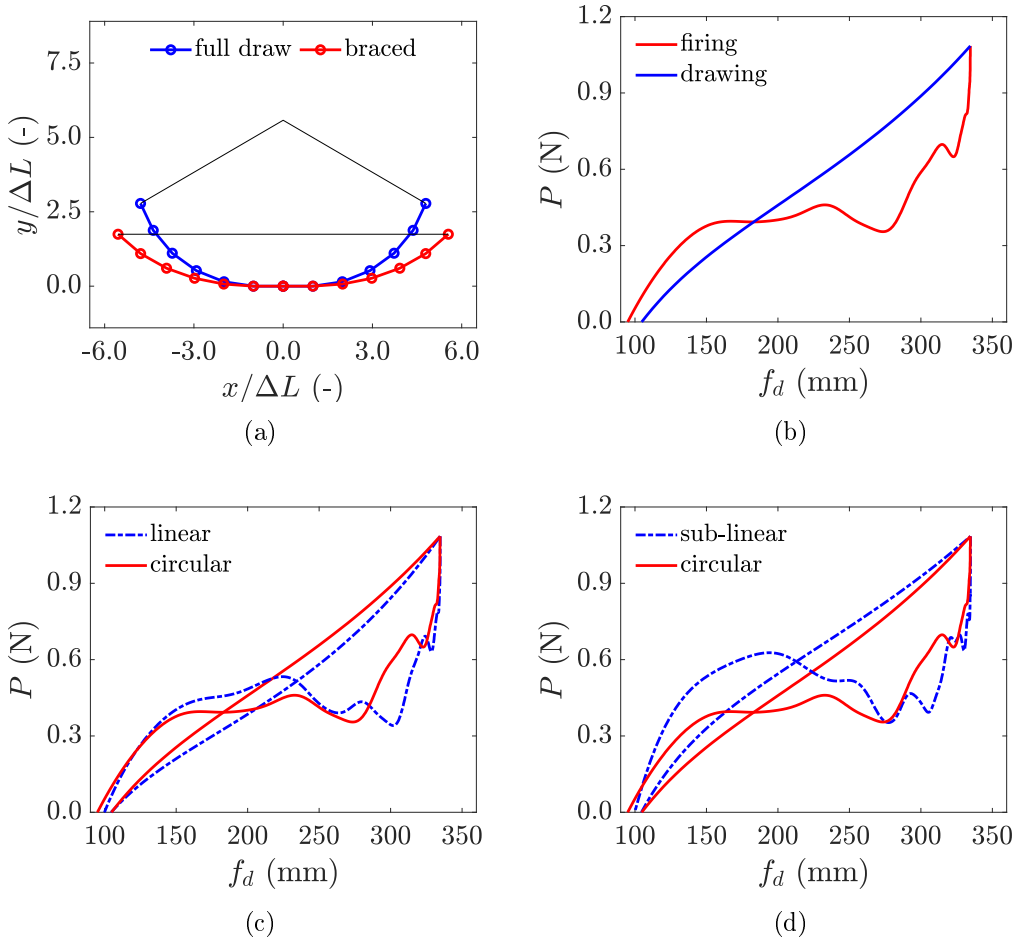

Figure 8.9. Behavior of the single stave circular bow. (a) Dimensionless shapes in the braced and fully-drawn configurations; (b) response curves for drawing and firing, for $c = 0$; (c) and (d) response curves compared with the flex-ten bow, linear and sub-linear case, respectively, for $c = 0$.

Table 8.2. Performance of the flex-ten bow, measured by the energetic ratios E_f/E_d and $E_d/(\bar{f}_d\bar{P})$ and by the exit speed v_e of the arrow, compared with the traditional circular-bent bow (case with no dissipation).

prototype	linear	sub-linear	circular
E_f/E_d (–)	0.88	0.84	0.79
$E_d/(\bar{f}_d\bar{P})$ (–)	0.31	0.38	0.34
v_e (m/s)	4.55	4.92	4.53

measured by the ratio E_f/E_d, but the exit speed is comparable; on the other hand, the flex-ten sub-linear bow is still more efficient than the circular bow, but it is much more effective in exit speed. Considering the ratio $E_d/(\bar{f}_d\bar{P})$, the linear bow is less user-friendly than the circular bow, which is also less user-friendly than the sub-linear bow.

Figure 8.10 reports the curves for the arrow exit speed v_e and for the efficiency ratio E_f/E_d as a function of the arrow mass M_a for various values of the mass per unit length m of the limbs, comparing the theoretical results obtained for the circular (traditional) bow with those for flex-ten bows. The sub-linear prototype always excels in exit speed v_e, regardless the arrow mass and the limb mass. The linear bow performs worse than the circular bow for the lighter limbs, becoming more effective for light-weighted arrows when the limb mass increases. Passing to the efficiency, evaluating both the actual value of E_f/E_d and the trend as the arrow mass M_a varies, the traditional bow worsen its performance as the limb mass increases and passes from being the more performing bow to being the less performing one, at least in the range of M_a here considered. Comparing the two flex-ten bows, the linear prototype is the best.

Of course the flex-ten bow can be further optimized, but this comparison shows its potentialities. In particular, a sub-linear constitutive relation for the internal lever arm a_i as a function of the relative segmental rotation $\Delta\varphi_i$ is more efficient in terms of arrow exit speed than the traditional linear elastic relationship, describing the deformation of the limbs of a traditional self bow. On the other hand, the linear flex-ten bow excels in terms of efficiency ratio.

8.3.5 Influence of number of segments

Let us now consider the influence of the number of segments on the response of the flex-ten bow. For brevity, only the linear prototype is analyzed. The geometric and constitutive parameters, with the only exception of the number of segments, are the same as in the previous Section 8.3.3: total length of the bow $L = 720\,\text{mm}$, brace

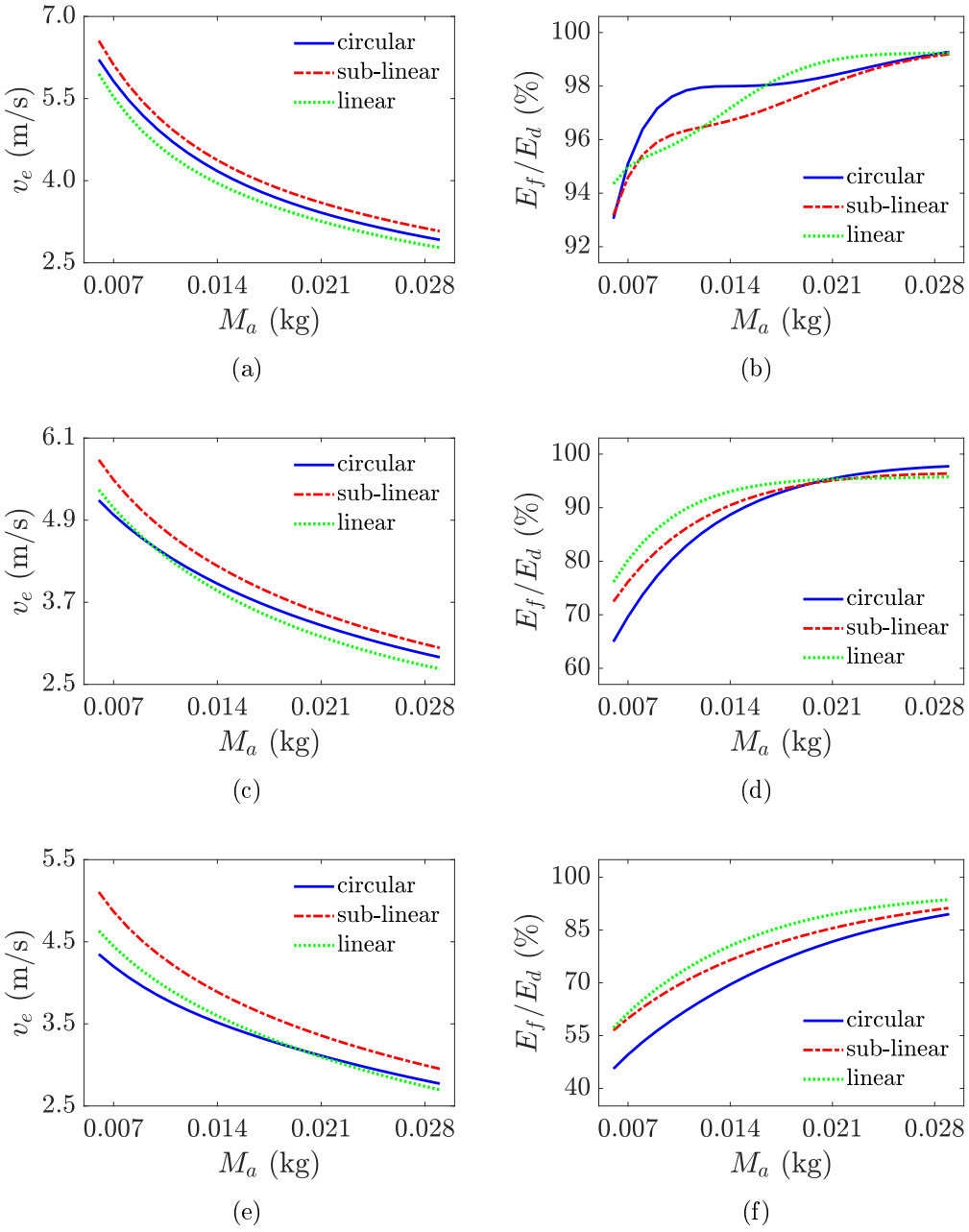

Figure 8.10. Efficiency of the flex-ten bow, with variable arrow mass M_a and for different values of the limb mass per unit length m, with respect to a single stave circular bow: (a) arrow exit speed v_e and (b) efficiency ratio E_f/E_d for $m = 0.0505\,\mathrm{kg/m}$; graphs plotted in (c) and (d) correspond to $m = 0.1515\,\mathrm{kg/m}$; graphs plotted in (e) and (f) correspond to $m = 0.3030\,\mathrm{kg/m}$. Condition with no dissipation.

height $f_0 = 105\,\text{mm}$ ($L_s \simeq 0.94\,L$), limb mass per unit length $m = 0.1515\,\text{kg/m}$, cable equivalent axial stiffness $K = 2.19\,\text{N/mm}$, and initial prestress $N_0 = 13\,\text{N}$; arrow mass $M_a = 0.0096\,\text{kg}$.

Following Figure 8.5(b), let again n represent the number of segments for the half bow. Figures 8.11(a) and 8.11(b) display the trend of the drawing force P as a function of the draw f_d, comparing the case of $n = 6$ (assumed as standard) with the case of $n = 49$ and $n = 9$, respectively. Figures 8.11(c) and 8.11(d) repeat the comparison in terms of deformed shape of the bow both in the strung and in the fully-drawn states. The slope of the linear relation of Figure 8.6(a) is adapted to the number of segments in order to have the same full draw height $\bar{f}_d$ and weight $\bar{P}$ as in Section 8.3.3: $\mathrm{d}a_i/\mathrm{d}\Delta\varphi_i = 48.4\,\text{mm/rad}$ for $n = 6$; $\mathrm{d}a_i/\mathrm{d}\Delta\varphi_i = 79.4\,\text{mm/rad}$ for $n = 9$, and $\mathrm{d}a_i/\mathrm{d}\Delta\varphi_i = 496.1\,\text{mm/rad}$ for $n = 49$.

The number of segments minimally affects the drawing curves, which almost perfectly overlap in Figures 8.11(a) and 8.11(b). Concerning the deformation of the limb, the configuration $n = 6$ is almost perfectly equivalent to the configuration $n = 9$, as per Figure 8.11(d). On the other hand, this is not the case of $n = 49$. This case well approximates the continuous nonlocal elastica discussed in Section 3.2.4, approaching a continuous deformed shape that appreciably differs from the polygonal line corresponding $n = 6$ (Figure 8.11(c)), although the drawing forces coincide in practice.

The cases reputed of practical interest for the fabrication of flex-ten bows are those corresponding to the number of segments comprised between 6 and 9 for the half bow, i.e., a total number of segments comprised between $5+5$ and $8+8$ for the limbs plus the handle, which has twice the length of the segments. For $n = 6$ and $n = 9$, Figures 8.11(e) and 8.11(f) compare both the static and dynamic response curves, considering $c = 0$ (no dissipations) or $c = 5 \cdot 10^{-3}\,\text{Nm s}$, respectively. The trend is very similar, although the curves do not perfectly overlap. Anyway, the difference in terms of drawing work is 0.6%, passing from $E_d = 113.3\,\text{Nmm}$ for $n = 9$ to $E_d = 112.6\,\text{Nmm}$ for $n = 6$; the energy released to the arrow passes from $E_f = 97.9\,\text{Nmm}$ for $n = 9$ to $E_f = 99.3\,\text{Nmm}$ for $n = 6$, when $c = 0$; and from $E_f = 94.7\,\text{Nmm}$ for $n = 9$ to $E_f = 93.9\,\text{Nmm}$ for $n = 6$, when $c = 5 \cdot 10^{-3}\,\text{Nm s}$, leading to a difference of 1.4% and 0.9% respectively. The exit speeds v_e coincide, up to the first decimal digit, when passing from $n = 6$ to $n = 9$, both for the damped (4.4 m/s) and for the undamped (4.5 m/s) firing scenario.

For the sake of comparison, we also include the case in which the deformation of the limbs is approximated via the shape function (4.2.18), which reduces the problem to the optimization of the single degree of freedom $\varphi_0(t)$, i.e., the rotation at the tip of the limb. For the linear bow, Figure 8.12 reports the comparison between the model with $n = 6$ and the SDOF approximation via shape function. The drawing phase almost perfectly coincides for the two cases (Figure 8.12(a)), but differences arise in the firing stage (case $c = 0$), as the shape function prescribes

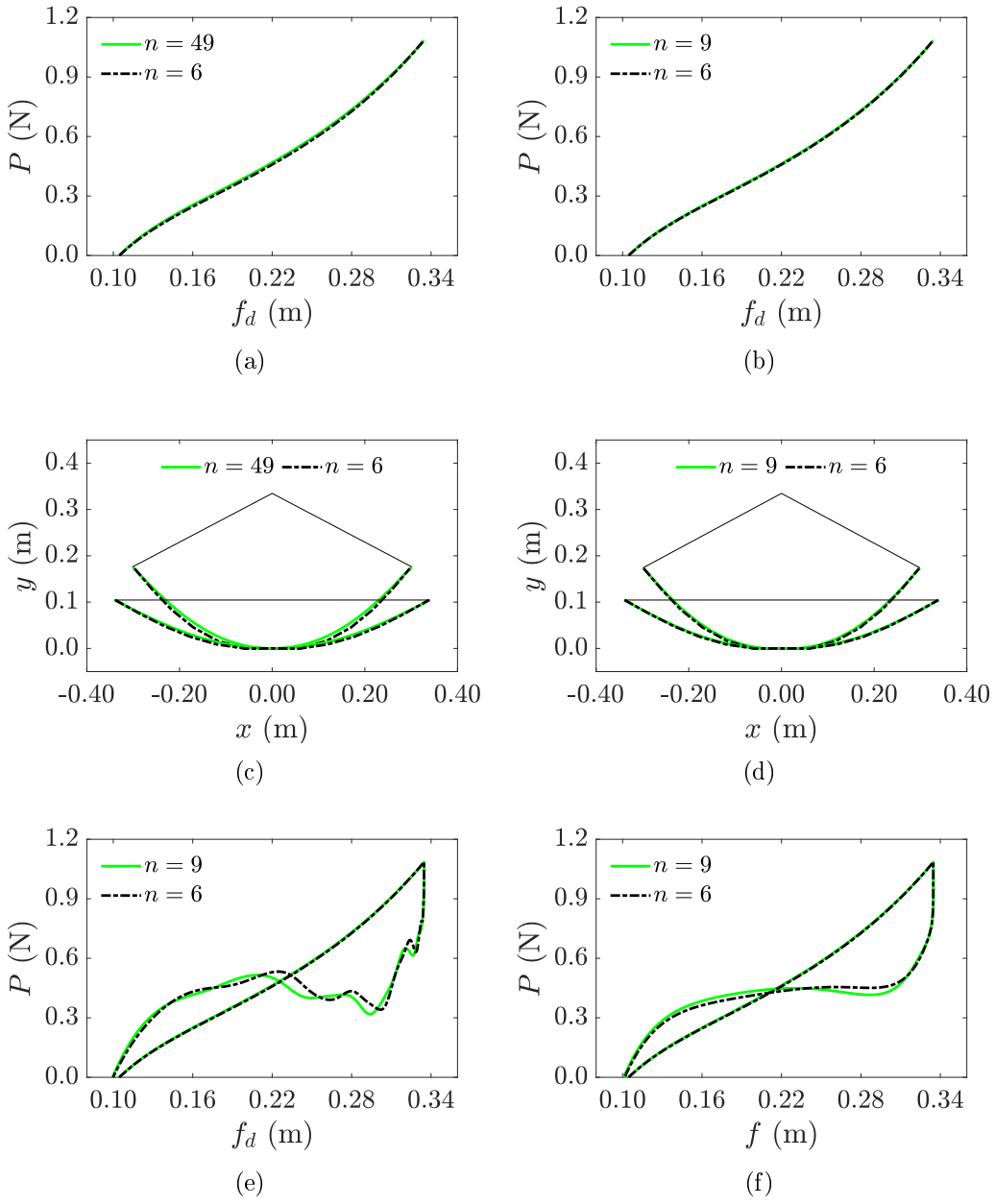

Figure 8.11. Influence of the number of segments (linear case). Comparisons in terms of: (a) force-draw curve for $n = 49$ and $n = 6$; (b) corresponding plots for $n = 9$ and $n = 6$; (c) bow in the braced and fully-drawn state for $n = 49$ and $n = 6$; (d) corresponding plots for $n = 9$ and $n = 6$; (e) drawing and arrow firing for $n = 9$ and $n = 6$, $M_a = 0.0096\,\mathrm{kg}$ and $c = 0$; (f) corresponding plots for $c = 5 \cdot 10^{-3}\,\mathrm{Nm\,s}$.

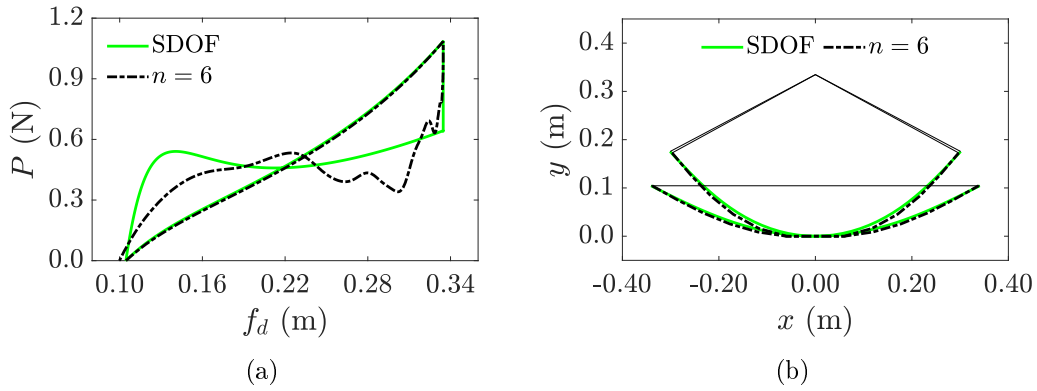

Figure 8.12. Comparison between the model with $n = 6$ (linear case) and the SDOF approximation via shape function for the deformation of the limbs: (a) force-draw and firing curves; (b) bow in the braced and fully-drawn state. Adopted parameters are $M_a = 0.0096\,\text{kg}$ and $c = 0$.

the deformed shape of the limbs and accounts only for the first mode of vibration. Similar arguments hold to interpret the differences for the bow in the braced and fully-drawn state (Figure 8.12(b)), with the additional consideration that the description via shape function approaches the continuum limit.

In conclusion, the differences in the response consequent to the number of segments is negligible, in practice, when this is comprised between 6 and 9 for the half bow. The configuration with $n = 6$, assumed as a paradigmatic example, will be prototyped and tested in the following.

8.4 Prototyping and testing

Two different types of flex-ten bows are now prototyped and tested, corresponding to the linear and sub-linear cases analyzed so far. Theoretical results are compared with the experimental findings.

8.4.1 Manufacturing of the prototypes

The prototypes were manufactured in polylactide (PLA) with the 3D-printing deposition method. Typical segments for the limbs and the handle are represented in Figure 8.13. The segments have been cut, carved and grid infilled (20% space density, covered by three external solid layers) in order to remove unnecessary

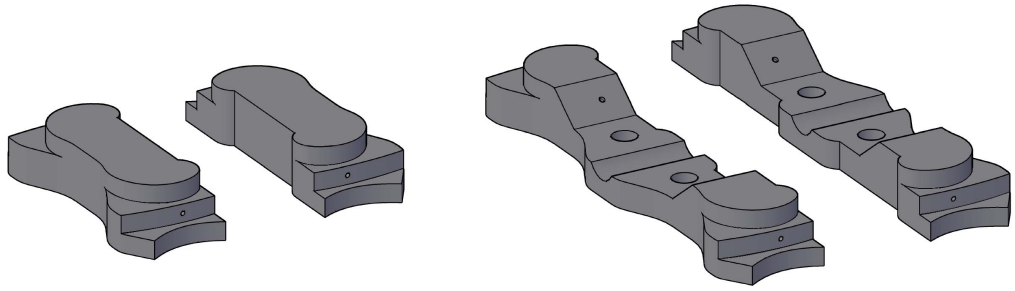

(a) (b)

Figure 8.13. Geometry of the flex-ten bow. 3D-CAD drawing of (a) the typical segment (3/4 view of belly side and back side) and of (b) the handle (3/4 view of belly side and back side).

material and diminish the weight of the bow. As a result, the mass per unit length is $m = 0.1515\,\mathrm{kg/m}$. The typical segmental length is 60 mm. The handle has twice the length of the segments (120 mm) and a groove has been made in it (Figure 8.13(b)), so to realize an arrow shelf and avoid the problems associated with the *archer's paradox* [138,139], i.e., the choice of the good flexural compliance for the arrow. The holes of the handle are used to pin it in a fixed position during the experimental tests.

The two prototypes clearly differ only for what concerns the moment-rotation constitutive equation at the contact hinges, consequent to either a linear or a sub-linear a_i vs. $\Delta\varphi_i$ relationship of the type indicated in Figures 8.6(a) and 8.6(c), as already discussed in Section 8.3.2. The overall geometry of the bow is the same for the two prototypes, as the only difference in the segments consists in the shape of the conjugate-profile contact surfaces, corresponding to the pitch lines. Figure 8.14(a) displays the assembled and braced flex-ten bow (here the linear prototype) with a bowstring length of 685 mm (tolerance ± 1 mm). Consequently, the brace height ranges from to 90 mm to 100 mm, depending upon the stringing process and upon the different bent shape, for the linear and sub-linear prototypes, respectively.

The limbs of both the prototyped bows are composed of five segments, coupled together by a polyamide 6.6 wire of diameter 0.8 mm; springs with elastic constant 5.45 N/mm are added in series. Consequently, the effective axial stiffness of the tendon is 2.19 N/mm. The disassembled components of the bow (the segments, the handle, the string, the series springs, the prestressing cable in two portions and the clamps for anchoring) are shown in Figure 8.14(b). Thanks to this modular design, the disassembled bow perfectly fits in a minimal prismatic box for easy transportation, as indicated in Figure 8.14(c).

(a)

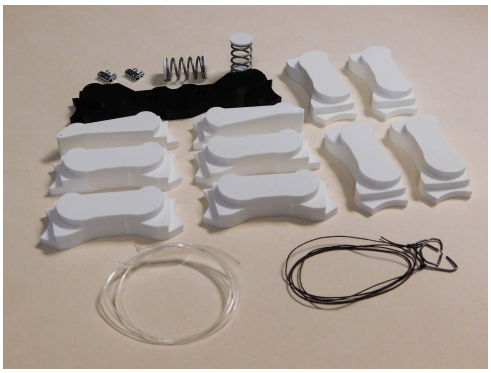

(b)

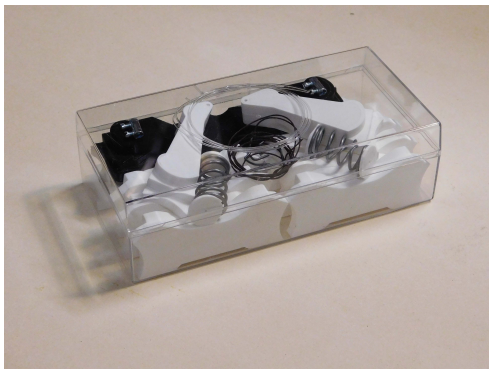

(c)

Figure 8.14. Prototype of the flex-ten bow (linear case) manufactured via 3D printing. (a) Assembled and braced bow; (b) disassembled components of the bow (segments, handle, string, clamps, cables and springs); (c) the disassembled bow perfectly fits in a small prismatic box for transportation.

8.4.2 Experiments

The prototypes of the flex-ten bows reproduce the cases theoretically considered in Section 8.3.3, the only difference being the cable prestress, which was experimentally measured from the shortening of the series spring with a Vernier caliper. The measured prestress is either $N_0 = 9.8\,\mathrm{N}$ or $N_0 = 16.4\,\mathrm{N}$ for the linear bow, and either $N_0 = 7.1\,\mathrm{N}$ or $N_0 = 17.2\,\mathrm{N}$ for the sub-linear case. The same value of prestress is used for both limbs, each one of which has a dedicated tendon.

The prototypes have been tested both in static and dynamic conditions. The setup for the static tests is schematically represented in Figure 8.15(a). The bow is kept in position at the handle, while the draw and the drawing force are measured by a ruler and a spring dynamometer with a precision of $\pm 0.05\,\mathrm{N}$. The test was performed in the vertical plane, with the drawing force opposite to gravity, so that one has to add to the work of external forces the contribution of self-weight ΔW_g, antagonistic to drawing, which reads

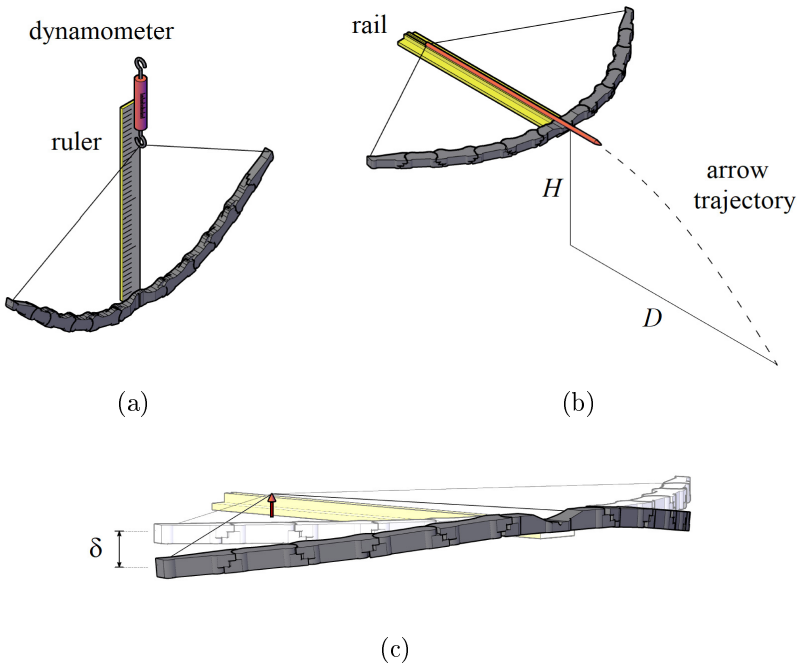

Figure 8.15. Schematic representation of the experimental setup: (a) static force-draw measurement with a ruler and a spring dynamometer; (b) measurement of the arrow exit speed from range, with a crossbow-like apparatus; (c) parasitic out-of-plane deflection of the cross-bow due to self-weight.

$$\Delta W_g = -mg\Delta L \sum_{i=1}^{n} \left[\left(\sum_{j=1}^{i} \Delta L \sin\varphi_j \right) - \frac{\Delta L}{2} \sin\varphi_i \right], \tag{8.4.11}$$

from the unstrung configuration $\varphi_i = 0$, for $i = 1 \dots n$, to the actual drawn state. Here, $mg\Delta L$ is the weight of each segment of length ΔL, and g is the gravity acceleration. Consequently, (8.2.2) becomes

$$\delta\,\Delta W = \frac{P(f_d)}{2}\,\delta f_d + \delta\,\Delta W_g\,. \tag{8.4.12}$$

In conclusion, the static response is governed by

$$N\big(a_i - a_{i-1}\big) - \frac{P\,\Delta L}{2\tan\vartheta}\sin\varphi_i + \frac{P\,\Delta L}{2}\cos\varphi_i - \Big(n - i + \frac{1}{2}\Big) mg\Delta L^2 \cos\varphi_i = 0\ , \tag{8.4.13}$$

for $i = 1 \dots n$. This is the counterpart of equation (8.2.6) when the bow is placed in vertical position and quasi-statically drawn, as in Figure 8.15(a).

Experimental results are collected in Figures 8.16(a) and 8.16(b), respectively for the linear and sub-linear prototypes, with reference to the aforementioned two values of initial prestress, and compared with the theoretical predictions. Despite measurement errors and manufacturing tolerances, the experimental points (black dots) well overlap with the theoretical trend (magenta solid curve). In general, the theory slightly overestimates the experimental value. This is probably due to construction tolerances and the approximations of the model, in particular the hypothesis of perfectly unbonded tendon.

The setup for the dynamic testing is represented in Figure 8.15(b). The bow

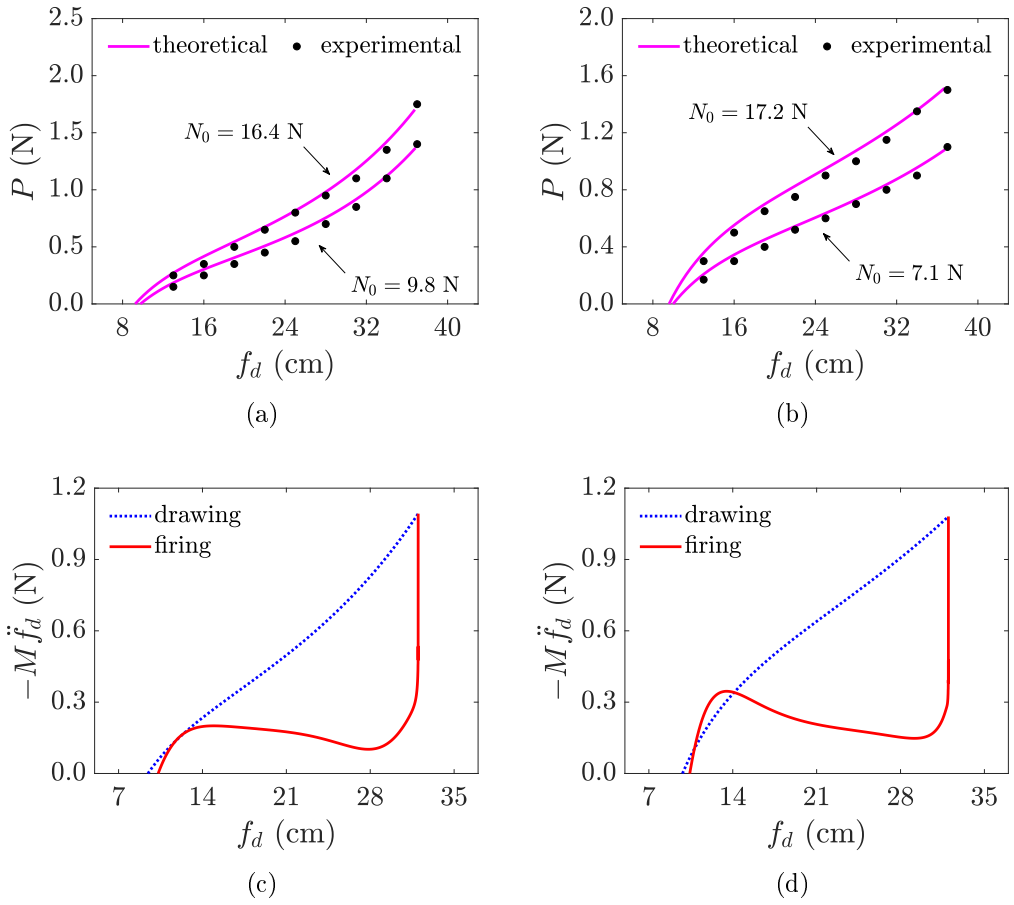

Figure 8.16. Experiments on the flex-ten bow: comparison between the theoretical and experimental results for quasi-static drawing for (a) the linear and (b) the sub-linear prototypes; theoretical response of the bow in the crossbow-like apparatus for (c) the linear and (d) the sub-linear cases, considering a tendon prestress $N_0 = 16.4\,\mathrm{N}$ and $N_0 = 17.2\,\mathrm{N}$, respectively.

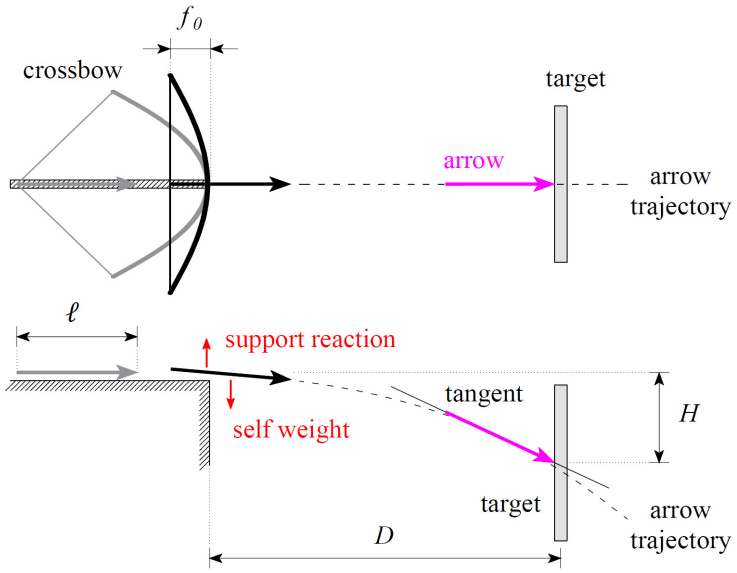

Figure 8.17. Schematic representation of the arrow flight: after detachment from the string, the arrow interacts with the edge of the supporting rail and rotates (upper and side views).

is placed horizontally, to rule out the effects of the self-weight on the in-plane deformation of the limbs, and fixed to a rail to guide the arrow while firing, as in a crossbow configuration. A polystyrene target, where the arrow can penetrate, was placed at a distance $D = 1.60\,\mathrm{m}$ from the crossbow-like apparatus, and the length H was measured from the point where the arrow had impacted. The arrow exit speed v_e is obtained by solving a ballistic problem, once the quantities D and H represented in Figure 8.15(b) are known.

Observe that the arrow is not a point mass and, therefore, the actual situation is that of Figure 8.17: when it detaches from the string and its center of mass moves out of the supporting rail, the arrow is subjected to the couple formed by its own weight and the contact reaction with the rail. Because of the conservation of angular momentum, the rotation increases during the flight of the arrow, until it reaches the target. However, experiments have demonstrated that the rotation is small, but one has to consider the length ℓ of the arrow, and the brace height f_0. Then, up to infinitesimal of higher order in the ration, the center of mass of the arrow travels the distance

$$\tilde{D} \simeq D - \frac{\ell}{2} + f_0\,. \tag{8.4.14}$$

Neglecting viscous drag dissipation through the air, one can write

$$\begin{cases} H = \dfrac{1}{2}\, g\, \bar{t}^{\,2} \\ \tilde{D} = v_e\, \bar{t} \end{cases} \quad \Rightarrow \quad v_e = \frac{\tilde{D}\sqrt{g}}{\sqrt{2H}}\,, \tag{8.4.15}$$

where $\bar{t}$ is the time of flight for the arrow, v_e is the exit (horizontal) speed, $g = 9.81\,\mathrm{m/s^2}$ is the gravity acceleration.

A first test for the calibration of the model was carried out for the higher values of the initial prestress, previously considered for the statics; the full draw was set equal to $\bar{f}_d = 0.32\,\mathrm{m}$, in order to achieve the same weight for both the linear and the sub-linear bows; the arrow length is $\ell = 28\,\mathrm{cm}$ and its mass $M_a = 0.002\,\mathrm{kg}$. The values $H = 0.35\,\mathrm{m}$ and $H = 0.26\,\mathrm{m}$ were obtained (mean of ten shots) for the linear and sub-linear prototypes, respectively, which correspond to $v_e = 5.9\,\mathrm{m/s}$ and $v_e = 6.8\,\mathrm{m/s}$.

The model with no dissipation provides the upper bound for the exit speeds, respectively equal to $v_e = 7.6\,\mathrm{m/s}$ for the linear bow and $v_e = 8.3\,\mathrm{m/s}$ for the sub-linear bow. There are, however, many uncertainties in the dynamic tests: the out-of-plane parasitic deflection of the limbs due to gravity; the consequent friction between the rail and the arrow; errors in the planarity for the crossbow (despite checked with spirit level); perturbations of the string at releasing; the creep of the prestressing cable, made of nylon (the bow is maintained braced for a few minutes during the tests); the neglected mass of the string; the simplifications in the ballistic problem to define the flight of the arrow. We repute that the most important contribution is that associated with the frictional contact between the arrow and the rail, because this is enhanced by the out-of-plane deflection of the limbs of the crossbow due to their self-weight, as schematically represented (not in scale) in Figure 8.15(c). The limb deformation δ presses the arrow against the rail (constraint reaction represented in Figure 8.15(c) with a red vector), so that frictional forces are greater than the value associated with the arrow weight.

In order to take into account this effect, condition (8.2.3c) shall be restated as

$$M_a\, \ddot{f}_d(t) = F_d - P(t)\,, \tag{8.4.16}$$

where, as before, P is the force on the string and F_d is the resultant of frictional forces from the contact with the rail. This force is supposed constant during firing and independent of the cable prestress N_0, because N_0, though affecting the out-of-plane stiffness of the limbs, is only mildly varying ($14 \div 19\,\mathrm{N}$ for the tests). By considering $F_d = 0.200\,\mathrm{N}$ and a coefficient $c = 5 \cdot 10^{-3}\,\mathrm{Ns}$ for viscous dissipation, the theoretical response of the bow is as displayed in Figure 8.16(c) for the linear prototype and in Figure 8.16(d) for the sub-linear prototype, corresponding to $N_0 = 16.4\,\mathrm{N}$ and $N_0 = 17.2\,\mathrm{N}$, respectively. Assuming that the arrow detaches

Table 8.3. Results of the dynamical tests in terms of arrow exit speed v_e compared with theoretical predictions for the linear and sub-linear bows. Arrow of mass 0.002 kg, fired from the crossbow with full draw $\bar{f}_d = 0.32$ m, for varying initial prestressing force N_0 .

linear prototype

prestress N_0 (N)	theoretical v_e (m/s)	experimental v_e (m/s)	error (%)
14.2	5.4	6.0	+ 10.0
16.4	5.9	5.9	+ 0.0
19.5	6.6	6.7	+ 1.5

sub-linear prototype

prestress N_0 (N)	theoretical v_e (m/s)	experimental v_e (m/s)	error (%)
14.2	6.2	6.3	+ 1.6
17.2	6.9	6.8	− 1.5
19.5	7.4	7.2	− 2.8

Table 8.4. Experimental results in terms of arrow exit speed v_e for different masses of the arrow, compared with the theoretical predictions, for the linear and sub-linear bow (full draw of 0.32 m and initial prestress $N_0 = 19.5$ N).

linear prototype

arrow mass M (kg)	theoretical v_e (m/s)	experimental v_e (m/s)	error (%)
0.0020	6.6	6.7	+ 1.5
0.0036	5.6	5.9	+ 5.1
0.0094	3.9	4.6	+ 15.2

sub-linear prototype

arrow mass M (kg)	theoretical v_e (m/s)	experimental v_e (m/s)	error (%)
0.0020	7.4	7.2	− 2.8
0.0036	6.1	6.1	+ 0.0
0.0094	4.3	4.6	+ 6.5

from the string when it is no more accelerated ($\ddot{f}_d = 0$), the theoretical exit speed v_e well agrees with the experimental finding, being the difference less than 1.5%.

Once the dissipative terms have been calibrated from the aforementioned cases, other experiments have been made while maintaining fixed the arrow mass $M_a = 0.002\,\text{kg}$ and the full draw $\bar{f}_d = 0.32\,\text{m}$, but varying the prestressing force N_0 of the tendon. The results are collected in Table 8.3 where, again, the arrow exit speed has been estimated as the mean value of ten measurements. Given all the possible uncertainties of the experimental apparatus and the simplicity of the model, the accuracy is reputed good, being the difference with the theory very small, of the order of $1 \div 2\%$, apart from the linear bow with the lowest prestress, for which it is about 10%. In all the cases, the sub-linear prototype performs better than the linear prototype.

For the sake of comparison, the most highly-prestressed bow ($N_0 = 19.5\,\text{N}$) has been tested with projectiles of increasing mass. Table 8.4 collects, for both the linear and the sub-linear prototypes, the experimental results and the theoretical

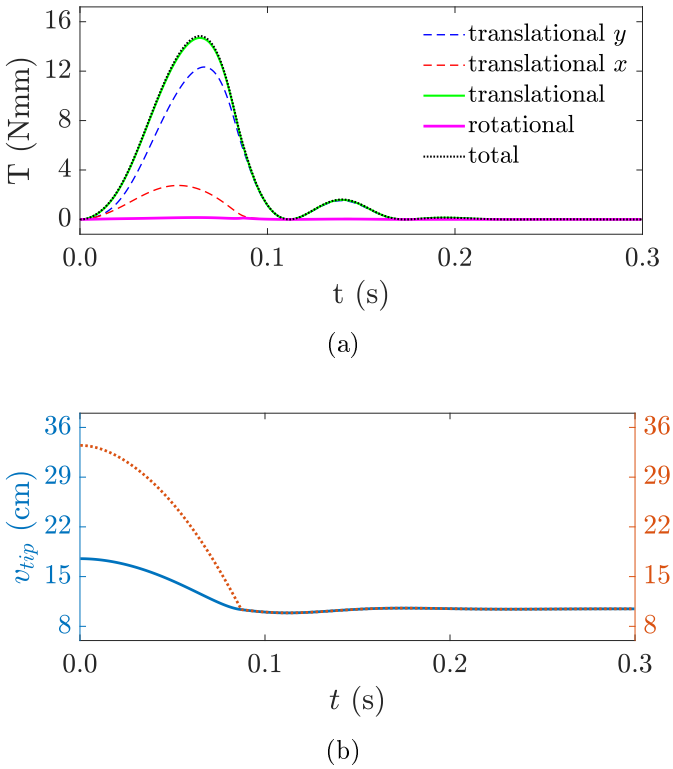

Figure 8.18. Limb of the sub-linear bow of Figure 8.7(d) during firing: (a) kinetic energy of the limb as a function of time, and (b) corresponding trend of the draw f_d and the vertical displacement v_{tip} of the tip of the limb. Case $c = 5 \cdot 10^{-3}\,\text{Nm s}$.

predictions for arrows with either mass $M_a = 0.0036\,\text{kg}$ and length $\ell = 28\,\text{cm}$, or $M_a = 0.0094\,\text{kg}$ and $\ell = 50\,\text{cm}$. To facilitate the comparison, the previous case ($M_a = 0.0020\,\text{kg}$ and $\ell = 28\,\text{cm}$) is repeated. The accuracy of the theoretical model worsens a little but it is still reputed good, taking into account the simplifications in the model and, in particular, the fact that the arrows differ not only in mass and length, but also in material (wood and plastic) and surface finishing, with diverse friction coefficients.

Remark. The model was developed by neglecting the rotary inertia of the segments. Here, we want to check *a posteriori* whether this assumption is consistent with the results computed with such a model.

Once the rotation field φ_i, for $i = 1 \dots n$, is known, the translational kinetic energy of the limb can be readily calculated from (8.2.4), while the rotational contribution is given as indicated in Footnote 2.

Figure 8.18(a) reports, as a function of time, the trend of kinetic energy during firing for the limb of the sub-linear bow of Figure 8.7(d). The various contributions to kinetic energy are highlighted: translational (x-direction, y-direction and sum of the two) and rotational contributions are plotted in the chart, together with total amount of kinetic energy. Remarkably, the translational contribution almost perfectly overlaps with the total amount of kinetic energy. For reference, Figure 8.18(b) shows the corresponding trend of the draw f_d and the vertical displacement v_{tip} of the limb tip, as a function of time, during the firing of the arrow.

From the graphs of Figure 8.18, it is clear that the rotational contribution is certainly negligible, thus justifying the assumption of overlooking it in our model.

Chapter 9

Application 2: propulsion in fluids

Many aquatic animals propel themselves by flapping their tails or tentacles. Indeed, cephalopods, fish, and aquatic mammals are extraordinary examples of how nature can find efficient strategies for propulsion in a fluid environment [151–153]. The flexural-tensegrity concept can be used to realize cable-controlled beam-like structures, capable of flapping and suitable for the specific application of propulsion in fluids.

Focusing on fish, two main modes of swimming can be identified, generally related to the shape of their body [154]. In slender-bodied fishes, such as eels, the whole lissome body tends to undulate at high amplitude in the so-called *anguilliform* mode. By contrast, fishes with a broad tail, compact body, and narrow caudal peduncle generally swim in the *carangiform* mode, oscillating only their tail [155]. These different swimming modes produce distinct vortex and wake structures in the fluid, with varying efficiencies. Experimental and computational results [154] show that carangiform swimmers are more efficient at high swimming speeds, while the anguilliform mode is preferable at low speeds.

Nature has long been a source of inspiration for artificial swimming devices. The robotic tuna [156] is a pioneering example of an efficient swimming machine but, even if the body shape and the swimming mode closely mimicked real tuna fish, the actuation was done with motors outside the testing tank. Recent advances in bio-inspired soft robotics and miniaturization [157] have enabled fish-like semi-autonomous robots for underwater exploration [158, 159]. Flexible oscillating tails for propulsion proved to be feasible also for *silent* operations of larger vessels [160]: moving fins minimize cavitation noise, which instead characterizes standard helix-based propellers. Indeed, the search for noise reduction or, more precisely, for low-level noise resembling a *biological sound*, is one of the goals of naval designers for stealth vessels and robotic rovers used for the exploration of natural environments. This context has motivated us to investigate the propulsion capacity of an

oscillating flex-ten tail in water.

Here, we explore the applicability of the flexural-tensegrity concept, declined as a snapping cantilever according to the design introduced in Chapter 6, to make active flapping devices for propulsion in fluid media, focusing on carangiform-mode oscillating tails. To characterize the fluid-structure interaction, precision experiments were performed and the thrust generated by the oscillating tail in a water tank was measured for different designs of the structure and the terminal fin, as the actuation frequency is varied. The device is simple and robust; the snapping is reversible and activated by a single cable; the actuation is a simple crank and crankshaft mechanism operated by a motor at low revs. A toy boat has been manufactured to demonstrate feasibility in the field. We believe that our innovative propulsion device, which differs from other active/passive non-snapping flappers, can find applications for swimming robots or silent vessels.

A summary of the present study is also reported in [161].

9.1 Definition of the problem

In Figure 9.1(a), a schematic diagram of the mid-surface layout of our segmented beam is presented. This adopts the design concept from Chapter 6. The tapered cantilever is composed of n hollow segments ($n = 7$ in Figure 9.1), which are held together by a pre-tensioned cable (drawn in red). The beam is clamped at the (fixed) segment $i = 2$, while the (control) segment $i = 1$ is rotated externally to trigger the snapping. The internal cavities, symmetric to the segment axis, are trapezoidal for the segments $2 \leqslant i \leqslant n-1$, and triangular at $i = 1$ and $i = n$, with the anchoring point of the cable at the vertices (points S and H, in Figure 9.1(a)). The contact surfaces are shaped according to circular pitch lines, with an equal radius for all joints; the toothed profiles prevent sliding. The cable is free to move inside the segments, constrained only by the cavity walls. This geometry makes the cable elongate by $\Lambda_i = \Lambda_i(\Delta\varphi_i)$ when segments i and $i+1$ are relatively rotated by $\Delta\varphi_i$. As a result of the rotation of all joints, the total elongation of the cable is $\Lambda = \sum_{i=1}^{n-1} \Lambda_i$, and the harnessed energy ΔU is expressed by (2.1.8).

The system is actuated by gradually rotating the segment $i = 1$, while segment $i = 2$ is kept fixed, causing the cable to move inside the cavities and elongate by Λ. Static equilibrium is attained as long as the cable passes through the pitch point of each joint $i \neq 1$ (condition of null lever arm), while Λ progressively increases (also increasing ΔU) until the equilibrium becomes unstable. At this point, Λ can be lowered by an infinitesimal perturbation, and the structure snaps, reversing its shape from configuration A to B, represented in Figure 9.1(b) together with the corresponding energy path. An orderly sequential snap of the contact joints

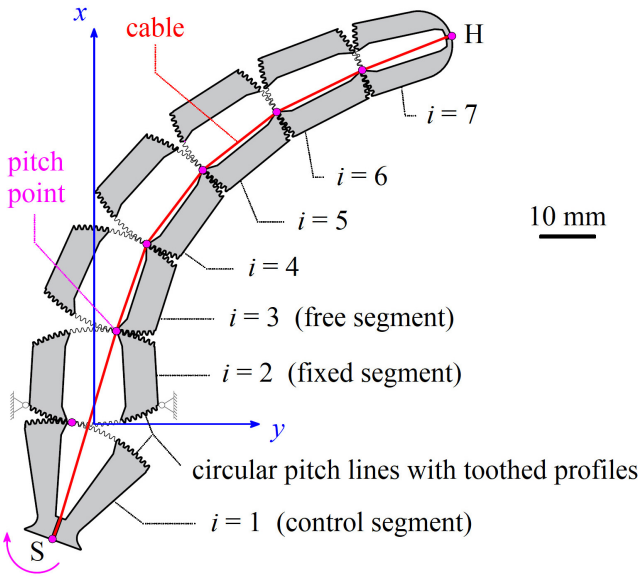

(a)

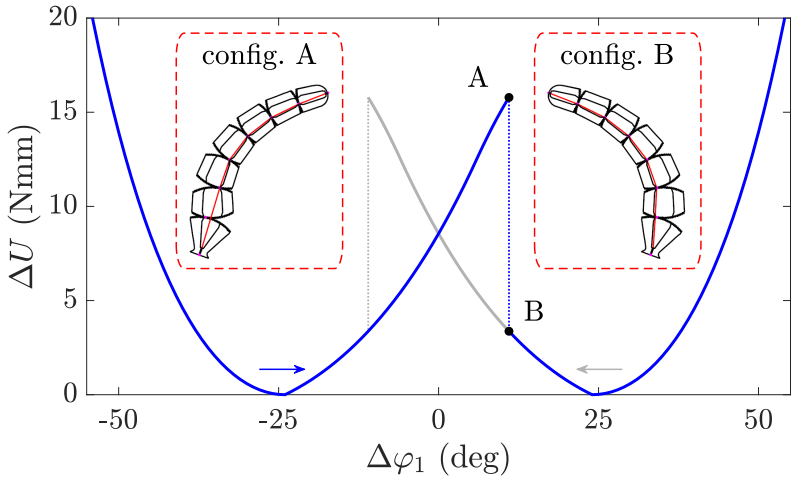

(b)

Figure 9.1. Schematic of the tail structure and its energy paths. (a) Mid-surface layout of the structured beam comprising a series of 7 segments held together by a cable (red line), which can move within the internal cavity (central non-shaded regions) and is blocked by lateral walls (shaded regions) of each element; note that the reference frame $x - y$ is now rotated with respect to the one adopted in Figure 6.2(a). (b) Quasi-static energy landscape: when moving along the path of increasing $\Delta\varphi_1$ (in blue), snapping occurs between the complementary equilibrium configurations A and B.

ensues, because the relative rotation of a pair of consecutive segments produces the snapping of the adjacent joint. Cyclically changing the sign of rotation of the control segment drives the beam to reverse its shape, alternately, acting as an oscillating tail. This oscillatory snapping motion will be interpreted for locomotion applications in fluid environments.

Fluid-structure interaction is a challenging problem to tackle predictively because of the non-trivial coupling of elastic, inertial, and fluid forces, which depend on time, geometry, and the physical properties of both fluid and structure. Developing analytical or computational models for this class of problems is particularly challenging in unsteady and turbulent flows, with added complexity in our system arising from the snap-though instability of the structure. Models for active/passive flexible/rigid flappers have been reported in the literature [162], but these usually consider simple geometries for the flapping foil, sinusoidal heave and pitch motions, small deflection theory, linearized terms, and inviscid fluid. Our system does not share the simple geometry of a rectangular plate, and it undergoes very large oscillations regulated by nonlinear contributions associated with the snap-through instability in a turbulent and dissipative medium. Therefore, the present study focuses exclusively on experiments aimed at a first quantitative characterization of the propulsive capacity.

9.2 Experimental apparatus

The photograph in Figure 9.2(a) shows the experimental apparatus, which includes a $100\times50\times50\,\mathrm{cm}^3$ water tank, whose plan dimensions are detailed in Figure 9.2(b). The samples, connected to a driving system, were immersed in the tank, while the driving system was mounted on the lab frame through a load cell to measure the reaction forces F_x and F_y (in the x and y directions reported in Figures 9.1(a) and 9.2(b)) arising from the fluid-structure interaction.

The samples (prototypes) consist of n segments of length 17.8 mm with a pitch line radius of 24.0 mm. Each segment is composed of three laser-cut layers bolted together. The two external layers (see Figure 9.3(a)) are made of *black* 6 mm-thick PMMA, shaped for the toothed contact profiles (indicated in Figure 9.1(a)); the central *white* 2 mm-thick PMMA layer is cut to form the internal cavities. The cable is a Nitinol wire of diameter 20 μm. A steel compression spring (elastic constant 5.9 N/mm) is added in series to the wire at the anchoring point to increase its compliance and measure the initial prestress N_0 from the spring shortening. The beam stiffness can be tuned by varying the prestress: the higher the prestress, the stiffer the beam. The value of $N_0 = 9.0\pm1.2\,\mathrm{N}$ (the uncertainty comes from the field measurement of the spring shorting) was found to be an appropriate compromise

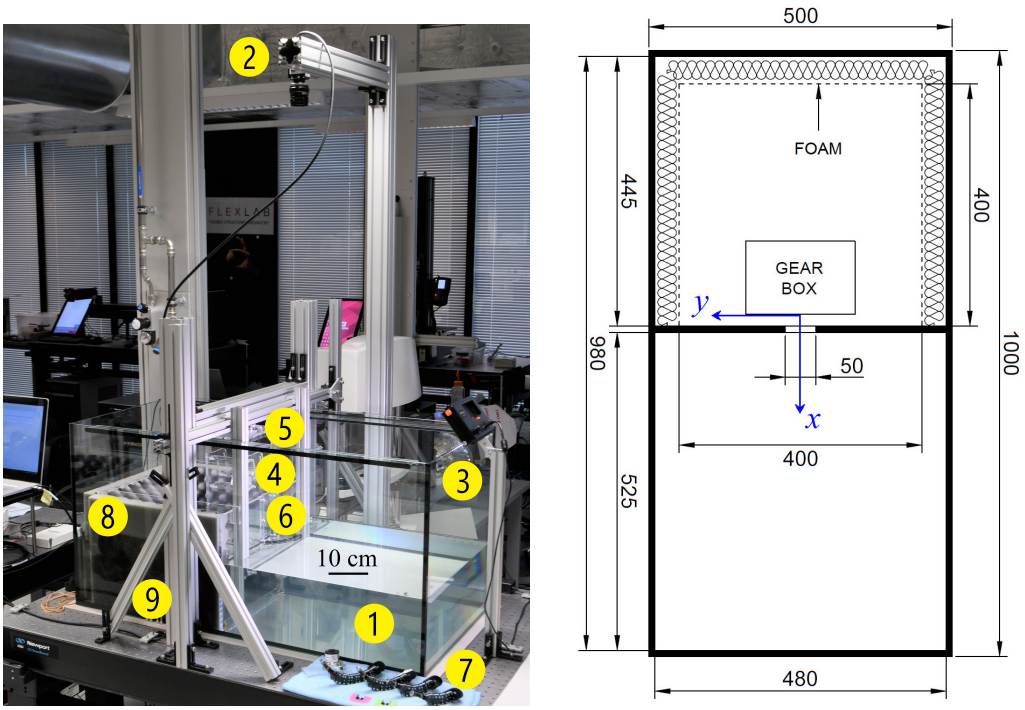

(a) (b)

Figure 9.2. Experimental setup and testing tank. (a) View of the setup with indication of: ① the testing tank, ② the camera, ③ the light, ④ the driving system, ⑤ the load sensor, ⑥ the separating barrier, ⑦ the prototypes to be tested, ⑧ the foam coating, and ⑨ the rigid lab frame. (b) Schematic plan view of the tank, with indication of the main dimensions [mm] and reference frame.

between beam stiffness, matched with viscous and inertial forces that come into play, and strength of the various components.

Each of prototypes shown in Figure 9.3(a) was equipped with a fin (see Figures 9.3(b) and 9.3(c)) to the end segment $i = n$, perpendicularly to the mid-surface. This fin was made out of PMMA (thickness 3 mm) and was effectively rigid in the considered regime of fluid loading. The trailing edge was designed convex to enhance thrust generation [163]. The connection of the fin to the end segment, $i = n$, was either clamped (Figure 9.3(b)) or pinned (Figure 9.3(c)). The pinned fins are equipped with a stop, limiting the maximum rotation angle to ϑ.

As shown in Figure 9.4, the segment $i = 2$ of the tail was bolted to a transparent PMMA box, the upper face of which was in turn connected to a load sensor (Schunk Mini40 SI-20-1), mounted on the test frame. This box housed the driving system comprising a gearbox coupled to both an electric 60 rpm 12V DC motor (Cramer 30827) and a crankshaft, supporting the crank that cyclically rotated the segment

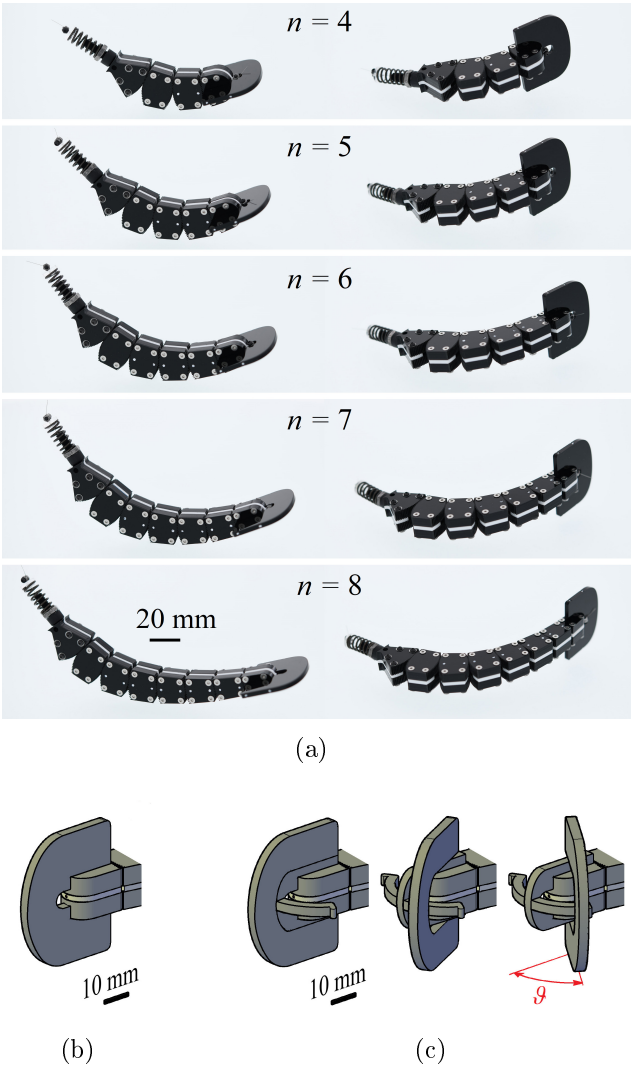

Figure 9.3. Prototypes and terminal fin. (a) Tested prototypes with variable number n of segments. Axonometric representation of the terminal fin: (b) fixed fin, clamped to the terminal segment; (c) pinned fin, in three different rotated configurations, with indication of the limit angle ϑ.

$i = 1$ of the prototype. To exemplify, in Figure 9.5, a schematic of the snapping of the tail, actuated by the crank, is presented. Multiple gears allowed us to vary the gear ratio with the motor, which ran at a constant velocity, in order to change the actuation frequency.

The tank was filled with water at room temperature ($\approx 20°$C) up to a height of 18 cm, so that the tail was fully submerged, 5 cm below the free surface. The tank was divided into two basins, as evidenced by the plan view of Figure 9.2(b). The

Figure 9.4. Detail of the driving system, mounted onto the load cell: the motor is connected through gears to a crankshaft and the snapping beam is actuated by a crank.

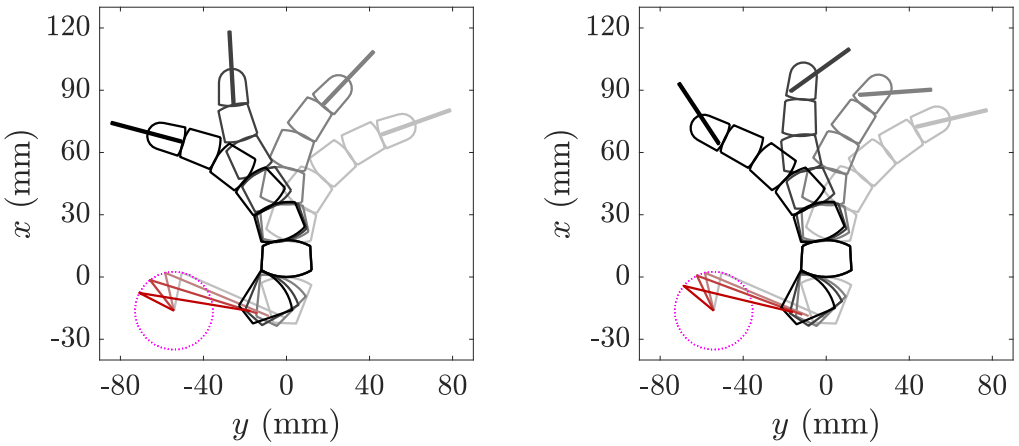

Figure 9.5. Schematic representation of the motion (actuating crank drawn in red color), reconstructed from the video recording of the experiments in water: (a) fixed fin and (b) pinned fin ($\vartheta = 45°$).

actuating system was hosted in the partition at the top of Figure 9.2(b) (left-hand side of Figure 9.2(a)), whose lateral walls were coated with foam panels to minimize contamination of the force signals due to wave reflections. The tail was placed in the partition at the bottom of Figure 9.2(b) (right-hand side of Figure 9.2(a)). The separating barrier between the upper and the bottom partitions contained an aperture where the tail passed through. In the absence of a background flow, the Reynolds number was estimated [164, 165] as $\mathrm{Re} = 2\pi\, f\, A\, L/\nu$, where L is the length of the oscillating tail from the clamped segment, A is the tip amplitude, f is the actuation frequency and $\nu = 1 \cdot 10^{-6}\,\mathrm{m}^2/\mathrm{s}$ is the kinematic viscosity of water. For the typical experimental values here concerned ($A \simeq 60\,\mathrm{mm}$, $L \simeq 90\,\mathrm{mm}$, and $f \simeq 1\,\mathrm{Hz}$), one finds $\mathrm{Re} \simeq 34000$.

During the experiments, the reaction forces F_x and F_y (x and y directions as per Figure 9.1(a)) were measured. These forces are those experienced by the driving box, connected to an external rigid frame (Figure 9.2(a)) through the load sensor. Given that the tail is integral with the box at segment $i = 2$, these forces are equivalent to the longitudinal (thrust) and transverse forces generated by the prototype oscillating in water. In particular, a parametric study was performed to investigate how the thrust is influenced by the number of segments n, the type of terminal fin (clamped or pinned), and the natural curvature of the tail at rest. During the experimental tests, the flapping of prototypes was captured by a digital camera (IDS UI-3370SE-M-GL) under controlled illumination conditions.

9.3 Characterization of the propulsion capacity

Experimental evidence on the propulsion capacity of flex-ten snapping tails is now reported. The most performing configuration was finally adopted to propel a toy boat, as proof-of-concept in the field.

9.3.1 Laboratory tests

The first tests concerned the evaluation of the "optimal" value of the prestress for the tail flapping in water. The focus was on the prototype shown in Figure 9.3(a) with $n = 7$ segments, manufactured according to the schematic of Figure 9.1(a). This design is referred to as "layout 1" (L1). Figure 9.6 compares the response of the flapping tail for three different values of initial prestressing force N_0 in the cable. In particular, Figure 9.6(a) reports the mean thrust force $\bar{F}_x$ (average value in the cycle), as a function of the actuation frequency f; the data points refer to the average of five measurements, and the corresponding standard deviations are represented as error bars. A fitted spline serves as a guide to the eye of each dataset.

As expected, the plot shows that the higher the prestress, the stiffer the beam. Consequently, a higher value of N_0 corresponds to a more powerful snapping, thus

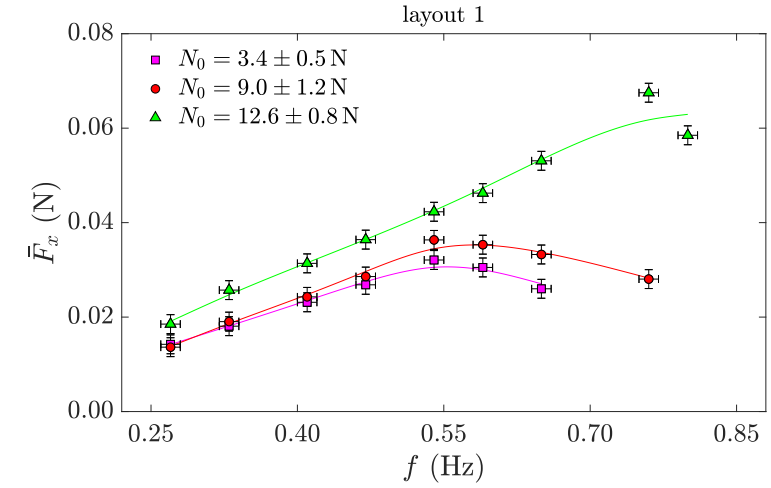

(a)

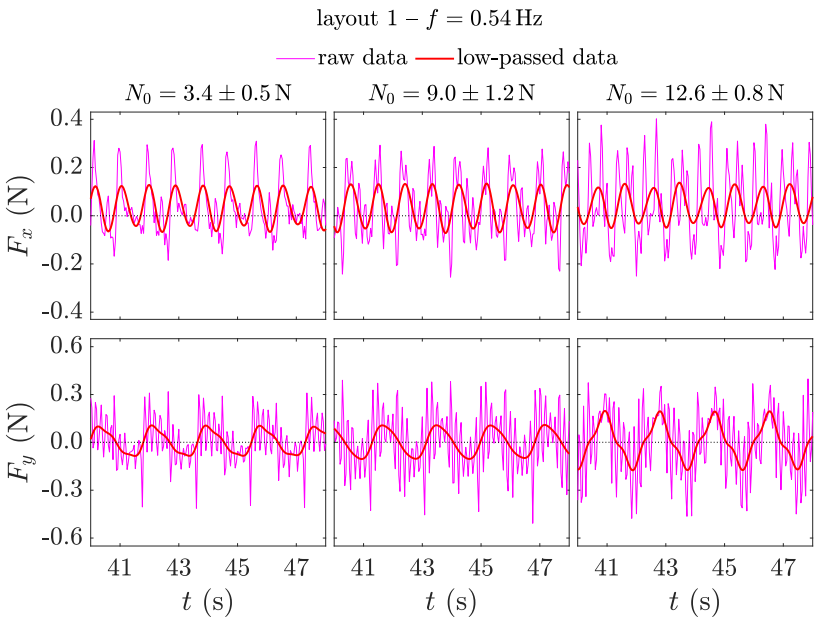

(b)

Figure 9.6. Experimental results for the snapping tail in the "layout 1" with $n = 7$ segments, equipped with a fixed fin and for different values of initial prestress N_0 in the cable: (a) mean thrust force $\bar{F}_x$ as a function of the actuation frequency f; (b) Time series of the recorded thrust (F_x) and transverse force (F_y), at the frequency $f = 0.54\,\mathrm{Hz}$.

increasing the forces F_x and F_y arising from the fluid-structure interaction. On the other hand, Figure 9.6(b) reports the time history of F_x and F_y for the three cases at the actuation frequency $f = 0.54\,\text{Hz}$.

Note that, at $f = 0.54\,\text{Hz}$, the mean thrust force $\bar{F}_x$ passes from $0.032\,\text{N}$ for $N_0 = 3.4 \pm 0.5\,\text{N}$, to $0.034\,\text{N}$ for $N_0 = 9.0 \pm 1.2\,\text{N}$, to $0.042\,\text{N}$ for $N_0 = 12.6 \pm 0.8\,\text{N}$, i.e., a difference of about -12% and $+16\%$ with respect to the case $N_0 = 9.0 \pm 1.2\,\text{N}$ (selected as standard). On the contrary, the peak value of F_y was found equal to $0.112\,\text{N}$ for $N_0 = 3.4 \pm 0.5\,\text{N}$, $0.119\,\text{N}$ for $N_0 = 9.0 \pm 1.2\,\text{N}$, and $0.208\,\text{N}$ for $N_0 = 12.6 \pm 0.8\,\text{N}$, which is a difference of about -7% and $+75\%$ with respect to the case $N_0 = 9.0 \pm 1.2\,\text{N}$. The advantage of the higher value of prestress N_0, related to the gain in generated mean thrust $\bar{F}_x$, is thus limited by the strong increase of lateral force F_y, which corresponds to a waste of energy in lateral direction and would cause undesired yaw movements in possible field applications. In addition, it was observed that the Nitinol wire is subjected to fatigue breakage after a few cycles (of the order of 10^2) for the higher prestress. For the aforementioned reasons, all the tests presented in the following adopted the value $N_0 = 9.0 \pm 1.2\,\text{N}$ for the initial prestress of the cable, which is, in our opinion, the best compromise between the stiffness of the beam, compared with viscous and inertial forces that come into play in the fluid, and the strength of the various components.

Observe that the high-frequency oscillations, which have been low-passed in the graphs of Figure 9.6(b), correspond to the noise due to reflections from the walls and interactions of the waves generated by the moving tail within the tank,

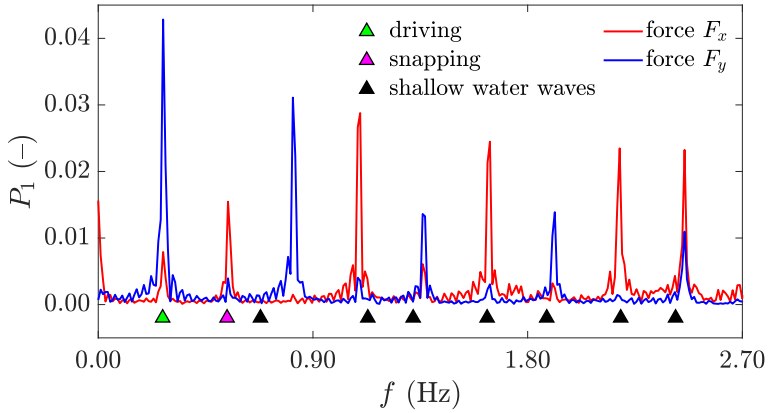

Figure 9.7. Single-sided amplitude spectrum, obtained with the Fast Fourier Transform, evidencing that the peaks in the force signal are due to the oscillations of the tail (driving frequency and snapping frequency), and to the waves generated inside the tank (shallow water waves). The plot refers to the L1 tail, with $n = 7$ segments and actuated at $f = 0.27\,\text{Hz}$, corresponding to the first experimental dot in Figure 9.6(a) for $N_0 = 9.0 \pm 1.2\,\text{N}$.

as well as to the snapping itself, which occurs like a whiplash. To ascertain this argument, at the start of the experimental campaign, the driving system was tested, running it with and without the connected tail, while measuring the force signal, in order to check whether the noise originated from the motor and gearbox of the driving system or if it was strictly related to the snapping of the tail. We also compared the single-sided amplitude spectrum, obtained with the Fast Fourier Transform (Figure 9.7) of the force signals, when the tail is moving in the fluid, with the frequencies obtained for stationary shallow water waves in inviscid fluid for the assumed tank dimensions[1]. In particular, Figure 9.7 reports the single-sided amplitude spectrum of the time history of the measured force signal for the L1 tail, with $n = 7$ segments and actuated at $f = 0.27\,\mathrm{Hz}$, corresponding to the first experimental dot in Figure 9.6(a) for $N_0 = 9.0 \pm 1.2\,\mathrm{N}$. The green and magenta triangular markers correspond to the driving frequency and to the frequency of the snaps, respectively: since two snaps occur in one cycle, clearly the snapping frequency is twice the actuation frequency. The black triangles mark the basic frequencies of resonant waves (fundamental plus harmonics) in the tank, under the hypothesis of the shallow water waves in inviscid fluid, for the assumed dimensions of the tank. Since the peaks in the measured force signal approximately correspond to the actuation frequency, the snapping frequency and the frequencies of shallow water waves, these results indicate the nature of the noise that is present in the graphs of Figure 9.6(b).

After having defined the reference value for the prestressing force in the cable, all the prototypes shown in Figure 9.3(a) were tested. These follow the design of Figure 9.1(a), previously indicated as "layout 1" (L1), with a clamped fin at the tip, while varying the number n of segments ($4 \leqslant n \leqslant 8$). The experimental results for the mean thrust force $\bar{F}_x$, as a function of the actuation frequency f, are reported in Figure 9.8. Each dataset corresponds to a prototype with a set number n of segments, and the data points refer again to the average of five measurements with standard deviation error bars. For each prototype, an optimal frequency value that provides maximal thrust can be found; the decreasing branch corresponds to oscillations progressively becoming less symmetric until the beam can no longer snap because the actuation is too fast to overcome inertial and viscous forces. The tails with $n = 6$ and $n = 7$ segments provide approximately the same maximum for $\bar{F}_x$. For the longest prototype $n = 8$, the motion becomes soon unstable when

[1] The free-surface modes [166] in a rectangular container, of plan dimensions $a \times b$ and filled with water up to the height h, are characterized by frequencies f_{ij} given by

$$f_{ij} = \frac{\omega_{ij}}{2\pi}, \quad \text{with} \quad {\omega_{ij}}^2 = g\, k_{ij} \tanh(k_{ij}\, h) \quad \text{and} \quad k_{ij} = \sqrt{\frac{i^2\,\pi^2}{a^2} + \frac{j^2\,\pi^2}{b^2}},$$

where $g = 9.81\,\mathrm{m/s^2}$ is the gravity acceleration, and i and j are integers.

the actuation frequency increases. For the short prototypes, $n = 4$ and $n = 5$, the expected peak value of $\bar{F}_x$ is not reached in the accessible range of frequencies, which could not be increased further without producing excessive vibrations in the experimental apparatus. Overall, the prototype with $n = 7$ provided the best compromise between thrust generation and smooth motion, therefore, becoming the reference for subsequent tests.

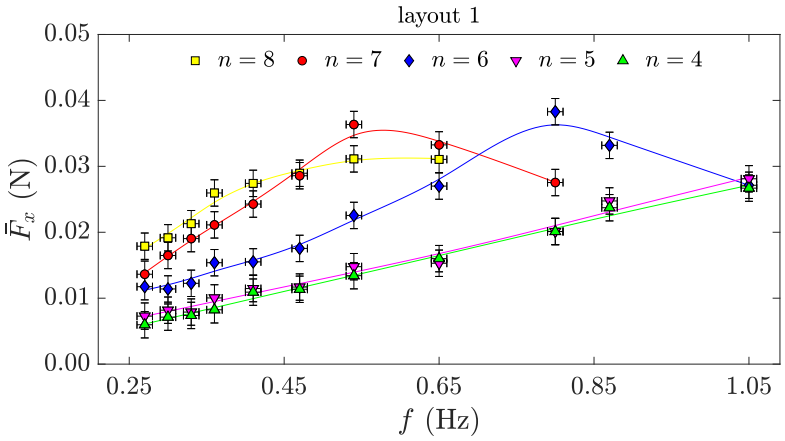

Figure 9.8. Experimental results for the snapping tail with a fixed fin and a different number of segments ($4 \leqslant n \leqslant 8$): mean thrust force $\bar{F}_x$ as a function of the actuation frequency f, for tails in the "layout 1", with initial prestress $N_0 = 9.0 \pm 1.2\,\mathrm{N}$ of the cable.

Having set $n = 7$, the investigation proceeded to find out whether a modification of the shape of the segmental cavities, providing different curvatures for the tail at rest, could enhance thrust. Hence, the "layout 2" (L2) prototype is introduced, which is "less bent" at rest than the L1 tail. For a quantitative characterization of the difference, at each segment i, one can define the curvature $\chi_i = 1/r_i$, where r_i is the radius of the circle passing through the centroids of segments i, $i + 1$ and $i - 1$. The difference between the L1 and L2 prototypes is shown in the left- and right-hand illustrations of Figure 9.9(a), respectively juxtaposing the values of χ_i, for $i = 3 \ldots 6$, and the shapes of the two tails at rest. Figure 9.9(b) compares the mean thrust $\bar{F}_x$: the response is similar between the L1 and L2 cases, except for a shift towards higher frequency for L2. Figure 9.9(c) shows the time series of thrust F_x and transverse force F_y, at the driving frequency corresponding to the peak thrust. Remarkably, the motion of the L2 tail was much smoother and symmetric (compare the plots of F_y) than the L1 tail. In fact, the more bent shape (at rest) of the L1 tail provides a more powerful snapping and a longer path of the fin, but this dissipates more energy in the lateral direction, producing more waves and causing more undesired vibrations. The milder and smoother snapping sequence of the L2 tail generates less noise in the measured force and is more efficient. Because of this

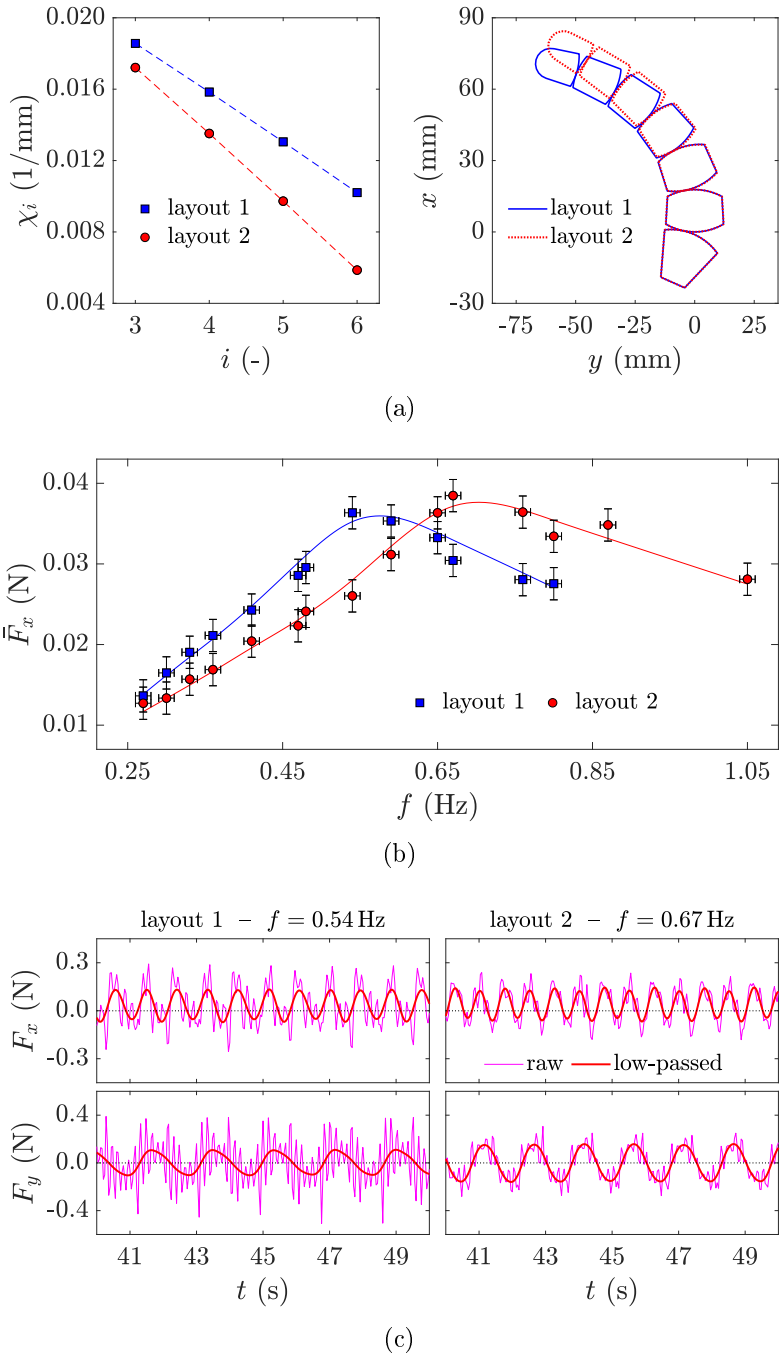

Figure 9.9. Comparison between the "layout 1" (L1) and "layout 2" (L2). (a) Characterization of L1 and L2 for tails with $n = 7$ segments in terms of: curvature χ_i at the i-th segment, $i = 3 \dots 6$, and reference shapes at rest. (b) Mean thrust force $\bar{F}_x$ as a function of frequency f for L1 and L2 with $n = 7$ segments. (c) Time series of the recorded thrust (F_x) and transverse force (F_y), at the frequency of peak mean thrust. Initial prestress of the cable: $N_0 = 9.0 \pm 1.2$ N.

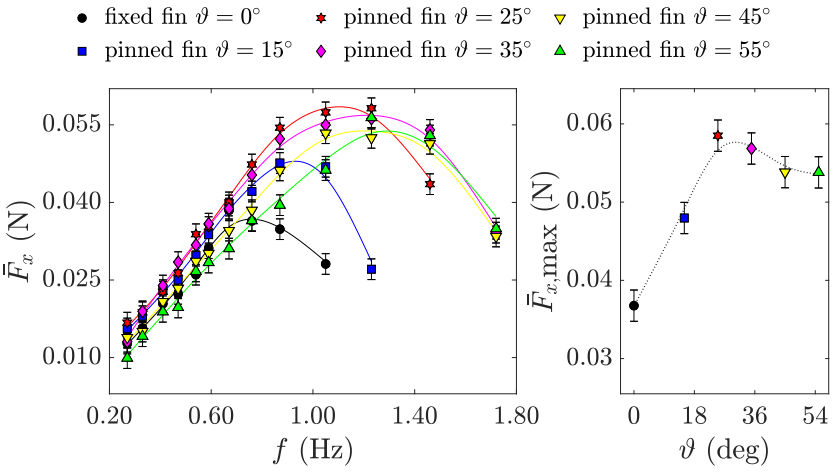

(a)

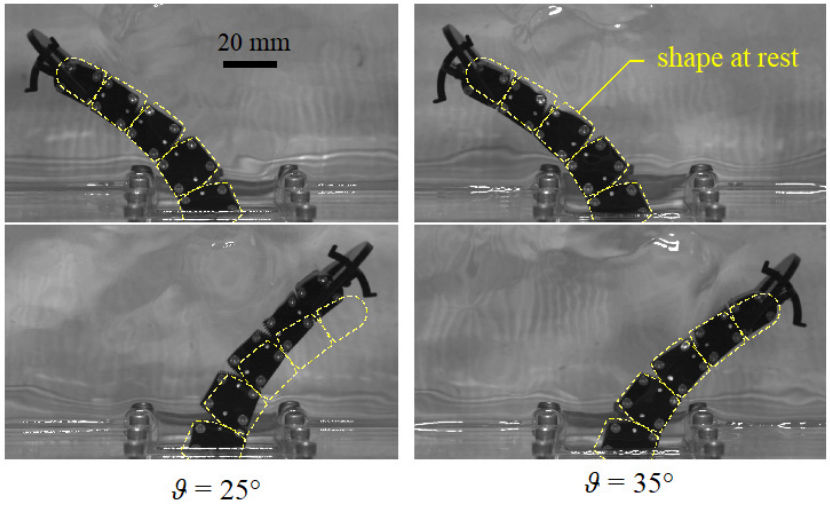

(b)

Figure 9.10. Experimental results for the "layout 2" prototype with $n = 7$ segments and pinned fin. (a) Measurements of generated thrust: mean thrust force $\bar{F}_x$ as a function of the actuation frequency f, for various limit angle ϑ for the fin, and corresponding peak value of the mean thrust force as a function of ϑ. (b) Comparison between the extremal configurations during the motion at $f = 1.05\,\text{Hz}$, corresponding to the peak thrust, for $\vartheta = 25°, 35°$ (shapes at rest are drawn, for reference, in yellow color).

finding, the L2 prototype with 7 segments was chosen as the new reference for the subsequent steps of the investigation.

In all of the experiments above, the prototypes were equipped with a clamped PMMA fin. Based on recent studies [167] suggesting that a pivoting fin may in-

crease performance, a new set of experiments was performed. The fin was pinned (instead of clamped) at the tip of the tail, and it could rotate freely, within an angular range $\pm\vartheta$, as per Figure 9.3(c). Five different cases were considered, with $\vartheta = 15°, 25°, 35°, 45°, 55°$. Figure 9.10(a) shows the measured mean thrust $\bar{F}_x$ as a function of the frequency f, for the L2 prototype with 7 segments and pinned fin, for different values of ϑ (each point corresponds to the average of five measurements). In the same figure, on the right-hand side, the corresponding values of peak thrust as a function of ϑ are also reported, evidencing that a maximum is obtained around 30°. These results confirm that the pinned fin allows attaining a more favorable angle of attack in the fluid, enhancing the thrust generated.

The case with $\vartheta = 25°$ provides the highest measured thrust at $f = 1.05\,\mathrm{Hz}$; however, the frames from the video, reported in Figure 9.10(b), indicate that the motion lacks symmetry and is not fully developed, as evidenced by the comparison with the theoretical rest shape (dashed yellow lines). Under these conditions, the actuation is too fast compared to the inertial and viscous forces. Therefore, for the field application that is presented in the next Section 9.3.2, concerning a toy vessel propelled by one single snapping tail, we will choose the case $\vartheta = 35°$ at the same frequency $f = 1.05\,\mathrm{Hz}$. From Figure 9.10(b), this case corresponds to symmetric oscillations at the cost of a (small) thrust loss of about 4%. In any case, the gain of thrust with respect to the clamped fin is more than 40%, passing from $0.038\,\mathrm{N}$ for $\vartheta = 0°$ at $f = 0.67\,\mathrm{Hz}$ to $0.055\,\mathrm{N}$ for $\vartheta = 35°$ at $f = 1.05\,\mathrm{Hz}$. Note that symmetric oscillations should be considered a design requirement to avoid parasitic deflections of the vessel trajectory when one tail is used for propulsion. Indeed, to achieve a nearly straight motion, the transverse force F_y at one stroke needs to be compensated by an equal force in the opposite direction at the following stroke.

9.3.2 Field application

As a proof-of-concept application in a field setting, a toy vessel was equipped with a snapping tail for propulsion and tested in a rectangular fountain basin (see photograph in Figure 9.11(a)). The top view of the moving vessel was video recorded using a digital camera (Samsung S5KGM1). The $300\times61\times50\,\mathrm{cm}^3$ tank had a water inlet on its left-hand side and an outlet on its right-hand side, with a morning-glory spillway producing a background flow with surface velocity estimated to be $\approx 9\,\mathrm{mm/s}$. A wire (highlighted in red in Figure 9.11(a)), kept straight by a hanging weight through a pulley, guided the vessel in the x-direction of the reference frame indicated in the same picture. This guidewire was needed because the vessel had no active control against external disturbances, such as wind.

Both vessel and tail, shown in Figure 9.11(b), were manufactured out of laser-cut acrylic plates and polypropylene shim stock, and bolted together. The interior

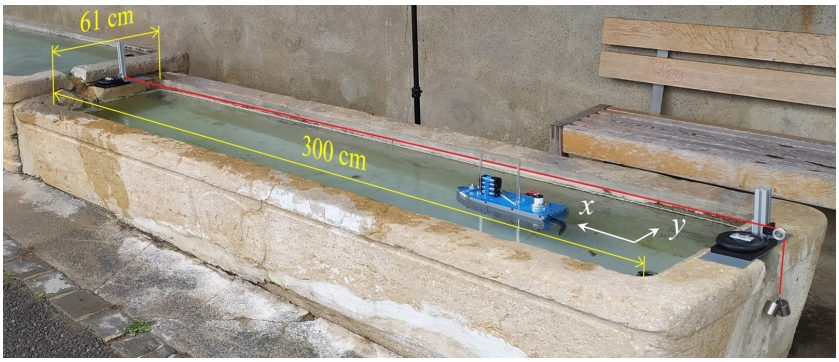

(a)

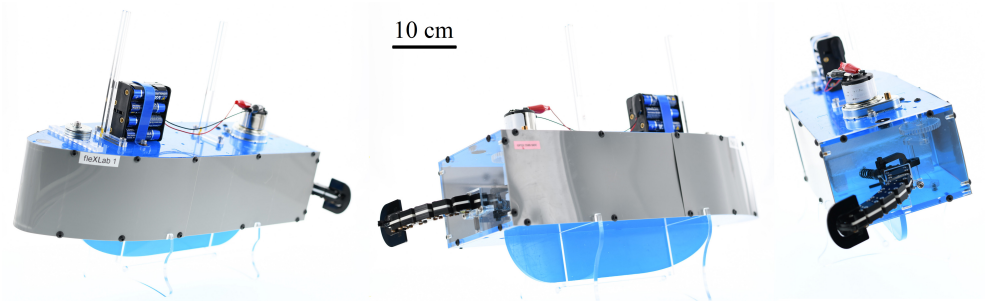

(b)

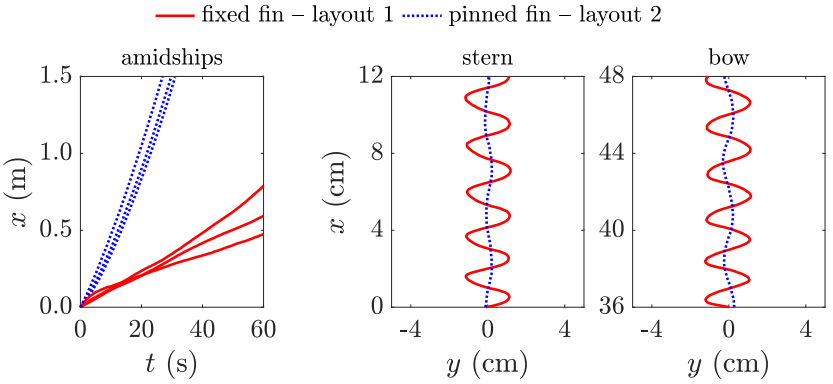

(c)

Figure 9.11. Field application of a toy vessel propelled by a flex-ten snapping tail. (a) View of the basin for the test, indicating the main dimensions, reference frame, and the guidewire (highlighted in red color). (b) Photograph of the manufactured vessel, evidencing the propulsive tail, the motor, the battery holder, and the keel. (c) Experimental results comparing the performance of a vessel propelled either by the 7-segment "layout 1" tail and fixed fin, actuated at $f = 0.54\,\mathrm{Hz}$, or by the "layout 2" tail with movable fin (limit angle $\vartheta = 35°$) at $f = 1.05\,\mathrm{Hz}$: vessel position x amidships as a function of time t, and trajectories of the stern and the bow.

of the boat was filled with polystyrene foam to increase buoyancy, while a vertical keel was used to improve stability. The hull was 38 cm long, with a tail of length approximately 12 cm, including the fin. The tail was submerged in water to a depth of 5 cm (same depth of the in-lab tests); it was actuated, through crank and crankshaft, by the same motor used in the experimental setup of Section 9.2. Two types of tails with $n = 7$ segments were considered: the L1 prototype with *fixed fin*, actuated at $f = 0.54$ Hz, and the L2 prototype equipped with a *pinned fin* with limit angle $\vartheta = 35°$, at $f = 1.05$ Hz. The first case corresponds to the highest mean thrust force, as per Figure 9.8; the second one to the best compromise between thrust and regularity of motion, according to Figures 9.10(a) and 9.10(b).

Figure 9.11(c) reports quantitative results for the motion of the vessel sailing in the fountain basin. The left-hand plot shows the x-position of the boat as a function of time t: the propulsion speed $\mathrm{d}x/\mathrm{d}t$ is ≈ 0.011 m/s for the L1 tail with fixed fin, and ≈ 0.049 m/s for the L2 tail with pinned fin, confirming in the field the advantages of the second design, as already indicated by in-lab experiments. Since the reference frame of Figure 9.11(a) is integral with the tank, $\mathrm{d}x/\mathrm{d}t$ is the absolute speed; the relative speed with respect to the fluid is obtained by summing up the background flow. The trajectories of the stern and the bow, represented in the two plots on the right-hand side of Figure 9.11(c), evidence the yawing motion for a vessel propelled by the L1 tail, which determines undesired oscillations and waste of energy in the lateral direction. The situation improves remarkably for the L2 tail with pinned fin, confirming again that this is the best design among all those considered.

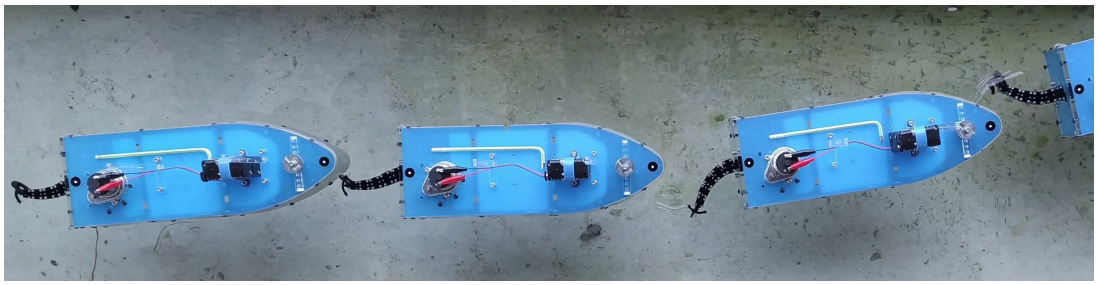

Figure 9.12. Sequence of superimposed snapshots showing the toy vessel sailing in the tank when propelled by the L2 tail with pinned fin ($\vartheta = 35°$, $f = 1.05$ Hz, no guidewire).

Figure 9.12 reports a sequence of superimposed photographs showing the toy vessel sailing in the tank when propelled by the L2 tail with pinned fin ($\vartheta = 35°$, $f = 1.05$ Hz). In this case the guidewire has been removed, thus evidencing that the motion is approximately straight with such a design for the propeller. In particular, this demonstrates that the yaw movement is reduced and, at each stroke, the transverse force compensates for the one in the opposite direction resulting from

the previous stroke; the slight deviation, when the right-hand side of the tank is reached, is due to the perturbations induced by the water inlet.

In order to compare our vessel with a swimming fish, reference can be made to the Strouhal number (St). This traditionally defines a similarity index for wakes and the frequency of vortex formation behind flow obstructions, but can also be applied to the alike wake structures generated by flapping foils in a fluid. For a swimming fish, St can be defined [154] as $\mathrm{St} = 2\,A\,f\,/\,V$, where A is the amplitude of oscillations for the tail beating at frequency f, and V represents the velocity of the fish with respect to the fluid. Fishes generally swim at $\mathrm{St} \simeq 0.3$ [156], considered a bio-motivated optimal value. For the toy vessel, with a background flow of 0.009 m/s, one has $V = 0.020\,\mathrm{m/s}$ for the L1 tail and $V = 0.058\,\mathrm{m/s}$ for the L2 case. Assuming $A \simeq 60\,\mathrm{mm}$, as measured in the tests, one obtains $\mathrm{St} = 3.24$ and $\mathrm{St} = 2.17$ for the L1 and L2 prototypes, respectively. These values are still considerably higher than those corresponding to a fish, indicating that there is ample room for improvement and further optimization in the design of both the hull and the propelling tail. Still, the Strouhal number closer to that of the fish corresponds to the L2 layout with pinned fin, confirming its superiority with respect to the L1 prototype with fixed fin.

Chapter 10

Other potential applications

Further applications of flex-ten structures, yet to be fully discovered and appreciated, are here proposed. In particular, the envisaged fields of applications range from soft robotics, to kinetic architecture, to industrial design. More specifically, cable-actuated robotic limbs are presented, kinetic structures to support envelopes for shielding and water collection are proposed, and a task lamp with a flex-ten tunable arm has been designed and prototyped.

10.1 Soft robotics

Linkages susceptible of large deformations are typically used in field applications for robotics, such as elephant-trunk or octopus-tentacle manipulators [168, 169], with also extensibility properties [170]. Most of them are cable-actuated, as flex-ten structures. More than one cable is generally used (at least 2 cables for plane motion or 3 cables for spatial motion); if just one cable is employed, it is usually confined in an eccentric sheath and the resulting bending motion is not symmetric [171].

Despite a one single cable can be used to fold a flex-ten beam with a proper design of the internal cavities (see Chapter 6), here a more classical design is concerned, with one cable that gives integrity to the assembly and dedicated tendons to control the folding of the beam. The aim is to show that flexural tensegrity represents a versatile structural concept, that can be used with minimal modifications in many fields, for example to manufacture grippers, as presented in [172] while discussing beam-to-beam and beam-to-rigid contacts, or robotic limbs with three-dimensional pitch-profiled-joints operated by cables, to achieve capacities comparable, e.g., to the manipulator presented in [170].

10.1.1 A cable-actuated picker

Using two cables a robotic segmental limb can be manufactured, which is capable of in-plane folding. As represented in Figure 10.1(a), one tendon (red color) passes through the segments in a centroidal tubular sheath to provide integrity to the assembly, while another tubular sheath, eccentric with respect to the segment centroid, houses the control cable (blue color). Both cables are anchored to the free tip of the limb at one end. At the opposite end, the red centroidal cable is pre-tensioned and anchored as well to the structure, thus representing the elastic bond that keeps the segments together. On the contrary, the blue control cable is connected to an actuator: by pulling this second tendon, the limb folds. Obviously, when the limb folds, the red centroidal cable is stretched and one has to win the increase of its elastic strain energy by acting on the tension force of the blue cable.

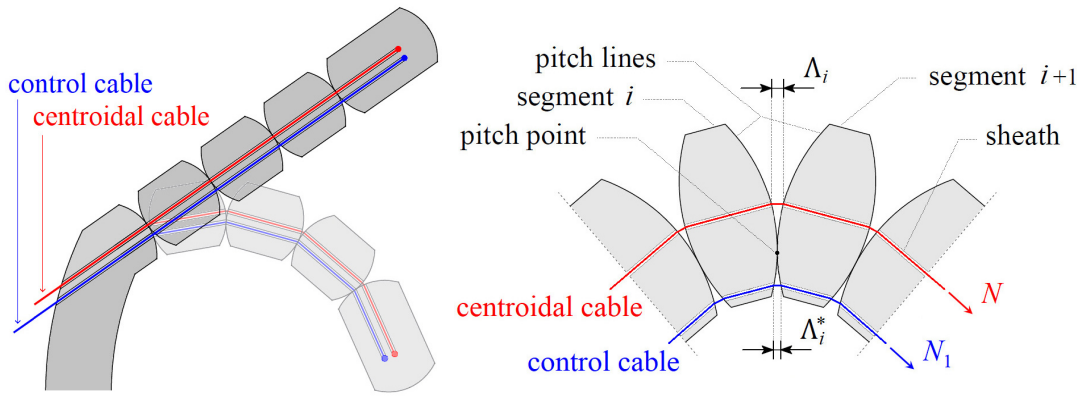

(a) (b)

Figure 10.1. Applications to robotics: the cable-controlled limb. (a) Schematics of the cable-actuated limb: the centroidal (red) tendon gives integrity to the assembly, while the eccentric (blue) one controls grasping when pulled. (b) Detail of the contact joint, evidencing the different elongations of the two cables in a folded state.

Let N_0 denote the initial prestress in the red cable and K its elastic axial stiffness. If N_1 is the external pulling force applied to the blue cable, whose elastic axial stiffness is K_1, then one has that the increase ΔU of elastic strain energy (under the hypothesis of rigid segments) and the work ΔW done by the external force respectively read

$$\Delta U = N_0 \sum_{i=1}^{n-1} \Lambda_i + \frac{1}{2} K \left(\sum_{i=1}^{n-1} \Lambda_i \right)^2 + \frac{1}{2} K_1 \left(\frac{N_1}{K_1} \right)^2 , \tag{10.1.1}$$

$$\Delta W = N_1 \sum_{i=1}^{n-1} (\bar{\Lambda}_i^* - \Lambda_i^*) + N_1 \frac{N_1}{K_1} , \tag{10.1.2}$$

where Λ_i and Λ_i^* are the portions of the cables, red and blue color respectively, that are exposed at joint i, between segments i and $i+1$, in the rotated state represented in Figure 10.1(b); n is the number of segments in the limb, and $\bar{\Lambda}_i^*$ represents the initial value of Λ_i^*, corresponding to the configuration in which the limb is straight (unfolded) and the blue cable is totally slackened (N_1 not yet applied, and $\Lambda_i = 0$). For the paradigmatic case of circular pitch lines of radius R, when the distance between the exit points of the blue and red cable is equal to $R\,\alpha$ along the pitch lines, one has

$$\Lambda_i = 2R \Big(1 - \cos \frac{\Delta\varphi_i}{2} \Big) , \tag{10.1.3a}$$

$$\bar{\Lambda}_i^* = 2R \Big(1 - \cos \alpha \Big) , \tag{10.1.3b}$$

$$\Lambda_i^* = 2R \left[1 - \cos \left(\alpha - \frac{\Delta\varphi_i}{2} \right) \right] , \tag{10.1.3c}$$

where $\Delta\varphi_i$ is the relative rotation between the consecutive segments, as usual.

One can select the rotations $\Delta\varphi_i$, for $i = 1 \ldots n-1$, as Lagrangian variables to describe the folding/unforlding of the limb. Hence, the problem is reduced to $\Delta U - \Delta W = \min$, if inertial effects can be neglected during the folding/unfolding process, otherwise one should consider the dynamic formulation according to what reported in Chapter 4.

Combining two of the limbs of Figure 10.1(a), a cable-actuated picker of the type shown in Figure 10.2(a) can be obtained; here, the contact joints can be manufactured according to the design introduced in Chapter 2, with a double couple of conjugate profiles, thus obtaining a 2D plane mobility for the limb. Such a limb is capable of grasping and collecting also very soft objects, by tuning the pulling force N_1 in the control cables. To exemplify, Figure 10.2(b) reports a sequence of photographs corresponding to the grasping of a plastic cup, without deforming it. Of course, in this example, the focus was on the structure, so that the folding was simply actuated by hand, visually tuning the pull of the control

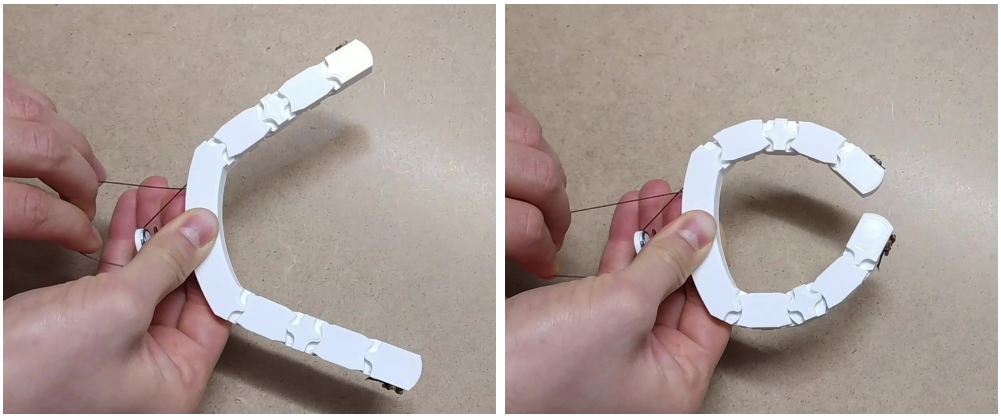

(a)

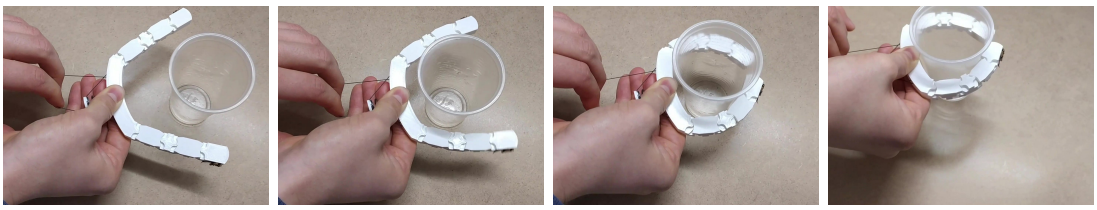

(b)

Figure 10.2. The cable-actuated robotic picker. (a) Robotic picker manufactured according to the principle of Figure 10.1(a). (b) Sequence of snapshots evidencing the capabilities of the cable-controlled picker: grasping of a plastic cup.

cable to avoid the deformation of the plastic cup. Anyway, this kind of picker could be readily equipped with pressure sensors on the segments, and the control cable can be driven by a stepper motor, with a closed-loop controller that adapts the tension force in the cable according to the pressure detected by the sensors.

10.1.2 A cable-controlled limb

Leveraging the design of the contact joints presented in Chapter 7, a more complex 3D mobility can be attained for the flex-ten robotic limb. Consider the sectioned CAD view of Figure 10.3. This is actuated by three cables, plus a centroidal cable for the integrity of the assembly. Moreover, the limb is now characterized by two different parts, i.e., the active and passive portions. In the active portion, the centroidal (red) tendon keeps the segments together in the straight state when the limb is at rest; on the other hand, the eccentric (blue) tendons, placed at 120° one another, control the 3D folding when pulled. In the passive portion, all the cables are confined in a neighborhood of the centroidal axis of the limb, thus providing

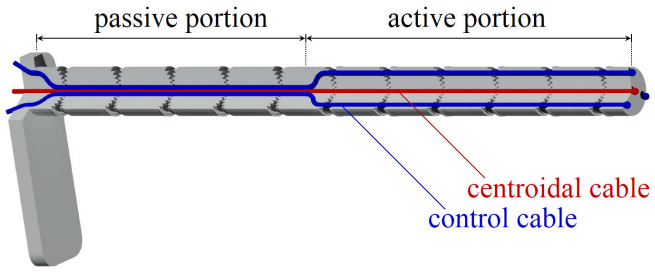

Figure 10.3. Schematics of the cable-actuated limb for 3D mobility: in the active portion, the centroidal (red) tendon gives integrity to the assembly, while the eccentric (blue) ones control folding when pulled; in the passive portion, all the cables are confined in a centroidal sheath, thus providing only elasticity to the assembly.

only elasticity and integrity to the assembly, which remains approximately straight if no external forces are applied except for the pull in the control cables. This is evidenced in Figure 10.4, which reports a sequence of photographs showing the capabilities of the cable-controlled limb.

Such a design, with a flexible (passive) portion that can elastically adapt to external constraints, while the active portion is capable of folding independently by pulling the cables, can find specific applications, apart from the general use as robotic limb to pick up and move objects. In particular, it can be suitable for robots for in-pipe traveling [173, 174], or to realize special endoscopes, also in the medical field. Indeed, the active head of the limb can be employed to select the desired path inside sharply curved pipes with bifurcations, or, in a miniaturized version, inside blood vessels. In addition, it can represent the basis to develop implants for prosthetics or other reconfigurable surgical tools such as catheters, possibly equipped with grippers actuated by the same tendon.

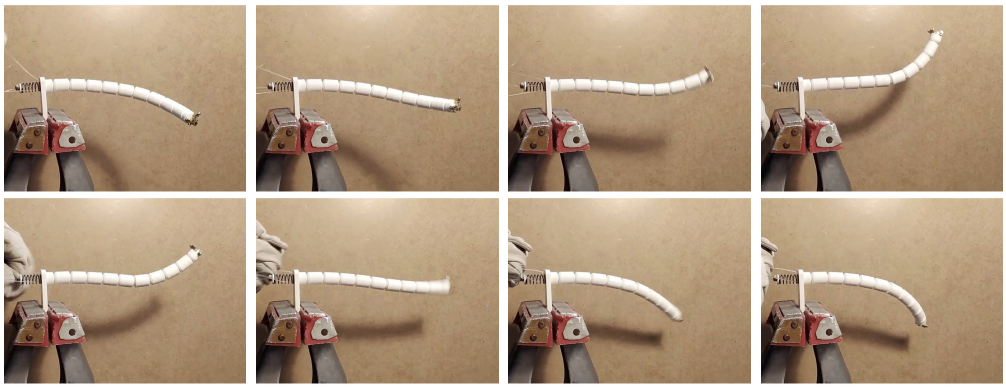

Figure 10.4. Sequence of snapshots evidencing the capabilities of the cable-controlled limb of Figure 10.3.

10.2 Kinetic architecture

The need for transforming spaces dedicated to human activities is pushing designers to think up and outline innovative structures in the broad field of kinetic architecture.

Probably one of the first examples of kinetic structures is represented by the drawbridge, typically present in fortresses dating back to the Middle Age. The application of movable structures to realize bridges is still leading in the field of civil engineering, being the Tower Bridge [175] and the Millennium Bridge [176] in London, or the El Ferdan Swing Bridge [177] on Suez Channel, classical examples among the others. Anyway, the mobility in these cases is usually obtained thanks to the standard technology of cylindrical or spherical hinges, and the actuation is generally made with steam or hydraulic power.

Novel applications come from the possibility to exploit the buckling of thin rods or the multi-stable mechanisms of curved plates due to local changes in the curvature field [178]. These structures do not need to be secured by additional devices in the deployed state, thanks to the high energy barrier separating the folded and the unfolded states. Nevertheless, a limitation is that such structures have only a few configurations, typically two, i.e., the open and closed ones.

Another class is represented by deployable tensegrity grids [179], while transforming origami façades [180] and reconfigurable vaults [181, 182] can be specifically conceived for shading and/or optimization of natural lighting of sustainable buildings. On the other hand, the light weight and the easy deployment and reconfiguration make these structures particularly suitable for the manufacturing of aerospace antennas [183] and shelters for rescue, scouting, military operations or extraterrestrial exploration [184].

The application of flexural tensegrities to kinetic architecture was envisaged in [19], where the structural concept was first proposed at the embryonal stage, and a methodology to tessellate generic plane curves with flex-ten segments was introduced. Here, we develop this idea and present possible applications to realize movable skeletons, with tunable shape, suitable for supporting envelopes devoted to shielding and water collection. Two examples are proposed in the following, which correspond to flex-ten arches and umbrellas; small-scale prototypes have been manufactured as a proof-of-concept.

10.2.1 Arches with tunable shape

In Figure 10.5(a), a flex-ten triumphal arch is proposed, which is made of concrete. The segments, shown in detail in Figure 10.5(b), are designed according to Section 2.1.1, with a double couple of conjugate profiles, because this layered construction

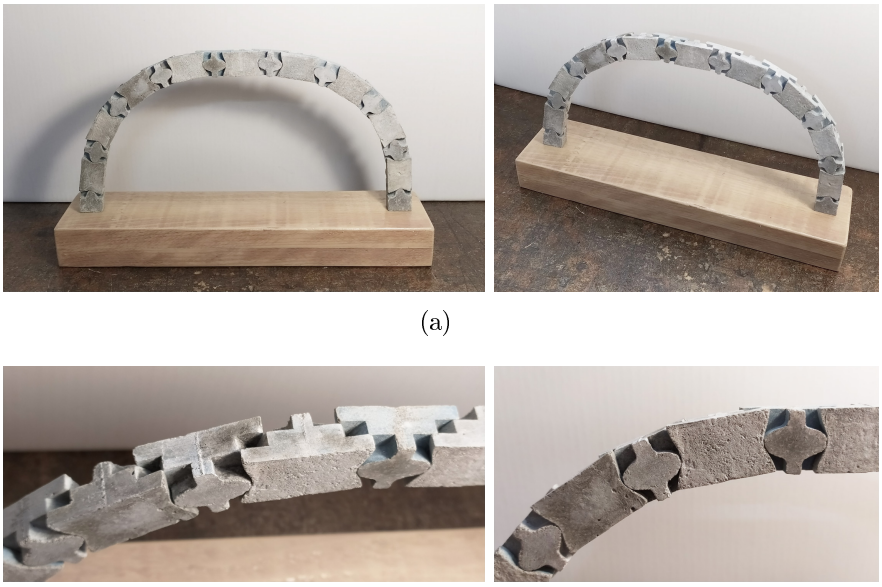

(a)

(b)

Figure 10.5. Applications to architecture: a small-scale flex-ten triumphal arch. (a) Front and 3/4 views of the arch, made of concrete; (b) detail of the segments.

is suitable for casting in molds (see Figure 2.5(c)). The segments are in contact along circular pitch lines of radius equal to the segmental length (28 mm). The holes inside the segments, that house the sheath for the cable, are now slightly eccentric with respect to the longitudinal axis of the segments, in order to tessellate the curved shape of the circular arch. The procedure to determine the position of the sheaths is reported in [19] for any given plane project curve, and it is summarized in Figure 10.6 for the case at hand, where the project curve is a semi-circle.

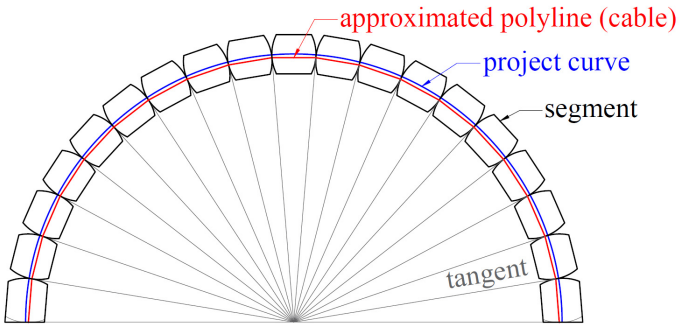

Figure 10.6. Geometric construction for the tessellation of the given project curve (semi-circle) with flex-ten segments of fixed length (28 mm), with circular pitch lines.

Arches of the type of Figure 10.5, but at a larger scale, can be used, as they are, as standing alone sculptures, similar to Snelson's tensegrities (see Figure 1.1). On the other hand, these arches, possibly composed of segments made of lightweight material, can be placed in sequence to realize the ribs of a flex-ten vault or dome, suitable for supporting a waterproof envelope to cover large spaces. Interestingly, by varying the initial tension force N_0 in the cable, the shape of the structure under service loads can be modified, thus obtaining kinetic structures that can optimize, for example, the exposed surface to solar irradiation.

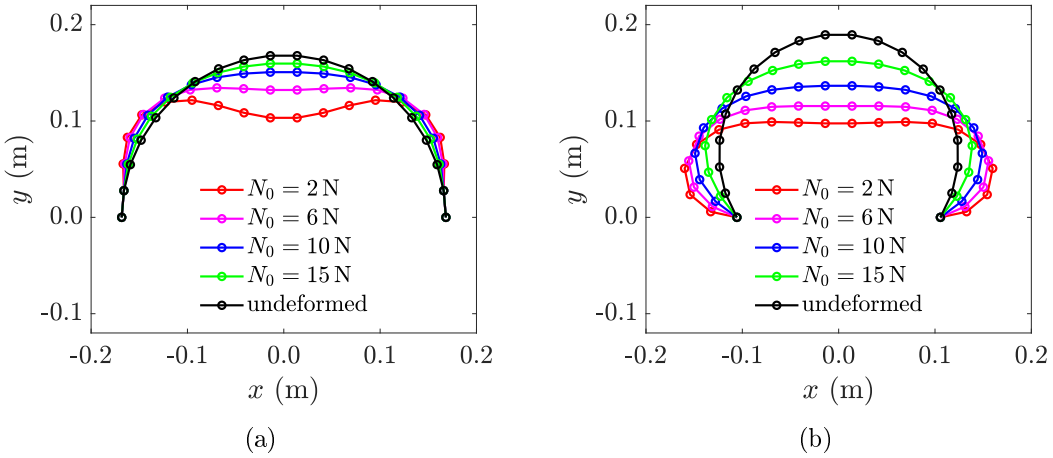

Figure 10.7. Tunable shape of a small-scale flex-ten arch under self-weight: (a) clamps and (b) hinges at the supports. Segmental length equal to 28 mm and segmental weight of 0.2176 N, corresponding to the case of Figure 10.5.

Figure 10.7(a) shows the mobility of the structure when the initial prestress N_0 of the cable is modified under self-weight. The arch is clamped at the supports and dimensions correspond to the case depicted in Figure 10.5; the own weight of each segment is 0.2176 N. Another example, for the same values of weight and length for the segments, is reported in Figure 10.7(b), where the supports are hinged, rather than clamped, and the span of the arch is different.

Note that the custom design of the hinge-based joints, with self-aligning properties when the cable is pulled, together with the possibility of a segmental construction, allows for the fabrication of modular structures that can be folded when the cable is slack and can be quickly unfolded by tensioning the cable. This can meet the specifications for a wide range of application in both the military and the rescue fields. Moreover, the tunable stiffness by controlling the tension force in the cable (see Section 4.2.3) may allow the aeroelastic tailoring and the reduction of vibrations.

10.2.2 Umbrellas for shielding and water collection

Architectural umbrellas are a typical example of deployable/collapsible structures, used to occasionally cover open spaces for sun shading and rain shielding. Figure 10.8 reports just one example, corresponding to Al-Masjid an-Nabawi Umbrellas in Medina. The umbrellas consist of a mast connected to the ground and supporting the ribs, to which a canopy is fixed. In folding umbrellas, such as those in Figure 10.8, the canopy is usually made with fabric or a waterproof polymeric membrane, but it is worth mentioning that it can be realized with different materials, such as glass or concrete. For instance, in the hypar-shaped umbrellas by Félix Candela [185,186], the structure is a point-supported thin shell made of reinforced concrete, but it cannot fold in the serviceability limit state.

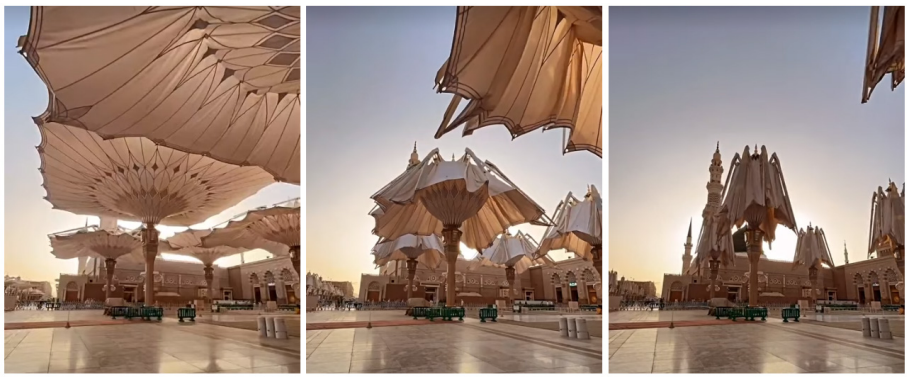

Figure 10.8. Folding sequence of the Al-Masjid an-Nabawi Umbrellas in Medina, placed to shade the pilgrims to the mosques (snapshots from YouTube video, public domain).

The flexural-tensegrity concept, thanks to the tailor design of the joints and the tunable deformation of the members under loads (by pulling/releasing the tendons), seems to be particularly suitable for the manufacturing of the ribs of foldable umbrellas. A first possibility, represented in Figure 10.9(a), consists of a flex-ten segmental cantilever beam placed vertically in the gravity field: the deployment is obtained by progressively releasing the tendon under the service load represented by self-weight. In Figure 10.9(a), the simplest case of circular pitch lines, with constant radius along the beam, is adopted for the joints; anyway, the bent shape of the cantilever can be functionally graded along the beam by tailor designing the pitch profiles of each joint. The disadvantage of this solution is that the beam is stabilized against external disturbances, such as wind, only by the own weight of the segments and the parasitic friction at the joints. As a result, the structure needs to be secured with additional devices, e.g., bolts at the joints or external cables connecting the tip of the ribs to the ground.

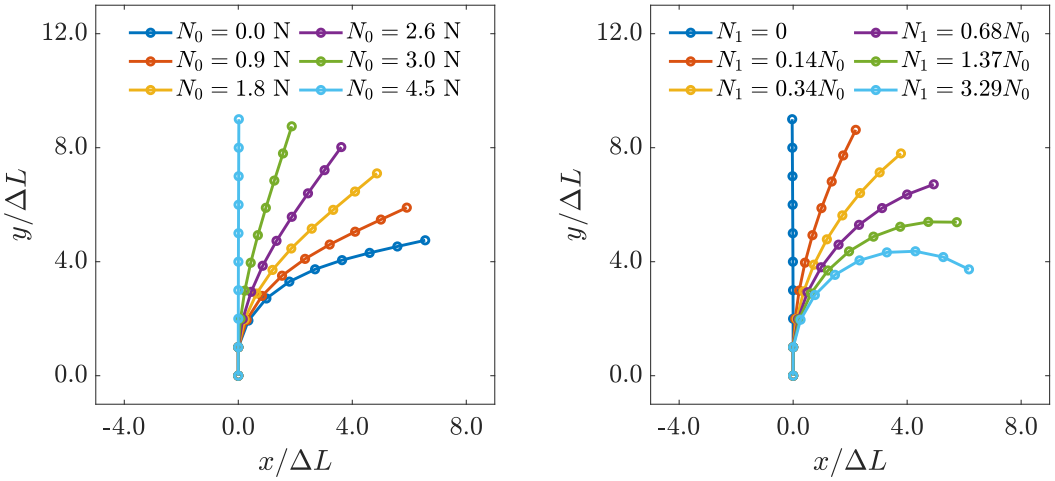

Figure 10.9. Tunable shape of a small-scale flex-ten umbrella rib: (a) solution with one cable, which is progressively released for the deployment of the rib under self-weight; (b) solution with two cables, one for integrity of the segmental assembly (prestress $N_0 = 10\,\text{N}$) and one for actuation (pulling force N_1). Segmental length equal to 17.4 mm and segmental weight of 0.0142 N; circular pitch lines of radius 13 mm.

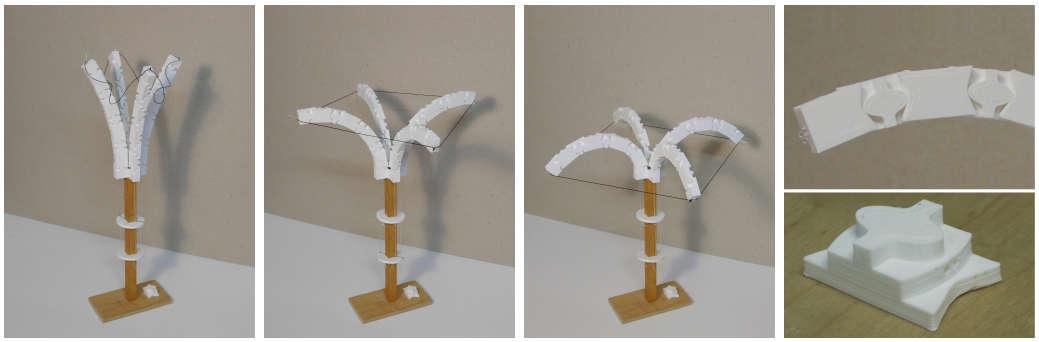

Figure 10.10. Manufactured ribs for a small-scale flex-ten umbrella under self-weight: (a) folded state, (b) semi-open state, and (c) totally deployed state; (d) detail of the segments. Segmental length of 17.4 mm and weight of 0.0142 N; circular pitch lines of radius 13 mm. Each rib has one tendon for integrity and one cable for actuation.

A second solution is represented in Figure 10.9(b). This case is similar to the robotic limb of Section 10.1.1, as two cables are used: the centroidal one is pre-stressed, thus giving integrity to the assembly and providing elasticity against

external loads; the eccentric tendon is used for actuation, to bend the rib. In particular, in Figure 10.9(b), different configurations for the rib are shown when the tension force N_1 applied to the actuation cable is expressed as a fraction of the prestress N_0 of the centroidal cable. In this case, thanks to the mutual action of the two tendons, the rib is always stable against external disturbances without the need of additional devices to secure it.

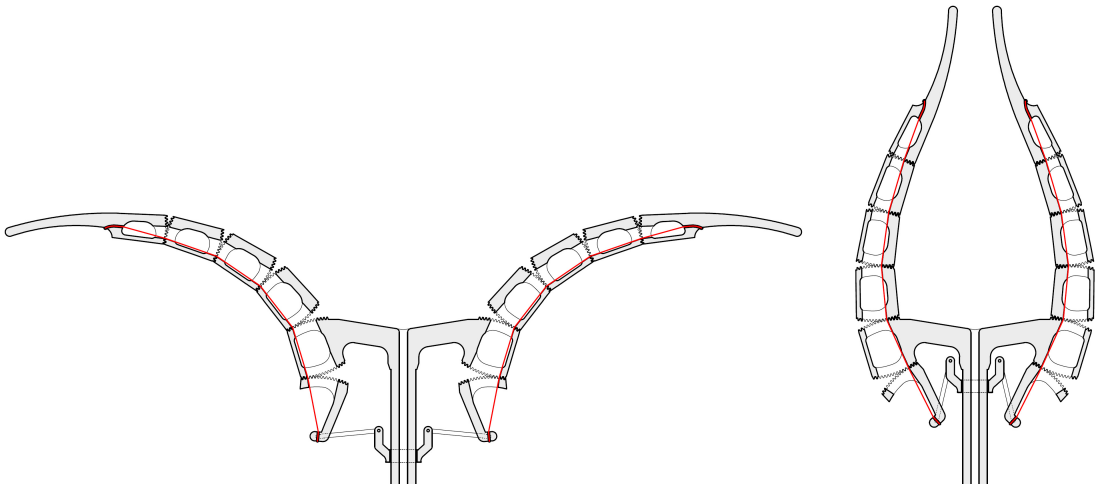

(a)

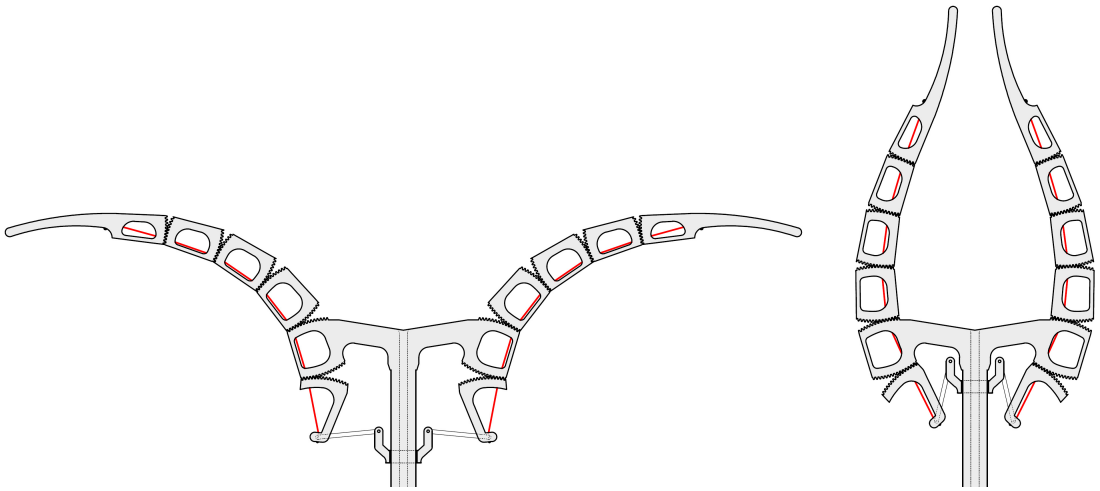

(b)

Figure 10.11. Schematics for the ribs of a snapping umbrella: (a) sectioned view of the open/closed configuration evidencing the cavities spanned by the cable, drawn as a red polyline; (b) another sectioned view of the open/closed configuration, for comparison, with the slicing plane that does not intercept the segmental cavities.

In Figure 10.10, a scale model of the umbrella with two tendons for each rib is presented. Each rib is composed of 9 segments, manufactured via 3D printing; the segmental length is equal to 17.4 mm, and each segment weights 0.0142 N; the radius of circular pitch lines is 13 mm. Note that these data correspond to the case theoretically analyzed in Figure 10.9(b). The folded state, the semi-open state, and the totally deployed configuration are depicted in Figures 10.10(a), 10.10(b) and 10.10(c), respectively, while a detail of the segments is reported in Figure 10.10(d).

A much more interesting solution to realize the ribs of a collapsible umbrella is represented by the snapping cantilever first introduced in Chapter 6. Referring to

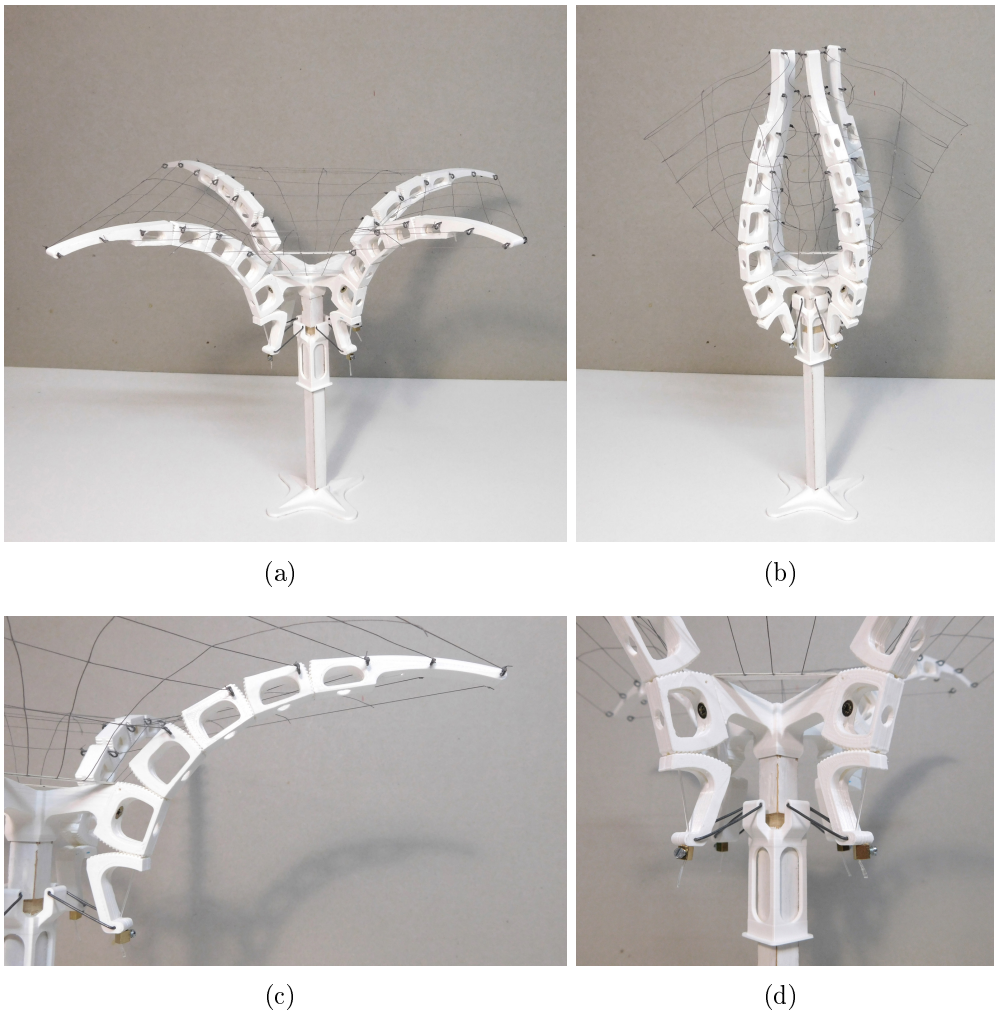

(a) (b)

(c) (d)

Figure 10.12. Manufactured small-scale flex-ten snapping umbrella under self-weight: (a) deployed state, and (b) folded state; (c) detail of the deployed rib; (d) detail of the actuation system. Segments are 3D-printed in PLA, with segmental length of 26.7 mm.

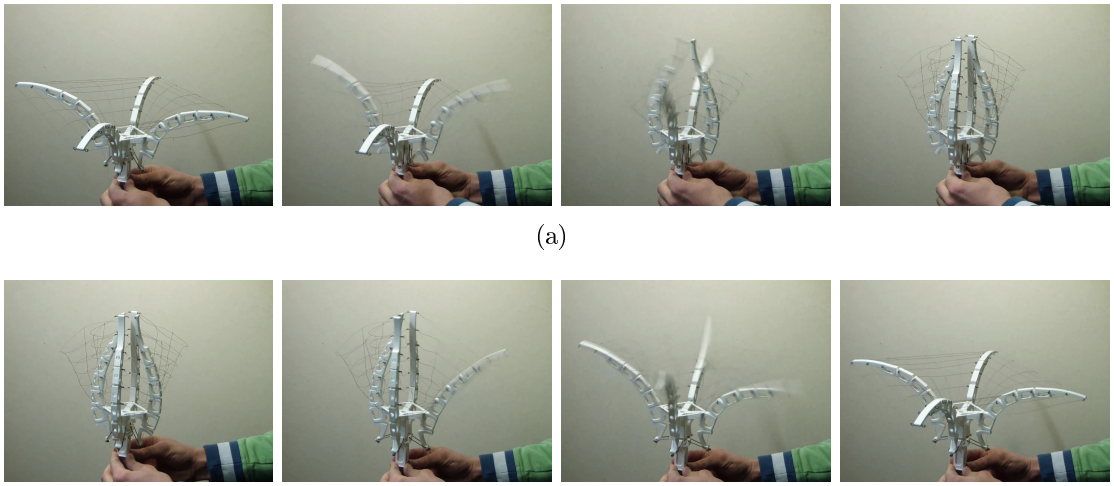

(a)

(b)

Figure 10.13. Mobility of the manufactured small-scale flex-ten snapping umbrella: (a) folding and (b) deployment process.

the schematics reported in Figure 10.11, each segments is holed to reduce the own weight; differently from the case of Chapter 6, the segmental cavities are now made non-symmetric with respect to the segmental longitudinal axis, in order to attain different curvatures (in absolute value) for each rib in the open and closed states, respectively. Moreover, a rigid appendix is added at the tip of the cantilever, to cover a wider space in the deployed state.

Figure 10.12 displays a small-scale prototype for such a snapping umbrella, manufactured via 3D printing in white PLA (segmental length of 26.7 mm). Here, a canopy made with a cable net is added, to define more accurately the structural volumes. The umbrella can open and close like a flower, by controlling the rotation of the L-shaped segments beneath the clamped one of each rib (see Figure 10.11). This is done through connecting rods hinged to a sliding sleeve on the mast (Figure 10.12(d)), which is externally raised or lowered.

Compared to a flower, the canopy plays the role of the petals, reinforced by the ribs, while the end segments recall the sepals. Remarkably, the prototype of Figure 10.12 resembles in shape the Tulipa Sylvestris. Flowers fold at night to protect stamens and ovary from the weather; on the contrary, the snapping umbrella can be deployed for sun shading or rain shielding, as well as for rainwater collection. Figure 10.13(a) reports the snapshots for the folding process of the umbrella, while Figure 10.13(b) is its counterpart for the deployment phases. Note that the energy barrier, separating the open and closed states, secures itself the structure in the two distant configurations without the need of external devices, while dampers can be added to control the structural vibrations after each snap.

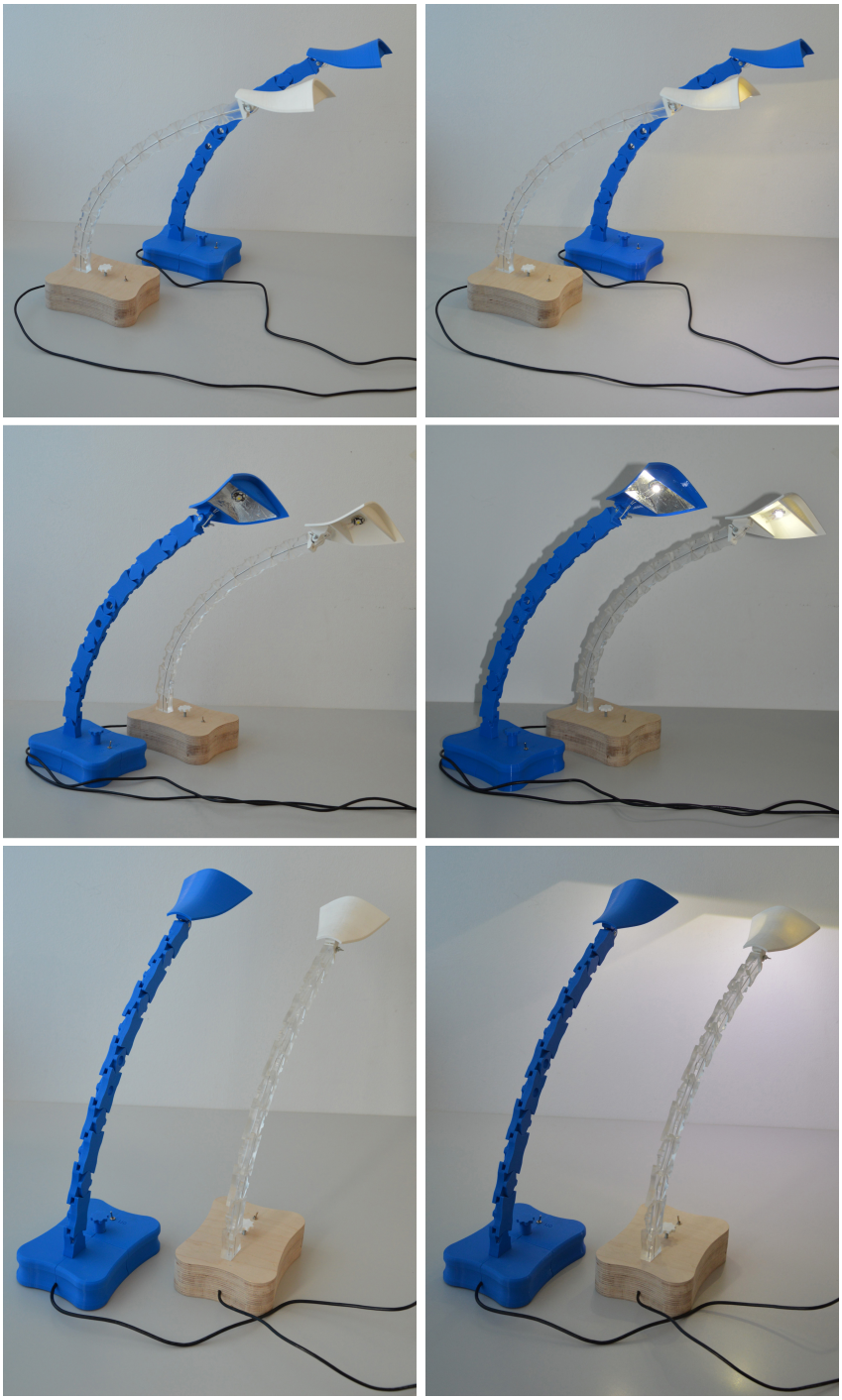

Figure 10.14. Different views of two manufactured prototypes, when the lamp is either switched off (left-hand side) or switched on (right-hand side). The blue prototype is entirely made of 3D-printed PLA, while the transparent one is made of acrylic, with a wooden base and a 3D-printed white lampshade.

Apart from the large-scale applications to kinetic architecture, such a snapping design can be used also to realize an innovative type of portable (inverse) umbrella.

10.3 Industrial design: the Dino-Lamp

At the scale of daily-life objects, the flexural-tensegrity concept can find application in the field of industrial design. Here, we discuss the possibility to realize a task lamp whose arm is made with a flex-ten cantilever beam. The segmental assembly together with the lampshade recalls the vertebrae and the skull of a dinosaur; hence, the proposed lamp has been named the "Dino-Lamp" ("LampaDino" in Italian, pun intended).

Since the Anglepoise lamp [187] was patented in the 1930s, most of task lamps is designed according to a spring-and-lever balancing mechanism [188], which allows to maintain the desired position of the arm, once it is initially set by hand. Here, the proposed design is somehow complementary, since the position of the arm is controlled by tuning the rotational stiffness of the spring-hinge joints of the flex-ten assembly, but the governing mechanism at each joint is still that of balancing an elastic return (of the springs in the Anglepoise lamp, of the elastic tendon in flex-ten beams) with an appropriate lever arm (see Figure 2.2).

In Figure 10.14 two manufactured prototypes are presented, depicted when the lamp is either switched off (left-hand side of the figure) or switched on (right-hand side of the figure). The blue prototype is entirely made of polylactide and was manufactured via 3D printing. On the contrary, for the second prototype, the arm was made of transparent acrylic, CNC milled and drilled from solid; the base was made of glued laminated timber, and the lampshade was 3D printed in white PLA. Inside the segments two twin tendons run parallel to keep the segments together and convoy electricity to the lamp. These can be made of carbon nanotube (CNT) fibers, which combine high tensile strength with a small cross-sectional area [189]

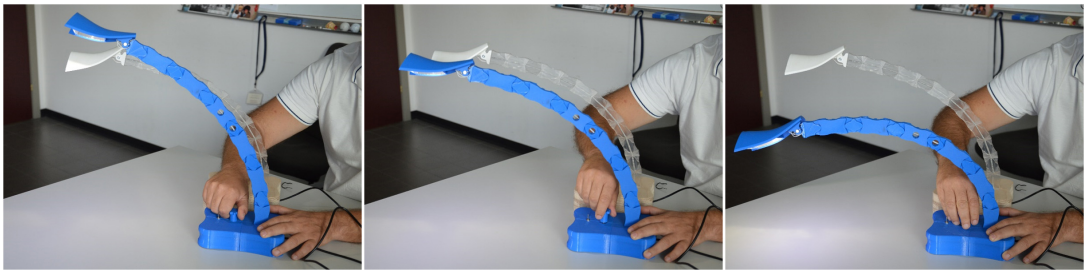

Figure 10.15. The height of the lamp can be tuned by pulling/releasing the tendons, manually acting on a knob.

and a reduced electrical resistance [190].

As shown in Figure 10.15, the height of the lamp can be tuned by pulling or releasing the tendons. This is achieved by manually turning a knob, placed on the base, to which the tendons are wound. A lock device, such as a ratchet mechanism, prevents the tendons from rolling out. Anyway, other solutions are possible to control the tension force of the tendons, such as electric actuators or

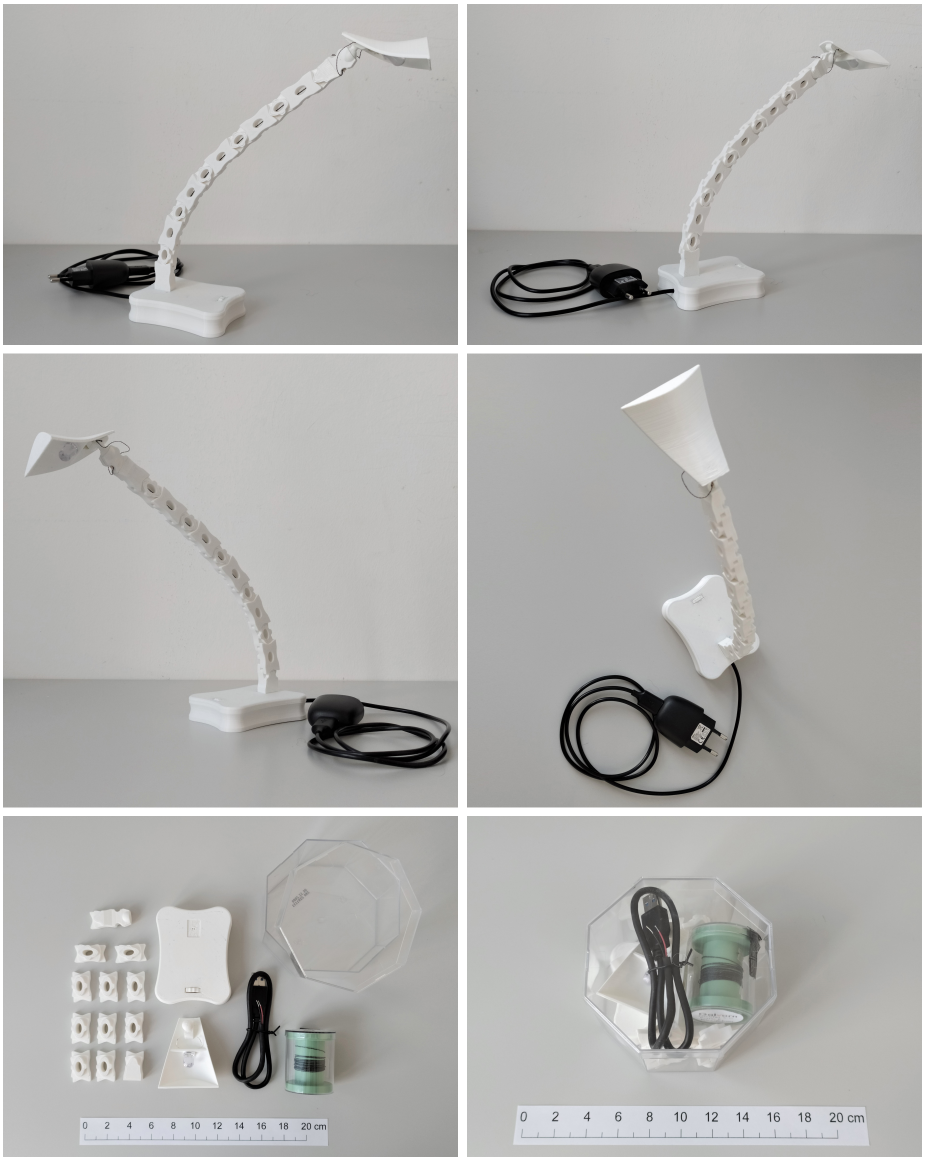

Figure 10.16. Different views of a third smaller prototype, made of 3D-printed PLA, in the assembled and disassembled configurations; the lamp can be packed in a small prismatic box for retailers.

miniaturized hydraulic jacks.

A third smaller prototype, made of 3D-printed PLA, is shown in Figure 10.16 in the assembled and disassembled configurations. The segmental construction is suitable for modular assemblies with different lengths of the arm, and the various components (segments, electric wire and plug, CNT tendons, lampshade, base and LED light) can be packed in a small prismatic box for retailers, so that the disassembled lamp can be sold as a kit project.

Observe that, in the manufactured prototypes, the segments have all the same dimensions and pitch profiles, but different curvatures for the arm can be attained by changing the shape of the design pitch lines. For instance, it is possible to have localized deformations of the arm when a certain rotation threshold is reached for a pair of consecutive segments, for example, by using a sub-linear law as per Figure 8.6; bi-stable joints, according to the design of Section 5.2.1, could also give to the arm a multi-stable response. On the other hand, by changing the configuration of the sheaths that house the tendons, moving them to eccentric positions with respect to the longitudinal axis of the segments, a sinusoidal shape, or even a more complicated one, can be obtained for the pre-tensioned arm.

Moreover, note that the design of the segments with a double couple of conjugate profiles, according to the layered construction of Section 2.1.1, is suitable for an industrialized manufacturing process, such as 3D printing in a wide range of plastic materials, casting in molds using synthetic resins, CNC milling from solid acrilic, aluminium, wood or glass, and die casting with thermoplastic polymers or metal alloys.

Chapter 11

From rolling to sliding: introduction to shear tensegrity

A different type of kinematics is now introduced, which represents the basis for a new type of tensegrity composite characterized by the sliding rather than the rolling of the segments in contact.

The kinematics, concerned so far, was defined by the pure rolling of the adjacent segments along tailor-designed pitch profiles. Now, we consider the sliding of initially-matching plates along wavy surfaces, and the resulting segmental assembly is declined as a laminar brickwork, rather than a beam-like chain of voussoirs. Since the sliding characterizes the response of such a structured material, this is named "shear tensegrity", in contrast to "flexural tensegrities", whose segments are rotated under bending.

Here, each lamella of the brickwork can relative slide with respect to the adjacent ones. As a result, in addition to the elasticity of the material matrix of the lamellae, the straining is due to the opening of gaps at the interfaces between the consecutive lamellae. The response of the laminate is analyzed within the structured deformation theory [191] and strongly depends on the shape of the contact profiles, as it happens for the complementary case of flex-ten beams under bending.

There exist natural materials whose response is governed by the sliding of platelets in mutual contact on rough surfaces, such as nacre [192]. Then, the theoretical model, which certainly deserves a specific and more accurate study in the future, is preliminary set with specific reference to nacre and materials that directly mimic the structural architecture of this naturally occurring composite. Anyway, apart from the specific interpretation of the mechanical response of nacre found in nature and the application to nacre-inspired laminates with a tailor design of the contact wavy profiles, this model has a much broader scope, since it can be suitable to interpret the complex structural behavior of new artificial metamaterials with

the propagation of disarrangements under loading, and it can inspire the design of novel bio-mimetic or bio-inspired self-assemblies and composites.

The chapter is organized as follows. In Section 11.1, the hierarchical structure of nacre is described, as it represents an example of biological shear tensegrity, and the model in introduced. Then, the theoretical analysis is developed in the following Section 11.2, while various geometric descriptions of the roughness of the lamellae composing the shear tensegrity are considered in Section 11.3. The theory is applied, in Section 11.4, to the mesolayers of different shear tensegrities under in-plane tension-compression; here, a comparison between the model and the response of real nacre is also reported. The theory and the main results here concerned are also available in [193].

11.1 An example of biological shear tensegrity

Nacre (mother-of-pearl), forming the iridescent internal layer of certain shells of mollusks, represents an example of the class of structured materials here referred to as *shear tensegrities*. In fact, it is arranged as a laminar assembly of tablets, in mutual interaction on rough surfaces. Nacre is composed of 95 wt% of a crystallographic form of $CaCO_3$, called *aragonite*, and 5 wt% of organic materials, such as proteins and polysaccharides [194]. It presents mechanical properties superior to those of monolithic aragonite thanks to an ingenious hierarchical microarchitecture that spans different length scales.

11.1.1 The hierarchical architecture of nacre

The hierarchical structure of nacre, represented in the scanning electron microscope (SEM) image of Figure 11.1(a), consists of thin lamellae composed of flat polygonal aragonite tablets, arranged in a Voronoi-like tiling of the type shown in Figure 11.1(b). There are various forms of micro-architecture, distinguished into two categories [195]: in the *columnar nacre* of Figure 11.1(c), typical of gastropods, the aragonite tablets have uniform size with nearly coinciding centers, whereas in the *sheet nacre* of Figure 11.1(d), which is found in bivalves, the tablets are stacked in a "brick wall" pattern. The overlap region in columnar nacre covers approximately 1/3 of the area of the tablets, but in sheet nacre the core and overlap cannot be distinguished [194]. The thickness of the aragonite tablets is approximately $0.5\,\mu$m for gastropods and $0.3\,\mu$m for bivalves [194], whereas their diameter is of the order of $10 \div 15\ \mu$m [196].

The architecture derives from a protein-mediated mechanism of growth. Each aragonite tablet is nucleated at one island. A thin organic membrane is spread from

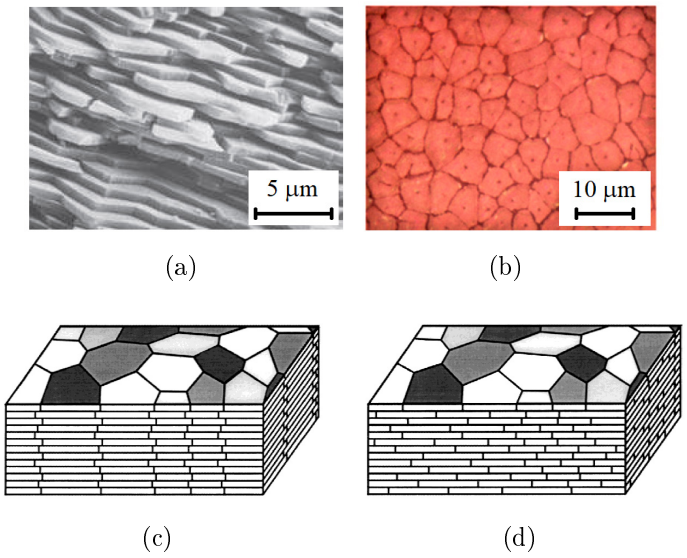

Figure 11.1. Microstructure of nacre. Image of nacre tablets: (a) view of a fractured section, adapted from [197], and (b) in-plane section showing the Voronoi-like tiling, adapted from [198]. Schematic illustration of (c) columnar nacre and (d) sheet nacre (pictures from [195]).

the top of the islands and determines the thickness of the layer: the membrane is permeable to calcium and carbonate ions but it restricts their flux to lateral growth only, until the layer closes [194]. The growth is arrested when the borders of adjacent tablets meet. The continuation of mineral growth from the preceding lamella of tiles to the successive lamella is due to *mineral bridges*, protruding through the membrane of proteins, creating the islands for the successive layer. The aragonite lamellae are bonded by interlayers, approximately $20 \div 50$ nm thick [195, 199], made of chitin or other silk-like proteins [197]. These consist of beta-pleated sheets folded into cross-linked polymer-like fibrils, shown in Figure 11.2(a), which can stretch out up to an elongation of 150 %, without becoming detached from the aragonite [194, 200].

Lin, Mayers and coworkers [199, 201] have demonstrated that a tensile straining in the lamellar plane produces the inelastic relative slip of the lamellae, restrained by the friction and interlocking between the undulating surfaces and the stretching of the organic bonds. As suggested by Evans et al. [192], friction is enhanced by nano-asperities on the surfaces of the tiles, which accompany the growth of the aragonite crystals. In abalone shells [199], SEM micrographs evidence a large number of asperities, about 50 nm in diameter, protruding outside the surface plane for less than 30 nm, as shown Figures 11.2(b) and 11.2(c). The asperities on the upper aragonite tablets interpose with those on the lower plane, providing

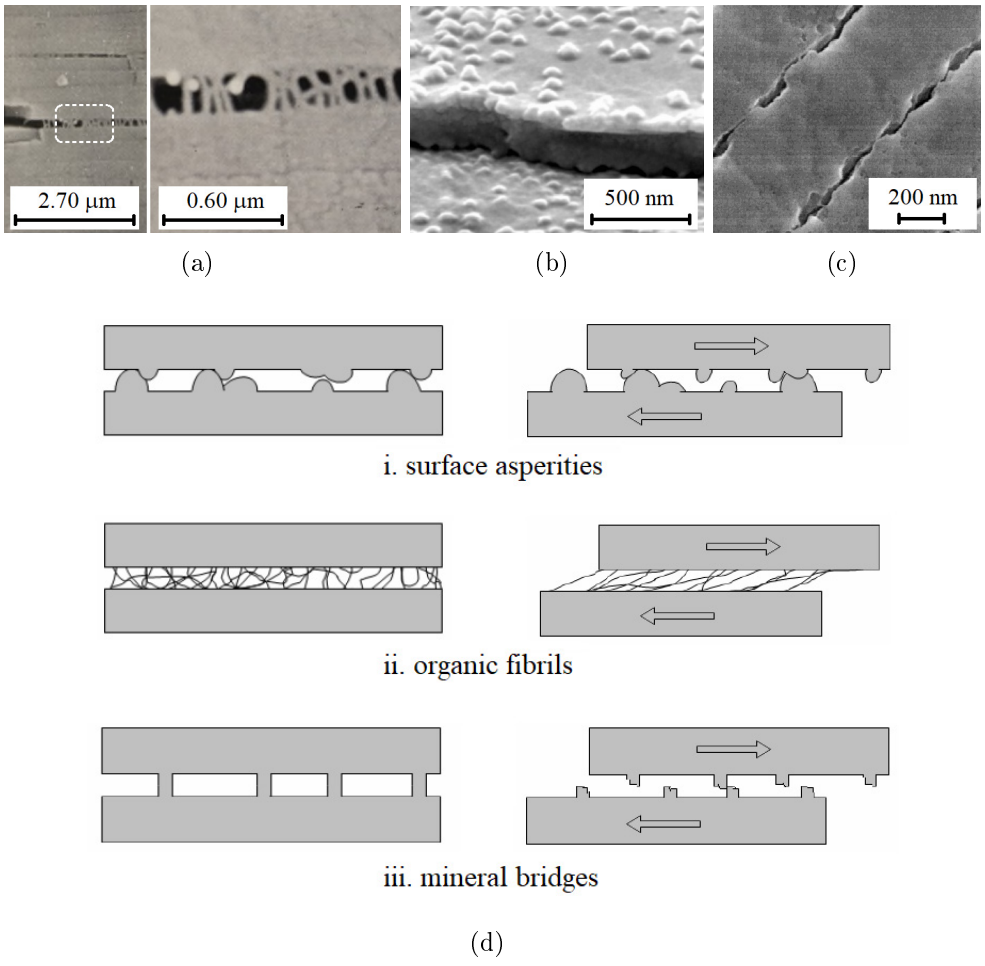

Figure 11.2. Micromechanics of the sliding aragonite tablets: (a) biopolymeric fibrils bridging the surfaces of adjacent tables during delamination tensile test, adapted from [200]; (b) SEM image of nano-asperities on the surface of aragonite tablets, taken from [199]; (c) cross sectional view of lamellae with evidence of their interlocking due to nano-asperities, adapted from [195]. (d) Schematic representation of the constraints in sliding plies [201]: i) nano-asperities interlocking , ii) bonding from the biopolymeric fibrils, iii) broken mineral bridges.

the interlocking of the two surfaces. Another source of roughness is represented by the broken mineral bridges connecting the individual tablets [199, 201], but their number is much smaller than the total number of the asperities. Restraints[1] of this

[1]Other microstructural imbrications, not considered in the model, are found in nacre: the Voronoi arrangement of tablets in each layer, screw dislocations with unique tessellated zig-zag morphologies and interconnected layer-to-layer spiral structures.

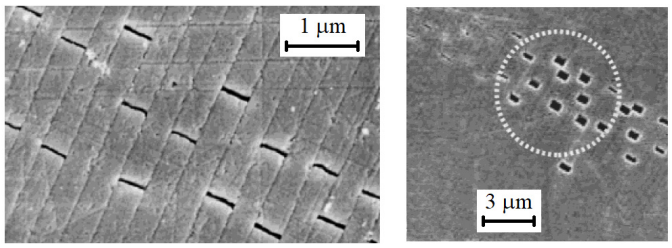

(a) (b)

Figure 11.3. SEM images of the dilatation bands found in nacre upon in-plane tensile straining: (a) aragonite lamellae with incipient gap formation [195] and (b) opening of gaps during the tensile test (adapted from [192]).

type are schematically indicated in Figure 11.2(d).

The constitutive properties of nacre are affected by the sliding of the rough interfacial surfaces and the stretching of the organic bonds, following the scheme of Figure 11.2(d). Apart from friction and cohesion, additional resistance to relative sliding between sheets results as the dilatation, that would occur when an undulating plate surmounts its mate, is constrained by non-slipping material outside the deformation band and by the stiffness of the organic fibrils. Straining in the plane of the lamellae produces disarrangements evidenced by the formation of *dilatation bands* [192], visible in Figure 11.3(a), located at the tablet terminations, which have a tessellated shape due to the regular microstructure. The inelastic in-plane strain derives from the opening gaps at these separations, shown in Figure 11.3(b), which derive from the slip of the adjoining interfaces of the aragonite tablets. Sliding of the aragonite tablets is facilitated by water, which softens the organic matrix. Indeed dry nacre is brittle, similarly to pure aragonite, whereas wet nacre shows a region of large inelastic strain [198].

Thanks to the "brickwork" arrangement of the platelets, which inhibits transverse crack propagation, the fracture toughness of nacre can be three to nine times the value of its basic calcium carbonate constituent [194]. There are various types of toughening mechanisms [202]: plastic deformation ahead of the crack tip, crack deflection, crack blunting, and tablet pull out. Several studies [203–207] have developed mechanical models spanning multiple length scales, which have inspired the creation of synthetic nacreous composite materials both at nanoscale [208–210] and at millimeter-scale. These include PMMA brickwork-like laminates [211] whose designs can be informed by optimization analyses [212]. These interesting aspects, however, will not be considered here. Our discussion will focus on the mechanical constitutive properties, under the assumption that the aragonite tablets remain sound and the deformation is dominated by the disarrangement of the "brickwork".

11.1.2 A multi-scale approach to shear tensegrities

To this aim, a multiscale approach is proposed, consisting in homogenizing the effects of disarrangements at the level of the representative volume element (RVE), with reference to the *structured deformation theory* by Del Piero and Owen [191, 213]. This powerful tool bridges mechanical responses at different length scales with macroscopic fields that can be set in a general thermodynamic framework. In fact, it is based on a two-scale representation that captures and recognizes, at the *macroscopic* level, the contributions of both smooth and non-smooth geometrical changes (disarrangements) at *sub-macroscopic* levels.

Two basic hypotheses are made, in agreement with Evans et al. [192]: (i) once the elastic limit is exceeded, the shear resistance of the plate interfaces is low enough to form dilatation bands rather than brittle cracks; (ii) large-scale inelastic distortions are due to the cohesive/frictional sliding of the aragonite tablets along rough interfaces. This approach spans multiple length-scales: (I) calcium carbonate and protein molecules (atomic scale); (II) characteristic height of the asperities on the surfaces of the aragonite tablets ($\leqslant 30\,\mathrm{nm}$); (III) thickness of the aragonite tablets forming each layer ($0.3 \div 0.5\,\mu\mathrm{m}$); (IV) diameter of the aragonite tablets ($10 \div 15\ \mu\mathrm{m}$); (V) thickness of the nacre mesolayers ($0.1 \div 1\,\mathrm{mm}$). We consider (I) by assuming a linear elastic response of the calcium carbonate of aragonite and introducing a constitutive law for the binding of the protein fibrils. Assuming a shape of the contact profiles takes into account (II). The characteristic size of the tablets provides for (III) and (IV). The mesolayers of (V) are supposed to be formed by a number of lamellae and determine the scale of the RVE.

The interfacial resistance to sliding is obtained via a generalized cohesive-frictional law, effective at the level of average separation plane. This approach accounts for the roughness of the interfaces, but eliminates the difficulties in solving in detail the contact problem and finding the stress concentrations at the asperity contacts; these can possibly be considered a posteriori. A key aspect is consideration of the dilatation due to the surmounting asperities of the sliding interface, which depends on their geometry; in fact, the bridging of the organic interlayer and, possibly, a transverse confinement pressure, can affect the constitutive properties. Structured deformation theory allows the representation of elastic and inelastic (disarrangements-driven) sources of deformation via continuum descriptors, which are set in a standard thermodynamic framework for irreversible processes for generalized materials [214]. Specifically, the lamellar sliding is treated as the internal variable associated with the corresponding thermodynamic force. A major peculiarity, discovered through this model, is the level to which the overall response of the composite is dictated by the geometry of the sliding profiles. For various shapes of the surface profiles, we derive the macroscopic response under monotonic and cyclic loading under in-plane stress, taking into account the

possible presence of a confining pressure.

The proposed model represents the development of what was proposed, at an embryonic level, in [215], in order to interpret the response of quasi-brittle materials under shear and confinement. That contribution was specifically conceived for masonry and concrete walls; it considered elementary surface shapes; it did not take into account the elastic bonding of the interfaces; it considered only the response under shear, for which the size and shape of the constituent bricks is not important. Here, we focus our attention on a completely different class of hierarchical materials; we consider the in-plane tensile response incorporating the length scale of the constituent tablets; we consider the presence of a binding interlayer; and we broaden the scenario by considering interface profiles of different shapes.

The model is inspired by the hierarchical structure of nacre, and specific reference to nacre is made throughout the chapter for illustrative purposes. However, this approach is much more general and can find applications in the design of new metamaterials, as well as in macroscopic applications, such as base isolators for seismic protection [216]. We demonstrate that, as a function of their geometry, pure kinematics of the sliding lamellae can provide a wide range of responses under tension tests, characterized by pinched hysteresis loops with branches of various shape, and serrated inelastic deformations. The hierarchical architecture can also represent a phenomenological model for interpreting the Portevin-Le Chatelier effect that characterizes the plastic deformation in steels [47], as well as a way of defining stick-slip frictional motion [217] without the need of distinguishing between static and kinematic friction.

11.2 Modeling of generalized shear tensegrities

The multi-scale mechanical model for shear tensegrities, inspired by nacre architecture, is presented next. The kinematics of sliding is set in a thermodynamical framework which provides the constitutive laws, the governing equations and the boundary conditions for the two dimensional problem of a laminate under generalized plane stress.

11.2.1 Structured deformation of lamellar materials

Consider a flat thin plate of nacre made by the assembly of several laminae formed by aragonite tablets. For convenience, introduce a reference frame $\{\boldsymbol{e}_1, \boldsymbol{e}_2, \boldsymbol{e}_3\}$, with $\{\boldsymbol{e}_2, \boldsymbol{e}_3\}$ parallel to the plate surface and $\boldsymbol{e}_1$ orthogonal to it. The major assumption is that the tablets are arranged according to a regular tessellation and that their surface asperities are isotropically distributed in the $\{\boldsymbol{e}_2, \boldsymbol{e}_3\}$ plane. This implies

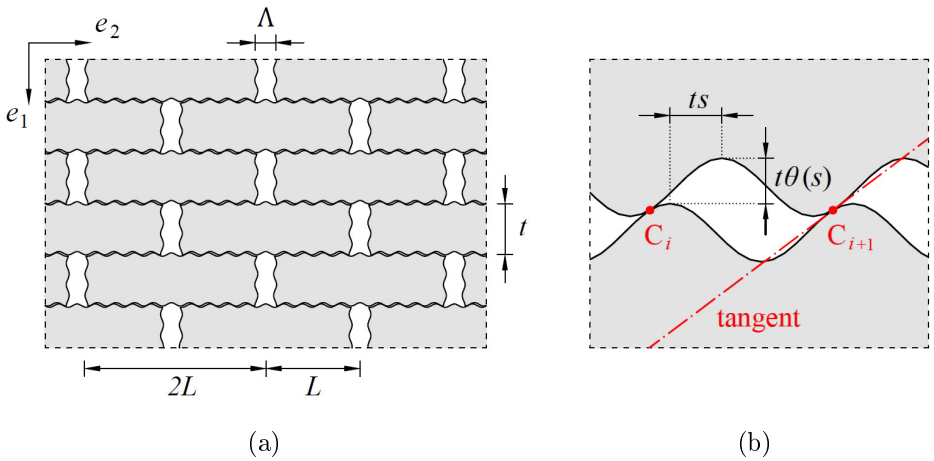

Figure 11.4. Schematic representation of the 2D model problem: (a) equivalent cross section of a mesolayer, composed of laminae of tablets, under uniaxial straining in the direction $\boldsymbol{e}_2$; (b) detail of the kinematics of contact for the wavy interface profiles.

that the relative sliding of any two adjacent laminae produces the same effects, in terms of stress and strain, whatever the in-plane direction of sliding.

The aforementioned regularity hypotheses allows us to consider an "equivalent" two-dimensional scenario. The term "equivalent" establishes a correspondence with the micro-mechanics of a three-dimensional arrangement for what concerns the mechanical properties, when the plate is in-plane strained in an arbitrary direction. This can be identified, without loosing generality, by the vector $\boldsymbol{e}_2$. The equivalent 2D kinematics, which strictly recalls the micro-photograph of Figure 11.3(a), is that indicated in Figure 11.4(a). The cross section shows a regular "brickwork" arrangement of rectangles of sides $2L \times t$, where L is the overlapping length between the interfaces and t is the thickness of the tablets forming the laminar layers, with $t \ll L$ as an order of magnitude[2].

Recall that the platelets are separated by interlayers of biopolymers. These provide, on the one hand, a bond that is sufficiently strong to impart a stiffness to the tile assembly during the deformation. But, on the other hand, they are sufficiently compliant to prevent their transverse breakage. Therefore, fractures are intergranular rather than transgranular. A macroscopic dilatation in the direction of $\boldsymbol{e}_2$ can only occur at the price of the opening of gaps in correspondence of the short sides of the rectangles [192], at a longitudinal pitch L, consequent to the sliding of the interfaces along the long sides. Denoting with Λ the gap opening, assume that $\Lambda \ll L$.

[2]In real nacre the lamellae are much longer than thick, because $t = 0.3 \div 0.5\,\mu$m and $L = 5.0 \div 7.5\,\mu$m (see Section 11.1.1), so that $t/L \simeq 0.05$.

The asperities of the platelets are modeled as wavy interface profiles: the kinematics of sliding is described by the requirement that the profiles remain in contact when they are sheared apart. In particular, a *dilatation* in the direction of $\boldsymbol{e}_1$ is provoked by the surmounting of the conjugate profiles (we define surmounting as the movement of a point on the surface of a tile along a path defined by the surface on an opposing tile to which it may be originally mated). This effect dictates the constitutive properties of the laminate, because the biopolymeric interlayers produce the springing back of the platelets, providing a cohesive-elastic restraint to the transversal dilatation. Indeed, the characterization of the kinematics of sliding for the wavy profiles represents a key point for the proposed model.

Observe that the model considers a regular arrangement, specifically for both the lamellar tessellation and the geometry of the wavy contact surfaces with interlayer bonds (organic fibrils). The potential randomness of nacre microstructure is not taken into account, but recent studies [218] have provided evidence that the macroscopic properties are only marginally affected by the underlying microstructural randomness, because of the staggered geometry and the shear load-transfer mechanism of brick-mortar microstructure. Although a more complicated model could take into account this aspect, the assumed regular arrangement is sufficient to motivate a wide scenario of possible responses and, in any case, it shall be considered as representative of an *effective geometry*, providing constitutive properties equivalent to the actual condition.

Consider a representative volume element of diameter w, with $w \gg L$, embracing a mesolayer. The macroscopic strain is due to the elasticity of the material and the disarrangements consequent to the cohesive-frictional sliding of the lamellae. We take a smeared view of this within *structured deformation theory* [191]. The gap Λ that opens between a pair of consecutive tablets, represented in Figure 11.4(a), reads $\Lambda = 2\,t\,s + \Lambda_0$, where $\Lambda_0 \geqslant 0$ is the gap in the reference state, which may also be due to a previous load history, and $t\,s$ is the slip between the upper and the lower lamella as per Figure 11.4(b). Note that the requirement that material does not overlap is fulfilled if $2\,t\,s \geqslant -\Lambda_0$. Consequently, one may define the average inelastic dilatation due to disarrangement in the $\boldsymbol{e}_2$ direction as

$$\lambda = \frac{\Lambda}{2\,L} = \frac{2\,t\,s + \Lambda_0}{2\,L}\,. \tag{11.2.1}$$

When $\Lambda_0 = 0$, the dilatation (11.2.1) becomes $\lambda = t\,s/L$, with $s \geqslant 0$.

In order to characterize the transversal structured strain in the $\boldsymbol{e}_1$ direction, refer to Figure 11.4(b). It is convenient to introduce the function $\theta(s)$ according to the following requirement: if $t\,s$ is the relative longitudinal displacement of the interface profile (in the $\boldsymbol{e}_2$ direction), the quantity $t\,\theta(s)$ represents the transversal relative displacement due to the surmounting (in the direction of $\boldsymbol{e}_1$). Since t is

the thickness of the lamellae, here taken as a representative length-scale, then s is the smeared shear strain in the lamellar layer and $\theta(s)$ the corresponding dilatation strain. In this description, the function $\theta(s)$ is completely characterized by the roughness of the lamellae; it will be referred to as the *opening* or *separation* function.

Introduce the $x-y$ reference frame, whose corresponding versors are respectively $\boldsymbol{e}_1$ and $\boldsymbol{e}_2$. The disarrangements due to sliding can be associated, in a smeared description, with the deformation gradient

$$\boldsymbol{M}(x,y) = \theta\left(s(x,y)\right)\, \boldsymbol{e}_1 \otimes \boldsymbol{e}_1 + \lambda\left(s(x,y)\right)\, \boldsymbol{e}_2 \otimes \boldsymbol{e}_2\,, \tag{11.2.2}$$

where[3] we have emphasized the dependence of s on (x,y) to cover the case in which the disarrangement is not homogeneous. Following the theory of [191], a *structured deformation* is given by a pair of functions $\boldsymbol{g}$ and $\boldsymbol{G}$, defined as

$$\boldsymbol{g}(x,y) = \left[x + u(x,y)\right]\boldsymbol{e}_1 + \left[y + v(x,y)\right]\boldsymbol{e}_2\,, \tag{11.2.3}$$

$$\boldsymbol{G}(x,y) = \nabla\boldsymbol{g}(x,y) - \boldsymbol{M}(x,y)\,, \tag{11.2.4}$$

where $u(x,y)$ and $v(x,y)$ represent the macroscopic displacement in the $\boldsymbol{e}_1$ and $\boldsymbol{e}_2$ directions, respectively. Roughly speaking, $\boldsymbol{g}$ is the macroscopic deformation, $\boldsymbol{M}$ the deformation gradient due to the disarrangements, and $\boldsymbol{G}$ that part of the deformation gradient due to the elastic distortion.

Assuming that the gradients of $u(x,y)$ and $v(x,y)$, as well as $\lambda\left(s(x,y)\right)$ and $\theta\left(s(x,y)\right)$, are small quantities of the first order, the Green's strain $(\boldsymbol{G}^T\boldsymbol{G} - \boldsymbol{I})/2$, due to the elasticity of the material, may be approximated by the *elastic infinitesimal strain*

$$\begin{aligned}\boldsymbol{\varepsilon}^e(x,y) &= \frac{1}{2}\left(\nabla\boldsymbol{g}(x,y) + \nabla\boldsymbol{g}^T(x,y)\right) - \boldsymbol{I} - \frac{1}{2}\left(\boldsymbol{M}(x,y) + \boldsymbol{M}^T(x,y)\right)\\ &= \boldsymbol{\varepsilon}(x,y) - \theta\left(s(x,y)\right)\, \boldsymbol{E}_{11} - \lambda\left(s(x,y)\right)\, \boldsymbol{E}_{22}\,,\end{aligned} \tag{11.2.5}$$

where $\boldsymbol{\varepsilon}(x,y)$ is the *macroscopic* (global) infinitesimal strain, and we have defined $\boldsymbol{E}_{11} = \boldsymbol{e_1} \otimes \boldsymbol{e_1}$ and $\boldsymbol{E}_{22} = \boldsymbol{e_2} \otimes \boldsymbol{e_2}$.

The quantity $\boldsymbol{\varepsilon}^s\left(s(x,y)\right) = \theta\left(s(x,y)\right)\, \boldsymbol{E}_{11} + \lambda\left(s(x,y)\right)\, \boldsymbol{E}_{22}$ represents instead the (infinitesimal) singular part of the strain, due to the disarrangements. The macroscopic strain $\boldsymbol{\varepsilon}$ is obtained with respect to the hypothesis of its partition in the elastic part $\boldsymbol{\varepsilon}^e$, due to the elasticity of the undamaged aragonite plates, and the structured deformation part $\boldsymbol{\varepsilon}^s$ due to the disarrangements. This leads to a plastic-like deformation splitting in the form

[3] Here, the symbol $\otimes$ represents the tensor product, i.e., $(\mathbf{a}\otimes\mathbf{b})\mathbf{v} = (\mathbf{b}\cdot\mathbf{v})\,\mathbf{a}$.

$$\boldsymbol{\varepsilon} = \boldsymbol{\varepsilon}^e + \boldsymbol{\varepsilon}^s \,. \tag{11.2.6}$$

In this way, it is possible not only to describe highly singular strains using continuous fields, but also to distinguish the contribution of the macroscopic deformation due to microstructural disarrangements from that consequent to the bulk distortions.

11.2.2 Thermodynamic framework

The state variables suggested by micro-mechanics are the total strain $\boldsymbol{\varepsilon}$ and the shear s due to disarrangements, which are now set in a thermodynamic framework. For convenience of notation, their dependence upon (x, y) will be dropped in the following. At constant temperature, the model is defined through the Helmholtz's free energy per unit mass Ψ and the yield function f.

Considering isothermal evolution, the Helmholtz's free energy coincides with the reversible elastic energy. There are two contributions to this energy: *i*) the elastic energy stored in the bent lamellae and *ii*) that associated with the elastic restraint offered by the bio-polymeric interlayer. If $\mathbb{C}$ represents the fourth-order isotropic elasticity tensor for the material forming the aragonite platelets, supposed to remain linear elastic (undamaged), the first contribution is associated with a strain energy per unit mass, which reads

$$\Psi_{elas} = \frac{1}{2\rho}\boldsymbol{\varepsilon}^e \cdot \mathbb{C}\,\boldsymbol{\varepsilon}^e = \frac{1}{2\rho}\boldsymbol{\varepsilon}^e \cdot \boldsymbol{\sigma} \,. \tag{11.2.7}$$

Here, ρ is the material density and $\boldsymbol{\sigma} = \mathbb{C}\,\boldsymbol{\varepsilon}^e$ is the stress tensor[4].

The second contribution is naturally associated with transversal relative displacement $t\,\theta(s)$ at the interface. We consider a general elastic constitutive law, expressed by the potential $\mathcal{K}\,(t\,\theta(s))$. Thinking again of a smeared view, where this contribution is averaged on the lamellar thickness t, the elastic energy per unit mass due to the elastic restraint of the disarrangements, reads

$$\Psi_{dis} = \frac{1}{\rho t}\mathcal{K}\,(t\,\theta(s)) \,. \tag{11.2.8}$$

For example, in the simplest case of a linear elastic constitutive law, one may assume $\mathcal{K}\,(t\,\theta(s)) = \frac{1}{2}\,\kappa\,(t\,\theta(s))^2$, where κ is the elastic constant per unit area, with dimensions $[M][L]^{-2}[T]^{-2}$. Representing the organic fibrils as elastic springs, and in particular the assumption that they are effective only for the dilatation

[4]The application of the fourth-order tensor $\mathbb{C}$ on the second-order tensor $\boldsymbol{\varepsilon}^e$ is denoted as $\mathbb{C}\,\boldsymbol{\varepsilon}^e$. The inner product between the two second-order tensors $\boldsymbol{\varepsilon}^e$ and $\boldsymbol{\sigma}$ reads $\boldsymbol{\varepsilon}^e \cdot \boldsymbol{\sigma}$.

component of deformation, is certainly a strong approximation. The model could incorporate a more general elastic-viscous-plastic response, of the type presented in [219], accounting for the shear s in addition to the dilation $\theta(s)$. However, this is not done here, because the simple term (11.2.8) will be sufficient to cover an exhaustive scenario.

In conclusion, by using the expression (11.2.5) for the elastic component of the strain $\boldsymbol{\varepsilon}^e$, the free energy per unit mass takes the form

$$\begin{aligned}\Psi(\boldsymbol{\varepsilon}, s) =& \frac{1}{2\rho} \left(\boldsymbol{\varepsilon} - \theta(s)\, \boldsymbol{E}_{11} - \lambda(s)\, \boldsymbol{E}_{22}\right) \cdot \mathbb{C} \left(\boldsymbol{\varepsilon} - \theta(s)\, \boldsymbol{E}_{11} - \lambda(s)\, \boldsymbol{E}_{22}\right) + \\ &+ \frac{1}{\rho t} \mathcal{K}\left(t\, \theta(s)\right) .\end{aligned} \tag{11.2.9}$$

The stress $\boldsymbol{\sigma}$, which corresponds to the derivative of $\rho\Psi$ with respect to $\boldsymbol{\varepsilon}$, reads

$$\boldsymbol{\sigma} = \mathbb{C}\left(\boldsymbol{\varepsilon} - \boldsymbol{\varepsilon}^s\right) = \mathbb{C}\left(\boldsymbol{\varepsilon} - \theta(s)\, \boldsymbol{E}_{11} - \lambda(s)\, \boldsymbol{E}_{22}\right) . \tag{11.2.10}$$

Since $\theta(0) = 0$ and $\lambda(0) = 0$, isotropic elasticity is readily recovered. It is possible to interpret the quantity $\boldsymbol{\varepsilon}^s(s) = \theta(s)\, \boldsymbol{E}_{11} + \lambda(s)\, \boldsymbol{E}_{22}$ to be equivalent to a plastic strain since, as in plasticity theory, from (11.2.9) the stress is given by $\mathbb{C}(\boldsymbol{\varepsilon} - \boldsymbol{\varepsilon}^s)$, but the similarity is just formal.

Following the standard generalized material framework [214], the thermodynamic force S associated with s is the partial derivative of the Helmholtz's free energy with respect to s, i.e., $S = -\partial(\rho\Psi)/\partial s$ (the minus sign is due to a thermodynamical convention). It is clear that here S represents the driving force for crack slip. In the case of isotropic materials, from (11.2.9) and recalling from (11.2.1) that $\mathrm{d}\lambda/\mathrm{d}s = t/L$, one obtains

$$\begin{aligned}S(\boldsymbol{\varepsilon}, s) =& \mathbb{C}\Big(\boldsymbol{\varepsilon} - \theta(s)\, \boldsymbol{E}_{11} - \lambda(s)\, \boldsymbol{E}_{22}\Big) \cdot \Big(\theta'(s)\, \boldsymbol{E}_{11} + \frac{t}{L} \boldsymbol{E}_{22}\Big) + \\ &- \theta'(s) \mathcal{K}'\left(t\, \theta(s)\right) ,\end{aligned} \tag{11.2.11}$$

where $\theta'(\cdot)$ and $\mathcal{K}'(\cdot)$ denote the first derivative of the functions $\theta(\cdot)$ and $\mathcal{K}(\cdot)$, respectively. Using (11.2.10), this expression can be conveniently rewritten in terms of the stress $\boldsymbol{\sigma}$ in the form

$$S(\boldsymbol{\sigma}, s) = \theta'(s) \Big[\boldsymbol{\sigma} \cdot \boldsymbol{E}_{11} - \mathcal{K}'\left(t\, \theta(s)\right)\Big] + \frac{t}{L}\, \boldsymbol{\sigma} \cdot \boldsymbol{E}_{22} . \tag{11.2.12}$$

Here, $\boldsymbol{\sigma} \cdot \boldsymbol{E}_{22}$ is the normal stress in the direction $\boldsymbol{e}_2$, related with the shear stress acting in direction parallel to the separation surface, while $\boldsymbol{\sigma} \cdot \boldsymbol{E}_{11}$ represents the normal component of stress in the direction $\boldsymbol{e}_1$. Thus, we infer from (11.2.12) that

not only the driving force S is produced by $t/L\,\boldsymbol{\sigma}\cdot\boldsymbol{E}_{22}$, but a significant role is also played by the component of stress work-conjugate with the "shear-induced dilation", as well as by the elastic reaction of the interface, represented by the term $\mathcal{K}'(t\,\theta(s))$.

It is natural to define the elastic region, or "convex of elasticity", with respect to the associated thermodynamic forces $\boldsymbol{\sigma}$ and S. In order to consider a cohesive-frictional response, one may introduce the yield function

$$f(\boldsymbol{\sigma},S)=|S|-\{B-\mu\,[\boldsymbol{\sigma}\cdot\boldsymbol{E}_{11}-\mathcal{K}'(t\,\theta(s))]\}\ . \tag{11.2.13}$$

Here, μ is the *effective* frictional coefficient and the constant B represents the cohesive contribution. This function defines the elastic domain through the condition $f(\boldsymbol{\sigma},S)<0$; yielding corresponds to $f(\boldsymbol{\sigma},S)=0$; states for which $f(\boldsymbol{\sigma},S)>0$ are not attainable. This is consistent with what observed in quasi-brittle materials [220] and recalls the cohesive fracture model by Barenblatt [221].

The term $\boldsymbol{\sigma}\cdot\boldsymbol{E}_{11}$ denotes the component of macroscopic stress at right angle to the sliding interface, defined at a material scale much larger than the characteristic length scale of surface roughness; similarly, the quantity $\mathcal{K}'(t\,\theta(s))$ denotes the elastic bridging provided by the biopolymeric interlayer. Observe that (11.2.13) does not exactly account for Coulomb's law, which should act according to the tangent plane to the contact profiles at the actual contact points, but it represents an "average" frictional law, effective at the level of mean separation plane between any pair of adjacent lamellae. In particular, μ denotes, in the aforementioned equivalence, the effective frictional coefficient, which is associated, but not necessarily coincides, with the actual frictional coefficient locally acting at the length scale of the contact profiles. Similarly, the dependence of the cohesion parameter B upon the local geometry of the contact profile is not made explicit, since B interprets the cohesive sliding of the mean interface plane between the adjacent lamellae.

The borderline case when $B=0$ corresponds to unilateral Coulomb's frictional law. When $B=0$, from (11.2.13), it follows that condition $\boldsymbol{\sigma}\cdot\boldsymbol{E}_{11}-\mathcal{K}'(t\,\theta(s))>0$ is not admissible. This means that the tensile stresses normal to the interface cannot overcome the elastic bridging. The elastic bridging, as well as a compressive normal stress $\boldsymbol{\sigma}\cdot\boldsymbol{E}_{11}<0$, all weighted by μ, increase the size of the elastic domain. The second limit case, $\mu=0$, corresponds to cohesive sliding. Now, we have from (11.2.13) that $|S|$ remains constant at yielding, independently of the compressive stress. The combinations of these two cases furnishes the admissibility condition

$$\boldsymbol{\sigma}\cdot\boldsymbol{E}_{11}-\mathcal{K}'(t\,\theta(s))\leqslant\frac{B}{\mu}\,. \tag{11.2.14}$$

This means that cohesion allows the transfer of tensile stresses that moderately overcome the elastic bridging.

At yielding ($f = 0$), the evolution for the state variable s is determined from the consistency equation $\mathrm{d}f = 0$ and generalized normality rule [214], stating that

$$\dot{s} = \frac{\partial f}{\partial S}\,\dot{\chi} = \mathrm{sgn}(S)\,\dot{\chi}\,, \tag{11.2.15}$$

where χ is analogous to the classic plastic multiplier, with $\dot{\chi} > 0$, the dot indicating derivative with respect to time. In this sense, the model can be considered associated, i.e., the dissipation pseudo-potential coincides with the yielding function. In particular, from equation (11.2.15), it is evident that $\dot{s}$ has the same sign of S, so that the yielding condition deriving from (11.2.13) can be written in the form,

$$\begin{cases} S = B - \mu\,[\,\boldsymbol{\sigma}\cdot\boldsymbol{E}_{11} - \mathcal{K}'\,(t\,\theta(s))]\,, & \text{if}\,\dot{s} > 0\,, \\ S = -\{B - \mu\,[\,\boldsymbol{\sigma}\cdot\boldsymbol{E}_{11} - \mathcal{K}'\,(t\,\theta(s))]\}\,, & \text{if}\,\dot{s} < 0\,, \\ |S| \leqslant B - \mu\,[\,\boldsymbol{\sigma}\cdot\boldsymbol{E}_{11} - \mathcal{K}'\,(t\,\theta(s))]\,, & \text{if}\,\dot{s} = 0\,, \end{cases} \tag{11.2.16}$$

where $B - \mu\,[\,\boldsymbol{\sigma}\cdot\boldsymbol{E}_{11} - \mathcal{K}'\,(t\,\theta(s))]$ is positive.

According to the second principle of thermodynamics, the intrinsic dissipation $\dot{D}$ must be positive. From the general theory [222], $\dot{D} = \sum_k A_k \dot{V}_k$, where A_k denotes the thermodynamic force associated with internal state variable V_k. For the case at hand, $A_k = S$ and $V_k = s$, so that, from (11.2.15), one obtains that the second principle is naturally fulfilled, i.e., $\dot{D} = S\,\dot{s} > 0$. Moreover, from (11.2.16), the intrinsic dissipation can be written as $\dot{D} = \{B - \mu\,[\,\boldsymbol{\sigma}\cdot\boldsymbol{E}_{11} - \mathcal{K}'\,(t\,\theta(s))]\}|\dot{s}|$, from which the admissibility condition (11.2.14) is recovered and turns out to be strictly correlated to the positiveness of the dissipation.

11.2.3 Equations for homogenous biaxial stress

Assume, for the shear tensegrity, that the stress state is homogeneous of the form $\boldsymbol{\sigma} = \sigma_{11}\,\boldsymbol{e}_1 \otimes \boldsymbol{e}_1 + \sigma_{22}\,\boldsymbol{e}_2 \otimes \boldsymbol{e}_2$, where $\boldsymbol{e}_1$ and $\boldsymbol{e}_2$ are as defined in Figure 11.4(a). This assumption, which neglects the stress concentrations due to local contact of the asperities, can be introduced in this particular theoretical framework, and represents one of the major advantages of the model.

From formula (11.2.12), the thermodynamical variable S associated with the slip s reads

$$S(s) = \theta'(s)\Big[\sigma_{11} - \mathcal{K}'\,(t\,\theta(s))\,\Big] + \frac{t}{L}\,\sigma_{22}\,. \tag{11.2.17}$$

In words, S is the sum of the imposed longitudinal stress σ_{22}, weighted by t/L, and

of the term $\theta'(s)\,[\sigma_{11} - \mathcal{K}'\,(t\,\theta(s))]$, which has a precise mechanical interpretation. Referring to Figure 11.4(a) and considering the equivalence in terms of resultant internal force, one has that the mean shear stress acting along the average interface of adjacent lamellae caused by the σ_{22} is $\sigma_{22}\,t/L$. On the other hand, with reference to periodic and symmetric contact profiles as per Figure 11.4(b), if the separation lips of the tablets are supposed to remain in contact during a relative translation, at each instant, the relative velocity of gliding is parallel to a common tangent plane to the separation lip profiles, whose slope is θ' with respect to the separation average plane. Hence, one can interpret $\theta'(s)\,[\sigma_{11} - \mathcal{K}'\,(t\,\theta(s))]$ as the amount of shear induced by the stress σ_{11} and the elastic bridging. The equivalence is also evident in energetic terms, since the dissipation reads $\dot{D} = S\dot{s} = [\sigma_{11} - \mathcal{K}'\,(t\,\theta(s))]\,\dot{\theta} + \sigma_{22}\,\dot{s}\,t/L$. Here, $\sigma_{22}\,\dot{s}\,t/L$ is the power dissipated by the shear induced by longitudinal stress and $[\sigma_{11} - \mathcal{K}'\,(t\,\theta(s))]\,\dot{\theta}$ represents the power of the lateral stress in the extension that accompanies sliding.

From (11.2.13) and (11.2.17), the elastic domain at a given state s is defined by the inequality

$$\left|\theta'(s)\Big[\sigma_{11} - \mathcal{K}'\,(t\,\theta(s))\Big] + \frac{t}{L}\,\sigma_{22}\right| \leqslant B - \mu\Big[\sigma_{11} - \mathcal{K}'\,(t\,\theta(s))\Big]\,, \tag{11.2.18}$$

where $B - \mu\,[\sigma_{11} - \mathcal{K}\,(t\,\theta(s))] \geqslant 0$ from the admissibility condition.

In the $\sigma_{11} - \sigma_{22}$ plane, equation (11.2.18) defines the region bounded by the two lines with the common point identified by the pair of coordinates

$$\left(\mathcal{K}'\,(t\,\theta(s)) + \frac{B}{\mu}\,,\, -\frac{BL}{t}\frac{\theta'(s)}{\mu}\right)\,, \tag{11.2.19}$$

and intersecting the $\sigma_{22}-$axis at points with ordinate

$$\frac{L}{t}\,\theta'(s)\,\mathcal{K}'\,(t\,\theta(s)) \pm \frac{L}{t}\Big[B + \mu\,\mathcal{K}'\,(t\,\theta(s))\Big]\,. \tag{11.2.20}$$

The situation can be better appreciated by plotting the elastic domain in the $\sigma_{11} - \mathcal{K}'\,(t\,\theta(s))$ vs. $\sigma_{22}\,t/L$ plane. This is bounded by two lines with the common point $(B/\mu, -B\theta'(s)/\mu)$ and intersecting the vertical axis at $+B$ and $-B$, as shown in Figure 11.5(a). The elastic domain may evolve between the upper and lower bounds determined by the maximum and minimum values attained by $\theta'(s)$. In particular, for the case of periodic and symmetric profiles in contact along convex surfaces, as indicated in Figure 11.4(b), these extremes are equal in absolute value, say $\pm M$, where $M > 0$ depends only upon the shape of the contact profiles. For varying s, the yielding surface takes two different shapes, according to the sign of the quantity $\mu - M$.

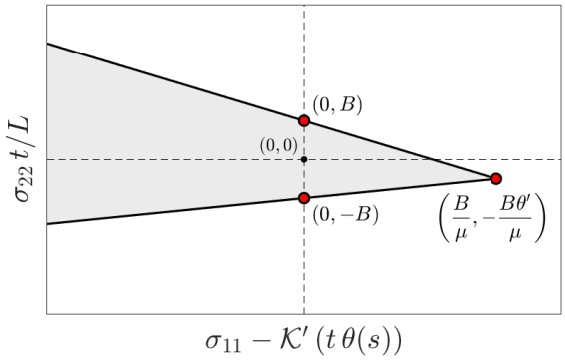

(a)

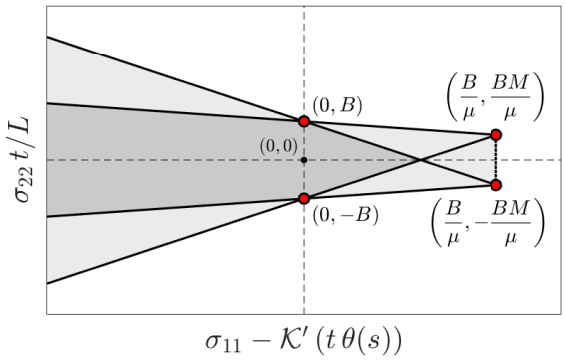

(b)

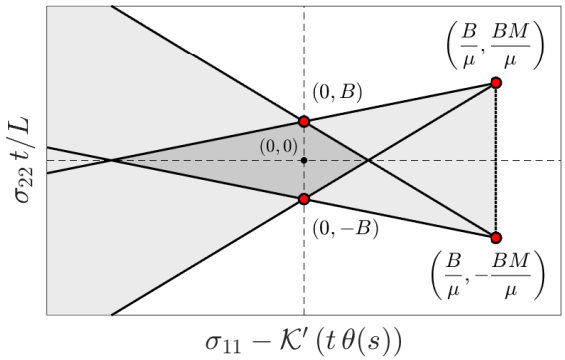

(c)

Figure 11.5. Representation of the elastic domain in the $\sigma_{11} - \mathcal{K}'\,(t\,\theta(s))$ vs. $\sigma_{22}\, t/L$ plane: (a) typical form of the elastic domain, bounded by two lines; (b) elastic domains in the case $\max\{\theta'(s)\} = M < \mu$ and (c) $\max\{\theta'(s)\} = M > \mu$.

Figure 11.5(b) illustrates the case $M-\mu<0$, corresponding to a material where the coefficient of friction μ is greater than the maximum slope M of the opening function, while Figure 11.5(c) displays the complementary case $M-\mu>0$. Here, parameters B and μ maintain the same values of Figure 11.5(a) and only M has been changed. Provided $\theta'(s)$ attains all the values in the interval $[-M,M]$ as s is varied, all admissible stress states lie in grey region represented in Figure 11.5. In particular, the dark-grey region, referred to as "always-elastic domain", corresponds to locally stable elastic stress configurations, i.e., every infinitesimal transformation from those states will remain elastic in the sense that they do not imply any modification of s.

11.3 Geometric characterization of sliding profiles

The constitutive properties of the material are strictly correlated with the roughness of the contact surfaces, which determines the form of the opening function $\theta(s)$. An important hypothesis is that the stress concentration due to the local contact of the asperities produces a *negligible* change in the shape of the profiles. The validity of this assumption will be checked later on in Section 11.4.3, while discussing the proposed examples. Our purpose, here, is to illustrate the wide scenario that can be obtained under this hypothesis, by just changing the geometry of the contacts.

Let $\omega:\mathbb{R}\to\mathbb{R}$ represent a piecewise regular, symmetric, even, periodic function, with period p, with the property that $\omega(x+p/2)=-\omega(x)$, $\forall x\in\mathbb{R}$. In order

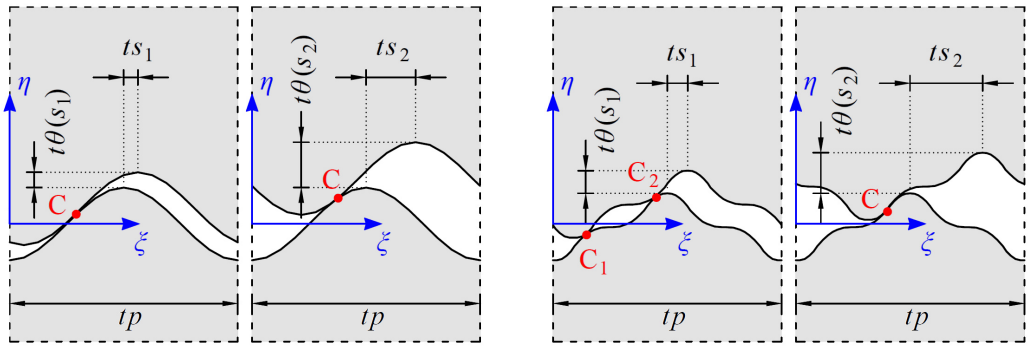

Figure 11.6. Schematic representation of the sliding profiles, with indication of contact points per period for increasing shearing. Case of (a) convex and (b) non-convex periodic profiles.

to define such a function it is sufficient to define the graph of its restriction in the interval $[0, p/4]$, since the successive branches can be obtained by alternately reversing this graph, mirroring and matching the pieces together. In other words, the graph can be made to coincide with itself after the combination of a reflection in its average line and a translation of half the wave-length. Without losing generality, assume that $\omega(0) < 0$.

We suppose that in the reference undistorted configuration the surfaces of the upper and lower lamellae perfectly match one another and are identified by the graph of the function $\eta = t\,\omega(\xi/t)$, where t is the thickness of the lamellae, here again chosen as a representative length-scale. Hence, the axis ξ defines the middle plane of each contact surface and is parallel to the direction of sliding, identified by the unit vector $\boldsymbol{e}_2$ in Figure 11.4(a); the axis η is orthogonal to ξ. Clearly the profiles are periodic curves of period $t\,p$ and they are the sequence of branches, which are one opposite to the other, alternately following with step $t\,p/2$. In particular, the assumed symmetry implies that

$$\omega(p/4 + \xi/t) = -\omega(p/4 - \xi/t), \quad \forall \xi \in \mathbb{R}\,, \tag{11.3.21a}$$

$$\omega'(p/4 + \xi/t) = \omega'(p/4 - \xi/t), \quad \forall \xi \in \mathbb{R}\,. \tag{11.3.21b}$$

It is supposed that, as the lamellae are sheared apart, the profiles remain in contact at points that are defined by their geometry, as represented in Figure 11.6. A distinction needs to be made between two cases. In the first, indicated in Figure 11.6(a), there is one point of contact per period. This occurs when the graph of $\eta = t\,\omega(\xi/t)$ is convex in the interval $[-t\,p/4, t\,p/4]$: because of this, profiles of this type will be called *convex*. The second, complementary, case is represented by the *non-convex* profiles of Figure 11.6(b). Now, there might be more than one point of contact for increasing shearing: more in general, the locus of the contact points is not represented by a continuous line, because the contact may "jump" from one branch of the profile to another.

The shearing is measured by the state variable s introduced in Section 11.2.1. The problem consists in calculating the opening function $\theta(s)$ once the shape of the contact profiles is assigned through the function ω.

11.3.1 Convex periodic profiles

When the upper lamella glides with respect to the lower one, as indicated in Figure 11.6(a), opening is due to surmounting. In the case of a convex profile, there is only one possible contact point C per period. Figure 11.6(a) illustrates this scenario for two different values s_1 and s_2 of the variable s. Without loosing generality, suppose that the lower profile remains fixed, so that it remains associated with the function

$\eta = t\,\omega(\xi/t)$; the upper profile, which is right-shifted of $t\,s$ if $s > 0$, is represented by the graph of the function $\eta = t\,\omega(\xi/t - s) + t\,\theta(s)$.

Due to the periodicity of the profiles, it is convenient to restrict the attention to the interval $-t\,p/2 \leqslant \xi \leqslant t\,p/2$ and consider a shearing such that $s \in [-p/2, p/2]$. Indicate with ξ_c the abscissa of the generic contact point C, which shall satisfy $-t\,p/2 \leqslant \xi_c \leqslant t\,p/2$ and observe that ξ_c has the same sign of s. The contact condition is that at C the tangent to the two profiles shall be the same, i.e.,

$$\omega'(\xi_c/t) = \omega'(\xi_c/t - s)\,, \qquad \text{for} \quad s \in [-p/2, p/2]\,. \tag{11.3.22}$$

Because of (11.3.21b), there exists some α for which

$$\begin{cases} \xi_c/t = p/4 + \alpha\,, \\ \xi_c/t - s = p/4 - \alpha\,, \end{cases} \qquad \text{if} \quad s \in [0, p/2]\,, \tag{11.3.23a}$$

$$\begin{cases} \xi_c/t = -(p/4 + \alpha)\,, \\ \xi_c/t - s = -(p/4 - \alpha)\,. \end{cases} \qquad \text{if} \quad s \in [-p/2, 0)\,. \tag{11.3.23b}$$

This distinction is necessary because ξ_c is positive (negative) when s is positive (negative). Eliminating α one obtains

$$\xi_c/t = s/2 + p/4\,, \qquad \text{if} \quad s \in [0, p/2]\,, \tag{11.3.24a}$$

$$\xi_c/t = s/2 - p/4\,, \qquad \text{if} \quad s \in [-p/2, 0)\,. \tag{11.3.24b}$$

The opening function $\theta(s)$ can be found from condition $\omega(\xi_c/t) = \omega(\xi_c/t - s) + \theta(s)$. Taking into account the symmetry of ω, as per (11.3.21a), $\theta(s)$ takes the form

$$\begin{aligned} \theta(s) &= \omega(p/4 + s/2) - \omega(p/4 - s/2) \\ &= 2\omega(p/4 + s/2)\,, \end{aligned} \qquad \text{if} \quad s \in [0, p/2]\,, \tag{11.3.25a}$$

$$\begin{aligned} \theta(s) &= \omega(p/4 - s/2) - \omega(p/4 + s/2) \\ &= -2\omega(p/4 + s/2)\,, \end{aligned} \qquad \text{if} \quad s \in [-p/2, 0)\,. \tag{11.3.25b}$$

This function is non-negative and its derivative is, in general, discontinuous at $s = 0$. It shall be periodically extended to cover the more general case in which s exceeds the interval $[-p/2, p/2]$.

Triangular profiles

A triangular wave profile of the type represented in Figure 11.7(a) corresponds to an expression of the form

$$\frac{\eta}{t} = \omega\Big(\frac{\xi}{t}\Big) = -\frac{A}{2} + A\,\mathrm{Tr}\Big(\frac{2\xi}{tp}\Big)\,, \tag{11.3.26}$$

where $\mathrm{Tr}(\cdot)$ is the period extension of the function $\mathrm{T}(\cdot)$, defined in the interval $[0,2]$ as $\mathrm{T}(x) = x$ for $x \in [0,1]$ and $\mathrm{T}(x) = 2 - x$ for $x \in (1,2]$. The opening function $\theta(s)$ is displayed in Figure 11.7(c) and can be expressed as

$$\theta(s) = A\,\mathrm{Tr}\Big(\frac{2s}{p}\Big)\,. \tag{11.3.27}$$

The derivative $\theta'(s)$ of the opening function is shown in Figure 11.7(e). It is piecewise constant function, i.e., $\theta'(s) = \pm 2A/p = \pm M$, with jumps at $s = kp$ and $s = kp/2$, $k \in \mathbb{Z}$.

Sinusoidal profiles

In the model proposed by Evans et al. [192], the roughness of the nacre lamellae has been considered sinusoidal in type. The profile shown in Figure 11.7(b) is the graph of the function

$$\frac{\eta}{t} = \omega\Big(\frac{\xi}{t}\Big) = -\frac{A}{2}\cos\Big(\frac{2\pi\xi}{tp}\Big)\,. \tag{11.3.28}$$

The opening function $\theta(s)$, displayed in Figure 11.7(d), can be expressed as

$$\theta(s) = A\left|\sin\Big(\frac{\pi s}{p}\Big)\right|\,. \tag{11.3.29}$$

Its first derivative $\theta'(s)$ is depicted in Figure 11.7(f). It is a monotonically decreasing piecewise cosine function, with jumps at $s = kp$, $k \in \mathbb{Z}$.

Observe that the slope of $\theta(s)$ at $s = 0^{\pm}$ is equal to $\pm\pi A/p$; for the same amplitude A, the triangle function provides $\theta'(0^{\pm}) = \pm 2A/p$, which is smaller in absolute value.

Circular profiles

A profile represented by a piecewise circular curve, where arcs of circle are continuously and smoothly connected one another, is referred to as a circular profile. It is convenient to use a parametric representation in the $\xi - \eta$ plane. When the

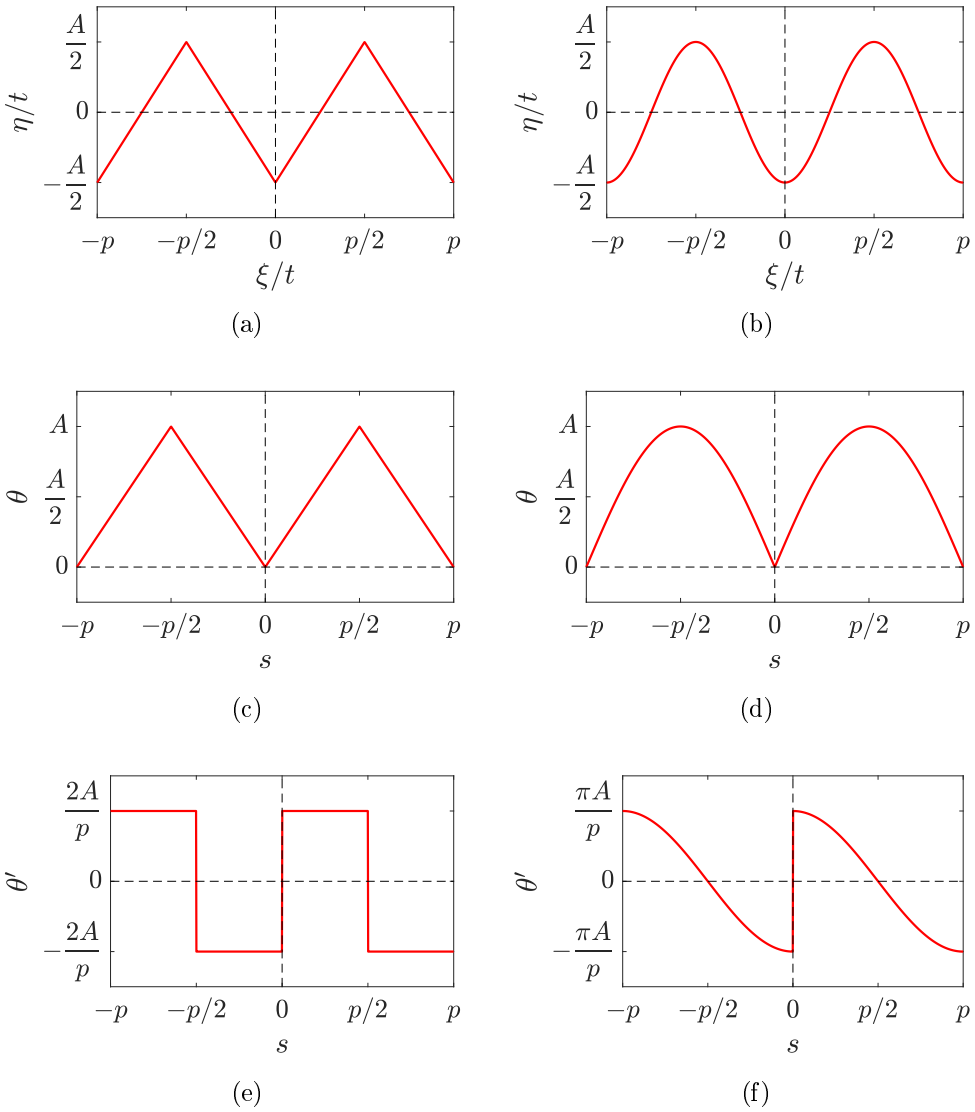

Figure 11.7. Triangular and sinusoidal contact profiles. Profile shape, opening function $\theta(s)$ and its derivative $\theta'(s)$ for (a)-(c)-(e) the triangular and (b)-(d)-(f) the sinusoidal cases, respectively.

profile is formed by semicircles as in Figure 11.8(a), so that the amplitude is R and the period $p = 4R$, one can write

$$\begin{cases} \xi/t = R\sin(\alpha) + 2kR\,, \\ \eta/t = -R\cos(\alpha + k\pi)\,, \end{cases} \quad \text{for} \quad \alpha \in [-\pi/2, \pi/2)\,, k \in \mathbb{Z}\,. \tag{11.3.30}$$

It is clear that α represents the angle between the η axis and the rotating radius of the constituting semicircles.

One can use the same parameter α to indicate a potential contact point. Simple geometry shows that the corresponding slide s takes the form

$$s = 2\left[R - R\sin(\alpha)\right] + 4kR\,, \qquad \text{if} \quad \alpha \in [0, \pi/2)\,, k \in \mathbb{Z}\,, \tag{11.3.31a}$$

$$s = -2\left[R + R\sin(\alpha)\right] + 4kR\,, \qquad \text{if} \quad \alpha \in [-\pi/2, 0)\,, k \in \mathbb{Z}\,, \tag{11.3.31b}$$

whereas the corresponding value of the opening θ reads

$$\theta = 2R\cos(\alpha)\ . \tag{11.3.32}$$

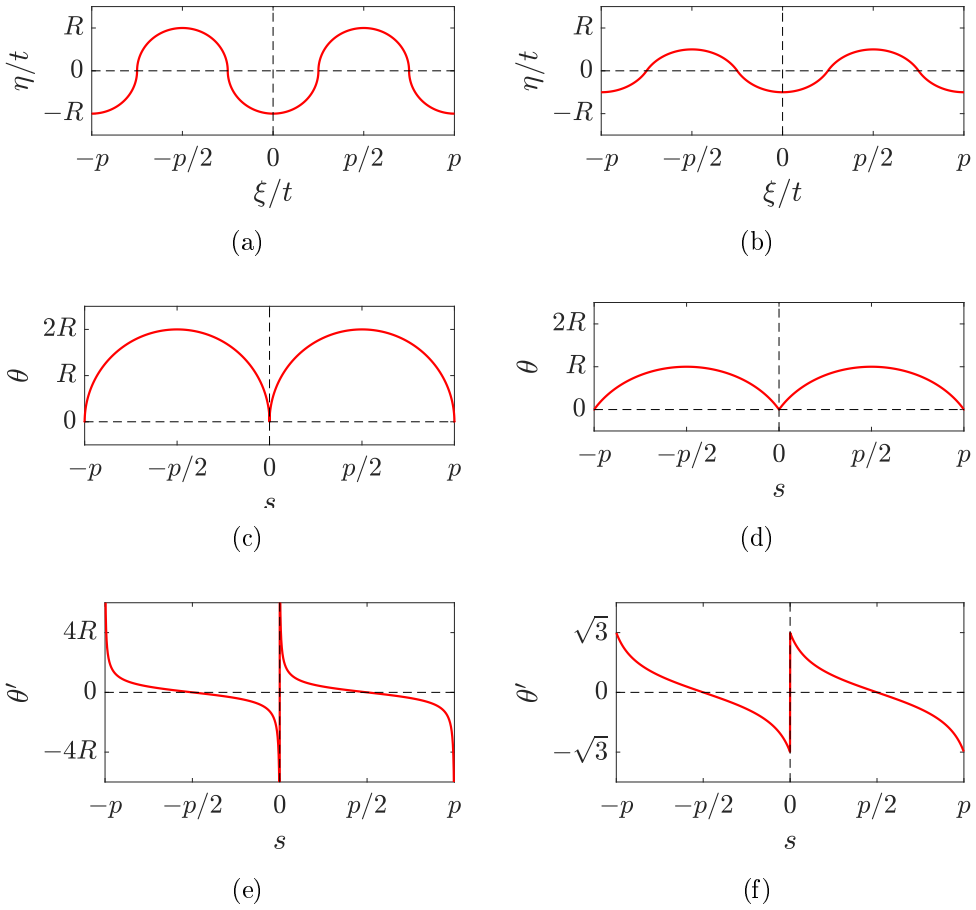

Figure 11.8. Circular contact profiles. Profile representation, opening function $\theta(s)$ and its derivative $\theta'(s)$ for (a)-(c)-(e) the semicircular toothing (parameter $\alpha \in [-\pi/2, \pi/2)$) and (b)-(d)-(f) the minor-arc toothing (parameter $\alpha \in [-\pi/3, \pi/3)$), respectively.

The equations (11.3.31) and (11.3.32) provide a parametric representation of the opening function $\theta(s)$, whose plot is represented in Figure 11.8(c). This is a piecewise semicircular curve of radius $2R$, with cusps at $s = kp$. Its derivative $\theta'(s)$, reported in Figure 11.8(e), presents vertical asymptotes at $s = kp$, $k \in \mathbb{Z}$.

The case in which the profile is formed by the smooth coupling of minor arcs of circles, can be similarly studied. One can write the same equations (11.3.30), (11.3.31) and (11.3.32), provided that the parameter α is made to vary in an interval smaller than $[-\pi/2, \pi/2)$, while considering that the centers of the connected circular arcs are no more aligned on the ξ axis. Figure 11.8(b) reports the graph of this minor-arc toothing for $\alpha \in [-\pi/3, \pi/3)$: the amplitude is $R/2$ and the period $p = 2\sqrt{3}R$. The corresponding plot of the opening function $\theta(s)$ is indicated in Figure 11.8(d). Observe that now the initial slope is no longer vertical, so that its derivative $\theta'(s)$, plotted in Figure 11.8(f), is bounded, with jumps at $s = kp$ between the values $\pm\tan(\pi/3)$.

11.3.2 Non-convex periodic profiles

This case is complicated by the fact that, as illustrated in Figure 11.6(b), the contact point may be not unique and may jump from one branch of the profile to another as the slide s is increased. Since condition (11.3.24) does not necessarily hold, the opening function $\theta(s)$ cannot be evaluated using (11.3.25). For the non-convex case, the direct approach is the most convenient. For any given value of the sliding $s = \bar{s}$, the corresponding value $\theta(\bar{s})$ is calculated, so that the upper profile $\eta/t = \omega(\xi/t - \bar{s}) + \theta(\bar{s})$ shares at least one point in common with the lower profile $\eta/t = \omega(\xi/t)$ and the inequality $\omega(\xi/t) \leqslant \omega(\xi/t - \bar{s}) + \theta(\bar{s})$ is fulfilled $\forall \xi \in \mathbb{R}$.

Figure 11.9 reports two examples. The shape shown in Figure 11.9(a) is obtained as the product of two cosine functions with different periods, in the form

$$\frac{\eta}{t} = \omega\Big(\frac{\xi}{t}\Big) = -\frac{A}{2}\cos\Big(\frac{2\pi\xi}{tp}\Big)\cos\Big(\frac{4\pi\xi}{tp}\Big)\,. \tag{11.3.33}$$

The corresponding opening function $\theta(s)$ and its derivative $\theta'(s)$ are reported in Figures 11.9(c) and 11.9(e), respectively. Figure 11.9(b) indicates instead a profile with smoothly connected arcs of circle of radius R and $2R$, for which $\theta(s)$ and $\theta'(s)$ are respectively plotted in Figures 11.9(d) and 11.9(f).

Multimodal functions for $\theta(s)$ are obtained, which correspond to complex constitutive responses. However, comparing Figure 11.9 with Figure 11.7, for the sinusoidal case, and with Figure 11.8, for the circular case, one infers that the non-convex case may be considered the superposition of convex cases. The constitutive equations shall be more complicated, but the difference is formal and not substantial.

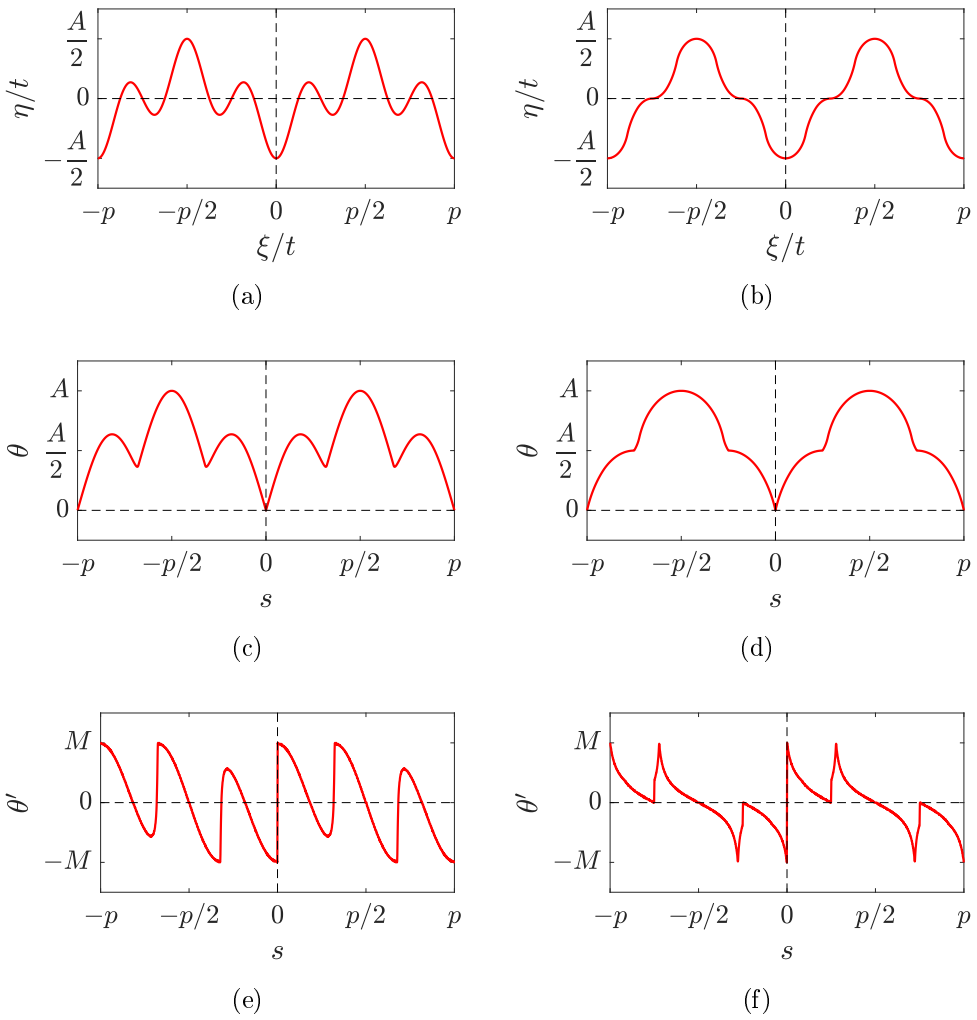

Figure 11.9. Non-convex contact profiles. Profile shape, opening function $\theta(s)$ and its derivative $\theta'(s)$ for (a)-(c)-(e) the piecewise sinusoidal and (b)-(d)-(f) the piecewise circular profiles, respectively.

Remark 1. A key property, which is in general shared by a wide class of profiles, is that $\theta'(s)$ is discontinuous at $s = kp$, $k \in \mathbb{Z}$, and attains its extreme values in a neighborhood of discontinuity points. The model calls for an interpretation of such discontinuities. For any infinitesimal variation of s in a neighborhood of $s = kp$, the yield surface would suddenly jump between the two distinct configurations, represented by the wedge-like domains of Figure 11.5, whose vertices are either at $(B/\mu, -BM/\mu)$ or at $(B/\mu, BM/\mu)$. Such a material instability is due to the assumed sharpness of the contact profiles, but one expects that in a real case

the profiles are smoothened, perhaps by micro-fractures that round the surfaces. Therefore, the discontinuous function $\theta'(s)$ should be interpreted as the limit case of a corresponding continuous function with a steep branch in a neighborhood of $s = kp$: this fact implies that $\theta'(s)$ attains all the values of the interval $[-M, M]$ in a neighborhood of $s = kp$.

This position reflects the spirit of classical Coulomb's frictional theory and the corresponding generalized functions. Referring to (11.2.18), all possible admissible states in the stress space, spanned while $\theta'(s) \in [-M, M]$ in a neighborhood of $s = kp$, $k \in \mathbb{Z}$, can be attained.

Remark 2. The model does not account for the reduction of the number of asperities during straining but, under the hypothesis that the shape of the asperities does not change, the results are not affected by this phenomenon. In fact, our model considers a frictional law that is valid at the level of the average contact plane, in such a way that the shear stress, consequent to the frictional restraint, depends on the resultant of the contact forces normal to this plane, and not on the single contact forces. If the number of contacts is reduced, the localized contact forces increase, but the resultant basically remains the same. Moreover, the opening function $\theta(s)$ does not change regardless the number of asperities still in contact, because this is dictated by the shape of the asperities, supposed rigid, that remain in contact.

Of course, the scenario becomes quite different if the elastic deformation of the asperities is taken into account, because, if the localized contact forces increase, the shape of the contact profiles is modified. Moreover, one expects that, as the relative sliding is increased, the cohesive ligaments break, thus reducing the cohesive contribution, but this is not taken into account here.

In any case, in real nacre, there is a high number of asperities. This implies that the length L of the overlapping lamellae is much greater than the characteristic wavelength $t\,p$ of the wavy profiles, and that the relative displacement Λ between sliding lamellae is much smaller than the length of the lamellae themselves (see Figure 11.4). As a result, the total number of asperities that remain in contact should not substantially vary during shearing. A more refined improved model shall take into account that the number of contacted asperities will decrease as the relative sliding increases, but this would require consideration of the elastic compliance of the lamellae, which is beyond the scope of the present work.

11.4 Response under homogeneous plane stress

Consider again the case developed in Section 11.2.3 for the biaxial state of stress $\boldsymbol{\sigma} = \sigma_{11}\,\boldsymbol{e}_1 \otimes \boldsymbol{e}_1 + \sigma_{22}\,\boldsymbol{e}_2 \otimes \boldsymbol{e}_2$, with $\boldsymbol{e}_1$ and $\boldsymbol{e}_2$ as in Figure 11.4(a). We calculate the

response under homogeneous straining for various shapes of the contact profiles, of the type characterized in Section 11.3.

From (11.2.16) and (11.2.17), one obtains that

$$\sigma_{22} = \frac{L\,B}{t} - \frac{L}{t}\Big[\mu + \theta'(s)\Big]\Big[\sigma_{11} - \mathcal{K}'\left(t\,\theta(s)\right)\Big]\,, \qquad \text{if} \quad \dot{s} > 0\,, \tag{11.4.34a}$$

$$\sigma_{22} = -\frac{L\,B}{t} + \frac{L}{t}\Big[\mu - \theta'(s)\Big]\Big[\sigma_{11} - \mathcal{K}'\left(t\,\theta(s)\right)\Big]\,, \qquad \text{if} \quad \dot{s} < 0\,. \tag{11.4.34b}$$

When $\dot{s} = 0$, the inequality (11.2.18) holds. From (11.2.1), (11.2.5), (11.2.6) and (11.2.10), the corresponding strain takes the form

$$\varepsilon_{22} = \frac{\sigma_{22}}{E} - \nu\frac{\sigma_{11}}{E} + \frac{2\,s\,t + \Lambda_0}{2L}\,, \tag{11.4.35}$$

where E and ν are the Young's modulus and the Poisson's ratio for the bulk material, supposed homogeneous and isotropic. In the following examples, unless otherwise stated, values compatible with those of a nacre tablet made of single crystalline aragonite are assumed for the mechanical properties. In particular, we will use $E = 87\,\text{GPa}$ as reported in [223], and $\nu = 0.28$ as derived from the bulk and shear moduli indicated in [224].

Assume that σ_{11} is given and fixed. For varying s the equations (11.4.34) and (11.4.35) provide a parametric representation of the "plastic" branches in the $\sigma_{22} - \varepsilon_{22}$ plane. The elastic branches correspond to $s = \bar{s}$, with $\bar{s}$ representing a constant value and $\dot{s} = 0$. In this case the inequality (11.2.18) implies that σ_{22} can vary within the interval defined by the limits (11.4.34a) and (11.4.34b); the corresponding ε_{22} results from (11.4.35).

The reference state is that in which $\sigma_{11} = \sigma_{22} = 0$ and $\varepsilon_{22} = 0$, which corresponds to $s = 0$ if $\Lambda_0 = 0$. However, since we are interested in considering reverse cyclic loading, it will be assumed that $\Lambda_0 > 0$, so that sliding of the interfaces can occur also in compression without material overlapping. According to (11.4.35), this would mean that $\varepsilon_{22} = 0.5\Lambda_0/L$ in the reference state, but this value is purely formal. For clarity, the graphs that will be drawn in the following will consider the *effective* value of ε_{22}, which represents its variation with respect to the reference value $0.5\Lambda_0/L$.

11.4.1 Constant interfacial confinement

For "interfacial confinement" we mean a restraint to the dilatation of the sliding interfaces, which can be generated by internal and/or external causes.

Table 11.1. Model parameters, including internal/external confinement and geometric characteristics of the contact profiles, used for the in-silico experiments of Figures 11.10, 11.11, 11.12 and 11.13.

profile	triangular		sinusoidal		circular		non-convex	
confinement	high	low	high	low	high	low	high	low
σ_κ (MPa)	1.43	0.48	0.96	0.31	1.64	0.55	0.37	0.12
σ_0 (MPa)	0.00	0.00	0.00	0.00	0.00	0.00	0.00	0.00
σ_y (MPa)	70.00	70.00	70.00	70.00	70.00	70.00	70.00	70.00
B (MPa)	0.5	2.5	0.4	2.5	0.5	2.5	0.4	2.5
μ ($-$)	0.1	0.1	0.1	0.1	0.1	0.1	0.1	0.1
p ($-$)	0.126	0.126	0.126	0.126	0.131	0.131	0.200	0.200
A ($-$)	0.126	0.126	0.126	0.126	0.038	0.038	0.300	0.300
t/L ($-$)	0.05	0.05	0.05	0.05	0.05	0.05	0.05	0.05

A constant external confinement is essentially a homogeneous compressive stress field orthogonal to the mean surface of interfaces, of the type $\sigma_{11} = -\sigma_0$, with $\sigma_0 > 0$. For example, in a underwater environment, this can represent the effect of the hydrostatic pressure when the nacre is protected by a waterproof skin.

The internal interfacial confinement is due to the biopolymeric fibrils bridging the interfaces, which has been modeled through the elastic potential $\mathcal{K}(t\,\theta(s))$ in Section 11.2.2. A *constant* confinement is achieved when the bridging stress, which is equal to $\mathcal{K}'(t\,\theta(s))$, is of the form

$$\mathcal{K}'(t\,\theta(s)) = \begin{cases} \sigma_\kappa\,, & \text{if } \theta(s) > 0\,, \\ 0\,, & \text{if } \theta(s) = 0\,, \end{cases} \qquad \text{with} \quad \sigma_\kappa > 0 \tag{11.4.36}$$

This represents the limit case of a superelastic response characterized by a tangent elastic modulus that rapidly decays to zero. Equivalently, it indicates a pure cohesive bridging, which recalls Barenblatt's crack model [221]. The superimposition of the two cases provides that $\sigma_{11} - \mathcal{K}'(t\,\theta(s)) = -\sigma_0 - \sigma_\kappa = -\sigma_c$, where $\sigma_c = (\sigma_0 + \sigma_\kappa) > 0$ will be referred to as *interfacial confinement* stress.

Figures 11.10, 11.11, 11.12 and 11.13 collect the graphs, drawn in the $\sigma_{22} - \varepsilon_{22}$ plane, which describe the responses for the triangular, sinusoidal, circular and non-convex (sinusoidal) contact profiles, respectively. The considered parameters are reported in Table 11.1.

The behavior is linear-elastic, with $s = 0$ and $\dot{s} = 0$, from the initial state $(0, 0)$

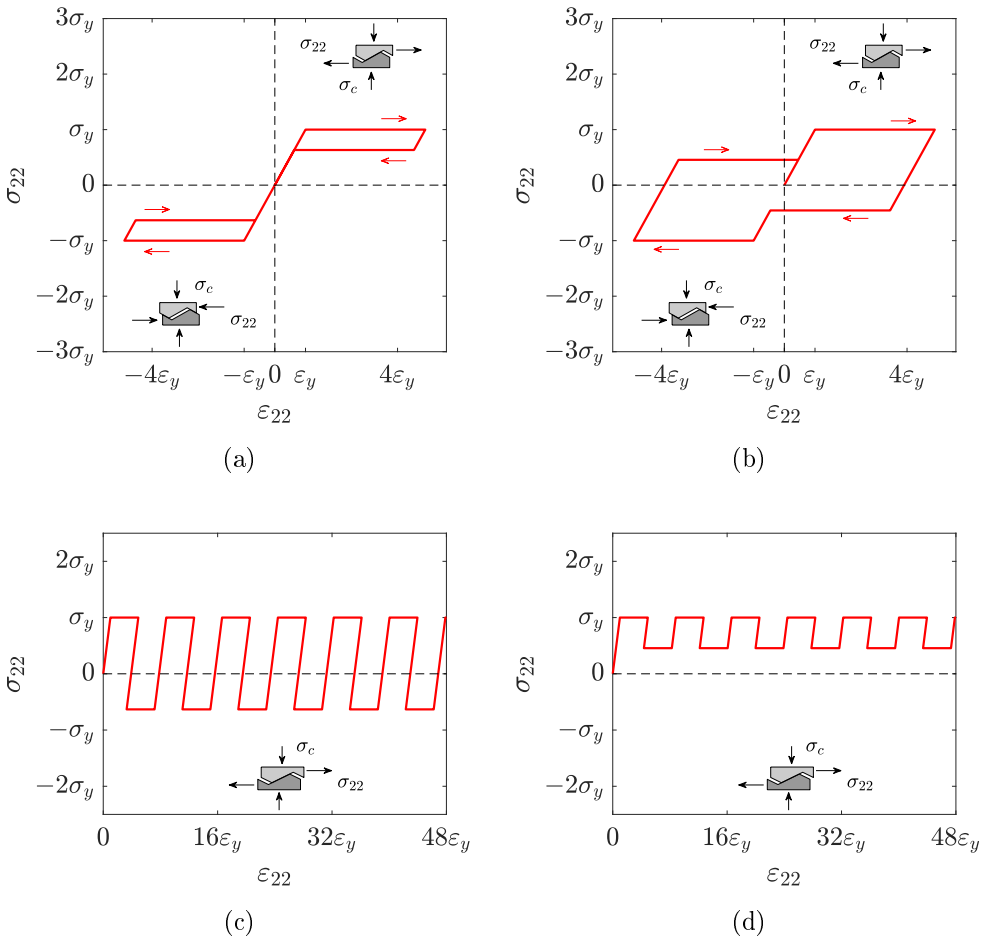

Figure 11.10. Response for the triangular contact profiles of Figure 11.7(a). Hysteresis loop for $s \in [-p/2, p/2]$: (a) "high" $\sigma_c > B/(\theta'(0^+) - \mu)$ and (b) "low" $\sigma_c < B/(\theta'(0^+) - \mu)$. Long tensile response ($s \gg p/2$) for (c) high σ_c and (d) low σ_c.

up to the point $(\varepsilon_y, \sigma_y)$ of first "yielding", for which $s = 0$ and $\dot{s} > 0$. Observe that the assumed value $\sigma_y = 70\,\text{MPa}$ is consistent to that of real nacre [198], while $t/L = 0.05$ complies with the dimensions of tablets detailed in the introductive Section 11.1.1. The subfigures (a) and (b) report the hysteresis loop consequent to strain-driven cycles, for which $s \in [-p/2, p/2]$, for two different values of σ_c. The subfigures (c) and (d) show, for the aforementioned σ_c, the "long" tensile response, corresponding to the case in which s can be very high ($s \gg p/2$), so that the surmounting of the asperities can occur several times as the interface profiles are progressively sheared apart. This tensile experiment corresponds to a closed-loop control imposing that the state variable s is monotonically increasing.

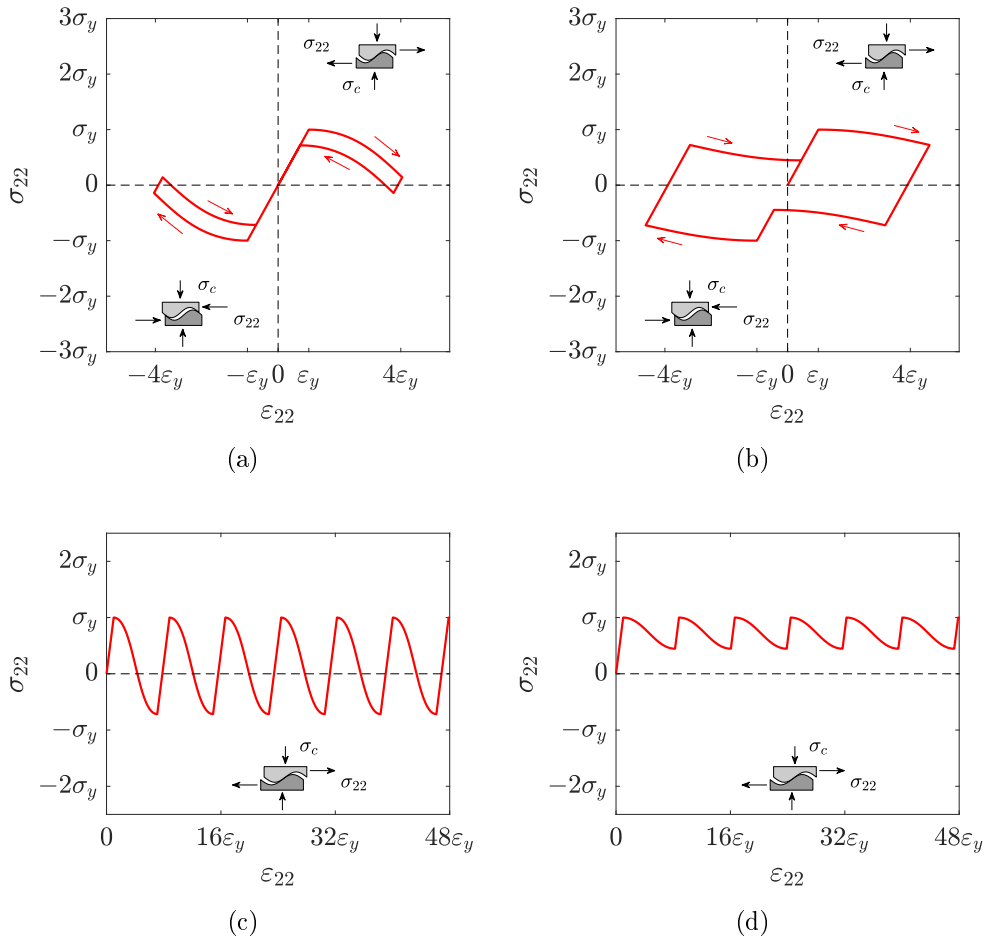

Figure 11.11. Response for the sinusoidal contact profiles of Figure 11.7(b). Hysteresis loop for $s \in [-p/2, p/2]$: (a) "high" $\sigma_c > B/(\theta'(0^+) - \mu)$ and (b) "low" $\sigma_c < B/(\theta'(0^+) - \mu)$. Long tensile response ($s \gg p/2$) for (c) high σ_c and (d) low σ_c.

Consideration of two different values for σ_c is important, because it confines the lateral dilatation and, hence, it has an effect on the sliding of the profiles. The case of "high" interfacial confinement σ_c is represented in subfigures (a) and (c). In the hysteresis loop of subfigure (a), the first unloading path is high enough to reconnect to the first linear-elastic branch at a point for which σ_{22} is positive (a specular response is obtained for negative stresses). For $s > 0$ and $\dot{s} < 0$, condition (11.4.34b) provides

$$\sigma_{22} = -\frac{L\,B}{t} - \frac{L}{t}\Big[\mu - M\Big]\sigma_c > 0 \quad \Rightarrow \quad \sigma_c > \frac{B}{M-\mu}\,, \tag{11.4.37}$$

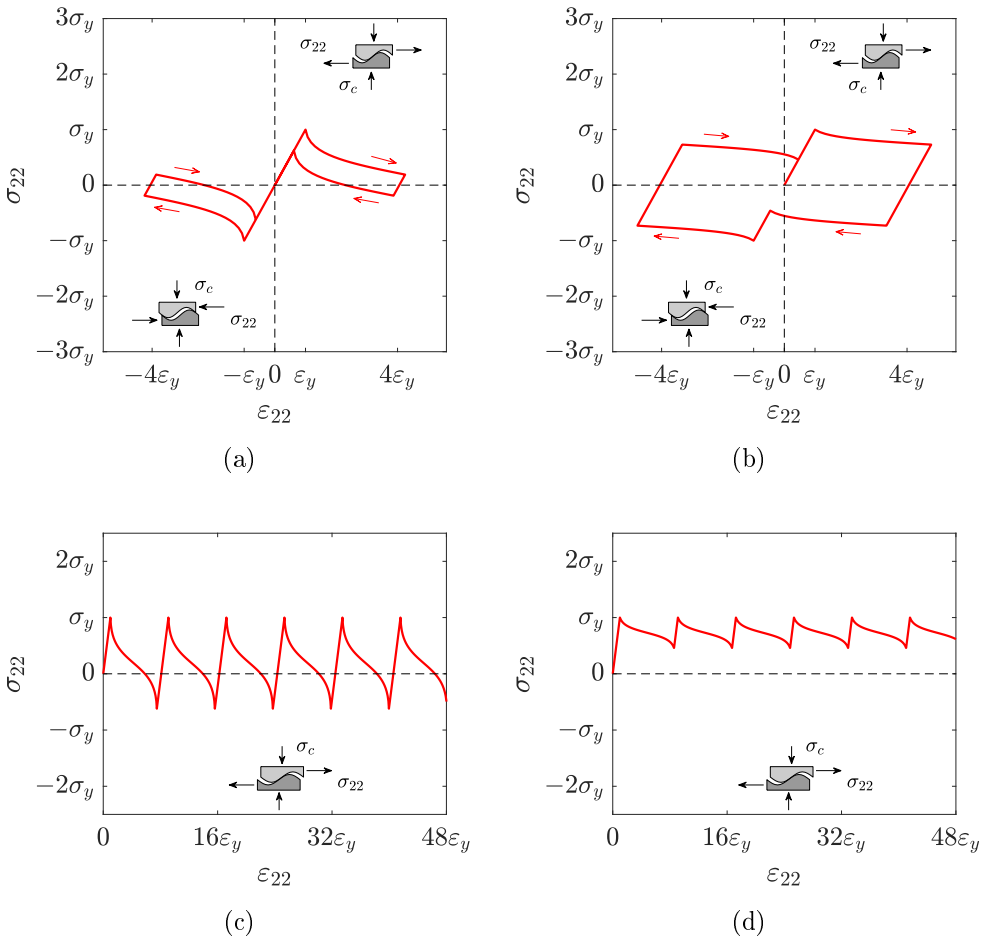

Figure 11.12. Response for the circular contact profiles of Figure 11.8(b). Hysteresis loop for $s \in [-p/2, p/2]$: (a) "high" $\sigma_c > B/(\theta'(0^+) - \mu)$ and (b) "low" $\sigma_c < B/(\theta'(0^+) - \mu)$. Long tensile response ($s \gg p/2$) for (c) high σ_c and (d) low σ_c.

where M ($-M$), as indicated in Section 11.2.3, represents the maximum (minimum) value of the function $\theta'(s)$. In all the profiles considered here $\pm M = \theta'(0^{\pm})$. Clearly, a strong interfacial confinement stress favors the return of the profiles towards the configuration where they match. This fact is evident also in the long tensile response, reported in subfigures (c). At the stage $s = p/2 + kp$, $k \in \mathbb{N}_0$, the profiles are at the maximum surmounting: immediately before (after) σ_c opposes (favors) sliding. The effect of σ_c, as stated by (11.4.37), overcomes that associated with the cohesive/frictional contact forces: hence, the stroke of the profiles must be braked by a negative σ_{22}. This is why the stress oscillates between positive and negative values.

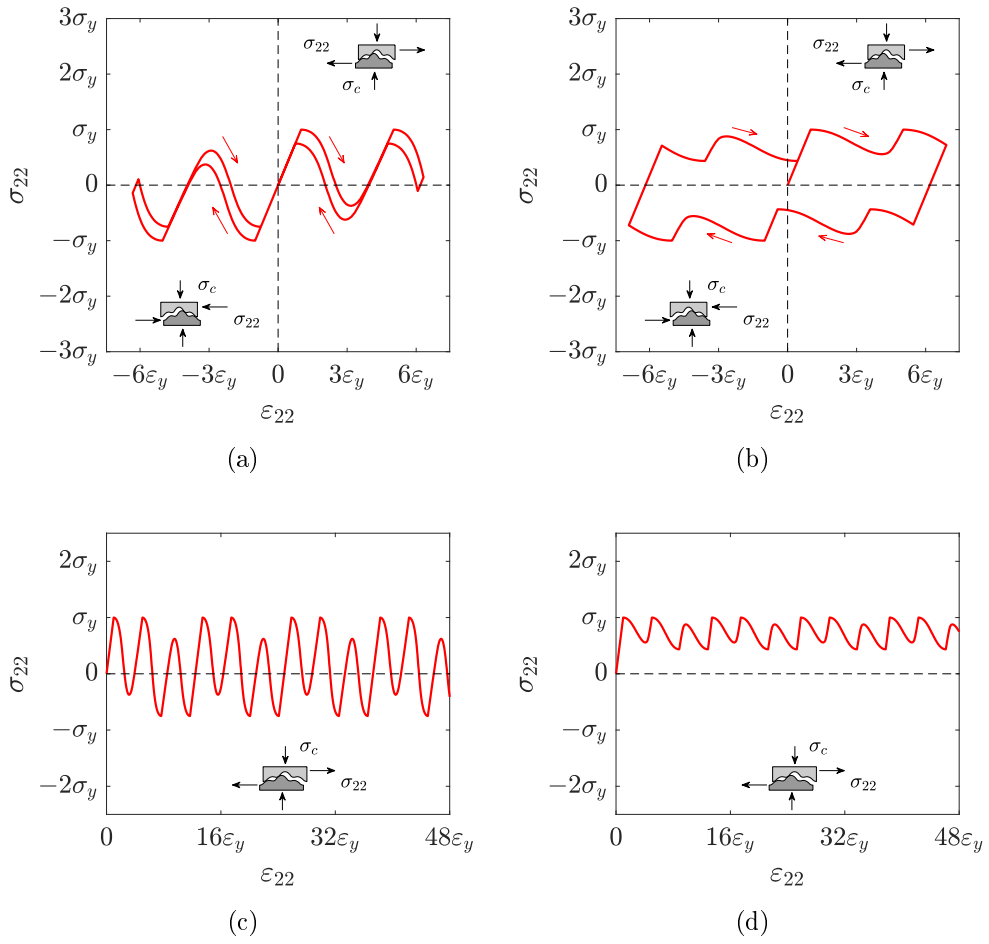

Figure 11.13. Response for the non-convex contact profiles of Figure 11.9(a). Hysteresis loop for $s \in [-p/2, p/2]$: (a) "high" $\sigma_c > B/(\theta'(0^+)-\mu)$ and (b) "low" $\sigma_c < B/(\theta'(0^+)-\mu)$. Long tensile response ($s \gg p/2$) for (c) high σ_c and (d) low σ_c.

The complementary case, illustrated in subfigures (b) and (d), corresponds to the condition of "low" interfacial confinement σ_c, when $\sigma_c < B/(M-\mu)$. Since $\sigma_c > 0$ and $B > 0$, this can occur only if $M > \mu$. Now the effect of σ_c cannot overcome the cohesive/frictional forces. Therefore, in the hysteresis loop of subfigures (b), the unloading branch requires in general a stress σ_{22} of opposite sign with respect to that for the loading branch. The oscillations in the long tensile response occur between positive values of the stress, because σ_c is not sufficient to make the profiles slide after the peak point of surmounting.

The response is similar, at the qualitative level, for all the three considered shapes of convex contact profiles. The hysteretic response exhibits an evident

pinched loop, which originates from the pinning associated with the waviness of the interface profiles. The oscillations that accompany the tensile response recall the Portevin-Le Chatelier effect that characterizes plastic deformation in steels [47]. The response of the non-convex (sinusoidal) profiles is more complicated, with more than one pinched loop, each of which corresponds to the surmounting of a local maximum of the curve describing the profile.

The elastic branches of the response are clearly linear in all the cases, but there are differences in the inelastic phase, associated with the progression of disarrangements, which depend upon the specific shape of the contact profiles. The plastic branches are horizontal in Figure 11.10, which corresponds to the case of triangular profiles. They show a strain-softening trend in the case of sinusoidal contact profiles, reported in Figure 11.11. The circular profiles of Figure 11.12 provide as well strain-softening branches in the plastic regime, but the concavity is opposite to that of the sinusoidal case. The non-convex case of Figure 11.13 exhibits two softening branches connected by a linear path, but the shape of each softening branch is similar to the corresponding sinusoidal case for the convex contact profiles.

11.4.2 Elastic interfacial constraint

In the following simulations, assume that $\sigma_{11} = 0$ and that the lamellae are held together by a *linear-elastic* interfacial constraint only. This is modeled as a bed of springs à la Winkler, with elastic constant per unit area equal to κ. Hence, the potential $\mathcal{K}(t\,\theta(s))$, introduced in Section 11.2.2, takes the form

$$\mathcal{K}(t\,\theta(s)) = \frac{1}{2}\,\kappa\,(t\,\theta(s))^2\,, \tag{11.4.38a}$$

$$\mathcal{K}'(t\,\theta(s)) = \kappa\,t\,\theta(s)\,. \tag{11.4.38b}$$

Figures 11.14, 11.15, 11.16 and 11.17 report the graphs, drawn again in the $\sigma_{22} - \varepsilon_{22}$ plane, for the responses of triangular, sinusoidal, circular and non-convex (sinusoidal) contact profiles, respectively. The parameters used in the plots are collected in Table 11.2.

Again, the behavior is linear-elastic from the initial state $(0, 0)$ up to the point $(\varepsilon_y, \sigma_y)$ of first yielding; then an inelastic branch, consequent to the development of disarrangements, develops if the strain is further increased. The subfigures (a) and (b) collect the hysteresis loop under strain-driven cycles, for $s \in [-p/2, p/2]$, for two different values of the interfacial spring stiffness, expressed by $\kappa\,t$ and referred to as "weak" and "strong" in Table 11.2. As in the previous Section 11.4.1, subfigures (c) and (d) show, for the aforementioned values of $\kappa\,t$, the long tensile response, characterized by $s \gg p/2$ and, hence, by multiple surmountings of asperities while the profiles are progressively sheared apart. As in Section 11.4.1, the

Table 11.2. Model parameters, including elastic interfacial constraint and geometric characteristics of the contact profiles, used for the in-silico experiments of Figures 11.14, 11.15, 11.16 and 11.17.

profile	triangular		sinusoidal		circular		non-convex	
interfacial springs	weak	strong	weak	strong	weak	strong	weak	strong
κt (MPa)	3.00	20.00	4.00	30.00	40.00	300.00	1.50	7.00
σ_y (MPa)	70.00	70.00	70.00	70.00	70.00	70.00	70.00	70.00
B (MPa)	3.5	3.5	3.5	3.5	3.5	3.5	3.5	3.5
μ ($-$)	0.1	0.1	0.1	0.1	0.1	0.1	0.1	0.1
p ($-$)	0.126	0.126	0.126	0.126	0.131	0.131	0.200	0.200
A ($-$)	0.126	0.126	0.126	0.126	0.038	0.038	0.300	0.300
t/L ($-$)	0.05	0.05	0.05	0.05	0.05	0.05	0.05	0.05

graphs correspond to a closed-loop control imposing that the state variable s is monotonically increased.

Consideration of two different values for κt allows to appreciate the effect of the interface constraints on sliding of the profiles: weak and strong interfacial springs are represented by the subfigures (a)-(c), and (b)-(d), respectively. The case of *strong* springs corresponds to a condition in which the *first* unloading inelastic path is characterized by points for which $\sigma_{22} > 0$ (a specular response is obtained for the other paths). At these points $s > 0$ and $\dot{s} < 0$; hence, from (11.4.34b), this happens when

$$\sigma_{22} = -\frac{L\,B}{t} - \frac{L}{t}\Big[\mu - \theta'(s)\Big]\kappa\, t\,\theta(s) > 0 \quad \Rightarrow \quad \kappa\, t > \frac{B}{(\theta'(s) - \mu)\theta(s)}\,. \tag{11.4.39}$$

Clearly, a strong elastic interface favors the sliding back of the profiles when the deformation is reversed. The complementary condition characterizes the case of *weak* springs.

A substantial difference with respect to the case of Section 11.4.1 is that the inelastic branches are smooth when $\dot{s}$ has a constant sign: the loops are not pinched any longer. This is a consequence of the fact that $\mathcal{K}'\,(t\,\theta(0)) = \mathcal{K}'\,(0) = 0$: the elastic interface does not oppose any resistance in a neighborhood of $s = 0$. Observe as well that when $s = kp$, $k \in \mathbb{Z}$, and $\dot{s} \neq 0$, equations (11.4.34) provide that $\sigma_{22} = \mathrm{sgn}(\dot{s})B\,L/t$, where $B\,L/t$ is the stress σ_y of first yielding.

The fact that the elastic branches are linear results from the straining of the constituent tablets, supposed linear elastic. The shape of the profile makes a dif-

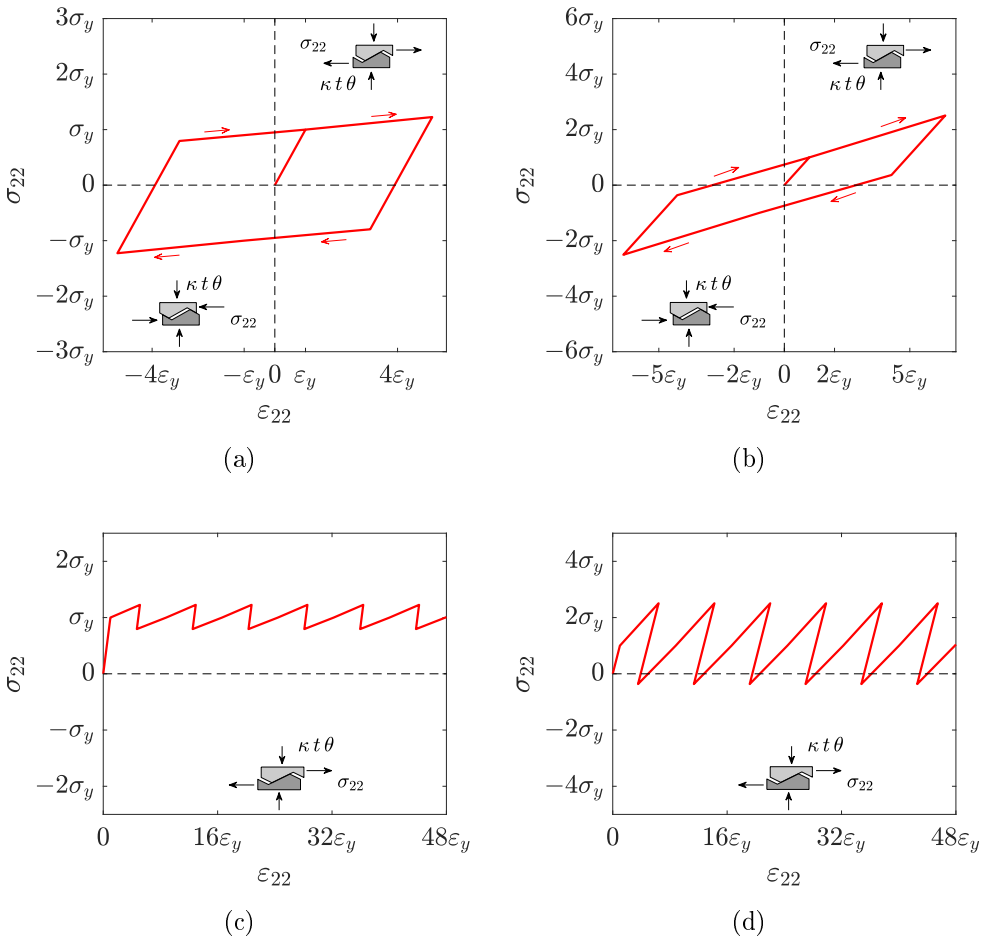

Figure 11.14. Response for the triangular contact profiles of Figure 11.7(a). Hysteresis loop for $s \in [-p/2, p/2]$: (a) "weak" interfacial springs and (b) "strong" interfacial springs. Long tensile response ($s \gg p/2$) for (c) "weak" and (d) "strong" interfacial springs.

ference in the inelastic phase, associated with the progression of disarrangements. For triangular profiles, the trend is linear and strain-hardening for $s \in [0, p/2)$, as per Figures 11.14(a) and 11.14(b); a sawtooth response characterizes the long tensile test of Figures 11.14(c) and 11.14(d). On the contrary, a smooth convex curve is obtained for both sinusoidal and circular contact profiles for $s > 0$ and $\dot{s} > 0$. Subfigures 11.15(a)-11.15(b) (sinusoidal) and 11.16(a)-11.16(b) (circular) indicate that the behavior is strain-hardening at the beginning, approximately for $0 < s < p/4$, and then strain-softening, for $p/4 < s < p/2$. The curves are anti-symmetric for $s < 0$ and $\dot{s} > 0$ with respect to the point $(\varepsilon_y, \sigma_y)$ of first yielding (the trend is analogous for $\dot{s} < 0$). Correspondingly, in the long tensile test the

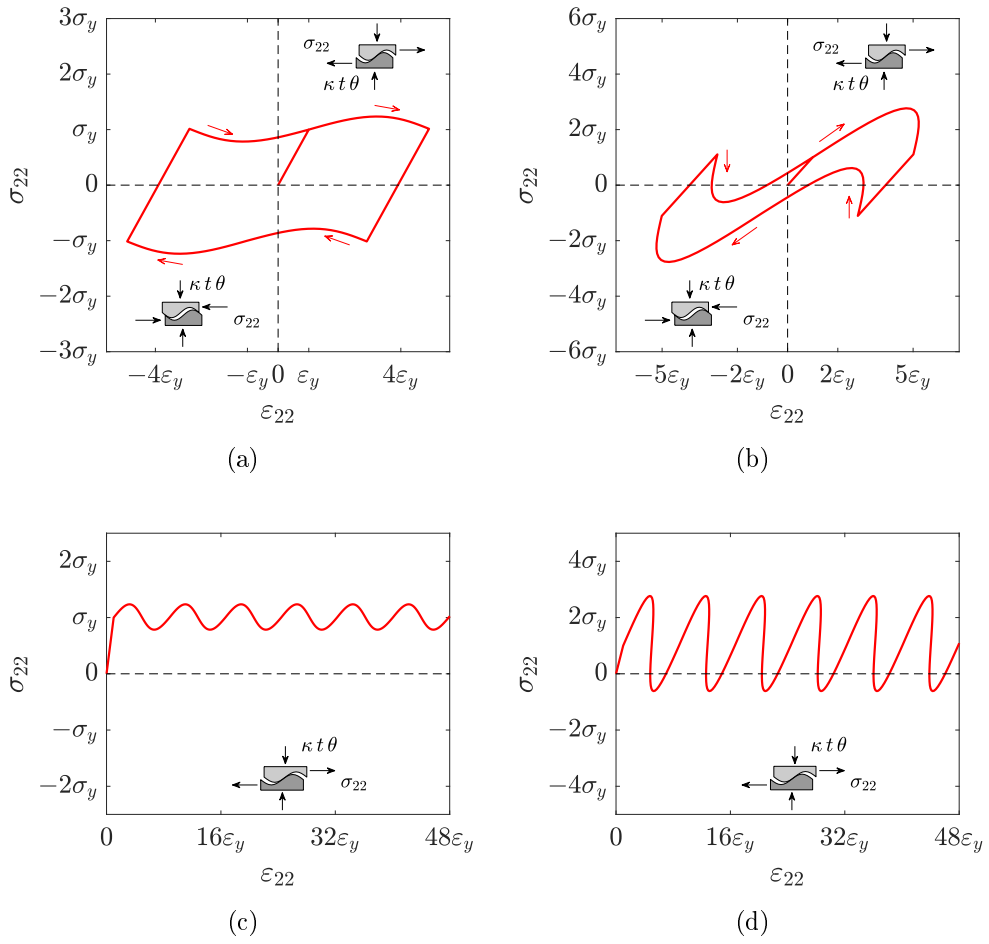

Figure 11.15. Response for the sinusoidal contact profiles of Figure 11.7(b). Hysteresis loop for $s \in [-p/2, p/2]$: (a) "weak" interfacial springs and (b) "strong" interfacial springs. Long tensile response ($s \gg p/2$) for (c) "weak" and (d) "strong" interfacial springs.

inelastic branch is described by a wavy smooth curve. Again, strong interfacial springs dictate that negative values of σ_{22} are attained during the oscillations, due to the powerful elastic return that accompanies the post-surmounting phase of the profiles. As before, the case of non-convex profiles of Figures 11.17 provides a more complicated response than the corresponding convex case of sinusoidal profiles (Figure 11.15), being now the path followed after the first yielding composed of a first strain-hardening branch which anticipates a strain-softening phase, a subsequent (short) linear branch and, again, a hardening and softening trend until $s = p/2$ is reached. Anyway, the difference is formal, but not substantial, with respect to the corresponding sinusoidal convex case.

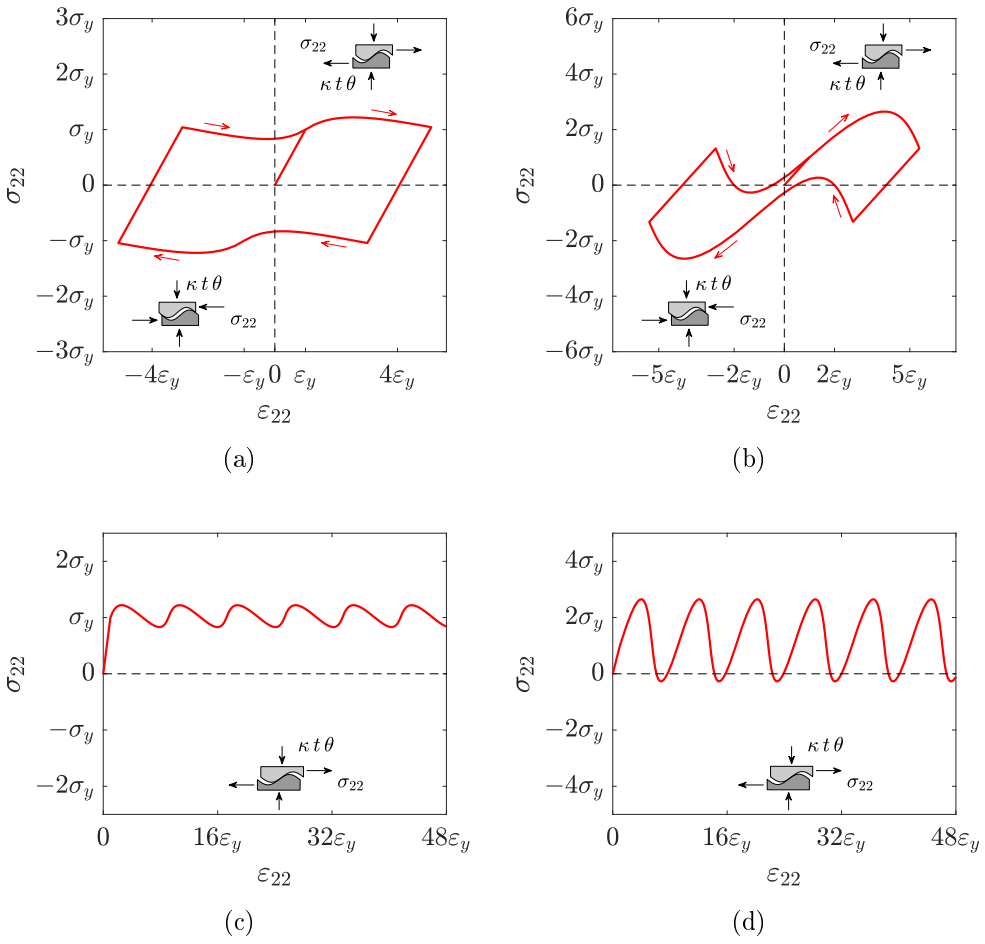

Figure 11.16. Response for the circular contact profiles of Figure 11.8(b). Hysteresis loop for $s \in [-p/2, p/2]$: (a) "weak" interfacial springs and (b) "strong" interfacial springs. Long tensile response ($s \gg p/2$) for (c) "weak" and (d) "strong" interfacial springs.

The comparison of Figures 11.14, 11.15, 11.16 and 11.17 with the corresponding Figures 11.10, 11.11, 11.12 and 11.13 of the previous Section 11.4.1, shows that the main difference introduced by the linear-elastic interfacial constraint is the strain-hardening character of the inelastic branches, after the first yielding. This is due to the fact that the interfacial forces increase as the shear induce dilatation increases. Observe that the long tensile response formally recalls the stick-slip frictional motion [217], in particular for the case of Figure 11.14(c) (triangular contact profiles), even if there is no distinction in the model between the cases of static and dynamic friction.

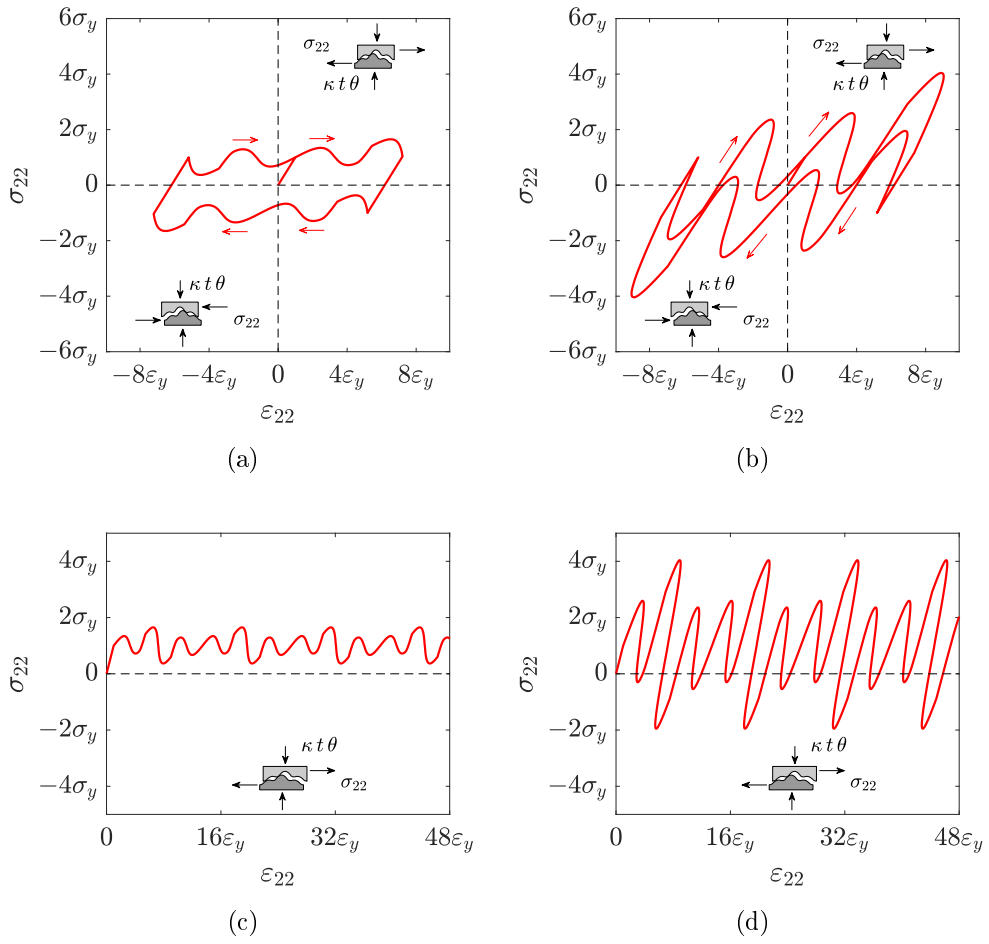

Figure 11.17. Response for the non-convex contact profiles of Figure 11.9(a). Hysteresis loop for $s \in [-p/2, p/2]$: (a) "weak" interfacial springs and (b) "strong" interfacial springs. Long tensile response ($s \gg p/2$) for (c) "weak" and (d) "strong" interfacial springs.

11.4.3 Effects of the localized contact

The assumption of negligible change in shape of the contact profiles during their reciprocal sliding greatly simplifies the calculations. In any case, the deformation consequent to the localized contact forces could be considered, and the same arguments, leading to the conclusions that the shape of the contact profiles dictates the macroscopic constitutive response, could be repeated, though at the price of a more sophisticated analysis of the contact problem. In order to validate the results of Sections 11.4.1 and 11.4.2, we now discuss the conditions for which the local deformation can be neglected.

Therefore, we now consider the localized contact between two curved surfaces by using a Hertzian-like approach [225] under plane stress assumption. If the size of the flattened contact area is small with respect to the characteristic size of the profiles, associated with the wavelength $t\,p$, the change in shape will be considered negligible. Viceversa, if this region is comparable with the wavelength, the compliance of the asperities shall be taken into account. The problem is affected by the mechanical properties of the material forming the lamellae, the level of

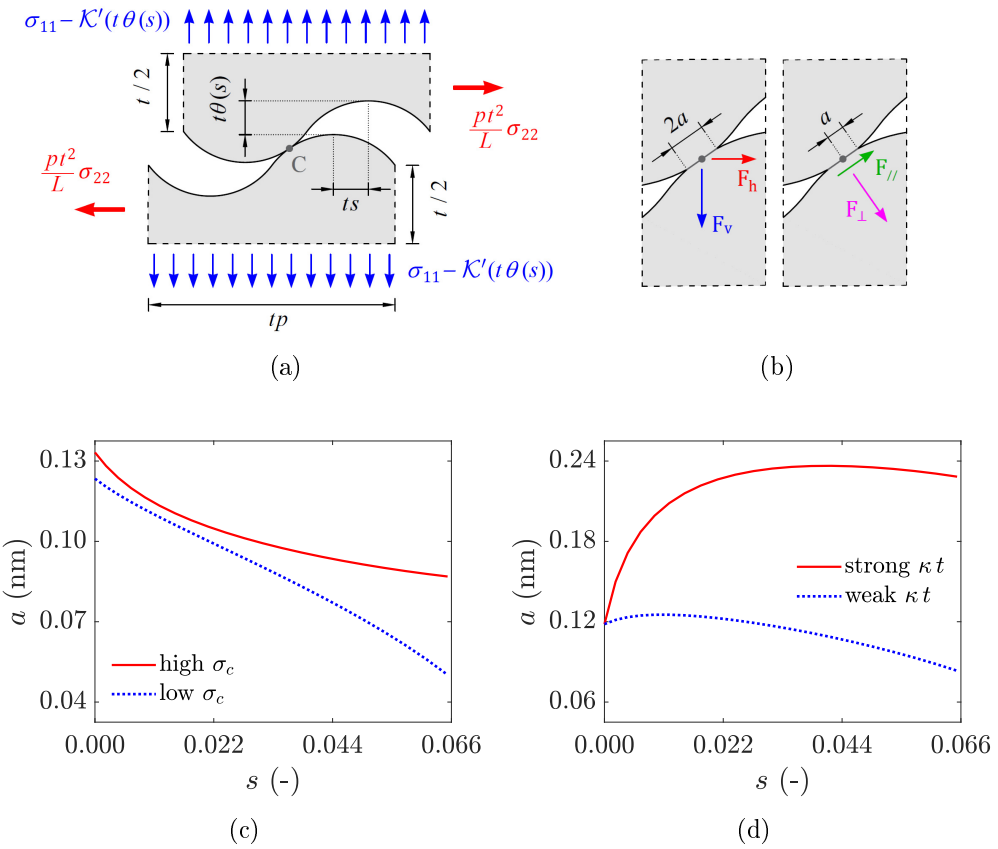

Figure 11.18. Effect of the localized contact on the circular profiles of Figure 11.8(b), during tensile test under constant interfacial confinement and elastic interfacial constraint. (a) Reference volume element, corresponding to a wavelength tp of the contact profiles. (b) Detail of the contact zone with indication of the flattened contact area (grey solid line) of width $2a$ and the contact forces transmitted by the upper profile to the lower profile (vertical and horizontal components F_v and F_h; normal and tangential components $\mathrm{F}_\perp$ and $\mathrm{F}_{//}$). Half-width a of the contact area as a function of the slide s for: (c) the case of "low" and "high" interfacial confinement σ_c, and (d) the case of "strong" and "weak" interfacial springs $\kappa\,t$.

transversal confinement and the slope of the contact profiles. The actual cohesive-frictional nature of the contact affects the norm and the direction of the localized reaction force, which could not be fully appreciated in the proposed model, where the Mohr-Coulomb law was defined on the inter-lamellar plane.

The triangular profiles of Figure 11.7(a) provide for a contact between two plane surfaces: the contact forces are distributed, so that a noteworthy change in the shape of the profiles is not expected. Of course, when the relative sliding s approaches one half of the wavelength ($s \to p/2$), the tip of the teeth are in direct contact, but this is a limit condition. In the real case, perfectly sharp teeth are not expected; on the other hand, the tip of a sharp tooth is prone to break, thus providing a blunt profile.

For curved profiles, Hertz's theory applies. To illustrate, consider the circular contact profiles of Figure 11.8(b). One can isolate a representative volume element corresponding to one wavelength $t\,p$, as per Figure 11.18(a). Assume that all the asperities equally respond to the tensile stress σ_{22} applied to the lamellae, so that the portions of Figure 11.18(a) are subjected to the net tensile stress $t\,p\,\sigma_{22}/L$ and to the confinement given by $\sigma_{11} - \mathcal{K}'(t\,\theta(s))$. Their resultant is balanced by the contact force F (per unit lamellar width) at the contact point C, with components F_h and F_v. Recalling (11.4.34a), these can be written as

$$\mathrm{F}_v = \big[\sigma_{11} - \mathcal{K}'(t\,\theta(s))\big]\,t\,p\,, \tag{11.4.40a}$$

$$\mathrm{F}_h = \sigma_{22}\,\frac{p\,t^2}{L} = t\,p\,B + \big[\mu + \theta'(s)\big]\,\mathrm{F}_v\,. \tag{11.4.40b}$$

Such components are detailed in the left-hand picture of Figure 11.18(b), where the flattened portion, of width $2a$, is also indicated. From these, one can calculate the components $\mathrm{F}_{/\!/}$ and $\mathrm{F}_\perp$, respectively parallel and normal to the tangent contact plane, indicated in the right-hand picture of Figure 11.18(b).

According to Hertzian theory [225], assume that the width $2a$ of the flattened contact region is dictated by $\mathrm{F}_\perp$, while the contribution of $\mathrm{F}_{/\!/}$ consists only in the modification of the contact stress field. Hence, if R denotes the radius of the contact profiles, one has

$$a = \sqrt{\frac{2\,R\,\mathrm{F}_\perp}{\pi\,\dfrac{E}{1-\nu^2}}}\,, \tag{11.4.41}$$

where E is the Young's modulus of the material and ν the Poisson's ratio.

Recall that, in the previous examples, the values $E = 87\,\mathrm{GPa}$ and $\nu \simeq 0.3$, compatible with a real nacre, were assumed. Figures 11.18(c) and 11.18(d) show

the trend of a as a function of the slide s for the case of *low* and *high* interfacial confinement σ_c, and for the case of *strong* and *weak* interfacial springs $\kappa\, t$, respectively. These correspond to the examples of circular profiles reported in Sections 11.4.1 and 11.4.2, whose parameters are collected in Tables 11.1 and 11.2. For nacre (see Section 11.1.1), one can assume $t \simeq 400\,\text{nm}$, so that $t\, p \simeq 50\,\text{nm}$. From Figure 11.18 one finds $2a \leqslant 0.47\,\text{nm}$, a value that is less than 1% of the wavelength of the asperities. This conclusion validates the hypothesis of negligible change in shape of the contact profiles during sliding.

11.4.4 Comparison with real nacre

The analysis of the previous sections has demonstrated the great potential of the proposed model in its capability to reproduce a wide spectrum of responses. It is now shown how the model parameters can be calibrated to specifically reproduce tensile tests on real nacre. Reference is made to the experimental results reported by *Barthelat et al.* [198] and by *Evans et al.* [192]. The model with the linear-elastic interfacial constraint should be preferred, because in real nacre the biological polymeric interlayer bridges the lamellae, without external confinement. Therefore, as in Section 11.4.2, consider $\sigma_{11} = 0$ and $\mathcal{K}'\left(t\,\theta(s)\right) = \kappa\, t\,\theta(s)$.

Figures 11.19(a) and 11.19(b) respectively show the experimental curves (green solid line) by Barthelat et al. [198] and Evans et al. [192]. In the same figures, the results (black dotted line) from the model are presented for the case of circular contact profiles, for which mechanical parameters are collected in Table 11.3. This case is referred to as "short yielding" because it corresponds to $s \in [0, p/2)$: surmounting of the contact profiles is not achieved. In fact the asperities are big enough (parameters p and A in Table 11.3) to cover the whole inelastic branch in this range. The agreement between theory and experiments is excellent.

Another possibility is to consider circular profiles with smaller asperities (parameter A) and shorter period (parameter p). In this way, with a mechanism analogous to that providing the *long tensile response* (Sections 11.4.1 and 11.4.2), the inelastic phase, associated with a horizontal plateau, results from multiple surmountings of the contact profiles. Figure 11.19(c) shows this second choice, referred to as "long yielding", for the parameters reported in Table 11.3. The comparison with the experiments reported in [192] indicates a less accurate fitting with respect to the short yielding case, especially for what concerns the fillet between the elastic branch and the plastic plateau, but the asymptotic tensile response can be accurately reproduced.

Since the thickness of aragonite tablets is of the order of $t \simeq 400\,\text{nm}$ (Section 11.1.1), the height of the asperities for the case of *short yielding* is $t\, A \simeq 32\,\text{nm}$. This value agrees with the size of asperities found in abalone nacre [199]. This

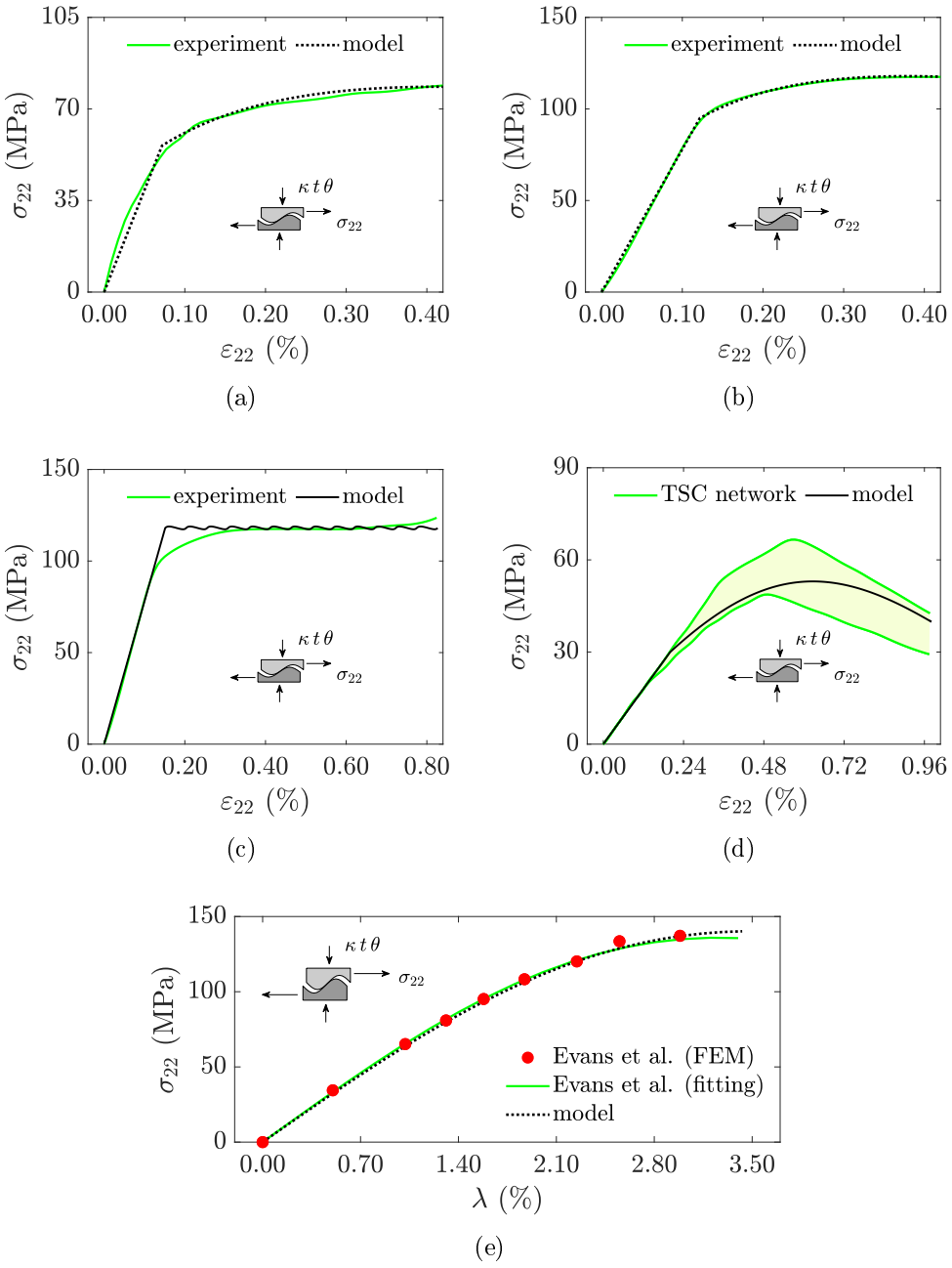

Figure 11.19. Comparison of the theoretical results with the experimental stress-strain curves for nacre. Case of "short yielding", with big asperities and $s \in [0, p/2)$, reproducing the dataset (a) by *Barthelat et al.* [198] and (b) by *Evans et al.* [192]. (c) Case of "long yielding" (small asperities and $s \gg p/2$), reproducing the test curve by *Evans et al.* [192]. Comparison with other models for nacre: (d) TSC network analysis by *Yan et al.* [218], and (e) finite element analysis by *Evans et al.* [192].

Table 11.3. Parameters for the cohesive-frictional model and the circular contact profiles, used to fit the experimental results reported in the plots of Figures 11.19(a), 11.19(b) and 11.19(c).

response	short yielding	short yielding	long yielding
reference	*Barthelat et al.* [198]	*Evans et al.* [192]	*Evans et al.* [192]
E (GPa)	78.00	78.00	78.00
$\kappa\, t$ (MPa)	20.00	28.00	28.00
σ_y (MPa)	56.00	95.00	118.00
B (MPa)	2.80	4.75	5.90
μ ($-$)	0.1	0.1	0.1
p ($-$)	0.3811	0.2771	0.0104
A ($-$)	0.1100	0.0800	0.0030
t/L ($-$)	0.05	0.05	0.05

Table 11.4. Parameters for the cohesive-frictional model and for the contact profiles, used in the comparison with other models reported in Figures 11.19(d) and 11.19(e).

comparison with	TSC network	FEM analysis
reference	*Yan et al.* [218]	*Evans et al.* [192]
profiles	circular	sinusoidal
E (GPa)	15.00	70.00
$\kappa\, t$ (GPa)	1.50	29.00
σ_y (MPa)	30.00	0.00
B (MPa)	12.00	0.00
μ ($-$)	0.1	0.2
p ($-$)	0.0416	0.2000
A ($-$)	0.0120	0.0100
t/L ($-$)	0.40	0.50

suggests that, in real nacre, the yielding mechanism develops with a short shearing of the contact profiles. In this case, the bridging provided by the biopolymeric fibrils can survive because their elongation is small. On the contrary, the condition of *long yielding*, with a pseudo-horizontal branch, corresponds to different mechanisms, in which one may expect the breakage of the extremely-elongated fibrils, and/or the blunting (due to localized breakage for stress concentration) of the teeth of the

contact profiles at their tip after their first surmounting. Moreover, it may be possible, especially in a stress-driven test, that the profiles directly slip over the peaks of the asperities after the first short-yielding phase, as detailed in [192]. Therefore, referring to the discussion reported in Remark 2 of Section 11.3, the case of *short yielding* is not in contrast with the hypotheses at the base of the model, in particular the invariability of the shape of contact profiles and of the cohesive contribution.

Further in-silico tests were performed to compare our model with other models. In particular, *Yan et al.* [218] developed a tension-shear-chain (TSC) network model, where linear-elastic tablets are connected by shear- and tension-resistant interfaces, such as in a brick-mortar arrangement. The authors accounted for microstructural randomness of the assembly, finding a family of curves in the $\sigma_{22}-\varepsilon_{22}$ plane. Although we do not consider microstructural randomness, by considering circular profiles with the same average geometrical parameters of [218], collected in Table 11.4, we find the curve shown in Figure 11.19(d) (black solid line). This is consistent with the findings by Yan et al. [218] with the TSC model, which provide a range of values (due to the random microstructure) within the green-shaded area reported in the same figure.

A second comparison is with the FEM analysis also reported by Evans et al. [192]. The authors considered two (half) lamellae with sinusoidal contact profiles, sheared apart in a numerical tensile experiment, for which the frictional contact was modeled along the actual contact wavy interface. In particular, we refer to the plot recorded in [192] for a friction coefficient equal to 0.1, for which results are provided in terms of the non-dimensional quantities Δ and Γ, which, according to our notation of Figure 11.4, are defined as

$$\Delta = \frac{\Lambda}{t\,p} \quad \xrightarrow{\Lambda_0=0} \quad \Delta = \frac{2\,t\,s}{t\,p} = \lambda\,\frac{1}{t/L}\,\frac{1}{p/2}\,, \tag{11.4.42a}$$

$$\Gamma = \frac{\sigma_{22}\,t^2}{E\,A t\,L}\left(1+\nu\frac{L}{t}\right) = \frac{\sigma_{22}}{E\,A}\,\frac{t}{L}\left(1+\frac{\nu}{t/L}\right), \tag{11.4.42b}$$

where $E = 70\,\mathrm{GPa}$ is the Young's modulus of the lamellae and $\nu = 0.2$ the Poisson's ratio, as in [192]. Given the values of Δ and Γ, one can plot the stress σ_{22} as a function of the inelastic elongation λ in the corresponding direction. In Figure 11.19(e), results from our model (black dotted line) are compared with those by Evans et al. [192], for which the red dots corresponding to the FEM simulations are fitted with a continuous semi-empirical curve. Remarkably, even if we do not consider the deformation of the profiles in contact, the agreement is very good, once the model parameters have been tuned according to the values of Table 11.4. Note that the non-dimensional parameters A, t/L and $2L/(pt)$ are the same as in [192], but the spacing between the "dilatation bands", as defined in [192], has

been set equal to the distance L, in order to obtain the a geometric correspondence with our model.

The above results show the possibility of reproducing the experiments on the real nacre through the proposed model for shear tensegrities. Remarkably, despite the simplifying hypotheses, the proposed model is not in contrast but complements the different models for nacre presented by other authors, while providing a mechanical interpretation of the mechanism through which structural capacity is achieved.

Chapter 12

Final remarks

12.1 Contributions

Flexural tensegrity represents an innovative structural concept, to achieve the flexural integrity of a chain of segments in unilateral contact by pressing them one another with tensioned cables (tendons), in order to form a beam-like structure with load bearing capacity under bending. The contact surfaces are curved and shaped in such a way that their relative movement is that of pure rolling along design pitch lines. The resulting contact constraint between the coupled segments is macroscopically equivalent to a spring hinge, but with nonlocal constitutive response. This is due to the interaction between all the joints, resulting from the fact that the tendon is unbonded, i.e., it is free to slide inside the segments, being anchored only at the end segments of the chain. In principle, any kind of constitutive response can be obtained, as a function of the tensile force in the cable and its axial stiffness, with a proper design of the pitch lines along which the segments roll. The construction is very simple, and the joints are made with massive components, without minute parts that are potentially subject to damage. Redundancy and structural robustness can be achieved by using more than one cable, defining a configuration with multiple prestressing tendons placed in parallel, or using a braided strand, so to avoid collapse if one wire of the strand breaks. The structure can be packaged and deployed by simply pulling the cables. Moreover, since the constitutive response of the spring hinges depends upon the tensile force in the cables, its active control can tune the structural response according to specific requirements. The concept can also be extended to two- and three-dimensional geometries, to form flexural-tensegrity plates, shells, and solids.

Starting with the simplest case in which the segments are held together by a centroidal cable, confined in a tubular sheath within the segments, the struc-

tural concept has been analyzed, modeled, prototyped and tested, as illustrated in Chapter 2. Despite a few simplifying hypotheses, such as the neglecting of frictional effects and the assumed rigidity of constituting segments, which will be considered in future work, a good agreement is found between the experimental results and the theoretical predictions.

In the continuum limit, presented in Chapter 3, it has been shown that the structure falls within the category of Euler's elastica. More precisely, since the tensile force in the tendon depends also upon the overall bending of the beam, the strain energy is characterized by a nonlocal contribution. In particular, the bending stiffness depends, through a squared Lebesgue norm, on the whole curvature field. For this reason, the theory provides a nonlocal model, recovering the classical Euler's elastica when the nonlocal term is negligible (first-order approximation, when the tensile stress in the tendon is supposed to remain constant). The continuum model does not carry the inconsistencies, especially for what concerns the edge conditions, of other nonlocal models for beams, in which the bending depends on the convolution of the curvature field with an averaging kernel, with either compact support or fast decay at infinity. The analytical research of the equilibrium configurations of the nonlocal elastica under imposed loads, relies upon the same methods of the classic Euler's elastica, implying the solution of elliptic integrals and the use of hypergeometric functions. This type of approach has been confirmed by a direct numerical calculation in paradigmatic model problems, for which the possibility of using shape functions to approximate moderate curvature fields has also been investigated.

The nonlinear effects in the dynamic response of flexural-tensegrity beams have been discussed in Chapter 4. The unbonded tendon is anchored to the end segments through the interposition of Kelvin-Voigt elements (linear spring and linear dashpot), but its tensile force may also be modified by an actuator. The kinematics is still driven by the shape of the intersegmental contact surfaces, which dictates the tendon elongation; this nonlinearly affects the reaction forces of the end springs and dashpots, thus modifying the dynamic response of the structure. Depending on the mechanical parameters of the cable and the Kelvin-Voigt elements, the response is that of either a harmonic or a Duffing oscillator. On the other hand, the modification of the tensile force in the tendon provides the variation of the bending stiffness of the beam, thus exciting or reducing the oscillations. Simple experiments on the free vibrations of cantilevers also allowed for a preliminary characterization of dissipation sources for the segmental assembly. These can be modeled by linear rotational dampers at the joints, i.e., providing a dissipative moment that linearly depends on the speed of relative rotation of the coupled segments, and through a constant parasitic friction moment at the joint.

In Chapter 5, a special subclass of flexural tensegrities, capable of exhibiting

multi-stable static states for certain values of the deformation, has been conceived, theoretically analyzed, prototyped and tested. In principle, it is possible to achieve a non-convex strain energy profile with arbitrary values of the energy wells, by properly designing the pitch lines that define the relative movement between the segments. However, there are limitations consequent to material interpenetration and sliding of the contact surfaces that realized the pitch profiles, which still need to be recognized and categorized in detail. The case of piecewise circular pitch lines for the contact surfaces, together with the enhancement of the tendon mobility inside hourglass-shaped cavities carved in the segments, fulfills the aforementioned physical constraints. It is then possible to obtain equilibrium states under pure bending that can be non-symmetric at certain levels of the applied actions (imposed rotations or couples at the ends), being characterized by diverse rotations (phases) at the various contact joints. Under monotonic loading, the stiffening due to the nonlocal action of the unbonded cable provides Maxwell paths and maximum hysteresis paths, which are strain-hardening in type, being characterized by final pseudo-linear growth, whose steepness increases with the rotations. Under cyclic actions, well defined hysteresis loops are obtained, with strain-hardening branches in the regions of phase (rotation) coexistence. This response qualitatively agrees with the experimentally measured pseudoelastic response of shape memory alloys, as well as with the response of biological tissues and macro-molecules, driven at the microstructural level by the breakage and rearrangement of internal bonds.

Thanks to a further improvement in the mobility of the cable inside broader segmental cavities, an innovative movable cantilever beam has been conceived. Theoretical model and experiments are recorded in Chapter 6. The new design allows for a multi-articulated global snapping between two distant globally-stable structural configurations, in response to one single perturbation, here represented by the relative rotation of a pair of segments. The major properties of such a structure are: i) the motion is autonomous, as it is activated by a slow perturbation (rotation) of one joint, with no need of special control devices; ii) the motion is reversible, since, by changing the sign of the perturbation, snapping occurs in the opposite direction; iii) the stable configurations do not need to be secured by locking devices, because they are well separated by an energetic barrier; iv) the driving system can be realized through a simple crank and crankshaft mechanism, connected to a motor at low revs; v) the structure is robust, since it is made of massive segments and the tendon can be composed of parallel wires, to avoid collapse in case of breakage of one wire. Since the structure behaves like a tail that flagellates, if cyclicly actuated, this can find specific applications to robotics, launching devices (such as catapults) and propulsion in fluids.

The extension of flexural-tensegrity beam-like structures to three-dimensional assemblies has been proposed in Chapter 7. They have been referred to as *flextegrity*

lattices, where flextegrity is the contraction of the coupled words flexural-tensegrity. They are composed of segments in a simple cubic arrangement, mimicking a compact assembly of spheres in pure rolling contact. The concept has been proposed, theoretically analyzed, prototyped in physical models and tested. Geometric compatibility provides a kinematic skeleton which constrains the energetic landscape, enforcing constitutive properties that are dictated, beside the stiffness and pretension of the tie tendons, by the shape of the pitch surface of the contact joints. The lattice can represent a mesoscopic model for the homogeneous microstructure of a crystal with interacting molecules, whose qualities as a whole depend upon the orientation of the molecules and the mutual forces acting between them. Metamaterials built upon flextegrity lattices enjoy particular bulk properties and are amenable of (molecular) vibrations, which suggests their use as resonators.
The static-kinematic analysis has also demonstrated that the lattice can support self-equilibrated stress states (eigenstress). This finding could be related to possible strategies for the growth of the crystal by the addition of layer after layers, and suggest a possible way by which contact forces can be increased by inserting molecules with different size into the lattice, as well as motivate the change in the microstructural orientation in response to the thermal expansion of the molecules. The particular kinematic, supplemented by the consideration of electric charges on the segments, could also represent a mesoscopic model for piezoelectric effects. The analyzed cases represent the simplest flextegrity lattices. One can imagine three-dimensional grids composed of segments with diverse geometry, different contact surfaces, possibly amenable of multiple equilibrium states, representing a transition from chiral to non-chiral phases as a consequence of thermal or mechanical stimuli. An improved model could account for the different response of the assembly under tension, compression and bending, by considering the detachment of segments. Anyway, the dynamics of the lattice, for what concerns either the global response of the whole, or the local vibrations at the segmental (molecular) level, possibly complicated by the fact that multi-stable contact joints may snap in response to localized perturbations, still need to be analyzed more in detail in future work.

The tailor design of hinge-based and self-aligning flexural-tensegrity structures with tunable response can have many potential applications at various length scales. Microfabrication allows to manufacture nano- to centimeter-scale devices for biomedical structures ranging from implants for prosthetics or for controlled drug delivery, to reconfigurable surgical tools such as catheters, possibly equipped with grippers actuated by the same tendons, which could also be designed to respond autonomously to specific chemical or temperature changes. In robotics, low-inertia cable-actuated compliant beams are particularly suitable for (humanoid) parallel reconfigurable arms and manipulators in different workspaces; moreover,

the structural system can mimic the movement of the limbs of microorganisms, such as the flagella of bacteria, or the mechanical characteristics of macromolecules, such as nucleic acids, especially in their capability of being transformed with very small variations at the level of the underlying microstructural constituents (here represented by the tuning of cable stiffness and prestress). Other potential applications are certainly in collapsible-deployable structures: foldable legs for camping furniture, landing sleds for drones, substructure for a membrane that folds and opens up like a flower, conveyors that work with movable villi or cilia.
At the bigger scale of aerospace applications, structures with morphing capability may define their aeroelastic properties. Moreover, the possibility of packaging, deployment and active control of the stiffness, possibly obtained with tendons made with shape-memory-alloy wires, permits the transport on spacecrafts, the segmental construction, the compliant adaptability and the reduction of the vibrations. In the broad field of architecture, the proposed structural element, used alone as a beam or an arch, or assembled in the form of spatial grids, may also meet the increasing demand for solutions capable of transforming the living space for anthropic and environmental needs, such as the optimization of solar radiation according to daily or seasonal changes. A few of these envisaged applications have been analyzed more in detail, to complement the theory with a feasibility study.

The first application is in archery, and it has been addressed to the manufacturing a new flex-ten bow, presented in Chapter 8. The bow is a launching device based on the elastic properties of the components, and represents a paradigmatic example to test the developed theory, comparing results of the dynamical model with experiments. Moreover, the possibility of tailor-shaping the pitch profiles, together with a tunable prestress for the cables, can be fully exploited to achieve a constitutive property in bending that meets the needs of the archer to optimize the firing performance. There is no need to use special materials to manufacture a flex-ten bow, because the constitutive properties result from geometry, i.e., from the shape of the contact surfaces between the segments. There are also further advantages in the modular construction: the components are simple and massive; the stiffness of the limbs can be modified by releasing/tensioning the tendons; segments with different contact surfaces are interchangeable; the bow length can be varied by adding/removing segments; the bow can be easily assembled/disassembled and the components packed in a small box.
The example of the bow is interesting because, in both professional and sports applications, it is necessary to take into account various performance indices, often antithetical and sometimes conflicting. Indeed, optimizing the bow properties is difficult and requires maximum freedom in the design parameters. Here, non-recurve flex-ten bows have been considered. Two designs have been proposed, which differ in terms of the laws describing, as a function of the segmental relative rotation,

the lever arm of the internal forces at each contact joint. It has been theoretically and experimentally demonstrated that a sub-linear law provides advantages with respect to a linear relationship in terms of arrow exit speed, while the opposite holds in terms of energetic efficiency. A limitation of this study is that only two categories of bow prototypes have been analyzed in detail. On the one hand, the shape and mass of the segments can certainly be further optimized; on the other hand, various different geometries for recurve bows could be obtained with segments of identical shape, simply by varying the position of the hole through which the tendon passes. The use of segments with multiple holes would give the archer the additional possibility to modify the geometry in the unbraced configuration, according to specific needs. In addition, the use of multiple cables, with different placements and prestressing forces, could increase the bow performance and make the device more structurally robust. All these potentialities have yet to be fully explored and appreciated.

The possibility, as an experimental proof-of-concept, of using flexural-tensegrity beams as propulsion mechanisms to mimic the swimming of fish has been investigated in Chapter 9. The proposed device adopts the design of the snapping flex-ten cantilever, and the propulsion capacity has been characterized by parametrically varying the number of segments and the shape of their internal cavities, also considering the effect of a terminal fin, either clamped or hinged to the cantilever tip. The concept has been finally demonstrated for the propulsion of a toy vessel. The results suggest that the flexural-tensegrity concept of the snapping cantilever could find application in marine propulsion. However, there are limitations, which can be hopefully addressed by future studies. For the cantilever and the tip fin, just a few elementary schemes were considered, which are presumably far from being optimal; flexible flappers with profiled geometries could be added; a limited range of frequencies was tested, only in water; theoretical modeling of the fluid-structure interaction is needed to rationalize the blending between elastic and inertial forces, together with drag and viscous forces in the fluid. Furthermore, to evaluate the real advantages of our system, it will have to be compared with other types of non-snapping simple flappers. Nevertheless, experimental findings indicate exciting new avenues for future investigations on bio-inspired flexural-tensegrity propulsion. Potential applications could be considered at different length scales: microthrusters for medical microrobots (capable not only of swimming in highly viscous human fluids, but also of climbing blood vessel walls or acting as stents), amphibious vehicles to move in marshes, and submarines with silent bio-mimetic propulsion units.

Further fields of application, explored in Chapter 10, range from kinetic architecture, to soft robotics, to industrial design. More specifically, kinetic structures to support envelopes for shielding and water collection have been proposed

and small-scale prototypes have been manufactured. In addition, cable-actuated robotic limbs have been presented, 3D-printed and tested in the field. Despite the structure was actuated by hand in the presented examples, electric or hydraulic actuators, and the related control systems, can be readily developed according to the specific need. Finally, a desk lamp with a flex-ten tunable arm has been designed and prototyped. Here, the bent shape of the flex-ten arm can be tuned by varying the tension force in the cables, which also convoy electricity, while the segmental construction allows for industrialized production. The lamp can be sold as an assembly kit.

To complement the study on flexural tensegrity, a different type of kinematics was explored in Chapter 11. This corresponds to the sliding of initially-matching plates along wavy surfaces, rather than the case of pure rolling along pitch profiles. This define a laminar brickwork-like segmental assembly, which has been called *shear tensegrity*. More in detail, the laminar material of shear tensegrities is formed by an assembly of tiles with rough contact surfaces. The considered microstructural arrangement is inspired by nacre (mother-of-pearl), composed of tablets of aragonite arranged in lamellae, connected by organic polymeric interlayers to form laminates. The model considers the disarrangements consequent to the sliding of the wavy contact surfaces between adjacent lamellae within structured deformation theory. The interfacial resistance to sliding is taken into account through an average cohesive-frictional law, effective at the level of average separation plane. The localized contact of the surface asperities is supposed to negligibly deform the contact profiles, and the conditions for which this hypothesis is consistent have been discussed. Similarly to what happens for the complementary case of flexural tensegrities under bending, the geometry of the contact profiles at the interface represents the main characteristic, which dictates the constitutive properties of the material when sheared in the lamellar plane. Another key point is represented by the gradual surmounting of the asperities of the interface profiles, which produces a shear-induced dilatation, constrained by the bridging offered by the (organic) interlayer, as well as by a transverse (external) confining stress.

The proposed model considers "on average" the elastic deformation of tablets and interlayers, thus bypassing the noteworthy difficulties associated with the solution of the microscopic contact problem. The model spans multiple length-scales, associated with the size of the surface asperities, the thickness and diameter of the tablets and the thickness of the interlayers. By changing the model parameters, it is possible to cover a wide spectrum of responses, characterized by pinched hysteresis loops under cycling strain-driven tests, and serrated inelastic deformations for long tensile tests. The shape of the inelastic branches can be linear, convex, concave, strain-hardening or strain-softening, according to the shape of the contact profiles, the stiffness of the interlayers and the possible external confining stress.

The relevant parameters can be calibrated to reproduce the experiments on real nacre, but the model is of much more general importance, because it can be applied to a broad class of hierarchical lamellar metamaterials.

Although more general loading scenarios can be considered, rather than the case of bi-axial plane stress here analyzed, and a direct experimental validation of the model is still missing, the proposed theoretical framework could guide the design of innovative organized arrangements of sub-components, with tailored enhanced constitutive properties. The insights gained through the analytical model offer promise for conceptual designs of isolators/dissipators, laminated composites, resilient shields, and deployable structures.

12.2 Conclusions

The term *flexural tensegrity*, in short *flextegrity* or *flex-ten*, is an invention: partially borrowing the original portmanteau *tensegrity*, coined by Buckminster Füller, it represents the contraction of *tension*-induced *integrity* under *flexure*. By extending Füller's concept, it describes a structural principle in which the shape deformation is governed, and the constitutive behavior is determined, by the geometry of discontinuous compression members pressed in unilateral contact by the force of continuous tensile elements. In the original tensegrities by Füller and Snelson, compression members are local islands, represented by floating struts, held together by a cable net. In flexural tensegrities, the compression islands are joined by isthmuses represented by the contact points, whose position depends upon geometry and deformation level, being detachment avoided by the tensile embracement of a few seamless prestressing tendons. This provides the ability to bend increasingly, without breaking or coming asunder, since the contact point represents a leverage fulcrum for which the geometry of neighboring compression members dictate the lever arm of the internal forces, arising from the stretched tendons, to balance the external loads.

Energy can be harvested in properly shaped systems and made available in response to localized stimuli. Three dimensional geometries can be achieved thanks to the multidirectional shaping of the contact surfaces. Through an ideal limit process, the segmental-chain construction can be conceptualized as a continuum rod, reducing to classical models, like Euler's elastica, but with non-classical characteristics, in particular the nonlocal character of the constitutive bending properties. The concept can be declined in the alternative form of *shear tensegrity*, for which the deformation is not any more flexural, but indicated by the relative sliding (shearing apart) of compressed lamellae with shaped surfaces, interconnected by a network of tensile fibrils. Other forms are yet to be fully explored and appreciated.

In the broad field of engineering structures, applications are in metamaterials, biomedical tools, robotic limbs, tunable aerospace scaffoldings, locomotion in fluids via tail-like propulsion units, and transforming (kinetic) architecture. The main advantages consist in the tailored constitutive relationships, the tunable stiffness, the self-aligning and foldable/deployable properties, all achieved with a very simple modular construction. Many natural systems, if properly understood, can be regarded as tensegrity structures, i.e., pure tensegrities in the classical sense, flexural tensegrities, shear tensegrities, or other variants. Examples have been proposed for material lattices with a kinematic skeleton of non-pointwise meso-particles (fullerite), as well as for biological laminates (nacre).

The theoretical framework is still limited and some simplifying hypotheses should be removed in a more general comprehensive approach. For what concerns the constitutive laws, a more detailed experimental activity is necessary for a better understanding of dissipative phenomena, i.e., those of frictional nature (between adjacent segments, and between the tendon and the segments), the damping due to the hysteretic material deformation and the interaction with the surrounding medium (air, water). In addition, the deformation of the segments renders the contact not anymore pointwise, as assumed in the theoretical models, with a consequent modification of the energy landscape. What I have proposed is just the conceptualizing model, which can be reliably programmed to reproduce structurings at various length-scales of humanly discernible magnitudes, at various levels of superficial and volumetric hierarchies.

Despite all the conceptual and practical limitations of my dissertation, I believe that I have been able to demonstrate, albeit tentatively, that the flexural-tensegrity concept, although very simple, has a lot of potential in various fields of application. Let me then conclude by citing one of the aphorisms by Buckminster Füller: “I am concerned with finding new technical ways of doing more with less”.

Bibliography

[1] S. Sadao, "Fuller on tensegrity," *International Journal of Space Structures*, vol. 11, no. 1-2, pp. 37–42, 1996.

[2] S. H. Juan and J. M. M. Tur, "Tensegrity frameworks: static analysis review," *Mechanism and Machine Theory*, vol. 43, no. 7, pp. 859–881, 2008.

[3] K. Snelson, "The art of tensegrity," *International journal of space structures*, vol. 27, no. 2-3, pp. 71–80, 2012.

[4] R. Connelly and W. Whiteley, "Second-order rigidity and prestress stability for tensegrity frameworks," *SIAM Journal on Discrete Mathematics*, vol. 9, no. 3, pp. 453–491, 1996.

[5] C. R. Calladine, "Buckminster Fuller's "tensegrity" structures and Clerk Maxwell's rules for the construction of stiff frames," *International Journal of Solids and Structures*, vol. 14, no. 2, pp. 161–172, 1978.

[6] C. Sultan and R. Skelton, "Deployment of tensegrity structures," *International Journal of Solids and Structures*, vol. 40, no. 18, pp. 4637–4657, 2003.

[7] M. Masic, R. Skelton, and P. E. Gill, "Optimization of tensegrity structures," *International Journal of Solids and Structures*, vol. 43, no. 16, pp. 4687–4703, 2006.

[8] A. G. Tibert and S. Pellegrino, "Review of form-finding methods for tensegrity structures," *International Journal of Space Structures*, vol. 18, no. 4, pp. 209–223, 2003.

[9] J. T. Hewes, "Seismic tests on precast segmental concrete columns with unbonded tendons," *Bridge Structures*, vol. 3, no. 3-4, pp. 215–227, 2007.

[10] M. Milan and F. Simonelli, "Padre pio church, foggia, italy," *Structural engineering international*, vol. 11, no. 3, pp. 170–172, 2001.

[11] C. Menn, *Prestressed concrete bridges*. Basel, CH: Birkhäuser Verlag, 1990.

[12] D. Huang and B. Hu, *Concrete Segmental Bridges: Theory, Design, and Construction to AASHTO LRFD Specifications.* Boca Raton, FL, USA: CRC Press, 2020.

[13] A. Pipinato, *Innovative bridge design handbook: Construction, rehabilitation and maintenance.* Oxford, UK: Butterworth Heinemann, 2021.

[14] J. E. Kristensen, "Precast segmental bridge construction." SunCam online education course, 2015. `https://www.suncam.com/`.

[15] C. Armanini, F. Dal Corso, D. Misseroni, and D. Bigoni, "From the elastica compass to the elastica catapult: An essay on the mechanics of soft robot arm," *Proceedings of the Royal Society A: Mathematical, Physical and Engineering Sciences*, vol. 473, no. 2198, 2017.

[16] M. Mahvash and P. Dupont, "Stiffness control of surgical continuum manipulators," *IEEE Transactions on Robotics*, vol. 27, no. 2, pp. 334–345, 2011.

[17] G. Cicconofri and A. DeSimone, "A study of snake-like locomotion through the analysis of a flexible robot model," *Proceedings of the Royal Society A: Mathematical, Physical and Engineering Sciences*, vol. 471, no. 2184, 2015.

[18] H. Mallikarachchi and S. Pellegrino, "Design of ultrathin composite self-deployable booms," *Journal of Spacecraft and Rockets*, vol. 51, no. 6, pp. 1811–1821, 2014.

[19] V. Beatini and G. Royer-Carfagni, "Cable-stiffened foldable elastica for movable structures," *Engineering Structures*, vol. 56, pp. 126–136, 2013.

[20] C. Boni, M. Silvestri, and G. Royer-Carfagni, "Flexural tensegrity of segmental beams," *Proceedings of the Royal Society A: Mathematical, Physical and Engineering Sciences*, vol. 476, no. 2237, p. 20200062, 2020.

[21] X. Wang, M. Jiang, Z. Zhou, J. Gou, and D. Hui, "3d printing of polymer matrix composites: A review and prospective," *Composites Part B: Engineering*, vol. 110, pp. 442–458, 2017.

[22] N. P. Belfiore, A. Di Benedetto, and E. Pennestrì, *Fondamenti di meccanica applicata alle macchine.* Milano, IT: Casa Editrice Ambrosiana, 2005.

[23] F. Freudenstein, "Higher path-curvature analysis in plane kinematics," *Journal of Engineering for Industry*, vol. 87, no. 2, pp. 184–190, 1965.

[24] A. B. Clemens, *Applied mechanics and strength of materials.* Scranton, PA, USA: International Textbook Company, 1906.

[25] H. Rothbart and T. H. Brown, *Mechanical Design Handbook, Measurement, Analysis, and Control of Dynamic Systems*. New York, NY, USA: McGraw-Hill Education, 2006.

[26] C. Boni and G. Royer-Carfagni, "A nonlocal elastica inspired by flexural tensegrity," *International Journal of Engineering Science*, vol. 158, p. 103421, 2021.

[27] L. Euler, *Methodus Inveniendi Lineas Curvas Maximi Minimive Proprietate Gaudentes sive Solutio Problematis Isoperimetrici Latissimo Sensu Accepti*, vol. 1. Lausanne & Geneve: M.-M. Bosquet & Socios, 1744.

[28] L. Euler, *Methodus Inveniendi Lineas Curvas Maximi Minimive Proprietate Gaudentes, sive Solutio Problematis Isoperimetrici Lattissimo Sensu Accepti: Additamentum 1 De Curvis Elasticis*. Leonhardi Euleri Opera Omnia, Series prima (Opera mathematica), Vol. XXIV, Auctoritate et impensis Societatis Scientiarum Naturalium Helveticae, Orell Füssli, Zürich, 1952.

[29] W. A. Oldfather, C. A. Ellis, and D. M. Brown, "Leonhard Euler's elastic curves," *Isis*, vol. 20, no. 1, pp. 72–160, 1933.

[30] W. Thomson and P. G. Tait, *Treatise on natural philosophy*, vol. 1, part 2. London, UK: C.J. Clay, M.A. & Son (Cambridge University Press Warehouse), 2 ed., 1883.

[31] A. Love, *A Treatise on the Mathematical Theory of Elasticity*. Cambridge, UK: Cambridge University Press, 4 ed., 1944.

[32] J. Diamant, A. Keller, E. L. H. M. Baer, M. Litt, and R. G. C. Arridge, "Collagen; ultrastructure and its relation to mechanical properties as a function of ageing," *Proceedings of the Royal Society of London B: Biological Sciences*, vol. 180, no. 1060, pp. 293–315, 1972.

[33] M. Tournus, A. Kirshtein, L. V. Berlyand, and I. Aranson, "Flexibility of bacterial flagella in external shear results in complex swimming trajectories," *Journal of the Royal Society Interface*, vol. 12, no. 102, p. 20140904, 2015.

[34] J. F. Wilson and J. M. Snyder, "The elastica with end-load flip-over," *Journal of Applied Mechanics*, vol. 55, no. 4, pp. 845–848, 1988.

[35] A. Yamada, M. Watari, H. Mochiyama, and H. Fujimoto, "A jumping robot based on the closed elastica," in *2007 International Symposium on Micro-NanoMechatronics and Human Science*, pp. 604–609, IEEE, 2007.

[36] J. S. Chen and C. W. Li, "Planar elastica inside a curved tube with clearance," *International journal of solids and structures*, vol. 44, no. 18-19, pp. 6173–6186, 2007.

[37] A. Søndergaard, J. Feringa, T. Nørbjerg, K. Steenstrup, D. Brander, J. Graversen, S. Markvorsen, A. Bærentzen, K. Petkov, J. Hattel, L. Knudsen, and J. Kortbek, "Robotic hot-blade cutting," in *Robotic Fabrication in Architecture, Art and Design 2016*, pp. 150–164, Springer, 2016.

[38] B. G. Newman, "Shape of a towed boom of logs," *Proceedings of the Royal Society of London. A. Mathematical and Physical Sciences*, vol. 346, no. 1646, pp. 329–348, 1975.

[39] P.-T. Brun, N. Ribe, and B. Audoly, "An introduction to the mechanics of the lasso," *Proceedings of the Royal Society A: Mathematical, Physical and Engineering Sciences*, vol. 470, no. 2171, p. 20140512, 2014.

[40] F. Bosi, D. Misseroni, F. Dal Corso, and D. Bigoni, "Development of configurational forces during the injection of an elastic rod," *Extreme Mechanics Letters*, vol. 4, pp. 83–88, 2015.

[41] C. Armanini, F. Dal Corso, D. Misseroni, and D. Bigoni, "Configurational forces and nonlinear structural dynamics," *Journal of the Mechanics and Physics of Solids*, vol. 130, pp. 82–100, 2019.

[42] F. Bosi, D. Misseroni, F. Dal Corso, and D. Bigoni, "An elastica arm scale," *Proceedings of the Royal Society A: Mathematical, Physical and Engineering Sciences*, vol. 470, no. 2169, 2014.

[43] F. Bosi, D. Misseroni, F. Dal Corso, and D. Bigoni, "Self-encapsulation, or the 'dripping' of an elastic rod," *Proceedings of the Royal Society A: Mathematical, Physical and Engineering Sciences*, vol. 471, no. 2179, p. 20150195, 2015.

[44] R. L. Fosdick and R. D. James, "The elastica and the problem of the pure bending for a non-convex stored energy function," *Journal of Elasticity*, vol. 11, no. 2, pp. 165–186, 1981.

[45] G. Royer-Carfagni, "Can a moment-curvature relationship describe the flexion of softening beams?," *European Journal of Mechanics, A/Solids*, vol. 20, no. 2, pp. 253–276, 2001.

[46] G. Royer-Carfagni and G. Buratti, "Plastic hinges as phase transitions in strain softening beams," *Journal of Mechanics of Materials and Structures*, vol. 2, no. 9, pp. 1677–1699, 2007.

[47] M. Froli and G. Royer-Carfagni, "A mechanical model for the elastic-plastic behavior of metallic bars," *International Journal of Solids and Structures*, vol. 37, no. 29, pp. 3901–3918, 2000.

[48] A. C. Eringen, "On differential equations of nonlocal elasticity and solutions of screw dislocation and surface waves," *Journal of Applied Physics*, vol. 54, no. 9, pp. 4703–4710, 1983.

[49] H.-T. Thai, "A nonlocal beam theory for bending, buckling, and vibration of nanobeams," *International Journal of Engineering Science*, vol. 52, pp. 56–64, 2012.

[50] G. Romano, R. Barretta, M. Diaco, and F. Marotti de Sciarra, "Constitutive boundary conditions and paradoxes in nonlocal elastic nanobeams," *International Journal of Mechanical Sciences*, vol. 121, pp. 151–156, 2017.

[51] G. Romano and R. Barretta, "Nonlocal elasticity in nanobeams: the stress-driven integral model," *International Journal of Engineering Science*, vol. 115, pp. 14–27, 2017.

[52] E. Jahnke and F. Emde, *Tables of functions with formulae and curves*. New York, NY, USA: Dover Publications, 4 ed., 1945.

[53] K. E. Bisshopp and D. C. Drucker, "Large deflection of cantilever beams," *Quarterly of Applied Mathematics*, vol. 3, no. 3, pp. 272–275, 1945.

[54] D. Bigoni, *Nonlinear solid mechanics: bifurcation theory and material instability*. Cambridge, UK: Cambridge University Press, 1 ed., 2012.

[55] G. Mingari Scarpello and D. Ritelli, "Exact solutions of nonlinear equation of rod deflections involving the lauricella hypergeometric functions," *International Journal of Mathematics and Mathematical Sciences*, vol. 2011, 2011.

[56] G. Lauricella, "Sulle funzioni ipergeometriche a piu variabili," *Rendiconti del Circolo Matematico di Palermo*, vol. 7, no. 1, pp. 111–158, 1893.

[57] MathWorks, "fsolve." `https://it.mathworks.com/help/optim/ug/fsolve.html#butbmfz-5`, 2020. Accessed: 2020-05-08.

[58] J. J. Moré, "The levenberg-marquardt algorithm: implementation and theory," in *Numerical analysis*, pp. 105–116, Springer, 1978.

[59] A. R. Conn, N. I. M. Gould, and P. L. Toint, *Trust region methods*, vol. 1. Philadelphia, PA, USA: Siam, 2000.

[60] A. H. Nayfeh and D. T. Mook, *Nonlinear oscillations*. New York, NY, USA: John Wiley & Sons Inc., 1995.

[61] D. W. Jordan and P. Smith, *Nonlinear ordinary differential equations*. New York, NY, USA: Oxford University Press, 4 ed., 2007.

[62] G. Duffing, *Erzwungene Schwingungen bei veränderlicher Eigenfrequenz und ihre technische Bedeutung*. Braunschweig, D: Vieweg u. Sohn, 1918.

[63] D. O. Fearnow, "Investigation of the structural damping of a full-scale airplane wing," tech. rep., National Advisory Committee for Aeronautics (NACA), 1951.

[64] A. Eichler, J. Moser, J. Chaste, M. Zdrojek, I. Wilson-Rae, and A. Bachtold, "Nonlinear damping in mechanical resonators made from carbon nanotubes and graphene," *Nature nanotechnology*, vol. 6, no. 6, pp. 339–342, 2011.

[65] C. Surace, K. Worden, and G. R. Tomlinson, "On the non-linear characteristics of automotive shock absorbers," *Proceedings of the Institution of Mechanical Engineers, Part D: Journal of Automobile Engineering*, vol. 206, no. 1, pp. 3–16, 1992.

[66] F. Alijani, M. Amabili, P. Balasubramanian, S. Carra, G. Ferrari, and R. Garziera, "Damping for large-amplitude vibrations of plates and curved panels, part 1: Modeling and experiments," *International Journal of Non-Linear Mechanics*, vol. 85, pp. 23–40, 2016.

[67] M. Amabili, "Nonlinear damping in large-amplitude vibrations: modelling and experiments," *Nonlinear Dynamics*, vol. 93, no. 1, pp. 5–18, 2018.

[68] M. Amabili, "Nonlinear damping in nonlinear vibrations of rectangular plates: derivation from viscoelasticity and experimental validation," *Journal of the Mechanics and Physics of Solids*, vol. 118, pp. 275–292, 2018.

[69] G. Royer-Carfagni, "Parametric-resonance-induced cable vibrations in network cable-stayed bridges. a continuum approach," *Journal of Sound and Vibration*, vol. 262, no. 5, pp. 1191–1222, 2003.

[70] E. Mathieu, "Cours de mathématique physique," 1873.

[71] A. Preumont, *Vibration Control of Active Structures*. Berlin, D: Springer, 2011.

[72] C. Boni and G. Royer-Carfagni, "Nonlinear effects in the vibrations of flexural tensegrity beams," *International Journal of Non-Linear Mechanics*, vol. 128, p. 103616, 2020.

[73] R. W. Clough and J. Penzien, *Dynamics of structures*. Berkeley, CA, USA: Computers & Structures Inc., 3 ed., 2003.

[74] R. E. Mickens, *Truly nonlinear oscillations: harmonic balance, parameter expansions, iteration, and averaging methods*. Singapore, SGP: World Scientific, 2010.

[75] A. Yeshmukhametov, K. Koganezawa, and Y. Yamamoto, "A novel discrete wire-driven continuum robot arm with passive sliding disc: design, kinematics and passive tension control," *Robotics*, vol. 8, no. 3, p. 51, 2019.

[76] G. Puglisi and L. Truskinovsky, "Mechanics of a discrete chain with bi-stable elements," *Journal of the Mechanics and Physics of Solids*, vol. 48, no. 1, pp. 1–27, 2000.

[77] C. Boni and G. Royer-Carfagni, "Equilibrium of bi-stable flexural-tensegrity segmental beams," *Journal of the Mechanics and Physics of Solids*, vol. 152, p. 104411, 2021.

[78] Z. Guo, H. Li, Q. Wan, X. Peng, and J. Wen, "A model to describe the magnetomechanical behavior of martensite in magnetic shape memory alloy," *Advances in Condensed Matter Physics*, vol. 2014, 2014.

[79] M. Rief, M. Gautel, F. Oesterhelt, J. M. Fernandez, and H. E. Gaub, "Reversible unfolding of individual titin immunoglobulin domains by AFM," *Sarticlecience*, vol. 276, no. 5315, pp. 1109–1112, 1997.

[80] J. L. Ericksen, "Equilibrium of bars," *Journal of elasticity*, vol. 5, no. 3-4, pp. 191–201, 1975.

[81] J. E. Dunn and R. L. Fosdick, "The morphology and stability of material phases," *Archive for Rational Mechanics and Analysis*, vol. 74, no. 1, pp. 1–99, 1980.

[82] I. Müller and P. Villaggio, "A model for an elastic-plastic body," *Archive for Rational Mechanics and Analysis*, vol. 65, no. 1, pp. 25–46, 1977.

[83] M. Froli and G. Royer-Carfagni, "Discontinuous deformation of tensile steel bars: Experimental results," *Journal of Engineering Mechanics*, vol. 125, no. 11, pp. 1243–1250, 1999.

[84] G. Puglisi and L. Truskinovsky, "Rate independent hysteresis in a bi-stable chain," *Journal of the Mechanics and Physics of Solids*, vol. 50, no. 2, pp. 165–187, 2002.

[85] O. U. Salman and L. Truskinovsky, "On the critical nature of plastic flow: One and two dimensional models," *International Journal of Engineering Science*, vol. 59, pp. 219–254, 2012.

[86] I. Benichou and S. Givli, "Structures undergoing discrete phase transformation," *Journal of the Mechanics and Physics of Solids*, vol. 61, no. 1, pp. 94–113, 2013.

[87] M. Caruel, J.-M. Allain, and L. Truskinovsky, "Mechanics of collective unfolding," *Journal of the Mechanics and Physics of Solids*, vol. 76, pp. 237–259, 2015.

[88] G. Puglisi and L. Truskinovsky, "A mechanism of transformational plasticity," *Continuum Mechanics and Thermodynamics*, vol. 14, no. 5, pp. 437–457, 2002.

[89] G. Florio and G. Puglisi, "Unveiling the influence of device stiffness in single macromolecule unfolding," *Scientific reports*, vol. 9, no. 1, pp. 1–11, 2019.

[90] L. Bellino, G. Florio, and G. Puglisi, "The influence of device handles in single-molecule experiments," *Soft Matter*, vol. 15, no. 43, pp. 8680–8690, 2019.

[91] L. Bellino, G. Florio, S. Giordano, and G. Puglisi, "On the competition between interface energy and temperature in phase transition phenomena," *Applications in Engineering Science*, vol. 2, p. 100009, 2020.

[92] D. Swigon, B. D. Coleman, and W. K. Olson, "Modeling the lac repressor-operator assembly: The influence of DNA looping on lac repressor conformation," *Proceedings of the National Academy of Sciences of the United States of America*, vol. 103, no. 26, pp. 9879–9884, 2006.

[93] R. Fosdick and G. Royer-Carfagni, "Multiple natural states for an elastic isotropic material with polyconvex stored energy," *Journal of Elasticity*, vol. 60, no. 3, pp. 223–231, 2000.

[94] C. Jianguo, Z. Yuhang, F. Jian, and X. Yixiang, "A bistable rolling joint for multistable structures," *Mechanics Research Communications*, vol. 79, pp. 1–6, 2017.

[95] M. Charlotte and L. Truskinovsky, "Lattice dynamics from a continuum viewpoint," *Journal of the Mechanics and Physics of Solids*, vol. 60, no. 8, pp. 1508–1544, 2012.

[96] A. Zareei, B. Deng, and K. Bertoldi, "Harnessing transition waves to realize deployable structures," *Proceedings of the National Academy of Sciences*, vol. 117, no. 8, pp. 4015–4020, 2020.

[97] C. Boni and G. Royer-Carfagni, "Energy harnessing in the snap-through motion of a flexural-tensegrity flagellum," *Mechanism and Machine Theory*, vol. 173, p. 104845, 2022.

[98] S. Mhatre, E. Boatti, D. Melancon, A. Zareei, M. Dupont, M. Bechthold, and K. Bertoldi, "Deployable structures based on buckling of curved beams upon a rotational input," *Advanced Functional Materials*, p. 2101144, 2021.

[99] R. Du, Z. Li, K. Youcef-Toumi, and P. Valdivia y Alvarado, *Robot fish*. Springer Tracts in Mechanical Engineering, Heidelberg (DE): Springer, 2015.

[100] Z. Zhang, Q. Yang, S. Gui, B. Chang, J. Zhao, H. Yang, and D. Chen, "Mechanism design for locust-inspired robot with one-dof leg based on jumping stability," *Mechanism and Machine Theory*, vol. 133, pp. 584–605, 2019.

[101] J. Yu, Y. Hu, J. Huo, and L. Wang, "Dolphin-like propulsive mechanism based on an adjustable scotch yoke," *Mechanism and Machine Theory*, vol. 44, no. 3, pp. 603–614, 2009.

[102] I. Virgala, M. Kelemen, E. Prada, M. Sukop, T. Kot, Z. Bobovskỳ, M. Varga, and P. Ferenčík, "A snake robot for locomotion in a pipe using trapezium-like travelling wave," *Mechanism and Machine Theory*, vol. 158, p. 104221, 2021.

[103] Z. Meng, M. Liu, Y. Zhang, and C. Q. Chen, "Multi-step deformation mechanical metamaterials," *Journal of the Mechanics and Physics of Solids*, vol. 144, p. 104095, 2020.

[104] Wolfram, "Minimize." `https://reference.wolfram.com/language/ref/Minimize.html`, 2003. Accessed: 2021-08-08.

[105] C. Boni and G. Royer-Carfagni, "Flextegrity simple cubic lattices." Manuscript submitted for publication, 2022.

[106] V. I. Erofeev and I. S. Pavlov, *Structural modeling of metamaterials*. Cham, CH: Springer, 2021.

[107] W. Thomson, *Baltimore Lectures on Molecular Dynamics and the Wave Theory of Light*. London: Clay and Sons, 1904.

[108] R. A. Del Carpio Minaya and Y. P. Atencio, "Applications of spring-mass model on crystalline lattices," in *2017 XLIII Latin American Computer Conference (CLEI)*, pp. 1–8, IEEE, 2017.

[109] A. H. Aly and A. Mehaney, "Low band gap frequencies and multiplexing properties in 1d and 2d mass spring structures," *Chinese Physics B*, vol. 25, no. 11, p. 114301, 2016.

[110] M. Lombardo and H. Askes, "Elastic wave dispersion in microstructured membranes," *Proceedings of the Royal Society A: Mathematical, Physical and Engineering Sciences*, vol. 466, no. 2118, pp. 1789–1807, 2010.

[111] B. Afra, M. Nazari, M. H. Kayhani, A. A. Delouei, and G. Ahmadi, "An immersed boundary-lattice boltzmann method combined with a robust lattice spring model for solving flow–structure interaction problems," *Applied Mathematical Modelling*, vol. 55, pp. 502–521, 2018.

[112] A. Santhanam, *Modeling, simulation, and visualization of 3D lung dynamics*. PhD thesis, School of Electrical Engineering and Computer Science, University of Central Florida, Orlando, FL, USA, 2006.

[113] A. Askar and A. S. Cakmak, "A structural model of a micropolar continuum," *International Journal of Engineering Science*, vol. 6, no. 10, pp. 583–589, 1968.

[114] Z. P. Bažant and M. Christensen, "Analogy between micropolar continuum and grid frameworks under initial stress," *International Journal of Solids and Structures*, vol. 8, no. 3, pp. 327–346, 1972.

[115] F. Qin, J. Chen, U. Aydemir, A. Sanson, L. Wang, Z. Pan, J. Xu, C. Sun, Y. Ren, J. Deng, *et al.*, "Isotropic zero thermal expansion and local vibrational dynamics in (Sc, Fe) F_3," *Inorganic chemistry*, vol. 56, no. 18, pp. 10840–10843, 2017.

[116] A. A. Vasiliev, "Modeling of micropolar type chiral structures," *Letters on Materials*, vol. 3, no. 3, pp. 248–251, 2013.

[117] A. A. Vasiliev and I. S. Pavlov, "Models and parameters of cosserat hexagonal lattices with chiral microstructure," in *IOP Conference Series: Materials Science and Engineering*, vol. 1008, p. 012017, IOP Publishing, 2020.

[118] P. Mora and D. Place, "A lattice solid model for the nonlinear dynamics of earthquakes," *International Journal of Modern Physics C*, vol. 4, no. 06, pp. 1059–1074, 1993.

[119] Y. Wang and P. Mora, "Macroscopic elastic properties of regular lattices," *Journal of the Mechanics and Physics of Solids*, vol. 56, no. 12, pp. 3459–3474, 2008.

[120] H. W. Kroto, J. R. Heath, S. C. O'Brien, R. F. Curl, and R. E. Smalley, "C60: Buckminsterfullerene," *nature*, vol. 318, no. 6042, pp. 162–163, 1985.

[121] A. M. Bubenchikov, M. A. Bubenchikov, D. V. Mamontov, and A. V. Lun-Fu, "Md-simulation of fullerene rotations in molecular crystal fullerite," *Crystals*, vol. 9, no. 10, p. 496, 2019.

[122] J. Nelder and R. Mead, "A simplex method for function minimization," *The computer journal*, vol. 7, no. 4, pp. 308–313, 1965.

[123] Wolfram, "Nminimize." `https://reference.wolfram.com/language/ref/NMinimize.html`, 2003. Accessed: 2022-05-18.

[124] B. W. Kooi and J. A. Sparenberg, "On the static deformation of a bow," *Journal of engineering mathematics*, vol. 14, no. 1, pp. 27–45, 1980.

[125] B. W. Kooi, *On the mechanics of the bow and arrow*. PhD thesis, Mathematisch Instituut, Rijksuniversiteit Groningen, NL, 1983.

[126] M. Loades, *The longbow*. Oxford, UK: Osprey Publishing Ltd, 2013.

[127] J. D. Latham and W. F. Paterson, *Saracen archery: an English version and exposition of a Mameluke work on archery (ca. AD 1368)*. London, UK: The Holland Press Ltd, 1970.

[128] R. Payne-Gallwey, *The Book of the Crossbow: With an Additional Section on Catapults and Other Siege Engines*. New York, NY, USA: Dover Publications Inc., 2012.

[129] M. Özveri, "Turkish traditional archery," 2005.

[130] L. Sung, K. Kesha, S. Avedschmidt, K. Root, and L. Hlavaty, "The modern compound bow," *Journal of forensic sciences*, vol. 63, no. 1, pp. 130–139, 2018.

[131] M. Kilic, Y. Yazicioglu, and D. F. Kurtulus, "Synthesis of a torsional spring mechanism with mechanically adjustable stiffness using wrapping cams," *Mechanism and Machine Theory*, vol. 57, pp. 27–39, 2012.

[132] B. W. Kooi, "The design of the bow," *Proceedings Koninklijke Nederlandse Akademie van Wetenschappen*, vol. 97, no. 3, pp. 1–27, 1994.

[133] C. Boni and G. Royer-Carfagni, "A new flexural-tensegrity bow," *Mechanism and Machine Theory*, vol. 164, p. 104398, 2021.

[134] M. Lombard and L. Phillipson, "Indications of bow and stone-tipped arrow use 64 000 years ago in kwazulu-natal, south africa," *Antiquity*, vol. 84, no. 325, pp. 635–648, 2010.

[135] M. Lombard and M. N. Haidle, "Thinking a bow-and-arrow set: cognitive implications of middle stone age bow and stone-tipped arrow technology," *Cambridge Archaeological Journal*, vol. 22, no. 2, p. 237, 2012.

[136] G. Mariani and M. Matsuo, "The static deformation of the asymmetric japanese bow: modelling bow asymmetries with the elastica theory," *Meccanica*, vol. 55, no. 9, pp. 1733–1752, 2020.

[137] E. McEwen, R. L. Miller, and C. A. Bergman, "Early bow design and construction," *Scientific American*, vol. 264, no. 6, pp. 76–83, 1991.

[138] P. E. Klopsteg, "Physics of bows and arrows," *American Journal of Physics*, vol. 11, no. 4, pp. 175–192, 1943.

[139] B. W. Kooi and J. A. Sparenberg, "On the mechanics of the arrow: archer's paradox," *Journal of Engineering Mathematics*, vol. 31, no. 2, pp. 285–303, 1997.

[140] J. O'Bryan, *A history of weapons: Crossbows, caltrops, catapults & lots of other things that can seriously mess you up*. San Francisco, CA, USA: Chronicle Books, 2013.

[141] T. G. Chondros, "Archimedes life works and machines," *Mechanism and Machine Theory*, vol. 45, no. 11, pp. 1766–1775, 2010.

[142] C. Rossi and F. Russo, "A reconstruction of the greek–roman repeating catapult," *Mechanism and Machine Theory*, vol. 45, no. 1, pp. 36–45, 2010.

[143] Leonardo da Vinci, "Codex atlanticus." `https://www.codex-atlanticus.it/`, 1478–1518. Accessed: 2021-02-05.

[144] C. N. Hickman, "The dynamics of a bow and arrow," *Journal of Applied Physics*, vol. 8, no. 6, pp. 404–409, 1937.

[145] B. Kooi and C. Bergman, "An approach to the study of ancient archery using mathematical modelling," *Antiquity*, vol. 71, pp. 124–134, 1997.

[146] Z. Kan, H. Peng, and B. Chen, "A simple linear complementarity approach for sliding cable modeling considering friction," *Mechanical Systems and Signal Processing*, vol. 130, pp. 293–314, 2019.

[147] Z. Kan, F. Li, H. Peng, B. Chen, and X. Song, "Sliding cable modeling: A nonlinear complementarity function based framework," *Mechanical Systems and Signal Processing*, vol. 146, p. 107021, 2021.

[148] N. B. H. Ali, A. C. Sychterz, and I. F. C. Smith, "A dynamic-relaxation formulation for analysis of cable structures with sliding-induced friction," *International Journal of Solids and Structures*, vol. 126, pp. 240–251, 2017.

[149] B. Zhu, X. Zhang, H. Zhang, J. Liang, H. Zang, H. Li, and R. Wang, "Design of compliant mechanisms using continuum topology optimization: a review," *Mechanism and Machine Theory*, vol. 143, p. 103622, 2020.

[150] P. Bilancia, G. Berselli, S. Magleby, and L. Howell, "On the modeling of a contact-aided cross-axis flexural pivot," *Mechanism and Machine Theory*, vol. 143, p. 103618, 2020.

[151] I. Nesteruk, G. Passoni, and A. Redaelli, "Shape of aquatic animals and their swimming efficiency," *Journal of marine biology*, vol. 2014, 2014.

[152] J. Ohlberger, G. Staaks, and F. Hölker, "Swimming efficiency and the influence of morphology on swimming costs in fishes," *Journal of Comparative Physiology B*, vol. 176, no. 1, pp. 17–25, 2006.

[153] R. O'Dor, "Telemetered cephalopod energetics: swimming, soaring, and blimping," *Integrative and Comparative Biology*, vol. 42, no. 5, pp. 1065–1070, 2002.

[154] E. D. Tytell, I. Borazjani, F. Sotiropoulos, T. V. Baker, E. J. Anderson, and G. V. Lauder, "Disentangling the functional roles of morphology and motion in the swimming of fish," *Integrative and comparative biology*, vol. 50, no. 6, pp. 1140–1154, 2010.

[155] M. Sfakiotakis, D. M. Lane, and J. B. C. Davies, "Review of fish swimming modes for aquatic locomotion," *IEEE Journal of oceanic engineering*, vol. 24, no. 2, pp. 237–252, 1999.

[156] M. S. Triantafyllou and G. S. Triantafyllou, "An efficient swimming machine," *Scientific american*, vol. 272, no. 3, pp. 64–70, 1995.

[157] S. Coyle, C. Majidi, P. LeDuc, and K. J. Hsia, "Bio-inspired soft robotics: Material selection, actuation, and design," *Extreme Mechanics Letters*, vol. 22, pp. 51–59, 2018.

[158] R. K. Katzschmann, A. D. Marchese, and D. Rus, "Hydraulic autonomous soft robotic fish for 3d swimming," in *Experimental Robotics*, pp. 405–420, Springer, 2016.

[159] R. K. Katzschmann, J. DelPreto, R. MacCurdy, and D. Rus, "Exploration of underwater life with an acoustically controlled soft robotic fish," *Science Robotics*, vol. 3, no. 16, 2018.

[160] R. Taggart, "Novel marine propulsion devices," *Journal of the American Society for Naval Engineers*, vol. 70, no. 4, pp. 643–652, 1958.

[161] C. Boni, P. M. Reis, and G. Royer-Carfagni, "Flexural-tensegrity snapping tails for bio-inspired propulsion in fluids," *Extreme Mechanics Letters*, p. 101853, 2022.

[162] A. J. Smits, "Undulatory and oscillatory swimming," *Journal of Fluid Mechanics*, vol. 874, 2019.

[163] T. Van Buren, D. Floryan, D. Brunner, U. Senturk, and A. J. Smits, "Impact of trailing edge shape on the wake and propulsive performance of pitching panels," *Physical Review Fluids*, vol. 2, no. 1, p. 014702, 2017.

[164] P. Leroy-Calatayud, M. Pezzulla, A. Keiser, K. Mulleners, and P. M. Reis, "Tapered foils favor traveling-wave kinematics to enhance the performance of flapping propulsion," *Physical Review Fluids*, vol. 7, no. 7, p. 074403, 2022.

[165] P. D. Yeh, Y. Li, and A. Alexeev, "Efficient swimming using flexible fins with tapered thickness," *Physical Review Fluids*, vol. 2, no. 10, p. 102101, 2017.

[166] M. E. McIntyre, "Flows with a free surface." `https://www.damtp.cam.ac.uk/user/mem/FLUIDS-IB/`. IB lecture notes on fluid dynamics.

[167] Q. Zhong, J. Zhu, F. E. Fish, S. J. Kerr, A. M. Downs, H. Bart-Smith, and D. B. Quinn, "Tunable stiffness enables fast and efficient swimming in fish-like robots," *Science Robotics*, vol. 6, no. 57, p. eabe4088, 2021.

[168] W. McMahan, B. Jones, I. Walker, V. Chitrakaran, A. Seshadri, and D. Dawson, "Robotic manipulators inspired by cephalopod limbs." Proceedings of the Canadian Engineering Education Association (CEEA), 2004.

[169] P. Handral and R. Rangarajan, "An elastica robot: Tip-control in tendon-actuated elastic arms," *Extreme Mechanics Letters*, vol. 34, p. 100584, 2020.

[170] G. Gao, H. Wang, J. Liu, and Y. Zheng, "Statics analysis of an extensible continuum manipulator with large deflection," *Mechanism and Machine Theory*, vol. 141, pp. 245–266, 2019.

[171] M. Calisti, A. Arienti, F. Renda, G. Levy, B. Hochner, B. Mazzolai, P. Dario, and C. Laschi, "Design and development of a soft robot with crawling and grasping capabilities," in *2012 IEEE International Conference on Robotics and Automation*, pp. 4950–4955, IEEE, 2012.

[172] M. Jin, B. Zhu, J. Mo, Z. Yang, X. Zhang, and L. L. Howell, "A CPRBM-based method for large-deflection analysis of contact-aided compliant mechanisms considering beam-to-beam contacts," *Mechanism and Machine Theory*, vol. 145, p. 103700, 2020.

[173] C.-Y. Yeh, S.-C. Chou, H.-W. Huang, H.-C. Yu, and J.-Y. Juang, "Tube-crawling soft robots driven by multistable buckling mechanics," *Extreme Mechanics Letters*, vol. 26, pp. 61–68, 2019.

[174] C.-Y. Yeh, C.-Y. Chen, and J.-Y. Juang, "Soft hopping and crawling robot for in-pipe traveling," *Extreme Mechanics Letters*, vol. 39, p. 100854, 2020.

[175] C. Welch, *History of the Tower bridge and of other bridges over the Thames built by the Corporation of London: Including an account of the Bridge House trust from the twelfth century, based on the records of the Bridge House estates committee.* London, UK: Smith, Elder and Company, 1894.

[176] P. Dallard, T. Fitzpatrick, A. Low, R. Ridsill Smith, and A. Flint, "The millennium bridge, london: problems and solutions," *Structural Engineer*, vol. 79, no. 8, 2001.

[177] N. Fuchs, K. Tomlinson, and R. Buckby, "El ferdan bridge, egypt: the world's longest swing bridge," in *Proceedings of the Institution of Civil Engineers-Bridge Engineering*, vol. 156, pp. 21–30, Thomas Telford Ltd, 2003.

[178] S. Pellegrino, "Deployable structures in engineering," in *Deployable structures*, pp. 1–35, Springer, 2001.

[179] R. Motro, *Tensegrity: structural systems for the future.* London, UK: Kogan Page Science, 2003.

[180] M. Barozzi, J. Lienhard, A. Zanelli, and C. Monticelli, "The sustainability of adaptive envelopes: developments of kinetic architecture," *Procedia Engineering*, vol. 155, pp. 275–284, 2016.

[181] H. Buri and Y. Weinand, "Origami-folded plate structures, architecture," tech. rep., 2008.

[182] A. Sorguç and S. A. Selçuk, "Origamics in architecture: A medium of inquiry or design in architecture," 2009.

[183] Y. Wei and S. Pellegrino, "Modular foldable surfaces: A novel approach based on spatial mechanisms and thin shells," in *4th AIAA Spacecraft Structures Conference*, p. 1345, 2017.

[184] A. P. Thrall and C. P. Quaglia, "Accordion shelters: A historical review of origami-like deployable shelters developed by the us military," *Engineering structures*, vol. 59, pp. 686–692, 2014.

[185] P. Cassinello, M. Schlaich, and A. Torroja, "Félix Candela. In memorian (1910-1997). From thin concrete shells to the 21st century's lightweight structures," *Informes de la construccion revista de informacion tecnica*, vol. 62, no. 519, pp. 5–26, 2010.

[186] S. Wang, J. A. Contreras-Jimenez, J. J. Jorquera-Lucerga, and M. Garlock, "Structural analysis of Félix Candela's hexagonal hyperbolic paraboloidal umbrellas," *Engineering Structures*, vol. 266, p. 114577, 2022.

[187] E. Doran, "The original 1227 desk lamp," *Plot(s) - Journal of Design Studies*, vol. 4, pp. 87–94, 2017.

[188] M. J. French and M. B. Widden, "The spring-and-lever balancing mechanism, george carwardine and the anglepoise lamp," *Proceedings of the Institution of Mechanical Engineers, Part C: Journal of Mechanical Engineering Science*, vol. 214, no. 3, pp. 501–508, 2000.

[189] D. Li, Q.-S. Yang, X. Liu, and J.-J. Shang, "Experimental investigation on tensile properties of carbon nanotube wires," *Mechanics of Materials*, vol. 105, pp. 42–48, 2017.

[190] P. Jarosz, C. Schauerman, J. Alvarenga, B. Moses, T. Mastrangelo, R. Raffaelle, R. Ridgley, and B. Landi, "Carbon nanotube wires and cables: near-term applications and future perspectives," *Nanoscale*, vol. 3, no. 11, pp. 4542–4553, 2011.

[191] G. Del Piero and D. R. Owen, "Structured deformations of continua," tech. rep., Carnegie Mellon University, Department of Mathematical Sciences, 1993.

[192] A. G. Evans, Z. Suo, R. Z. Wang, I. A. Aksay, M. Y. He, and J. W. Hutchinson, "Model for the robust mechanical behavior of nacre," *Journal of Materials Research*, vol. 16, no. 9, pp. 2475–2484, 2001.

[193] R. Ballarini, C. Boni, and G. Royer-Carfagni, "Geometry of sliding lamellae dictates the constitutive properties of nacre-like hierarchical materials," *Journal of the Mechanics and Physics of Solids*, vol. 167, p. 105000, 2022.

[194] J. Sun and B. Bhushan, "Hierarchical structure and mechanical properties of nacre: a review," *Rsc Advances*, vol. 2, no. 20, pp. 7617–7632, 2012.

[195] R. Z. Wang, Z. Suo, A. G. Evans, N. Yao, and I. A. Aksay, "Deformation mechanisms in nacre," *Journal of Materials Research*, vol. 16, no. 9, pp. 2485–2493, 2001.

[196] F. Nudelman, B. A. Gotliv, L. Addadi, and S. Weiner, "Mollusk shell formation: mapping the distribution of organic matrix components underlying a single aragonitic tablet in nacre," *Journal of structural biology*, vol. 153, no. 2, pp. 176–187, 2006.

[197] J.-P. Cuif, Y. Dauphin, and J. E. Sorauf, *Biominerals and fossils through time*. New York: Cambridge University Press, 2010.

[198] F. Barthelat, H. Tang, P. D. Zavattieri, C.-M. Li, and H. D. Espinosa, "On the mechanics of mother-of-pearl: a key feature in the material hierarchical structure," *Journal of the Mechanics and Physics of Solids*, vol. 55, no. 2, pp. 306–337, 2007.

[199] M. A. Meyers, A. Y.-M. Lin, P.-Y. Chen, and J. Muyco, "Mechanical strength of abalone nacre: role of the soft organic layer," *Journal of the mechanical behavior of biomedical materials*, vol. 1, no. 1, pp. 76–85, 2008.

[200] A. P. Jackson, J. F. V. Vincent, and R. M. Turner, "The mechanical design of nacre," *Proceedings of the Royal society of London. Series B. Biological sciences*, vol. 234, no. 1277, pp. 415–440, 1988.

[201] A. Y.-M. Lin, *Structural and functional biological materials: abalone nacre, sharp materials, and abalone foot adhesion*. Dissertation, San Diego, 2008.

[202] J. D. Currey, "Mechanical properties of mother of pearl in tension," *Proceedings of the Royal society of London. Series B. Biological sciences*, vol. 196, no. 1125, pp. 443–463, 1977.

[203] L. T. Kuhn-Spearing, H. Kessler, E. Chateau, R. Ballarini, A. H. Heuer, and S. M. Spearing, "Fracture mechanisms of the strombus gigas conch shell: implications for the design of brittle laminates," *Journal of Materials Science*, vol. 31, no. 24, pp. 6583–6594, 1996.

[204] S. Kamat, X. Su, R. Ballarini, and A. H. Heuer, "Structural basis for the fracture toughness of the shell of the conch strombus gigas," *Nature*, vol. 405, no. 6790, pp. 1036–1040, 2000.

[205] S. Kamat, H. Kessler, R. Ballarini, M. Nassirou, and A. H. Heuer, "Fracture mechanisms of the strombus gigas conch shell: Ii-micromechanics analyses of multiple cracking and large-scale crack bridging," *Acta Materialia*, vol. 52, no. 8, pp. 2395–2406, 2004.

[206] Y. Shao, H.-P. Zhao, X.-Q. Feng, and H. Gao, "Discontinuous crack-bridging model for fracture toughness analysis of nacre," *Journal of the Mechanics and Physics of Solids*, vol. 60, no. 8, pp. 1400–1419, 2012.

[207] J. Liu, Z. Yu, and X. Wei, "A multiscale analytical framework for mode i crack in staggered composites," *Journal of the Mechanics and Physics of Solids*, vol. 145, p. 104157, 2020.

[208] C.-A. Wang, Y. Huang, Q. Zan, H. Guo, and S. Cai, "Biomimetic structure design - a possible approach to change the brittleness of ceramics in nature," *Materials Science and Engineering: C*, vol. 11, no. 1, pp. 9–12, 2000.

[209] H. Wei, N. Ma, F. Shi, Z. Wang, and X. Zhang, "Artificial nacre by alternating preparation of layer-by-layer polymer films and $CaCO_3$ strata," *Chemistry of materials*, vol. 19, no. 8, pp. 1974–1978, 2007.

[210] S. Bueno and C. Baudin, "Design and processing of a ceramic laminate with high toughness and strong interfaces," *Composites Part A: Applied Science and Manufacturing*, vol. 40, no. 2, pp. 137–143, 2009.

[211] F. Barthelat and D. Zhu, "A novel biomimetic material duplicating the structure and mechanics of natural nacre," *Journal of Materials Research*, vol. 26, no. 10, pp. 1203–1215, 2011.

[212] F. Barthelat, "Designing nacre-like materials for simultaneous stiffness, strength and toughness: Optimum materials, composition, microstructure and size," *Journal of the Mechanics and Physics of Solids*, vol. 73, pp. 22–37, 2014.

[213] R. Choksi, G. Del Piero, I. Fonseca, and D. Owen, "Structured deformations as energy minimizers in models of fracture and hysteresis," *Mathematics and Mechanics of Solids*, vol. 4, no. 3, pp. 321–356, 1999.

[214] B. Halphen and Q. S. Nguyen, "Sur les matériaux standard généralisés," *Journal de mécanique*, vol. 14, pp. 39–63, 1975.

[215] M. François and G. Royer-Carfagni, "Structured deformation of damaged continua with cohesive-frictional sliding rough fractures," *European Journal of Mechanics-A/Solids*, vol. 24, no. 4, pp. 644–660, 2005.

[216] J. M. Kelly, "Aseismic base isolation: review and bibliography," *Soil Dynamics and earthquake engineering*, vol. 5, no. 4, pp. 202–216, 1986.

[217] J. D. Byerlee, "The mechanics of stick-slip," *Tectonophysics*, vol. 9, no. 5, pp. 475–486, 1970.

[218] Y. Yan, Z.-L. Zhao, X.-Q. Feng, and H. Gao, "Nacre's brick–mortar structure suppresses the adverse effect of microstructural randomness," *Journal of the Mechanics and Physics of Solids*, vol. 159, p. 104769, 2022.

[219] H. Tang, F. Barthelat, and H. D. Espinosa, "An elasto-viscoplastic interface model for investigating the constitutive behavior of nacre," *Journal of the Mechanics and Physics of Solids*, vol. 55, no. 7, pp. 1410–1438, 2007.

[220] A. K. Maji and J. L. Wang, "Experimental study of fracture processes in rock," *Rock mechanics and rock engineering*, vol. 25, no. 1, pp. 25–47, 1992.

[221] G. I. Barenblatt, "The mathematical theory of equilibrium cracks in brittle fracture," in *Advances in applied mechanics*, vol. 7, pp. 55–129, Elsevier, 1962.

[222] J. Lemaitre, *A course on damage mechanics*. Berlin: Springer-Verlag, 1992.

[223] N. Zhang, S. Yang, L. Xiong, Y. Hong, and Y. Chen, "Nanoscale toughening mechanism of nacre tablet," *Journal of the mechanical behavior of biomedical materials*, vol. 53, pp. 200–209, 2016.

[224] L.-G. Liu, C.-C. Chen, C.-C. Lin, and Y.-J. Yang, "Elasticity of single-crystal aragonite by brillouin spectroscopy," *Physics and Chemistry of Minerals*, vol. 32, no. 2, pp. 97–102, 2005.

[225] P. Villaggio, "An elastic theory of coulomb friction," *Archive for Rational Mechanics and Analysis*, vol. 70, no. 2, pp. 135–143, 1979.

Acknowledgements

Firstly, I would like to express my sincere gratitude to my supervisor, Prof. Gianni Royer-Carfagni (University of Parma), for the continuous support during my adventure in the Ph.D. program, for his teachings, his patience, his advice and his guidance. The concept of flexural tensegrity would never have been developed up to this point without his supervision and brilliant ideas.

I would also like to thank Prof. Pedro Miguel Reis (fleXLab, EPFL, Lausanne), who made available his well-equipped laboratory and supervised the experimental work during my exchange period in Switzerland. Thanks to his expertise and direction, I managed to successfully carry out the experimental study on flex-ten snapping tails for propulsion in fluids during my stay at fleXLab.

A special thank goes to Dr. Laura Galuppi (University of Parma), for her advise and support during the past three years, especially for her insightful comments inside and outside the field of Structural Mechanics.

I would like to mention the collaboration with Prof. Roberto Ballarini (University of Houston), for the development of the theory of shear tensegrities, and with Prof. Juan José Castellón (Rice University, Houston), who suggested the idea of the flex-ten umbrella for architectural applications.

I would also like to acknowledge Dr. Fabio Corradini (formerly at University of Parma; now at SUPSI, Lugano), Dr. Giovanni Fortese (TP Engineering, Parma) and Dr. Samuel Poincloux (formerly at fleXLab, EPFL, Lausanne; now at University of Tokyo) for their help and advice while using laboratory equipments, such as 3D printers, laser cutters, and testing machines.

I also thank Andrea Rossi (University of Parma), who accurately milled the segments for the Dino-Lamp from solid acrylic according to my design drawings.

Finally, I must express my very profound gratitude to my parents, Pietro and Claudia, and grandparents, Ivo, Guglielma and Carmen, for providing me with unfailing support and continuous encouragement throughout my years at university.